AN ENGINEERING STUDY INTO THE BIOSONAR SYSTEM OF FRUITBATS IN THE GENUS *ROUSETTUS*

Simon Whiteley

Submitted in April 2013

for the degree of Doctor of Philosophy

Centre for Ultrasonic Engineering
Electronic and Electrical Engineering Department
University of Strathclyde
204 George Street, Glasgow,
G1 1XW, UK

This thesis is the result of the author's original research. It has been composed by the author and has not been previously submitted for examination which has led to the award of a degree.

Signed:

Date:

TABLE OF CONTENTS

Acknowledgements

Firstly, my sincere thanks must go to my supervisor, Professor Gordon Hayward. Over the course of the past 15 or more years that I have known him, he has been a constant source of inspiration and opportunity. There is certainly no doubt that had it not been for Gordon, this Thesis would not exist. It may be late, but it's finally arrived. And as Gordon recently told me, I will be his last Ph.D. student. An honour indeed. Cheers!

Dr. Gareth Pierce, who also supervised this work, was also of immense help over the years and his input is very much appreciated. I also now have a working knowledge of the Conditions of Carriage of Britain's railways!

Given my background in engineering, the undertaking of a piece of work so imbued with a biological background was as daunting as it was exciting. Smoothing the path for me was Dr. Dean Waters, formerly of the University of Leeds. His enthusiasm and chiropteran knowledge was invaluable, as was his ability to handle the fruitbats we used during the course of a very interesting few days spent in a flight corridor in Leeds. His input and support is very much appreciated.

Dr. Gerry Harvey, of Weidlinger Associates, also deserves a special mention. His expertise in PZ Flex, the finite element analysis package, was invaluable. He is also one of life's good guys. The original data that made the FEA of bat ears possible at all was provided by Dr. Rolf Müller, of the University of Shandong, China. The spirit in which this data was provided, with no favour requested nor received, was very much appreciated.

In no particular order, I would also like to express my thanks to various members, past and present, of the Centre for Ultrasonic Engineering at the University of Strathclyde. Dr. Tony Gachagan, Dr. Richard O'Leary, Walter Galbraith, Tommy McCunnie, Alex Ward, Lynn Morrison, Dr. Joe Jackson, Dr. John Mackersie, Dr. David Atkinson, Dr. Stephen Kelly and others too numerous to mention all contributed to the success of this Thesis and to making CUE an enjoyable and rewarding place to be.

To my parents, thank you for your continued support. You have always backed me in whatever path I have chosen through life, and that has always been appreciated. You are the best parents I could have wished for…and maybe this time you can make it to the graduation ceremony? And to my sister Ali – you're always there for me and are a light in anyone's life. Thank you for being you.

And finally, to my family. My beautiful wife Gill – Thank you for always believing that I could do this. I think you are the only person who never wavered, always encouraged and cajoled, and never questioned if this Thesis could be completed. For that I will always be grateful, and I will always love you. And Emily - my "little sausage". Though you may never read this, you make life the most amazing journey. I promise to always try to fascinate you with the world around us, and to try to see that world through your eyes. And to the most recent addition to the family, Martha – welcome to the world baby girl, it is a truly wonderful place to be.

Abstract

The history of research into biosonar has a long and fascinating history, beginning with the documented experiments of Lazarro Spallanzani in the late 18th century. It was some 150 years before the mechanism of echolocation was to be demonstrated. Since that discovery, the acuity with which bats can perceive their surroundings has itself become a wonder for scientists and engineers, and furthermore an *inspiration* for improving human sonar systems. This Thesis provides further understanding of the signals and processes involved, and indeed replicates these in the laboratory.

The calls of the echolocating fruit-bat *Rousettus aegyptiacus* are recorded using a novel design of wireless ultrasonic microphone sensor, which uses biomimetic variable gain to enable both the emitted signal *and* the return echoes to be recorded from the bat as it echolocates in flight. This demonstrates the complexity of the echoes returning to the bat, indicating the difficulty inherent in decoding these signals to image the bat's surroundings. It is further demonstrated using the finite element analysis (FEA) technique, that *Rousettus* echolocation signals, when combined with the response of its ear, do not produce obvious monaural spectral cues that could be used to indicate the location of the source. It is interesting to note that this is different to results reported in the literature for some species of microchiropteran bat, indicating that the nature of megachiropteran echolocation may be rather different.

There is also the potential to apply biological techniques and signals in engineering systems. This Thesis documents inexpensive, piston-mode electrostatic transducers that have been designed to generate wideband ultrasonic signals in air. A rigorous characterisation of the operation of these transducers is presented, with detailed surface motion and field measurement data. These transducers are used to replicate echolocation calls to investigate bats' ability to detect targets of cross-section considerably smaller than the wavelength of the signals they emit. It is demonstrated that, partially enabled by their aural gain-control mechanism, this feat is made possible by the dynamic range over which bats can operate. In its entirety, this Thesis presents a multi-disciplinary investigation into biosonar systems, and their replication in human engineered systems.

Glossary of Terms

A/D – Analogue to Digital Convertor

AFG – Arbitrary Function Generator

AGC – Automatic Gain Control

B&K - Brüel & Kjær

CF – Constant Frequency

CF2 – Prominent 2nd harmonic of CF call

CM – Cochlear Microphonic

CT – Computed Tomography

CW – Continuous Wave

DC – Direct Current

DSC – Doppler Shift Compensation

EMFi – Electro-Mechanical Film

EMG – Electromyography

cMUT – capacitive Micromachined Ultrasonic Transducer

FEA – Finite Element Analysis

FFT – Fast Fourier Transform

FM – Frequency Modulated / Frequency Modulation

HRTF – Head Related Transfer Function

IF – Intermediate Frequency

IID – Inter-aural Intensity Difference

IL – Insertion Loss

ITD – Inter-aural Time Difference

LDV – Laser Doppler Vibrometer

MD – Maximum Dimension

NDE – Non-Destructive Evaluation

NiMH – Nickel Metal Hydride

NPL – National Physical Laboratory

PCB – Printed Circuit Board

PLL – Phase-Locked Loop

PVDF - polyvinylidene fluoride

RC – Resistor / Capacitor

RF – Radio Frequency

RMS – Root Mean Square

SD – Standard Deviation

SEM – Scanning Electron Microscope

SNR – Signal to Noise Ratio

SPL – Sound Pressure Level

TS – Target Strength

VC – Vitreous Carbon

VCO – Voltage Controlled Oscillator

VGA – Variable Gain Amplifier

CHAPTER 1

INTRODUCTION

1.1 Background

The biosonar systems of bats have been studied in earnest since the first documented evidence that they use the echoes from high-frequency calls to navigate and feed. In the decades since that pioneering work of the 1940s, this ability and the techniques that underpin it have been studied using a number of methods. The echolocation calls of many bat species have been recorded, both in the wild and in captive environments. This has demonstrated the variety of signals that are used, often specifically suited to a given task. Furthermore, by presenting a captive bat with an echolocation task in a controlled environment, the limits of the biosonar system can be ascertained. In recent times, technological advances have enabled researchers to study echolocation signals in different ways. For example miniature wireless microphones have been mounted on bats in captivity, recording their echolocation calls whilst in flight. Furthermore, computer simulation techniques have been used to investigate how the origin of a sound can be encoded into the echo, through interaction with the bat's head and ears.

The insights provided through these methods have, of course, provided a greater understanding of the techniques employed by bats. However, understanding of the methods used can also provide inspiration for the improvement of human sonar systems, or air-coupled ultrasonic devices and techniques. Bats catch small insect prey in some particularly difficult acoustic environments, such as amongst the moving branches and leaves of trees. Other bats have adapted their sonar signals to detect fish as they break the surface of the water looking to feed, which they then catch as prey. In captivity, they have demonstrated the ability to detect and avoid wire obstacles with a cross section significantly smaller than the ultrasonic wavelengths they emit, while their capability to detect the angular position and range of targets with great accuracy has also been demonstrated. These feats are tasks that the human engineer would use a sonar array to perform; the bat uses just its mouth and two ears. To replicate this performance using only a single transmitter and two receivers would be impressive indeed. The further exploration of this ability is the inspiration behind the work presented in this Thesis.

1.2 Aims and Objectives of the Thesis

This Thesis takes an engineering approach to investigate the biosonar techniques of bats in general, and fruitbats in the genus *Rousettus* in particular. In undertaking this study, a range of scientific and engineering disciplines have been employed, including biology, electronics, acoustics and Finite Element Analysis. These have all been necessary to achieve the main aims of the work,

The work focuses on the sonar system of fruitbats in the order *Rousettus*. Specifically, this concerns the closely related species *Rousettus aegyptiacus* and *Rousettus leschenaultii*. The aim of this work was to further explain the mechanisms of biosonar echolocation, and to generate technology and devices that could take advantage of such mechanisms for bio-inspired air-coupled sonar systems. This will be achieved through the following goals:

- To investigate the echolocation calls used by *Rousettus*, both the signal emitted by the bat and the echo that returns
- To design and build wideband air-coupled ultrasonic transducers capable of recreating bat echolocation calls in the laboratory; and to fully characterise the operation of these devices
- To reproduce bat echolocation experiments in the laboratory using the wideband transducers
- To simulate the interaction of the calls and ears of *Rousettus*, to investigate the possibility that the location of the origin of the sound is encoded into the echo via interaction with the external ear structure.

1.3 Overview of the Thesis

Given the multidisciplinary nature of the work undertaken, a comprehensive review of the fields involved was performed, and presented in Chapter 2. This includes the history of biosonar research, from its origins in the late 19th century, to the present day, with a detailed account of significant discoveries relating to bats' echolocation expertise, particularly in terms of the resolution with which they can perceive their environment. Subsequent sections review the methods used to record biosonar

signals, techniques that have been employed to ascertain the sounds bats actually hear (these being the signals bats decode to obtain an image of their surroundings after interaction with their head and ears, rather than the raw echo that returns), and air-coupled ultrasonic techniques and devices capable of reproducing wideband echolocation calls.

Chapter 3 presents the design of a miniature wireless ultrasonic sensor. The sensor was mounted on the back of the fruitbat *R. aegyptiacus*, and used to detect its echolocation calls whilst the bat flew in a captive environment. Through use of a voltage controlled oscillator, the detected calls were transmitted wirelessly, and demodulated using an FM tuner to be recorded digitally for later processing. In addition to recording the emitted echolocation calls, the sensor was also capable of detecting the relatively faint echoes returning from acoustic targets. This was achieved through replication in electronics of a gain control mechanism demonstrated in some bats, whereby the gain is gradually increased after the point of call emission. In bats, and indeed the sensor, the function of this gain control is two-fold. Firstly, it prevents the sensitive receivers from being damaged or saturated by the intense emitted call; and secondly it provides gain compensation, whereby echoes arriving later in time, and hence having been subject to greater propagation attenuation, are amplified by a larger gain. The return echoes recorded in this fashion demonstrated their complex nature, even when echolocating in the relatively simple environment of a corridor.

Chapter 4 demonstrates the manufacture and test of a range of affordable air-coupled electrostatic transducers, designed to enable the replication of wideband bat echolocation calls. Through measurement of the acoustic fields generated, using a calibrated microphone, and characterisation of the motion of the active membrane using a laser doppler vibrometer (LDV), it was demonstrated that these devices were capable of near piston-mode operation over 20kHz-250kHz, encompassing the frequency range of bat echolocation. The combined measurement of the emitted field and membrane motion ensured that the operation of these devices was fully characterised and understood, a significant omission in the literature. Furthermore,

through optical and mechanical metrology of the surface of the transducer backplates, the link between surface features and device operation was demonstrated.

In addition, a field simulation tool was developed. A previously-developed technique based on Huygen's theorem was used to simulate the theoretical field generated by a piston-mode source. However, the method was extended to allow the propagation of an arbitrary signal to be simulated, by first calculating the complex FFT of the signal and simulating the propagation of each spectral component. This method allowed the intricacies of the field generated from a transducer by a non-continuous (e.g. toneburst) signal to be simulated. Furthermore, the propagation of bat echolocation calls is also possible. Since this method of field simulation is so flexible, based on superposition of individual signal components travelling from a series of discretised points on the transducer surface, it could also be used in conjunction with the measured LDV data to simulate the field emitted by the transducer. This provides a very flexible and efficient method of characterising the behaviour of a transducer.

Chapter 5 demonstrates the use of these electrostatic transducers, in combination with a pre-equalisation technique, to accurately replicate airborne biological and biologically-inspired wideband acoustic signals. These signals were then used to replicate the wire-avoidance experiments that bats have undertaken in captivity, indicating that detection of objects with a small cross-section is dependent on dynamic range. If a large enough signal can be transmitted into the environment, then detection of small targets is made possible via the capability to detect signals that may be up to 100dB attenuated from the emitted signal. It would appear that bats, aided by their acoustic gain control mechanism, possess precisely this capability.

Finally, in Chapter 6, the function of the external ear of the bat is investigated using a novel combination of rapid prototyping and finite element analysis (FEA) techniques. The ear of a *R. leschenaultii* individual, which was scanned using x-ray computed tomography techniques, was rendered in a soft polymer material using a micro-stereolithography machine. The response of this ear was then measured in transmission using a calibrated microphone. Next, a 3D representation of the ear was imported into PZ Flex, a FEA package, allowing the experimental procedures to be

repeated in the virtual environment, thereby verifying the simulation technique. FEA was then used to simulate the response of the bat ear to a variety of biological echolocation signals (including the *R. aegyptiacus* calls recorded using the wireless sensor, as documented in Chapter 2) and biologically-inspired FM chirps. This showed how the direction from which an echo originates could be encoded into the spectral peaks and notches generated in an FM chirp through its interaction with the external ear structure. In contrast, no obvious monaural cues were shown to be generated from the calls of *R. aegyptiacus*, perhaps indicating that these echolocating fruitbats do not use monaural cues as an aid to elevation sound localisation.

1.4 Original Contributions of the Thesis

- A miniature wireless sensor capable of being mounted on a flying bat for detecting the echolocation calls emitted by the bat. This sensor mimics the variable gain seen in some bats to detect the echoes reflected back to the bat.
- Two designs of relatively inexpensive air-coupled electrostatic transducers. These devices are capable of operating in a piston-mode fashion over a bandwidth that encompasses the range of bat echolocation.
- Reproduction of bat echolocation calls in the laboratory, using linear transducers and a spectral-compensation technique.
- The link between the magnitude and phase response of the membrane of electrostatic transducers and the field generated was quantified, using laser vibrometry and field measurement techniques.
- The relationship between the surface features of the electrostatic transducer backplate and its motion has been demonstrated using laser vibrometry and surface metrology techniques.
- Investigation of bats' capability for detecting objects with a cross-section considerably smaller than the wavelength of the incident echolocation call, using echolocation calls replicated in the laboratory.
- A finite element analysis technique for simulating the response of a bat ear to an incoming sound signal. This demonstrated that the calls and ears of bats of the genus *Rousettus* do not combine to generate obvious or systematic sound-

localising monaural cues, in contrast to results demonstrated for various microchiropteran species.

1.5 Publications Arising From the Thesis

Whiteley, S.M., Papadopoulos, T., Waters, D. and Farr, I. "Encoded information contained in target echoes produced by real and modelled bat echolocation", Proceedings of Biological Approaches for Engineering, Southampton, UK, 17-19 March, Posters, 2008, 167-171

Whiteley, S.M., Waters, D.A., Farr, I., Pierce, S.G. and Hayward, G. "Wireless monitoring of in-flight bat calls and echoes from the echolocating fruit bat Rousettus aegyptiacus" , Proceedings of the Institute of Acoustics 31(1) Fifth International Conference on Bio-Acoustics, 2009, 159-164

Whiteley, S.M., Pierce, S.G. and Hayward, G. "Reproducing the calls of bats using inverse filtering and broadband transducers" presented at US Navy Workshop on Acoustic Transduction Materials and Devices, Pennsylvania, USA, 2009

Whiteley, S.M., Waters, D.A., Hayward, G., Pierce, S.G., and Farr, I., "Wireless recording of the calls of Rousettus aegyptiacus and their reproduction using electrostatic transducers." Bioinspiration and Biomimetics, 5, 2010, 1-10 026001

Jackson, J.C., Summan, R., Dobie, G., Whiteley, S., Pierce, S.G. and Hayward, G. "Time of flight measurement techniques for airborne ultrasonic ranging", IEEE Transactions on Ultrasonics, Ferroelectrics and Frequency Control (In Press)

1.5.1 Further Planned Publications

Whiteley, S.M., Harvey, G. and Hayward, G. "The response of the ear of *Rousettus leschenaultii*, simulated using the Finite Element method", Journal of the Acoustical Society of America.

Whiteley, S.M. and Hayward, G. “Field measurement of electrostatic transducers and the effect of their magnitude and phase response”, IEEE Transactions on Ultrasonics, Ferroelectrics and Frequency Control.

CHAPTER 2

HISTORICAL REVIEW OF BIOSONAR RESEARCH

2.1 Introduction

Given the multi-disciplinary nature of this work, the areas encompassed by it are varied and broad-ranging. For example, Chapter 3 deals with the design of a wireless microphone sensor for recording the echolocation calls of a flying bat. This encompasses the fields of: electronics; circuit design; microphone design and characterisation; RF wireless transmission and reception; and bioacoustics. Chapter 4 deals with the design of a wideband electrostatic transducer, specifically aimed at accurately replicating bat echolocation calls in the laboratory. As such, this Chapter covers: air-coupled ultrasonic transduction; transducer characterisation through impulse response, field measurement and simulation, and laser vibrometry techniques; ultrasonic propagation in air; and echolocation call characteristics. Chapter 5 investigates the application of these transducers in echolocation replication experiments in the laboratory, which deals with signal processing and channel equalisation. Chapter 6 documents the experimental and theoretical investigation of the response of a bat ear to acoustic signals. As such, this deals with: rapid prototyping techniques; sound field characterisation; and Finite Element Analysis (FEA) for ultrasonic wave propagation. To deal with the state of the art of each of these topics would require far more space than is available here and so the approach taken has been to review only the literature that directly affects the aims, objectives and applications presented. As such, state of the art digital radio system-on-a-chip is not reviewed as that type of system requires too much power, and hence mass, to be used in the bat-mounted sensor; any work related to bat-mounted radio transmitters is, however, discussed in detail. Similarly, the field of air-coupled ultrasound is not reviewed in its entirety, but is discussed in detail as it relates to the reproduction of wideband signals. It is therefore the aim of this Chapter to document the history and current thinking published in the literature, but only where that impacts directly on the work presented. This approach has been taken as a prudent way by which all the relevant information can be demonstrated within the scope of this work. There is one general exception to this. Since this Thesis is aimed primarily at an engineering audience, bat echolocation is covered in more detail than might be necessary for a biological text, including a background and history against which to base this work. This aside, the review has a distinct leaning towards bioacoustics, since the central

aim of this Thesis is based around investigation of the echolocation signals and systems of the fruitbat *Rousettus aegyptiacus*.

2.2 Biosonar

With a few exceptions, there are two groups of mammals that use active biological echolocation. Mammals classified in the suborder Odontoceti (toothed whales) and the order Chiroptera (bats) have developed sophisticated sonar systems, which can be used for navigation and finding prey in cluttered and visually difficult environments. The toothed whales (including dolphins, porpoises, orcas, sperm and beaked whales) use sonar extensively (Lockley, 1979). Since visibility can be limited by water turbidity or lack of light due to depth, and their olfactory systems are poor, whales use sonar for navigation and catching prey; they also use sound for communication. However, it is the bats with which this work is concerned.

With its almost unique exploitation of the aerial nocturnal niche, and the potential insect prey that it brings, the order Chiroptera has evolved to be highly successful, colonising every continent except Antarctica. Indeed, it is the second largest mammalian order (after Rodentia, the rodents) comprising some 1100 species. Within the order Chiroptera are two suborders: Megachiroptera (megabats); and Microchiroptera (microbats). Of the megabats, only *Rousettus* (a genus of fruit bat) is known to use sonar (Sales and Pye, 1974; Waters and Volrath 2003, Holland *et al*. 2004), which it generates by clicking the tongue within the mouth. The microbats, on the other hand, produce sound via the larynx and have developed a large variety of echolocation calls, which have adapted to a wide range of habitats and tasks (Schnitzler and Kalko, 2001; Ulanovsky and Moss, 2008).

2.2.1 The Biological Mechanics of Bat Echolocation

Excepting the echolocation oddity that is *Rousettus*, bats produce sound in much the same fashion as humans (or indeed most mammals) via the larynx. The larynx connects the lungs, via the trachea (windpipe) to the pharynx. The pharynx is the tube-like structure in the neck that is common to both the respiratory and digestive system; the epiglottis acts like a flap that closes over the opening to the larynx to

direct food into the oesophagus when swallowing. Figure 2.1 illustrates this arrangement in humans for reference.

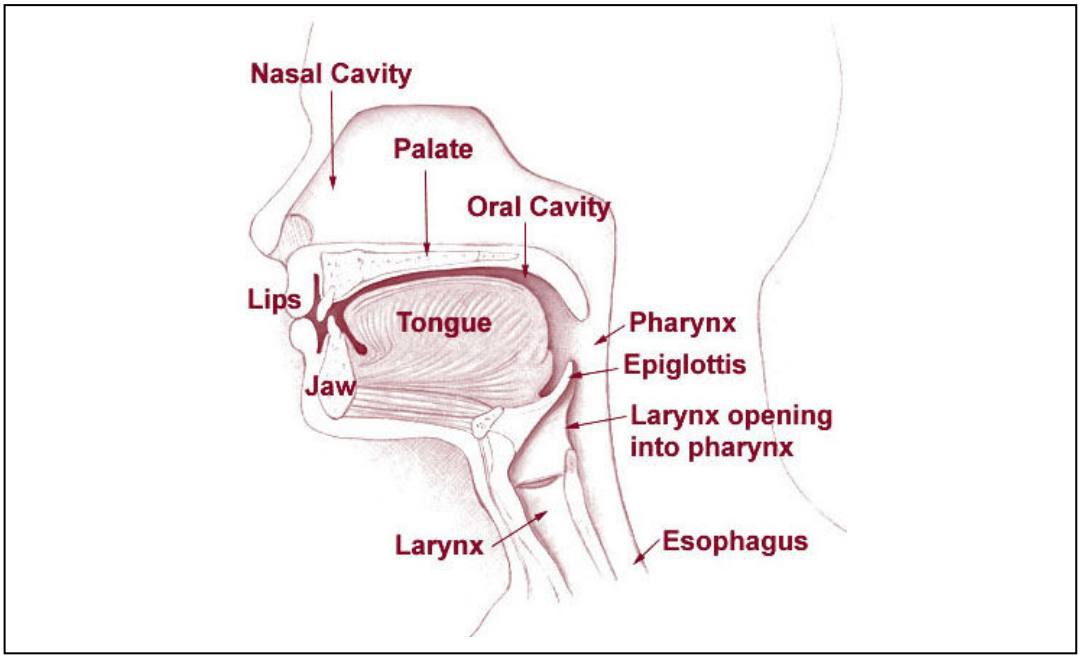

Figure 2.1. Cross-section of the human upper respiratory tract (http://upload.wikimedia.org/wikipedia/commons/d/d4/Illu01_head_neck.jpg)

Phonation (literally, production of sound) is achieved by expelling air from the lungs through the larynx; the vocal cords (or vocal folds) regulate this flow of air, and are caused to vibrate in the air column generating sound which is further modified by changes in the oral cavity to produce speech. The vocal cords, then, serve two purposes in humans: firstly regulation of airflow (they can fully close to stop airflow altogether, forming the glottal stop); and secondly production of sound. Figure 2.2 shows a view of the vocal folds as would be seen from above with a laryngoscope, illustrating their location and function as described above.

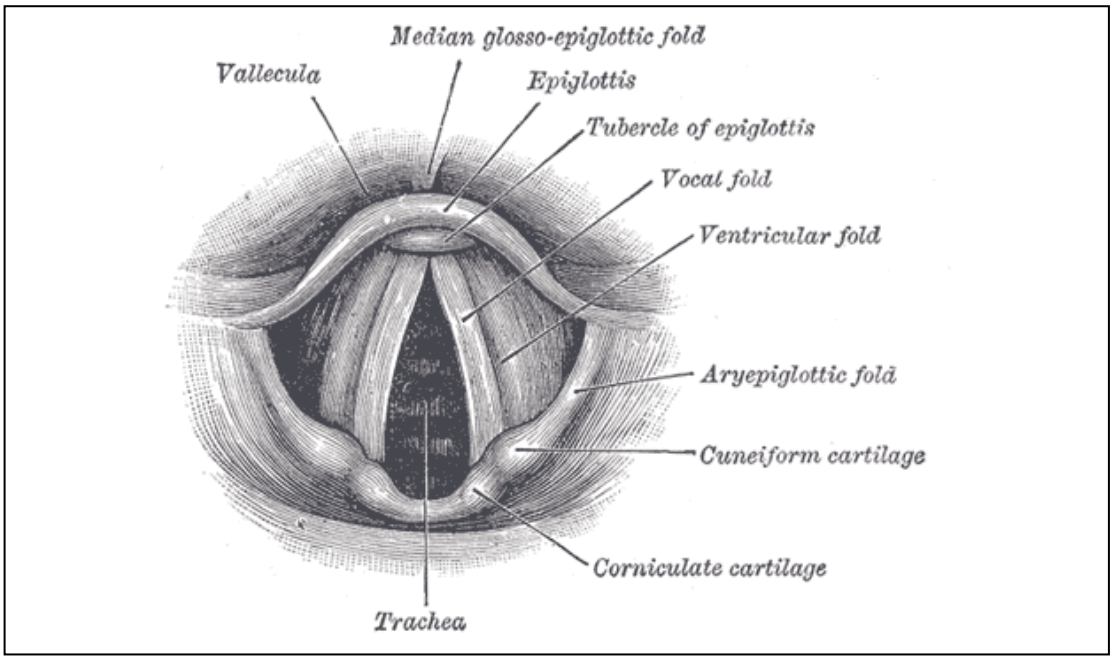

Figure 2.2. View of vocal folds across the entrance to the trachea (http://upload.wikimedia.org/wikipedia/commons/5/50/Gray956.png)

In bats, the functionality of the larynx is slightly different. The vocal folds (and membranes) are still responsible for the production of sound through vibration in the expired air stream (Griffin 1958), however they do not regulate the flow of air. The cricothyroid muscles (see Figure 2.3, label D) are responsible for both these functions in that they vary the tension on the vocal membranes, hence varying pitch, and also control the laryngeal opening, regulating airflow (Suthers, 2004). This use of a single group of muscles to control both timing and pitch of phonation is a rather elegant technique for generating efficient, rapid and frequency modulated calls. As the CT muscles contract prior to call emission, the vocal membranes are put in tension and the glottis is closed, then as the CT muscles relax, the glottis is opened and the expiring airflow causes the relaxing membranes to vibrate producing a downward sweeping tone. Figure 2.3 shows a cross-section of the larynx of a big brown bat for reference; in this image expired air flows upward from the trachea across the vocal membranes and into the pharynx. The comparison of human and bat phonation is a valid one. Mergell *et al*. (1999) state that the "mammalian larynx exhibits little structural variation compared to sound-producing organs in other taxa, such as birds or insects." However, there are some variations, notably the vocal membranes (see Figure 2.3, label A), which act to improve phonation efficiency by lowering the pressure at which phonation can be sustained (Mergell *et al*., 1999).

Furthermore, this effect is “most pronounced at high frequencies”. It is unsurprising that bats, being small mammals capable of producing sounds estimated at in excess of 140dB (Surlykke and Kalko, 2008) have evolved mechanisms to improve vocalisation efficiency. This will be discussed later in the Chapter in relation to coupling of wingbeat muscle energy into echolocation call production (Speakman and Racey, 1991).

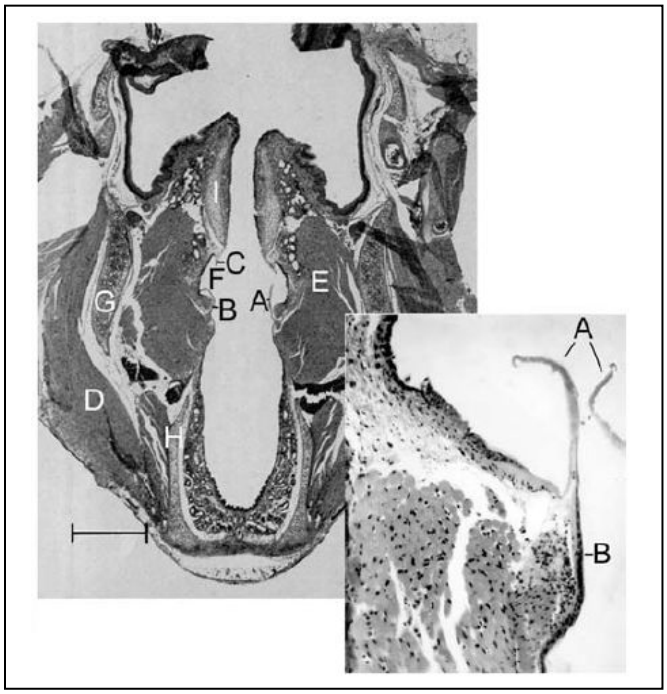

Figure 2.3. Cross section of big brown bat (Eptesicus fuscus) larynx showing: A, vocal membrane; B, vocal fold; C, ventricular membrane; D, cricothyroid muscle; E, thyroid artenoid muscle; F, ventricle of Morgagni; G, thyroid cartilage. Inset: close-up of vocal membrane (A) and vocal fold (B) (Suthers and Fattu, 1973; Suthers, 2004).

The mechanics of bat hearing can also be compared to that of humans. Mammalian ears consist of three main sections: the outer, middle and inner ear. The main components of mammalian hearing are illustrated in Figure 2.4. The outer ear consists of the pinna and ear canal up to the surface of the eardrum (or tympanic membrane). It is the function of the outer ear to focus sound from the external environment onto the eardrum, which transmits energy into the middle ear via direct contact with the malleus bone. The middle ear is an air filled cavity beyond the eardrum, that includes the three small ear bones, or ossicles: the malleus; incus; and stapes. These bones act to transfer energy from the deflecting eardrum to the inner

ear via direct contact of the stapes with the oval window, transmitting pressure waves to the inner ear. The inner ear consists of the cochlea, which relates to hearing, and the vestibular system (the inner ear labyrinth) which contributes to sense of balance. The cochlea translates incoming mechanical energy into electrical impulses, which are carried to the brain by one of the cranial nerves. The cochlea is coiled, with the oval window at one end and the round window at the other; the round window, as with the oval window, is a membrane-covered opening that allows for movement of the (non-compressible) fluid within the cochlea. It is this movement against the cochlea inner hair cells that generates the electrical impulses via which the brain interprets sound.

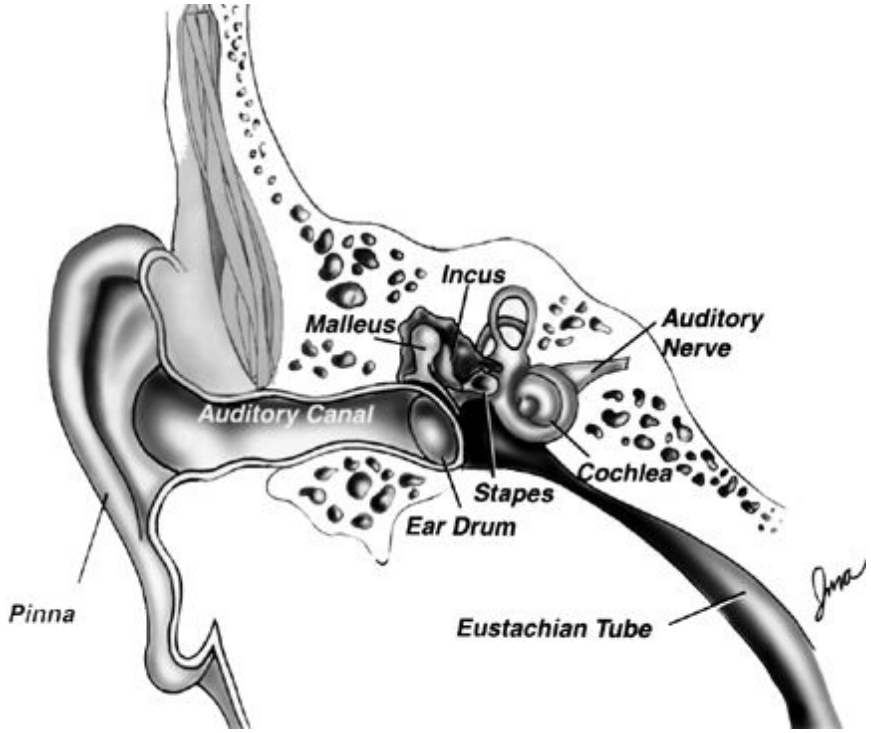

Figure 2.4. Diagram of the human ear, featuring the main functional components of mammalian hearing. (http://www.nidcd.nih.gov/health/hearing/innear.html)

The interaction between incoming sounds (i.e. reflected echolocation calls) and the external ear structures is important for bats' ability to discern the angular direction of a sound source. It has been shown that the sound arriving at the eardrum has spectral cues encoded in it as to the azimuth and elevation angle of the sound source (e.g. Lawrence & Simmons 1982; Wotton *et al.*, 1995) as will be covered in detail in

Section 2.4.1. The operation of the pinna of the fruitbat *Rousettus aegyptiacus* is examined in detail in Chapter 6, through a combined experimental and simulation approach.

2.2.2 The History of Bat Echolocation Research

It is thought that laryngeal echolocation might have evolved in bats between 85 and 65 million years ago, and that ancestors of the echolocating megabats firstly lost the ability, before it re-evolved into the clicking mechanism it is today (Jones & Teeling 2006). The echolocation ability of microbats and their ancestors has never been lost, but has continued to evolve, as it does to this day.

The earliest records of experiments being performed on bats in order to understand their ability to navigate in the dark are attributed to Abbé Lazaro Spallanzani, an 18th century Italian monk who devoted much of his life to scientific experimentation. His experimentation on bats commenced in 1793, and was to occupy him until the time of his death in 1799. During those six years, Spallanzani and his peers, shed more light on what became known as "Spallanzani's bat problem" than would be achieved in the succeeding century and a half.

The discovery of bat echolocation is a fascinating story. The interested reader is directed to Griffin (1958) for an excellent and detailed account, from which the following brief summary has been produced. The catalyst for Spallanzani's consideration of bat navigation was when he noticed that a captive owl, but not a captive bat, would become disoriented if the candle in its room was extinguished and would proceed by crashing into walls and other objects. To confirm that this was not simply due to bats being able to see when the light was too dim for man or owl, he blinded the bats (firstly by tying hoods over their heads, and thereafter by burning the cornea out with a red-hot wire or by pulling the eyeball out and cutting it off) and then confirmed that their ability to fly unharmed was still intact. His experiments on five species of bat confirmed the same behaviour; in marked contrast to results from the same experiments conducted on "birds, quadrupeds, amphibians, fish and insects." From these experiments, Spallanzani concluded that the bat must possess "some new organ or sense which we do not have and…can not have any idea."

Having written letters on the results of these experiments, and indeed requested that other academics may repeat his experiments to confirm the findings, subsequent discoveries were made. Charles Jurine, a member of the Geneva Natural History Society to which Spallanzani had presented his work in a letter, repeated the experiments but added a significant insight. If the ears of the bat were plugged with wax, its powers of navigation in the dark were very much reduced. These results however, served only to confuse Spallanzani; how could it be that navigation can be achieved through hearing? He did suggest that it may be sounds from the wingbeats reflected from objects which might aid navigation. This was closer to the solution than anyone would get for over a century. However, he also found that their abilities were reduced with a blockage placed in the mouth. By the time of his death, he appeared to be struggling with the evidence:

> "Can it then be said that…their ears rather than their eyes serve to direct them in flight? I can say only that deaf bats fly badly and hurtle against obstacles in the dark and…that blinded bats avoid obstacles in either light or dark."

There were many dissenting voices to the findings of Spallanzani and Jurine; it appeared the weight of established scientific thinking was against them, as summed up by George Montagu, the English naturalist, when he asked facetiously: "Since bats see with their ears, do they hear with their eyes?"

It was to be a hundred years or more before any significant results were reported on the question of bats' navigation in the dark. By this point the work of Spallanzani and his peers, much of it unpublished, was largely forgotten. In 1900, Rollinat and Trouessart, two French zoologists, returned to the problem and unknowingly repeated some of the earlier experiments. However, often they impaired two or more of the senses and failed to shed much light on the mystery. Shortly after this in 1908, the American zoologist WL Hahn again repeated these experiments but this time added regularly spaced wires as obstacles in order to obtain qualitative measurements of the bat's performance. Again, plugging of the ears was shown to greatly reduce the ability of bats to steer clear of the obstacles. Hahn put his conclusions in rather

vague terms, attributing the bat's navigational ability to "sense organs located in the internal ear" and "a sixth sense, that of direction"

In 1912, Sir Hiram Maxim (the American inventor of the Maxim machine gun) suggested a system that could prevent a repeat of the Titanic disaster. He suggested that sound generated from bat wingbeats at ~15Hz, and then reflected was the basis of their navigational ability. This hypothesis he extended to a system that would transmit low frequency underwater sound, which could be used to warn of approaching icebergs. It was only in 1920 that the correct explanation was finally suggested. The English physiologist Hamilton Hartridge (Hartridge, 1920) knew that if the wavelength of sound is large compared to an object it strikes, then the reflection does not form "sharp shadows." He noted that if sounds of a sufficiently short wavelength were used then sound casts shadows and obeys similar reflection laws to that of light. From these insights, and armed with the knowledge of the previous experiments that proved bats' reliance on hearing for navigation, Hartridge hypothesized that "bats during flight emit a short-wavelength note and that this sound is reflected from objects in the vicinity."

Finally, in 1939 and 1940, evidence was gathered to demonstrate that bats do indeed emit such short-wavelength sounds. Donald Griffin (Griffin, 1944) reported that, together with Dr. Robert Galambos, he made measurements of "bats' intense supersonic cries," which he stated as being made up primarily of frequencies between 30kHz and 70kHz. These measurements were only made possible by the development of a superheterodyne ultrasonic receiver (Noyes and Pierce, 1938), which Pierce made available for the purpose. Galambos and Griffin (Griffin, 1944) further demonstrated specifically that a bat required use of both its mouth and ears to be able to navigate competently, repeating one of Spallanzani's early results. They then proceeded to show that the "supersonic clamour" emitted by the bats increased as they neared objects, which they then proceeded to avoid, indicating that bats adapt their echolocation technique to their immediate environment. The trail was completed when further work (Galambos, 1942) demonstrated that the cochlea of bats generated electrical potentials when exposed to sound waves up to nearly

100kHz in some species; in comparison the cochlea of the guinea pig elicited measurable potentials up to only 40kHz.

So with the work of Galambos and Griffin in the early 1940s, the mystery of how bats navigate in complete darkness had been solved. Furthermore, Griffin compared this skill to the operation of an echo sounder on a ship and hence coined the term (Griffin, 1944) still in use today for a bat's ability to locate obstacles and prey using sound: echolocation. He even went as far as to suggest that a closer analogue is the operation of radar but that the bat "manages to achieve results which I think any radar engineer might envy." Certainly in terms of the bat's sonar ability, this is an envy which still drives engineers to this day and in some ways is also the inspiration for the work reported here.

2.2.3 Characterisation of Bat Echolocation Calls

As well as characterising bats by their genus, bats are often distinguished by the type of echolocation call they emit. Many species of echolocating bat have been studied in some detail, allowing broad classification of bats according to their echolocation characteristics. An excellent overview of the characteristics of these signals is provided by Grinnell (1995), and also by Schnitzler and Kalko (2001). In order to feed, each echolocating bat must be able to detect and locate prey; in some cases bats have also been shown to be able to identify prey insects based on wingbeat frequency (von der Emde and Menne 1989, Roverud *et al*. 1991). To achieve this, a wide variety of species- and habitat-specific signal types have evolved which vary in a number of ways.

Broad categorisation is achieved based on the frequency characteristics of the signals, and specifically the relative proportion of constant frequency (CF) and frequency modulated (FM) sections. Although some researchers have used up to seven categories for identifying bat echolocation calls (Simmons and Stein, 1980), which take into account the number of harmonics, and length and order of CF and FM sections, generally researchers use less than this, often distinguishing simply between CF (or CF/FM) and FM species. These categories are useful for classifying a bat species, but are completely insufficient to describe the wide variation in

echolocation calls that even a single species of bat might use given varying habitat or task. As an example of this see Figure 2.5, which illustrates the spectrogram representation of the echolocation calls of four genii of bat in the search, approach and terminal phases of insect predation. It can be seen that *Eptesicus* exhibits classic FM bat behaviour, with ever-steepening FM signals as the target is approached. *Pteronotus* demonstrates short CF/FM signals in the search phase that adapt to steeply-modulated FM signals in the approach and terminal phases. *Rhinolophus*, generally known as a CF bat can be seen to have a long CF portion with rising and falling initial and terminal FM sections, respectively, in the search phase. However, with approach to the target, the CF section shortens considerably and the FM sections become more prominent. Finally, *Tadarida* can be seen to alter its call from a very shallow FM, almost CF call to a steeply modulated FM call in the terminal phase. As such, the general classification of a CF or FM (or sometimes short CF/FM, long CF/FM or FM) bat is only really useful to define the type of call a species will use in free flight whilst searching for prey or using sonar for orientation. These call characteristics are matched to the bat's specific task and its local environment (Simmons, Lavender *et al*. 1978, Faure & Barclay 1994, Schnitzler & Kalko 2001, Schnitzler *et al*. 2003). Across this range of signals, other characteristics also vary widely. Dominant frequency content has been measured as low as 11 kHz and as high as 212 kHz (Jones, 1999), whilst the duration of calls can be less than a millisecond (Schumm *et al*., 1991) or up to around 100msec (Grinnell, 1995).

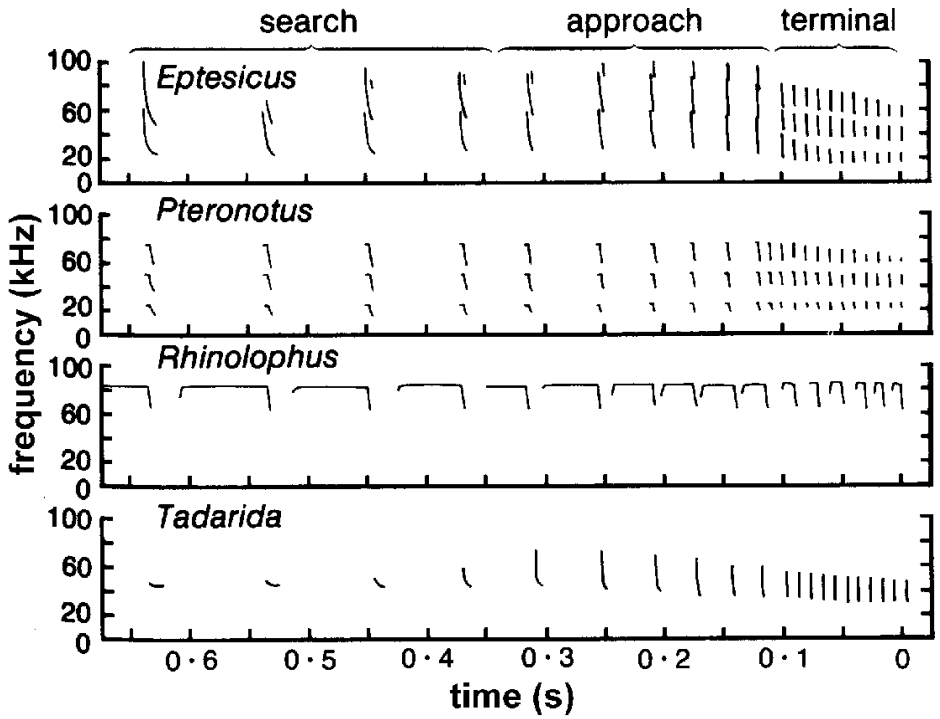

Figure 2.5. Sonograms illustrating a variety of bat echolocation calls (Hill and Smith, 1984).

2.2.4 Echolocation Signal Dynamic Range

Bat echolocation calls cover a wide range of amplitudes. In a summary of emitted sound pressure level (SPL) measurements from the literature, Waters and Jones (1995) reported a range of peak SPL of 77dB – 115dB, although bats certainly emit much lower level sound than this during echolocation, with <60dB quoted by Griffin (1958) and recent research in the field has revealed insectivorous bats producing sound in excess of 140dB (Surlykke and Kalko, 2008). That bats require to emit such high amplitude signals is due to searching for small prey items in a highly attenuative environment; the combination of these effects means that signal attenuation over the return path is considerable. The attenuation of ultrasound in air is highly frequency dependent (Bass *et al.*, 1995), increasing from approximately $0.5dBm^{-1}$ to $8dBm^{-1}$ over 20kHz to 200kHz, the approximate frequency range of bat echolocation (it is also dependent on humidity and temperature though to a lesser extent). In addition to this, the target strength of a prey insect can vary from (Waters *et al.*, 1995) approximately -35dB for larger moths, to -70dB for small flies such as midges. As such, a bat trying to locate a small fly with a high-frequency echolocation signal may

encounter round-trip attenuation in excess of 100dB for a distance of just two metres. That such a small mammal can even emit sounds of this amplitude is quite incredible. In fact this feat appears to be achieved with relatively little additional cost in terms of energy consumption over that required for flight (Speakman and Racey, 1991), by coupling energy generated from the flight muscles into contracting the abdominal wall to produce high sub-glottal pressure to power intense vocalisations (Lancaster *et al.*, 1995).

To enable them to deal with the large dynamic range (possibly in excess of 100dB as described previously) and small return echoes, bats (in common with most mammals) are able to detect signals close to 0dB SPL at their most sensitive frequency (e.g. Neuweiler *et al.*, 1984; Koay *et al.*, 1998; Koay *et al*., 2003). However, this causes the bats a further problem – how to prevent damage of the sensitive hearing system when emitting intense calls. This is solved by employing biological automatic gain control (AGC). Research has shown that species including *Tadarida brasiliensis mexicana* (Henson, 1965), *Myotis lucifugus* (Jen and Suga, 1975), and *Eptesicus fuscus* (Kick and Simmons, 1984), have evolved a mechanism that helps them to overcome the dynamic range between emitted and reflected signals, whilst protecting the hearing system from damage. By contraction of the middle ear muscles just prior to emission of the echolocation call, a temporary reduction in hearing sensitivity is achieved for the period of call emission. This sensitivity is then *gradually* restored as the muscles relax post emission, causing sensitivity to increase as the propagation loss incurred by echoes increases (Kick and Simmons, 1984; Simmons *et al*., 1992). Hence, the bat employs gain control in order to regulate the perceived loudness of the returning echoes, thereby increasing the dynamic range of signals it can use and process. It has also been shown that bats take measures to restrict the dynamic range between emitted and reflected signals by reducing the amplitude of the emitted signals as they approach a target to account for the reduced path-loss. Hiryu *et al*. (2007) showed that *Pipistrellus abramus* reduced the intensity of its emissions as a target wall was approached at a rate of 6dB per halving-of-distance. It was also retrospectively reported that the work reported in Hiryu *et al*. (2005) had found that *Hipposideros terasensis* decreased its call intensity by 6.5dB per halving-of-distance. These figures broadly agree with the findings of

Hartley *et al.* (1989) and Hartley (1992) for the fish-catching bat *Noctilio leporinus* and for *E. fuscus*, respectively. Through the combination of these techniques (reduced sensitivity through AGC and reduce emission intensity) it has been demonstrated (Hartley, 1992) that bats can stabilise the SPL at which echoes return, aiding the dynamic range issue as well as allowing the bat to detect any level changes that are caused by the object itself, such as glints from the wings of prey insects (Henson *et al*. 1987, Moss and Schnitzler, 1995; p.134). In the context of this Thesis, AGC as employed by bats has significance for two reasons. Firstly, it provided inspiration for the wireless sensor presented in Chapter 3, which used electronic AGC to enable both the emitted and reflected echolocation signals from a flying fruitbat to be recorded. Secondly, although AGC aids bats by avoiding hearing damage and maintaining a stable echo intensity, the reduced hearing sensitivity has an effect on the level at which sound can be detected, and so the size of objects detectable using echolocation. This is investigated with respect to target wire diameter in Chapter 5.

2.2.5 The Information Content of Bat Echolocation Signals

The information that a bat can gather from its sonar echoes is mainly dependent on the frequency characteristics (Simmons *et al*., 1978) of its calls. Long CF signals, with their single-frequency frequency content, are useful for detecting and characterising prey insects via doppler shifts in the echo frequency. Such shifts can be used to infer insect motion Also, if this long CF signal is viewed as a carrier frequency, then amplitude and frequency modulation due to the fluttering of insect wings can provide classification information about the insect (von der Emde and Menne 1989, Roverud *et al*. 1991). Furthermore, amplitude modulation of the signal by insect wingbeats also produces ‘glints’ when the insect wings are momentarily perpendicular to the incident sonar signal. A glint is characterised by a short amplitude peak, up to 20dB above the amplitude of the echo from the insect with the wings in any other orientation (Henson *et al*. 1987, Moss and Schnitzler, 1995 (p.134)) that can aid long-range detection of prey. So it can be seen that the long CF portion of the signal is very useful both for initial detection and for selection, if a bat is choosy about its favoured meal. Shorter CF signals, on the other hand are less

useful in classifying an insect and are generally used to aid the initial detection of a prey insect. If the CF portion of signals is for longer-range detection and classification, then the FM portion is ideally suited to more detailed image construction and ranging, for locating an insect in space. These signals, with their short time duration and rapidly changing frequency profile can provide excellent ranging information from any cross-correlation techniques the bat might use (e.g. Simmons, 1973; Moss and Schnitzler, 1995 (pp.106-107); Moss and Schnitzler, 1989).

It can be seen from the preceding discussion, that these different sonar signals are suited to different tasks. For these reasons, bats emit calls with a mix of these characteristics, and alter these characteristics as it goes through the search, approach and terminal phases of insect predation (e.g. Simmons, *et al.* 1978, Henson *et al*. 1987). Similarly, these call characteristics can also be matched to the primary habitat in which the bat hunts and some bats alter the composition of their calls as they move between habitats (Schnitzler & Kalko, 2001).

2.2.6 Spatial Resolution Capabilities of Bats

Much experimental work has been devoted to measuring how accurately bats can resolve targets in space, in terms of range and angular position. This has been made possible by behavioural experiments, in which a bat is trained to make a choice based on discrimination between two different real or simulated echoes from its echolocation calls. In the early 1970s, Simmons and Vernon (1971) published the original work in this area, demonstrating bats trained in a two-choice simultaneous discrimination procedure. This method has proven to be successful for investigating bats' resolution capabilities. For a bat to locate a sound source in space, three separate variables are measured: time delay (range); azimuth (horizontal angle); and elevation (vertical angle). These three measurements are made using different processes in the brain, and bats' accuracy in each has been demonstrated in the literature.

2.2.6.1 Range Resolution

An early study of bat range resolution was published by Simmons (1973), showing that four species of bat, which use FM or short CF/FM signals could resolve range difference between two separate targets of 10mm - 30mm, a result that was relatively unaffected by the absolute range of the targets, from 30cm – 240cm. Subsequent work in this area, which is summarised by Moss and Schnitzler (1995, pp.106-107) produced similar results, with most species of bat that are able to use FM signals exhibiting absolute range resolution of 8mm - 15mm. These results were tempered by the knowledge that the bat moved its head during echolocation experiments, "changing the true distance to the targets by several millimetres." This suggested that range resolution (or rather, time resolution of the echo delay) of the bat is actually more accurate than these figures. Indeed subsequent jitter discrimination tests (where a bat must select between two artificially-generated echoes – one which is stationary in time-delay and one which is jittered, altering the time-delay between subsequent echoes by a small amount) suggested that bats may be capable of distinguishing delay resolution of 10ns (Simmons *et al*., 1990). Whilst these results have attracted criticism – notably from Pollack (1993) – it would appear that bats can certainly discriminate between jittered and non-jittered targets, with a jitter level of less than 1μs (Menne *et al*. 1989; Moss and Schnitzler 1989; Simmons 1979) corresponding to a range difference of tens of μm. This level of discrimination has been explained by the possibility that bats use some sort of cross-correlation technique to obtain timing and therefore range information (Moss and Schnitzler, 1989; Simmons *et al*., 1990).

Similar methods were used to determine the detection resolution of multiple reflectors on a single target, known as the two-point threshold. Initially this was done by drilling two holes in a Plexiglas plate and determining the depth difference at which a bat could no longer select the shallower hole. Simmons *et al*. (1974) drilled an 8mm deep hole and a second one of 6.5mm – 7.6mm deep. *E. fuscus* was shown to be capable of resolving differences of less than 1mm. A study by Habersetzer and Vogler (1983) on *Myotis myotis* produced very similar results. More recently, Simmons revisited the subject and used an electronic target simulator (essentially producing artificial echoes from a bat echolocation call) to demonstrate that *E. fuscus*

has a two-point threshold of 2μs – equating to a range difference of 0.35mm. As the authors state, this threshold is "far in excess of what would be needed just to capture individual flying insects" but it would enable the bat to "determine the location of multiple reflecting surfaces and to perceive the shape of a complex target in spatial terms." This could be used by the bat for target identification or to recreate complex spatial environments.

2.2.6.2 Angular Resolution

Bats' perception of angular resolution has also received attention. Since bats, like most mammals, have two ears, mounted on either side of the head, they use different methods by which to resolve azimuth (horizontal) and elevation (vertical) angles. *E. fuscus* has been demonstrated to be capable of discriminating between horizontally-spaced pairs of rods separated by approximately 1.5˚ (Simmons *et al*., 1983). Elevation angular discrimination was reported to be less accurate, at 3˚ (Lawrence and Simmons, 1982; Wotton *et al*., 1996). Interestingly, deflecting the tragus of the bat prompted a significant decrease in elevation angle discrimination, to between 14˚ (Lawrence and Simmons, 1982) and 20˚ (Wotton *et al*., 1996) without affecting horizontal angle acuity. This demonstrates the importance of the transfer function of the outer ear in determining elevation angles. Azimuth resolution has been explained by interaural time difference (ITD) and interaural intensity difference (IID) since sounds originating from either side of the median sagittal plane are separated in arrival time and have a different intensity at each ear (Simmons *et al.*, 1983; Wotton *et al*, 1995). Recent work (Aytekin *et al.*, 2004) also demonstrated in some detail the interaural difference in spectral cues associated with both azimuth and elevation, which provides further cues for sound localisation as discussed in the following section.

2.2.6.3 Binaural and Monaural Cues for Angular Discrimination

The three components that indicate the location of a sound source in space (range, azimuth angle and elevation angle) are calculated via different processes in the brain. Range, as discussed earlier, is determined via the time-delay of an echo. Although the precise nature of the process is still debated, a form of cross correlation in the

time and / or frequency domain appears to play a role. In relation to this Thesis, discrimination of source angle is of more importance as will become clear. The location of a sound source in azimuth could be ascertained via binaural information, that is the ITD and IID that exists between the signals arriving at the right and left ears (any echoes arriving at the right and left ears with no ITD or IID would have originated on the median sagittal plane). Returning to the horizontal angular resolution of 1.5˚, Simmons *et al.* (1983) suggest that this can be explained by the bat's ability to perceive sub-μs time-delay resolution in the ITD between echoes to its two ears. However, whilst this binaural information can provide cues as to the horizontal angle to a sound source, it cannot help the bat discriminate elevation. This is especially true if the sound source is located on the median sagittal plane, due to head symmetry providing no ITD or IID cues. The mechanism for determining the elevation is implied by the fact that deflecting the tragus of an echolocating bat leads to its vertical acuity being significantly reduced (Lawrence and Simmons, 1982; Wotton *et al*., 1996). The vertical angle of an echo source is encoded into the (broadband) echo as it interacts with the head, body and external ear before it impacts on the ear drum. The effect of this interaction, known as the head-related transfer function (HRTF) is to alter the nature of the incoming sound, convolving the returning echo signal with the HRTF. As regards the vertical angle of the sound source, this produces a series of spectral notches in the sound transferred to the eardrum, which encode the vertical angle of the sound source. This mechanism has been demonstrated in a number of mammals, including humans (Wightman and Kistler, 1989) and cats (Huang and May, 1996), as well as in echolocating bats (Wotton *et al.*, 1995; Wotton *et al*., 1996; Aytekin *et al.*, 2004). As such, the azimuth and elevation angle can be computed separately in the brain. It would appear that azimuth angle is computed through *binaural* cues, whilst vertical angle is computed through *monaural* cues. There has been some debate over the years as to whether subjects can accurately detect the vertical location of a sound source using one ear only, with current research indicating that the signals from both ears are required to achieve this accurately and robustly (Wightman and Kistler, 1997; Van Wanrooij and Van Opstal, 2004 and 2006). However, although the signals detected by both ears appear to be required, it cannot be refuted that these cues are *generated* monaurally

in each ear individually, rather than from a comparison of the signals occurring at each ear, as is the case with ITD and IID. As such, finite element analysis (FEA) of the response of a single ear, as is presented in Chapter 6, is a valid method by which to investigate the characteristics of the signals generated at the ear drum, after transformation via the pinna. The FEA approach is certainly more flexible than previously documented methods, such as inserting microphones into the ear canal of a dead bat mounted in an acoustic test chamber (Wotton *et al.*, 1995) or training a bat to respond to acoustic cues (Wotton *et al.*, 1996; Wotton and Simmons, 2000). There are a handful of publications that have demonstrated FEA of a bat's ear; these are summarised in section 2.4.2.

2.2.7 Detection of Targets With a Small Cross Section

The capability of any sonar system to detect a target decreases with the cross section of the target, as a function related to the wavelength of the sonar signal. As an example of this, consider the target strength (TS) of a sphere of radius a. In general TS varies with a^2, however for an incident wavelength (λ) much greater than the radius, TS varies with a^3/λ^2 (Urban, 2002). This indicates that for reducing radius with respect to wavelength, TS decreases rapidly. It is interesting that the neurologist and anatomist Stephen Polyack (Griffin, 1958) commented in 1946 that "the use of ultrasonic sounds…cannot be accepted as guiding the feeding sense, for the size of the prey is too small for reflection." Of course this capability is now accepted as a matter of course, and the ability of bats to detect objects with a cross section smaller than the wavelength of their echolocation calls has been demonstrated via wire-avoidance experiments. In these tests, a series of wires are placed as obstacles within a captive flight environment. The bats are trained to fly from one side of the enclosure to the other, avoiding wires of successively smaller diameter, which are moved between each experiment to avoid the bat memorising the layout of the wire obstacles. Gustafson and Schnitzler (1979) showed that the bat *Asellia tridens* was capable of avoiding wires down to a diameter of 65μm, in comparison with a minimum wavelength within its echolocation call of approximately 3mm, corresponding to the CF portion of its CF/FM call at 115kHz. As such, the bat is detecting, locating and avoiding targets with a cross-section of $\lambda/46$. This result is not

unique. Mogdans *et al*. (1988) reported that the greater horseshoe bat (*Rhinolophus ferrumequinum*) could detect and avoid wires down to at least 60μm. *R. ferrumequinum* has an echolocation call that is generally classified as CF, though it can have initial and/or terminal FM portions. The highest frequency in the call is the CF portion at approximately 83kHz, indicating that the bat can detect wires with a cross-section of λ/70. Furthermore, a similar capacity has been demonstrated in the megachiropteran fruitbat *R. aegyptiacus* (Waters and Vollrath, 2003) which was found to be capable of detecting and avoiding wires of 6mm diameter, and also "took evasive action" when within approximately 500mm of wires of 1.3mm diameter, although the bat did not always manage to avoid contact. This is in comparison with a peak component at 20kHz (17mm), with little energy above 40kHz (λ≈8.6mm). This capability is investigated in Chapter 5, using replicated echolocation calls in the laboratory.

2.3 Recording the Echolocation Calls of Bats

The previous sections have detailed the level of perception with which bats can discern targets in their surrounding environment using echolocation. However, the nature of the echolocation calls themselves have received little attention thus far. The format of the signals used by the bat is crucial to its success, as evidenced by the way in which bats match call characteristics to a given task or environment (Schnitzler and Kalko, 2001). As such, the first problem to be overcome in understanding how these calls are used is to record the emitted call itself.

Having been responsible for demonstrating bats' emission of ultrasonic sounds, Griffin (1958) set about recording these signals in the field, to demonstrate their use for insect predation. This he achieved by rigging various pieces of laboratory equipment for operation from a generator and employing them at a local pond where bats were present at dusk. Through heterodyning he was able to listen to a frequency-shifted representation of these calls and hence determined how the echolocation calls went through specific stages as the bats made the characteristic "rapid turns and dives" of insectivorous feeding. From this point onwards, echolocation call recording was achieved using a static microphone attached to some sort of recording media,

such as analogue tape (e.g. Simmons 1973; Gustafson & Schnitzler 1979), but more recently digital media (e.g. Holland *et al*. 2004). Generally these recordings have been made using solid dielectric capacitance microphones, mounted in a stationary position or handheld. This method of recording has inherent problems for accurate recording of the emitted echolocation call, as summarised by Waters and Jones (1995):

- Non-linear frequency response (generally low-pass) of capacitance microphones
- Unpredictable behaviour with respect to temperature, humidity and membrane tension of capacitance microphones
- Frequency-dependent directionality of sonar emitted by bat
- Frequency-dependent directionality of receiving microphone
- Frequency-dependent (low-pass) attenuation of sound in air

In addition to these factors, with a stationary microphone and a moving bat, doppler effects alter the component frequencies of the recorded calls. Furthermore, as the bat moves the cumulative effect of these factors varies, making post-processing to obtain the original signal almost impossible.

Given the difficulties of recording bat echolocation calls, many studies have been performed in a captive environment, with bats flying in a flight room (e.g. Waters and Jones, 1995; Kick and Simmons, 1984; Boonman and Jones, 2002) or being held in a pendulum, which can be swung towards a prey object (and microphone) eliciting a range of echolocation calls (e.g. Henson *et al.*, 1987). Indeed, this method has been used with some success, although the bat is in a somewhat unnatural situation. It is also noted by Waters and Jones (1995) that the characteristics of calls recorded in captive bats can differ from those recorded in the wild, so perhaps recordings obtained from captive bats will always leave some echolocation behaviour unexplained. To this end, recent studies have undertaken recordings in the wild, with echolocation call recording linked to 3D positioning systems (Holderied *et al.*, 2005; Surlykke and Kalko, 2008) to extrapolate source SPL in the wild, as well as recording natural echolocation sequences of feeding bats. It should be noted that

reconstruction of the emitted signal is still practically impossible using post-processing techniques, which have been limited to SPL estimation.

In the course of these recordings, echoes have surely been detected by handheld or static microphones. However, it has been impossible using this approach to record the echo signal the bat actually hears. It can be imagined that to gain an insight into how bats use sonar to navigate and feed, it is the information that returns directly to the bat which is of the utmost importance. To this end, a new approach to bat recordings has recently emerged. This approach involves attaching an ultrasonic sensor directly to a captive bat, which is then wirelessly linked via a radio transmitter to a remote recording system. As the bat echolocates in flight, albeit in a captive environment, the echolocation calls are recorded. There are several pieces of work that have demonstrated this approach.

2.3.1 Recording of Bat Calls Using Wireless Telemetry

There are many examples in the literature of telemetry being used to track the movement of bats. In these studies bats were captured, had a radio tag attached, and then released in order to study their foraging behaviour (e.g. Bernard & Fenton, 2003; Hamilton & Barclay, 1998; Bontadina *et al.*, 2002). The mass of the radio tag was generally kept below 5% of the bat's body mass in order to ensure that the presence of the tag did not affect the flight and behaviour of the bat, as reported by Aldridge & Brigham (1988). However, these studies were only of use for gleaning information about the routes a bat might take to or from its roost, or where and for how long the bat is foraging for food.

Of more interest to the work being undertaken here, are a number of publications arising from two research groups using bat-mounted telemetry sensors to monitor sonar and physiological information for bats in flight. The first research group is based at the University of North Carolina (Chapel Hill, NC, USA). In the first relevant publication, Henson *et al.* (1987) reported using a telemetry system to study biosonar signals of the moustached bat, *Pteronotus parnellii*, which emits a CF call preceded and terminated by a brief (1-3ms) FM portion. The second harmonic (CF2) at approximately 61kHz, is the most prominent and is matched to the most sensitive

frequency of the bat's hearing. It is noted that the FM portions of the signal are readily useful for ranging and locating acoustic targets, while the CF portion can be used to detect motion of the target as well as detecting wingbeat frequency. This appears to be born out by the fact that *P. parnellii* is selective about its prey, deciding from a considerable distance whether to attack based on wingbeat frequency encoded into doppler shift of the reflected CF signal (Kober and Schnitzler, 1990; Roverud *et al.*, 1991). In many ways, though this is the first reported use of a bat-mounted telemetry system, the study is more diversely interesting than its successors. The authors set out with two specific objectives: firstly, to extend the understanding of how *P. parnellii* uses its sonar, especially in the active pursuit and capture of insects; and secondly, to use telemetry and signal processing techniques to obtain detailed information on the nature of the signals actually detected by the ear of the bat. For these purposes, two separate transmitters were used with either one or the other being mounted on a bat at any one time. It was noted that bats with a sensor attached to the head "could fly normally but tended to tire very quickly". It should be noted that the mass of the sensor was up to 1.8g, representing some 14% of the bat's 13g. Another problem the authors noted was "the irregularity in [wirelessly transmitted] signal-to-noise levels in different parts of the recording chamber" which made recording from flying bats difficult. Despite these issues, some good recordings of biosonar signals were achieved from bats in flight, using a sensor based on a microphone (of unspecified construction) an amplifier and oscillator. The recordings even included representations of the call echoes. An interesting point was noted about the telemetered signals as opposed to those recorded from a static microphone – beating was shown to occur between the outgoing sonar signal and the overlapping doppler-shifted echo, which could well be used to infer target motion. This is an effect that could only be detected using this technique.

Further experiments were carried out with the bat strapped into a pendulum device, presumably to limit the bat's position in order to achieve good SNR in transmitted wireless signals, as well as saving the bat from the arduous task of carrying the sensor. These experiments were especially interesting, since as well as measuring emitted echolocation calls, a telemetry sensor with biological implants was also used to monitor cochlear microphonic (CM) potentials elicited by the transmitted and

echoed signals. Interestingly, the high intensity calls emitted by the bat did not elicit strong potentials in the cochlea, due to the highly tuned nature of the ear of *P. parnellii* (and also, possibly, the same AGC mechanism discussed previously). However echo signals, which had been doppler shifted in frequency *did* generate good CM signals, which showed a strong response to both glints and the beating mentioned previously. Neither of these features was obvious when the signal from a microphone located directly in front of the bat was analysed. Hence with a combination of signals, the authors show how the bat might use its sonar signals to identify prey in a noisy environment, and also then how it might track that prey.

Five years after this study, some of the issues regarding the telemetry system had been resolved as reported by Lancaster, Keating and Henson (1992). Nulls in the RF transmission pattern were still proving to be a "significant hindrance" however. In this study, the wireless sensor had evolved somewhat, consisting of a Knowles 1759 electret microphone, coupled to a variation of a Clapp oscillator; the inductive element of the oscillator was provided by a coil of wire that also doubled as the antenna, with alteration of its geometry providing the tuning inductance. Telemetry signals were received on a commercial tuner (Harmon and Kardon T403). The sensor had a mass of just 0.85g, and was attached to the head of the bat using latex adhesive. Once in place it was reported that an 11g bat (again, *P. parnellii*) could fly without significant impairment for periods of up to one hour.

The experiments consisted of a bat flying in a mesh enclosure with a target opening in one wall allowing the bat egress to a larger room. A microphone was located at the opening, such that static recordings (with doppler-induced shift) could be compared with recordings from the bat-mounted sensor. During flight tests it was shown that, although the SNR on signals from the static microphone was significantly better, bat calls were accurately reproduced by the received signals from the wireless sensor. These were used to demonstrate a number of findings. Firstly, it enabled in-flight calls to be monitored, both with (static recording) and without (wireless recording) doppler effects. This showed that flying bats maintained echo frequencies in a narrower band than emitted frequencies, indicating that the bats were doppler-shift compensating (DSC). This is done in order to keep echoes at the frequency at which

the ear is most sensitive, in this case a narrow band between 61.8kHz and 62.0kHz. The corresponding doppler-compensated calls were in a wider band between 61.0kHz and 61.6kHz. This technique had earlier been suggested by Gustafson and Schnitzler (1979) after analysis of a series of static microphone recordings; use of the wireless sensor provided direct evidence.

Further experiments performed on bats mounted on a pendulum showed a number of differences when compared with bats in free flight. Firstly, the bats were less accurate with their frequency compensation. In free flight 59% of all echoes fell within 150Hz of the reference frequency, with 93% within 500Hz; this dropped to 23% and 72% respectively with the bat on the pendulum. Secondly, the timing associated with calls was also different, both in terms of the duration of calls and intervals between calls, both of which were generally longer for a bat on the pendulum. This indicated that it may be necessary to study bats in free flight in order to properly interpret their use of sonar.

Another study (Lancaster *et al*., 1995) conducted by the same group used telemetry to show a link between activity in the respiratory muscles and vocalisations in *P. parnellii*. In this case a similar wireless sensor was used, but with two adaptations. Firstly the electret microphone was replaced with a "ceramic-crystal" microphone with its resonant frequency tuned to the dominant 61kHz call frequency. Secondly, an electrode was added to the sensor that was used to record signals from various muscles. The electrode was inserted into the muscle of choice to monitor the electromyographic (EMG) signals, or electrical potentials, generated by muscle activity. These low frequency (<10kHz) signals were then summed with the higher frequency vocalisation signals, and this combined signal was then transmitted for later examination. The findings of this study show that bats synchronise (as often as possible) the production of sonar pulses with the muscle activity associated with wingbeats. This is done in order to make "double use of the force generated by the great muscles of downstroke: to power flight and to assist in the production of pressure for intense echolocation vocalisations." Speakman *et al.* (1989) had demonstrated that the energetic cost to the bat *Pipistrellus pipistrellus* of emitting ten echolocation pulses per second whilst at rest was 9.5 times its base measurement.

However, Speakman and Racey (1991) established that whilst in flight, echolocation was achieved without significant additional energy expenditure. Only by monitoring both the calls and muscle activity (or wingbeat cycle) of bats in free flight could the mechanics of this phenomenon be demonstrated; without telemetry this would have been impossible. It should be pointed out that the study did find that intense calls were not always linked to flight muscle activity. In cases where the bat was undertaking a more complex echolocation task (e.g. landing or obstacle avoidance) which required a higher pulse repetition rate, pulses could be emitted at any stage of the wingbeat cycle as necessary. However, once this task was completed the bat would immediately restore the coincidence of wingbeat with call.

The second group conducting telemetry studies is based at Doshisha University (Kyotanabe, Japan). The sensor was first detailed by Riquimaroux and Watanabe (2000) at the seventh Western Pacific Regional Acoustics Conference (WESTPRAC VII). The sensor (dubbed 'Telemike') consisted of "a small transmitter and a ¼" titanium condenser microphone which weighed 3g". The results from this paper were added to and repeated by Riquimaroux *et al*. (2002) at the Forum Acustica Sevilla. By recording the Taiwanese leaf-nosed bat (*Hipposideros terasensis*) in flight with a high-speed video camera, and simultaneously recording their calls, a correlation was found between call timing and wingbeat cycle, backing up the findings of Lancaster *et al.* (1995). This link has since been demonstrated in a number of species, for example *Pteropus gouldii* (Thomas, 1981); *Myotis dasycneme* (Britton *et al.*, 1997); *Pipistrellus pygmaeus* (Wong and Waters, 2001). However, the paper also reported how *H. terasensis* demonstrated doppler-shift compensation while in flight. This result is obtained using the Telemike to record the frequency of the emitted pulse at the head, and it was suggested that Telemike also detected some echoes which return to the bat, from which frequency information can be gleaned. The frequency of the pulse at a static microphone was also recorded and – as reported by Lancaster *et al*. (1992) – it was found that the returned echo was kept in a narrower band of frequencies than the emitted pulse.

These findings were followed up by a further publication from the group (Hiryu *et al*., 2005). In this study the echolocation calls of *H. terasensis* were examined in

relation to two different flight scenarios: firstly a direct flight towards a wall on which the bat landed; and secondly a flight in which a wall was approached, but a u-turn manoeuvre performed to fly away again. The flights were again monitored by both microphone and video camera. However, in this case, two high-speed video cameras were used that allowed the bat's position in space and velocity to be calculated. Based on the velocity at which the bat was calculated to be travelling, the frequency of the CF2 component required to compensate for the doppler-shift was estimated. In both flight scenarios, this estimation was shown to correlate well with the frequency of the Telemike recordings, although estimated frequencies did tend be slightly low. The authors explained this by assuming that the bats would switch attention between the wall directly in front of them and the side wall in order to accurately plot their surroundings. This meant that the angle at which echoes returned to the bat from the side walls would change; by taking this angle into account, the estimated frequency agreed with the recorded frequency of bat calls. This assumption seems valid on consideration of the u-turn flight scenario, which showed a periodic error between the original estimate and the measured frequency. As the bat performed the u-turn manoeuvre it monitored both the front and side walls in order to build an accurate picture of its surroundings and successfully complete the manoeuvre. In the direct flight to land on the front wall, the side walls are of less consequence. These data provide an interesting insight into the methods used by bats for building up their mental image of the surroundings.

It is interesting to note that Hiryu *et al*. (2005) used estimated frequencies to confirm that *H. terasensis* was indeed using DSC. If it was possible for the Telemike system to discern the returning echoes which the bat actually hears, then there would be no need for this estimation. Again, the attenuation of sound in air was problematic in this respect; the returning echoes are simply too faint to be reliably detected. This is one of the issues which the work reported here aimed to address (see Chapter 3).

Further work with Telemike was carried out and reported by: Hiryu *et al*. (2007); Hiryu *et al*. (2008); and Shiori *et al*. (2009). Hiryu *et al*. (2007) reported its use for measuring the intensity change of the emitted echolocation calls of *Pipistrellus abramus* as a target wall was approached. This reduction in intensity was measured

at 6dB per halving-of-distance. It was also retrospectively reported that the work reported in Hiryu *et al*. (2005) had found that *H. terasensis* decreased its call intensity by 6.5dB per halving-of-distance. Similar findings on echo intensity and frequency stability were reported for the Japanese horseshoe bat (*Rhinolophus ferrumequinum nippon*) by Hiryu, Shiori *et al*. (2008). These findings concur with earlier measurements (Kick and Simmons, 1984; Simmons *et al*., 1992; Hartley *et al.*, 1999) that demonstrate the 6dB reduction in call strength per halving-of-range. As reported previously, this reduction combines with the AGC of the bat to stabilise the level of returning echoes (Hartley, 1992).

Hiryu *et al*. (2007) demonstrated that pulse production by *P. abramus* in the approach phase differed between field recordings and those made in the laboratory using Telemike. Finally, *R. ferrumequinum nippon* was again used, by Shiori *et al*. (2009), with DSC being demonstrated. Results presented by Henson *et al.* (1987) were confirmed, with the retuning CF calls of *R. ferrumequinum nippon* overlapping with subsequently emitted calls to create beating of the signal the bat hears, which the authors again suggest could be used for target localisation by the bat.

It can be seen that the literature contains a wealth of information on the signals that bats use for echolocation, and also the methods they employ to make best use of these signals, in terms of altering frequency, repetition rate, call duration or intensity. It is obvious that the success of microchiroptera is very much reliant on these biological engineering techniques.

2.4 Investigating the Sounds Actually Heard by Bats

Wireless microphone systems such as those documented in the previous section have brought great understanding of many aspects of the echolocation process. Some of the previous studies have detected returning signals, for example allowing the DSC generally used by CF bats to be investigated, or detailing the beating of overlapping emitted and reflected CF calls. However, these techniques alone cannot be used to understand the sounds the bat actually hears. One study, discussed in the previous section, (Henson *et al*., 1987) actually measured electrical impulses in the brain stimulated by the cochlear on hearing returning echoes. However, this gave an

indication of the intensity of the signals as perceived by the bat, rather than their structure. Behavioural studies have been used to infer how bats use artefacts (such as spectral notches) imposed on returning echolocation calls by the HRTF (Wotton *et al*., 1996; Wotton and Simmons, 2000). However, direct measurement and modelling techniques have recently been developed in an attempt to calculate the signals the bat actually hears, by simulating the effect that the HRTF has on these returning echoes.

2.4.1 Measuring the Head Related Transfer Function of Bats

Several studies have been published that used dead bats to measure the HRTF. The bat (or part of a bat) is within an acoustic test environment, with one or two microphones inserted into the ear canal to replace the eardrum. Sounds are then transmitted from a range of locations, toward the bat head and recorded using the microphones. The signals detected by the microphones can then be analysed for characteristics (generally spectral) that can be used to infer azimuth and elevation. Some studies have been conducted that investigate the directionality of bat ears from many species using these methods (Jen and Chen, 1988; Obrist *et al.*, 1993). These are not covered in detail here as they did not provide a measure of the HRTF, although obviously the data gathered is related.

One of the first examples of this type of measurement was reported by Lawrence and Simmons (1982). After observing that deflection of the tragus in *E. fuscus* decreased its ability to perceive changes in the vertical separation of pairs of rods from 3˚ to 12˚-14˚, a microphone was inserted into the ear canal of a dead bat and a "broadband acoustic impulse" was transmitted towards the bat. A strong reflection of the impulse was detected, which varied in time delay from the initial impulse received with elevation angle. The reflected impulse was also "greatly attenuated by removal of the tragus". This time-dependent reflection within the external ear is responsible for the spectral nulls or notches found in later publications. When the time delay is equal to half the period of an incident wave, then the initial and reflected signals are 180˚ out-of-phase, and so cancel each other in the ear canal, generating the notch in the frequency domain corresponding with that time delay.

The first detailed investigation of the effect of the HRTF on incoming sounds was reported by Wotton *et al.* (1995) on *E. fuscus*. Either the right or left eardrum of an intact bat head (or half-head) was replaced with a microphone and a 0.5ms FM sweep (100kHz – 10kHz) was transmitted towards the bat head. The results investigated the relationship between the position of sharp notches and wider peaks in the HRTF, with elevation varying over ±45˚ and azimuth varying from 0˚ (directly ahead) to 70˚. For any given azimuth, the frequency at which the notch appeared in the spectral representation of the HRTF was shown to decrease systematically with decreasing elevation. There were a number of interesting features of the HRTF. Firstly, the "elevation dependence of the most prominent notch…is largely restricted to elevations below the horizontal" which fits well with the authors' assertion that "the bat usually places the target in a position below its eye-nostril plane". As such, the target is generally kept in a position where its elevation can be determined from the frequency of the main spectral notch. Furthermore, although these notches do vary with azimuth angle, bats tend to point their head towards the prey object (Simmons, 1989), thus keeping it on the median sagittal plane (at least with respect to the head orientation) and therefore maintaining the quality of elevation cues available in the echoes. The influence of the tragus was again investigated through removal and repetition of measurements, which demonstrated that the systematic variation in the peaks of the HRTF in the time domain (or nulls in the spectral domain) largely disappeared. This indicated the importance of the tragus to *E. fuscus*, and is especially interesting given the lack of a prominent tragus in the *Rousettus* genus. This work was followed up (Wotton *et al.*, 1997) to generate what was termed the "echolocation combination" which combined the measured directionality of the sonar emission (Hartley and Suthers, 1989) with the HRTFs measured previously. The results indicated that "spectral peaks are sharpened and there is greater contrast in intensity between peaks and notches when compared to the spectra of the ear alone." Furthermore, the authors commented that the results indicated that spectral localisation cues were available for sound sources "restricted to a cone of space of approximately ±30˚" and that this is a far smaller range of sensitivity than demonstrated by humans. This is another example of the specialism of bats, with their forward-facing echolocation system allowing them to focus attention on a prey

object that they attempt to keep directly in front of them whilst hunting (Simmons, 1989).

Similar methods were used by Fuzessery (1996) with the pallid bat (*Antrozous pallidus*) to measure ear directivity and gain with respect to frequency, as well as the HRTF. *A. pallidus* is an interesting bat, in that it gleans its prey (that is, locates it by passive listening to the sounds generated by prey insects as they move) whilst using echolocation for general orientation. As such, its ears have characteristics that are different in some respects to other echolocating bats, with a relatively low frequency for maximum directivity (35kHz) and large acoustic gain at low frequencies, to aid detection of prey-generated, rather than echolocation, signals. However, the measured HRTFs indicated very similar trends in terms of spectral nulls as demonstrated with *E. fuscus*, with the frequency of the main spectral null varying linearly with elevation.

Aytekin *et al.* (2004) used similar methods to provide detailed findings regarding both monaural and binaural information available to *E. fuscus* for discerning the angular location of a sound source. However, in this work, a whole bat was used so as to include the influence of the entire body, rather than just the head or ears. The results demonstrated that the primary spectral null moves linearly from 30kHz to 55kHz with elevation angle increasing from -60˚ to 20˚, broadly agreeing with the observations of Wotton *et al.* (1995). The variation of notch frequencies with azimuth as well as elevation was also confirmed. Furthermore, the role of binaural cues was investigated for angular perception, with IID demonstrated to vary with both azimuth and elevation and so the authors proposed a model for sound localisation based on a combination of monaurally-generated cues, such as the notch frequencies, with binaural information such as IID. These studies documenting the HRTF of bats has therefore produced a greater understanding of the signal features, and therefore processing, that allow a bat to locate a sound source in space.

2.4.2 Modelling the Response of the Ears of Bats

Recently, a different approach has been introduced to investigate the response of bat ears. Rolf Müller, whilst working at the University of Southern Denmark, pioneered

a technique of using x-ray microtomography to scan the ear structure of a bat and therefore enable it to be rendered as a 3D CAD-compatible model. This allowed the response of the bat ear to be simulated, with Müller and his colleagues subsequently publishing a number of papers in this area as detailed in the following paragraphs.

The first publication, (Müller, 2004) examined the ear of *E. fuscus*, and specifically investigated the role of the tragus in sound field structure. The severed ear of a dead bat was scanned using a Skyscan 1072 (Skyscan, Kontich, Belgium) x-ray tomography scanner, which generated a series of 2D tomographic slices through the ear. After postprocessing, these images were stacked to generate a 3D representation of the ear. The directionality of the ear was examined using Finite Element Analysis (FEA) that simulated the ear as a loudspeaker, with an acoustic source located in the ear canal. The ear structure was placed in an air surround, which was itself limited in size to within the near field of the structure. This was done to limit computation time, but necessitated that the directivity in the far field was calculated through "forward projection" using a Kirchoff integral formulation. FEA itself was performed in the time domain, with the results obtained at the boundaries of the model being transformed into the frequency domain prior to the forward projection process. Interestingly, this would appear to be practically the same process as that used during validation of the FEA technique used in Chapter 6 of this Thesis (although the "forward projection" process is known as *extrapolation*). This process, then, allowed the directivity of the ear to be simulated. The role of the tragus was investigated by manually altering the elevation (angle) at which the tragus was inclined in the 3D representation (a cuboid of voxels that included the tragus was selected and rotated, with any gaps that were introduced filled accordingly).

With the forward projection method used, only directivity of the sound field could be calculated, and the aim of the publication was to examine the influence of the tragus position. It was demonstrated that the strength of an asymmetric side-lobe was dependent on tragus elevation; the location and shape of the sidelobes were also demonstrated to vary, though this was less significant. In the near field, where the time-domain characteristics of the wave could be investigated, side-lobe generation was linked to diffraction around the tragus. It was seen that the relative phase of the

wavefront on either side of the tragus would cause the interference required for side-lobe generation.

Similar methods were used by Müller *et al*. (2006) to investigate the response of the ear of the Chinese Noctule (*Nyctalus plancyi*). It was found that the influence of a prominent tragus and thicker lower edge of the pinna rim combined to produce a directivity pattern that varied with frequency, alternating between a strong mainlobe and conical arrangement of sidelobes, with this pattern caused by the phase of the wavefronts surrounding the tragus and pinna rim. Through use of digital manipulation it was also demonstrated that small movements of the pinna rim or tragus could be used to make considerable alterations to its beam pattern, thereby providing the bat with a method by which it could obtain acoustic information from varying spatial directions, to aid in location of a sound source.

Further publications followed, employing the same methodology. The ear of the brown long-eared bat (*Plecotus auritus*) was investigated (Müller *et al.*, 2008). A similar result was demonstrated, with a sidelobe of the ear directivity being scanned spatially in frequency, with a flap on the pinna identified as playing a pivotal role in its formation. This would therefore provide the bat with an indication of angular location of a sound source via spectral content of return echoes. Wang and Müller (2009) investigated the effect of the pinna-rim skin of the lesser false vampire bat (*Megaderma spasma*). Pinna rim skin in several species somewhat broadens the appearance of the base of the ears, but in *M. spasma* this rim forms a connection between the two pinnae above the nose of the bat. It was demonstrated that this skin causes the ear beamwidth to significantly decrease, generating small regions of high sensitivity that may be useful for detecting faint sounds or precise localisation.

The approach described in these publications is similar to that used in this work, described in Chapter 6. However, the method presented in this Thesis is extensively validated through comparison of simulated results with experimental results obtained from a 3D rendering of the bat ear through rapid prototyping techniques. Furthermore, the FEA performed during this work allowed the actual time domain signals that would propagate into the ear canal of a bat to be simulated. In this way,

the detailed signals (rather than directivity data only) could be investigated in a fashion that was not previously possible. It should be pointed out that the microtomography data that allowed the ear of a fruitbat (*Rousettus leschenaultii*) to be rendered physically and in the virtual FEA environment was very kindly provided by Rolf Müller himself.

2.5 Echolocation Call Reproduction

With the wealth of knowledge acquired on the echolocation signals and systems of bats, and the published details of their accuracy in perceiving their surroundings, it is surprising to find that research using such signals is almost non-existent. This is perhaps related to the difficulty of producing wideband ultrasonic signals in air. There are a variety of methods that are suitable for ultrasonic transduction in air (Manthey *et al*., 1992) including electrostatic, piezoceramic or piezocomposite, and piezopolymer devices, but most of these are narrowband and so unsuitable for generation of the wideband chirps of most echolocation calls. For example, piezoceramic devices have an acoustic impedance so mismatched with that of air (approximately 72000 times greater) that it greatly limits their use. Even composite piezoceramic devices with an added passive polymer phase that reduces the acoustic impedance of the device, struggle to achieve sensitivity in air without a suitable matching layer (Kelly *et al*., 2004). Such a matching layer allows great improvement of the device sensitivity, but its operating frequency is matched to that of the resonance of the transducer, thereby further limiting its fractional bandwidth (defined as the 3dB bandwidth divided by the centre frequency) to a few percent. Piezopolymer membrane transducers, such as PVDF (polyvinylidene fluoride) or copolymers of PVDF and trifluoroethylene, would appear to offer the capability for wideband operation, but these suffer from poor sensitivity (Takahashi and Ohigashi, 2009) and / or radial modes on the membrane surface thereby disrupting the field structure (Hayward *et al*., 2000). Recently, EMFi (Electro-Mechanical Film; Paajanen *et al*., 2000) has also been investigated for air-coupled transduction. EMFi is an electret film with a cellular internal structure. The charged dipoles within the electret mean that application of an external force generates a charge across the material as is the case with a piezoelectric material; conversely applying a charge

across the material generates mechanical deformation. One study in particular (Streicher *et al*., 1995) had the stated objective of producing a broadband transducer for bat echolocation research. However, although devices were manufactured and operation was demonstrated across the required frequency range, no production of wideband acoustic signals was documented, possibly due to its poor transmit sensitivity (Jimenez *et al*., 2008) requiring up to 600V drive to generate output signals in the regions of 100dB SPL (Streicher *et al*., 1995).

However, there is one type device that can achieve wideband transduction in air – the electrostatic transducer. Electrostatic (or capacitive) transducers with a solid backplate have long been used as a source of a generating and detecting ultrasound in air, since first described by Kuhl *et al*. (1954). The general construction of an electrostatic device has not altered much over the intervening period. The two main parts are the transmitting membrane, formed of a thin film (generally 1μm – 25μm) of polymer, and an electrically conductive backplate. The polymer membrane is held over or against the backplate, with the non-contact surface of the membrane being metallised. A constant bias voltage, typically hundreds of volts, providing direct current (DC) is applied between the metallised surface of the membrane and the backplate, generating an electrostatic force between the two, which attracts the membrane into contact with the surface of the backplate. This bias voltage also helps to linearise the device operation. Depending on the surface finish of the backplate, air pockets of varying size will be trapped between the membrane and backplate. The further addition of a time-varying voltage superimposed onto the bias voltage causes the electrostatic force to vary and hence the membrane to vibrate over the air-pockets, generating sound through direct contact with the molecules in the air. In reception, the inverse process occurs: pressure variations associated with an incident ultrasonic wave, cause the membrane to deflect, varying the average membrane/backplate separation, and hence generating a net capacitance change. This change, in the presence of the applied bias voltage, causes the charge on the device to vary, which can be amplified and measured via suitable electronic circuitry.

Many modern electrostatic devices (and related cMUTs covered later in this Section) are capable of generating wideband ultrasound. However, as recently as the early

1990s, most devices tended to be quite narrowband (e.g. Rafiq and Wykes, 1991; Oksanaen *et al*., 1997), with backplates having regular machined features, such as grooves. These regular features produced devices with relatively narrowband operation (typical fractional bandwidth of approximately 30%), whilst the depth and spacing of these grooves (100μm minimum) ensured that the centre frequency was relatively low (sub-200kHz). The operational characteristics of these grooved devices are well understood in terms of centre frequency, bandwidth and factors that affect sensitivity (Rafiq and Wykes, 1991; Hietanen *et al.*, 1993; Hietanen, 1998; Ge, 1999).

In general, the physical characteristics of the backplate and membrane can give a guide to its operating characteristics Schindel *et al*. (1995), with a thin membrane used in conjunction with a smooth backplate tending to produce a device with a high centre-frequency (up to 1MHz) and wideband response (approximately 100% fractional bandwidth). These devices, as well as those manufactured earlier by Suzuki *et al*. (1989), were based on silicon micromachining of the backplate in an attempt to regularise their response and achieve piston-mode operation and repeatability. It was considered that the "roughening techniques" applied to backplates to obtain operation above 200kHz (as opposed to the machining used below 200kHz) were not controlled enough to allow either repeatable operation, or investigation of the mechanisms of operation of the devices. Two devices were manufactured by Schindel *et al*. (1995) and demonstrated to have an almost identical frequency response, and were further characterised (Bashford *et al*., 1997) by having their emitted fields mapped, demonstrating very similar characteristics to piston-mode fields over a range of frequencies from 200kHz up to 1.5MHz; they had a centre frequency of approximately 900kHz and a stated 6dB bandwidth extending from <100kHz to 2.3MHz. These devices have subsequently been employed for a variety of purposes, ranging from traditional application areas such as surface profiling, damage detection in solids and detection of ultrasonic surface waves in solid plates (Schindel and Hutchins, 1995) to more recent activities such as evaluation of food materials (Pallav *et al*., 2009).

A close relative of the silicon backplate electrostatic transducer is the confusingly-named capacitive micromachined ultrasonic transducer, or cMUT. It can be appreciated that such a description could easily apply to the devices of Schindel *et al*.; indeed, prior to the introduction of the term cMUT, an early example of this type of transducer (Haller and Khuri-Yakub, 1996) was described as a "surface micromachined electrostatic ultrasonic air transducer". The cMUT, however, is manufactured and operates rather differently. Whereas the micromachined backplate transducers have a separate thin metallised polymer stretched across the backplate to complete the structure, cMUTs may be manufactured using silicon processing techniques that create the pit and membrane as part of the technique, with no separate membrane required. cMUT devices are manufactured via a series of deposition, oxidisation and etching processes that produce a series of small silicon nitride (coated with either gold or aluminium for conductivity) membranes supported on posts of remaining oxide material. The individual membrane dimensions are small, typically 10s of μm across with an air or vacuum gap (Hansen *et al*., 2004) of typically a few μm or less. As such, these devices tend to operate above 1MHz and are of limited interest for the application investigated here.

Development of traditional electrostatic transducers (i.e. those composed of a separate backplate and membrane, as opposed to cMUTs) has received less attention over the past decade or so, with many papers and developments referring back to the publications of Schindel and his colleagues. Recent work has included building focussed transducers, whether cylindrical (Robertson *et al*., 2002) or spherical (Song and Chimenti, 2006), or forming a number of individual electrostatic transducers into a 2D array (Blum *et al*., 2005).

However, the devices produced through silicon micromachining cannot be custom manufactured without access to specialised equipment. For that reason, the work reported here demonstrates a number of inexpensive and relatively simple designs of electrostatic devices that operate in a piston-mode fashion across the frequency range of interest, and beyond. The design and operation of these devices is detailed in Chapter 4, with their application to generating wideband echolocation calls and reproducing echolocation experiments with small cross-section targets reported in

Chapter 5. Not only does this work produce a transducer that is relatively inexpensive, but its operation has also been more thoroughly characterised through use of laser doppler vibrometry (LDV) techniques (to demonstrate piston-mode operation) and a calibrated microphone to measure absolute output pressure. As such, the operation of these transducers has been more fully characterised than anything that currently exists in the literature.

2.6 Summary

This Chapter has presented the technical background and state-of-the art in a number of fields that are covered within the scope of this Thesis. With regards to the following Chapters, wireless microphone sensors used to detect bat echolocation calls have been reviewed; Chapter 3 documents the design of a wireless ultrasonic sensor with biologically inspired automatic gain control. The nature of current air-coupled transducer technology has also been described; Chapter 4 details the design and characterisation of wideband electrostatic transducers, with the specific aim of reproducing bat echolocation calls in a laboratory environment. The lack of such replication in the literature has been discussed, and in Chapter 5 the electrostatic transducers are used with a spectral equalisation technique to accurately replicate a wide range of bat echolocation calls and biologically-inspired FM chirps. These signals are then used to investigate the acoustics involved in the wire-avoidance tests documented in the literature. Finally, publications investigating the bat head related transfer function and ear response have been discussed; in Chapter 6 a novel technique combining finite element analysis (FEA) with experimental validation is presented that can accurately and quickly provide a measurement of the transfer function of a bat's ear, with similarities to the HRTFs discussed previously. In combination, this multi-disciplinary approach will be demonstrated to offer a unique insight into the signals and systems associated with the wonder of bat echolocation.

CHAPTER 3

INVESTIGATING THE CALLS OF ROUSETTUS AEGYPTIACUS USING A WIRELESS SENSOR

3.1. Introduction

Bats use a range of echolocation signals, each designed to meet the specific requirement of the bat at that point in time. This can be seen in the way the signals are matched to either task (in the phases of predation) or environment (e.g. Schnitzler and Kalko, 2001). Hence it stands to reason that recording of the emitted echolocation signals will provide an insight into the echolocation process. As covered in Chapter 2, accurate recording of calls that are representative of those the bat uses for echolocation in flight is not trivial. This is due to a combination of factors: frequency-dependent directionality of the emitted call; frequency-dependent directionality of the microphone; frequency response of the microphone; and frequency-dependent attenuation of ultrasonic energy in air. Given these factors, *accurate* recording of an emitted call relies on the bat and microphone being oriented such that the more directional high-frequency components of the call are incident on the microphone. Essentially, the bat must be emitting its call directly towards the recording microphone, and the distance must be such that these high-frequency components are not lost due to attenuation - as an example, the attenuation of ultrasound in air rises from approximately $0.5dBm^{-1}$ at 20kHz to approximately $8dBm^{-1}$ at 200kHz (Bass *et al.*, 1995).

Because of these factors, restraining the bat in front of the microphone might be attractive. However this leads to the bat emitting calls that are not representative of those it would use whilst echolocating in flight (Waters and Jones, 1995), at least partly due to their calls being energetically coupled (Speakman and Racey, 1991; Lancaster *et al*., 1995). As such, recording of representative echolocation calls relies on the capability to capture these calls from the bat whilst in flight. One such method has been to deploy a miniature sensor on the bat (e.g. Lancaster *et al*., 1992; Hiryu *et al*., 2005) to detect the emitted calls and relay these via a wireless interface to be recorded remotely. This is the approach used here, although the design of the wireless sensor differs from those in the literature. Recent developments in the field have involved miniaturising the device (Hiryu *et al.,* 2007, 2008) for use with various small bats emitting CF or FM calls. However, the approach taken here has been to use a larger species of bat, which allows a larger and heavier sensor to be

designed. This additional size and weight has been used to design a sensor with variable gain to allow the echoes returning to the bat, as well as the emitted calls, to be recorded.

3.2. Wireless Sensor Design and Operation

3.2.1 Design Considerations

Designing a sensor which is capable of detecting both the emitted signal and the echoes which bats use in echolocation is a significant challenge in terms of the dynamic signal range of the sensor. This is further complicated with the requirement that the sensor has to be small enough and light enough to be carried by a bat. Emitted echolocation calls have been measured with a peak pressure in excess of 140 dB peSPL (peak equivalent SPL) in the field (Surlykke and Kalko, 2008), whilst 120dB SPL is commonly reported. Audiograms of bats indicate a hearing threshold (in common with most mammals) in the region of 0dB (Neuweiler *et al*., 1984; Koay *et al*., 2003). This 0dB limit represents the accepted level at which sound is detectable, rather than the level at which the sound becomes useful and useable to the bat. Furthermore, a flying bat will have to overcome environmental noise and masking generated by airflow into and around the ears; Surlykke and Kalko (2008) estimated this may set a useful threshold at approximately 20dB SPL, although there appeared to be no scientific validation for this figure. A variety of bats have been demonstrated as responding to acoustic stimuli ranging between 0dB SPL and in excess of 70dB SPL (Moss and Schnitzler, 1995). Certainly the dynamic range over which bats operate is significant – in excess of 100dB is possible between the emitted call and reflected echo. In terms of electronics, this represents an enormous dynamic range with which a sensor system may be required to cope to study the emitted call, as well as the echoes audible to the bat.

The intended test subject for the wireless sensor was the fruit bat *Rousettus aegyptiacus*, a member of the only genus within the suborder megachiroptera that echolocates. This species uses echolocation to navigate through the caves in which it roosts; in sufficiently light conditions, it uses both echolocation and visual clues for orientation. The echolocation signals of this bat generally consist of pairs of clicks

produced with the tongue, and have been described as “rudimentary” in comparison to the “specialized” signals employed by microchiropterans (Koay *et al.,* 1998), suggesting the echolocation system to be simpler. However, a study of the echolocation performance of *R. aegyptiacus* (Waters and Vollrath, 2003) indicates that its performance in wire avoidance tests is comparable to that of microchiropterans, in that it can detect the presence of wires with a cross section significantly smaller than the minimum wavelength of its echolocation signal. This study subjected several *R. aegyptiacus* individuals to wire avoidance tests using wires with a cross section of either 6mm or 1.3mm. Although the percentage of clear flights dropped with the 1.3mm wires, there was still evidence of the bat taking “evasive action” when approaching these wires in total darkness. This suggests that wires of approximately 1mm cross section are detectable by *R. aegyptiacus* using echolocation alone. This result agrees with an earlier study by Griffin *et al.* (1958) which indicated that a single *R. aegyptiacus* individual was capable of detecting wires with a 1mm cross section, and possibly even smaller. Since the signals used by *Rousettus* are wideband clicks, their frequency content is somewhat subjective. Waters and Vollrath (2003) indicate a peak output at 19kHz, with a relative energy level at least 30dB reduced from this above 60kHz. The highest frequency component useful to the bat is debatable, but given this result in combination with the measured audiogram (Koay *et al.*, 1998) it is certainly reasonable to suggest that no components above 60kHz will be useful. At 60kHz, the wavelength of sound in air is 5.75mm, considerably longer than the cross section of the detectable wires.

This species is fairly large and robust, which combined with its echolocation performance, make it an ideal candidate for flight experiments with a wireless microphone sensor. In terms of mass requirements, long term studies involving load carrying, such as using radio telemetry transmitters, should not impose more than a 5% increase in mass (Aldridge and Brigham, 1988). However, for short term laboratory-based studies, loads of up to 10% of the bat body mass should not impose any undue strain since gravid bats often reach a 20-30% increase in body mass in the latter stages of pregnancy (Korine et al. 2004). It was originally intended that future developments of the sensor would be aimed at smaller FM and CF-FM bats. As such,

the target frequency range for the sensor was 20kHz-200kHz, adequately covering the frequency range of calls emitted by these species.

Wireless sensors reported in the literature consist of a microphone coupled via a simple amplifier to a suitable oscillator for radio frequency (RF) transmission. Since the aim of this work was to produce a sensor capable of operating across a wide dynamic range, a simple fixed amplifier would not suffice. Research has indicated that some bats, such as *Myotis lucifugus* (Jen and Suga, 1975), *Tadarida brasiliensis mexicana* (Henson, 1965) and *E. fuscus* (Kick and Simmons, 1984), have evolved a mechanism which helps them to cope with the dynamic range between emitted and reflected signals. By contraction of the middle ear muscles just prior to emission of the echolocation call, a temporary reduction in sensitivity is achieved for the period of call emission itself. Furthermore this sensitivity is *gradually* restored as the muscles relax post emission, causing hearing sensitivity to increase as the return echo strength decreases due to propagation losses (Kick and Simmons, 1984; Simmons *et al*., 1991). Effectively, the bat employs gain control in order to regulate the perceived loudness of the returning echoes, at least over the first 3-5m. It would seem reasonable to assume that any bat that emits high intensity sound may use this process to avoid self-deafening by the emitted call and enhance its echolocation performance. Through use of a variable gain amplifier (VGA) and suitable control circuitry, this process can be recreated electronically. Additionally, the wireless sensors in the literature are not calibrated, or certainly it is not reported that they are. In order that the influence of the sensor on the signal it is designed to record is known, it is imperative that its response is known. With this in mind, the sensor designed and built for this work had each of its component parts fully characterised, and this process is also detailed in this Chapter.

3.2.2 Wireless Sensor Components

The main components of the sensor system were a microphone, instrumentation amplifier, VGA and voltage controlled oscillator (VCO) for transmission of FM radio frequency (RF) energy. In addition there was timing circuitry for control of the VGA and a battery. The microphone selected for use was the Knowles (Itasca, IL,

USA) FG3329 electret microphone, the same model as used by Hiryu *et al.* (2005, 2007, 2008). This device combines small size (2.5mmØx3mm) and mass (0.1g) with a useable sensitivity extending from the audible range to over 100kHz. The microphone also had no need for a biasing voltage due to its electret element and has very low power requirements (24μA at 1.3V). Manufacturer data indicates the device exhibits sensitivity of approximately -53dB re. 1V/μbar at 20kHz (-33dB re. 1V/Pa). Its response decreases beyond this frequency, but maintains some sensitivity above 100kHz making it applicable for use in this system. In the course of this investigation, it was shown that the response of this microphone is seriously impaired at frequencies above 130kHz, as will be discussed in Section 3.3.1. The microphone was coupled directly to an instrumentation amplifier, the AD623 from Analog Devices (Norwood, MA, USA), that provided an initial gain stage as well as common-mode noise immunity, at less than 500μA of current for 3V supply voltage. Variable gain was provided by the AD8330 VGA from Analog Devices, which manufacturer data indicates is capable of in excess of 100dB of variable gain, typically drawing 20mA from a 3V supply; gain through this device is set by the voltage level on two control pins. The amplified signal was then applied to a Maxim (Sunnyvale, CA, USA) MAX2606 VCO that can generate FM signals across a wide range of frequencies, including the commercial (88MHz – 108MHz) FM band. The sensor was completed by control circuitry and a battery. Control was provided by a timer circuit based on a National Semiconductor (Santa Clara, CA, USA) LM761 comparator and the Texas Instruments TLC555 device. Finally, the battery selected for use with the sensor was a 3.6V nickel-metal hydride (Ni-MH) rechargeable cell. The high level of current required (mainly attributable to the VGA) necessitated the higher energy density of the Ni-MH cell, as opposed to lighter technologies such as silver-oxide or zinc-air. By using the Ni-MH cell, the sensor can be powered for more than 20 minutes between charging, which is sufficient to conduct flight tests in captivity. Two circuit diagrams of the sensor are illustrated in Figure 3.1, with part (a) illustrating the signal flow more clearly, while part (b) gives a more detailed illustration of the circuit.

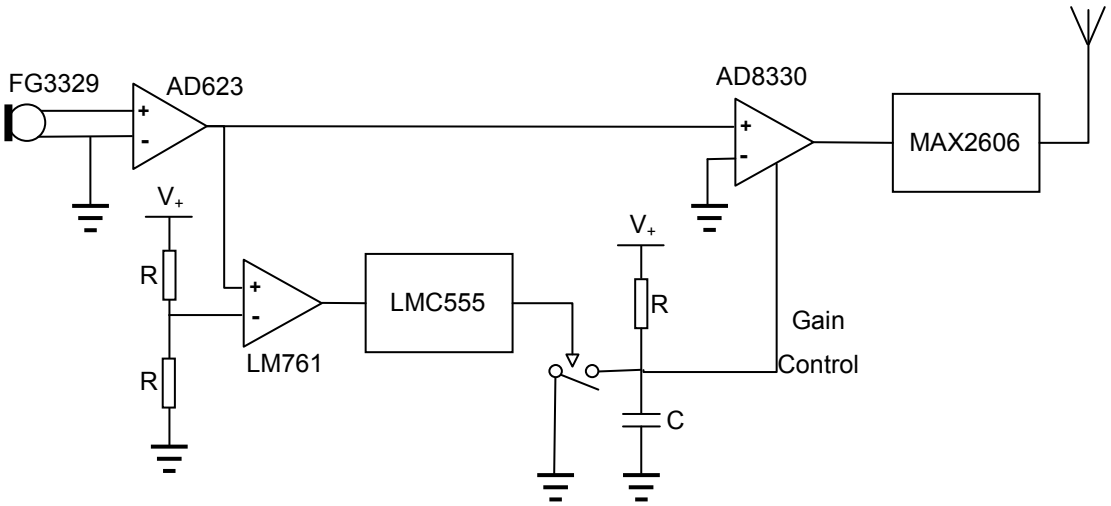

(a)

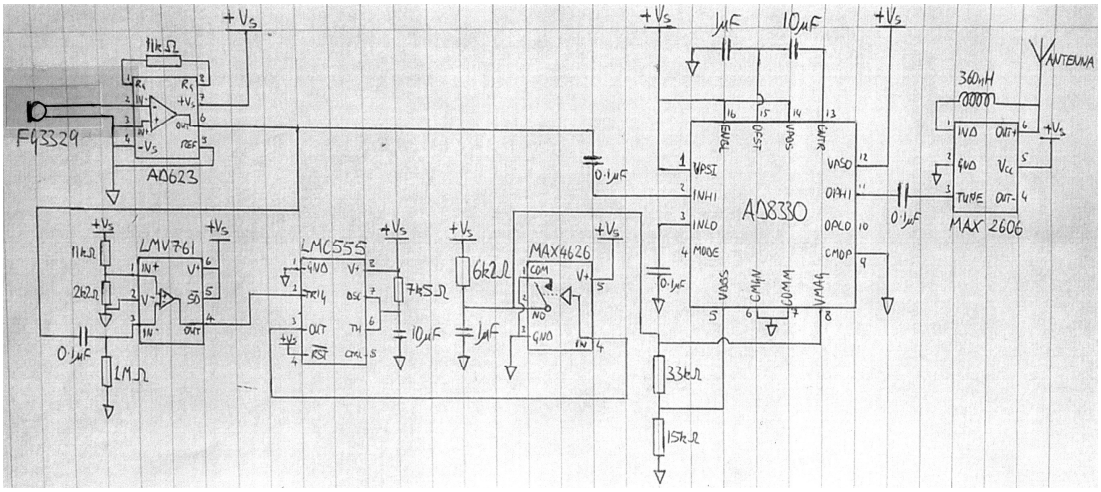

(b)

Figure 3.1. Circuit diagrams of sensor: (a) for clarity of signal flow; and (b) showing the full circuit diagram.

3.2.4 Wireless Sensor Operation

The sensor operates as follows: it is set to its lowest gain as the default state; when an emitted echolocation call is detected by the microphone, this signal triggers the timing circuit which switches in a resistor / capacitor (RC) charging circuit for a user-defined time period. The charging voltage drives the gain-control pins of the VGA, providing time-varying gain through the device; these amplified signals are then used to drive the VCO. Hence, echo signals are subjected to additional gain dependent on their time of arrival, as is the case with the gain control mechanism seen in the auditory pathway of bats. The level of gain variation and time over which

this is applied is programmable through component selection. Importantly, the time of emission of the echolocation call provides a reference point, since it is the emitted call that triggers the rise in gain to be initiated. The gain characteristic is defined and repeatable.

Targeting *R. aegyptiacus* meant that a weight limit of 10g was imposed; the actual sensor weighs 6.8g, with 4.0g attributable to the battery. The prototype wireless sensor is pictured in Figure 3.2, with attached whip antenna for FM transmission. The transmitted FM signal was received by a standard FM tuner (Philips, model FT930), used in one of two ways: firstly without modification; and secondly by using a custom-built phase locked loop (PLL) circuit to demodulate the 10.7MHz Intermediate Frequency (IF) signal generated by the RF-IF mixer. Using the tuner without modification, the demodulated signal was extracted prior to baseband filtering and allowed signals up to approximately 100kHz to be received. The addition of the PLL circuit provided the capability to demodulate signals across the full 20kHz-200kHz range. The performance of the sensor and tuner (in both modes of operation) is detailed in the following section.

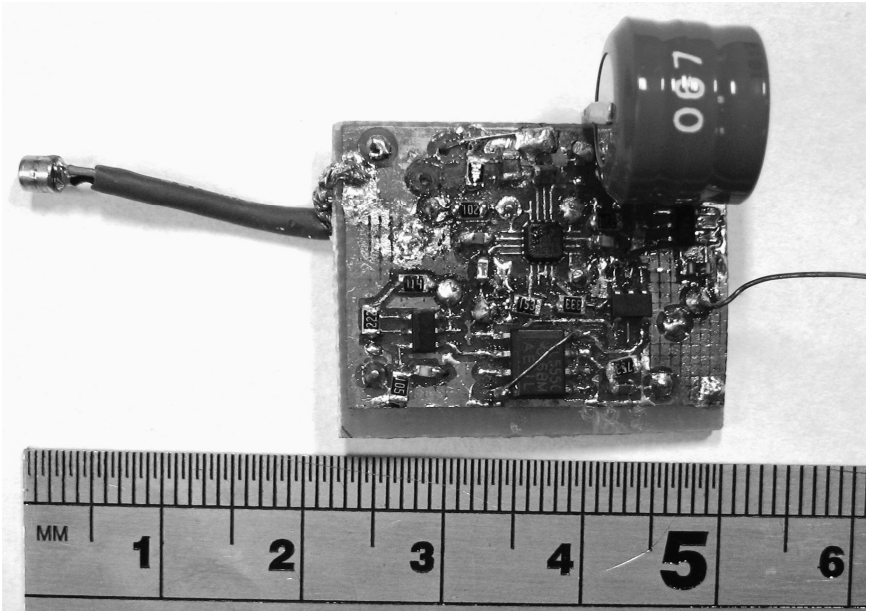

Figure 3.2. Wireless sensor, with rule for scale.

3.3 System Calibration

To gain an understanding of how the received signals would be affected by the sensor, its response, and that of its constituent parts, were characterised in the laboratory. Since it was intended that further development would enable the sensor to be used with FM bats, a larger frequency range than was necessary for *R. aegyptiacus* was considered. Hence, the sensor response has been examined up to 200kHz.

3.3.1. Microphone Calibration

The FG3329 microphone has been characterised by the manufacturer up to 50kHz: its response is flat to within ±1dB between 1kHz and 20kHz, with a sensitivity of -53dB re. 1V/µbar. It is predicted by the manufacturer that the response will roll off beyond this point at approximately 10dB per octave (33dB per decade) to have a sensitivity of approximately -88dB re. 1V/µbar at 200kHz. This however, was extrapolated data and required verification.

Microphone characterisation was performed using the substitution method: the transmission frequency response of a custom-built wideband electrostatic transducer (see Chapter 4) was measured using a calibrated Brüel & Kjær (B&K) condenser microphone (Type 4138) with a calibrated Nexus 2690 preamplifier. The FG3329 electret device was then substituted to ascertain its frequency response. The calibration was carried out by driving the electrostatic transducer with a series of narrowband toneburst signals. This process was automated using LabVIEW (National Instruments, Austin, Texas, USA) to configure an Agilent 33120A Arbitrary Function Generator (AFG), while the received signal was captured from a Gage analogue to digital converter (A/D) card, also under the control of LabVIEW. Figure 3.3 displays the results of this test, firstly comparing the calibrated response of the transducer (measured using the B&K device) with the response from the FG3329, then displaying the calculated response of the FG3329 microphone. These results indicate a roll off of approximately 6dB/octave between 20kHz and 120kHz, with a steeper roll-off above this and profound nulls at approximately 150kHz and approximately 170kHz. This will restrict sensor use to below approximately 120kHz.

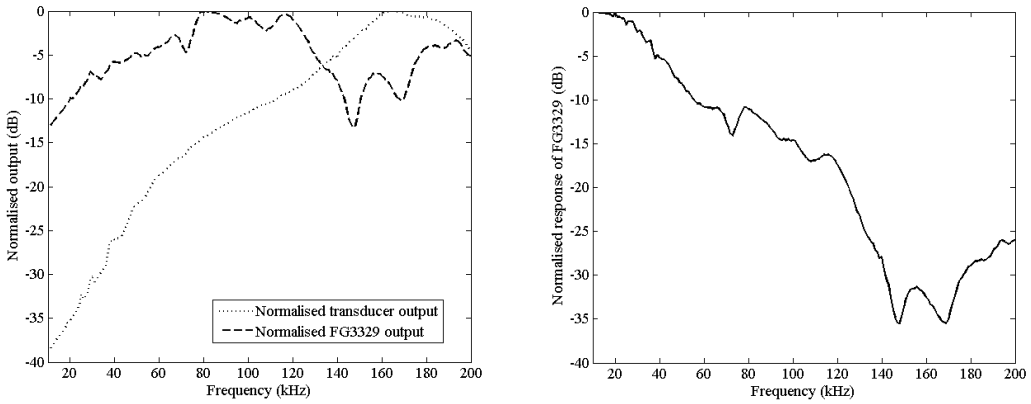

(a) (b)

Figure 3.3. Calibration of FG3329 microphone response using the substitution method: (a) normalised output of electrostatic transducer calibrated with B&K Type 4138 microphone vs. response from FG3329; (b) calculated response of FG3329.

3.3.1.1 Microphone Case Modal Analysis

The null in the response of the Knowles microphone is not predicted by the manufacturer. It was hypothesised that a resonance set up in the case of the microphone may be responsible for the null, and this was investigated using COMSOL Multiphysics Finite Element Analysis (FEA) software (Comsol, Burlington, MA, USA). COMSOL Multiphysics allows the user to build a structure that may have a variety of physical phenomena occurring within it, and simulate their effect. In this case, COMSOL was used to carry out a modal analysis of the cylindrical microphone case. Modal analysis allows the natural vibration "modes" within a structure to be found, providing the frequency and vibration shape of each mode. By subjecting the structure of the microphone case to this analysis it can be found whether natural resonances within the case itself are responsible for the considerable reduction in output amplitude at 150kHz – 170kHz. It should be noted that these resonant modes are a product of the dimensions of the case itself, and are not in any way related to the electronic operation of the microphone components. As such, the parameters of interest are the dimensions of the microphone casing.

The specifications of the microphone case were provided by the manufacturer. It was constructed of type 305 stainless steel with a thickness of 0.127mm. The case was cylindrical in design with an external diameter and length of 2.565mm. Using these measurements, a cylinder of air of the dimensions within the microphone case

(2.311mm in diameter and height) was created, with the boundaries simulated as a solid wall. Modal analysis of this structure predicts modes of vibration as illustrated in Figure 3.4, where the colours indicate local variation of pressure, from low (blue) to high (red). As such, it can be seen that COMSOL predicts a half-wavelength resonance across the height of the case (a) at 74kHz, a full-wavelength mode at twice this frequency (b) and a radial mode at 180kHz (c). The author would like to express his gratitude to David Mackie for construction of the COMSOL model.

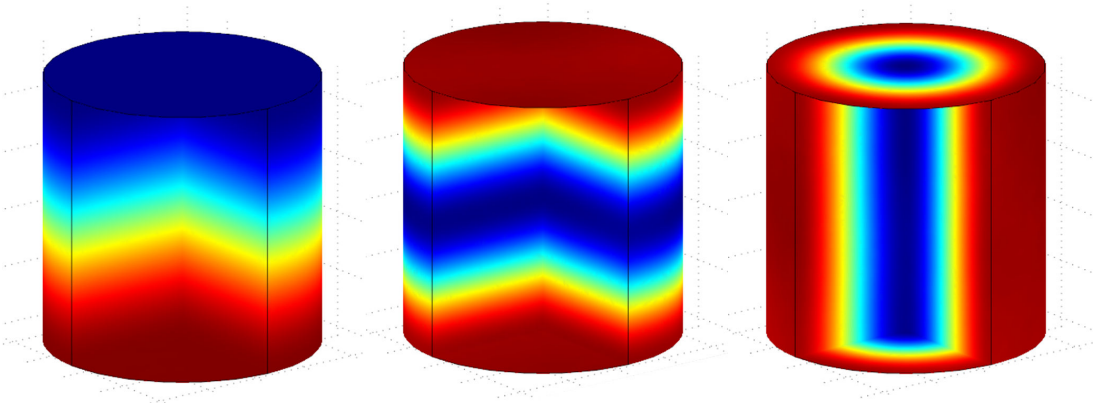

(a) (b) (c)

Figure 3.4. Vibrational modes of the microphone case as predicted by Comsol: (a) half-wavelength resonance across the height of the case at 74kHz; (b) single wavelength resonance across the height of the case at 148kHz; (c) wavelength resonance across the diameter of the case at 180kHz.

On examination of Figure 3.3, it can be seen that the higher frequency modes, at 148kHz and 180kHz, correlate well with the double-null observed in characterising the microphone, at 147kHz and 170kHz. Furthermore, the lower frequency mode predicted at 74kHz also agrees well with another dip in microphone sensitivity observed at 72kHz. This result indicates that resonant modes in the case are indeed responsible for the reduced sensitivity in these regions. The internal height of the microphone case is 2.311mm, which if set as the wavelength, corresponds to a frequency of 148.5kHz assuming $c=343ms^{-1}$ for the speed of sound in air. Given that the diameter of the case is the same as its height, then the wavelength (radial) resonance across that dimension is at a similar frequency, though apparently modified by the circular cross section of the case. It can be seen that, even though these reductions and nulls in the response were not predicted by the manufacturer, simple analysis of the structure would indicate that resonant activity within the case

would have some effect at these frequencies. This correlated well with the experimentally measured operation of the microphone being limited to approximately 120kHz. However, for the calls of *R. aegyptiacus*, the microphone covers more than sufficient bandwidth.

3.3.2. Variable Gain Amplifier Characterisation

The selected VGA (AD8330) has a constant bandwidth of 150MHz for all available levels of gain, and so is not a factor in the frequency response of the sensor; this was verified experimentally. However, its dynamic gain performance is of crucial importance to the operation of the sensor.

As stated previously the gain of the device is controlled via two control pins, VMAG and VDBS. The total gain (ratio) through the device is defined by the manufacturer:

$$A_V = \frac{VMAG}{0.5} 10^{\left(\frac{VDBS}{0.6}\right)} \tag{3.1}$$

Assuming a nominal 3V supply, VMAG can be driven by the full supply voltage, while VDBS is limited to 1.5V. By driving these two pins simultaneously (varying VMAG over the range 1mV – 3V, while VDBS receives half that) the gain has a theoretical range of over 100dB, as illustrated in Figure 3.5.

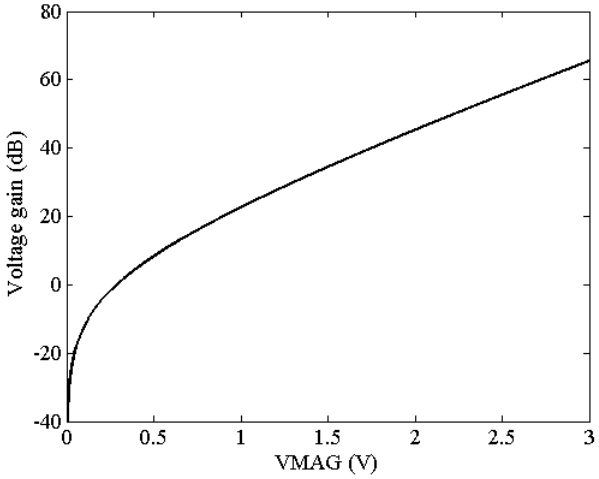

Figure 3.5. Theoretical variation of gain through the AD8330 variable gain amplifier indicating over 100dB of user-programmable gain variation.

The practical gain range is limited by the configuration of the gain control circuit and the lowest magnitude of signal which can drive the VCO. For these reasons, the sensor was configured such that VMAG was varied from 56mV – 2.75V, while VDBS was limited to VMAG/2.75, or 20mV – 1.0V. This provided a gain range of -27dB to +40dB, a variation of 67dB. This was the same variation predicted by Equation (3.1), although experimental data are some 10dB reduced from the absolute values predicted. This is due to the signals being single-ended rather than differential, as well as loading effects on the amplifier output. This difference is illustrated in Figure 3.6, where theoretical and measured values are plotted over the gain range. Since this gain curve is generated by the repeatable charging characteristic of the RC circuit, the gain through the device can be predicted at each point in time, with the emitted bat call as the reference.

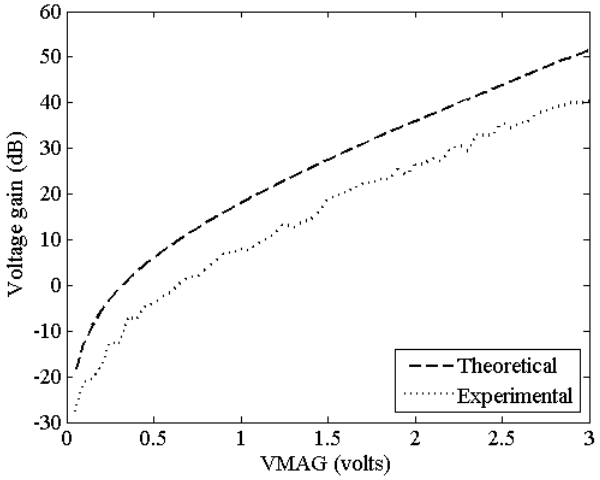

Figure. 3.6. Theoretical and experimental values of voltage gain through AD8330 plotted against voltage applied to VMAG pin, with VDBS = VMAG/2.75.

3.3.3. Wireless Electronic System Characterisation

The VCO that facilitated FM transmission from the sensor had a low-pass response and also required characterisation. Its response can be considered in conjunction with the sensor amplifiers (although these have a flat response over the frequency range of interest) and FM receiver to obtain a response for the electronic and wireless section of the system – only the microphone is not considered here. In some respects, the low-pass characteristic of the VCO is actually useful, since it reduces high-frequency noise in the transmitted signal. Characterisation was achieved with a

similar automated process to that used with the microphone, driving the sensor instrumentation amplifier with a series of single-frequency tonebursts, and capturing the demodulated signal via the A/D card. The gain through the VGA was set to approximately 0dB. Demodulation was performed with the FM tuner, used in the two ways described at the end of Section 3.2.4: firstly without modification; and secondly using the PLL demodulation circuit. The response of the system is illustrated in Figure 3.7. It can be seen that the wideband response of the system is considerably improved with the PLL demodulator, although the response of either method, in conjunction with the microphone response, will lead to significant emphasis of signals at the lower end of the ultrasonic frequency range.

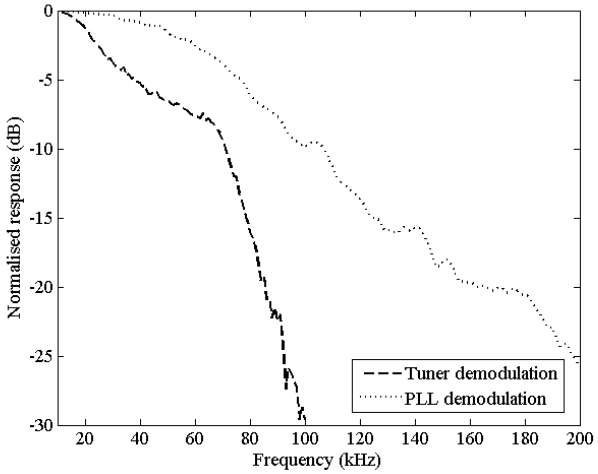

Figure 3.7. Frequency response of the RF system, using either the in-built circuit in the FM tuner, or a custom built PLL circuit, to demodulate the 10.7MHz IF signal.

3.3.4. Full sensor characterisation

To demonstrate the response of the whole sensor system, the substitution method was again used, employing the calibrated electrostatic transducer as the acoustic source. The VGA was configured to have a static gain of approximately 0dB and the wireless interface was used to transmit the signals, which were received using the FM tuner with and without the PLL demodulator as previously described. This resulted in the frequency response depicted in Figure 3.8. With the unmodified tuner, signals above 100kHz were not detectable, while the PLL demodulator extended this range somewhat. It can be seen by comparison with the results in the previous sections, that the response is dominated by that of the wireless system below

100kHz, while the significant reduction in sensitivity above 120kHz is due to the microphone response.

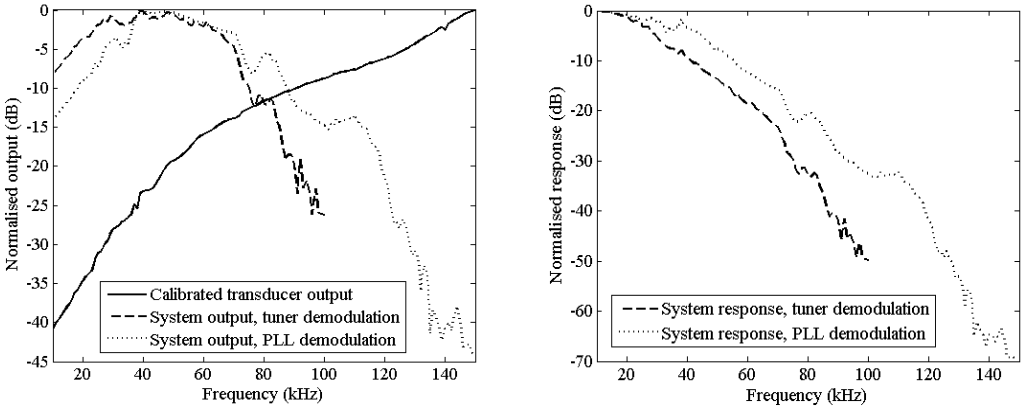

(a) (b)

Figure 3.8. Calibration of the full sensor system response using the substitution method: (a) response of the system compared with calibrated transducer response; (b) calculated response of system using in-built tuner demodulation and PLL demodulation.

Since, it is preferable the system has a flat response it could be equalised through use of a high-pass filter on the wireless sensor. This was disregarded as it would necessarily reduce the sensitivity at lower frequencies which was deemed imprudent in an application where SNR may already be limited. Since the application was dynamic, methods for improving SNR, such as averaging, were not applicable.

3.3.5. System Testing

It has been shown that the sensor system is capable of detecting ultrasonic signals and relaying these via its FM interface to a receiver for digitisation and storage. However, to have confidence in the design, the fidelity of the system to both emitted and reflected signals was tested. The calls of *R. aegyptiacus* consist of pairs of "clicks" produced by the tongue. This typically creates pulses of a few cycles in length with peak energy at approximately 19kHz (Waters and Vollrath, 2003). Most energy (-6dB) is concentrated in the 15-25kHz band, with little energy (-15dB) below 15kHz or above 40kHz. The peak pressure expected is in the region of 100dB SPL. For this reason, testing of the sensor was carried out with 10-cycle tonebursts at a range of frequencies up to 50kHz, generated by the same calibrated transducer as

used previously, delivering a peak SPL of approximately 100dB at 100mm. A vertical steel bar with a square cross section of 10mm located approximately 1.4m from the transmitter was used as a target. The sensor and B&K microphone were located approximately 200mm from the emitter, in the path of acoustic energy between emitter and target. The signals detected using both the wireless system and B&K microphone were captured using a digitising oscilloscope. This configuration, depicted in Figure 3.9, was designed to test the response of the sensor to direct and reflected signals allowing the variable gain functionality to be demonstrated.

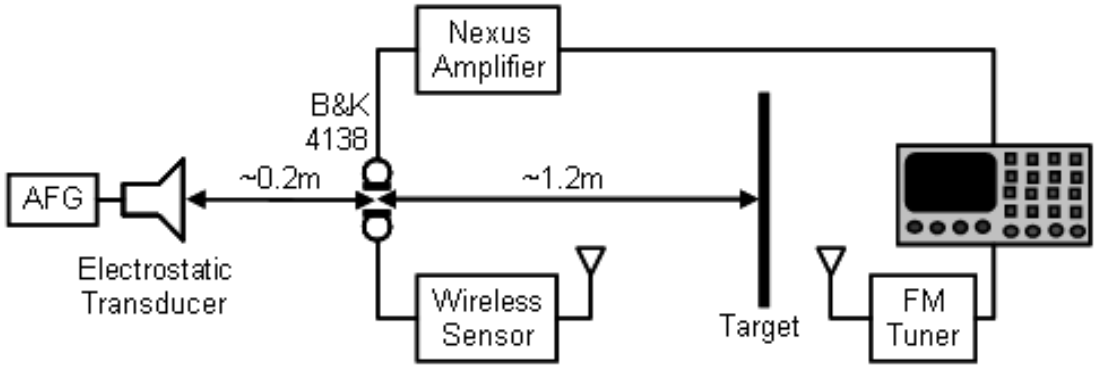

Figure 3.9. Experimental configuration of test for wireless sensor.

Waveforms resulting from the test carried out with a 40kHz toneburst are depicted in Figure 3.10. Figure 3.10(a) depicts the response from the B&K microphone and wireless sensor to both emitted and reflected signals; the wireless sensor output is magnified 30 times, and both signals DC-shifted for clarity of display.

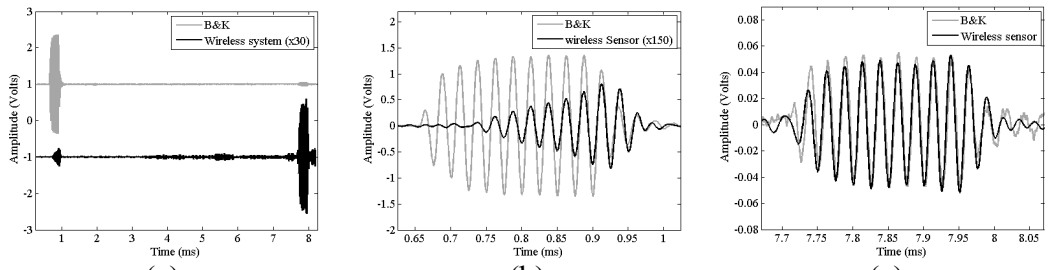

(a) (b) (c)

Figure 3.10. Signals from laboratory testing of the wireless sensor demonstrating fidelity of the detected signal and dynamic gain performance. Also shown are signals obtained with a calibrated B&K Type 4138 microphone, for comparison: (a) emitted and reflected signals (both DC level-shifted, with the wireless signal amplitude multiplied by 30 for clarity); (b) emitted signal (wireless signal amplitude multiplied by 150 for comparison); (c) signal reflected from target.

It can clearly be seen how successfully the variable gain performs from the comparative amplitude of emitted and reflected signals from each detector. The drop in amplitude from transmitted to reflected signal is in the order of 30dB, as illustrated by the reduction in B&K microphone output between these signals. Figures 3.10(b) and (c) show the transmitted and reflected signals in more detail, and it can be seen how accurately the wireless sensor detects the acoustic signal by comparison with the trace from the B&K microphone. The effect of the variable gain is plainly visible in Figure 3.10(b), in the increasing envelope of the signal from the wireless system. Obviously this configuration has a detrimental effect on the wireless recording of the emitted signal, and for this reason the sensor was redesigned. By placing an additional TLC555 timer IC immediately prior to the one already on the sensor, the "initial gain" setting could be maintained for a user-defined period. After this time, the second TLC555 device switched in the charging circuit to vary the gain through the VGA as already described. With this modification, the test was repeated with the results displayed in Figure 3.11. Again, part (a) depicts the response from both systems with a DC-offset and the wireless signal amplified for clarity of display, with parts (b) and (c) comparing the transmitted and reflected signals obtained with each system. The sensor was configured to have a gain variation of approximately 45dB between its lower and upper limits, in order to preserve the clarity of the signals displayed in Figure 3.11(a). The accuracy of the wireless sensor is evident from the correlation between its output and that of the B&K system. It should be noted that no averaging of the resulting waveforms was performed, since the sensor is designed for use in a dynamic environment where this would simply not be possible.

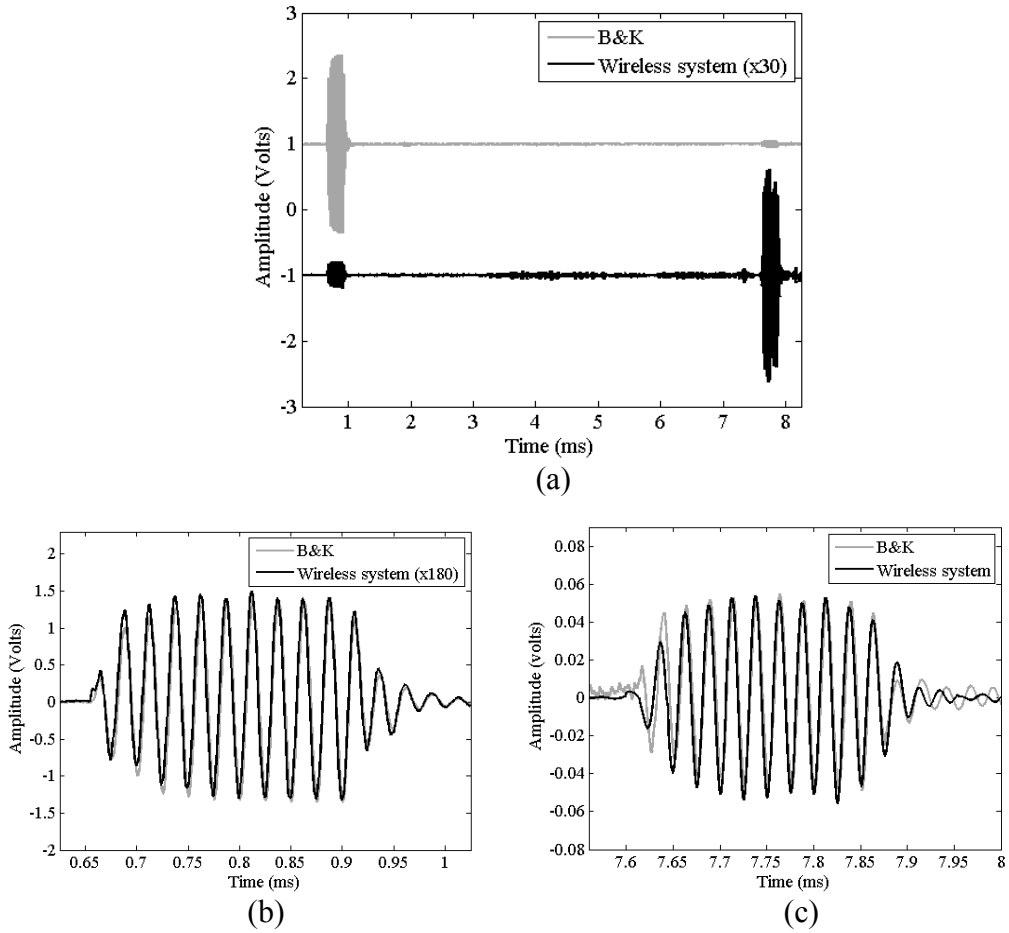

Figure 3.11. Signals from laboratory testing of the wireless sensor after addition of the second TLC555 timer device. Also shown are signals obtained with a calibrated B&K Type 4138 microphone, for comparison: (a) emitted and reflected signals (both DC level-shifted, with the wireless signal amplitude multiplied by 30 for clarity); (b) emitted signal (wireless signal amplitude multiplied by 150 for comparison); (c) signal reflected from target.

3.4. Capturing signals from *R. aegyptiacus* in flight

Six *R. aegyptiacus* individuals were loaned from Tropical World, Leeds and maintained on a 12h light, 12h dark reversed photoperiod, in a cage provided with fruit and water throughout their stay. Experimental flights were conducted in a 14m × 2.5m × 1.5m corridor situated adjacent to the room containing the cage. A mesh suspended at one end of the corridor served as an artificial roost, while a 100mm diameter metal planar disk was suspended as an acoustic target halfway along the corridor. Each bat performed up to 16 flights along the corridor. The sensor was attached to the bat using Velcro, with one piece attached dorsally, between the shoulders of the bat, while the mating piece of Velcro was attached to the underside

of the sensor. This method was used rather than a more permanent means, as the sensor required removal for battery replacement after 20 minutes of operation. The sensor mounted on the bat can be seen in Figure 3.12. All handling of the bats was performed by a colleague from the University of Leeds, Dr. Dean Waters. For this, and all his invaluable help in organising and carrying out these tests, the author would like to extend a great deal of gratitude.

Figure 3.12. *R. aegyptiacus* with wireless sensor mounted dorsally, between the shoulder blades.

The FM signal transmitted by the sensor from the bat in flight was picked up by two receiving FM antennas placed on the floor of the corridor. Two antennas were used to improve the reception quality of the signal as the bat flew along the corridor. The demodulated acoustic signals from the FM tuner were digitised using a National Instruments 6251 USB A/D converter, at a sampling rate of 400 kHz and 16 bit resolution using a routine written in LabView. Simultaneously, video data were recorded using a Kodak SR-500 Motion Corder high speed video camera at 500 frames per second. The acoustic and video data capture was triggered by a manually generated trigger from a Thurlby Thandar TGP110 pulse generator. The flight corridor is shown in Figure 3.13, with acoustic target, artificial roost, FM antennas and video camera plainly visible.

Figure 3.13. Photograph of the corridor in which flight tests were conducted, showing video camera, antennas and circular target.

With *R. aegyptiacus* producing a double-click echolocation call approximately every 86ms (Waters and Vollrath, 2003), there was the potential for gathering large amounts of data on each 3s flight recording. In practice, not all flights produced noise-free recordings. The corridor where the flights took place was not electromagnetically screened, which meant that interference from FM radio stations was an issue. In configuring the sensor, care was taken to set the centre frequency of the VCO to a region where there was no radio station present by adjusting the DC level fed to the Tune pin of the VCO. However, as the battery drained over its 20-minute life cycle, the DC level would drop causing the centre frequency of the VCO to decrease. Hence as tests with each battery progressed, the tuner was retuned to follow the VCO frequency and ensure reception of the sensor signal. This meant that the signal could come into the same frequency band as a radio station, causing interference. Another cause of interference was that heavy plant machinery was being operated on site, which caused intermittent interference throughout the

experiments. Despite these factors, many recordings were made in suitable conditions, with over 700 individual calls identified in recordings. The sensor was operated in either of two modes: static gain mode, where the gain control voltage was set to provide fixed gain through the VGA; and variable gain mode, where the gain control voltage was controlled by the timer and RC charging circuitry.

3.4.1. Static gain recordings

Although the sensor was designed to operate with variable gain, the majority of the recordings were made with the sensor in static gain mode. It can be seen by referring to Figures 3.10 and 3.11, that variable gain mode necessarily reduces the sensitivity of the sensor to the emitted call since the sensor is configured for low gain at emission. To allow accurate recordings of the emitted calls to be made with the best available signal to noise ratio (SNR) required the sensor to be used with an optimal level of static gain. The optimum gain was set during laboratory configuration such that the maximum signal was generated at the VCO (without overdriving it and causing distortion in the transmitted FM signal) for the expected level of emitted acoustic signal.

As noted previously, the recording conditions in the corridor were not ideal, with electromagnetic interference producing noisy recordings in a number of cases. Furthermore, if the bat was flying in close proximity to a reflecting object, the recorded echolocation signal may not appear clean but have overlapping echoes, even with the sensor in static gain mode. In addition to this, it became clear during preliminary examination of the data that differences were detectable between the first and second calls within a pair. For these reasons, not all calls detected by the sensor have been included for analysis. Specifically only interference- and echo-free *pairs* of calls were selected for analysis. This allowed any difference between the first and second calls to be examined and also allowed the timing within a pair of clicks (intra-pair), and between successive pairs (inter-pair), to be measured. Given these criteria, a total of 362 pairs of clicks were selected for analysis. A typical example of a recording is displayed in Figure 3.14, as described in Section 3.4.1.2.

The calls recorded from each bat revealed some differences in the calls emitted both between bats and also within individuals. The general structure and specific details of these differences will be covered in the following sections. Four bats yielded useful data from the static gain sensor, here labelled bats 1, 4, 5 and 6; these will be covered in order.

3.4.1.1 Static gain recordings – call statistics

The four bats that provided useful echolocation data performed a total of 49 flights, of which 40 contained useable data. The data from each bat was analysed separately, as call characteristics were shown to differ between individual bats. Table 3.1 displays the number of runs, number of runs that yielded useful data, number of call pairs and the mean intra- and inter-pair call intervals for each bat.

	No. flights	Useful flights	No. call pairs	Mean interval (ms ± S.D.)	
				Intra-pair	Inter-pair
Bat 1	6	4	32	26.7±3.8	124.3±21.7
Bat 4	13	12	112	26.9±3.3	115.0±30.4
Bat 5	16	13	149	21.9±2.7	112.6±24.8
Bat 6	14	11	69	29.1±4.6	132.4±30.5
All Bats	**49**	**40**	**362**	**25.3±4.5**	**117.6±27.4**

Table 3.1. Echolocation call statistics for each bat, and all bats combined.

In terms of call timing it can be seen that both the intra- and inter-pulse intervals are longer than recorded by Waters and Vollrath (2003). However, the figures quoted in that paper are based on a small sample (n = 7) and furthermore, the bat was faced with a wire avoidance task. This may have induced an increased frequency of call emission to tackle a more complex echolocation environment. It is interesting that the calls are almost always emitted in pairs, as is generally the case within this genus. This means that the unambiguous range for any return echo is different depending on whether it originated from the first or second call of the pair. Taking average figures from Table 3.1, the unambiguous range for the first call is 4.3m ($25.3ms/2\times345ms^{-1}$), compared with 15.7m ($117.6ms/2\times345ms^{-1}$) for the second.

3.4.1.2 Static gain recordings – call analysis

As previously stated, *R. aegyptiacus* emits calls as a series of double clicks. This characteristic pattern can be seen in the second half of Figure 3.14(a), which depicts 2s of data recorded using the wireless sensor with bat 1 flying in the corridor.

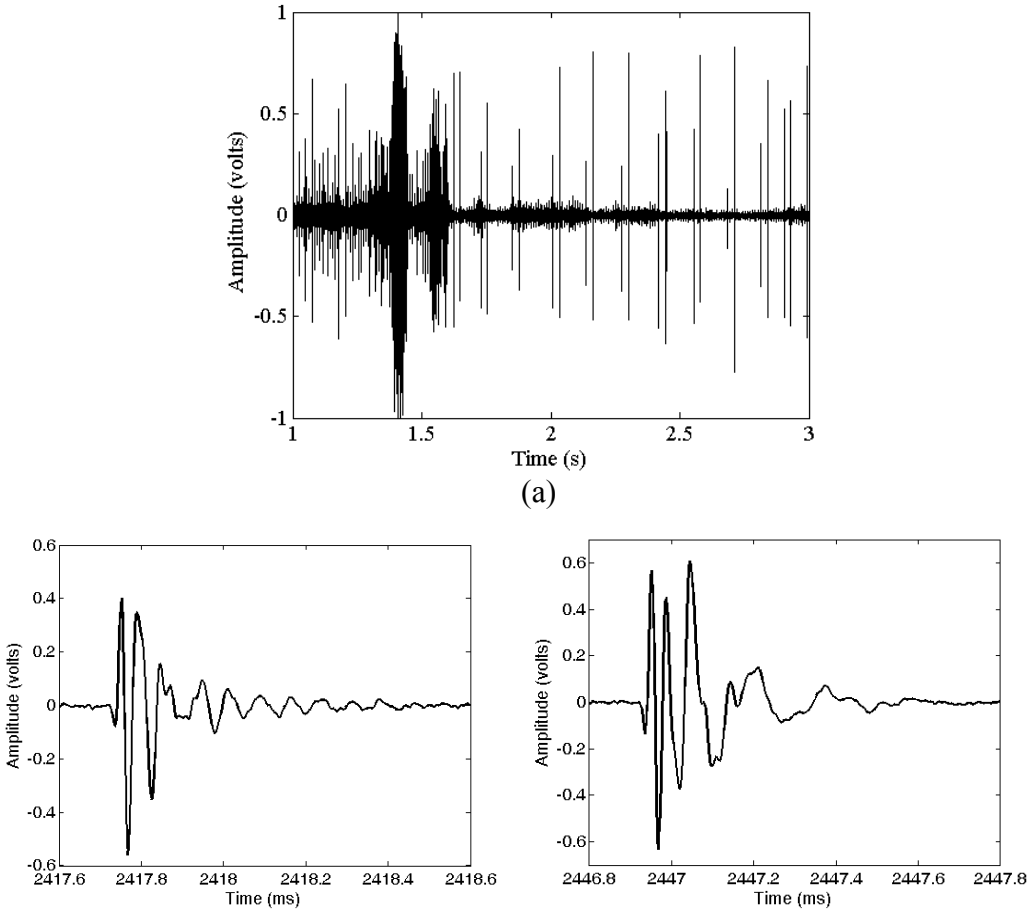

Figure 3.14. Echolocation signals captured using the wireless sensor mounted on bat 1 whilst in flight: (a) sequence of double-click calls; (b) expanded image of first call from double click; (c) expanded image of second call from double click.

As with many flights there is significant interference present, but the section from approximately 1.7s-3s contains a sequence of ten double-clicks recorded with usable clarity. For brevity and to avoid repetition, similar sequences are not reproduced here for each bat. This sequence is representative of those gathered on each flight, with sections of useful data and sections of interference from which no calls were analysed, even if detectable in the noise. Figures 3.14(b) and (c) depict a representative example of the first and second click within a pair for bat 1. It can be

seen that these signals differ somewhat, with the second call having more low frequency content, especially noticeable toward the end of the trace. Fourier analysis of each call indicates that this difference is consistent enough to be evident in the average spectrum of the odd- and even-numbered calls (first and second clicks within each pair) as illustrated in Figure 3.15.

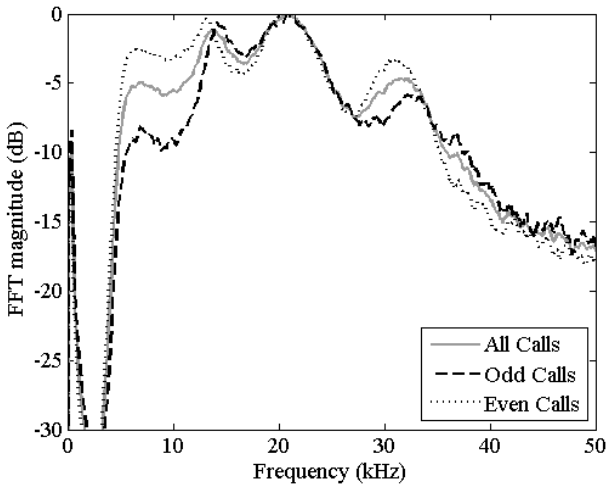

Figure 3.15. Magnitude of the FFT of calls emitted by bat 1, illustrating difference in frequency content between odd- and even-numbered calls.

There are subtle differences in the calls produced by each bat, and this is can be seen in both the time and frequency domain. Figures 3.16 – 3.18 give representative examples of odd- and even-numbered calls produced by each of the three other bats, alongside the average magnitude of the FFT of these calls. It can be seen that each of these three bats has a significant low-frequency component at approximately 1kHz, which is particularly evident in the second call of each pair. The FFT illustrates that even-numbered calls have increased low frequency content on average; this is evident even with bat 1, though its calls have no 1kHz component. It should be noted that the average FFT spectra are normalised, and so the increase in low-frequency content is illustrated either by the low-frequency components appearing stronger on the plot (bats 1 and 4) or in a relative decrease in the strength of the higher frequency components (bats 5 and 6). In comparing calls within bats it is clear that the presence of increased low-frequency content has little or no effect on the higher frequency components. Rather, the higher components are superimposed on top of the low-frequency one. This can plainly be seen in the time domain signals of bats 4-6.

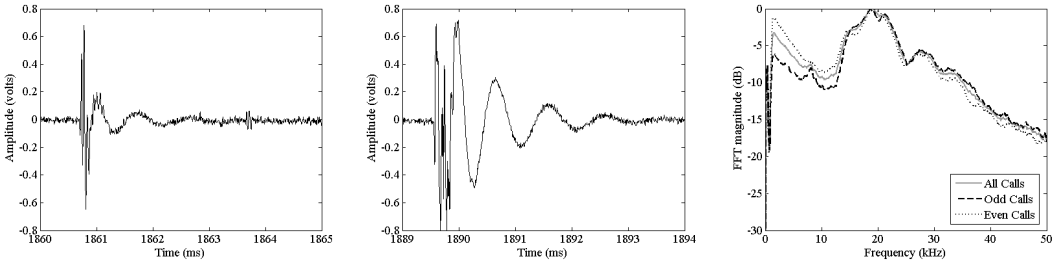

(a) (b) (c)

Figure 3.16. Calls recorded from bat 4 whilst in flight using wireless sensor: (a) representative example of an odd-numbered call; (b) representative example of an even-numbered call; (c) frequency content of calls from bat 4.

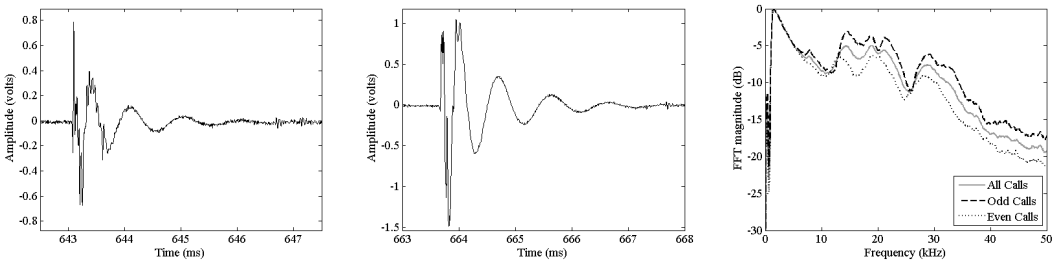

(a) (b) (c)

Figure 3.17. Calls recorded from bat 5 whilst in flight using wireless sensor: (a) representative example of an odd-numbered call; (b) representative example of an even-numbered call; (c) frequency content of calls from bat 5.

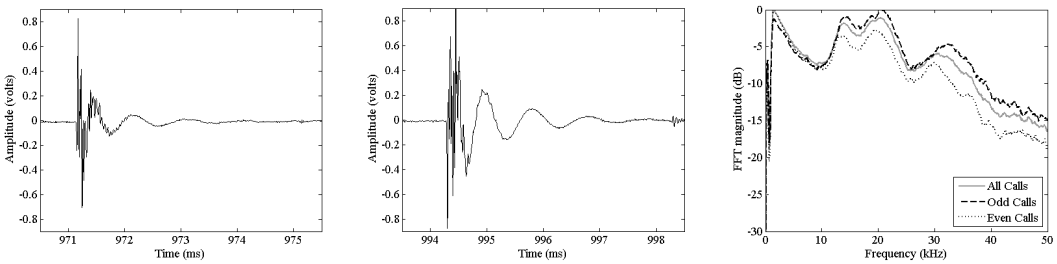

(a) (b) (c)

Figure 3.18. Calls recorded from bat 6 whilst in flight using wireless sensor: (a) representative example of an odd-numbered call; (b) representative example of an even-numbered call; (c) frequency content of calls from bat 6.

In all bats, there are certain similarities in the call spectra recorded. They all have significant content in the 12kHz-22kHz region, with another peak between 28kHz and 32kHz. These results tie in broadly with observations made in the literature. Griffin *et al.* (1958) noted that across the genus as a whole, the "bulk of the energy appears to be in the range 12kHz to 18kHz" with "additional energy scattered from 6.5kHz to over 100kHz with a second maximum at about 20kHz to 40kHz". Roberts (1975) broadly agreed with this, indicating a "major component" between 10kHz and

17kHz. Interestingly, through use of a capacitive device to record components above 10kHz, and a microphone to record components below 10kHz, the spectrograms Roberts published indicate significant energy below 10kHz, extending down into the 1kHz region. Roberts also indicated that the successive peaks in the energy spectrum are consistent with resonances in the buccal [oral] cavity; so the calls are produced with the tongue, but their structure is dependant on the characteristics of the oral cavity. Waters and Vollrath (2003) indicated a peak at 19kHz, with a second peak at approximately 30kHz. It can be seen that the data obtained using the wireless sensor is in good general agreement with the literature.

3.4.2. Variable gain recordings

Only bat 2 was used to make recordings using the sensor in variable gain mode. The signals obtained from only a handful of flights with this bat were sufficient to demonstrate the efficacy of the sensor used in this mode, and to gain an insight into the echoes returning to the bat. Figure 3.19 shows signals recorded using this configuration. Figure 3.19(a) is provided for direct comparison with Figure 3.14(a) having the same timespan. This illustrates the quantity of reflected signals returning to the bat detectable through use of variable gain. Given the hearing range of *R. aegyptiacus* extends down to approximately 0dB SPL (Koay *et al.*, 1998), these signals would be audible (assuming the pinnae are oriented correctly – see the discussion in Section 3.5). Figure 3.19(b) depicts a single echolocation call and its associated echoes as recorded using variable gain including reflected signals originating from an object approximately 5m from the bat. Also displayed, on the same scale for comparison purposes, is a DC-shifted trace captured using static gain, which illustrates the value of using variable gain to examine the reflected signals. As can be seen from Figure 3.19(c), which depicts the emitted call and echoes originating from close to the bat (up to approximately 1m) the sensor was deployed prior to the modification that added the second timer. As such, the sensor applied the increasing gain as soon as the emitted call is detected, generating the rising envelope seen in the recorded signal (as shown in sensor testing, Figure 3.10(b)). Obviously the recorded signal is not an accurate representation of the emitted signal due to the increasing gain characteristic. Unfortunately, there was no subsequent opportunity to

use the modified sensor on the bat. Figure 3.19(d) is an expanded image of the echoes returning to the bat from approximately 5m distance. Interestingly, this is from the second click of a pair; if it were from the first, then its range could well be ambiguous as its delay of approximately 30ms exceeds the mean interval between calls within a pair.

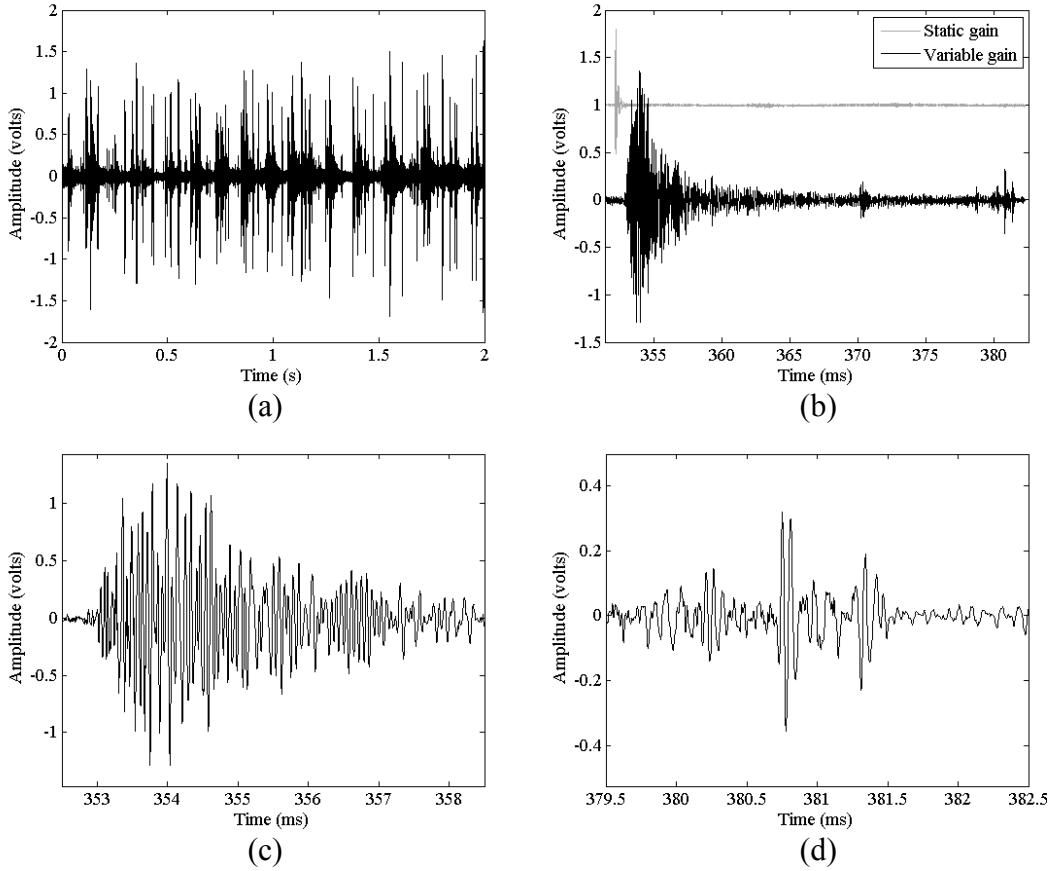

Figure 3.19. Calls recorded from bat 2 using the sensor in variable gain mode: (a) sequence of echolocation calls and echoes; (b) a single call and associated echoes, displayed with a DC-offset trace recorded using static gain for comparison; (c) expanded view of emitted call and echoes originating from close to (up to ~1m) the bat; (d) echoes returning from ~5m from the bat.

It is immediately apparent from these recordings that, even in the relatively simple environment of a corridor, the bat must decipher a complex combination of overlapping echoes from multiple objects and surfaces. Indeed, the images in Figure 3.19 were specifically selected for the fact they contained distinct echoes; many of the sequences recorded had few of these. Rather, they generally contained a complex combination of overlapping reflected signals as illustrated in Figure 3.20. It is these

signals the bat must be able to decipher to obtain an image of the environment in which it is flying.

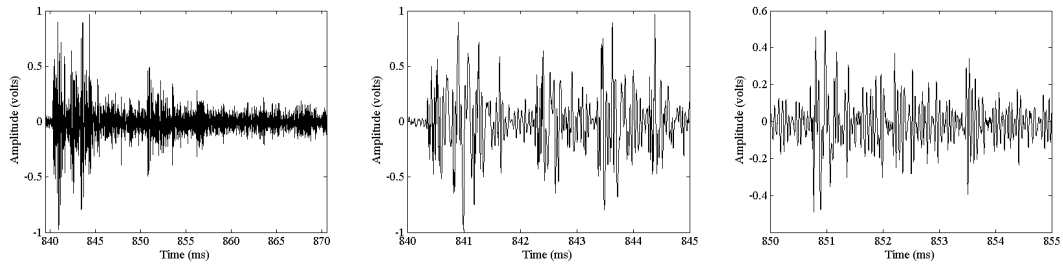

(a) (b) (c)

Figure 3.20. Calls recorded from bat 2 using the sensor in variable gain mode illustrating the complex nature of returning echoes. (a) A single call and associated echoes. (b) Expanded view of emitted call and echoes originating from close to (up to ~1m) the bat. (c) Echoes returning from ~1.5m-2.5m from the bat.

3.5 Call Synchronisation with Wingbeat

It has been previously reported in microchiropteran species that echolocation calls are emitted regularly, with one call emitted per wingbeat cycle, and that the point at which the call is emitted is linked to the angle of the wing (Kalko, 1994). This link has been explained by considering that some of the energy used for flight is coupled into producing sufficient sub-glottal pressure to emit high intensity calls (Lancaster *et al*., 1995) without incurring any extra energy cost (Speakman and Racey, 1991). However, these microchiropteran species produce calls from the larynx, whilst fruitbats of the genus *Rousettus* produce calls by clicking the tongue. As such, the bat need not use the flight muscles to compress the lungs to aid echolocation call production, apparently removing the requirement for a link between wingbeat cycle and call emission. This hypothesis was tested using the wireless sensor in conjunction with high-speed video footage of the flights undertaken by *R. aegyptiacus*. The data for this section was analysed by Dr. Dean Waters, and again the author would like to note his gratitude.

In addition to the equipment previously documented, the high-speed video data were recorded using a Kodak SR-500 Motioncorder (Kodak, Rochester, NY, USA) at 500 frames per second. This was triggered by the same signal as used to begin sound recording, ensuring synchronisation. This type of analysis has been reported in the

literature using a static microphone in conjunction with a high-speed 3D video system. For each call that is detected, the video is used to calculate the position of the bat with respect to the microphone at the time of emission. This allows the timing of call and wingbeat to be correlated. Through the use of simultaneously recorded video and wireless acoustic signals, this timing can be measured directly. A total of 303 calls were isolated that had suitable audio and video signals for analysis, yielding the following results. In the vast majority of cases, both calls of a "double-click" echolocation were emitted during the same phase of the wingbeat, either on the downward (70%) or upward (13%), with a significant minority having the first call on the downstroke and second on the upstroke (11%) or vice versa (6%). Furthermore, the angle at which the calls were emitted (measured with respect to 0˚, defined as vertical) was reasonably consistent. When both calls were emitted on the downstroke, the first was emitted at 54.2˚±25.3˚ (mean ± standard deviation) while the second was emitted at 82.8˚±26.2˚. When both calls were emitted on the upstroke, the first call was emitted at 58.9˚±32.2˚ and the second at 30.2˚±13.35˚. Similar distributions were found for the situation of the first call on the upstroke and second on the downstroke (21.2˚±10.0˚; 37.2˚±12.0˚), or first call on the downstroke and second on the upstroke (87.9˚±26.8˚; 69.6˚±22.2˚). This apparent link between wingbeat timing and echolocation call is interesting, since the coupling of energy from flight into call generation seems redundant given the mode of call production. These measurements were made far simpler than if the wireless sensor had not been available, and the findings will be discussed in the following section.

3.6. Discussion

A wireless sensor has been described that was used to detect the echolocation calls emitted by *R. aegyptiacus* whilst in flight. The sensor can be operated in one of two modes, employing either static or variable gain through the sensor amplifiers. Static gain mode was used to obtain accurate recordings of the emitted call, with the sensor gain set to achieve the best possible SNR. Variable gain mode allowed the reflected signals returning to the bat to be recorded. This mode of operation is inspired by the automatic gain control which some bats use to mitigate the large dynamic range between emitted calls and their echoes, allowing both emitted and reflected

echolocation signals to be recorded. Through accurate calibration of the sensor system, its effect on the recorded signals can also be understood. With the signals emitted by *R. aegyptiacus* having little energy above 40kHz, the sensor contributes an error of less than ±5dB across the range of these signals, demonstrating the importance of accurate calibration.

The calls emitted by *R. aegyptiacus* have been examined in some detail, with their frequency content yielding an interesting result. It was shown that, of each double-click echolocation pair, the second call generally had increased low-frequency (<10kHz) components. In three of the four bats this took the form of a large 1kHz component with higher frequency components superimposed on top. The reason for the increase in low-frequency content is not obvious. In fact, since the hearing of *R. aegyptiacus* is significantly (approximately 70dB) less sensitive at 1kHz than in the 10kHz-25kHz range (Koay *et al.*, 1998), it is surprising to see the bat using signals in this frequency regime at all. Notwithstanding this, it could be argued that the lower frequency components would allow the bat to probe further into its environment, using the longer unambiguous range (15.7m on average) available to the second click in a pair, as opposed to the first (4.3m). However, all four bats have significant energy content at or below 15kHz. Whilst the attenuation increases 7-fold in that interval (0.046dBm^{-1} at 1kHz; 0.326dBm^{-1} at 15kHz), the attenuation for the longest unambiguous range (31m round-trip) is only 10dB at 15kHz, as opposed to 1.4dB at 1kHz. This difference in attenuation is small enough to cast doubt on whether the lower frequency would be required to facilitate increased range echolocation for the bat. The consistency of the increased low frequency content in even-numbered calls certainly suggests that this effect should serve a purpose, but the reason for it is not apparent at this point. It is interesting that only one other source (Roberts, 1975) indicated call components in the region of the 1kHz signal recorded here, although this was not commented on by the author. It is also the only paper which specifically indicated that equipment was used that was capable of detecting such signals. Often, echolocation calls are recorded using a bat detector (e.g. Waters and Vollrath, 2003) which tend to have a high-pass filtering characteristic to ensure that low frequency background signals do not swamp the ultrasonic signals which are of interest. This may be the reason why such a component has not been noted previously.

The corridor in which these tests were carried out is a similar acoustic environment to the caves in which this bat roosts, consisting of large, high strength reflecting surfaces. The reflected signals detected by the variable gain sensor, then, give some understanding of the complexity of the task facing the bat when echolocating. It is this complex combination of overlapping echoes that the bat must decipher to obtain an image of the environment in which it is flying. It should be noted however, that while these signals were recorded returning to the bat, it does not necessarily hear them all. There are two of reasons for this. Firstly, unlike the sensor, the bat has pinnae that it is known to actively scan (Holland and Waters, 2005) whilst echolocating. This will provide directional filtering of the returning echoes not available to the sensor microphone. The response of the pinna was investigated in some detail, and is reported in Chapter 6 of this thesis. Secondly, there is no evidence that *R. aegyptiacus* uses any kind of AGC to process return echoes; the wireless sensor may have generated a more complex image of the environment than the bat itself is aware of. Even if these echoes are detected by the bat, it has a further tool it can use to extract information from them. Directionality is encoded into echoes via the binaural head related transfer function (HRTF) of the bat (e.g. Aytekin *et al.*, 2004). Through decoding of these cues, the bat may be able to obtain accurate spatial information from the plethora of reflected signals that are available. With the sensor using a single microphone, any potential for gathering this type of information is lost. Given the "impulsive" nature of the signals, the correlation-based techniques that the microchiroptera appear to use (Moss & Schnitzler, 1989) would be of less benefit to *Rousettus*. Cross correlation of the microchiropteran coded FM waveforms provides significant pulse compression to aid timing and hence range-finding; this is not the case with the impulsive clicks used by *Rousettus*.

When considering how the bat uses and analyses return echoes, another possibility should be considered. Unlike most of the microchiroptera, the genus *Rousettus* does not use echolocation for predation, but rather for navigating through the dark caves in which they roost. This being the case, it may be that their sonar acts as a form of collision avoidance, identifying the free space directly ahead of the bat into which it is flying, or is used to select a roost site. As such, there may be no requirement for the bat to build up a detailed image of its environment from its reflected calls.

Certainly it would appear that the type of complex scene analysis that the microchiroptera are capable of (Moss & Surlykke, 2001), may not be required by *Rousettus*.

The sensor has been successful in its aim of recording both emitted and reflected echolocation signals. There is, however, room for improvement. Firstly, given the amplitude and quality of the signals that were obtained, it would have been preferable to have employed a high-pass filter on the sensor to provide a more level frequency response. It was originally considered that this approach would have been imprudent, given its limiting factor on the available SNR. However, the signal levels that were captured would have allowed for a filter to be designed into the sensor. In fact, a bandpass filter should have been implemented, that would have allowed a flat operation bandwidth to be defined, with enhanced roll-off in the high frequency region. Another improvement has already been covered in Section 3.3.5. The additional TLC555 timer IC should have been added prior to flight tests with the bats, hence allowing both emitted and reflected calls to be recorded on each flight, rather than using separate sensors. If there had been the opportunity to spend further time working with the bats, these improvements would have been made.

One further aspect of the calls of *R. aegyptiacus* that the sensor proved useful for investigating was call timing and its relationship to wingbeat. It was found that, in general there was a link between these data, with over 80% of double-click echolocation calls occurring during the same cycle (either downstroke or upstroke) of the wingbeat. Furthermore, the angle of the wing at which these calls were emitted was also reasonably consistent. Given the mode of call generation of the genus *Rousettus*, this link was unexpected, since the microchiropteran use of flight muscles to generate the sub-glottal pressures required for intense call emission would appear to be redundant. As such, the reason for such a strong link between the two remains unknown.

CHAPTER 4

WIDEBAND AIR-COUPLED ELECTROSTATIC TRANSDUCER DESIGN AND CHARACTERISATION

4.1 Introduction

Air-coupled ultrasound has numerous industrial and research uses, including gas-flow measurement, range finding and proximity detection. It can also be used in applications ranging from non-destructive evaluation (NDE) and materials characterisation, to researching how bat calls interact with prey or propagate through air, all of which require ultrasound to be launched effectively into the air medium. The type of signal used depends on the application. For NDE, it may be sufficient for a narrowband toneburst to be transmitted into the test structure via an intermediate layer of air. In this case the use of piezocomposite devices, especially with a matching layer (Kelly *et al*., 2004), may be suitable. However, wideband signals such as chirps, or other frequency modulated (FM) constructions, are increasingly used in ultrasonic applications such as sonar or ranging. This necessitates the use of a transducer that, for most air-coupled applications operates in the sub-1MHz frequency regime (due to the frequency-dependent attenuation in air) but may be required to have significant bandwidth. For such applications, the use of traditional piezoelectric materials is not viable; their resonant nature restricts their ability to produce wideband energy, especially in air. In addition to requiring large bandwidth, it is also advantageous to achieve piston-mode operation of the device. This is no different for a wideband device, it is simply required that this is achievable across the entire bandwidth of interest, placing further restrictions on the device design.

As reviewed in Chapter 2, there are a variety of methods and materials that allow transfer of acoustic and ultrasonic energy into air, although few of these are suitable for *wideband* use. Those that do offer the capability of wideband operation may alternatively suffer from poor transmit sensitivity (e.g. Electromechanical Film (EMFi); Jimenez *et al.*, 2008), poor magnitude and phase correlation across the transducer surface (e.g. PVDF; Hayward *et al.*, 2000) or are expensive to produce (e.g. silicon-micromachined electrostatic transducers; Schindel *et al.*, 1995, and related capacitive micromachined ultrasonic transducers (cMUTs); Haller and Khuri-Yakub, 1996).

In the present study a range of inexpensive air-coupled electrostatic transducers were designed and manufactured, and characterised over an extended frequency range. The original aim of this work was to produce piston-mode transducers capable of operating over the frequency spectrum that bats use; this extends from the audible range to in excess of 200kHz (Fenton and Bell, 1981). Since audible transducers can be irritating when used, the frequency range of interest was limited to that lying between 20kHz and 250kHz. It is pertinent to note that this range has a centre frequency of 135kHz, with a fractional bandwidth (-3dB bandwidth divided by centre frequency) of 170%, which is a considerable challenge.

This frequency range would allow replication of practically any bat echolocation call in the laboratory. Furthermore, given the increasing attenuation of ultrasound in air with frequency (e.g. 0.5dBm^{-1} at 20kHz; 12dBm^{-1} at 250kHz; 42dBm^{-1} at 500kHz; 162dBm^{-1} at 1MHz; for 20°C, 50% relative humidity and atmospheric pressure) as described by the equations of Bass *et al.* (1995), these frequencies allow substantial propagation of ultrasonic energy. As will be described, the transducers produced were actually capable of operating up to a significantly higher frequency range, which may enable the use of these devices in other engineering disciplines in the future, such as NDE.

4.2 Theoretical Field Simulation

In characterising air-coupled devices, one important measurement is that of the emitted field structure. Generally, this is done by measuring the peak pressure of a selected set of points in a 2-D plane through the centre-line of the transducer; the set of points and their spatial resolution are selected to provide an accurate image of the structure of the field. This measured field can then be compared with the theoretical field emitted by an ideal plane-piston device of the same dimensions to provide a "figure of merit" for the transducer. The method used for predicting the field from such an ideal device (and from real devices using LDV measurements, as will be discussed in Section 4.5.4), uses a discretised version of the Rayleigh integral as described by Benny *et al.* (2000), which expands on the work of Lerch and Friedrich

(1986). An overview of the derivation of the discretised integral is repeated here, but the interested reader is directed to the work of Benny *et al.* for further detail.

The Rayleigh integral calculates the pressure at a point in the field through summation of the spherical wavelets emitted by each small area, *dS*, of the discretised surface of the transducer (or aperture) *S*:

$$p(R,t) = \frac{\rho}{2\pi}\frac{\partial}{\partial t}\int_S \frac{v(R,t-R/c)}{R}dS \tag{4.1}$$

Where p is the sound pressure, ρ the medium density, v the velocity component normal to the transmitting surface, R the distance from dS to the point in the field, c the velocity of sound in the medium and S the radiating surface itself. If the attenuation incurred in a lossy environment is included, and the excitation is assumed to be continuous (harmonic), then an equation in the frequency domain can be expressed as follows:

$$p(R,\omega) = \frac{\rho}{2\pi} j\omega \int_S \frac{a\exp(-(\alpha + jk)R)}{R}dS \tag{4.2}$$

Where ω is the angular frequency, a the velocity magnitude at dS normal to the surface, α the attenuation coefficient in the medium, j the imaginary unit, and k the wavenumber ($k=\omega/c$). The attenuation coefficient was calculated using a formulation of the equations provided by Bass *et al.* (1995), with temperature set to 20°C, humidity to 50% and atmospheric pressure to 1 bar.

This equation was then discretised into a form that can be rendered in computer code for calculation:

$$p_\omega = \frac{\rho\omega}{2\pi}\sum_N \frac{a\exp(j\varphi - \beta R)}{R}dS \tag{4.3}$$

Where p_ω is the pressure at a given point in the field, N the number of points used to discretise surface S, φ the phase associated with the amplitude a, and $\beta=(\alpha+jk)$. The use of this discretised Rayleigh calculation, whilst computationally intensive, is highly adaptable, allowing the magnitude and phase of each discrete point on the transducer surface to be manipulated individually.

The discretised version of the Rayleigh integral was based on the assumption of continuous wave (CW), or harmonic, operation. However, in finite space and without access to an anechoic environment, CW operation presents problems due to reflections when experimentally measuring emitted field structures. Indeed, Benny *et al.* measured the pressure field produced by a transducer driven using a toneburst of 20 cycles. In this work, a 10-cycle toneburst, apodised with a Hanning window was used to drive the transducers. In Benny's case, using a resonant piezoelectric transducer, toneburst excitation approximates CW operation. However, with a wideband transducer, which is more capable of reproducing a time-limited signal such as a toneburst, the field generated is not an exact match to that generated by under CW conditions.

To predict the field produced using such a toneburst, the discrete Rayleigh integral was employed in a different fashion. Firstly, the complex spectral components of the excitation signal were calculated through use of the Fast Fourier Transform (FFT). These components were then applied in turn to the Rayleigh integral, accounting for the attenuation of each component by calculating its individual attenuation coefficient, and applying each component at the appropriate phase indicated by the complex FFT. This modification allowed the structure of an arbitrary signal at any point in the field to be predicted through performing the inverse FFT on the signals calculated by the Rayleigh integral, prior to summation for each spectral component. The field profile was then found by extracting amplitude information from the predicted signal. This allowed the subtle effects of toneburst operation to be predicted, as discussed in Section 4.5.3.1. The discretised Rayleigh integral and attenuation equations were coded and executed in Matlab (The Mathworks, MA, USA).

4.3 Principles of Operation of Electrostatic Transducers

Given the limitations of some materials and mechanisms for generating and detecting air-coupled ultrasound, a range of electrostatic transducers was designed for this work. Electrostatic (or capacitive) transducers with a solid backplate have long been used as a source of a generating and detecting ultrasound in air, since first described by Kuhl *et al.* (1954). The general construction of an electrostatic device has not altered much over the intervening time period. The two main parts are the transmitting membrane, formed of a thin film (generally 1μm – 25μm) of polymer, and an electrically conductive backplate. The polymer membrane is held over the backplate, with the non-contact surface of the membrane being metallised. A constant bias voltage, typically 50V – 500V direct current (DC) is applied between the metallised surface of the membrane and the backplate, generating an electrostatic force between the two which attracts the membrane into contact with the surface of the backplate. This bias voltage also helps to linearize the device operation. Depending on the surface finish of the backplate, air pockets of varying size will be trapped between the membrane and backplate. The further addition of a time-varying voltage superimposed onto the bias voltage causes the electrostatic force to vary and hence the membrane to vibrate over the air-pockets, producing vibration in the load through direct contact with the molecules in the air. In reception, the inverse process occurs: pressure variations associated with an incident ultrasonic wave, cause the membrane to deflect, varying the average membrane/backplate separation, and hence generating a net capacitance change. This change, in the presence of the applied bias voltage, causes the charge on the device to vary, which can be amplified and measured via suitable electronic circuitry.

4.3.1 Operational Trends of Electrostatic Transducers

The operational characteristics, in terms of frequency response and sensitivity, of an electrostatic transducer are generally defined by the interaction between the membrane and backplate surfaces. Many modern electrostatic transducers (and related cMUTs) are capable of generating wideband ultrasound. However, as recently as the early 1990s, most devices tended to be quite narrowband (e.g. Rafiq

and Wykes, 1991; Oksanaen *et al.*, 1997), with backplates having regular machined features, such as grooves. Such regular features produced devices with relatively narrowband operation (typical fractional bandwidth of approximately 30%), whilst the depth and spacing of these grooves (100μm minimum) ensured that the centre frequency was relatively low (sub-200kHz). In general, the physical characteristics of the backplate and membrane can give a guide to its operating characteristics as demonstrated by Schindel *et al.* (1995). A rougher backplate will produce larger air pockets and preferentially operate at a lower frequency, and have a smaller bandwidth, than a device with a smoother backplate. Similarly, a thinner membrane will preferentially generate higher frequencies and have a larger bandwidth than a thicker membrane. A thinner membrane will also tend to improve the sensitivity of the device. The bias voltage can also have an effect on these characteristics, causing the sensitivity, frequency and bandwidth of a device to increase with bias voltage, although this relationship is only maintained up to a point; the response of the device tends to reach a plateau whereupon additional increase in bias voltage has a minimal, or even detrimental, effect. Through knowledge of the operational trends of electrostatic transducers, then design for a specific application and operational characteristics becomes possible.

4.4 Electrostatic Transducers

Modern electrostatic transducers (e.g. Schindel *et al.*, 1995; Bashford *et al.*, 1997), are capable of wideband operation, with a fractional bandwidth greater than 100% and operation extending into the low MHz region. They are manufactured using precision engineering processes (e.g. silicon micromachining of the backplate) to control the characteristics of the device. These devices have been characterised and shown to produce field structures that compare well with a theoretical piston-mode device (Bashford *et al.*, 1997), across a range of frequencies. However, these manufacturing techniques are not widely available and are costly. One of the objectives of this work was to produce a range of electrostatic transducers capable of piston-mode operation across the frequency range of interest, which are relatively inexpensive to manufacture.

4.4.1 Transducer Manufacture and Operation

The construction of the electrostatic transducer was as follows. The 30mm diameter backplate was housed within an insulating PVC shoe of 34mm diameter, and further contained within an aluminium case of external diameter 55mm. The polymer film (metallised on the non-contact surface with evaporated aluminium) was held within an aluminium ring (external diameter 55mm, internal diameter 34mm) which was screwed to the case. This ring provided the capability to tension the membrane over the backplate, and provided electrical connection between the case and the metallised front face of the membrane. A diagrammatical illustration of this configuration is provided in Figure 4.1(a), with a photograph of a fully- and partially-constructed device in Figure 4.1(b).

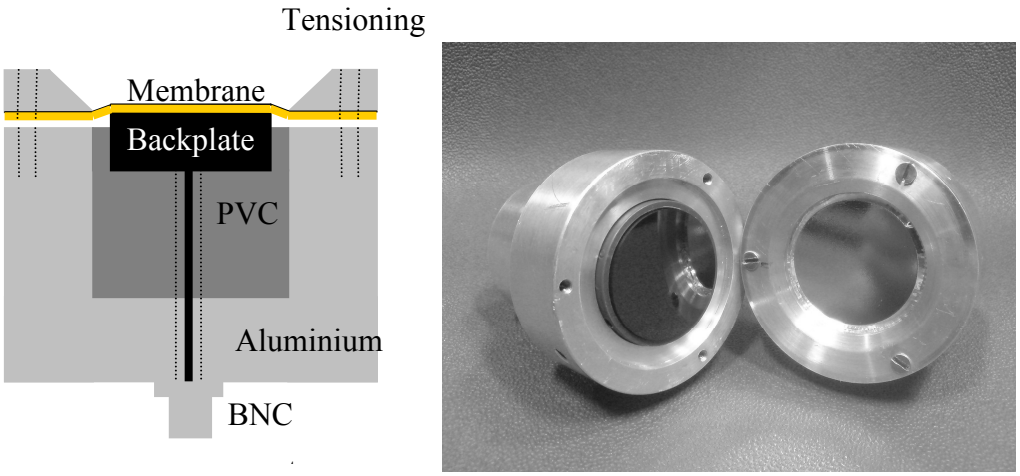

Figure 4.1. Design and manufacture of electrostatic transducers. (a) Diagram of cross section of device illustrating component parts. (b) Photograph of partly (left) and fully constructed devices, showing a backplate of polished vitreous carbon.

The bias and time-varying voltages required to drive the transducers were provided as illustrated in Figure 4.2. The bias voltage, of up to 500V, was provided by a high-voltage (HV) power supply (475R photomultiplier power supply, Brandenburg, Dudley, UK), whilst the time varying voltage was generated using an Arbitrary Function Generator (AFG), either the 33120A or 33250A (Agilent, CA, USA). In the case of impulse response measurement, a Panametrics 5052PR pulser unit (Olympus Corporation, Tokyo, Japan) was used to generate the characterising impulse, and provide amplification in pulse-echo mode. The DC and time-varying signals were

summed together via the resistor and capacitor combination in the bias decoupling circuit. The resistor (100kΩ) was employed as a current limiting device between the HV supply and the transducer; the capacitor (5.6μF; 630V dc breakdown) provided DC protection between the HV supply and the AFG output. Further protection of the AFG was provided by the buffer circuit, based around a BUF634T (Texas Instruments, TX, USA) high-speed buffer IC. This circuit had a dual purpose. Firstly, it performed the duty of a sacrificial buffer in the (rare) event that an electrical breakdown occurred across the membrane. In this case the bias voltage, of up to 500V, would discharge via the short circuit, creating a transient signal that would be passed by the blocking capacitor, and travel towards the AFG output socket, risking damage to the AFG output circuit. This was avoided since the buffer IC would instead be damaged, and could be easily (and cheaply) replaced. Secondly, the buffer provided a high-current output stage to aid the driving of a high-capacitance load, as is the case with the electrostatic transducer.

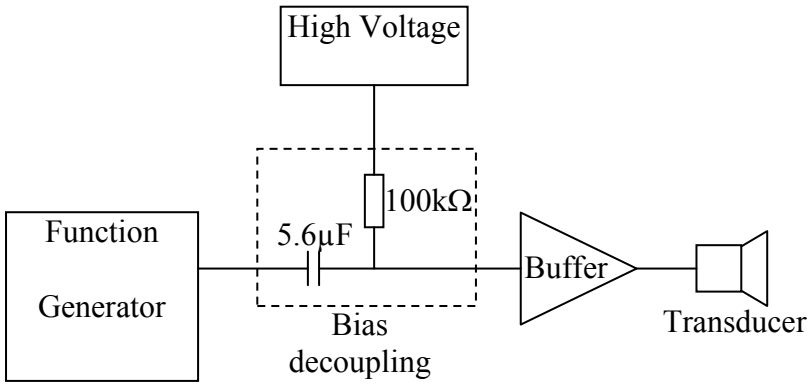

Figure 4.2. Circuit for supply of bias voltage and drive signal.

Two different backplate materials were used to manufacture devices. These were vitreous carbon (VC) and FR-4 glass reinforced epoxy resin. VC, a glasslike form of carbon, was selected for two main reasons: firstly it can be supplied with a well-controlled polished finish; and secondly it is electrically conductive. Backplates were purchased (Sigradur G; HTW Hochtemperatur-Werkstoffe GmbH, Thierhaupton, Germany) ready for use as 30mmØ x 5mm discs, with one side polished flat to within 50nm, as specified by the manufacturer; measurement using a white light interferometer system (Wyko NT1100 Optical Profiling System, Veeco, NY, USA) indicated that the average surface roughness, $R_a \approx 10$nm, with a maximum variation,

$R_t \approx 60$nm. FR-4 is the base material used in most electronic printed circuit boards (PCBs). After further lamination with a layer of copper, the board is processed to produce the tracks for carrying electronic signals. In this work, 30mm diameter disks of blank (unprocessed) FR-4 PCB were used as an alternative backplate material. Surface profiling using the Wyko system indicated how the weave of the glass fibres gives the PCB a rougher surface finish: $R_a \approx 100$nm; $R_t \approx 3\mu$m. The well-defined nature of both materials allowed a number of devices to be manufactured having similar operational characteristics, whilst the variation in surface finish between the two produced contrasting results that were investigated.

4.5 Characterisation of Electrostatic Transducer Operation

Each transducer was characterised in a number of ways: its impulse response was used to attain a measure of its wideband response; absolute narrowband output sensitivity was characterised through measurement with a calibrated microphone; the acoustic field generated was measured through use of a scanned detector; and the motion of the membrane was measured using a Laser Doppler Vibrometer (LDV) system. Through a combination of these measurements, the operational characteristics of each device can be fully understood.

4.5.1 Operational Trends of Electrostatic Transducers: Impulse Response

Through manufacture of prototype devices, the operational trends of electrostatic transducers were measured to ascertain how the variables of device manufacture and operation affected their operation. The variables examined were: bias voltage; membrane thickness; and backplate surface. The impulse response of the device was measured in pulse-echo mode using the Panametrics pulser unit as previously described, with a block of crown glass as the reflector, positioned approximately 10mm from the front face of the transducer. With each experiment, care was taken to align the transducer so as to elicit maximum sensitivity and bandwidth from the system. This was done by observing the multiple echoes generated by reverberation of energy between the transducer and glass block; when a maximum number of multiple echoes of maximum achievable magnitude was observed, then the alignment was judged to be correct. Each received time-domain signal was digitised

at a sampling frequency of 2GHz using an Infiniium oscilloscope (Agilent, CA, USA), and saved for analysis. The spectral content of this signal was then calculated using a Fast Fourier Transform (FFT) routine, coded in Matlab.

A PCB backplate transducer was manufactured, and operated using a range of bias voltages and membranes. Firstly, 8µm polyimide (Kapton; DuPont, Wilmington, DE, USA), metallised with evaporated aluminium, was used as the membrane and its impulse response measured whilst varying the bias voltage from 50V to 500V. The magnitude of the FFT of the received acoustic pulse at each bias voltage is illustrated in Figure 4.3(a) showing how the response of the device becomes more wideband with increased bias voltage, although the *peak* sensitivity is reduced. Figure 4.3(b) shows how the impulse response varies with membrane thickness and material, for a bias voltage of 300V. Membranes were constructed of Mylar (DuPont, Wilmington, DE, USA), a polyester film of 12µm, 5µm and 2.5µm; and of 8µm Kapton (DuPont, Wilmington, DE, USA), a polyimide film. It can be seen that as the thickness decreases, the centre frequency and fractional bandwidth of the transducer increases, although there *is* a decrease in fractional bandwidth between the 5µm and 2.5µm Mylar membranes of approximately 25%. These trends generally agree with those of Schindel *et al.* (1995) and indicate that a thin membrane with a high bias voltage will give the highest frequency, and widest bandwidth, operation, though not necessarily the greatest sensitivity. The results from these impulse response tests are presented in Table 4.1 for quantitative comparison.

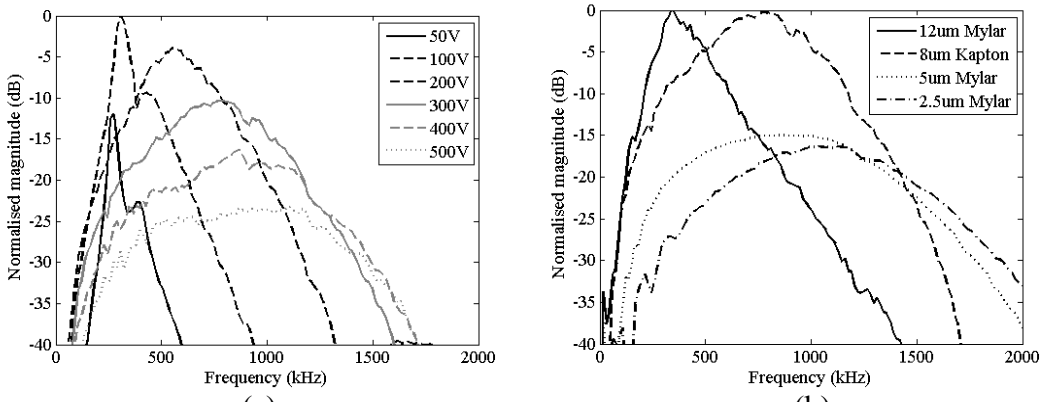

(a) (b)

Figure 4.3. Frequency domain representations of the pulse-echo impulse response of the electrostatic transducer with a range of configurations. (a) Varying bias voltage; (b) Varying membrane.

Backplate	Membrane	Bias Voltage	Centre frequency	Fractional bandwidth
PCB	8µm Kapton	50V	275kHz	20%
PCB	8µm Kapton	100V	305kHz	28%
PCB	8µm Kapton	200V	565kHz	70%
PCB	8µm Kapton	300V	779kHz	82%
PCB	8µm Kapton	400V	870kHz	92%
PCB	8µm Kapton	500V	870kHz	129%
PCB	12µm Mylar	300V	336kHz	81%
PCB	8µm Kapton	300V	779kHz	82%
PCB	5µm Mylar	300V	885kHz	128%
PCB	2.5µm Mylar	300V	1038kHz	101%

Table 4.1. Frequency characteristics of PCB backplate electrostatic transducer, with varying bias voltage and membrane.

Given the original aim of this work was to reproduce bat echolocation calls in the lab, within the frequency range of 20kHz – 250kHz, the highest operating frequency and largest bandwidth were not necessarily the deciding factors in device construction. Two transducer configurations were used for most of this work, consisting of an 8µm Kapton membrane and either a PCB or VC backplate. The Kapton membrane was selected as it produced a device with a good combination of sensitivity and wideband characteristics. Furthermore, these transducers generated a linear output across the frequency range of interest and demonstrated reasonable correlation with piston-mode operation, as will be illustrated and discussed in the following Sections. The impulse response data for these two particular transducers are displayed in greater detail in Figure 4.4, in the time, 4.4(a), and frequency, 4.4(b), domains. It can be seen from these results that the impulse response of the smoother VC backplate has a higher centre-frequency (885kHz) and a higher fractional bandwidth (123%) compared to the rougher PCB (779kHz; 82%), as expected. It should be noted that the response of these transducers, when measured at such a short distance, demonstrate significant operation into the MHz region. Ultrasonic energy at such frequencies is rapidly attenuated in air however (by over 160dBm^{-1} at 1MHz for example) and as such these frequencies are present only in small amplitudes in the far-field of these devices. Most of the work was conducted at frequencies below

300kHz; what this characterisation illustrates is the capacity for these transducers to operate significantly in excess of this frequency range.

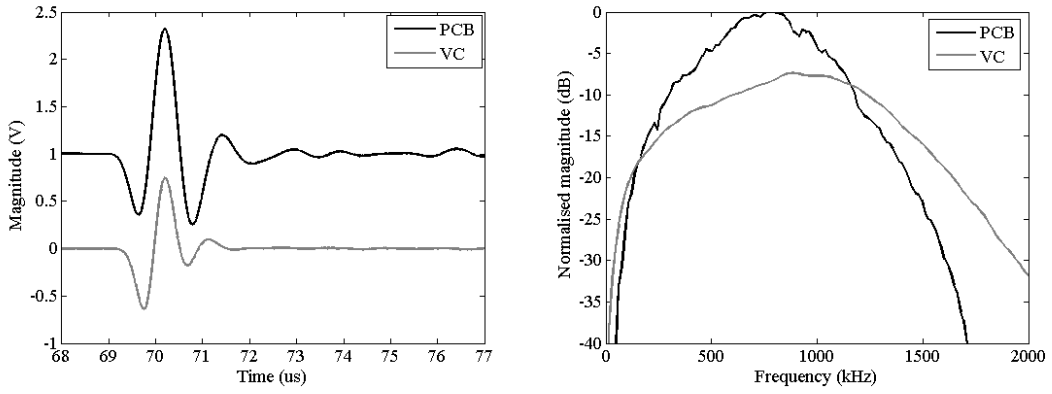

(a) (b)

Figure 4.4. Impulse response of PCB and vitreous carbon (VC) transducers with 8μm Kapton membrane and a bias voltage of 300V: (a) Time domain (PCB trace dc-level shifted for clarity); (b) Frequency domain.

This exercise in identifying trends in the operation of electrostatic transducers is both necessary and useful. Not only does it identify those operational features that allow a wideband device to be constructed, but it also indicates the combination of factors that may be useful in designing a transducer for a specific application in any given frequency regime. The work reported in Chapter 5 relating to the replication of biological echolocation signals draws on this information in selecting the correct combination of backplate, membrane and bias voltage for any given signal. Indeed the bias voltage used throughout the work conducted for this thesis was 300V. It is worth noting at this point that no transducer has a flat response across the frequency range of interest. For this reason, generation of wideband bat calls uses a spectral inversion technique to achieve accurate replication. This is detailed in Chapter 5.

4.5.2 Sensitivity Measurement

The sensitivity of the electrostatic transducers is measured in two ways. Firstly, the output Sound Pressure Level (SPL) is measured using a calibrated microphone, and secondly the Insertion Loss (IL) of a transmit / receive pair is measured for comparison with existing air-coupled piezocomposite devices.

4.5.2.1 Calibrated Measurement of Output Pressure

The impulse response provides a relative measure of the frequency response of the transducers. However, by its nature, it lends itself to a normalised measurement, providing no information on the absolute pressure levels that can be generated by the device. To measure this, the narrowband (toneburst) response of the device was measured using a calibrated microphone, over a range of frequencies. This was performed using a Brüel & Kjær (B&K, Nærum, Denmark) Type 4138 1/8" microphone, used in conjunction with a Nexus 2670 preamplifier (also supplied by B&K). The preamplifier was purchased with the high-frequency option, allowing calibrated operation up to 200kHz. Calibration data was provided for the microphone in graphical format; for information on the process used to calibrate pressure measurements made with this microphone, refer to Appendix A.

An Agilent 33120 AFG was configured to emit a succession of single-frequency tonebursts, at 1kHz intervals across the frequency range 10kHz – 200kHz. The peak output from the microphone was measured via a CS82G GaGe analogue to digital (A/D) converter card (Dynamic Signals, IL, USA). Both the AFG and A/D card were configured using LabVIEW (National Instruments, TX, USA) to automate data collection. The microphone was positioned 100mm from the front face of the transducer, the standard reference distance for an acoustic source in air. It is interesting to consider the influence of this distance on the measured sound field with varying frequency. The boundary between the near- and far-field, N, is defined by equation 4.1:

$$N = \frac{a^2}{\lambda} = \frac{a^2 f}{c} \tag{4.4}$$

Where a is the transducer radius (15mm in this case), λ the wavelength of the radiated ultrasound, f its frequency and c the speed of sound in air (assumed to be $345 ms^{-1}$). As such, at 153kHz the microphone is situated exactly on the boundary; for frequencies below this value the microphone is in the far-field, while for those above this value, it is in the near-field. As such, calibration at this distance does not indicate

the *maximum* pressure the transducer can deliver at any given frequency, it provides a standard measure by which to compare a number of sources.

The calibrated narrowband frequency response for both the VC and PCB transducers are displayed in Figure 4.5. Two transducers of each type were constructed to demonstrate repeatability. These results are for an applied AC voltage of 20Vp-p with a 300V bias. It can be seen that at frequencies over 100kHz, the VC transducer is capable of generating approximately 100dB SPL, with the PCB transducer exceeding this by approximately 10dB. Bat calls have been estimated with a maximum level of over 140dB SPL in the field (Surlykke and Kalko, 2008) referenced to 100mm from the mouth, with average maximum call strength in the region of 120dB SPL – 130dB SPL. As such, it can be seen that these transducers, fall some way short of the peak pressures attained by bats in the field. However, these results were obtained using the 20Vp-p drive signal, so with some amplification greater pressures could be attained if necessary. Indeed, the PCB transducer was driven via a power amplifier to generate drive signals of 50Vp-p and 100Vp-p, giving an improvement of 7.4dB and 13.5dB, respectively – a linear response – allowing the PCB transducer to generate in excess of 120dB SPL for 100Vp-p excitation signal.

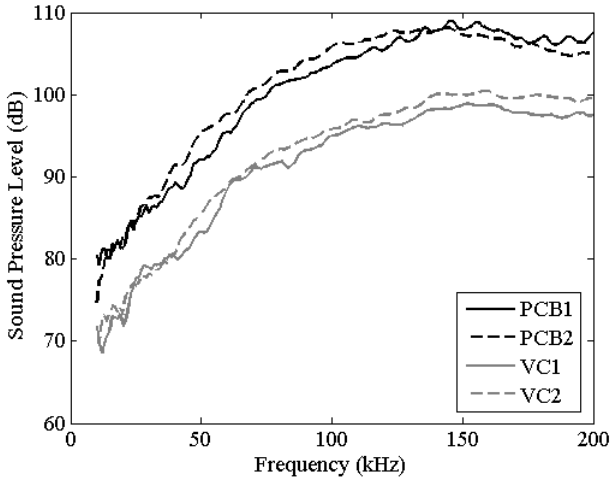

Figure 4.5. Narrowband calibration of absolute output pressure at 100mm from the transducer front face, from the PCB and vitreous carbon (VC) backplate electrostatic transducers. Two examples of each transducer were manufactured.

One feature of note in the data is the slight dip in the pressure output at just beyond 150kHz. This is not due to the pressure output from the transducer reducing at these frequencies (it can be seen from the impulse response data in the previous Section that the peak output is at a significantly higher frequency) but rather due to the far-field boundary moving beyond the microphone at these frequencies. As such, the microphone starts to drop down the pressure field curve towards the final local minimum, causing the measured pressure to reduce.

4.5.2.2 Insertion Loss Measurement

Impulse response characterisation has illustrated that both the VC and PCB backplate are capable of operating over the original target range of 20kHz – 250kHz. Results presented in Chapter 5 will also demonstrate how these devices can be used to replicate a wide range of biological and biologically-inspired acoustic signals. The frequency range of these devices, with peak output at approximately 800kHz, recommends them to other applications such as NDE, which currently use piezocomposite devices. Indeed, the wideband nature of the electrostatic transducer has undoubted advantages over the narrowband piezocomposite. For example, coded ultrasonic signals could be used to improve SNR and for pulse compression to obtain accurate timing / imaging data. Furthermore, the capability to generate energy over a wide bandwidth would enable Lamb waves to be launched into plates of varying thickness, with a fixed angle of incidence. Since electronically varying the frequency of a signal is easier than mechanically altering the angle at which a transducer is inclined with respect to an inspection surface, this would be a significant benefit. For this to be viable, however, its sensitivity would need to be considerably improved as is revealed by comparison with an air coupled piezocomposite transducer with suitable matching layer (Kelly *et al.*, 2004), a device which is similar to those used in a number of air-coupled NDE applications such as testing of aerospace components using through transmission of Lamb waves (Kelly *et al.*, 1996).

Comparison of the sensitivity of these devices can be achieved through measurement of the transmit / receive insertion loss (IL). IL is defined as:

$$IL = 20\log_{10}\left(V_R \big/ V_I\right) \tag{4.5}$$

Where V_R is the voltage generated by the receiving transducer into a matched load, and V_I the voltage produced by the electrical source into a matched load. As such, it is a measure of the loss produced with respect to the available voltage from the source, providing a measure of the loss inherent in the entire system, both electrical and acoustic. In practice, V_I was measured directly into the 50Ω input of an oscilloscope (to match to the 50Ω output impedance of the AFG), while V_R was calculated as half the open-circuit voltage (measured into the high-impedance input of the oscilloscope).

The highest sensitivity electrostatic devices – those with the PCB backplate – were measured. The measurement was made using a narrowband toneburst of 10 cycles duration across a range of frequencies. The peak response of the PCB electrostatic devices was at approximately 750kHz, with an IL of 56.0dB. This was measured at approximately 20mm, with the transmitter driven using the same bias box and buffer arrangement as previously; the receiver was connected to the oscilloscope via another bias box, used to decouple the bias voltage from the oscilloscope input. For comparison, it is interesting to review the results obtained by Gachagan *et al.* (1996). The method used differs slightly, in that the measurement of input and output voltage is defined as being into the high input impedance of an oscilloscope; essentially V_I and V_R are defined as the open circuit voltage response. However, the resulting IL is directly comparable, since V_I and V_R are both doubled in comparison to the definition used above. The electrostatic results are similar, with an IL of 57.2dB reported for a transducer pair with a rough brass backplate and a 5μm Mylar membrane (a better result of 50.8dB was obtained for a device with a 2.5μm membrane but, as previously documented, transducers with such a thin membrane were prone to electrostatic breakdown across the membrane and were hence rather unreliable). However, Gachagan *et al.* also measured the piezocomposite devices described in the opening paragraph of this section, generating a figure of 28.4dB. This is some 22dB – 29dB more sensitive than the electrostatic devices measured. If electrostatic devices are to be used in similar applications, then future development should

undoubtedly concentrate on increasing their sensitivity, without significantly reducing the bandwidth.

4.5.3 Measurement of the Emitted Acoustic Field

The emitted field from each transducer was measured directly, using the B&K microphone system in conjunction with a three-axis scanning system. The transducer was mounted on a two-axis (x-y) scanning system, with the microphone mounted on a single-axis (z) stage, housed within a purpose-built Perspex case (2000mm×650mm×700mm) to provide environmental protection, as pictured in Figure 4.6. Each axis was driven via a stepper motor, in turn controlled by a stepper-motor controller (C560, Physik Instrumente UK, Cranfield, UK). This was conducted in a temperature-controlled room. Measurement of the acoustic field was automated using LabVIEW to drive the stepper-motor controller so as to scan the microphone within the acoustic field. Measurements of peak-to-peak amplitude were made at each selected point in the field via the GaGe A/D card. For comparison purposes, the theoretical field generated by an ideal 30mm diameter piston-mode transducer was predicted using the discretised Rayleigh integral, as described in Section 4.2.

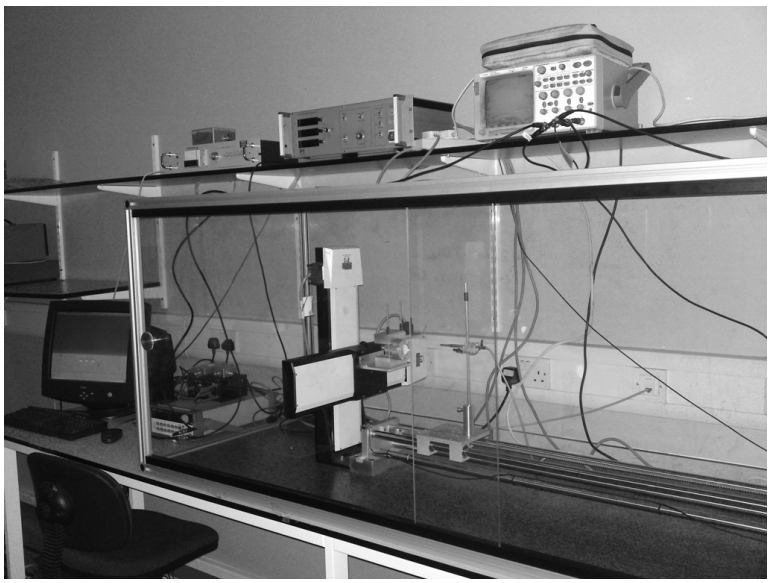

Figure 4.6. Air-calibration system, with 3-axis scanner enclosed in Perspex case.

4.5.3.1 Influence of Microphone Directionality and Toneburst Excitation

The pressure field emitted by the transducers, as measured by the B&K microphone, differs from that predicted by the plane-piston CW Rayleigh integral due to two factors. Firstly, the directional response of the microphone affects the measurement of the field (since the field measurements are made at a single frequency, the frequency response of the microphone has no impact). Secondly, the non-continuous nature of the drive signal (a 10-cycle, Hanning windowed toneburst was used) affects the field actually emitted by the transducer.

The microphone response, as can be seen in Appendix A, dictates that the amplitude measured from any obliquely-incident signal is subject to a reduction with respect to a normally-incident signal. This is important since it is the coincidental arrival of edge and plane waves, with their varying relative phases, that produces the local maxima and minima of the near field. This is particularly noticeable on the acoustic axis of a circular device, which displays alternating maxima and minima that vary between the acoustic maximum (attenuation notwithstanding) and zero pressure. Since the edge wave necessarily arrives at a greater angle of incidence, the microphone attenuates these components with respect to the plane wave, causing the local maxima and minima to be less extreme.

The toneburst nature of the acoustic signal has a very similar effect, but for a different reason. In the time domain, this can be explained by the non-continuous nature of the acoustic signal, meaning that complete overlap of the planar and edge wave components from the circular aperture is not possible. For a finite-duration drive signal, complete overlap would require the two components to have the same path length, which is obviously not possible. For example, consider the pressure on the acoustic axis of a 30mm diameter transducer, being driven by a 10-cycle toneburst at a centre frequency of 250kHz. With the toneburst having a duration of 40μs, any path length difference of greater than 40μs leads to no overlap whatsoever. As such, the two components arrive entirely separately, and so the combined amplitude is half what it would be if they arrived *entirely* in phase (causing constructive interference). As the distance on the acoustic axis increases, so the overlap between the two components increases. However, due to the reduced envelope of the signal at its extremities, the overlap initially has little effect,

gradually increasing as the difference between path lengths decreases on approach of the far-field boundary, where the difference is exactly a wavelength (at the centre frequency of the toneburst). This produces the largest signal due to constructive interference, but it is still reduced from the case of CW operation. In the frequency domain, this effect can be explained by the multiple frequency components present in a windowed tone-burst. Each of these frequencies has a slightly different location for each local maximum and minimum in the near field, thereby 'smearing' the interference effect present with a single-frequency CW signal.

These effects are illustrated in Figure 4.7, which compares the predicted field at 250kHz from a 30mm diameter aperture under various conditions: CW operation, 4.7(a); 10-cycle Hanning-windowed toneburst, 4.7(b); and a 10-cycle Hanning-windowed toneburst, with the additional influence of the B&K microphone, 4.7(c). The effect can possibly be seen most clearly in Figure 4.7(d), which shows the pressure variations on the acoustic axis in the near field. It can be seen from Figure 4.7(d) that the time-limited drive waveform has rather more of an effect than the microphone directionality, greatly reducing the variation in pressure between successive maxima and minima. In comparing the field profiles, it can be seen that, except for the subtle effect on the near-field interference pattern and the far-field beamwidth, neither of these factors has a significant effect on the measured field.

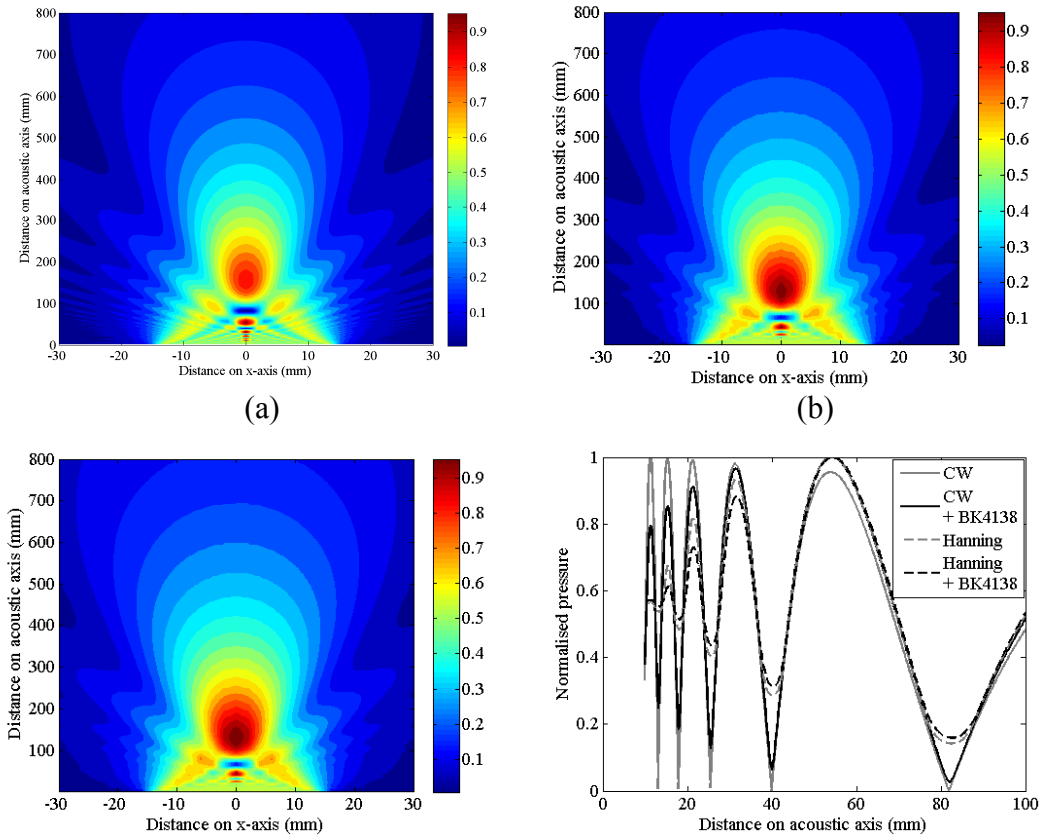

Figure 4.7. Simulation of the influence of windowed-toneburst excitation and microphone directionality on the predicted acoustic field at 250kHz from a 30mm diameter transducer: (a) Simulated field under CW excitation; (b) Simulated field with 10-cycle Hanning-windowed toneburst excitation; (c) as (b) but including directionality of B&K 4138 microphone; (d) On-axis comparison of CW and Hanning-windowed 10-cycle excitation, with and without microphone directionality.

The effect of both the windowed excitation function and the microphone directionality are included in all theoretically predicted results in this Chapter. The effect of the windowed-toneburst could only be calculated through use of the modified Rayleigh integral, including the FFT. The method by which the microphone directionality was calculated is detailed in Appendix A.

4.5.3.2 Field Measurement Results

Field measurements were made in the horizontal plane through the centre-line of the transducer, and were performed identically for both VC and PCB transducers. These measurements are compared with the theoretical field calculated from a piston-like radiator of 30mm diameter (accounting for both microphone directionality and windowed toneburst excitation). These comparisons are displayed in Figure 4.8, from 20kHz to 250kHz, where the measured and predicted pressure fields are normalised. It can be seen that the field emitted by the vitreous carbon transducer correlated exceptionally well with the predicted piston-mode field, over the entire frequency range. This is true, even in the near field where the pattern generated by the interference of plane and edge waves is well replicated. The fields produced by the PCB backplate do not replicate this near-field interference quite so well, especially at the higher frequencies. The reasons for this will be examined in Section 4.5.4 by measuring the motion of the transmitting membrane using the LDV system.

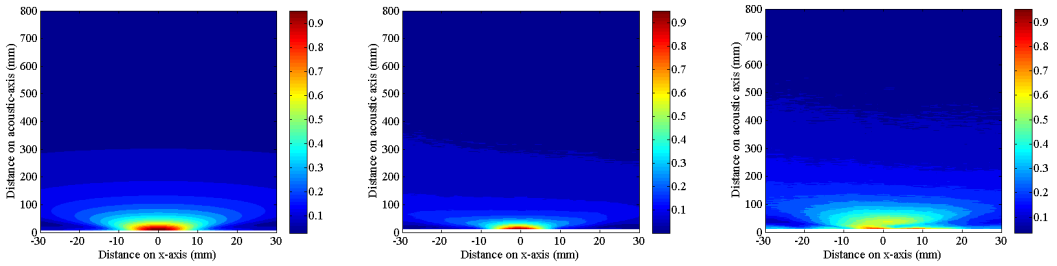

(a) 20kHz: Piston mode prediction; VC field; PCB field

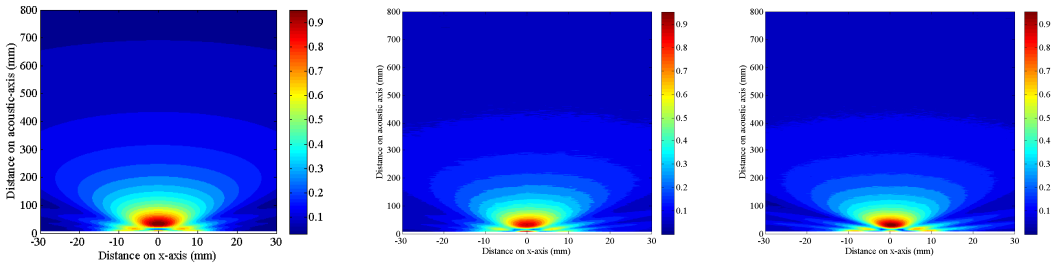

(b) 50kHz: Piston mode prediction; VC field; PCB field

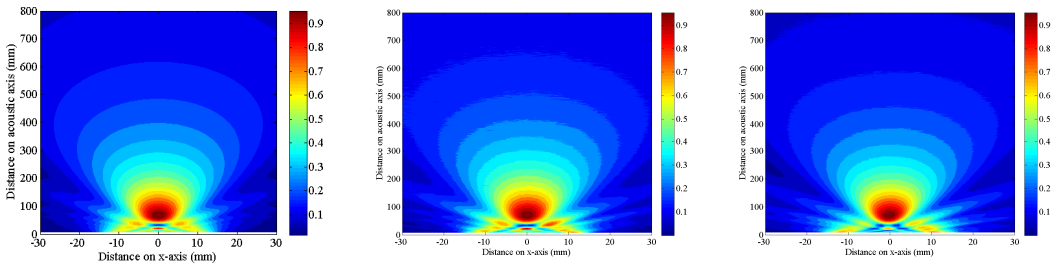

(c) 100kHz: Piston mode prediction; VC field; PCB field

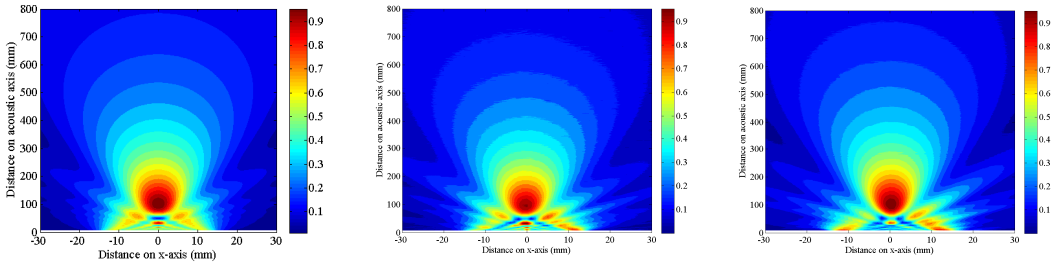

(d) 1500kHz: Piston mode prediction; VC field; PCB field

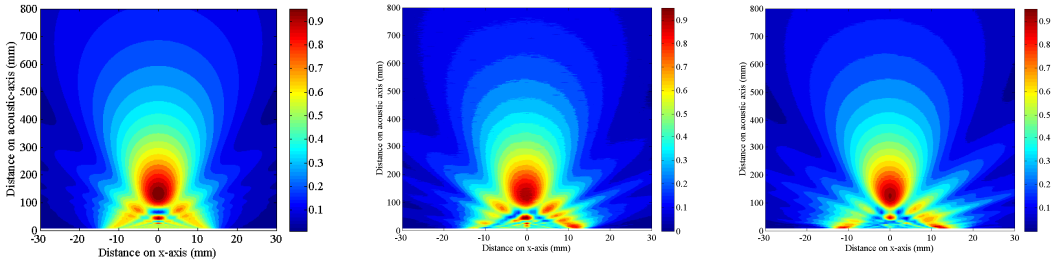

(e) 200kHz: Piston mode prediction; VC field; PCB field

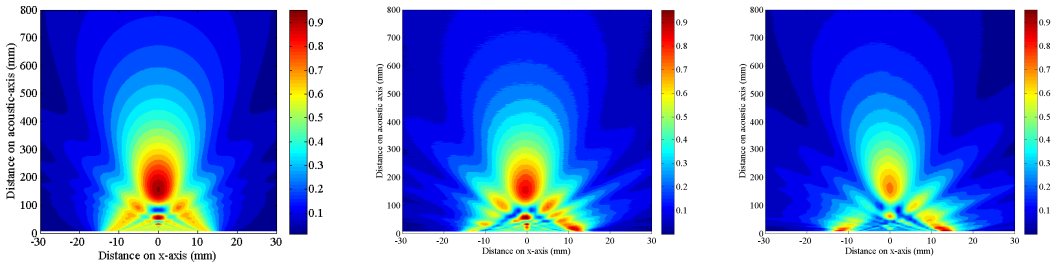

(f) 250kHz: Piston mode prediction; VC field; PCB field

Figure 4.8. Comparison of normalised ideal (plane-piston) and measured acoustic pressure fields from VC and PCB transducers: (a) 20kHz; (b) 50kHz; (c) 100kHz; (d) 150kHz; (e) 200kHz; and (f) 250kHz, with plane-piston (left), vitreous carbon (VC) measured field (middle) and PCB measured field (right) in each row.

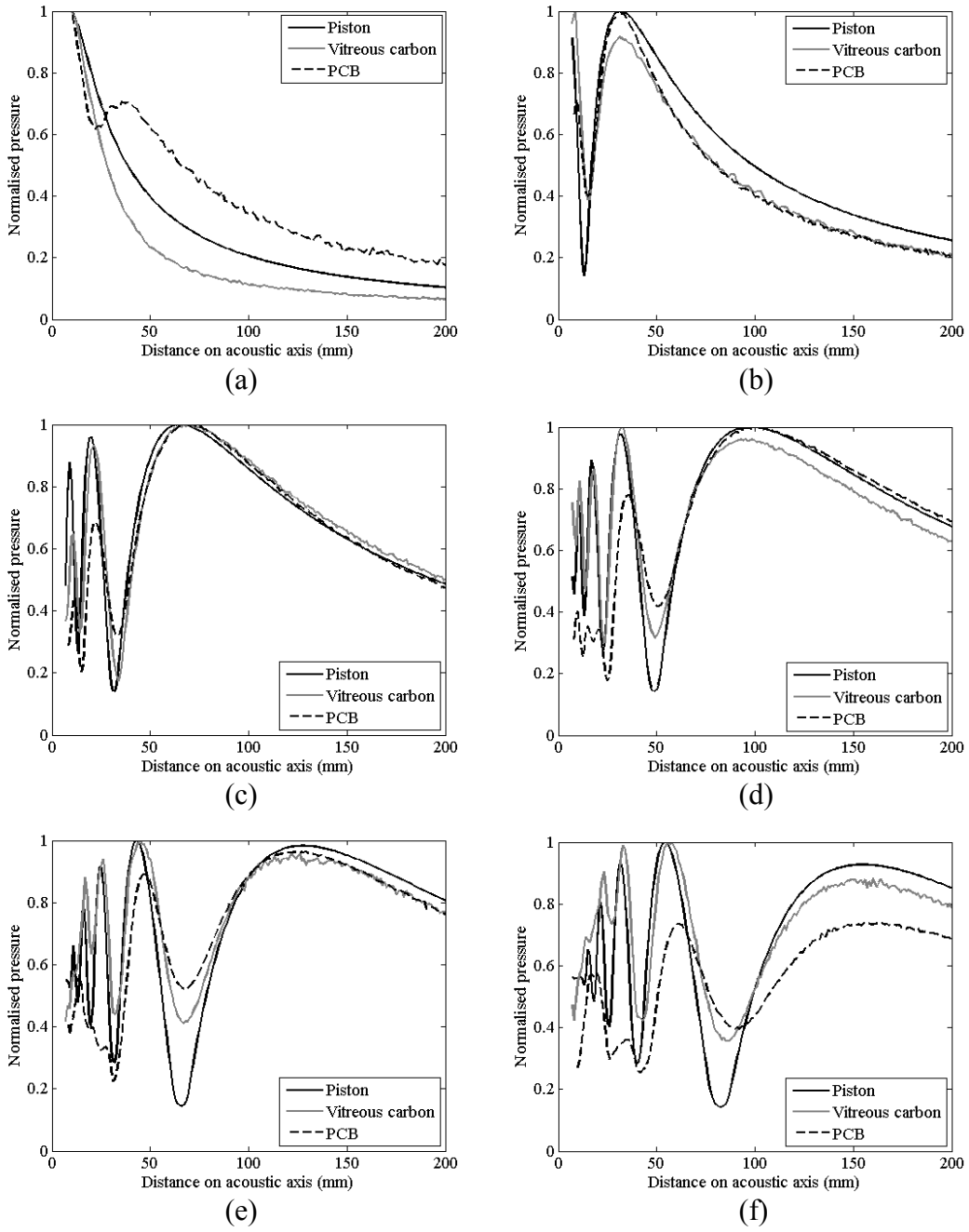

Figure 4.9. Comparison of normalised ideal (plane-piston) and measured on-axis acoustic pressure: (a) 20kHz; (b) 50kHz; (c) 100kHz; (d) 150kHz; (e) 200kHz; and (f) 250kHz.

The correlation between measured and theoretical profiles can perhaps be more easily considered by examining the pressure profiles on the acoustic axis in the near field, as displayed in Figure 4.9.

It is particularly noticeable at 200kHz and 250kHz, that the vitreous carbon response is better matched with that of the plane-piston, than the PCB response. This is also the reason for the relatively low amplitude of the peak at the far-field boundary for the PCB transducer at 250kHz; examination of Figure 4.8(f) indicates that the maximum amplitude occurs at the edges of the transducer, a short axial distance from the front face. A further point of interest is the noticeable reduction in variation between localised maxima and minima in Figure 4.9, due to the combination of the toneburst drive signal and the microphone directional response.

Given the accurate generation of piston-like fields by the VC transducer, it might be considered that this device would be used for most applications. However, there is a sensitivity advantage with the PCB device, as demonstrated by the calibration of absolute output pressure. In terms of transducer design, it is a goal to produce devices capable of piston-mode operation, generating piston-like fields as they are efficient (producing components that sum in-phase in the field) and generate well-defined, easily predicted field structures. However, as can be seen from the PCB fields, they are similar (especially so in the far field) to those produced by the vitreous carbon. In terms of practical use of such devices, most applications are carried out in the far field where the minor variations in the near field structure are of little significance. Furthermore, in air coupled ultrasound, signal-to-noise ratio (SNR) is often a limiting factor and so the transducer capable of generating higher pressure output may be selected.

4.5.4 Measurement of Membrane Motion Using Laser Doppler Vibrometry

The operation of the transducers was further characterised through measurement of the motion of the transmitting membrane whilst being driven by single-frequency CW signals, across the frequency range of interest. This was performed using a Polytec PSV400 Laser Doppler Vibrometer (LDV) system (Lambda Photometrics, Hertfordshire, UK). This is a powerful technique, allowing the motion of thousands of user-defined points on an object to be individually measured. These measurements then combine to produce a set of data that defines the motion of the entire surface.

When applied to the surface of a transducer, this allows its actual motion to be visualised and so compared with ideal piston-mode vibration.

Prior to commencing a measurement scan, the LDV system must be configured as follows:

1. Focus the laser on the measurement surface. Correct focussing maximises the return energy and so minimises noise in the measurement. It also minimises the spot-size of the laser on the measurement surface; using the standard laser optics, the spot size when focussed is approximately 18μm (Polytec data).
2. Perform 2-D alignment of the laser to align the scan surface in the local coordinate environment of the system.
3. Define an array of scan points on the transducer surface. With a surface of diameter 34mm and a spatial resolution of 150μm (λ/9 at the highest frequency of 250kHz), approximately 40000 data points were defined.
4. Configure the system A/D card to perform the measurement. This was configured to measure the velocity of each point, using 8 (complex) averages, in the frequency domain mode with a FFT bin-width of 1kHz.

This method allows the motion of the membrane to be measured directly. As will be discussed in Section 4.6, measurement of a piston-like field cannot be taken as evidence of piston-mode operation of the transducer, and so the measurements presented thus far do not necessarily indicate piston-mode motion of the transducer surface – though they *do* indicate that the fields produced are piston-like. As such, LDV measurement also provides a quantitative measure of how efficient the transducer is, since for any given magnitude of vibration, maximum energy is transferred to the load when all points on the transducer surface are operating in phase. The LDV system allows the motion of the membrane to be measured across an extended frequency range. This enables the variation in operation demonstrated in previous Sections to be analysed with respect to the vibration characteristics of each transducer, in terms of the magnitude and phase of the motion of the membrane surface.

For comparison purposes, the response of the transducers was measured using the LDV up to 250kHz. The operation of these devices at frequencies above this target range is documented in Section 4.7. The data gathered using the LDV system has been processed and displayed in a number of ways. Firstly, velocity magnitude and phase data was extracted and displayed visually; this data was further processed to extract statistical information to provide a quantitative measure. Furthermore, magnitude and phase data can be applied directly to the discretised Rayleigh integral, allowing field predictions to be made from LDV scan data. This is only useful, however, if the field predicted from LDV measurement is shown to be consistent with that measured directly using the scanned microphone. These comparisons are presented in Section 4.5.4.3.

4.5.4.1 Visual Magnitude and Phase Data from LDV

The velocity magnitude and phase data exported from the LDV system was plotted using Matlab to visualise the membrane motion across its surface, as displayed in Figure 4.10. Both the vitreous carbon and PCB transducers were measured across the frequency range of interest, and are displayed together for comparison, with the appropriate colourbar scaling indicated beside each plot.

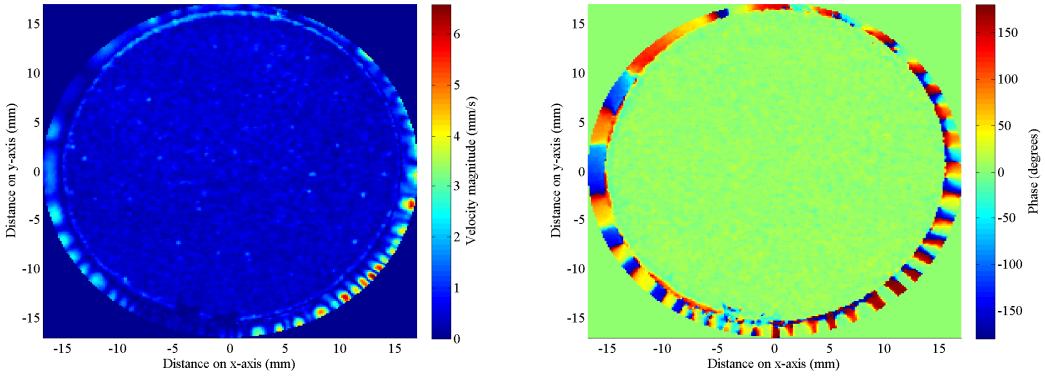

(a) VC 20kHz LDV measurement: Magnitude; Phase

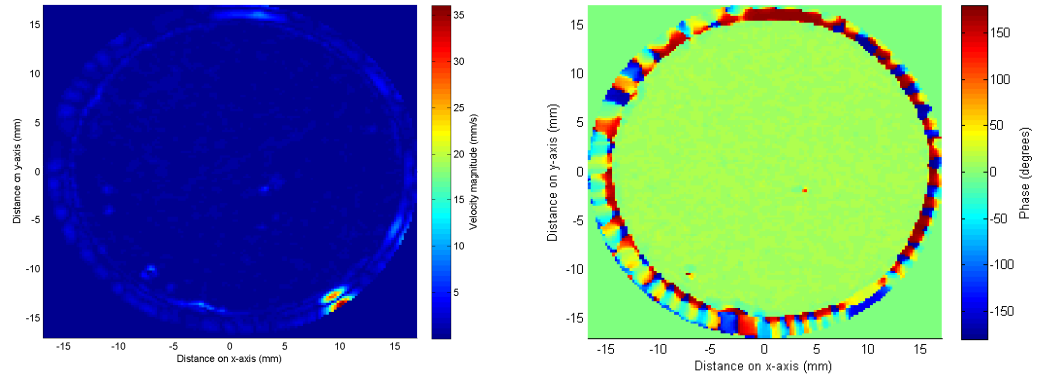

(b) PCB 20kHz LDV measurement: Magnitude; Phase

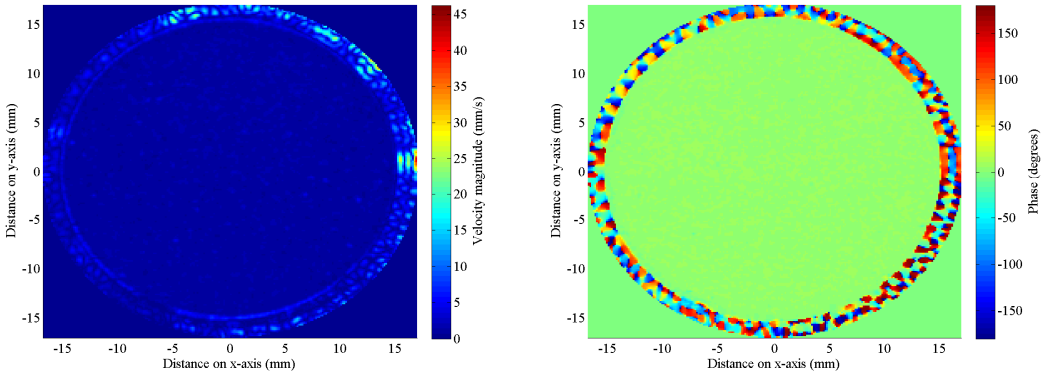

(c) VC 50kHz LDV measurement: Magnitude; Phase

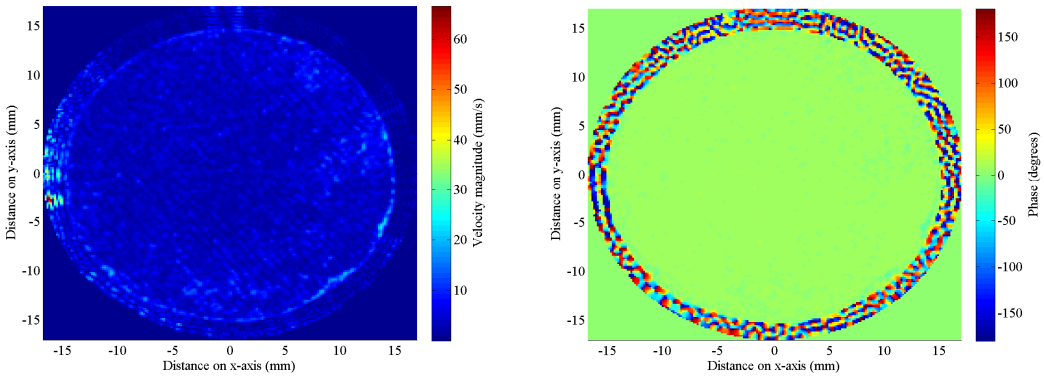

(d) PCB 50kHz LDV measurement: Magnitude; Phase

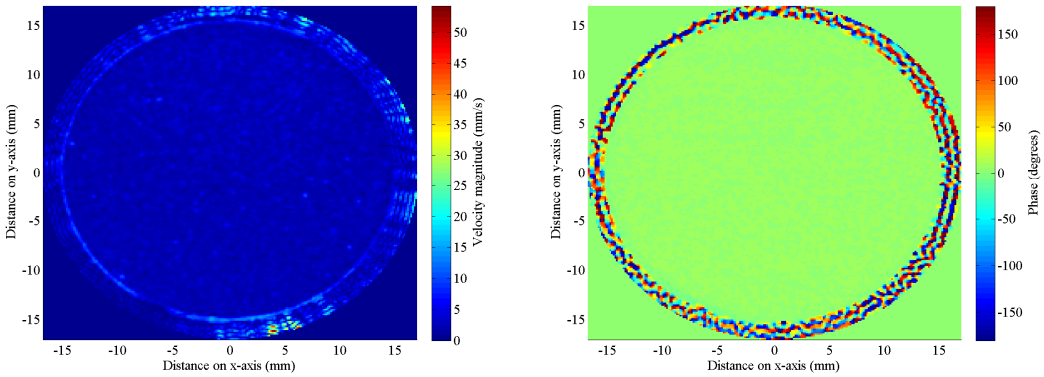

(e) VC 100kHz LDV measurement: Magnitude; Phase

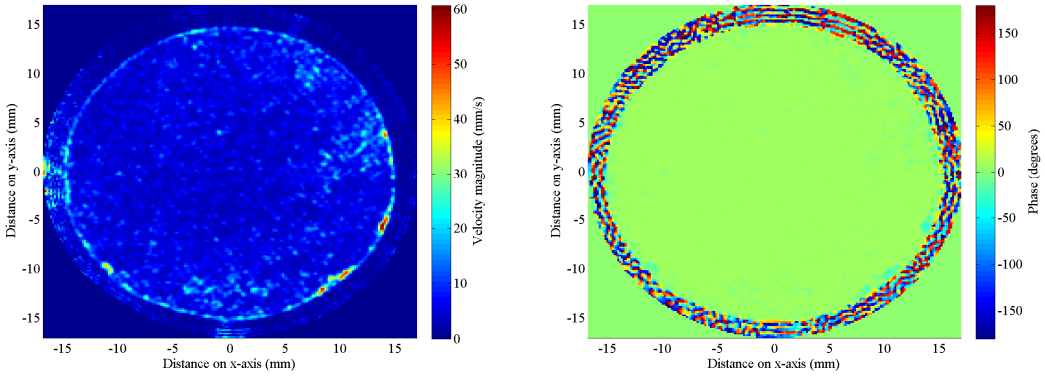

(f) PCB 100kHz LDV measurement: Magnitude; Phase

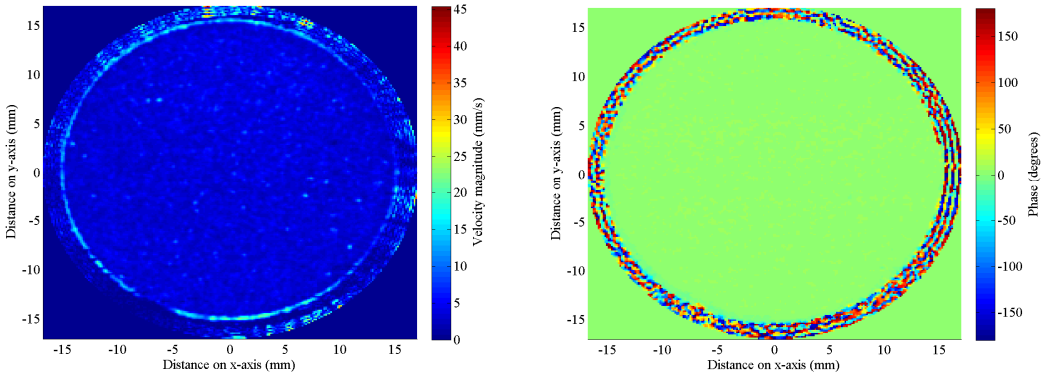

(g) VC 150kHz LDV measurement: Magnitude; Phase

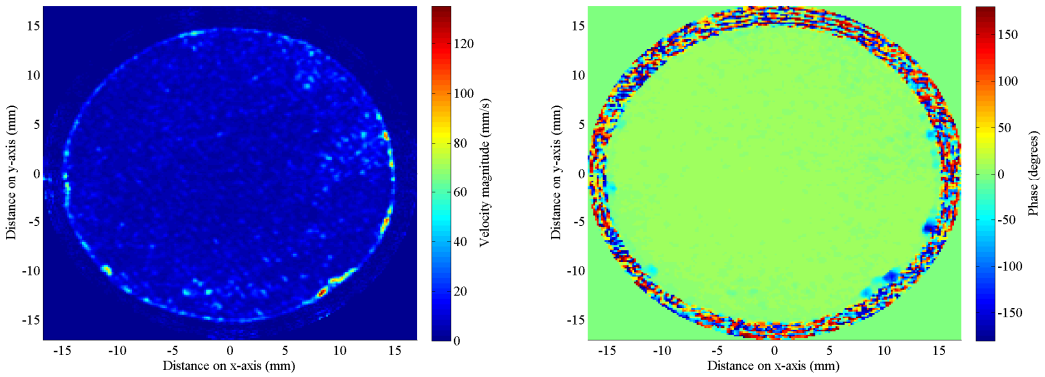

(h) PCB 150kHz LDV measurement: Magnitude; Phase

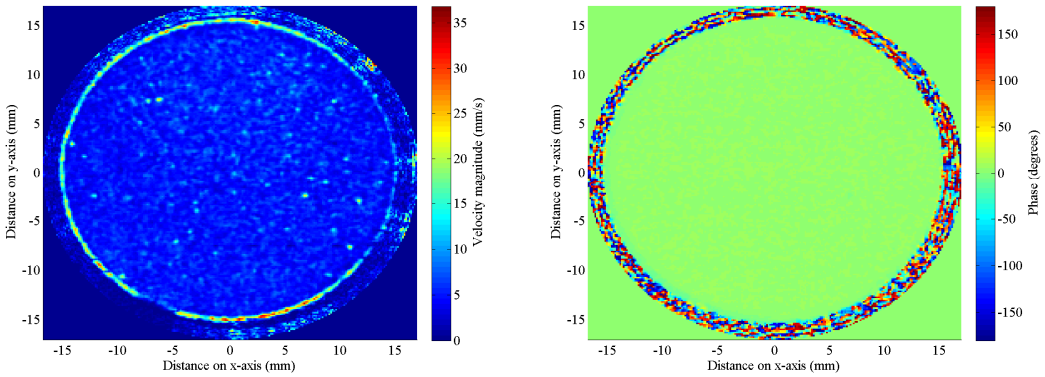

(i) VC 200kHz LDV measurement: Magnitude; Phase

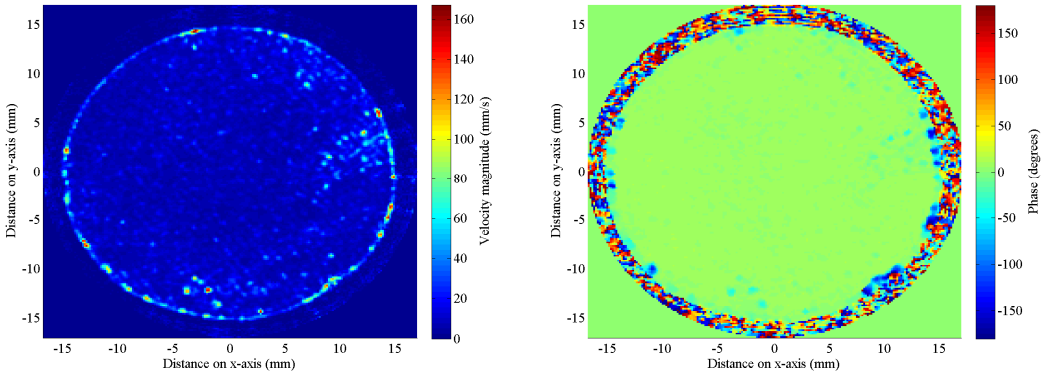

(j) PCB 200kHz LDV measurement: Magnitude; Phase

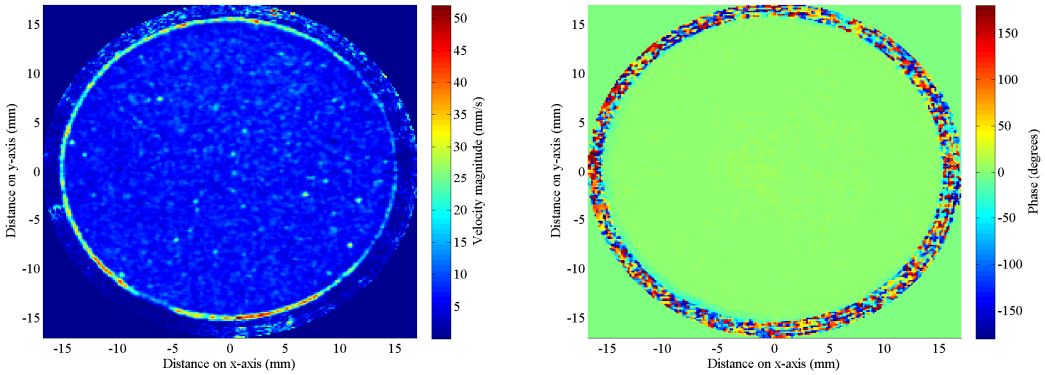

(k) VC 250kHz LDV measurement: Magnitude; Phase

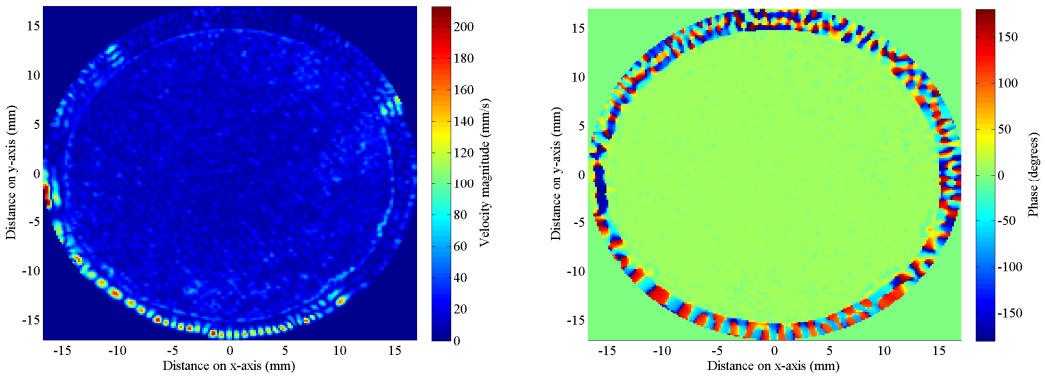

(l) PCB 250kHz LDV measurement: Magnitude; Phase

Figure 4.10. Measured magnitude and phase of the velocity of the full 34mm diameter transmitting membrane of VC and PCB transducers: (a) VC 20kHz; (b) PCB 20kHz; (c) VC 50kHz; (d) PCB 50kHz; (e) VC 100kHz; (f) PCB 100kHz; (g) VC 150kHz; (h) PCB 150kHz; (i) VC 200kHz; (j) PCB 200kHz; (k) VC 250kHz; and (l) PCB 250kHz, with magnitude (left) and phase (right) in each row.

With reference to Figure 4.1(a), which illustrates the transducer construction diagrammatically, it can be seen that there is an region of membrane that is unsupported by the backplate, being stretched between the backplate and the

tensioning ring. It is this area of membrane that accounts for the annulus of more varied magnitude and phase distribution apparent at the outer edge of the LDV plots of Figure 4.10. It would appear that this behaviour is due to the membrane being unconstrained by the backplate surface. As a result, it vibrates due to being physically connected to the rest of the membrane, rather than being controlled directly by the bias and time-varying voltage, and associated electric field, applied to the backplate. Furthermore, the magnitude of vibration of this region tends to exceed that of the backplate-clamped membrane area. It might be expected that this would seriously affect the field structure. However, as illustrated in Section 4.5.3.2, the emitted fields compares well with the theoretical piston-mode fields of a 30mm diameter aperture, especially for the VC backplate. The reason for this was investigated and documented in Section 4.5.5.

It can be seen from the LDV data that the inner region of the membrane appears to vibrate, for the most part, with uniform magnitude and phase. However, due to the large variations in the outer ring, the detail of the central area of membrane is lost. For this reason, the data has been replotted, examining only the central 28mm diameter Section, in Figure 4.11. This series of results illustrates in more detail how uniformly the central portion of the membrane is vibrating, especially as regards phase with a far more constrained distribution of phase angles than for the entire 34mm diameter membrane. The statistical data from these scans gives a more quantitative measure of the membrane vibration, and this is detailed in the following Section. Another point to note in both Figure 4.10 and 4.11 is how the weave of the glass fibre in the PCB backplate is evident in the magnitude plots from the LDV, running diagonally from top-left to bottom-right. This illustrates how the local surface profile of the backplate has a direct effect on the vibration magnitude of the membrane in contact with it. Through optical surface profiling techniques, this relationship was investigated and is reported in Section 4.6. A further point to note is how the phase correlation across the membrane of the PCB transducer is somewhat poorer than that of the VC transducer, especially for the higher frequency scans. This agrees with the trend identified from the field scans of the field profile degrading as the frequency is increased.

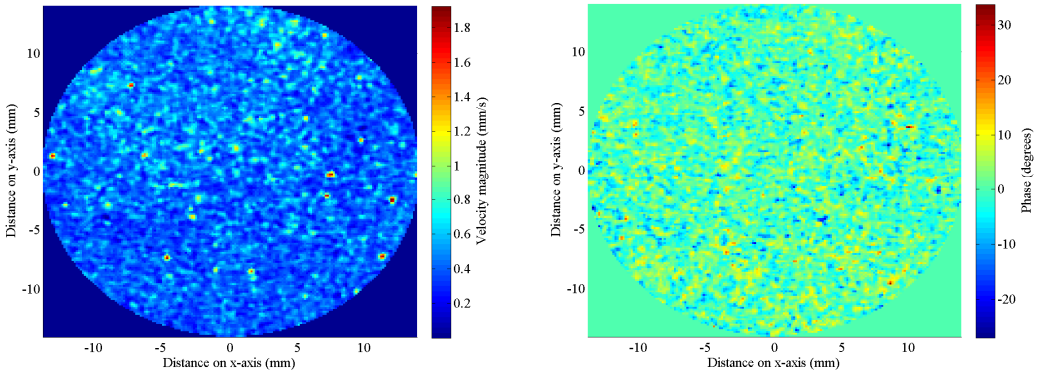

(a) VC 20kHz LDV measurement: Magnitude; Phase

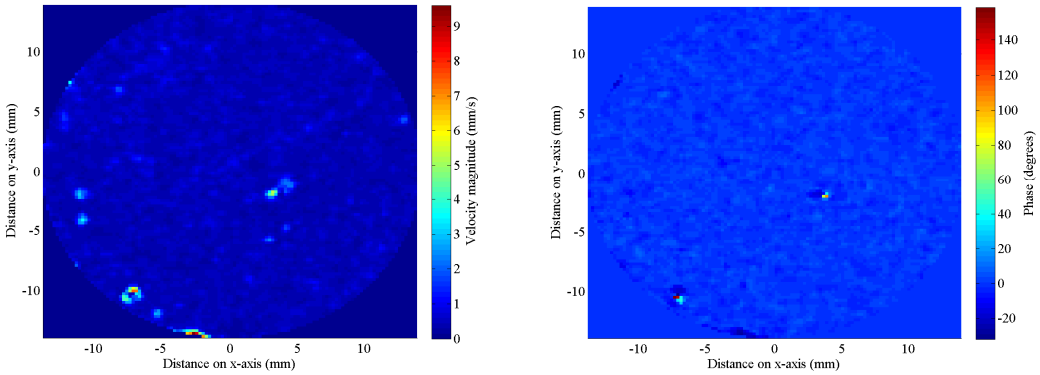

(b) PCB 20kHz LDV measurement: Magnitude; Phase

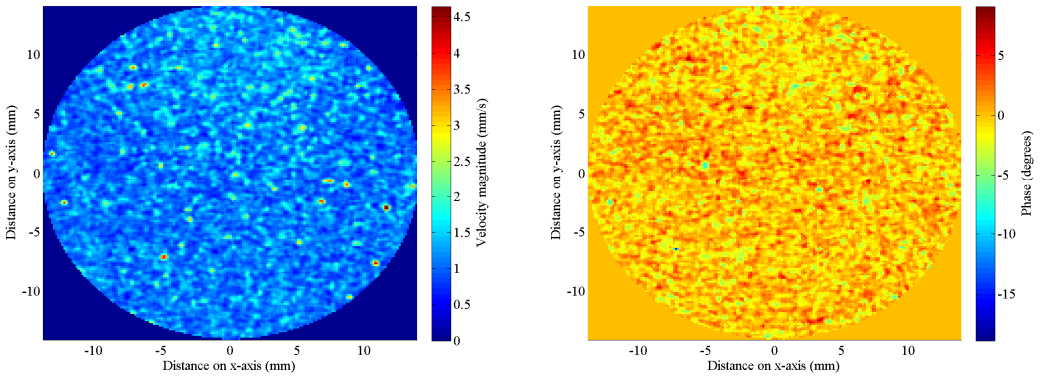

(c) VC 50kHz LDV measurement: Magnitude; Phase

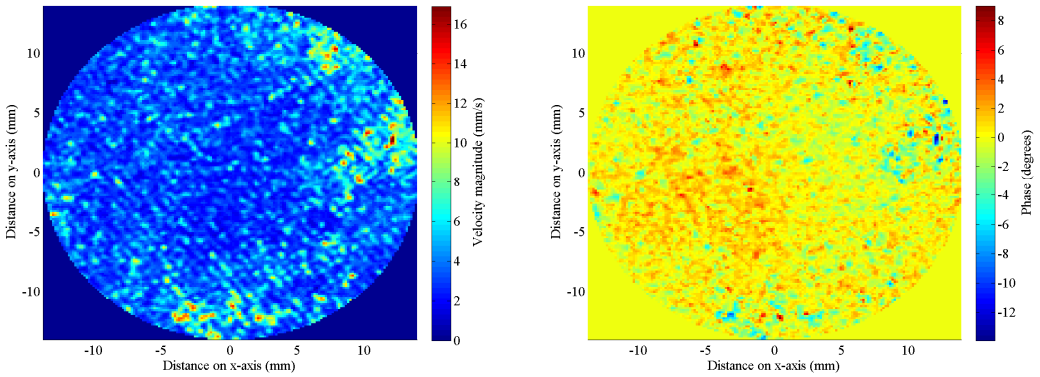

(d) PCB 50kHz LDV measurement: Magnitude; Phase

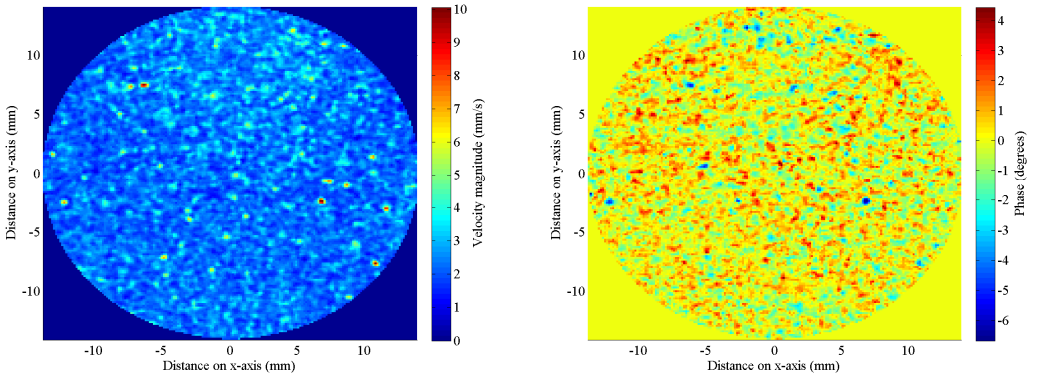

(e) VC 100kHz LDV measurement: Magnitude; Phase

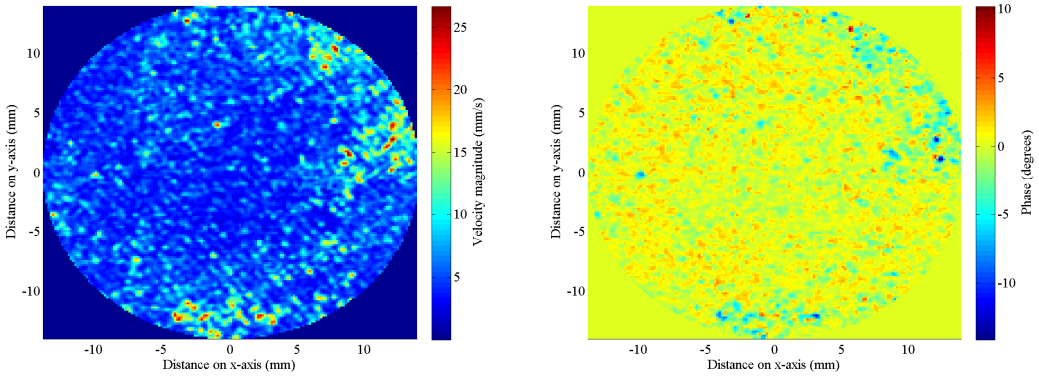

(f) PCB 100kHz LDV measurement: Magnitude; Phase

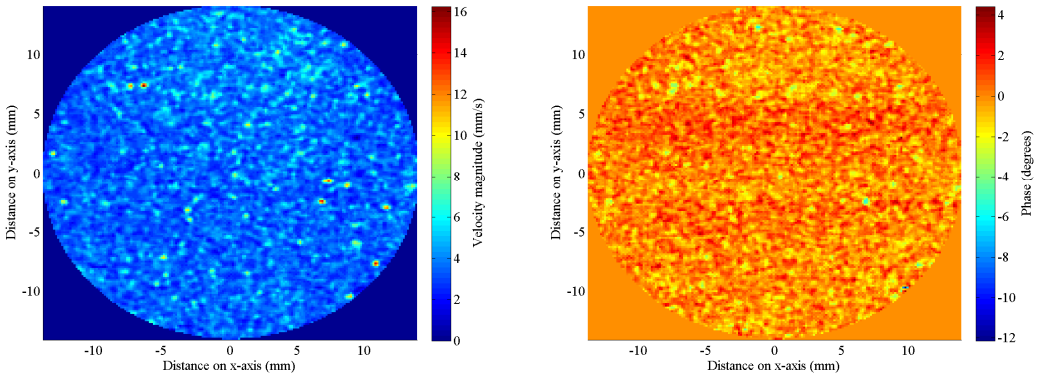

(g) VC 150kHz LDV measurement: Magnitude; Phase

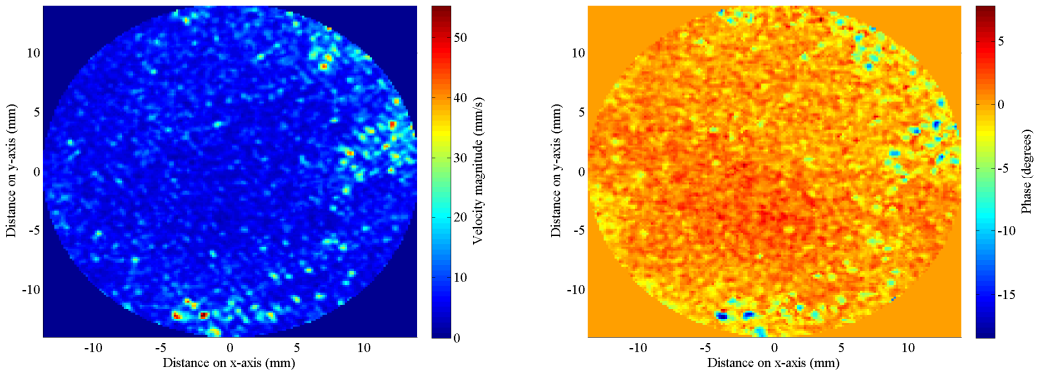

(h) PCB 150kHz LDV measurement: Magnitude; Phase

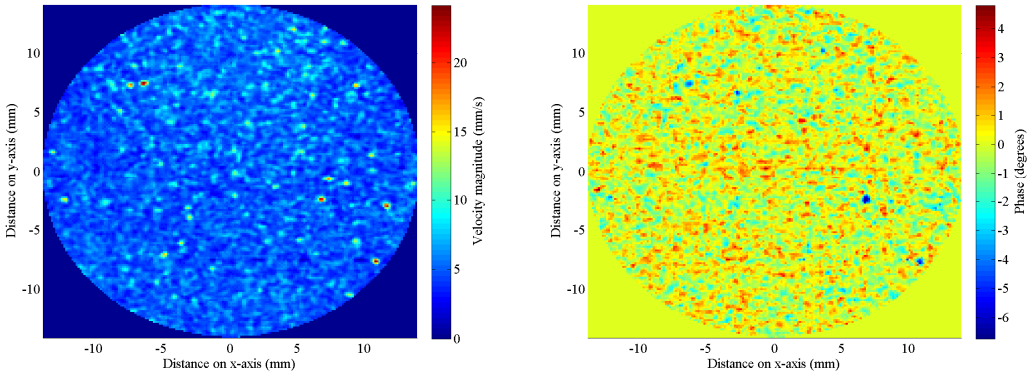

(i) VC 200kHz LDV measurement: Magnitude; Phase

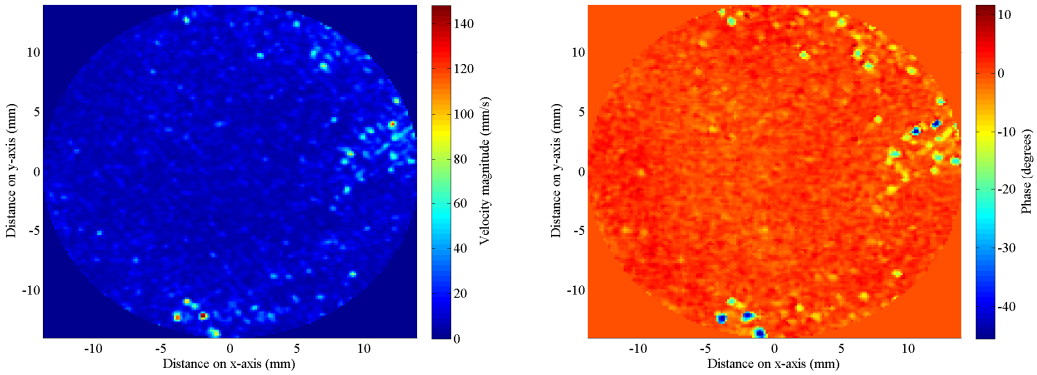

(j) PCB 200kHz LDV measurement: Magnitude; Phase

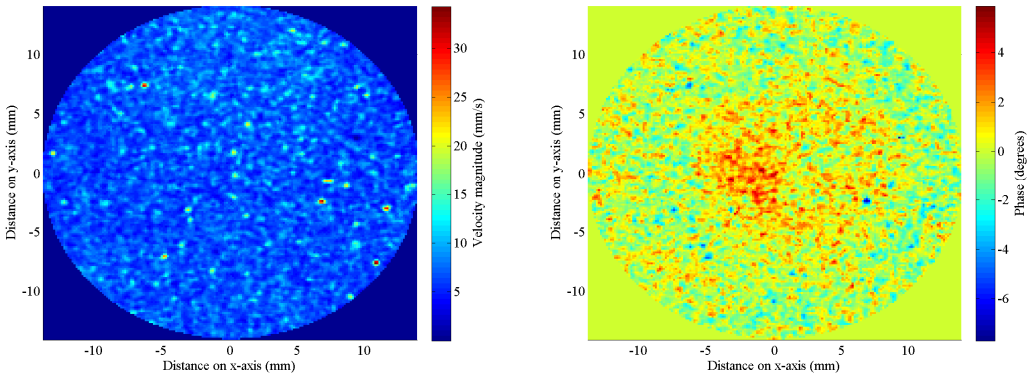

(k) VC 250kHz LDV measurement: Magnitude; Phase

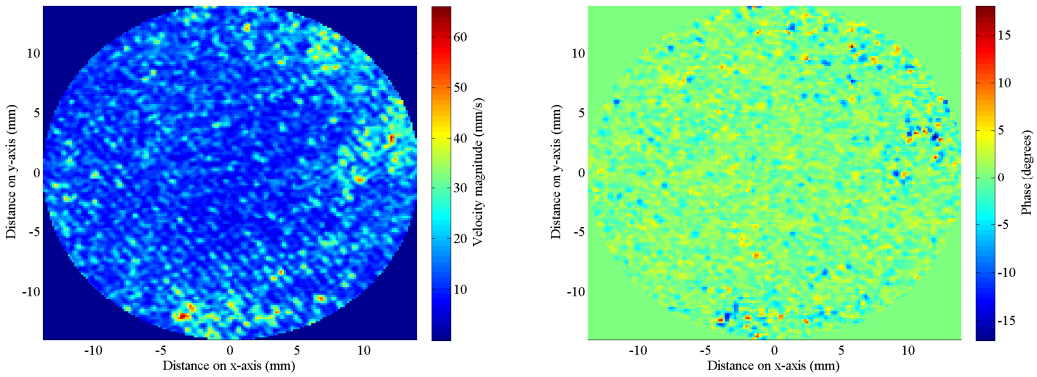

(l) PCB 250kHz: Magnitude; Phase

Figure 4.11. Measured magnitude and phase of the velocity of the inner 28mm diameter section of the transmitting membrane of VC and PCB transducers: (a) VC 20kHz; (b) PCB 20kHz; (c) VC 50kHz; (d) PCB 50kHz; (e) VC 100kHz; (f) PCB 100kHz; (g) VC 150kHz; (h) PCB 150kHz; (i) VC 200kHz; (j) PCB 200kHz; (k) VC 250kHz; and (l) PCB 250kHz, with magnitude (left) and phase (right) in each row.

4.5.4.2 Statistical Data from LDV Surface Velocity Measurements

In its visual format, the data measured by the LDV system provides qualitative information on the membrane vibration. For this reason, the raw data was processed to provide statistical data by which the transducer operation could be quantified and compared. Statistical analysis was performed to extract the mean and standard deviation values for the magnitude data; standard deviation alone is provided for the phase data, since to accurately calculate this, the phase data was processed to set the mean value to zero degrees. As with the visual plots, the data was examined as a whole, and as a subset including only those points within a 28mm diameter, thereby eliminating the contribution from the unsupported membrane around the device edge. This data, provided in Table 4.2, shows how the membrane motion varies with frequency, and also how these figures compare between the VC and PCB transducer.

	34mm diameter			28mm diameter		
Backplate / Frequency	Avg.Vel. (mms^{-1})	Vel.SD. (mms^{-1})	Vel. Phase SD (degs.)	Avg.Vel. (mms^{-1})	Vel. SD (mms^{-1})	Vel. Phase SD (degs.)
VC 20kHz	0.55	0.47	41.4	0.44	0.13	4.4
PCB 20kHz	0.79	1.51	50.0	0.48	0.32	3.5
VC 50kHz	1.82	2.38	43.7	1.16	0.29	1.5
PCB 50kHz	4.11	2.95	48.6	3.89	1.72	1.5
VC 100kHz	2.95	2.34	44.5	2.39	0.60	1.0
PCB 100kHz	5.75	4.35	49.1	5.74	2.78	1.4
VC 150kHz	4.06	2.59	44.5	3.66	0.92	0.9
PCB 150kHz	7.65	7.30	49.1	7.63	4.25	1.8
VC 200kHz	5.35	3.11	45.6	5.18	1.32	0.9
PCB 200kHz	10.58	10.93	50.1	10.35	7.29	3.0
VC 250kHz	7.24	4.46	42.8	6.99	1.78	1.2
PCB 250kHz	17.93	16.49	47.6	14.29	6.19	2.0

Table 4.2. Statistics calculated from the magnitude and phase data from LDV scans of both VC and PCB transducers across the frequency range of interest.

The first, very noticeable trend from the data is the difference in statistics presented for the entire membrane as opposed to the central Section only. This demonstrates the impact that the unsupported 2mm width ring of membrane has on the statistics, despite accounting for only 22% of the surface area. The standard deviations of the magnitude and phase populations are markedly different in all cases; the nature of the vibration of this Section of membrane skews the data. As can be seen from the 28mm diameter data, the central Section of the membrane actually vibrates with approximately uniform phase (it cannot be said that the membrane operates in piston mode, given the standard deviation of the magnitude). If the magnitude data across the frequency range (phase data are sufficiently similar between both transducers) are compared with the narrowband calibration data presented in Figure 4.5, it can be seen that the same trends exist – vibration magnitude and measured output pressure both increase with frequency, with the PCB transducer having greater magnitude and hence greater pressure output. Furthermore, it is known from the impulse response (see Figure 4.4) that peak output for both devices is above the frequency range of interest, and it can be seen here that the velocity magnitude increases across the frequency range without peaking. Another feature to note in this data is that,

although the phase spread is tighter for the vitreous carbon device, the difference is minor. This explains why the field plots displayed in Figure 4.8 are similar for these devices, with only a minor degradation illustrated in the PCB fields.

4.5.4.3 Field Profile Prediction from LDV Surface Velocity Measurements

With the data provided by the LDV system, there is a further powerful tool available for transducer characterisation. The magnitude and phase data obtained from the LDV system can be applied directly to the discretised Rayleigh integral described earlier. The only processing required is to map the LDV coordinate system to the spatial dimensions of the transducer. Each LDV measurement point is given a U and V coordinate, which relates to the angular displacement in the horizontal and vertical directions. The absolute distance coordinates cannot be provided directly since the vibrometer is configured to make measurements on a 2-D surface, through a user-controlled alignment process. This allows the system to position the laser at the correct location for each data point on the transducer surface through angular alignment of mirrors. With the distance to the target being undefined, the absolute distance between points cannot be known by the system. However, since the diameter of the circular scan area are known to the user, a mapping of the (u,v) coordinate system directly to (x,y) was performed as follows:

1. Find Δu, the difference between u_{min} and u_{max}.
2. Find Δv, the difference between v_{min} and v_{max}.
3. Specify d, the diameter of the scan in mm.
4. Map x-coordinates to $[u - (u_{min} + \Delta u/2) \times d/\Delta u]$
5. Map y-coordinates to $[v - (v_{min} + \Delta v/2) \times d/\Delta v]$

This translates the (u,v) coordinate system to (x,y), removing any offset on both axes to position the centre of the scan at (0,0). The Rayleigh integral then reads in the (x,y) coordinate data, applies the corresponding magnitude and phase measurements, and the field profile is computed as previously. This is a powerful and flexible tool, since obtaining LDV data may take only a matter of minutes; performing a field scan can take hours, or even days depending on the obtainable SNR and the associated

number of averages required at each measurement point. However, this tool is only useful if it is proven to produce results that correlate well with those produced by the direct field measurement process.

The LDV scan data, of both the VC and PCB transducers, obtained to produce Table 4.2 was applied to the Rayleigh integral to obtain predicted field plots for each transducer at each frequency. The full 34mm diameter scan data was used, and the field prediction from this displayed alongside the measured field data (previously presented in Figure 4.8, but reproduced here for comparison purposes) in Figure 4.12. Additionally, a comparison of the measured and predicted near-field pressure profile on the acoustic axis is also displayed. The effects of both the Hanning-windowed toneburst excitation and microphone directionality are included in the predicted results. Comparison of the plots in Figure 4.12 illustrate that the measured and predicted fields do, in the main, correlate well. This is particularly evident in the acoustic-axis near-field comparisons. There are some exceptions however, with 20kHz and 250kHz predictions having discrepancies with the measured data. For example, at 250kHz, the field plots indicate that the LDV data predicts lower pressure at the far-field boundary. Inspection of the axial comparison, however, indicates that this variation is not as large as the field plot suggests, with the colour scaling somewhat exaggerating these differences.

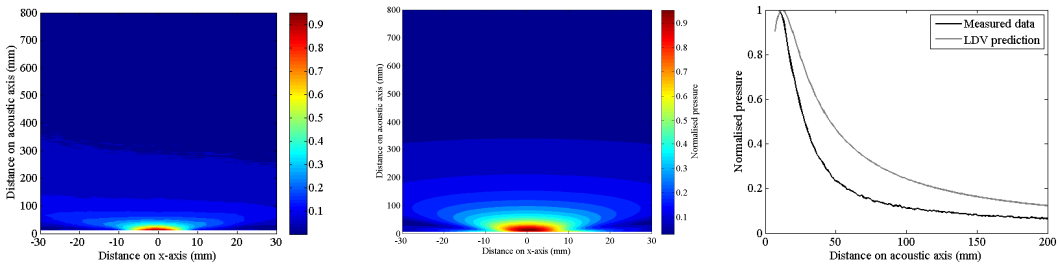

(a) VC 20kHz: Measured field; Predicted field; On-axis comparison

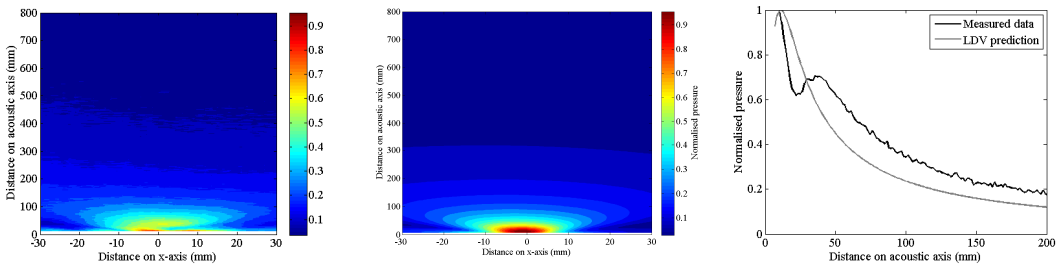

(b)PCB 20kHz: Measured field; Predicted field; On-axis comparison

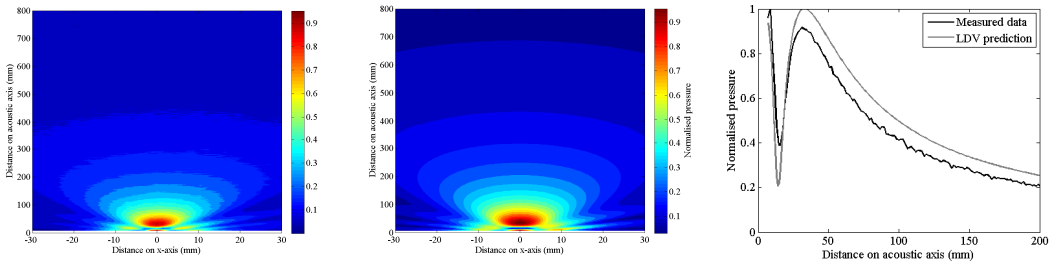

(c)VC 50kHz: Measured field; Predicted field; On-axis comparison

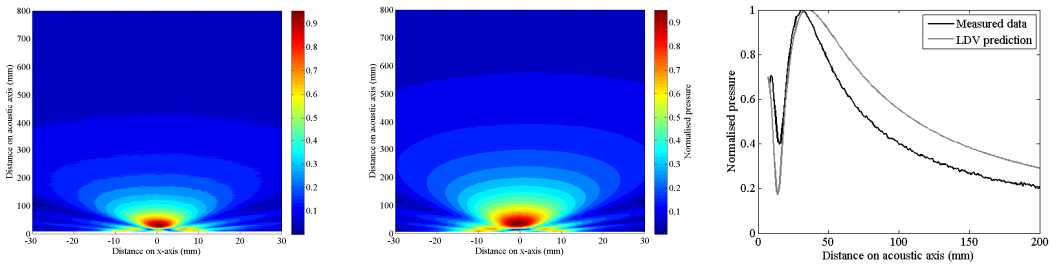

(d)PCB 50kHz: Measured field; Predicted field; On-axis comparison

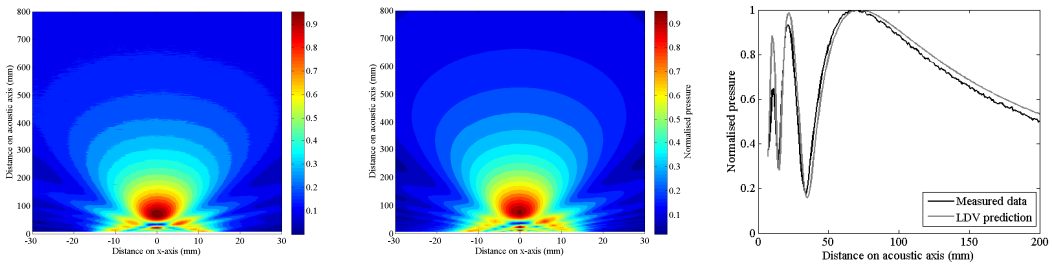

(e)VC 100kHz: Measured field; Predicted field; On-axis comparison

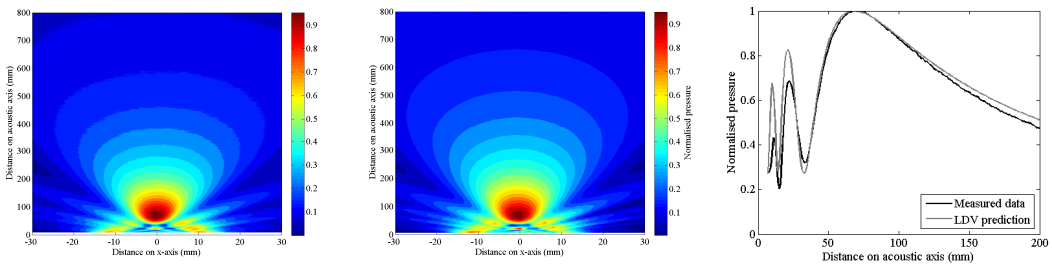

(f)PCB 100kHz: Measured field; Predicted field; On-axis comparison

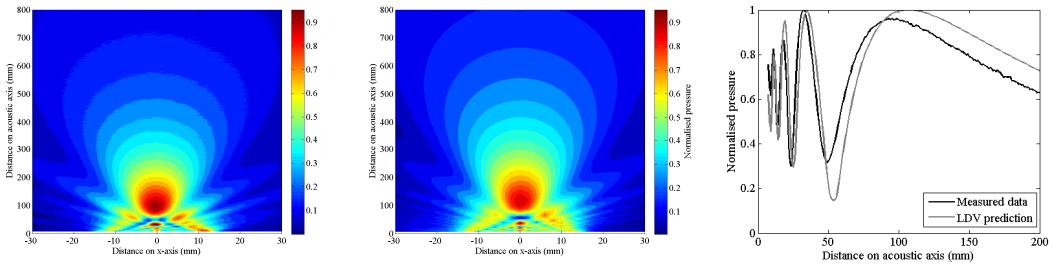

(g) VC 150kHz: Measured field; Predicted field; On-axis comparison

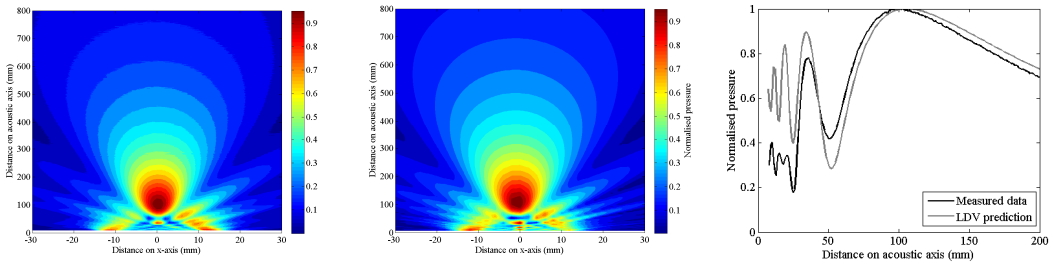

(h) PCB 150kHz: Measured field; Predicted field; On-axis comparison

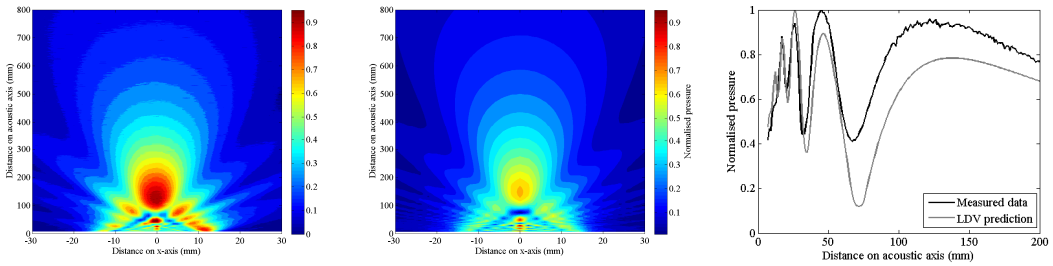

(i)VC 200kHz: Measured field; Predicted field; On-axis comparison

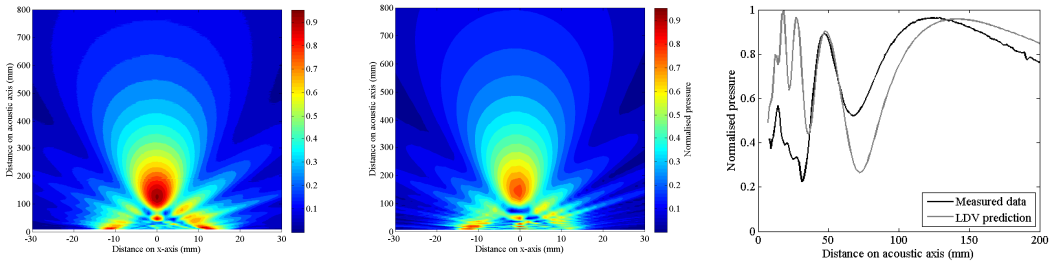

(j)PCB 200kHz: Measured field; Predicted field; On-axis comparison

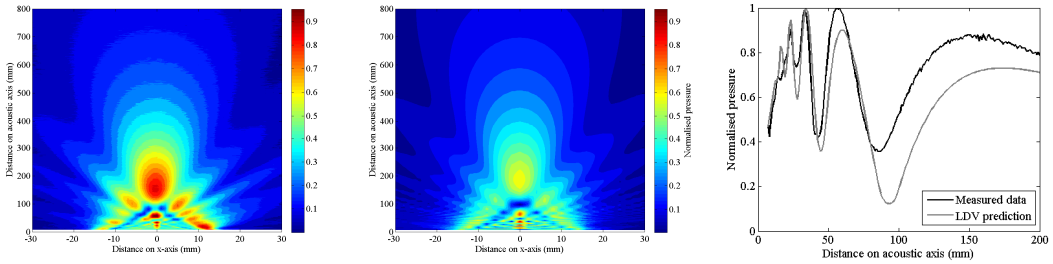

(k)VC 250kHz: Measured field; Predicted field; On-axis comparison

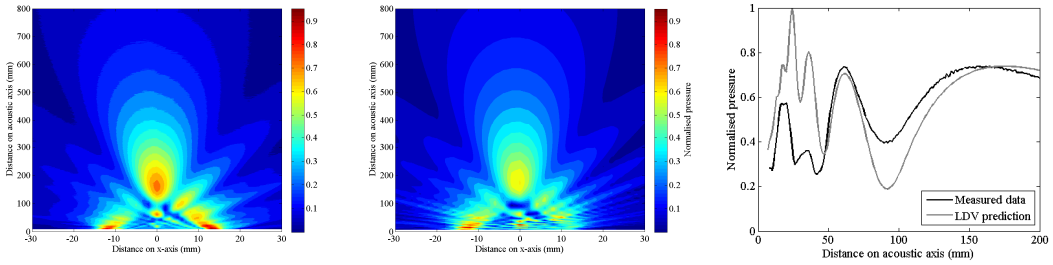

(l)PCB 250kHz: Measured field; Predicted field; On-axis comparison

Figure 4.12. Normalised measured field in comparison with the field predicted from LDV data: (a) VC 20kHz; (b) PCB 20kHz; (c) VC 50kHz; (d) PCB 50kHz; (e) VC 100kHz; (f) PCB 100kHz; (g) VC 150kHz; (h) PCB 150kHz; (i) VC 200kHz; (j) PCB 200kHz; (k) VC 250kHz; and (l) PCB 250kHz, with measured field (left), predicted field (centre) and on-axis comparison (right) in each row.

4.5.5 Investigating the Effect of the Outer Annulus of Unsupported Membrane

As previously illustrated through LDV measurement of the vibration of the transducer membrane, the outer ring of unsupported membrane between the backplate and tensioning ring has a far larger phase variation than the rest of the membrane. Furthermore, the vibration magnitude is equal to, if not greater than, that of the inner portion of the membrane, with a significantly larger SD. However, through field measurement and prediction from LDV data, this appears to have little effect on the emitted field, which compares well in most cases to that produced by a 30mm piston-mode radiator. The reason for this was not clear. However, it appeared from the LDV plots, that the phase distribution of the outer ring of membrane was fairly random. If this was the case, with phase distributed over the full 360°, then the components in the field would destructively interfere to produce little output, dependent on the magnitude distribution. This hypothesis was tested and indeed shown to be the case.

The magnitude and phase data from the LDV was divided into two regions: one from the membrane in contact with the backplate; and one from the annulus of unsupported membrane. Firstly, the phase distribution of the points on the outer ring was calculated and plotted. As an example, Figure 4.13(a) displays the phase distribution for the LDV points on the outer annulus of the VC transducer, at 250kHz. Figure 4.13(b) displays the normalised cumulative sum of the probabilities across all 360° of phase, in 1° bins.

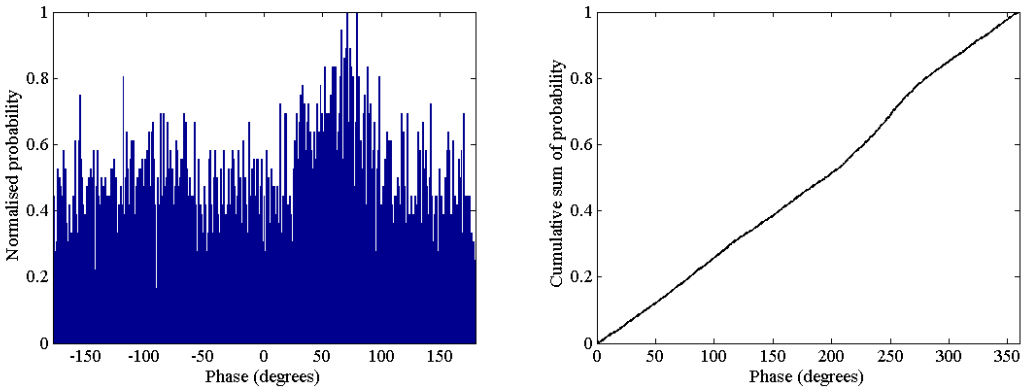

(a) (b)

Figure 4.13. Measured phase distribution of the points on the outer unsupported ring of membrane of a VC transducer operating at 250kHz: (a) Normalised probability density function, expressed as a histogram. (b) Cumulative sum of the probability density function.

These plots indicate that the phase distribution is, to all intents and purposes, a normal distribution with an equal probability of having any particular phase angle. As such, if these phases are also randomly distributed throughout the annulus, then the output field from this region should be close to zero. To check this, the field was predicted using only those points outside the 30mm diameter of the backplate. This field is depicted in Figure 4.14(a), where the magnitude has been scaled as a fraction of the maximum of the field predicted from the whole 34mm diameter scan. This shows that the maximum magnitude of the field generated by the outer annulus is approximately 12% of that generated by the whole device. The contribution of this outer annulus was further investigated by calculating its contribution as a fraction of each individual point in the field. This result is depicted in Figure 4.14(b), on a logarithmic scale. Here it can be seen that, although the maximum field strength produced by the outer annulus is significantly lower than the maximum of the device as a whole, there are regions where the annulus contribution is actually *reduced* by the contribution from the rest of the device (i.e. the field from the outer annulus is actually *greater* than the field from the whole device), indicated by a positive relative value in the plot. However, these regions are small, and restricted to the outer reaches of the field, and at small axial distances. This is illustrated in Figure 4.14(c), which shows the same data as 4.14(b), except that a -20dB limit has been imposed for clarity. As such, this plot illustrates where the contribution from the outer annulus to the total output pressure is greater than 10%, as those regions shaded deep blue. This

gives an excellent illustration of why it is that the field emitted by the electrostatic transducers compares well with that of a piston-mode 30mm diameter device, despite the large magnitude and phase variations present in the outer annulus of the membrane. This region does not contribute in a meaningful fashion to the field as a whole, especially in the far field of the transducer where most use will occur.

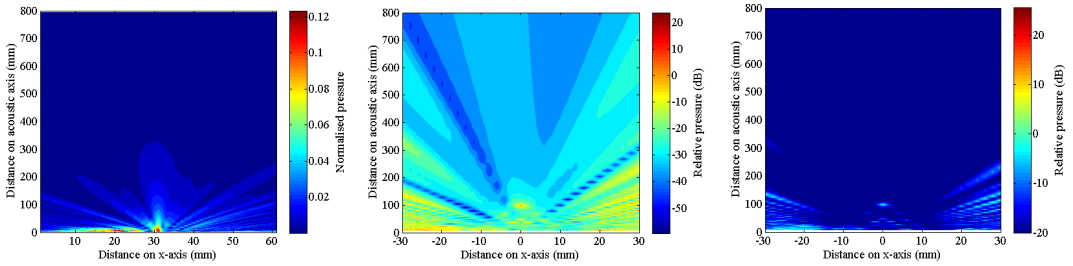

(a) (b) (c)

Figure 4.14. Predicted field contribution from the outer annulus of unsupported membrane of VC transducer at 250kHz: (a) Output field strength, normalised to that of the device as a whole; (b) Output field strength, normalised to that of the device as a whole, expressed in dB; (c) as (b) but limited to -20dB.

4.6 The Effect of Membrane Magnitude and Phase Variability

It can be seen from previous Sections that the output pressure and field structure from an electrostatic transducer depends on the magnitude and phase response of the membrane across the backplate. Previous studies (e.g. Rafiq & Wykes, 1991; Hietanen 1998; Oksanen *et al.*, 1997) have linked the structure of the backplate to operational characteristics of the transducer such as peak frequency or sensitivity, but only for backplates with regular machined features, such as grooves. In the present study, the surface of three different backplates was profiled and the link between this and the magnitude and phase of the associated membrane investigated. Furthermore, the effect that magnitude and phase variation of membrane motion has on the transmitted field was investigated theoretically and experimentally to demonstrate the fundamental link between the backplate surface profile, magnitude and phase variation and the operation of the transducer.

4.6.1 Theoretical Effect of Magnitude and Phase Variation on Field Structure

Piston-mode operation has long been a goal of transducer design. However, no practical ultrasonic transducer is capable of perfect piston motion; some variation,

however minor, of both the magnitude and phase response across the transducer surface will occur. A well-designed transducer may be capable of operation that approximates piston motion, whereby a small deviation in amplitude and phase is present across the transmitting surface, as has been demonstrated with the VC electrostatic transducers. However, there is little investigation of how such deviation affects transducer output reported in the literature. This was examined theoretically using the discretised Rayleigh integral detailed in Chapter 4, assuming CW operation to simplify the computation. A series of simulations was run, applying randomisation to either the amplitude or phase of the velocity of each point on a discretised 30mm disc. These simulations were performed at 250kHz, which was selected for two reasons: firstly, with a 30mm diameter aperture, there is a significant near-field, allowing the influence of amplitude and phase variation to be observed; and secondly, the transducers and microphone are sensitive enough at this frequency (and attenuation in air is not too large) to make clear experimental measurements for comparison. The disc was discretised at a resolution of 0.5mm, exceeding the two points per wavelength (λ=1.38mm) required for the Rayleigh integral to produce accurate field predictions. This resolution was maintained for all theoretical calculations.

Firstly, the field structure generated by a 30mm plane piston, discretised at a resolution of 0.5mm, was calculated as a reference. The generated field was discretised at 1mm resolution over a 60mmx800mm horizontal plane, which was sufficient to visualise the near field interference patterns as well as far-field spreading. The predicted normalised field structure is depicted in Figure 4.15(a). Next, the velocity magnitude of the discretised membrane was subjected to increasing levels of randomisation, applied with a uniform distribution. This process took the mean amplitude, defined as unity for ease of calculation, and added a randomised value drawn from the standard uniform distribution on the interval (-0.5,0.5), multiplied by the specified level of randomisation. As such, with a specified randomisation of 50%, each point would have an amplitude drawn from the interval (0.75,1.25), with equal probability of each point lying anywhere within that range. It was found that neither the field structure nor transmitted energy level suffered any practical degradation, even with an applied randomisation of 100% (i.e. the mean

value ±50%). The predicted field is not reproduced, since it is visually identical to Figure 4.15(a). However, a comparison of the near-field on-axis normalised sound pressure is displayed in Figure 4.15(b), starting at 10mm for clarity.

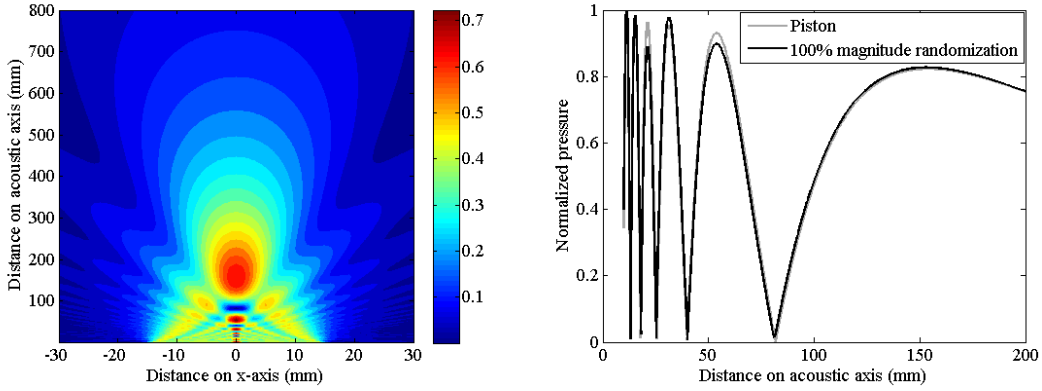

(a) (b)

Figure 4.15. Normalised pressure output from a 30mm diameter source driven at 250kHz in continuous-wave mode as predicted by the discretised Rayleigh integral including air attenuation. The source was originally assumed to be a plane-piston (a). 100% magnitude randomisation was then applied across the aperture, with the axial pressure profile of these two modes of operation compared in (b).

There are a number of points to note in Figure 4.15. Firstly, the classical Rayleigh integral predicts that the near field interference pattern should fluctuate between zero pressure and the normalised maximum. Here, the effect of attenuation in air is evident from the reduction in amplitude of successive interference peaks as the far-field boundary is approached, whilst the minimum pressure points do not reach zero, due to a combination of the discretisation of both the aperture surface and the sound field. Secondly, the variation evident in the on-axis profile due to magnitude randomisation is minor, and only affects the extent to which local minima and maxima are recreated. This demonstrates that the field produced by a transducer is robust as regards amplitude variation across the aperture. Note that this applies only when the amplitude is *randomised*, and not if an identifiable trend exists across a dimension of the transducer, such as a radial mode (Hayward *et al.*, 2000) or a distribution of higher amplitudes in a specific area (Benny *et al.*, 2000). However, this type of randomisation has been observed in real radiating structures, as will be illustrated in the following Section.

The effect of phase variation was studied in the same fashion, applying increasing levels of phase randomisation (again with a uniform distribution) across the discretised 30mm diameter aperture. This produced the results illustrated in Figure 4.16, for phase randomisation of 90° (i.e. ±45°), 180° (±90˚) and 270° (±135˚) at 250kHz. It can be seen that the field structure becomes increasingly degraded and loses output amplitude for increasing levels of phase variation. This is illustrated particularly well in Figure 4.16(d), which compares the pressure on the acoustic axis. The normalised amplitude at the far field boundary was 75%, 53% and 25% of the value for piston-mode operation, for phase randomisation of 90°, 180° and 270° respectively.

It is necessary here to describe the normalisation process that produced the images in Figure 4.16. The data was normalised *across all* data points (rather than *within each* field prediction) to enable the relative transmitted pressures to be compared, rather than field structures only. To perform a full comparison, the piston mode prediction was repeated as part of this series of results. The reason its on-axis pressure did not peak at normalised full pressure, as in Figure 4.15(b), is due to the phase randomisation producing a maximum pressure (across all the results) at a point located off the acoustic axis in the 270° randomisation simulation. As such, all data used to produce Figure 4.16 are normalised with respect to that point.

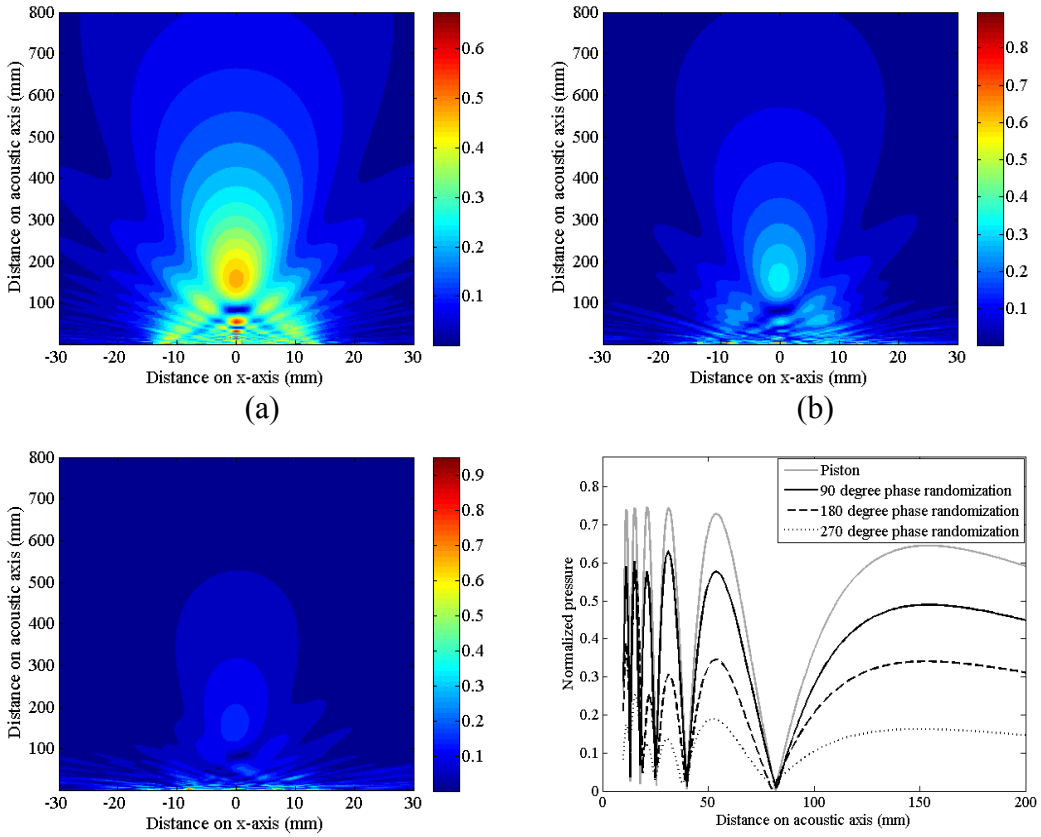

Figure 4.16. Comparison of predicted pressure output for a 30mm radiating aperture, discretised at 0.5mm, excited with increasing levels of phase randomization: (a) 90˚; (b) 180˚; (c) 270˚; (d) On axis comparison.

It is perhaps surprising that the field structure maintains much similarity with piston-mode operation, certainly beyond 90° phase randomisation. However, it should be noted that since both the magnitude and phase are being randomised across all radiating points, then the resulting field structure will tend to remain constant, reducing only in amplitude as the phase variation causes a reduction in the magnitude of the added vectors. Indeed, the reason the field structure can be seen to degrade in the phase randomisation simulations is due to the level of discretisation employed. If a larger number of points were taken on the radiating surface, then the field would tend towards the original piston-mode structure, by virtue of the added vectors tending towards a combined phase angle of 0˚. Nevertheless, the investigation is instructive as to the nature of fields emitted in the presence of such phase variation.

4.6.2 Experimental Investigation of Magnitude and Phase Effects

The previously documented VC transducer was again used, with its tight phase correlation across the aperture providing a useful control for investigation. A variety of rougher materials were tested to contrast with this operation, to study the effect that variation of the magnitude and phase response would have on the emitted field structure. As such, P240 sandpaper, with a conducting layer of silver paint, was used as the second backplate, mounted on a 30mm disc of aluminium. As defined by FEPA (Federation of European Producers of Abrasives), P240 sandpaper has a mean grain size of 58.5μm. It was considered that this randomly rough substrate would promote magnitude and phase randomisation across the membrane to compare with the operation of the vitreous carbon device.

4.6.2.1 Experimental Characterisation of VC and P240 Transducers

The operation of the electrostatic transducers was characterised in two ways: firstly through use of the Polytec LDV system and subsequently through direct measurement of the emitted field, using the B&K microphone. Through these two methods, the relationship between the motion of the transmitting membrane and the emitted field structure was investigated.

For LDV measurement, the membrane surface was discretised at a resolution of 150μm, in order to obtain detailed data on the membrane motion; as such, some 31000 points were measured across the membrane, allowing a quantitative evaluation of how "piston-like" the motion of each transducer was. Figure 4.17 shows the results of these measurements, plotted as normalised probability functions for both the velocity magnitude and phase across the radiating membrane. These plots are normalised histogram data displayed as a linear plot to accommodate multiple results in a single figure for comparison. Measurements were made across a range of frequencies, with those made at 100kHz and 250kHz presented here as representative examples. In Figure 4.17(a) it can be seen that the membrane motion of the vitreous carbon transducer increases between 100kHz and 250kHz, whereas that of the P240 sandpaper transducer decreases. (In comparison with the VC transducer having a peak output at 885kHz and a fractional bandwidth of approximately 120%,

measurement on the P240 transducer indicated a peak at 63kHz, and a fractional bandwidth of less than 30%). Figure 4.17(b) illustrates the phase response of the two transducers, with a single set of data displayed as the phase data at 100kHz and 250kHz was practically identical for both transducers. Since the data was normalised for comparison, some detail is lost; it is instructive that peak phase probability (with a histogram bin-width of 1˚) for the VC transducer accounts for some 18% of all measured points; for the P240 transducer, the peak accounted for 1%.

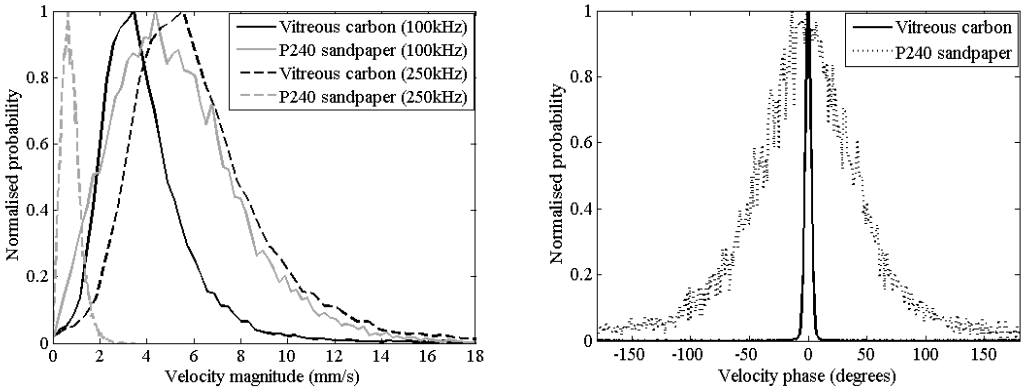

(a) (b)

Figure 4.17. Normalised probability density functions for displacement magnitude (a) and phase (b) of points on the radiating membrane of the electrostatic transducers measured using the LDV.

Further understanding of the results in Figure 4.17 can be gained from their statistical mean and standard deviation (SD) as displayed in Table 4.3. This indicates that the standard deviation of the velocity amplitude was approximately 50% of the average value for both transducers at both frequencies. There are two interesting points to note from this. Firstly, even with the rougher surface of the sandpaper, the peak membrane velocity between these two measurements is approximately the same at 5mms^{-1}. Secondly, it appears that the greater roughness did not promote additional variation of the velocity amplitude, since the ratio of SD to mean value remains fairly constant; it did however have the desired effect of causing the phase correlation to break down.

Frequency	Vitreous carbon transducer			P240 transducer		
	Avg. Vel. (mms^{-1})	Vel. SD (mms^{-1})	Vel. Phase SD (degs.)	Avg. Vel. (mms^{-1})	Vel. SD (mms^{-1})	Vel. Phase SD (degs.)
100kHz	4.03	2.33	1.6	5.31	2.78	48.4
250kHz	4.79	2.96	2.3	0.81	0.42	54.1

Table 4.3: Statistical data from LDV measurement of the displacement amplitude and phase across the membrane of each transducer, at 100kHz and 250kHz.

Given the results from the LDV measurement, it was interesting to investigate how these characteristics transferred to the field structure generated by each transducer. Measurements were made at each point in the field, on a 1mm×1mm grid for direct comparison with the theoretical results and are compared with the theoretical field expected from a piston-like radiator of 30mm diameter driven with a 10-cycle Hanning-windowed toneburst, as predicted by the modified Rayleigh integral (including FFT) introduced in Section 4.2. These comparisons are displayed in Figure 4.18, where the measured and predicted pressure fields are normalised within each individual field measurement.

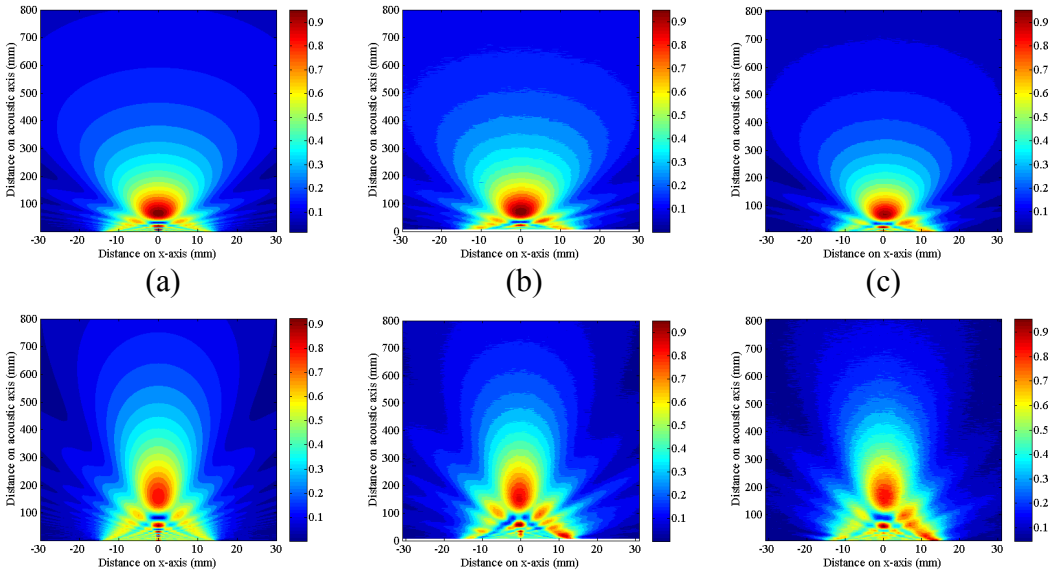

Figure 4.18 Comparison between predicted piston-mode pressure output for a 30mm radiating aperture and measured output pressure from the electrostatic transducers. (a) – (c) 100kHz: (a) Predicted piston mode field; (b) Measured field from vitreous carbon transducer; (c) Measured field from P240 grade sandpaper transducer. (d) – (f) 250kHz: (d) Predicted piston mode field; (e) Measured field from vitreous carbon transducer; (f) Measured field from P240 sandpaper transducer.

As previously reported (but repeated here for comparison purposes) the field emitted by the VC transducer correlated exceptionally well with the predicted piston-mode field. However, the fields produced from the P240 sandpaper, with far greater phase variation across the membrane surface, do not show major degradation in the field structure, even in the near field. One noticeable difference between the fields is the increased level of noise in the 250kHz field from the sandpaper-backed transducer (visible as the blurring of the boundaries in Figure 4.18(f)). This is due to the reduced pressure (and so decreased SNR) generated by the transducer, which resulted from the combination of the reduction in amplitude and increase in phase variation of the membrane velocity, as measured by the LDV. The measured pressure at the far-field boundary was reduced by approximately 24% and 73% for the sandpaper-backed transducer, at 100kHz and 250kHz respectively, although this is obviously not visible in the normalised measurements.

4.6.2.2 Regarding Backplate Surface Profile: its Link to Magnitude and Phase Response

The results reported in the previous Section illustrate how variation in magnitude and phase, either artificially randomised or experimentally occurring, can affect the output field. However, it is interesting to investigate potential mechanisms that would cause such variation in the first place. The surface profile of three different backplates was measured, to ascertain to what extent this characteristic could be linked to the motion of the membrane. The backplates examined were the VC and P240 sandpaper, and the PCB documented previously. The backplates were profiled using two techniques, by the National Physical Laboratory (NPL; Teddington, UK). Firstly, the roughness of each sample was measured using a PGI 1000 (Taylor Hobson, Leicester, UK) contact stylus instrument. The profile evaluation lengths of 0.4mm, 4mm and 8mm for the VC, PCB and P240 backplates, respectively, were selected according to ISO 4288: 1996. Roughness was characterised through measurement of R_a, which is the arithmetic average of the absolute height values measured on the surface. The value of R_a (±SD) for each sample was: 2.23nm (±0.15nm) for VC; 500nm (±45nm) for PCB; and 16.2μm (±1.3μm) for P240. It will

become apparent that this measurement, given the relatively short and linear extent of the measurement points, is designed to give an indication of surface roughness over a relatively small area. This indication is rather different to what metrologists might term *form*, or the larger-scale variation over a surface. This was indicated by the second set of measurements, which was performed using a PGK 120 (Mahr, Göttingen, Germany) surface metrology instrument. This set of measurements allowed the surface profile of the backplates to be mapped, and so compared graphically with the LDV measurements of the membrane motion, to investigate the link between membrane motion and the backplate surface. The original data provided by NPL was mapped using Matlab, and is displayed in Figure 4.19. The data presented are square, since the contact method of surface profile measurement involved a raster scan of the measurement head and so the central 19mm square section was examined. It can be seen from these images that there is not necessarily a link between a low value for roughness (R_a) and the flatness or form across the entire backplate. For example, the VC backplate varies in height across the entire sample by slightly more than ±3µm; the PCB backplate varies by less than this, despite having a roughness figure some 200 times greater. In practical terms what this means is that the VC sample is smooth, but has a larger degree of variation in form (it can be seen from the data that the sample actually has a shallow saddle-type form), whereas the PCB is rougher, but has a smaller variation in form, and so may be seen as "flatter" (as opposed to "smoother") over its entire surface.

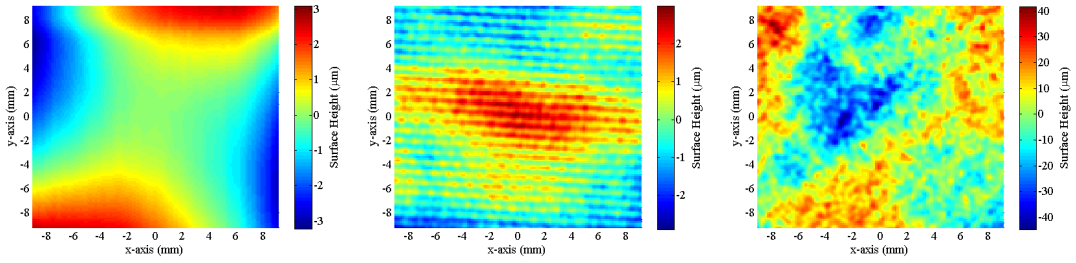

(a) (b) (c)

Figure 4.19. Surface profile data for the three backplates as measured by NPL: (a) VC; (b) PCB; and (c) P240.

Two views of a cross-section of the VC sample are illustrated in Figure 4.20. Although the curved nature of the profile is exaggerated by the aspect ratio of the axes, the variation of just 2µm across the surface means that the membrane can

adhere closely to it across the entire surface. Indeed, this was seen on the device when the bias voltage was applied. Figure 4.21 presents the magnitude and phase response over the corresponding region of the membrane at 100kHz and 250kHz. The magnitude and phase response, at both frequencies, appear to have an arbitrary pattern. This was confirmed by rebuilding the transducer, which yielded a similar range of values, but a rather different pattern as can be seen in the LDV data of Figure 4.22. What can be discerned, however, is the similarity in the pattern of the magnitude data at 100kHz and 250kHz within each figure. This demonstrates that the trapped air behind the membrane defines its motion at each frequency. However, the smooth nature of the VC material means that any air that does get trapped under the membrane is organised arbitrarily, since there are no surface features to regulate this. The defining feature of the VC transducer is its very tightly grouped phase response, due to the motion of the membrane being regulated by the large electric field caused by the proximity of the backplate over its entire surface.

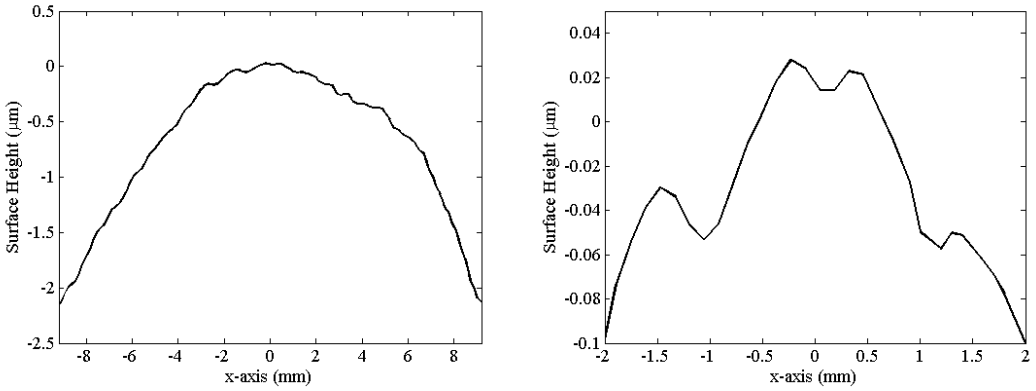

(a) (b)

Figure 4.20. Cross section of VC backplate across (a) entire sample, (b) central 4mm section.

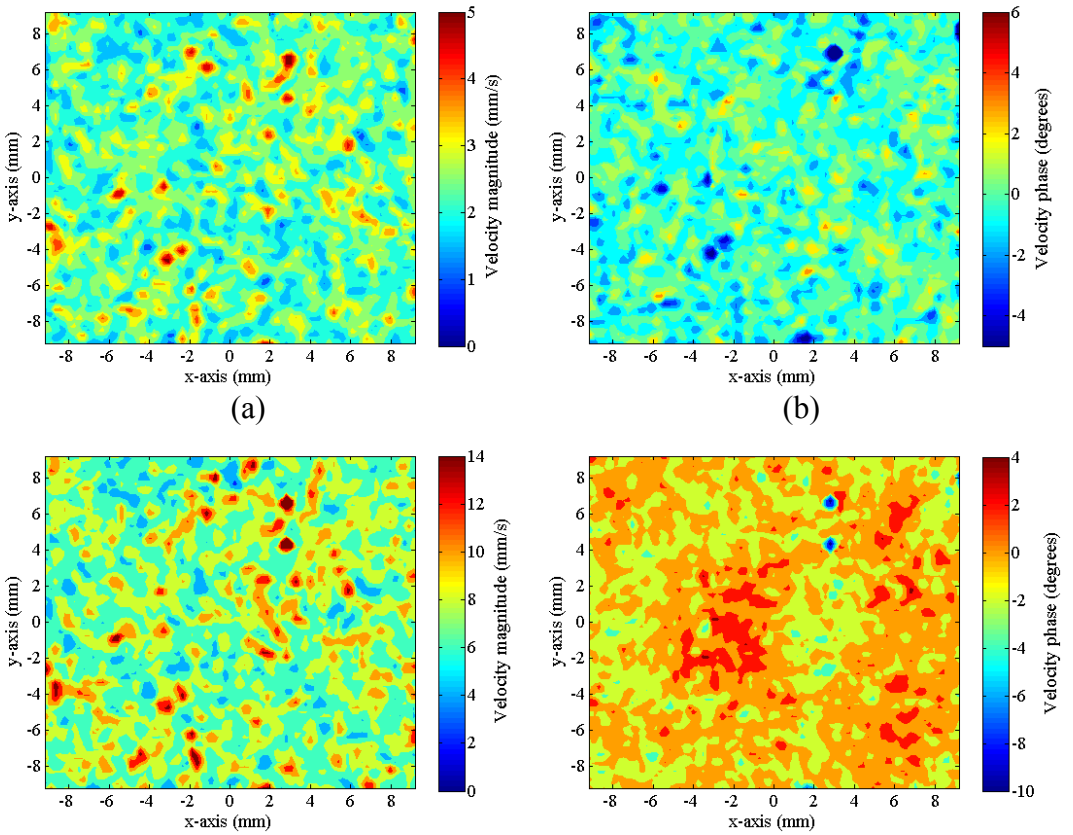

Figure 4.21. LDV membrane velocity data for VC transducer: (a) 100kHz magnitude; (b) 100kHz phase; (c) 250kHz magnitude; and (d) 250kHz phase.

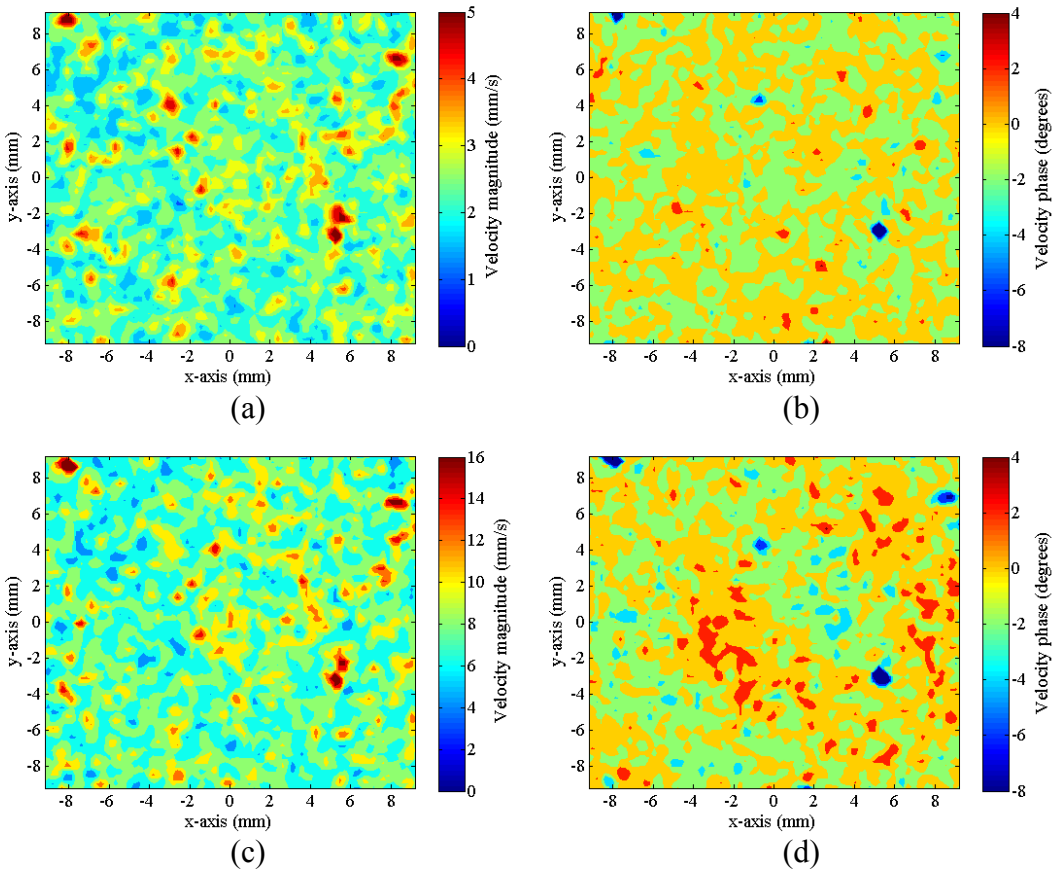

Figure 4.22. LDV membrane velocity data for the rebuilt VC transducer: (a) 100kHz magnitude; (b) 100kHz phase; (c) 250kHz magnitude; and (d) 250kHz phase.

In order to see the local variation of the PCB and P240 samples, the form of the surface was removed using a 2-D averaging filter. This was performed to more clearly display local variation in surface height, without deviation over the whole sample obscuring it. The result of this is displayed in Figure 4.23 for the PCB sample. By removing the larger variation in form, then the local maxima and minima, caused by the weave of the glass fibres, can be easily discerned. It is those points of greater elevation that should clamp the membrane more tightly under the influence of higher electrostatic field, caused by greater proximity. It is also instructive to consider that the membrane conforms to the surface of the PCB, allowing the weave pattern of the material to be discerned through the membrane after application of the bias voltage. This demonstrates how closely the membrane adheres to the backplate, similarly to the VC backplate.

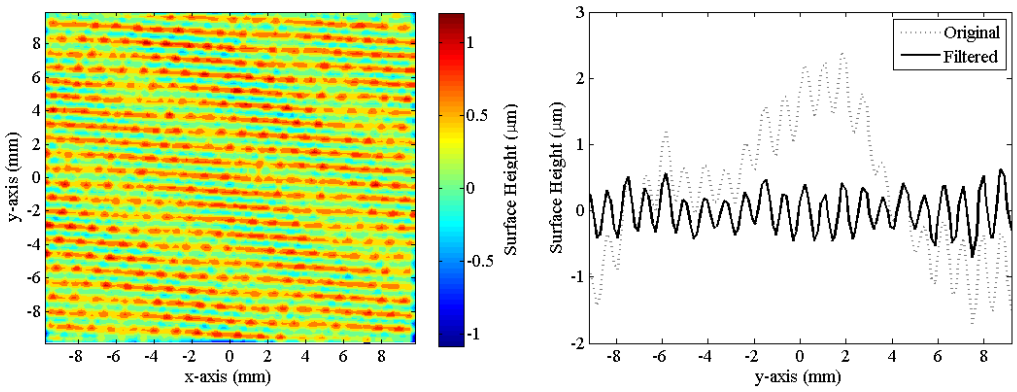

(a) (b)

Figure 4.23. Spatially filtered surface profile data for PCB (a), with a single cross section comparison (b).

With this map of the surface of the backplate it is interesting to compare the magnitude and phase of the membrane motion of this device in operation. These results are displayed in Figure 4.24, where correlation between the surface profile and the velocity magnitude images can be seen for both 100kHz and 250kHz. The correlation in the phase images is less clear. Comparing the magnitude data with the surface profile, it is interesting to note that the lines of greater membrane velocity correlate precisely with the dips or valleys in the surface profile. As such, it would appear that the peaks do indeed cause the membrane to be more tightly clamped, allowing air to gather in between, over which the membrane has more freedom of motion. The close proximity across the backplate still produces close phase correlation, though with a larger spread than for the VC device.

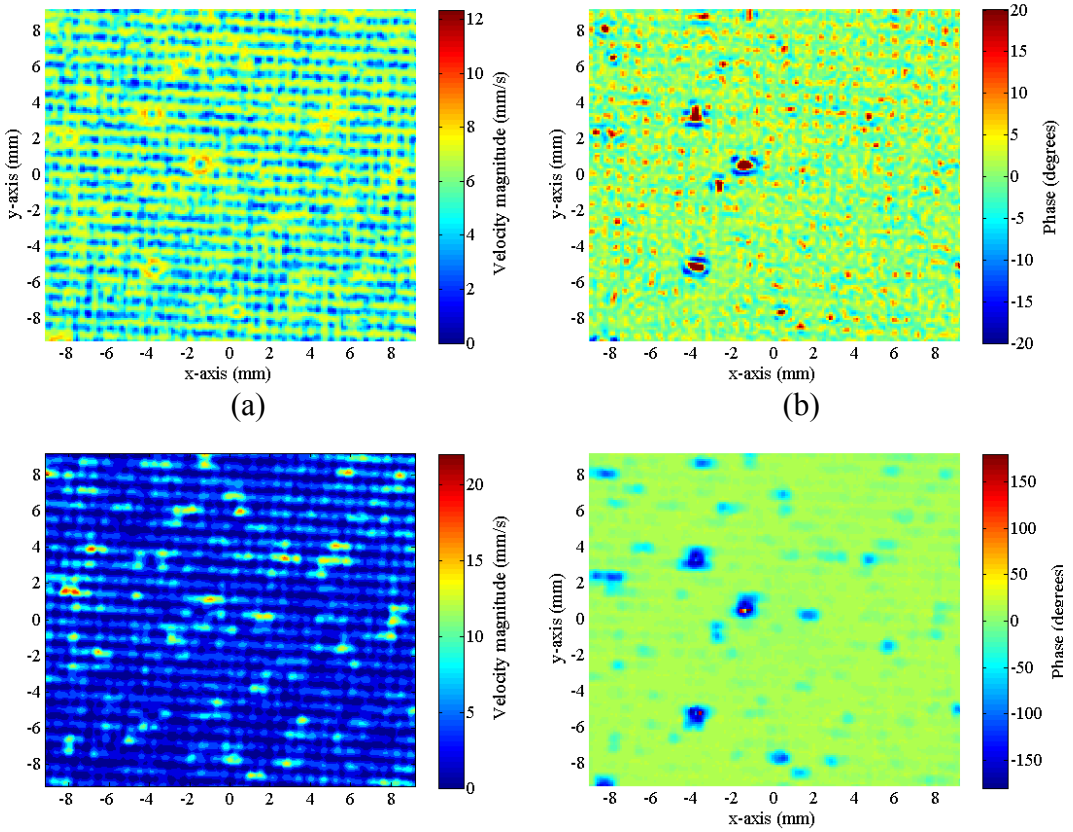

Figure 4.24. LDV membrane velocity data for PCB transducer: (a) 100kHz magnitude; (b) 100kHz phase; (c) 250kHz magnitude; and (d) 250kHz phase

Similar results for the P240 device are displayed in Figures 4.25 and 4.26. The filtered surface profile data indicates a lack of the structured surface obvious with the PCB material, with arbitrary location of peaks and troughs. Furthermore, there is no obvious correlation between the surface structure of the backplate and the membrane motion. Indeed, in some ways, this is similar to that of the VC device. However, due to the membrane being subject to a reduced electric field from the backplate over most of its surface (due to the reduced proximity), the phase response across the transducer has a far greater spread with a much larger SD. The hypothesis that the "randomly" rough sandpaper backplate could be used to generate a wide range of phase across the aperture holds true and has allowed this aspect of electrostatic operation to be investigated. This has demonstrated that normalised fields measured from a transducer cannot be taken to imply piston-mode operation of the transducer, as has been done in the literature (e.g. Bashford *et al.*, 1996). It has been shown here that the P240 transducer certainly does not operate in piston-mode, but that the phase

variation is distributed randomly enough across the transducer surface to generate a field that compares well with piston theory. It is only by combining this data with LDV measurement of the membrane motion that the transducer operation can be fully characterised.

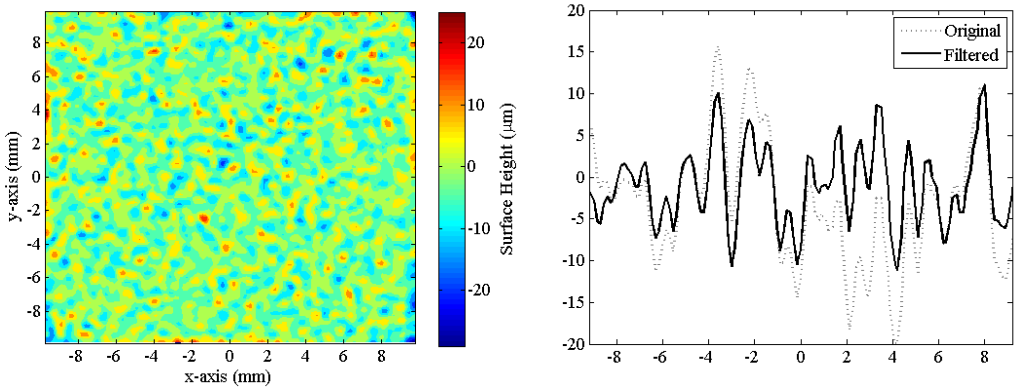

(a) (b)

Figure 4.25. Spatially filtered surface profile data for P240 sandpaper (a), with a single cross section comparison of original and filtered data (b).

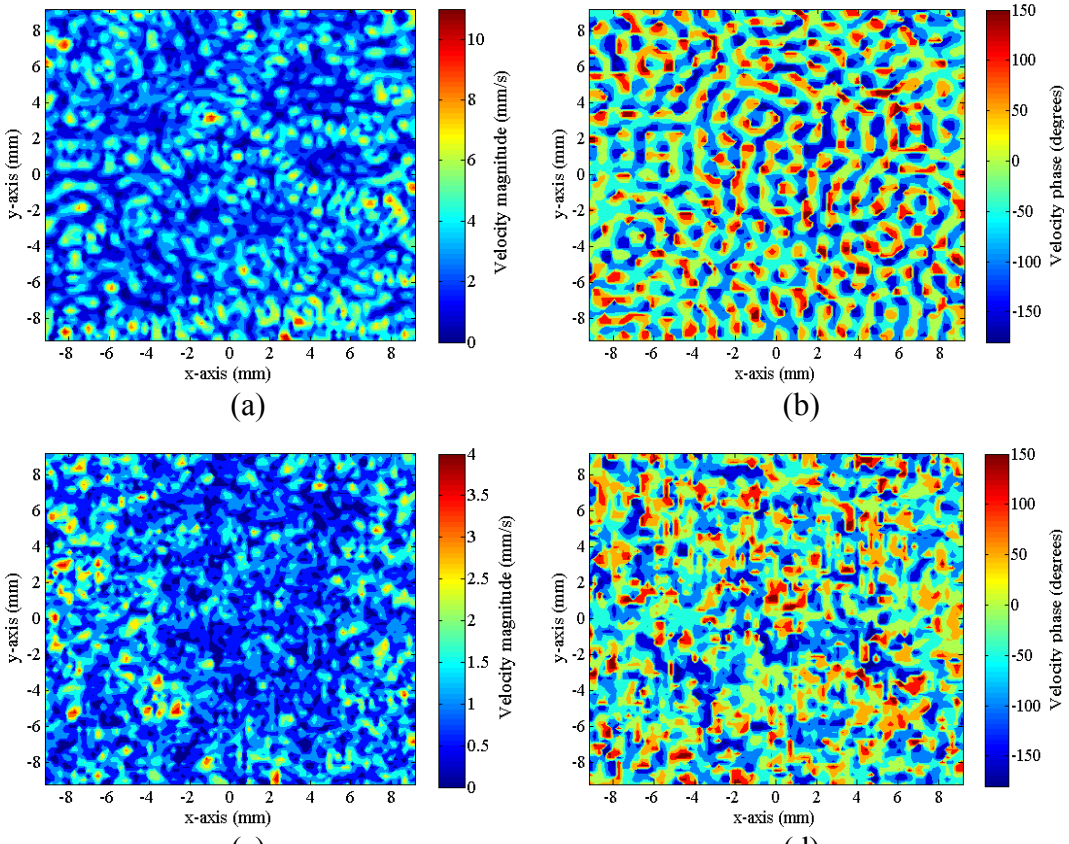

(a) (b)

(c) (d)

Figure 4.26. LDV membrane velocity data for P240 transducer: (a) 100kHz magnitude; (b) 100kHz phase; (c) 250kHz magnitude; and (d) 250kHz phase.

Finally, to quantify the relationship between the surface of the backplate and the motion of the membrane over it, the 2D cross-correlation of the surface profile and LDV data was calculated for each transducer at both 100kHz and 250kHz. The surface profile and LDV magnitude data were both normalised and then the 2D cross correlation performed. Figure 4.27 displays the results at 100kHz for the VC, PCB and P240 sandpaper backplate. It can be seen that the form of the VC backplate dominates the response of the cross correlation, meaning that no useful information can be gleaned regarding how the surface profile affects membrane motion. However, it has already been demonstrated that the membrane motion has an arbitrary pattern with the VC backplate (Figures 4.21 and 4.22). The result of the 2D cross correlation of the PCB and P240 sandpaper data is interesting however. As would be expected when two sets of data correlate well, the PCB cross correlation shows a peak at the centre, where the two sets of data align. The P240 sandpaper data do not show this, indicating no correlation between the surface structure and membrane motion. At 250kHz (Figure 4.28) similar results are demonstrated, although the correlation in the PCB data is not as exact as at 100kHz. To demonstrate how precise the correlation of the PCB surface data and velocity is, an expanded image of the central section of the data is presented in Figure 4.29. It can be seen that the peak of the cross correlation function occurs exactly in the centre of the data.

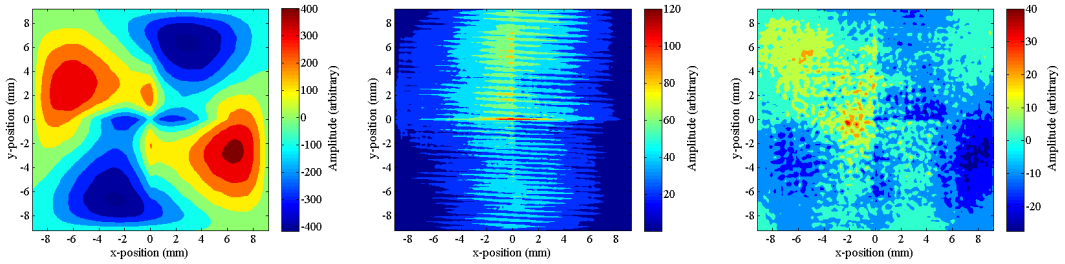

(a) (b) (c)

Figure 4.27. 2D cross correlation of the measured surface profile with measured membrane velocity magnitude: (a) VC backplate at 100kHz; (b) PCB backplate at 100kHz; (c) P240 sandpaper backplate at 100kHz.

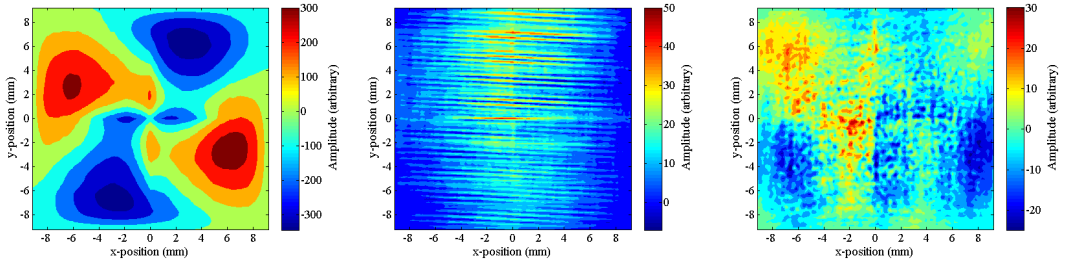

(a) (b) (c)

Figure 4.28. 2D cross correlation of the measured surface profile with measured membrane velocity magnitude: (a) VC backplate at 250kHz; (b) PCB backplate at 250kHz; (c) P240 sandpaper backplate at 250kHz.

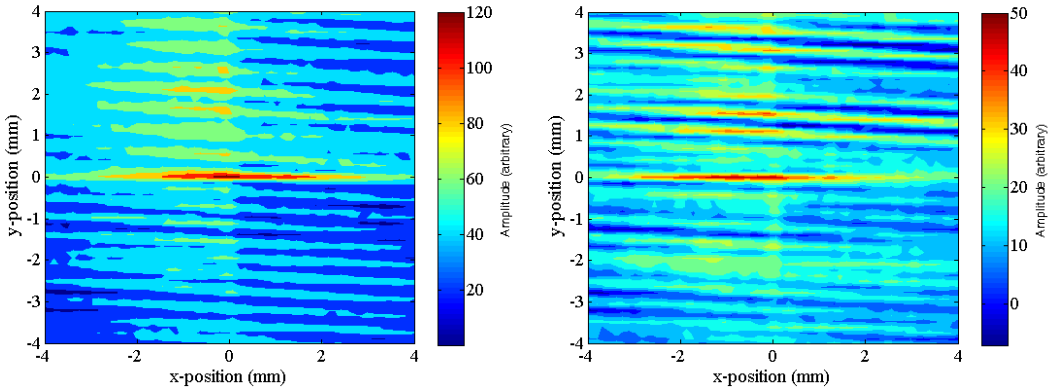

(a) (b)

Figure 4.29. Close-up of the centre of the 2D cross correlation of the PCB surface data and LDV magnitude data: (a) 100kHz; (b) 250kHz

4.7 Laser Micromachining of the Transducer Backplate

As indicated by the insertion loss measurements, the sensitivity of the electrostatic devices is poor in comparison with that achievable using air-coupled piezocomposite devices, albeit with a far greater bandwidth. It would be of immense benefit to fields such as NDE that the wideband nature of these devices could be combined with improved sensitivity. The increased sensitivity of the PCB backplate is a product of

the increased velocity of the membrane when in operation, as measured using the LDV system. Vibrometry data indicated that this increase occurred as a result of the surface structure allowing a greater volume of air to be trapped under the membrane, which in turn allows a greater freedom of motion of the membrane. However, the smooth nature of the vitreous carbon does have the advantage of promoting in-phase motion across the membrane. It is important to maintain this phase correlation, especially at the higher frequencies associated with NDE, and even more so since air-coupled NDE often involves working in the near field of the transducer. As such, the mechanism used to promote increased sensitivity was also intended to allow the phase correlation of the membrane to be maintained. It was considered that generating small pits in the backplate surface would allow additional air to be trapped between the membrane and backplate over which the membrane can vibrate. It should be noted that it was not the intention of this process to generate *resonant* cavities. Such a technique, whereby cavities (and in some cases matched pipes) of specific dimensions are machined into the backplate structure, has been used to improve the transmission sensitivity of electrostatic devices (Campbell *et al*., 2006). However, due to the resonant nature of the backplate structures, this generates narrowband improvement in sensitivity. The aim here was to generate small pockets of air under the membrane to allow it a greater range of motion, over its entire operational frequency. Furthermore, by producing pits on the micron scale, and spacing them apart so that the remaining surface is unaffected, the aim was to improve sensitivity without disrupting the in-phase nature of membrane vibration.

There are many examples of micromachined backplates (generally through silicon etching using a similar process to that used in IC manufacture by the electronics industry) in the literature (e.g. Haller and Khuri-Yakub, 1996; Schindel *et al.*, 1995) but the impact of this micromachining on sensitivity has not been reported; rather it was performed to produce backplates that operated in a repeatable fashion. Silicon micromachining is an expensive technique, requiring specialist equipment and materials, as well as expertise. However, laser-micromachining offers a method by which pits on a similar scale can be created in a range of material, including vitreous carbon.

The apparatus used for this was a MP100 copper vapour laser micromachining system (Oxford Lasers, Didcot, UK). The laser was operated in percussion drilling mode, supplying a single 2mJ pulse of 1ms duration to a spot size of approximately 10µm. Due to maintenance issues with the laser system, only a cursory investigation into this method for sensitivity improvement could be made. One backplate was processed in this fashion, producing a series of pits at a spacing of 375µm, arranged on a square grid as illustrated in the scanning electron microscope (SEM) images in Figure 4.30. The pits in the surface were roughly elliptical with major and minor axes of approximately 30µm and 15µm, respectively, as can be seen in Figure 4.30(c). The depth of these pits is not known as there was no reasonable way to measure this dimension. An attempt was made to measure depth by angling the sample in the SEM field of view. By measuring the apparent length of the side wall of the pit (from the surface to the bottom) and measuring the angle of tilt, then the actual depth could be known. However, the pit bottom was not visible using this method. A further attempt using a NT1100 (Veeco, Plainview, NY, USA) optical profiling system was attempted, but the nature of the pits meant that there was not sufficient light returned to make a measurement.

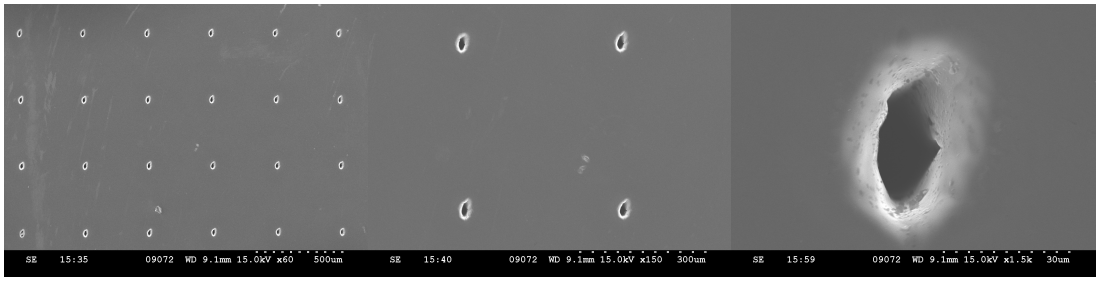

(a) (b) (c)

Figure 4.30. SEM images of pits in VC produced using laser micromachining, at various scales indicated by scale bars.

The elliptical nature of the pits is thought to be a result of a focussing issue with the laser. However, the SEM images show that VC is well-suited to this type of micromachining, producing a well-defined pit, with no damage to the surface surrounding the pit. This was not the case with all materials, as illustrated when the same technique was used on a PCB backplate. SEM images (Figure 4.31) indicate both wide area damage to the PCB substrate around the pits (a), as well as significant

damage from the rapid heating, melting and cooling of the copper surface immediately surrounding the pits (b).

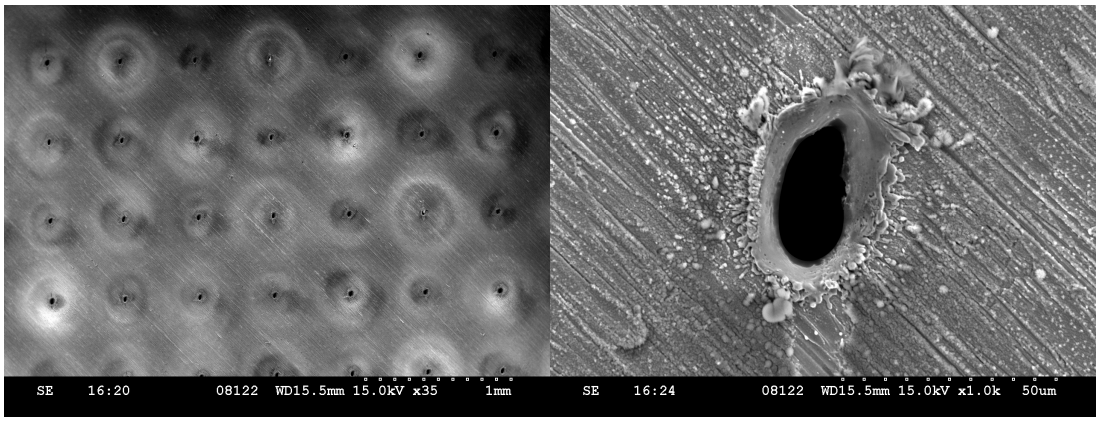

(a) (b)

Figure 4.31. SEM images of pits in PCB produced using laser micromachining, at various scales indicated by scale bars.

Another issue with the PCB material arose since the micromachining process disrupted the electrical continuity of the backplate surface. As such, it was necessary to recoat with a conductive material. This was not straightforward, as the surface contained sharp discontinuities and was considerably roughened by the laser drilling procedure. After evaporation of a layer of aluminium onto the surface, it quickly oxidised, leading to large areas of non-conductivity. The VC material, in addition to its well-defined pits and undamaged surrounding surface, has a further advantage in that it is electrically conductive, and so requires no additional procedure to ensure electrical continuity across its surface and into the pits.

Since the main aim of micromachining the backplate was to improve sensitivity, the frequency response of the new device was measured first, via its impulse response and narrowband response measured using the B&K calibrated microphone. The results of these measurements are presented in Figure 4.32. The impulse response indicates a very similar response over the entire frequency range, with the B&K calibration confirming this in the sub-200kHz range.

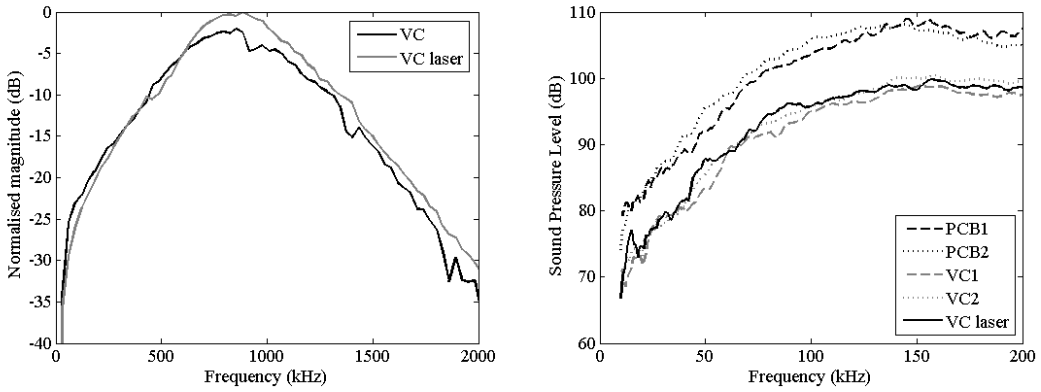

(a) (b)

Figure 4.32. Frequency response of the laser micromachined VC transducer, measured using the impulse response method (a) and using narrowband tonebursts into the B&K microphone.

It may be that this method could be successful, but that the density of pits requires to be increased. At 375µm spacing, there are approximately 5000 pits on the backplate surface, each with an area of approximately $1.41\times10^{-9}m^2$, giving a total area of $7.05\times10^{-6}m^2$. The backplate itself has a surface area of $7.06\times10^{-4}m^2$ and so the total pit area accounts for just 1% of the surface area of the backplate. In comparison, the backplates produced by Schindel *et al*. (1995) using silicon micromachining had pits of 40µm diameter, with a centre-centre spacing of approximately double that, meaning that the pits themselves accounted for some 20% of the backplate area. However, no vibrometry data has ever been published on these, or similar, devices. Nor has there been a published comparison of a micromachined and non-micromachined device, and so no conclusions can be drawn about the effect of these pits on transducer operation.

A transducer constructed using the micromachined backplate was also subjected to measurement using the LDV system, both to measure the velocity amplitude and ensure that the phase correlation across the membrane surface had not been lost. These results are depicted statistically in Table 4.4.

	Avg. Vel. (mms^{-1})	Vel. SD (mms^{-1})	Vel. Phase SD (degs.)
VC Laser 20kHz	0.51	0.16	2.6
VC Laser 50kHz	1.21	0.34	1.2
VC Laser 100kHz	2.36	0.63	1.4
VC Laser 150kHz	3.44	0.94	1.3
VC Laser 200kHz	5.67	1.28	1.3
VC Laser 250kHz	6.59	1.76	1.5

Table 4.4. Statistical data from LDV scan of the micromachined VC device.

By comparing these data with those for the central 28mm of the VC transducer in Table 4.2 (page 114), it can be seen that the magnitude and phase characteristics are very similar, as expected from the SPL measurement. As such, the micromachining did not affect the phase correlation of the device, but neither did it have the desired effect of improving device sensitivity.

4.8 High Frequency Characterisation

Although the target frequency range of operation was limited to those approximately covered by bat echolocation calls, it is clear from the impulse response of both transducers that their greatest sensitivity is actually above this range. This potentially opens the way for these devices to be used in other applications. One that is of particular interest to CUE is air-coupled NDE, which generally uses frequencies of 500kHz and above, due to the high velocities, and hence long wavelengths, in most NDE test structures. For this reason, the operation of the VC device was characterised using the LDV at frequencies up to 1MHz. As with lower frequency scans, visual magnitude and phase plots, as well as statistical data, is presented in Figure 4.33 and Table 4.5, respectively.

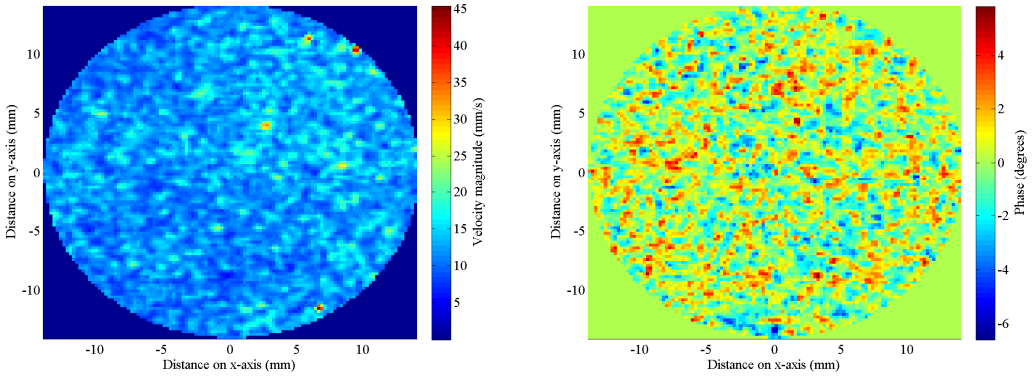

(a) VC transducer 400kHz LDV measurement; Magnitude; Phase.

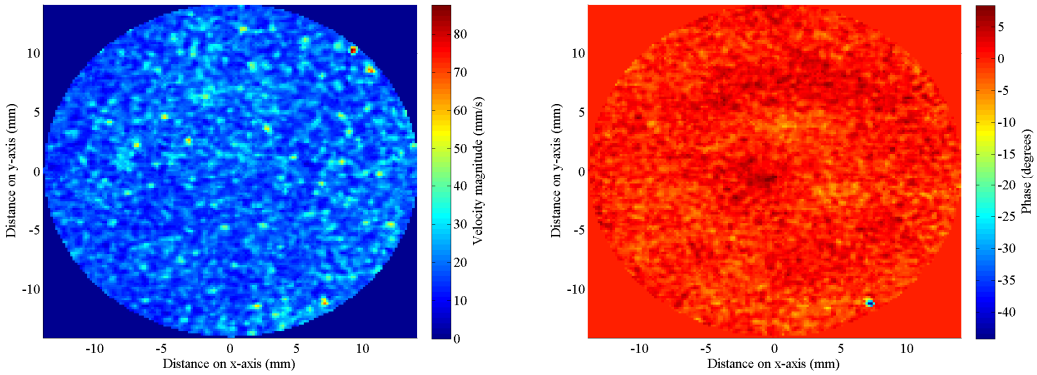

(b) VC transducer 500kHz LDV measurement; Magnitude; Phase.

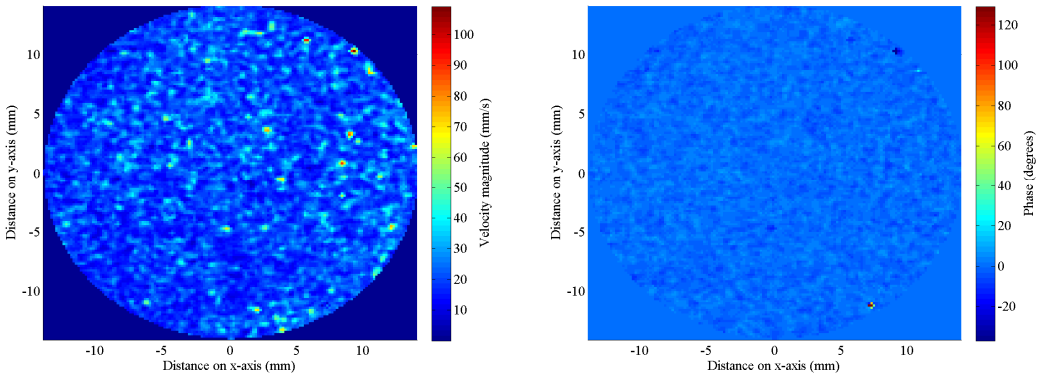

(c) VC transducer 600kHz LDV measurement; Magnitude; Phase.

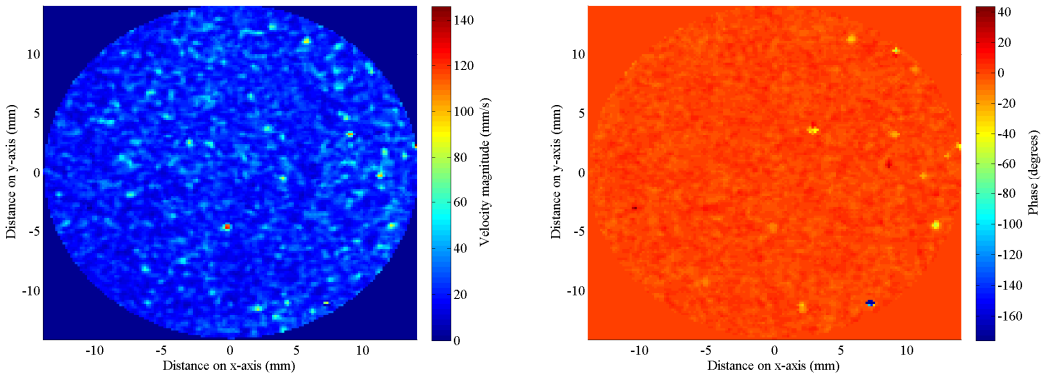

(d) VC transducer 700kHz LDV measurement; Magnitude; Phase.

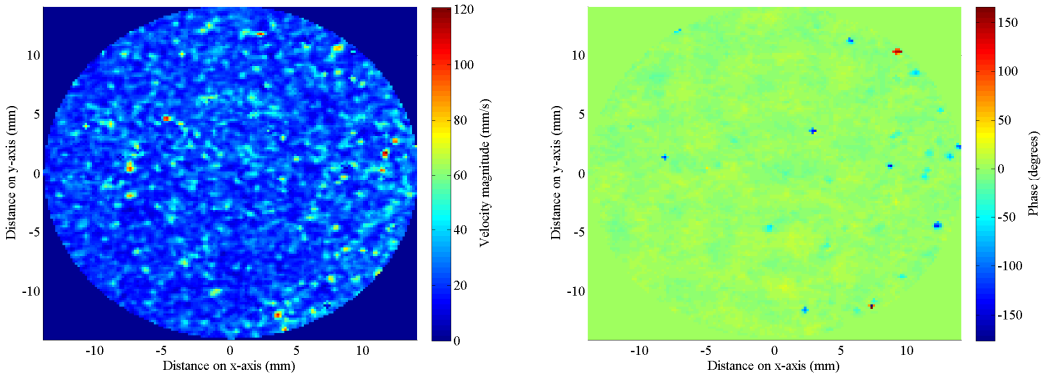

(e) VC transducer 800kHz LDV measurement; Magnitude; Phase.

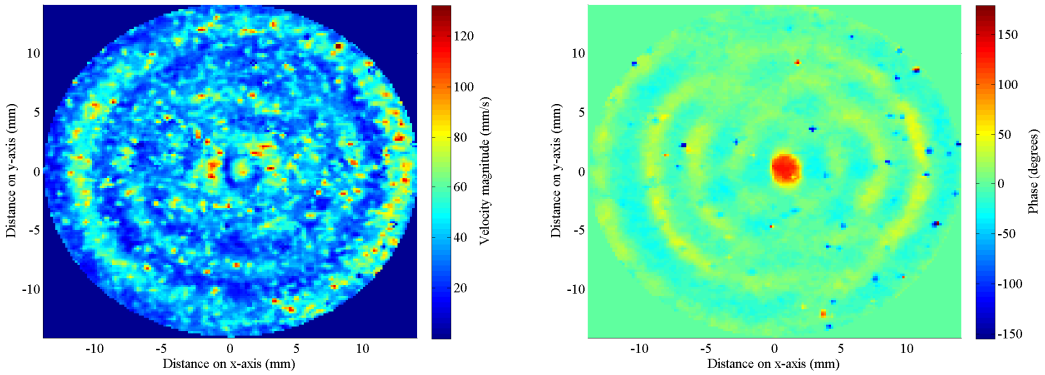

(f) VC transducer 900kHz LDV measurement; Magnitude; Phase.

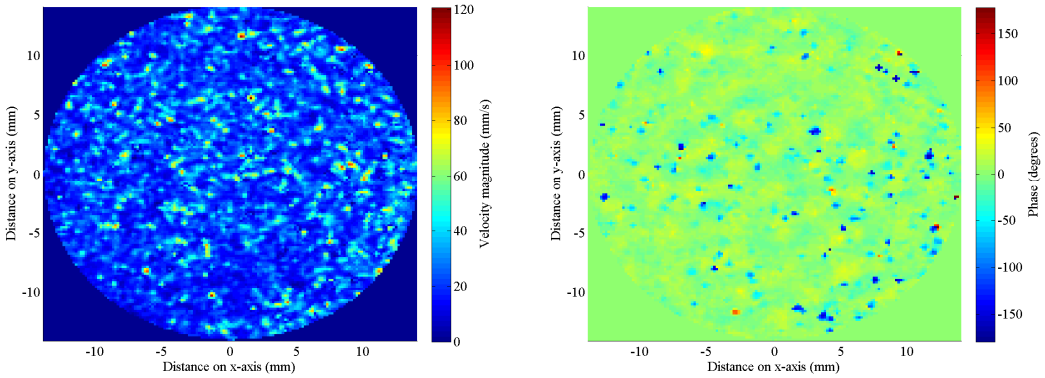

(g) VC transducer 1MHz LDV measurement; Magnitude; Phase.

Figure 4.33. Measured magnitude and phase of the membrane velocity of the central 28mm diameter of the VC transducer: (a) 400kHz; (b) 500kHz; (c) 600kHz; (d) 700kHz; (e) 800kHz; (f) 900kHz; and (g) 1MHz, with magnitude (left) and phase (right) in each row.

	Avg. Vel. (mms^{-1})	Vel. SD (mms^{-1})	Vel. Phase SD (degs.)
VC 400kHz	12.35	2.62	1.56
VC 500kHz	18.90	5.64	2.30
VC 600kHz	20.98	6.72	2.94
VC 700kHz	22.26	7.86	4.84
VC 800kHz	23.99	9.17	7.44
VC 900kHz	40.84	15.59	17.26
VC 1MHz	24.34	11.85	18.97

Table 4.5. Statistical data from high-frequency LDV characterisation of 28mm VC transducer.

It is clear from both the visual and statistical data that, up to approximately 800kHz, the phase distribution across the membrane continues to be fairly tight, with a SD of only 7.4° at 800kHz. The data at 900kHz, which coincides with the region of maximum sensitivity indicated by the impulse response (Figure 4.4(b)), is unusual. The statistics indicate a considerable increase in average velocity of the membrane, whilst in the visual data of Figure 4.33(f), it can be seen that some form of standing wave has been set up across the aperture, or possibly a Lamb wave in the membrane. This frequency is also the point at which the phase correlation appears to break down, with far larger values of phase SD at 900kHz and 1MHz than at lower frequencies. However, the results presented here indicate that the use of electrostatic transducers for air-coupled NDE may be possible, although a mechanism for improvement of sensitivity appears to be required. The capability for use of wideband energy in air-coupled NDE would certainly be a welcome addition.

4.9 Discussion and Conclusions

This Chapter has documented the design, manufacture and test of a range of affordable wideband electrostatic transducers. These devices have been demonstrated to be capable of producing piston-like fields across the frequency range of interest: 20kHz – 250kHz, covering the calls of most echolocating bats. Furthermore, from a standard 10Vp-p laboratory function generator, the transducers are capable of generating up to 110dB SPL at a distance of 100mm from the front face in the region

of 100kHz, which is comparable to the pressure levels generated by echolocating bats.

The transducers were manufactured in-house, and consisted of an aluminium casing that housed the backplate, with a membrane of 8μm metallised Kapton (polyimide) polymer held in place via a tensioning ring screwed to the front face of the device. Two different backplate materials were used: PCB and vitreous carbon (VC). These were selected after investigating the performance of a number of transducers, with a variety of backplate materials and membranes, since they provided a good combination of sensitivity, wideband performance, repeatability and robustness. The transducers were capable of operation at considerably higher frequencies than the target range, into the low-MHz region as demonstrated by both their impulse response and characterisation using narrowband toneburst signals. In fact the transducers were very wideband, with a maximum fractional bandwidth in excess of 120% at a centre frequency of 880kHz. This compares favourably with devices in the literature (e.g. Schindel *et al*., 1995), which were produced using specialist silicon micromachining techniques. The maximum centre frequency and bandwidth was achieved with the VC transducer; this wideband performance could be sacrificed slightly with the PCB transducer, in the process gaining approximately 10dB in output pressure level. Since the frequency range of interest is considerably below the centre frequency of these devices, the increased output level could be the deciding factor between the two devices, as will be discussed in the following Chapter.

Frequency response is only one figure of merit for transducer operation. The field structure emitted by the device is of great importance, and this was measured by scanning a detector in the field of the transducer using a three-axis scanning system. This revealed that the field emitted by the VC transducer correlated exceptionally well with that of a theoretical plane-piston device, across the entire 20kHz-250kHz frequency range of interest. The PCB transducer achieved similar results, with some deterioration at the higher frequencies. This deterioration was evident only in the complex interference pattern of the near field, which was not reproduced quite as accurately with the PCB transducer. In some ways, these minor discrepancies are of little consequence in the practical use of the device, since most applications at these

frequencies will occur in the far-field of the device. However, the accuracy of reproduction of the near-field interference pattern can be an indicator of how piston-like the motion of the transmitting surface is. This is important since piston-mode motion transfers energy more efficiently into the load.

Field structure measurements, then, implied that both transducers are operating as piston-mode devices. However, this can only be confirmed through measuring the motion of the transmitting membrane itself. This was performed using a laser doppler vibrometer (LDV) system. These measurements demonstrated that there were two distinct areas of the membrane that operated in a very different fashion. Firstly, the area of membrane that was in contact with the backplate operated with a high degree of phase correlation across the entire surface, though not as a plane piston since the SD of the magnitude population was considerable. Secondly, there was an area of membrane that was unsupported by the membrane, being stretched between the outer edge of the backplate and the transducer case. This annulus of membrane had a large degree of both magnitude and phase variation, with its magnitude often larger than that of the central portion of membrane. This being the case, it might have been expected that this area would have a significant detrimental effect on the field produced by the transducer. However, both field scans and predictions from LDV measurement demonstrated that the emitted fields were well correlated with those of a piston-mode 30mm diameter device. This was investigated and demonstrated to be due to the almost uniform distribution of the phase components of the annulus motion, practically cancelling each other out in the field.

Finally, it was shown that the fields predicted from LDV measurements correlated well with those measured using the scanned microphone. This is important since LDV scans of the device surface take a fraction of the time required to perform a field scan, and as such accurate operational characteristics can be obtained far more quickly, and over an extended frequency range using this method.

Given the considerable deviation in magnitude, and smaller deviation in phase, across the membrane surface, the effect that such variability has on the field emitted by such devices was investigated. Firstly, through simulation of magnitude and phase

variation, it could be seen that the piston-like field was actually fairly robust to statistical randomisation across the aperture. In fact this can be explained through vector addition in the field producing an average phase of 0˚, although with the magnitude reduced due to the non-coincident phases of the individual components. Such behaviour was demonstrated in a device constructed using P240 sandpaper as the backplate. This illustrated that measurement of a piston-like field cannot be accepted as evidence of a piston-mode transducer, as has sometimes been assumed in the literature. Vibrometry data of the P240 transducer indicated that the device was, in fact, far removed from piston-mode with a considerable SD in the phase of the membrane motion. This indicated the transducer was not as efficient in transfer of energy into the field.

The link between the surface profile of the backplate and measured LDV data of membrane motion was then investigated, with three backplates having their surface profiles mapped by NPL. This demonstrated contrasting modes of operation for three backplates with differing surface characteristics. The very smooth surface of the VC, with no features to regulate the pooling of air between the membrane and backplate led to an arbitrary pattern of membrane vibration. However, the proximity of the backplate and membrane led to the membrane motion being closely regulated, producing a high level of phase coherence. This contrasted to the irregularly rough P240 sandpaper backplate, which promoted a similar level of SD in the velocity magnitude across the membrane, but generated a far higher spread of phase angles with the backplate exerting less control over the membrane motion. Both of these contrasted with the regularly patterned weave of the PCB material, which promoted greater motion in the regions of membrane positioned above the troughs of the weave. With the membrane capable of adhering to the contours of the backplate with the bias voltage applied, the membrane motion was still closely regulated and so had a similar level of phase coherence as the VC device. In both simulated and experimental data, it was phase coherence of the transducer face that was shown to be important for the structure of the field, as well as the transmit sensitivity with the components generated from each point on the transducer operating in phase.

One additional development of the transducer design was investigated. The VC backplate was pitted using a micromachining laser system in an attempt to increase the output pressure of the device. However, no increase in either membrane velocity or output pressure was facilitated. It is felt that future developments of electrostatic transducer technology should focus on the need to improve sensitivity, since measurement of transmit / receive insertion loss indicated that existing piezocomposite transducers are 10dB-20dB more sensitive than these electrostatic devices. If it were possible to produce electrostatic devices with greater sensitivity, however, their wideband nature would be of significant benefit in future NDE systems. Potential mechanisms for this are discussed in the final Chapter.

CHAPTER 5

REPLICATION OF WIDEBAND BIOSONAR CALLS USED IN WIRE-AVOIDANCE EXPERIMENTS

5.1 Introduction

Any transducer system is designed to transfer energy from one form into another, generally with the output being an accurate representation of the input signal. In acoustics this accurate reproduction is important whether the driving signal is electrical and the output acoustic, in the case of a loudspeaker, or vice versa, as is the case with a microphone. In either case, the output signal should trace precisely the time varying waveform of the input, so that the sound is accurately reproduced to the listener, or accurately recorded onto some medium. As such, the transducer itself should only transfer energy from one form to another, it should not be responsible for the addition of any artefacts that are not present in the original signal. This Chapter is concerned with the accurate reproduction of wideband biomimetic and bioinspired echolocation signals, as a means to examine the echolocation process itself, as well as to apply such signals to engineering applications such as ranging. In each of these situations, precise replication of the signal is important, as will be demonstrated later in this Chapter. The electrostatic transducers described in the previous Chapter are used to reproduce a variety of bioacoustic and biologically-inspired wideband signals. As reported previously, the frequency response of these transducers is not flat and so an equalisation process was required to allow accurate reproduction of wideband signals. The necessity for this process is also demonstrated.

As described in Chapters two and four, there is a variety of transduction mechanisms suitable for producing ultrasonic signals in air. However, few of these are suitable for generation of wideband signals over the frequency range of bat echolocation of 20kHz – 250kHz. In the literature, one study using Electro-Mechanical Film (EMFi; Streicher *et al*., 2005) had the stated objective of producing a broadband transducer for bat echolocation research. However, although devices were manufactured and operation was demonstrated across the required frequency range, no production of wideband acoustic signals was documented. Transducers built from EMFi suffer from low sensitivity, with driving signals up to 600V required to produce output pressure in the region of 100dB SPL (Streicher *et al*., 2005). One other study that reproduced bat echolocation calls is that by Waters and Jones (1995). In this work a commercially available (Ultra Sound Advice, Wimbledon, UK) electrostatic

loudspeaker was used to replicate the recorded calls of UK bats for energy measurement purposes. The authors reported that "examination of the broadcast call revealed no major changes in frequency or temporal structure from the original call", and a frequency spectrum of a single call from *Myotis nattereri* was provided as evidence. However, no numerical techniques were used to examine the accuracy of replication, and furthermore, the call is relatively narrowband with a 3dB bandwidth extending from approximately 75kHz – 115kHz. These studies aside, reproduction of wideband bioacoustic signals has had little attention in the literature, despite the benefit that can be afforded in both biological and engineering application areas.

5.2 System Response and Equalisation

5.2.1 Background

As described in Chapter 4, the response of the transducers is not constant across the frequency range of interest; see, for example, the impulse response of a PCB and vitreous carbon (VC) electrostatic transducer repeated in Figure 5.1. This response would lead to different spectral components being subjected to relatively more or less amplification, dependent on their frequency. For example, a wideband signal occupying the frequency range from 30kHz-300kHz would have its higher spectral components significantly amplified with respect to its lower ones. In fact, the component at 300kHz would be subject to an additional 20dB-30dB of amplification in comparison to one at 30kHz, depending on the transducer used. It can readily be appreciated that the generated ultrasonic signal would not be an accurate reproduction of the driving electrical function.

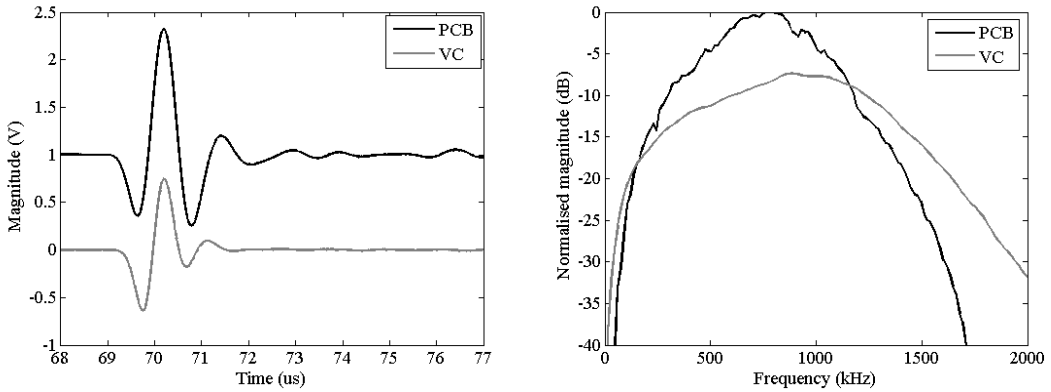

(a) (b)

Figure 5.1. Impulse response of PCB and vitreous carbon (VC) transducers with 8µm Kapton membrane and a bias voltage of 300V: (a) Time domain (PCB trace dc-level shifted for clarity); (b) Frequency domain.

Given this non-uniform response, an equalisation method was required, such that a given signal could be accurately reproduced. This method involved processing the input signal to compensate for the system response, so that a pre-equalised signal was applied to the transducer, thereby generating the required acoustic signal. Through laboratory measurements, it was shown that the response of the transducer was linear across the frequency range. Given this linearity, the response of the system is fully described by its impulse response, such that the output, y(t), is defined as the convolution of the input, x(t), with the impulse response, h(t):

$$y(t) = h(t) * x(t) \tag{5.1}$$

This calculation can be simplified by transforming into the frequency domain using a Fast Fourier Transform (FFT), where convolution of two signals is calculated by multiplication. Hence the output, Y(f), is the product of the input, X(f), and the impulse response, H(f), where all terms are complex:

$$Y(f) = H(f)X(f) \tag{5.2}$$

If a desired output signal is defined and the impulse response of the system is measured, then the input signal necessary to generate the desired output can be calculated, by rearrangement of (5.2):

$$X(f) = \frac{Y(f)}{H(f)} \tag{5.3}$$

Now, by transforming back to the time domain using the inverse FFT, the input signal required to generate the desired output can be found:

$$x(t) = iFFT\left(\frac{Y(f)}{H(f)}\right) \tag{5.4}$$

Hence, by measuring the impulse response of the system, the input signal required to generate a defined output signal from the system can be calculated. This method produces a pre-distorted version of the required signal that, when used as the input signal, compensates for the impulse response of the system and hence allows accurate reproduction of the required signal.

It is important to note here that it is the *system* response that is equalized. This means that any component in the system that contributes to the signal measured in the impulse response is compensated. This includes both transmit and receive transduction mechanisms, plus associated electronics and the propagation channel. In the case that generated the results of Figure 5.1, the transmitter and receiver are the same since the device was characterized in pulse-echo mode, so this is compensated for, along with the attenuation characteristics of the transmission medium. However, often the receiver will be a different device altogether, such as a microphone or remote sensor used to detect and characterise the transmitted energy. In applications such as ranging, which may use a cross-correlation type calculation, this becomes important since the received signal will be an accurate reproduction of the input signal producing the strongest cross correlation function possible. These issues will be discussed later in the Chapter.

5.3 Reproduction of Wideband Ultrasonic Signals in the Laboratory

To demonstrate the effect of the system response, an artificial wideband signal was transmitted using a VC transducer and received on the B&K 4138 microphone system. As can be seen in Appendix A, the response of the microphone varies by less

than 6dB up to approximately 60kHz; across this range of frequencies the transducer response increases by in excess of 20dB, and so its response will dominate the system response. The impulse response was measured with the 5052 pulser unit used as previously to drive the transducer, with the generated acoustic signal detected using the B&K microphone. The time and frequency domain representations of this are depicted in Figure 5.2, demonstrating the response described above. It can be seen that the wideband response of the transducer is narrowbanded by the response of the microphone system.

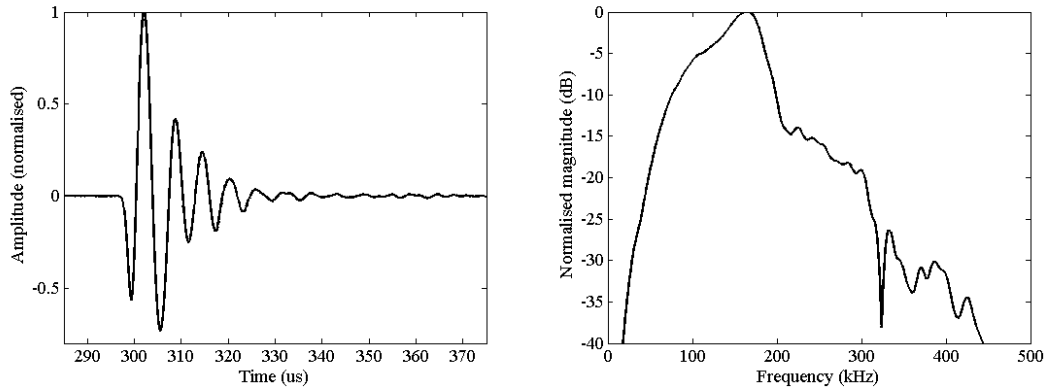

(a) (b)

Figure 5.2. Time (a) and frequency (b) domain of the impulse response of a VC transducer as measured using the B&K 4138 microphone, at a range of 100mm.

A similar response can be demonstrated using a wideband multi-harmonic FM chirp. The signal was created in Matlab using a quadratic FM chirp, with an initial frequency of 60kHz and a terminal one of 30kHz, as the fundamental component. Four harmonics (starting at 120kHz, 180kHz, 240kHz and 300kHz, respectively) each sweeping downward over an octave of bandwidth, were added to the fundamental. The resulting signal was then windowed using a Tukey window. A Tukey window, also known as a cosine-tapered window, is a cosine window convolved with a rectangular window, producing a window with cosine-tapered outer sections and a flat central portion. The window used in this work had a 25% ratio of tapered to constant sections - as such, the constant amplitude portion makes up 75% of the function. This window is illustrated in Figure 5.3.

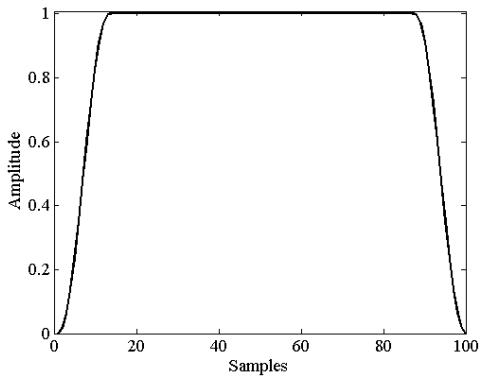

Figure 5.3. Tukey window, 100 samples in length with a taper-ratio of 0.25.

The response of the system to these chirps amply demonstrated the necessity for pre-processing if accurate replication is required, as illustrated in Figure 5.4, where the transmitted and received chirps are shown in the time-frequency space of a spectrogram. The spectrograms were generated using a sliding Hanning-windowed FFT, with a window length of 256 samples. The combined effect of the transducer and microphone frequency response can be seen by comparing parts (a) and (b) of Figure 5.4, with (a) showing the spectrogram of the original desired signal, and (b) the signal detected by the microphone with the original signal applied to the transmitting transducer. The combination of the high-pass frequency response of the transducer, with the bandpass effect of the microphone means that the energy content of the signal is concentrated in the second and third harmonics, as well as the lower frequency components of the fourth harmonic, of the recorded signal. Similarly, the high-pass response of the transducer, coupled with the reduced response of the microphone at frequencies in excess of 150kHz, means that the fundamental and fifth harmonics are comparatively weak with respect to the original signal. However, by employing the pre-equalisation described in the previous section, the combined effect of both transducer and microphone can be mitigated. By applying a pre-equalised version of the signal to the transducer, the signal illustrated in Figure 5.4(c) is detected by the microphone. Comparison with Figure 5.4(a) demonstrates the efficacy of the technique in maintaining the original frequency content.

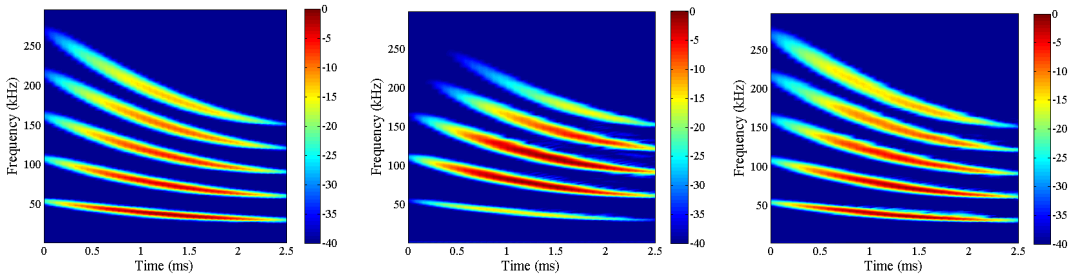

Figure 5.4. Spectrograms demonstrating inversion processing for reproduction of multi-harmonic wideband FM chirp: (a) original signal; (b) signal produced by applying original signal to the transducer; (c) signal produced by applying pre-equalised signal to the transducer.

A further demonstration of how well the inversion process works can be illustrated by examining the cross correlation of the original and reproduced signals, and comparing this with the auto-correlation function of the original signal itself - this comparison is pictured in Figure 5.5. It can be seen that the cross correlation function generated from the signal reproduced using the inversion process is very similar to that of the auto-correlation function, whereas the cross correlation function produced from the signal reproduced without inversion has significant differences. This demonstrates both the effectiveness and necessity of the inversion process. If these correlation functions were used in a ranging algorithm, the presence of the large sidelobe in the non-inversion correlation function could introduce errors, especially in the presence of noise, leading to inaccurate estimation of time-delay and range.

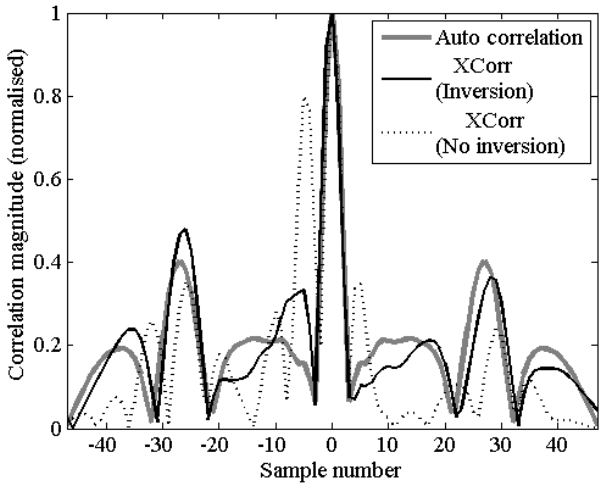

Figure 5.5. Comparison of the auto-correlation function of the five-harmonic FM chirp, with the cross correlation of the original and reproduced signals, with and without the pre-equalisation spectral inversion process.

5.4 Reproduction of Bat Echolocation Calls

Microchiropteran bats echolocate by producing sounds via the larynx, in common with most mammals including humans. Between them, these bats produce a wide variety of echolocation calls that can be broadly categorised according to the relative constant frequency (CF) or frequency modulated (FM) components within their call, with components ranging from the audible to in excess of 200kHz (Fenton and Bell, 1981). As something of an echolocation oddity, the Megachiropteran genus *Rousettus* echolocates via clicks of its tongue, producing wideband impulse-like signals, generally in the sub-50kHz frequency range, and extending down to audible frequencies. It was an aim of this work to enable accurate reproduction of the call of any bat, and the multi-harmonic chirp in the previous section demonstrates that the electrostatic transducers are capable of operating across the entire frequency range. However, two examples of bat echolocation call have been selected to demonstrate reproduction of actual echolocation calls in the laboratory. The first was a signal recorded using the wireless system documented in Chapter 3, mounted on the fruitbat *R. aegyptiacus*. The second is a wideband, multiharmonic FM-CF call from the European common pipistrelle bat (*Pipistrellus pipistrellus*) recorded in the field.

5.4.1 Reproduction of the Calls of *Rousettus aegyptiacus*

The echolocation calls of *R. aegyptiacus*, in common with those produced by other species within its genus, are produced by clicking the tongue against the roof of the mouth. This species also produces social calls and whistles, though these are not considered here. The echolocation calls actually contain considerable low-frequency content (see Section 3.4.1.2) and are audible to the human ear. With most of the frequency content present at below 50kHz, this is in the part of the spectrum that the electrostatic transducers are least efficient and most variable with frequency, making them rather challenging to produce. However, the spectral compensation method does allow these signals to be accurately reproduced, as illustrated in Figure 5.6. The resulting signal is depicted in part (a) where it can be seen that good correlation is achieved with the original recording in the time domain. The need for the inversion process is demonstrated by making a comparison with the signal transmitted by the transducer using an unmodified input signal. This result is illustrated in Figure 5.6(b), in the frequency domain for clarity. It can be seen that, as expected, the high-pass nature of the transducer / microphone response across this frequency range promotes the higher frequency components, which is compensated by the inversion process.

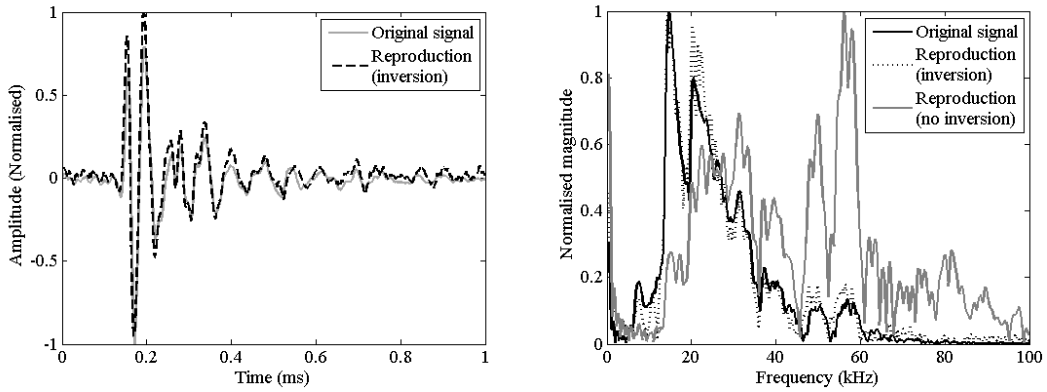

(a) (b)

Figure 5.6. Reproduction of *R. aegyptiacus* echolocation call, comparing the original with a reproduction based on the inversion process in the time domain (a) and frequency domain (b). Also included in (b) is the frequency spectrum of a signal reproduced without use of the inversion process, applying the recorded echolocation call directly to the transducer.

5.4.2 Reproduction of the Calls of *Pipistrellus pipistrellus*

Pipistrellus pipistrellus is generally classified as a FM bat, although its calls, especially in the search phase, generally have a CF tail of similar duration to the leading FM portion. An example of a call from this species is illustrated in the spectrogram of Figure 5.7(a), with energy content from 180kHz to 45kHz, distributed within its three harmonics. This call was recorded in the field using a Pettersson D-1000x (Pettersson Elektronic AB, Uppsala, Sweden) bat detector. Figure 5.7(b) shows the call as reproduced in the laboratory through direct application of the original signal to the transducer, while Figure 5.7(c) shows the signal reproduced using the spectral inversion process. It can be seen again that the higher frequency components are emphasised by the transducer, causing the CF portion of the fundamental component to lose energy with respect to the second and third harmonics. In this case, with little energy present above 150kHz, the reduced sensitivity of the microphone above this frequency is of little consequence.

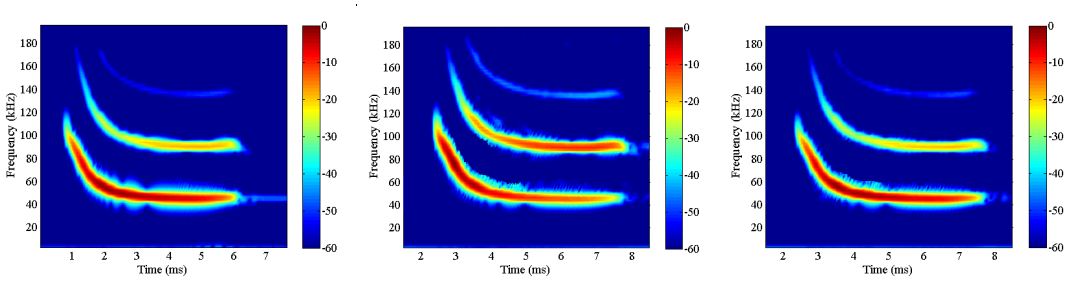

Figure 5.7 Reproduction of the call of *P. pipistrellus*. (a) depicts the original signal in spectrogram format; (b) depicts the signal reproduced by applying the original signal as the drive function; (c) depicts the signal reproduced using the inversion process.

5.5 Bats in Wire Avoidance Experiments

The ability to produce wideband airborne acoustic signals could lead to applications in NDE, ranging and SONAR. Another avenue of research that can be investigated is the use of the echolocation signals themselves, and their interaction with target objects. For example, through accurate replication of echolocation signals, scenarios that bats have been faced with that are reported in the literature can be recreated to examine the behaviour of echolocation calls. One such scenario involves bats being

presented with a series of wires, placed as obstacles within a captive flight environment. The bats are trained to fly from one side of the enclosure to the other, avoiding wires of successively smaller diameter, which are generally moved between each experiment to avoid the bat memorising the layout of the wire obstacles. In these experiments, it is common for the bats to use echolocation alone to detect and avoid wires with a cross-section considerably smaller than the wavelength of the calls they emit. For example, Gustafson and Schnitzler (1979) showed that the bat *Asellia tridens* was capable of avoiding wires down to a diameter of 65μm, in comparison with a minimum wavelength within its echolocation call of approximately 3mm, corresponding to the CF portion of its CF/FM call at approximately 115kHz. This means that the bat is detecting targets with a cross-section of λ/46. This result may seem surprising, though it is not unique. Mogdans *et al*. (1988) reported that the greater horseshoe bat (*Rhinolophus ferrumequinum*) could detect and avoid wires down to at least 60μm. *R. ferrumequinum* has an echolocation call that is generally classified as CF, though it can have initial and/or terminal FM portions; the highest frequency in the call is the CF portion at approximately 83kHz. As such, the bat is detecting wires with a cross-section of approximately λ/70. Furthermore, a similar capacity has been demonstrated in the megachiropteran fruitbat *R. aegyptiacus* (Waters and Vollrath, 2003) which was found to be capable of detecting and avoiding wires of 6mm diameter, and also "took evasive action" when within approximately 500mm of wires of 1.3mm diameter, although the bat did not always manage to actually avoid contact. This is in comparison with a peak component at 20kHz (17mm), with little energy above 40kHz (λ≈8.6mm). All these experiments illustrate that bats are capable of detecting wires with a diameter significantly smaller than the wavelength of their emitted echolocation call. How bats achieve such resolution is not answered in these publications, however. To attempt to resolve this, the experimental setup described is recreated in the laboratory using the electrostatic transducers and calibrated B&K microphone previously described. Through a series of controlled experiments, the fundamental physics of the wire-detection problem is examined to determine the nature of bats' capability to detect these small cross-section targets.

5.5.1 Replication of Bat Echolocation Calls from Wire Avoidance Experiments

A range of biological and bio-inspired signals were used for recreating the wire-avoidance experiments. The call of *R. aegyptiacus* used for these experiments was that demonstrated in section 5.4.1, as recorded from the wireless sensor. However, there was no access to recorded calls of the other species documented as having completed such experiments. As such, the call of *A. tridens* was artificially generated in Matlab from descriptions and spectrograms provided in Gustafson and Schnitzler (1979), as a CF call of 115kHz terminated with a linear FM sweep ending at 85kHz. The call of *R. ferrumequinum* was approximated by a constant 83kHz tone, as a comparison with the CF/FM call of *A. tridens* and the impulsive click of *R. aegyptiacus*. Two further biologically-inspired signals were used in the wire echolocation experiments; a multiharmonic FM chirp composed of a fundamental quadratic sweeping from 60kHz to 30kHz with two further harmonics, and a quadratic FM chirp descending from 180kHz to 30kHz in a single harmonic. The spectrograms of these signals, as received by the B&K microphone at 100mm (after spectral pre-equalisation) are displayed in Figure 5.8. All signals were windowed using a Tukey window with a taper ratio of 25%. This is the reason for the frequency content of the FM chirps not extending up to 180kHz, since the initial samples are reduced in amplitude by the windowing function. Due to the nature of a quadratic chirp, with its rate of frequency change slowing over the signal duration, the lower-frequency components are more completely represented. One aspect of Figure 5.8 that is worthy of note is the relative width of the spectrogram traces, in comparison to the multi-harmonic calls of Figures 5.3 and 5.7. The reason for this is simply the duration of the signals involved, and the corresponding smaller number of samples. Since the spectrogram is a sliding FFT window, the accuracy of the time and frequency information is a trade off. A long window will allow the frequency content to be accurately located in a small number of FFT bins; however, the time at which those frequencies occur will be somewhat blurred (carrying this argument to its logical conclusion generates the FFT of the entire signal, providing the most accurate information on the frequency content of the signal, but no timing information). Conversely, a shorter window allows the point in time of a given

frequency component to be accurately located, but the frequency information is spread over a greater number of FFT bins, reducing its accuracy. The signals in Figures 5.3 and 5.7 have a long duration, and therefore a high number of samples, allowing accurate time and frequency information to be displayed in the spectrograms. The signals constructed for the wire echolocation experiments were reduced in duration, for the reason that the space within which the experiments were to be conducted is finite, and that longer signals would have an effect on the minimum range at which experiments could be conducted. As such, the spectrograms of Figure 5.8 are displayed with the best compromise between accuracy of time and frequency data, using a Hanning-windowed 512-point FFT.

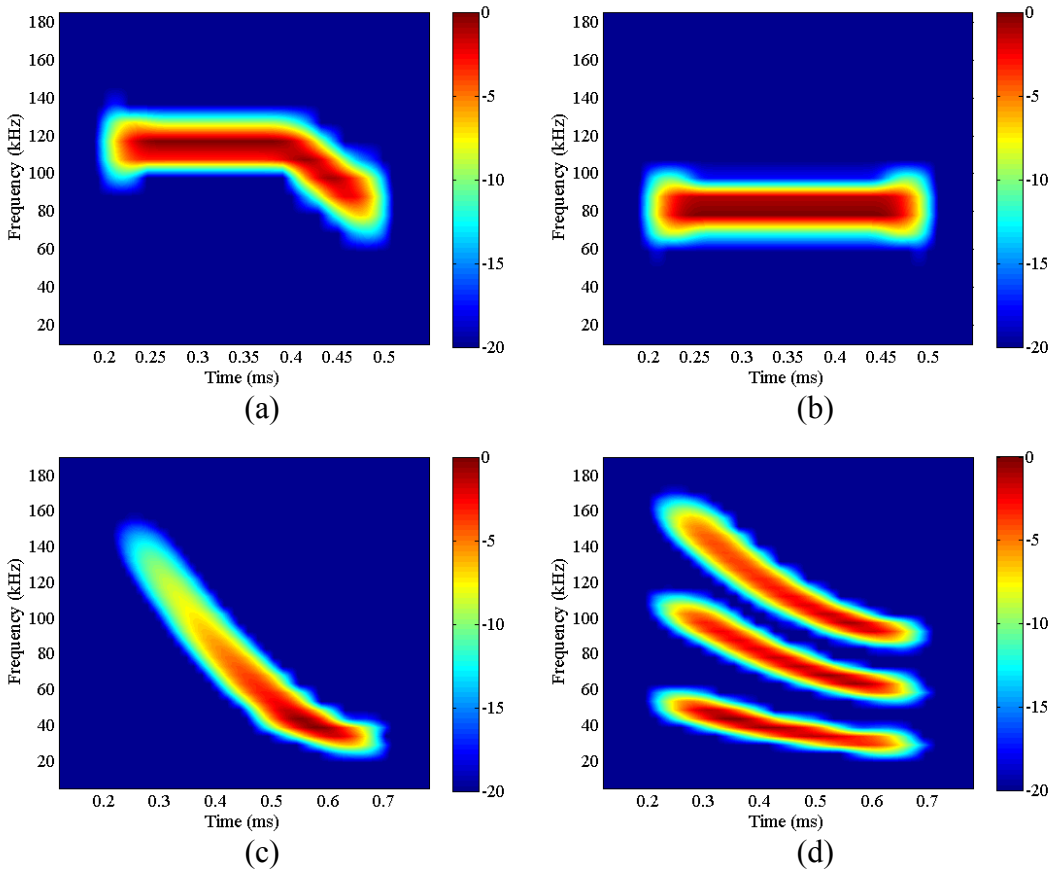

Figure 5.8. Spectrograms of the signals used in the wire echolocation experiments as recorded using the B&K microphone at a range of 100mm: (a) representation of *A. tridens* CF/FM call as described by Gustafson and Schnitzler (1979); (b) CF 83kHz, representative of the call of *R. ferrumequinum*; (c) multi-harmonic quadratic FM chirp, composed of a fundamental component sweeping from 60kHz to 30kHz, with two additional harmonics; (d) single-harmonic quadratic FM chirp sweeping from 180kHz to 30kHz. All signals are windowed with a Tukey window, having a taper ratio of 25%.

The amplitude of each driving electrical signal was altered such that the pressure detected by the B&K microphone at 100mm was 100dB pSPL (peak SPL). This meant applying different amplitude signals to the transducer, dependent on the driving function, but allowed a more rigorous comparison of the relative merits of each of these echolocation calls to be made than if the same electrical signal amplitude (and therefore varying acoustic pressures) had been used. In calculating the generated pressure, the peak frequency of each signal, and the microphone calibration at that frequency was included in the calculation. In this case peak SPL was used to enable comparison of the impulse-like asymmetric clicks of *R. aegyptiacus* with the longer duration CF and FM signals.

The echolocation tests were performed in the same temperature controlled Perspex case as was used for the transducer characterisation in the previous Chapter. This environment was not ideal to carry out echolocation testing since the walls of the case generated significant echoes. Care was taken to position the transducer, microphone and target in such a way that these echoes had no effect on the echolocation procedure. In addition to this, the repetition rate of the driving signal was selected to allow reverberation of the acoustic signal within the case to completely fade before the next signal was applied The configuration of the test is illustrated in the photograph of Figure 5.9 illustrating the arrangement of the transmitting transducer, receiving microphone and target wire. The transducer / microphone arrangement was mounted on the z-stage of the x-y-z scanner described in section 4.5.3. The wire was mounted vertically via a small hole in the top of the Perspex case, and secured within the case, directly in line with the transducer / microphone, situated 300mm and 350mm respectively from each side, and approximately 1.2m from the end, of the case. The z-stage was used to vary the target distance.

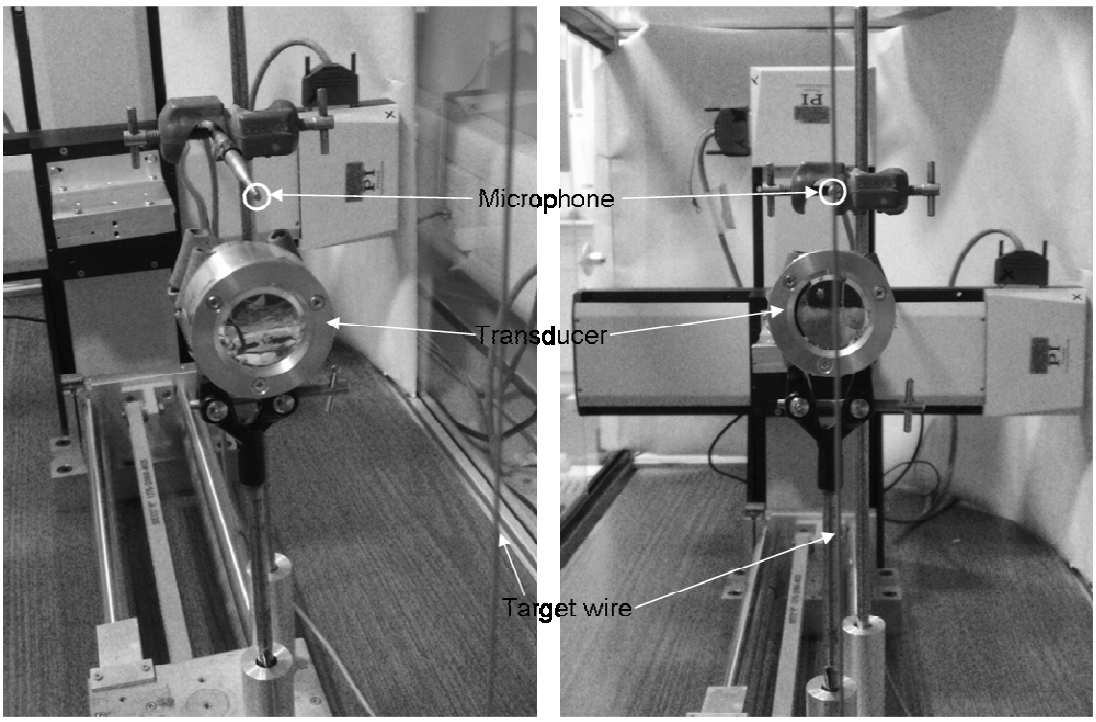

Figure 5.9. Photograph illustrating the arrangement of the transducer, microphone and target wire in perspex case.

Each echolocation call was presented to seven targets, with diameters of 5mm, 3mm, 1mm, 600µm, 340µm, 250µm and 125µm respectively. Furthermore, six discrete target distances were used: 50mm; 100mm; 200mm; 300mm; 400mm; and 500mm. In addition to this the effect of noise on the echolocation signals was also investigated through varying the number of averages performed on the recorded signal.

There is some evidence in the literature that bats make use of the fine detail of the cross-correlation function as covered in Chapter 2. Certainly it appears that bats use some sort of correlation based method by which to ascertain the time of arrival (and hence range) of an echo from a target. For this reason, cross correlation of the emitted (in this case the signal recorded at 100mm from the emitter) and received signal was performed as a method by which to enhance detection of the target echo.

5.5.2 Echolocation Call Recording and Processing

Each echolocation procedure obtained a number of signals, illustrated in Figure 5.10, using a quadratic FM chirp as an example. Firstly, the emitted echolocation call was

recorded using the B&K microphone situated at a distance of 100mm from the emitter; Figure 5.10(a). There were two reasons for doing this. Firstly, the driving signal amplitude could be adjusted to generate an acoustic signal with a peak amplitude of 100dB pSPL. Secondly, this recorded signal acted as the reference signal for the correlation procedure, in the same way as the bat may use its emitted call. The microphone was then moved into position above the transmitter (as pictured in Figure 5.9) to enable echolocation testing to be performed.

The experiment was configured over a number of steps as follows. The target wire was secured in place and the range set to 300mm. At this point the transducer position was adjusted by hand to enable the largest amplitude echo to be received from the target. This target range was selected to enable sufficient signal to be detected in order to perform the alignment, but wasn't so close as to require substantial vertical tilt of the transmitter; if 50mm had been used, then the transducer would have been significantly inclined upwards to obtain the largest echo, resulting in misalignment at larger distances. The target wire was then removed and a signal recorded for each target distance, to act as a 'no-target' control signal; Figure 5.10(b). As with all the figures in this section, the traces are stacked in order of target range, from 50mm at the bottom to 500mm at the top. The wire was then replaced and the target distance sequentially increased from 50mm to 500mm, with the signal detected by the microphone being recorded at each point; Figure 5.10(c). It can be seen in this figure that the emitted and reflected signals can overlap, especially at closer range. Furthermore, there are reflected signals evident throughout the 'no-target' trace, due to the finite environment provided by the case. As such, the trace recorded without the target was used a control trace, which was subtracted from the trace recorded with the target in place to leave only the signals attributable to the target; Figure 5.10(d). For reasons of brevity, this trace will be called the 'subtracted' trace throughout this section.

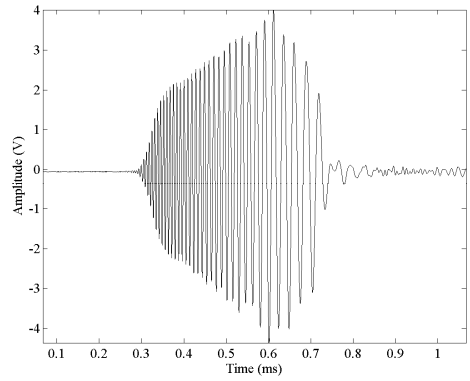
Amplitude (V)
Time (ms)

(a)

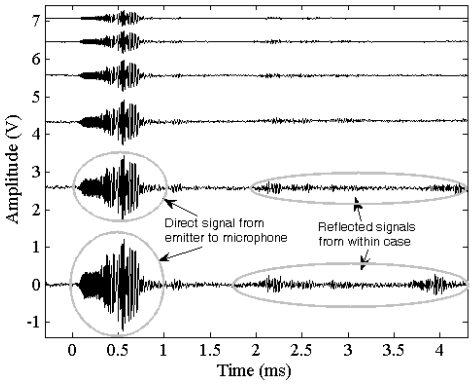
Amplitude (V)
Direct signal from emitter to microphone
Reflected signals from within case
Time (ms)

(b)

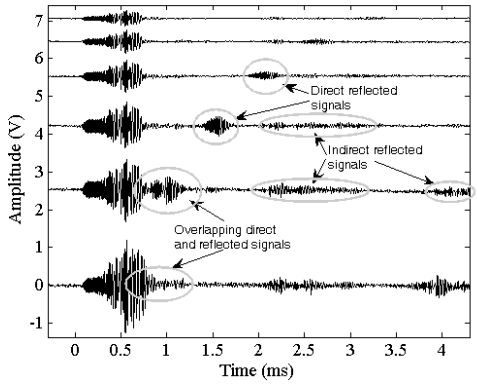
Amplitude (V)
Direct reflected signals
Indirect reflected signals
Overlapping direct and reflected signals
Time (ms)

(c)

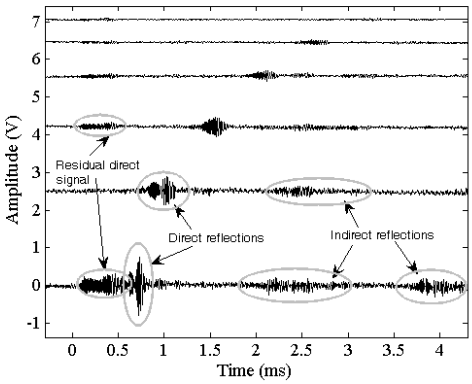
Amplitude (V)
Residual direct signal
Direct reflections
Indirect reflections
Time (ms)

(d)

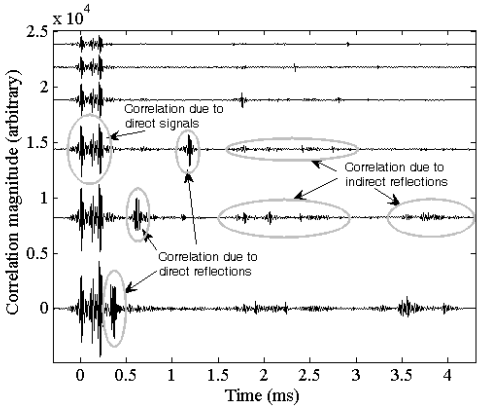
x 10^4
Correlation magnitude (arbitrary)
Correlation due to direct signals
Correlation due to indirect reflections
Correlation due to direct reflections
Time (ms)

(e)

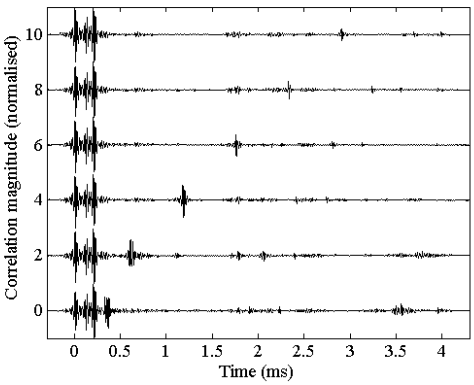
Correlation magnitude (normalised)
Time (ms)

(f)

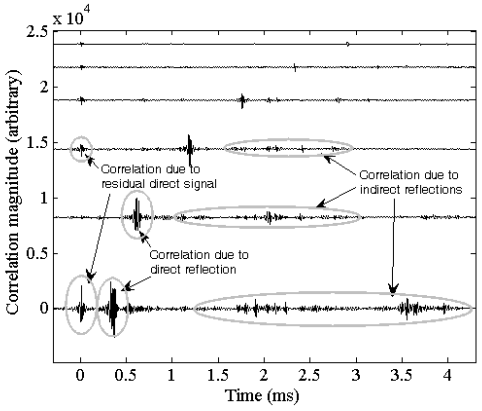
x 10^4
Correlation magnitude (arbitrary)
Correlation due to residual direct signal
Correlation due to indirect reflections
Correlation due to direct reflection
Time (ms)

(g)

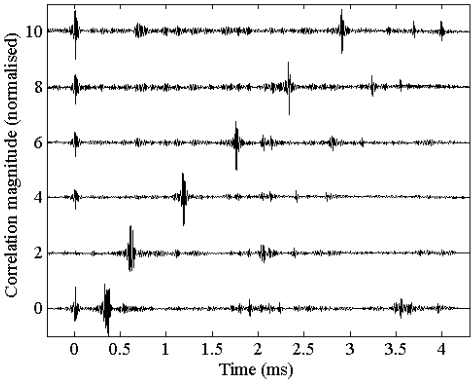
Correlation magnitude (normalised)
Time (ms)

(h)

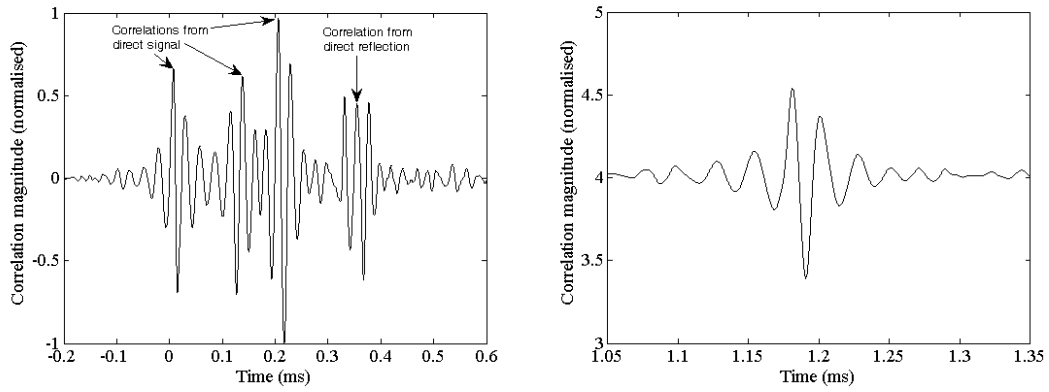

(i) (j)

Figure 5.10. Signals and processing of echolocation signals from wire-avoidance experiments. Each figure has multiple traces, one for each of the ranges: bottom to top is 50mm; 100mm; 200mm; 300mm; 400mm; and 500mm. (a) Reproduced echolocation signal at 100mm from the transmitter; (b) recorded signal with no target in place; (c) signals recorded with 1mm target; (d) signals recorded with target minus those without target, i.e. (d) – (c); (e) cross correlation of the emitted signal (a) with the trace recorded from the target (c); (f) normalised version of (e); (g) cross correlation of the emitted signal (a) with the subtracted trace from the target (d); (h) normalised version of (g); (i) close-up of cross-correlation function of directly-detected signal and direct echo from 1mm target at 50mm range; (j) close-up of cross-correlation function of return echo from 1mm target at 200mm range.

The next step was to perform a correlation between the emitted signal and the returning series of echoes. Firstly the cross-correlation of the signal (a) and recorded echolocation trace (c) was performed and is displayed in Figure 5.10(e). This was then further processed to produce the normalised version of each trace (f). Similarly, the cross-correlation of the signal (a) and the subtracted trace (d) is presented in Figure 5.10(g), with its normalised version in Figure 5.10(h). As expected, the pulse compression capability of cross-correlation of chirp signals allows the presence of multiple echoes within the returning trace to be separated, as can be seen in parts (e) and (f) in comparison with (c). It even appears that the direct signal between the transmitter and microphone is actually comprised of at least three distinct chirps, as can be seen from the close-up view of its correlation function in part (i). It can also be seen in this image that the cross correlation of the echo returned from the wire target may not be a distinct single chirp signal, as shown by the ambiguity of the peak of the correlation signal; possibly, there is a small amount of directly-coupled energy at this point interfering with the reflection. It can be seen as the target distance is increased, that the correlation function was a sharper peak as

demonstrated in (j) at 200mm range. For all subsequent results, only the subtracted and normalised cross-correlation traces will be displayed. Generally 256 averages were used to obtain these signals, allowing the noise level to be reduced and an accurate sound pressure level measured for the returning echoes. The effect of averaging is covered in a later section.

5.5.3 Wire Target Echolocation: *Rousettus aegyptiacus* call

As discussed previously, *R. aegyptiacus* has been subjected to wire-avoidance tests (Waters and Vollrath, 2003). In that study it was shown that this species was capable of consistently detecting and avoiding wires of a cross section of 6mm, whereas with wires of 1.3mm cross-section, more collisions occurred but the bats did execute "evasive action" when within "ca. 50cm of the wires". Documentation of the echolocation calls used by these bats illustrate their similarity to those recorded using the wireless sensor (see Chapter 3) and hence reproduced here. The signal traces obtained using the emitted signal displayed in Figure 5.6(a) are shown in Figure 5.11. It can be seen that the return echoes from the 5mm diameter target are easily identified up to 400mm in both the raw (averaged) and cross-correlation traces. At 500mm the echo is still discernible, though there is some scope for ambiguity given its amplitude in comparison with other acoustic signals not associated with the wire target. However, given the "impulse-like" nature of the *R. aegyptiacus* echolocation signal, cross correlation does not provide the same pulse-compression and noise reduction that is present when used with a longer CF or FM signal, as already illustrated in Figure 5.10 and further discussed later.

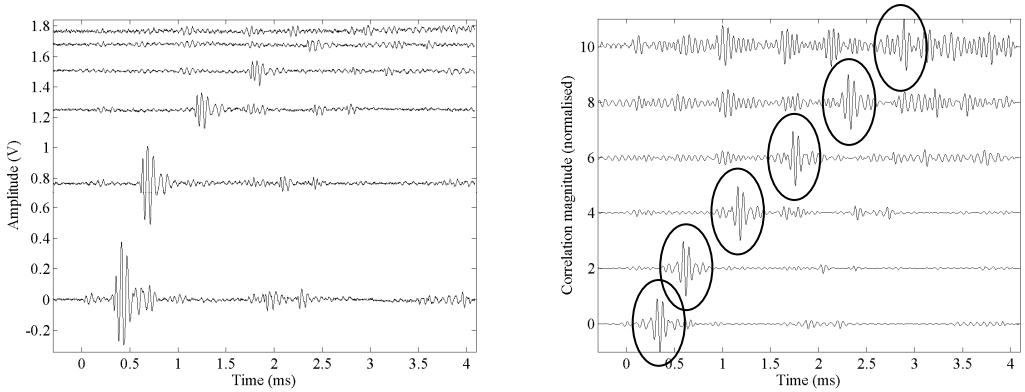

(a) (b)

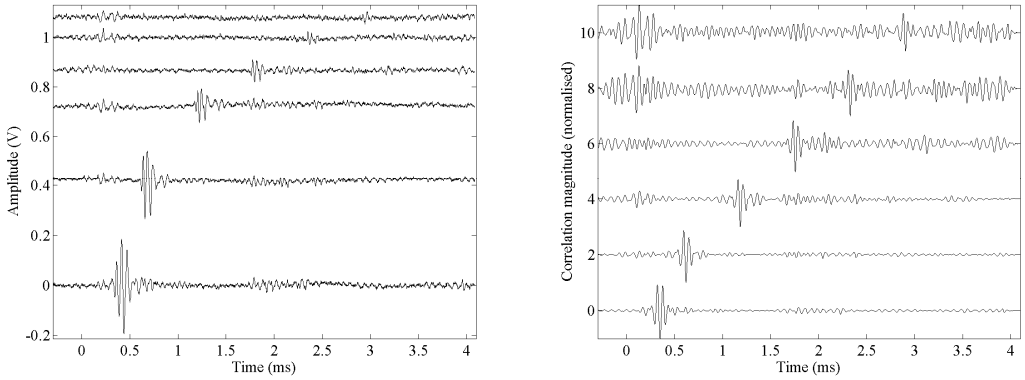

(c) (d)

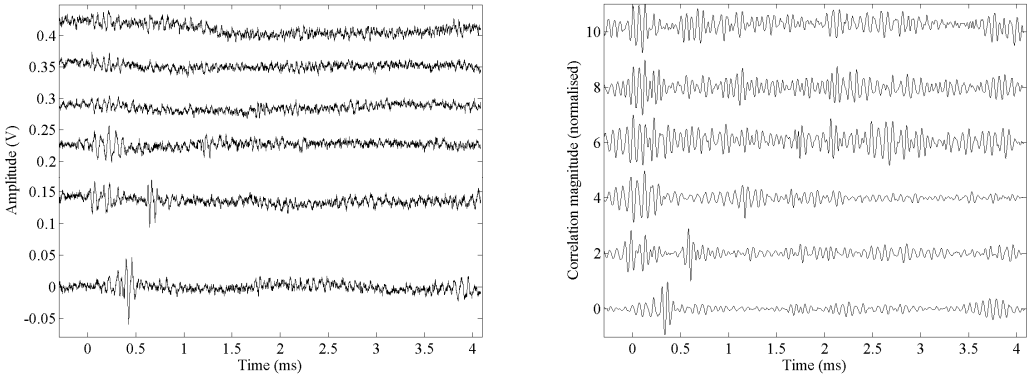

(e) (f)

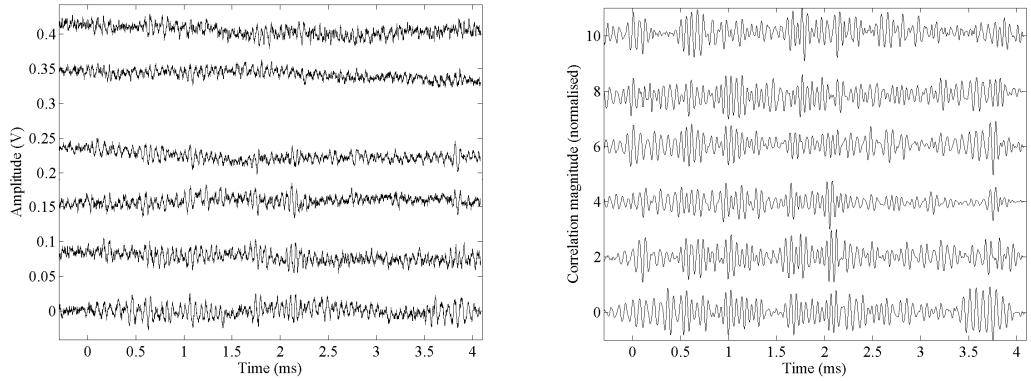

(g) (h)

Figure 5.11. Series of figures depicting signals from wire-target echolocation tests using a reproduced call from *R. aegyptiacus*: (a) subtracted and (b) normalised cross-correlation trace for 5mm cross-section target (with location of target echoes circled); (c) subtracted and (d) normalised cross-correlation trace for 3mm cross-section target; (e) subtracted and (f) normalised cross-correlation trace for 1mm cross-section target; (g) subtracted and (h) normalised cross-correlation trace for 600μm cross-section target.

As expected, with reducing diameter of target, the capability of the *R. aegyptiacus* signal to generate a return echo is reduced. The return signals from the 3mm wire show similar results to the 5mm target, though with reduced amplitude. The 1mm target can only be discerned to a distance of 100mm-200mm; the 600μm target cannot be detected at any distance. For obvious reasons, the traces obtained with targets of less than 600μm diameter have not been reproduced here. The location of the return echoes for the 5mm target are circled in Figure 5.11(b); since these obviously do not change location, they are only circled in this single figure.

These findings agree well with those published by Waters and Vollrath (2003) indicating the bat to be easily capable of detecting targets of 3mm and above, but with the return echoes being seriously degraded at the approximately 1mm target diameter level. Indeed, the results here indicate that the return signal from the 1mm target would only become discernible as the bat approached the target, possibly enabling it to take "evasive action", but not having the time to consistently avoid the target. It will be interesting to compare this performance with that of the microchiropteran and bio-inspired signals used subsequently. However, it still bears mention that the maximum frequency component of the *R. aegyptiacus* call is approximately 40kHz, with a corresponding wavelength of 8.6mm, while its peak component at approximately 15kHz has a wavelength of 23mm, in comparison with the 1mm diameter of the target wire.

The strength of the return echo will be covered in a later section in order to provide an analysis of this parameter with respect to target range, target diameter and echolocation signal. However, as an indication, the lowest return signal that can be detected and discerned from the background noise (e.g. 3mm target at 400mm or 1mm target at 200mm) is in the region of 50dB pSPL. This is a reduction of some 50dB on the emitted signal, and has also been extracted from the environmental noise through use of averaging (n = 256). As with analysis of the returning signal strength, noise analysis and the effect of averaging and signal structure on the detection of an echo will be documented in a later section.

5.5.4 Wire Target Echolocation: 83kHz CF Echolocation Call

Another bat that has had its wire avoidance capabilities assessed in the laboratory is the CF bat *Rhinolophus ferrumequinum* (Mogdans *et al.*, 1988). *R. ferrumequinum* emits calls with a strong CF component at approximately 83kHz, with a short initial and/or terminal FM section. The length of the CF section, and frequency range of the FM portions can vary with task but the calls are generally classified as CF. Since the use of FM chirps in echolocation is examined in subsequent sections, the call of *R. ferrumequinum* is here approximated as a 250μs long 83kHz toneburst, apodised by a Tukey window with a taper-ratio of 25%. The duration of the toneburst was selected to enable a CF call to be replicated, but without being too long to cause considerable problems operating in a finite space.

Mogdans *et al.* (1988) indicated that *R. ferrumequinum* was capable of detecting and avoiding wires down to at least 60μm – this was the smallest diameter of wire used. Although the bats' performance dropped for 80μm and 60μm wires, it was still considerably above the calculated chance level, for both horizontally- and vertically-oriented wires. The 60μm diameter represents approximately λ/69 at the CF of 83kHz. The echolocation traces obtained using the signal displayed in Figure 5.8(b) are shown in Figure 5.12. It can be seen that the return echoes from each target down to 600μm cross-section are easily discerned at all ranges, with the characteristic triangular envelope of the auto-correlation function of a toneburst clearly evident. It can be seen that as the target diameter decreases, or the range increases, thereby reducing the amplitude of the returning signal, that the SNR of the correlation function decreases. With the 340μm wire, the return echo is less distinct from the noise, though still identifiable, whilst the echoes from the 250μm wire are increasingly difficult to extract. No return echoes can be perceived from the 125μm target. Even so, it should be noted that the 340μm wire represents approximately λ/12 of the 83kHz signal, whilst 250μm is λ/16. Furthermore, examination of the 340μm and 250μm results indicate that the echoes from the targets are actually quite evident and distinct from any noise-floor that is present. Their location and detection is only made ambiguous by the presence of "coherent noise" in the form of echoes from within the limited space of the experimental case. As such, although the echoes

may not seem particularly distinct in Figures 5.12(i)-(l), these echoes are enough to be accurately measured for echo amplitude and signal-to-noise ratio analysis of the subsequent sections.

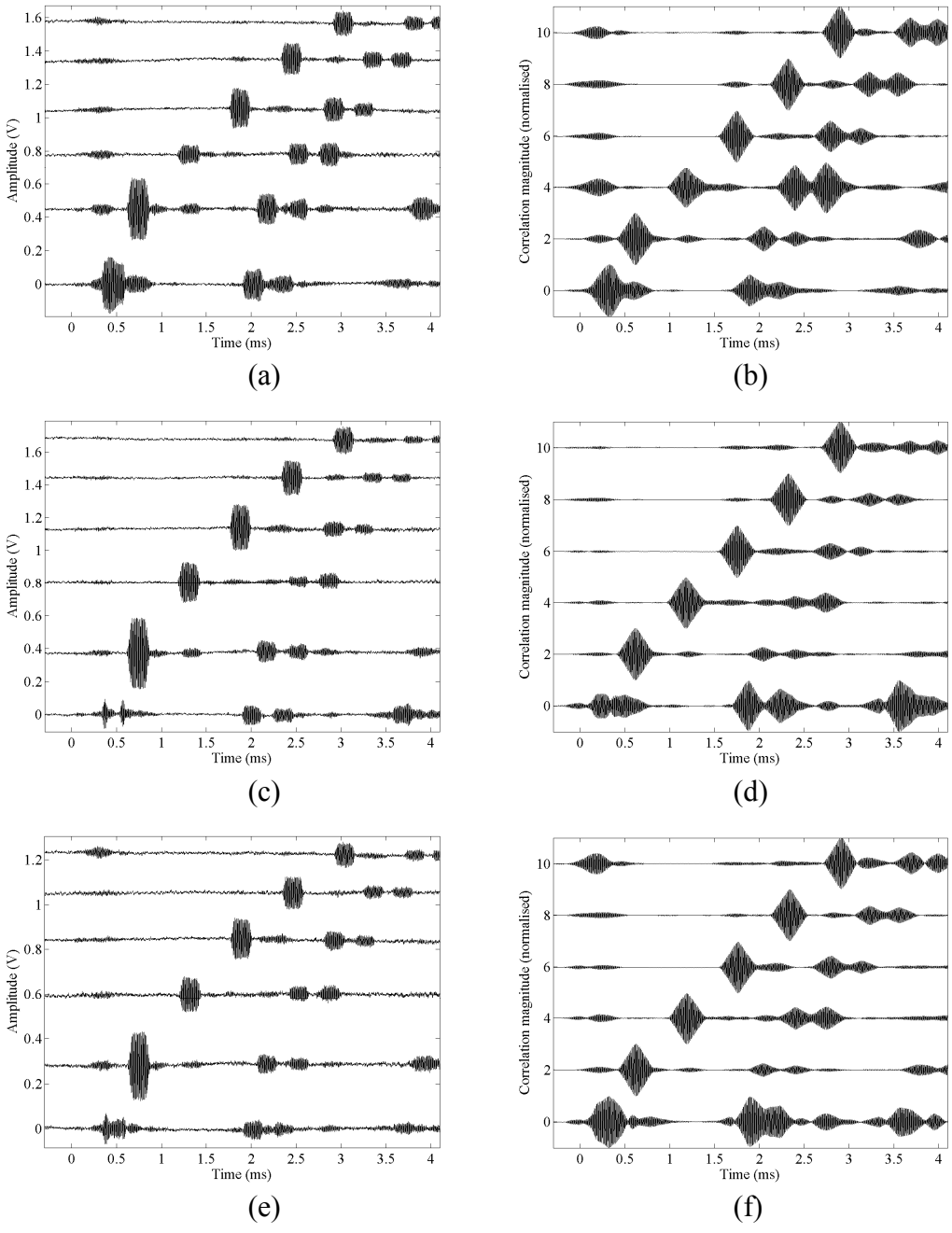

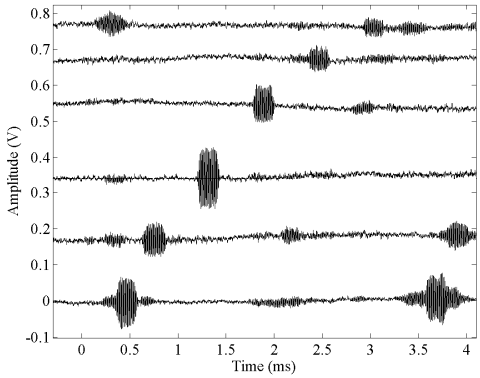
Amplitude (V)
Time (ms)

(g)

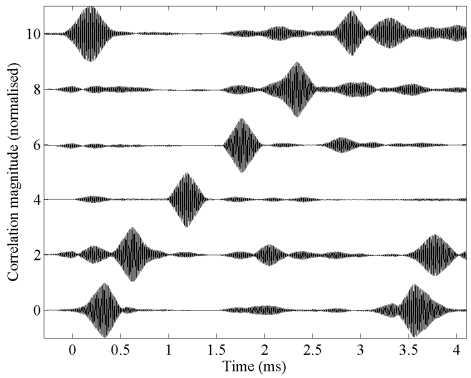
Correlation magnitude (normalised)
Time (ms)

(h)

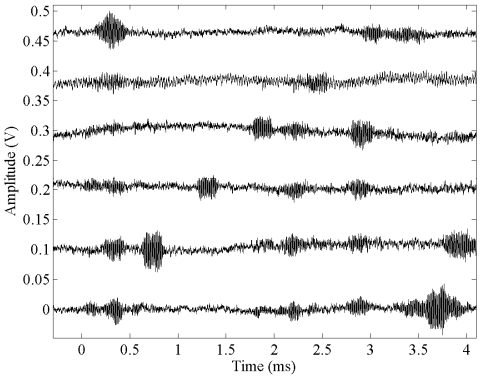
Amplitude (V)
Time (ms)

(i)

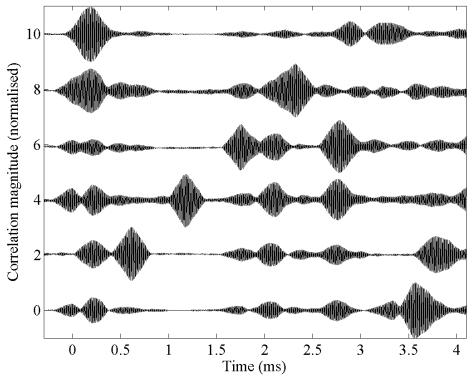
Correlation magnitude (normalised)
Time (ms)

(j)

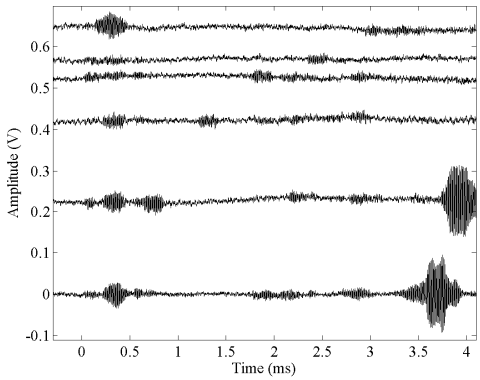
Amplitude (V)
Time (ms)

(k)

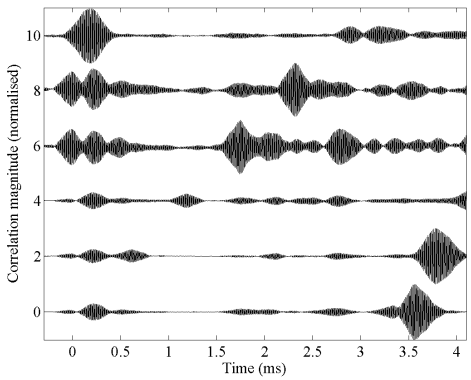
Correlation magnitude (normalised)
Time (ms)

(l)

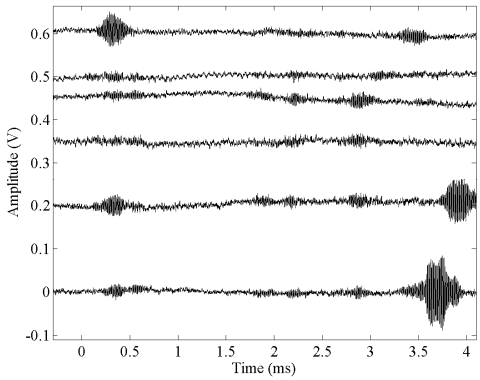
Amplitude (V)
Time (ms)

(m)

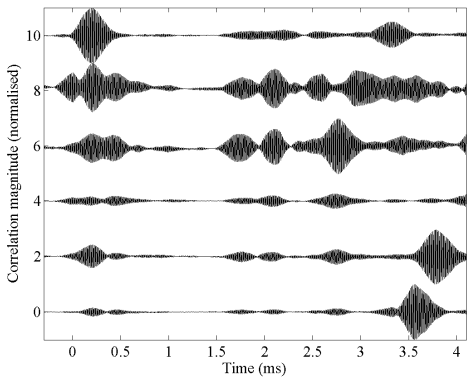
Correlation magnitude (normalised)
Time (ms)

(n)

Figure 5.12. Series of figures depicting signals from wire-target echolocation tests using a 250μs windowed 82kHz tone-burst: (a) subtracted and (b) normalised cross-correlation trace for 5mm cross-section target; (c) subtracted and (d) normalised cross-correlation trace for 3mm cross-section target; (e) subtracted and (f) normalised cross-correlation trace for 1mm cross-section target; (g) subtracted and (h) normalised cross-correlation trace for 600μm cross-section target; (i) subtracted and (j) normalised cross-correlation trace for 340μm cross-section target; (k) subtracted and (l) normalised cross-correlation trace for 250μm cross-section target; (m) subtracted and (n) normalised cross-correlation trace for 125μm cross-section target.

5.5.5 Wire Target Echolocation: *Asellia tridens* echolocation call

Gustafson and Schnitzler (1979) studied the wire avoidance capabilities of the bat *A. tridens*. Its echolocation call is described as consisting of a "CF component followed by a FM terminal downward sweep of 19-21kHz" where the CF part "constitutes about 7/10 of the entire signal" and varies "between 111-124kHz" in 18 individuals. From this description, and spectrograms contained in the paper, an artificial version of the signal was constructed in Matlab consisting of a 200μs CF section at 115kHz, with a terminal FM sweep decreasing to 85kHz over 100μs, producing a signal with a total duration of 300μs. Using this signal, as illustrated in Figure 5.8(a), the wire detection echolocation traces displayed in Figure 5.13 were captured.

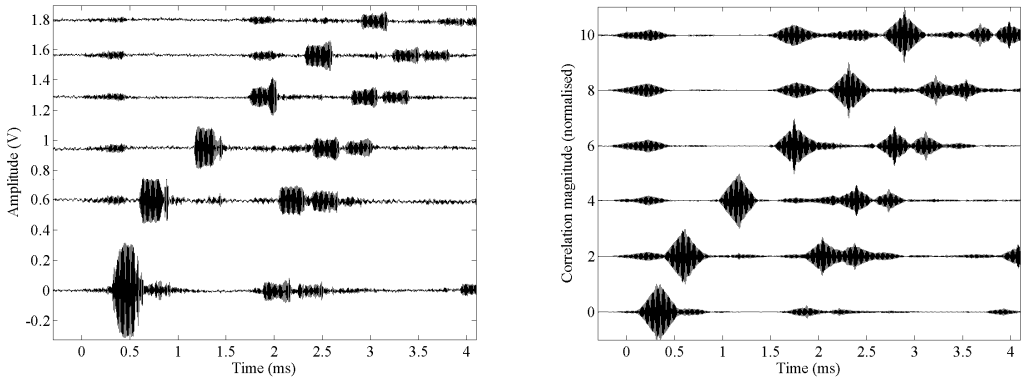

(a) (b)

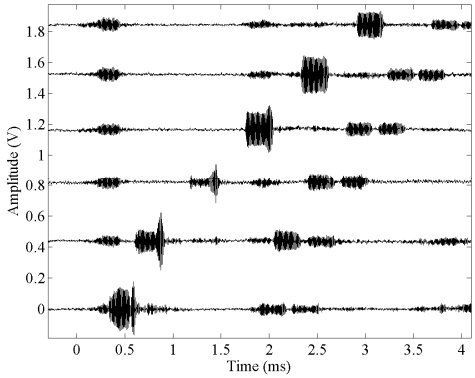
Amplitude (V)
Time (ms)

(c)

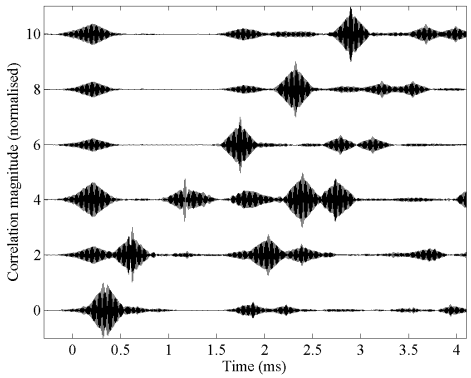
Correlation magnitude (normalised)
Time (ms)

(d)

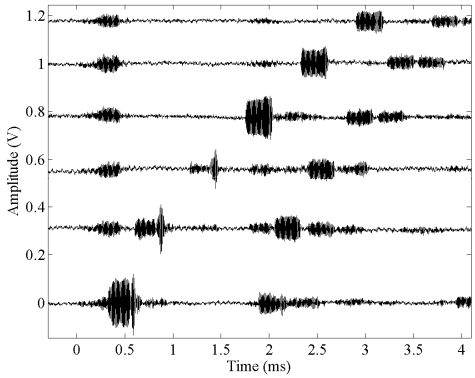
Amplitude (V)
Time (ms)

(e)

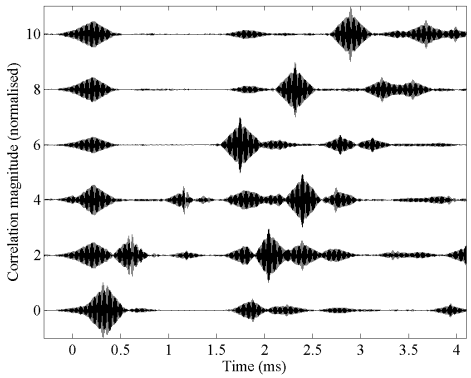
Correlation magnitude (normalised)
Time (ms)

(f)

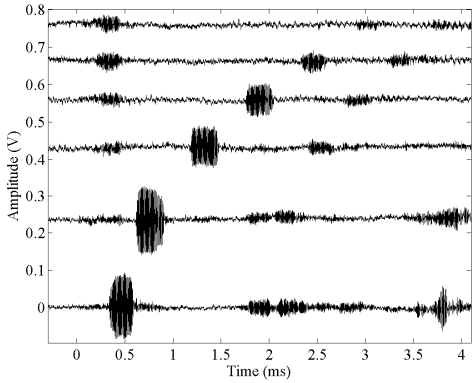
Amplitude (V)
Time (ms)

(g)

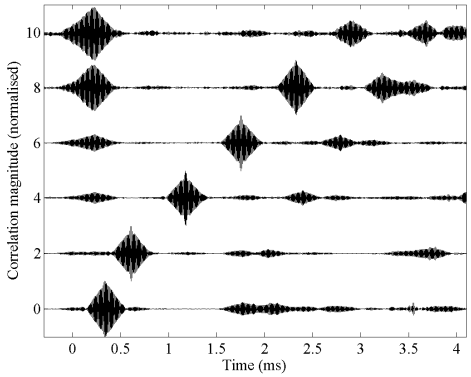
Correlation magnitude (normalised)
Time (ms)

(h)

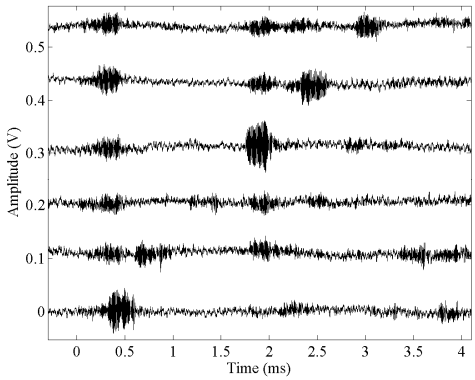
Amplitude (V)
Time (ms)

(i)

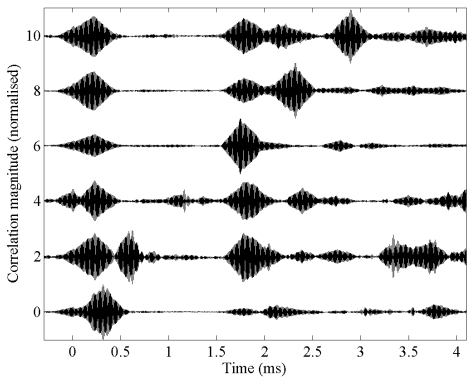
Correlation magnitude (normalised)
Time (ms)

(j)

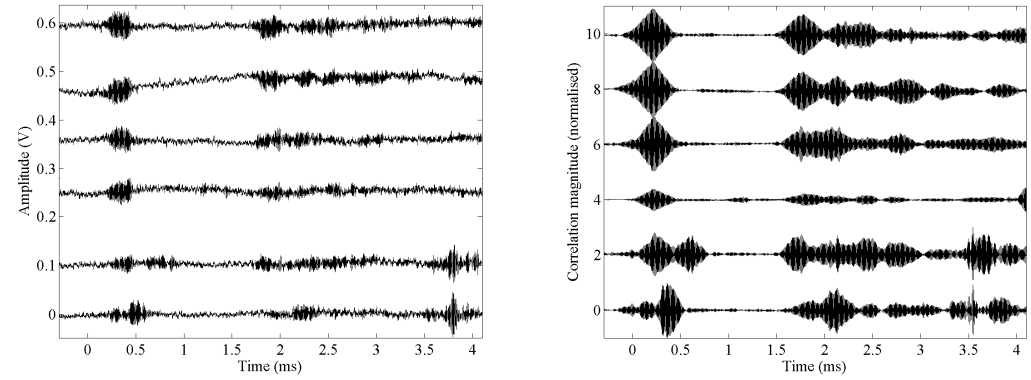

(k) (l)

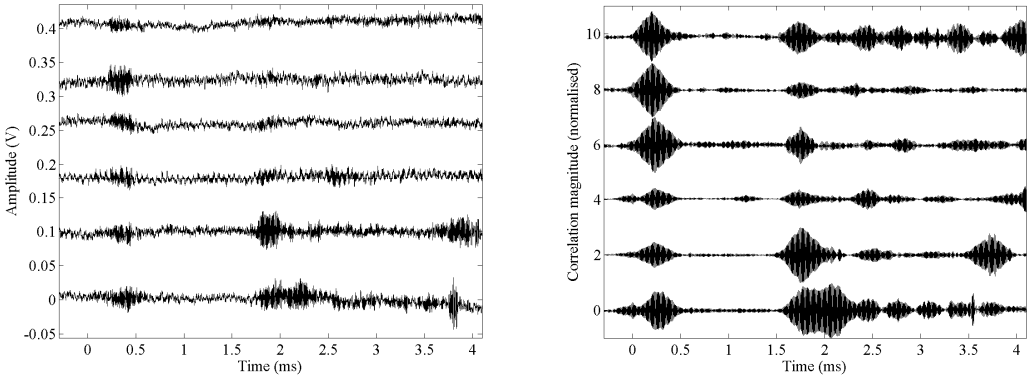

(m) (n)

Figure 5.13. Series of figures depicting signals from wire-target echolocation tests using a 300μs representation of an *Aselia Tridens* call: (a) subtracted and (b) normalised cross-correlation trace for 5mm cross-section target; (c) subtracted and (d) normalised cross-correlation trace for 3mm cross-section target; (e) subtracted and (f) normalised cross-correlation trace for 1mm cross-section target; (g) subtracted and (h) normalised cross-correlation trace for 600μm cross-section target; (i) subtracted and (j) normalised cross-correlation trace for 340μm cross-section target; (k) subtracted and (l) normalised cross-correlation trace for 250μm cross-section target; (m) subtracted and (n) normalised cross-correlation trace for 125μm cross-section target.

It can be seen in comparing the correlation traces from this signal with those from the CF signal in Figure 5.12 previously, that the additional terminal FM sweep produces a sharper peak in the correlation function due to pulse compression. This amply demonstrates the advantage of the additional bandwidth in terms of localising the arrival time, and hence range, of an echo. In terms of the targets detectable through echolocation, this signal generates easily detectable echoes from the 600μm target, up to the full 500mm range, whilst those from the 340μm target are discernible, though less distinct with respect to spurious signals within the trace. The 250μm

target does appear to generate detectable echoes at 50mm and 100mm, whilst again no echoes are detectable from the 125μm wire., with only echoes from within the case being detected.

5.5.6 Wire Target Echolocation: Artificial FM chirps

After echolocation experiments were completed using the calls of bats that have been subjected to wire-avoidance tests in the literature, it was decided to use artificial biologically-inspired FM chirps. These signals were composed to cover practically the entire frequency spectrum utilised by microchiroptera in their echolocation calls, covering the range from 180kHz to 30kHz. Two signals were created, the first a single quadratic FM chirp with an initial and terminal frequency of 180kHz and 30kHz, respectively; the second signal was comprised of a fundamental 60kHz to 30kHz quadratic chirp component, with a second (120kHz to 60kHz) and third (180kHz to 90kHz) harmonic added to the fundamental. Each signal was again windowed using a 25% taper-ratio Tukey window. These signals occupy the same frequency space, but have their energy concentrated in different energy bands as can be seen in Figures 5.8(c) and 5.8(d). The traces recorded using the 180kHz-30kHz chirp are displayed in Figure 5.14, while those recorded with the multiharmonic signal are in Figure 5.15. There is an immediately obvious difference between the correlation functions produced using these wideband signals (even given the reduction in high-frequency content due to windowing, the fractional bandwidth is still in excess of 130%; in comparison, the FM portion of the *A. tridens* is less than 25%) and those produced by the previously used signals. The pulse compression produced by the correlation function produces the sharp peaks that are especially evident in the traces produced by the larger cross-section targets in Figures 5.14 and 5.15. This is one obvious advantage of using a wideband signal; it provides the capability for generating accurate timing data, limited only by the precision with which the peak of the correlation function can be located. In terms of detecting the thinnest wires in this series of tests, however, these chirps are actually less effective than either the CF or CF/FM signals previously investigated with the 340μm wire far more difficult to detect than the 600μm wire. In reality it appears that it is difficult to

separate the reflected signal from the 340μm wire from the noise, certainly beyond approximately 100mm-200mm.

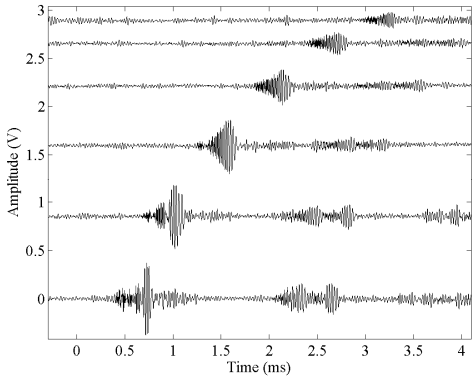

(a)

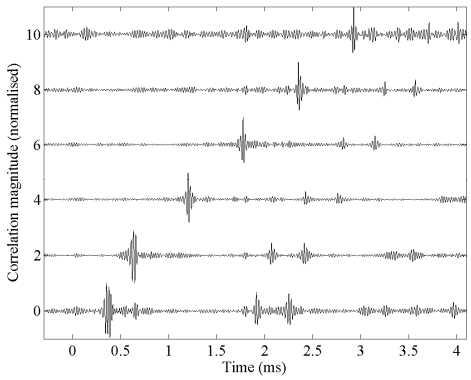

(b)

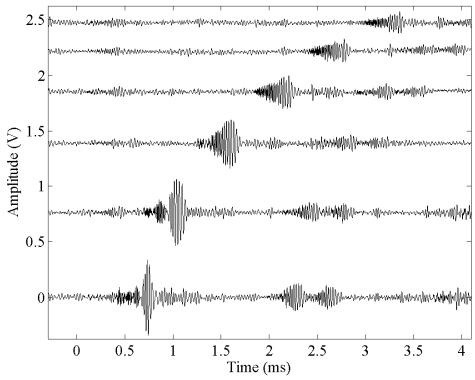

(c)

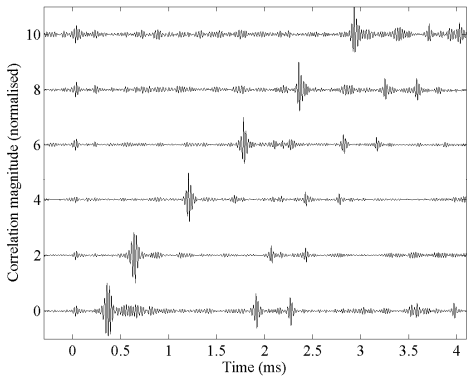

(d)

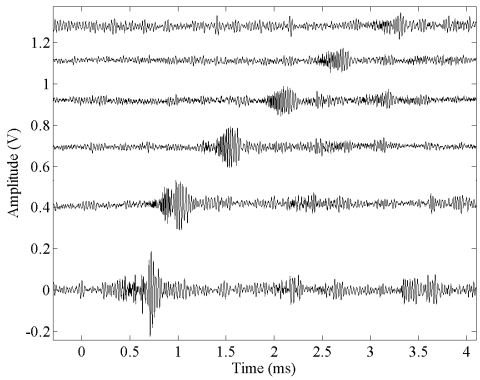

(e)

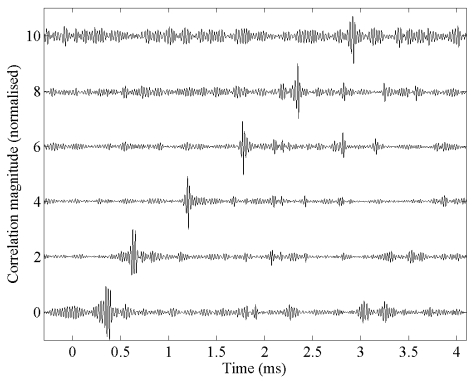

(f)

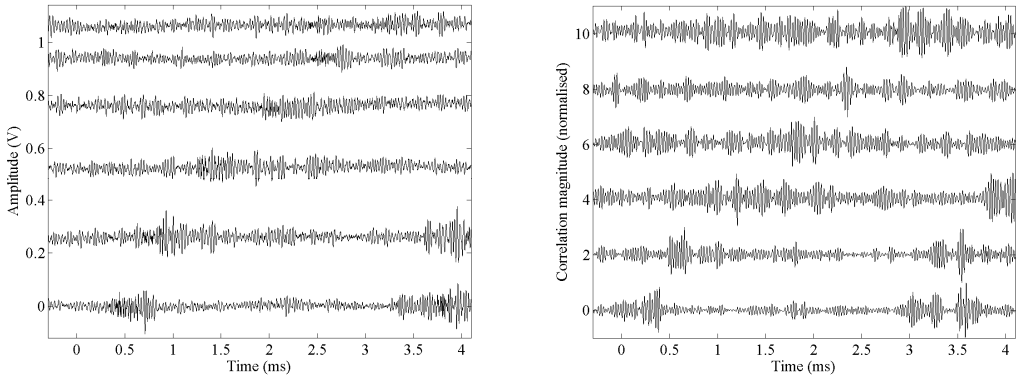

(g) (h)

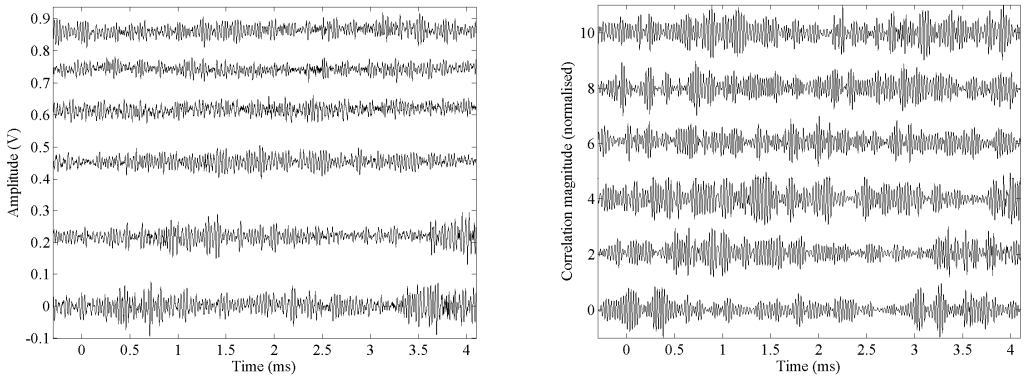

(i) (j)

Figure 5.14. Series of figures depicting signals from wire-target echolocation tests using a 500μs quadratic FM chirp, with initial and terminal frequencies of 180kHz and 30kHz, respectively: (a) subtracted and (b) normalised cross-correlation trace for 5mm cross-section target; (c) subtracted and (d) normalised cross-correlation trace for 3mm cross-section target; (e) subtracted and (f) normalised cross-correlation trace for 1mm cross-section target; (g) subtracted and (h) normalised cross-correlation trace for 600μm cross-section target; (i) subtracted and (j) normalised cross-correlation trace for 340μm cross-section target.

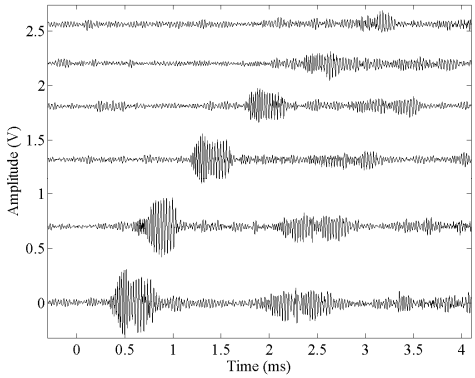
Amplitude (V)
Time (ms)

(a)

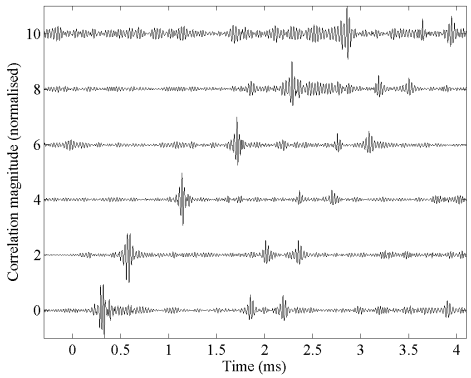
Correlation magnitude (normalised)
Time (ms)

(b)

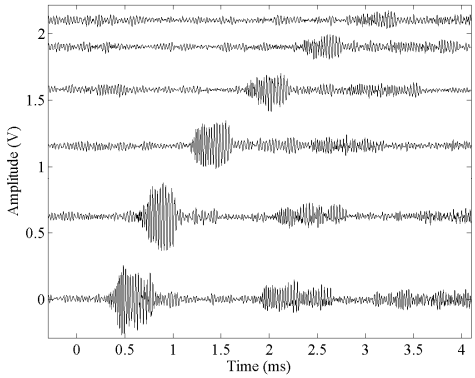
Amplitude (V)
Time (ms)

(c)

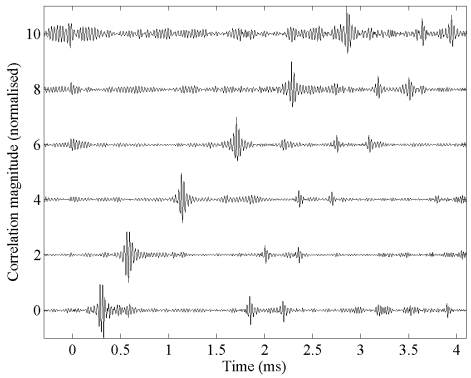
Correlation magnitude (normalised)
Time (ms)

(d)

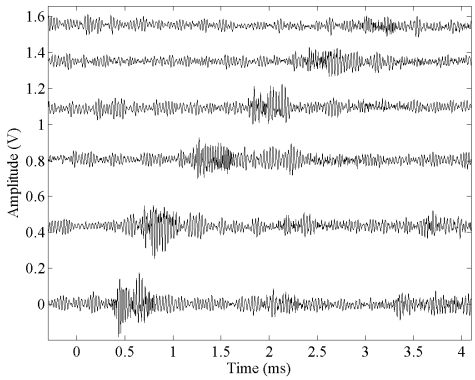
Amplitude (V)
Time (ms)

(e)

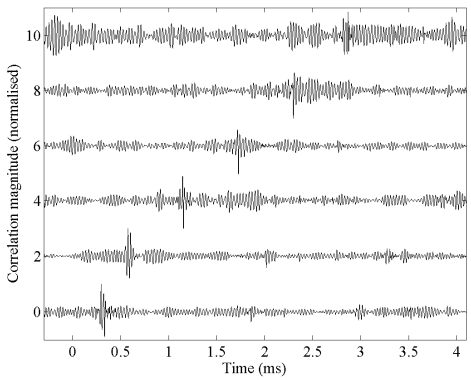
Correlation magnitude (normalised)
Time (ms)

(f)

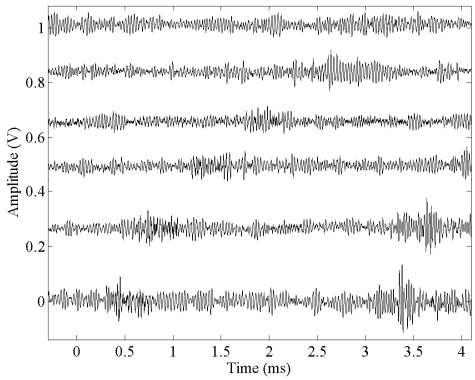
Amplitude (V)
Time (ms)

(g)

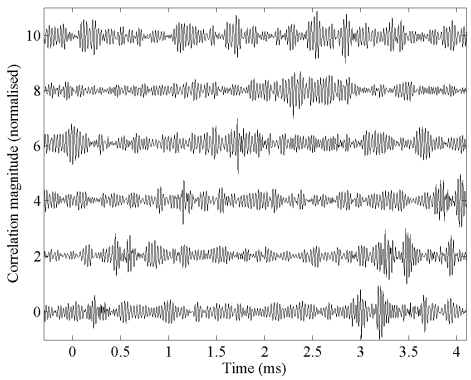
Correlation magnitude (normalised)
Time (ms)

(h)

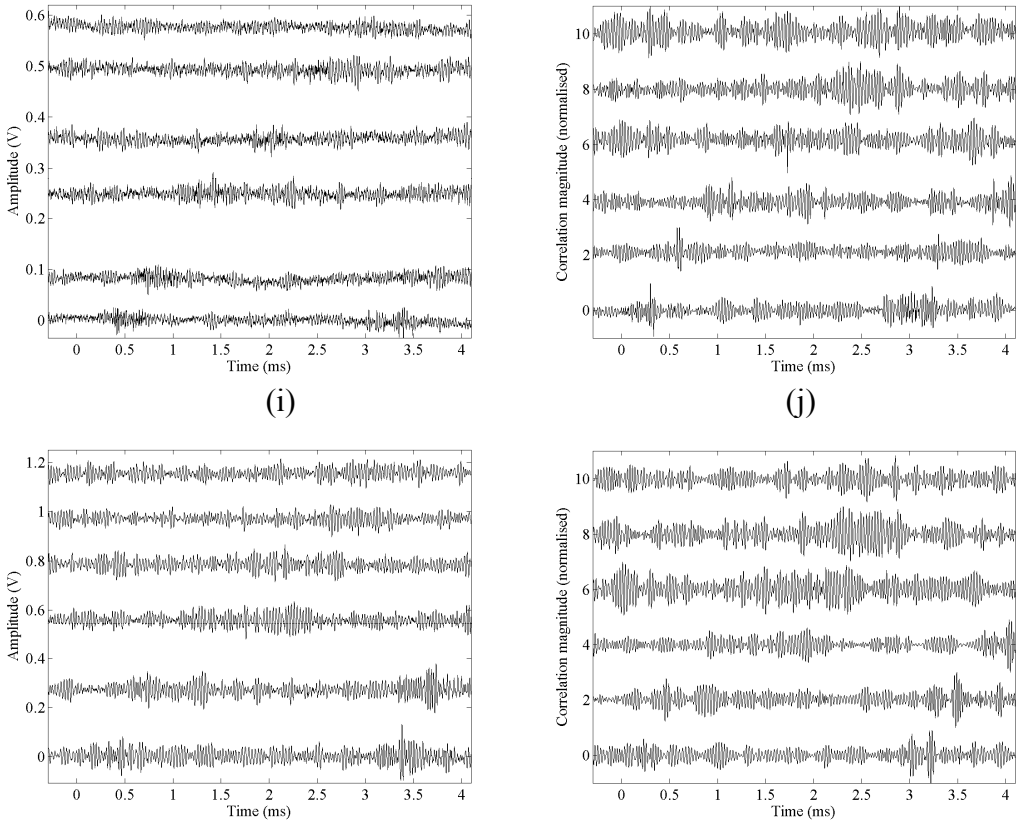

Figure 5.15. Series of figures depicting signals from wire-target echolocation tests using a 500μs multiharmonic chirp, consisting of a fundamental quadratic chirp with initial and terminal frequencies of 60kHz and 30kHz, respectively, plus the second and third harmonics of that signal: (a) subtracted and (b) normalised cross-correlation trace for 5mm cross-section target; (c) subtracted and (d) normalised cross-correlation trace for 3mm cross-section target; (e) subtracted and (f) normalised cross-correlation trace for 1mm cross-section target; (g) subtracted and (h) normalised cross-correlation trace for 600μm cross-section target; (i) subtracted and (j) normalised cross-correlation trace for 340μm cross-section target; (k) subtracted and (l) normalised cross-correlation trace for 250μm cross-section target.

5.6 Analysis of Returning Echo Strength

The strength of the returning echo is dependent on a number of factors: the geometry of the transducer; the characteristics of the echolocation signal; the diameter of the wire target; and the range travelled. These factors can be examined separately by interpreting sets of results to illustrate how each factor directly affects the returning echoes, independently of the other factors.

Each of these factors is examined in this fashion, with one exception. Since the transducer was constant, its characteristics are fixed throughout. However, given the varying frequency characteristics of the signals used, the dimensions of the transducer have an effect on the field structure emitted and hence the signal that impacts on the target, thereby affecting the return echo. As such, any effect the transducer geometry has is illustrated by examining the effect of signal on the return echo strength. The two effects are obviously linked, but given the constant transducer, its effect is implied through examination of the different echolocation signals.

It can be seen from the preceding results that not all targets at all ranges will provide a reliable estimation of the return echo amplitude, since for increasing range or smaller target diameter, the return echo is often not detectable. As such, averaged results are examined initially to ascertain which sets of results can be reliably used to obtain valid estimations of the effect each of these variables has on the return echo. To do this, it was initially assumed that all traces contained a return echo, the position of which was found using the largest reflector. These samples were then extracted from each trace for processing using a Matlab script. Conclusions are drawn later in the section, with regard being paid to the appropriate sets of data.

5.6.1 Absolute Values of Echo Sound Pressure Level

Initial examination of the return echoes focussed on the absolute peak value of SPL of each return echo. This was defined as peak SPL (pSPL) to enable comparison of the impulse-like *R. aegyptiacus* calls with the chirps and tonebursts of the other signals. As such, the maximum peak output voltage from the microphone was calculated and converted to dB and this value is the one used throughout this Chapter.

Initially return echo pressure was plotted against range and target diameter. These plots are displayed in Figure 5.16, with part (a) plotted against target range (with separate traces for each target diameter) and part (b) plotted against target diameter (with separate traces for each target range). Each of these traces is produced by

averaging the return echo strength across all echolocation calls; the effect of each echolocation call is covered in the following section.

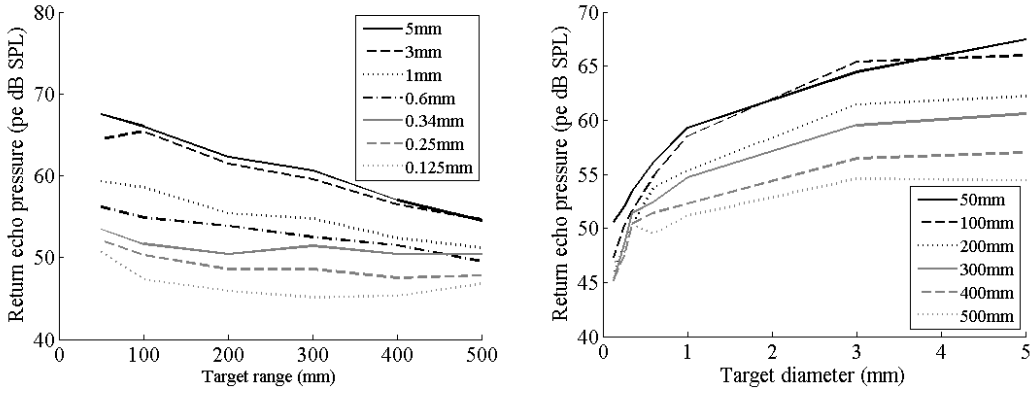

(a) (b)

Figure 5.16. Average peak pressure of return echo from each wire target diameter at each target range: (a) Echo pressure plotted against target range, with a separate trace for each diameter; (b) Echo pressure plotted against target diameter, with a separate trace for each range.

The results displayed in Figure 5.16 are instructive on a number of aspects of the echolocation experiments, not simply in the relationship of return echo against each independent variable. Inspection of Figure 5.16(a) indicates that, as expected, the average return echo pressure reduces as target range increases. However, it can also be seen that this relationship is far stronger for the larger-diameter targets. As the target diameter decreases, the curves flatten out across target range and also begin to overlap on the graph. This is due to the script assuming that an echo is present and estimating its SPL from the extracted samples, when in fact little more than noise is being measured for the smaller targets. This relationship is also illustrated in Table 5.1, which displays the change in recorded echo SPL between the 50mm and 500mm target range for each target diameter.

Target diameter (mm)	5	3	1.3	0.6	0.34	0.25	0.125
Maximum difference (dB)	13.0	10.8	8.12	6.65	3.1	4.5	5.5

Table 5.1. Maximum change in return echo pressure over the range 50mm-500mm, tabulated against target diameter. The maximum difference is the difference between the maximum and minimum (average) values across the target range as plotted in Figure 5.16(a).

A similar relationship can be seen in Figure 5.16(b), which demonstrates an expected reduction in echo strength with decreasing target diameter. In this case, however, the relationship is stronger for the shorter target ranges; as range increases, the curves flatten out. This is illustrated in Table 5.2, which displays the difference in return echo SPL between the 5mm and 125µm diameter wires, at each target range.

Target range (mm)	50	100	200	300	400	500
Maximum difference (dB)	16.9	18.7	16.4	15.5	11.7	7.8

Table 5.2. Maximum change in return echo pressure between the 5mm and 125µm diameter wires, tabulated against target range. The maximum difference is the difference between the maximum and minimum (average) values across the target diameters as plotted in Figure 5.16(b).

The correlation between reducing echo strength and either increasing target range or decreasing target diameter is affected by the extent to which the samples extracted for analysis actually contain a return signal that is distinguishable above the noise floor. It has previously been illustrated that most echolocation signals did not produce a detectable return echo from the smaller targets, and so the true relationship between target range and return echo is not illustrated by the results from the smaller-diameter targets. Similarly, as the target range increased, some experiments did not obtain a distinguishable target echo. As such, a similar effect occurs whereby increased range causes the true relationship between return echo strength and target diameter to be obscured. For these reasons, in the following sections, conclusions about the direct effect of both target range and diameter are drawn from reduced sets of results that can be relied upon as having distinct and measurable target echoes.

It should be borne in mind that the purpose of these experiments was three-fold. Firstly, the fundamental question of *how* bats detect targets with a cross section significantly smaller than the wavelength of their echolocation signals, was to be investigated. Secondly, the relationship between the various echolocation calls and their efficacy for detection of a given target was to be examined, with these findings linked to those found through wire-avoidance experiments in the literature. Thirdly, the relationship between echo amplitude and both target range, and target diameter,

was to be investigated. These aims are related, but require the data to be examined from different viewpoints, as detailed in the following sections.

5.6.2 Echo Strength as a Function of Echolocation Call and Target Range

To illustrate the effect that each echolocation call has on the strength of the return echo, it is difficult to display simply one graph with multiple traces, since the effect of both range and target diameter have to be considered. For this reason, two series of graphs are presented, demonstrating the effect of varying echolocation call against target range and against target diameter.

In Figure 5.17, four graphs are presented illustrating the variation in return echo SPL with target range, from (a) the 5mm diameter wire, (b) the 3mm wire, (c) the 1mm wire and (d) the 0.6mm wire. Only the results from the 5mm, 3mm and 1mm wire are used to draw conclusions regarding the performance of each signal with range, since smaller targets do not give reliable results across the 500mm target range. This is the reason for including plot (d) to illustrate why the results from smaller targets were not used to ascertain a relationship between target range and return echo strength: it can be seen that the link between target range and return echo SPL that is so evident in the first three plots is less so in the fourth one.

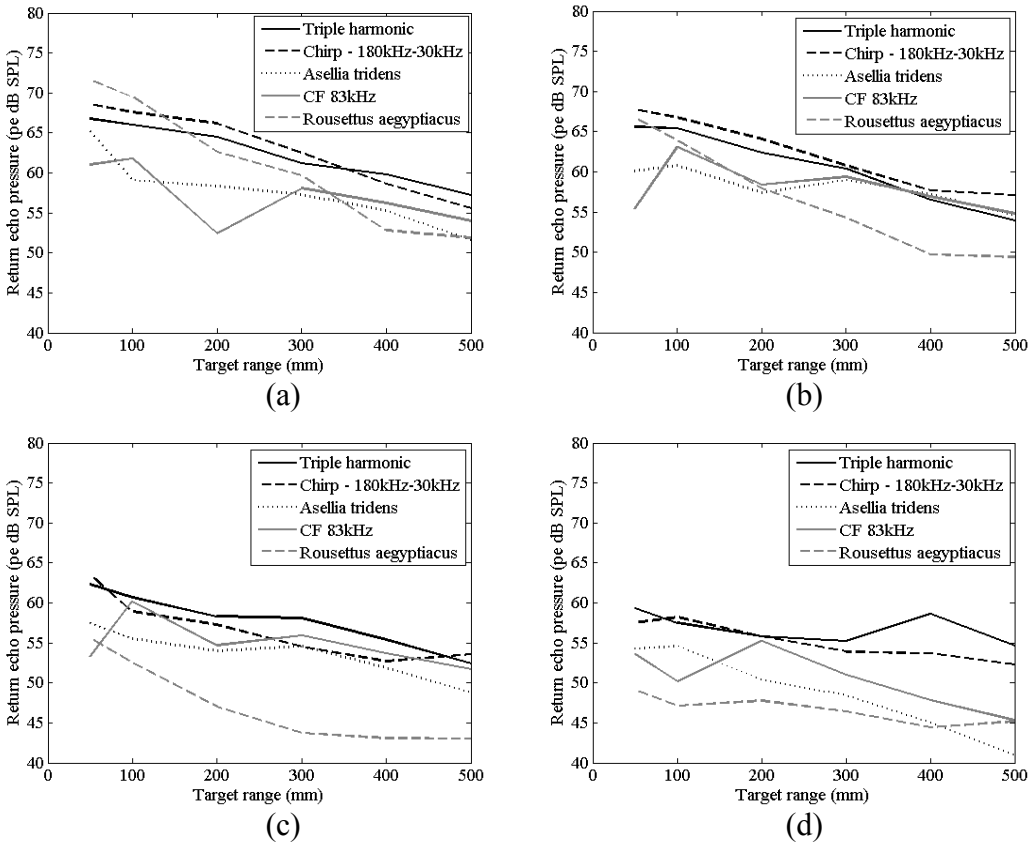

Figure 5.17. Graphs illustrating the effect of echolocation call on the return echo SPL with varying target range with (a) 5mm target; (b) 3mm target; (c) 1mm target; (d) 0.6mm target.

There are several interesting aspects illustrated by these plots. Firstly the 83kHz CF call, being a windowed toneburst of a single frequency, has a rather different relationship with target range than the other signals, with its maximum return amplitude generally occurring at 100mm – 200mm range. There are several possible reasons for this. Firstly, with a single frequency of excitation, the field structure will be composed of the familiar near-field and far-field as described in Chapter 4. As such, the target could be situated at a point in the near field where the pressure profile is close to a minimum. In fact, this is not the case – the far-field boundary for a 30mm diameter piston mode transducer occurs at an *axial distance* of approximately 54mm, and so the target range of 50mm is situated almost exactly at the maximum associated with the boundary. In fact it seems that this effect is a result of the way in which the experiment was configured. As previously described, the transducer was aligned with the target to produce the maximum return echo at a range of 300mm. Assuming that the largest return echo would be achieved for a

reflection that directs the central lobe of the emitted beam profile towards the microphone then the required angle of tilt, θ, is:

$$\theta = \tan^{-1}\left(\frac{d}{D}\right) \tag{5.5}$$

Where d is half the vertical separation between the transducer and microphone centres (25mm), and D is the target range. This provides the following results:

Target range (mm)	50	100	200	300	400	500
Angle of incidence	23.8°	12.4°	6.3°	4.2°	3.1°	2.5°

Table 5.3. Required transducer angle of incidence to direct maximum amplitude of return echo from target towards microphone at each target range.

As such, the transducer would be aligned with a tilt angle of approximately 4° to the horizontal plane. This means that there is an increasing mismatch between the optimal angle and the transducer angle as the range is reduced; at 50mm this angular 'error' is in excess of 19°. This is critical for the CF signal, since at 83kHz the emitted field is narrow, with a 3dB beamwidth of approximately ±4.5° at 50mm, meaning that the large offset in transducer angle is particularly damaging to the echo SPL. Hence the amplitude of the return echo of the CF signal is higher at 100mm-200mm than it is at 50mm, as the loss due to angular offset decreases. The *A. tridens* signal exhibits a similar, though less pronounced, effect. This signal has its CF portion at 115kHz followed by a 115kHz-80kHz sweep. As such, at 50mm, the target is in the near-field of the transducer at 115kHz, where it has a beamwidth of ±10°, more than twice that of the 83kHz signal at the same distance, thereby reducing the effect of the transducer angular offset. The wideband nature of the remaining FM chirps ensures that there are frequency components in the signal with sufficient beamwidth that this effect does not occur, whilst the low frequency components of the *R. aegyptiacus* call ensure a wide beamwidth (±24° 3dB beamwidth at 15kHz).

These effects notwithstanding, there are further interesting points to note. By examining a set of results restricted to only the 5mm, 3mm and 1mm diameter targets

(as pictured in Figure 5.17) then the reduction in performance of each signal with increasing target range can be ascertained. The call of *R. aegyptiacus* suffers the most significant reduction in echo amplitude with increasing target range of any of the signals used. Its echoes lose an average of over 16dB between the 50mm and 500mm over these three targets. As such, even though it produces the largest return echo of any signal tested (71.7dB for the 5mm target at 50mm range), with increasing range it becomes the least effective echolocation call. The remaining echolocation calls lose an average of 9dB – 10dB as indicated in Table 5.5. The reduction is calculated as an average of the reduction for each of the targets of 1mm diameter and above, over the 50mm-500mm range.

Echolocation Call	Triple harmonic	Chirp (180-30kHz)	*A. tridens*	CF 83kHz	*R. aegyptiacus*
Echo SPL reduction (dB) (50mm-500mm target range)	8.9	9.7	10.1	9.0	16.6

Table 5.4. Reduction in return echo SPL over the target range 50mm-500mm, tabulated against echolocation call. This figure is an average of the loss encountered with the 5mm, 3mm and 1mm cross-section targets.

The reason for the large reduction in return echo amplitude over this particular target range for *R. aegyptiacus* is its low frequency content, which means that the transducer operates with very little near field (at 15kHz the far-field boundary, *N*, is approximately 10mm axially distant from the face of the transducer) and so the transducer acts as a pseudo point source, with a reduction in signal strength of 6dB per doubling of range due to spherical spreading. This is not the case for the other signals used with higher frequency content (e.g. *N*=54mm and 75mm at 83kHz and 115kHz, respectively). It appears that up to 500mm, the additional attenuation of these higher frequency signals (2.7dBm^{-1} at 83kHz; 3.8dBm^{-1} at 115kHz) as opposed to at 15kHz (0.3dBm^{-1}) is more than compensated for by the beamshape. Of course as range increases this advantage would gradually be lost.

The remaining echolocation signals actually demonstrate quite similar performance with each target at each range, notwithstanding the close-range variability related to

the 83kHz CF call already detailed above. To remove this variability, data was examined over just the 200mm-500mm range, with the average return echo SPL varying by just 4.0dB between all four remaining calls.

It is interesting to note that the sonar industry has a standard method for dealing with the variation in signal strength at a target that occurs for short target ranges. Two proximity criteria are defined for piston-mode sources: that the target range must be greater than the maximum dimension (*MD*) of the transducer and also that it must be greater than (MD^2/λ). At ranges smaller than this, a correction factor is defined which is dependent on the target distance, *MD* (in this case, the transducer diameter) and the signal wavelength. This method, known as spherical wave correction (pp. 121-133, Bobber, 1988) provides an estimate of the correction required when these proximity criteria are breached. Although these corrections are necessarily narrowband (specified for a given wavelength-to-diameter ratio), it is instructive to examine figures specified by the correction curves (Fig 3.17, Bobber, 1988) at certain frequencies of interest. For example, at 83kHz (the frequency of the CF portion of the *R. ferrumequinum* call), the correction value is approximately 5dB, 1.25dB and 0.6dB at 50mm, 100mm and 200mm, respectively. As such, this would necessarily add 5dB to the loss figure quoted in Table 5.4 for the CF 83kHz call. On the other hand, the call of *R. aegyptiacus*, with its 15kHz peak, would be subjected to a correction of less than 1dB, even at the shortest distance. This illustrates that the loss quoted over distance for these two calls would be similar, within approximately 3dB.

5.6.3 Echo SPL as a Function of Echolocation Call and Target Diameter

The link between echolocation call and echo SPL with varying target diameter can be investigated via the second series of plots referred to in the previous section and depicted in Figure 5.18.

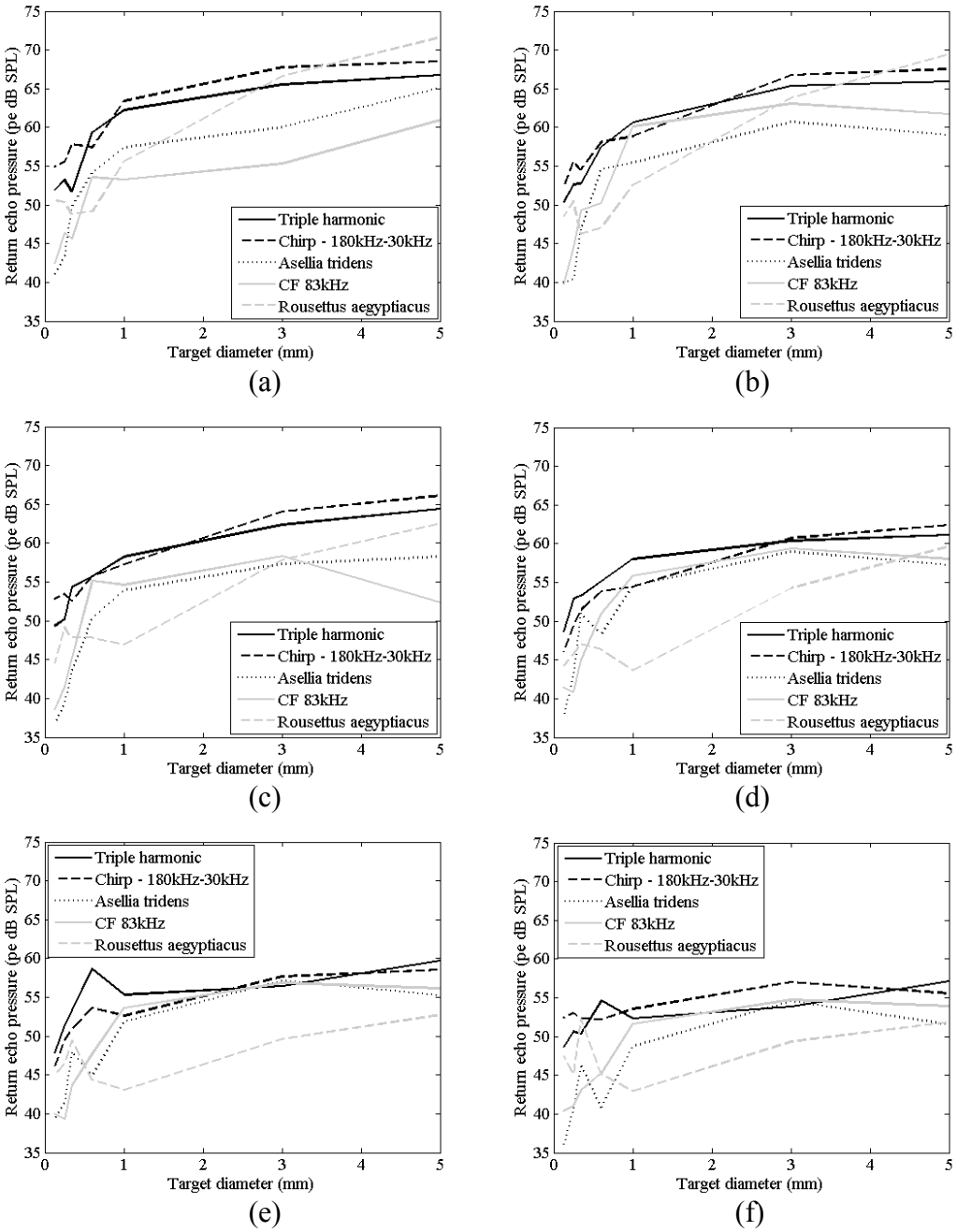

Figure 5.18. Graphs illustrating the effect of echolocation call on the return echo SPL with varying target diameter: (a) 50mm range; (b) 100mm range; (c) 200mm range; (d) 300mm range; (e) 400mm range; (f) 500mm range.

These plots indicate that as the target diameter decreases to 0.34mm and below, the expected reduction in return echo SPL does not hold true for all traces (e.g. the triple harmonic, 180kHz-30kHz chirp, and *R. aegyptiacus* traces in 5.18(a)). Again, this is due to the script extracting samples that do not contain an actual target echo. It can be seen from Figure 5.16(b), that on average the reduction in echo SPL does continue

across the range of target diameters. To investigate this link, the reduction in echo SPL between the 5mm target and each other target was calculated and is presented in Table 5.5:

Echolocation Call	Triple harmonic	Chirp (180kHz-30kHz)	*A. tridens*	CF 83kHz	*R. aegyptiacus*
Echo SPL reduction (dB) (5mm-3mm target)	1.9	1.3	2.4	2.6	4.4
Echo SPL reduction (dB) (5mm-1mm target)	4.7	6.7	5.4	4.4	13.9
Echo SPL reduction (dB) (5mm-0.6mm target)	6.6	8.4	9.5	8.9	15.9
Echo SPL reduction (dB) (5mm-0.34mm target)	9.9	10.1	10.2	11.3	16.1
Echo SPL reduction (dB) (5mm-0.25mm target)	10.9	11.0	13.4	13.6	16.1
Echo SPL reduction (dB) (5mm-0.125mm target)	13.1	12.7	17.2	16.7	16.9

Table 5.5. Reduction in return echo SPL between all target diameters, tabulated against echolocation call. This figure is an average of the loss encountered at each individual range up to 500mm.

It is interesting to note how the reduction in echo SPL behaves very differently for the call of *R. aegyptiacus* than it does for all other signals. With the *R. aegyptiacus* signal, 90% of the reduction occurs over the 5mm to 0.6mm targets, whereas for the other four the reduction is more continuous across all target diameters. As such, the reduction between the 5mm and 0.125mm targets is relatively similar for all echolocation signals. However, what this does indicate is that the call of *R. aegyptiacus* is not very effective for detecting targets of less than 1mm, whilst the other four signals are capable of detecting more of these smaller targets as indicated

by the gradual reduction in echo SPL (the relatively constant SPL of echoes from the 0.6mm to 0.125mm targets for *R. aegyptiacus* indicates that the signal being measured is essentially noise).

As with target range, the call of *R. aegyptiacus* again suffers the most rapid reduction in return echo SPL with reducing target diameter. However, plotted against these target diameters, the reduction is particularly marked and rapidly makes this call the least effective for detecting small-diameter targets. Again this is due to its low frequency components. With little energy above 40kHz, corresponding to a wavelength of approximately 8.6mm, all the targets actually have a cross-section smaller than the minimum wavelength component in the call. This is further exacerbated by the fact that the *peak* energy occurs at approximately 15kHz, or $\lambda \approx 23$mm. This compares with wavelengths of approximately 4.1mm at 83kHz, approximately 3.0mm at 115kHz and approximately 2.1mm at 160kHz, which is the approximate maximum frequency of the artificial FM signals.

In terms of the most effective signals for detecting sub-mm targets, it can be seen from the preceding sections that there is some variability between the remaining four signals. Whilst the call of *A. tridens* generates distinct echoes from the 340μm diameter wire, and the 83kHz CF call even generates some from the 250μm wire, return echoes are difficult to perceive from the 340μm target using the FM chirps. The reasons for this reduction in performance of the FM chirps in investigated at the end of section 5.7.2.

5.6.4 Comparing Experimental Results with Wire Avoidance Experiments

It is interesting to look at the results obtained from the wire detection experiments in the light of the published wire-avoidance tasks referenced earlier. Waters and Vollrath (2003) stated that *R. aegyptiacus* was capable of avoiding 6mm wires, but that with wires of 1mm diameter caused the bats more problems. It was reported that the bats took “evasive action” when approaching to within 500mm of the narrower wires, but that they would strike these wires significantly more often than those of the larger diameter. This suggests that the bat was capable of detecting the wires, though not able to locate them with sufficient accuracy to avoid them. Alternatively,

this information is possibly decoded too late for the evasive manoeuvres to be successful. The results collected during the wire detection experiments correlate reasonably well with these findings. The artificial *R. aegyptiacus* calls have been demonstrated to be capable of detecting the 5mm and 3mm wires across the 500mm target range. However, the 1mm wire resulted in detection at a maximum of 100mm to 200mm, with any targets smaller than that being completely undetectable by the experimental equipment. Examination of the SPL of the returning echoes also illustrates significant reduction between the 5mm and 1mm target. The study by Waters and Vollrath only presented two diameters of wires (6mm and 1.3mm) to the bats, and so it is difficult to say where the threshold of detection / avoidance lies for this species, in comparison with the data gathered in this investigation.

The other two species that have been studied with regards to wire avoidance skills were *A. tridens* (Gustafson and Schnitzler, 1979), and *R. ferrumequinum* (Mogdans *et al.*, 1988). Each of these species was subjected to more rigorous testing, using a larger range of wire diameters. The findings were similar, with *A. tridens* capable of avoiding vertical wires of 65µm in diameter, though not 50µm, whilst *R. ferrumequinum* was found to be capable of avoiding both vertical and horizontal wires of 60µm. *R. ferrumequinum* was not presented with any smaller targets, though at 60µm its performance had reduced to approximately 75%, from above 90% for wires of 200µm in diameter. As such, the established trend showed distinct similarity to that of *A. tridens*. In comparison with the shortest wavelength of their calls, *A. tridens* and *R. ferrumequinum* detected and avoided targets with a cross section of approximately λ/46 and λ/69, respectively. Since the experiments performed in this investigation were incapable of detecting reflections from such objects, it is not possible to directly measure the SPL of echoes from these targets. However, employing curve fitting techniques to the results obtained here can provide estimated values.

Curve fitting was carried out using a curve-fitting toolbox available for Matlab (http://www.mathworks.com/matlabcentral/fileexchange/10176-ezyfit-2-40), with Figure 5.19 showing the curves generated for two series of results. Since the CF and *A. tridens* call were the signals of interest, these were the only ones used for curve

fitting. Furthermore, since these signals generated echoes from smaller target diameters, it was considered that these would provide the most accurate estimation of return echo from a 65μm target. In Figures 5.19(a) and (b), the process is demonstrated using the results from the *A. tridens* call at 200mm range, with echo SPL limited to targets of 340μm and above since these echoes were reliably detected. A logarithmic curve-fitting law is used, which fits a curve to the data in the form of equation 5.6:

$$y(x) = a\log_{10}(bx) \tag{5.6}$$

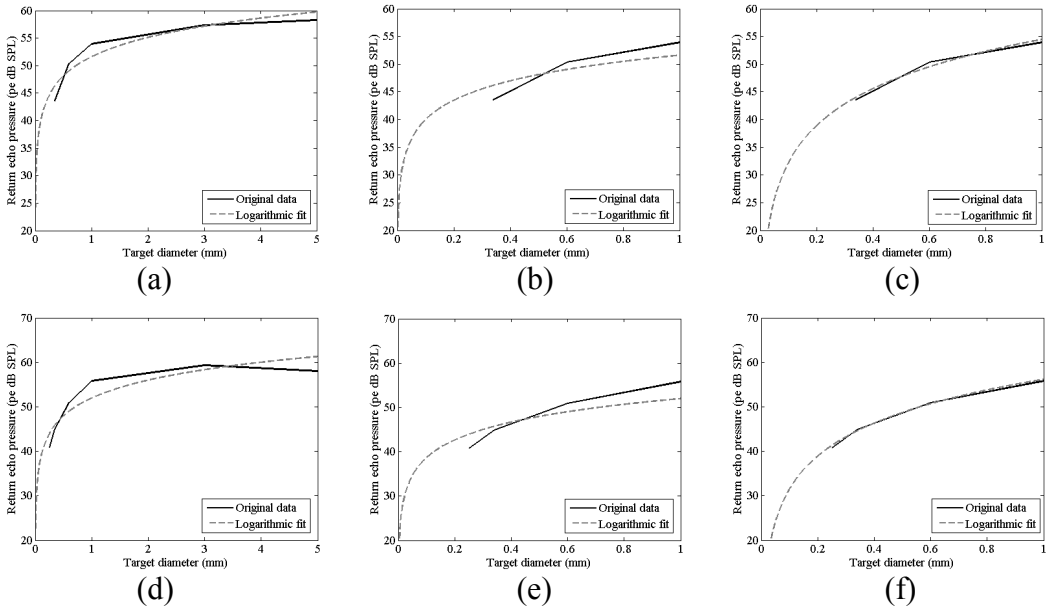

Figure 5.19. Plots demonstrating the logarithmic curve-fitting process for estimation of the echo SPL from a 65μm diameter wire. Results from A. tridens: (a) at 300mm target range; (b) expanded version depicting only sub-mm target diameters; (c) curve fitting to results generated only from sub-mm diameter targets. Results for 83kHz CF signal: (d) at 300mm target range; (e) expanded version depicting only sub-mm target diameters; (f) curve fitting to results generated only from sub-mm diameter targets.

This process is repeated in Figure 5.19(d) and (e) for the echo SPL values obtained using the 83kHz CF call that is representative of *R. ferrumequinum*. With this signal, the curve was fitted to data obtained from targets of 250μm and above, again because these echoes were reliably detected. Using this procedure, the echo SPL from a 65μm target was estimated to be 37.7dB for *A. tridens* and 40.9dB for *R. ferrumequinum*. Visual examination of these curves and their fit with the data, particularly in the sub-

mm target range of plots (b) and (e), tended to suggest that the echo SPL from a 65µm target may be overestimated using this procedure. As such, a more accurate estimation of the return echo from a 65µm target may be obtained by curve-fitting to a subset of the data points for the smaller diameter targets. Figure 5.19(c) and (f) illustrate this process for each echolocation signal, but only using those data points for target diameters of 1mm and less. For *A. tridens* this indicated an echo of 28.1dB for a 65µm target, and 28.8dB for *R. ferrumequinum*. Examination of Figures 4.19(c) and (f) indicates that this method does generate a closer match to the available data, and so it is these results that have been used. To have significance, these calculated values were then referenced to the echo SPL for a 1mm target, so that a figure was calculated for the additional reduction in echo SPL from the reliable figure obtained for a 1mm target. An average value was then calculated, which estimated the additional reduction to be 22.0dB for the *A. tridens* call and 24.6dB for *R. ferrumequinum*. Using this averaged data produces the following estimated figures for the return SPL of an echo from a 65µm target at 50mm to 500mm target range.

Target range (mm)	50	100	200	300	400	500
Echo SPL (dB) (*A. tridens*)	35.5	33.5	32.0	32.6	29.9	26.8
Echo SPL (dB) (CF 83kHz)	28.7	35.6	30.1	31.3	29.1	27.1

Table 5.6. Predicted return echo SPL from a 65µm cross-section wire at each range using either the CF-FM call of *A. tridens* or a CF 83kHz call.

To relate these results to the situation of an echolocating bat, it is useful to think about these figures both in terms of the dynamic range between emitted and reflected signals, as well as the absolute amplitudes as displayed in Table 5.6. Since the emitted calls were set to 100dB SPL at 100mm from the source, the dynamic range of these signals is approximately 65dB – 75dB. This is a considerable challenge to overcome, but comparable to that which might be expected from prey insects; one study by Waters *et al.* (1995) measured the target strength of prey insects as varying from approximately -35dB for the larger moths, to -70dB for small flies such as midges. The dynamic range challenge is undoubtedly aided by the "automatic gain control" (e.g. Kick and Simmons, 1984; Simmons *et al.*, 1992) that bats exhibit

whereby they contract the muscles of their inner ear to self-deafen as the emit echolocation sounds. This process reduces the bat's sensitivity to its emitted call, thereby similarly reducing the dynamic range of the signals with which its hearing system must cope. However, the corollary of this process is that the bat necessarily reduces its sensitivity to echoes that arrive before its hearing has been fully restored. Since the bat's sensitivity is gradually restored as the muscles relax post-emission, the sensitivity follows a curve that can be plotted against time or range. Kick and Simmons (1984) indicated that at a target range of 0.2m, the detection threshold of *Eptesicus fuscus* was approximately 25dB worse than at 1m. Assuming this figure is added to the 'quiet threshold' found during laboratory experiments, then the post-emission detection threshold at the 50mm-500mm target range examined during the echolocation experiments begins to approach the estimated SPL of an echo from a 65µm wire expressed in Table 5.6 of 27dB – 35dB pe SPL. Furthermore, an echolocating bat in flight is subjected to additional environmental noise (including the wind noise created by the bat itself as it moves through the air) that is not the case in static experimental conditions in a quiet laboratory. As such, it is difficult to estimate the required SPL for detection by a flying echolocating bat; Surlykke and Kalko (2008) estimated this to be 20dB SPL, though there appears to be no scientific validation provided for this figure. Certainly some additional margin would have to be accounted for, and as such the figures of Table 5.6 seem to be a reasonable estimate of the detection threshold of a flying echolocating bat, operating at a range where its detection threshold is necessarily increased due to its gain control process. It is also interesting to note that the logarithmic curves fitted to the sub-mm target data estimate that the reduction in SPL between a 65µm and 50µm wire for the call of *A. tridens* is just 1.6dB on average, however this is enough for its performance to fall from 85% successful (no collision) flights for 65µm wires, to less than 50% successful flights for 50µm wires.

5.7 The Effect of Averaging and Noise

As previously stated, all the echolocation experimental results presented thus far were obtained using time-based averaging, which was done by the Agilent Infiniium Oscilloscope. Each result was averaged 256 times, and since noise is reduced by the

square root of the number of averages, this would imply a reduction by a factor of 16, or 24dB, over the raw figure. This amount of averaging was selected through empirical trials as a compromise between the required amount of noise reduction, and the length of time the process took. This was necessary to produce traces suitable for reproduction to demonstrate the experimental results, and also to allow accurate measurement of the amplitude of the returning signals (as opposed to signal plus noise). However, bats obviously do not use any similar techniques during their echolocation process. Indeed, they have to be capable of detecting returning echoes buried within environmental noise in order to survive. Given this, it is interesting to investigate the raw noise level and the effect that averaging has on this. Furthermore, one method potentially used by bats to enable signals to be extracted from noise will be investigated with respect to each of the echolocation signals used in these experiments.

5.7.1 Averaging and Noise Level

To illustrate the effect of averaging on the signal recorded from the B&K microphone system, a series of traces was captured of the background noise in the Perspex case, as depicted in Figure 5.20. These traces show the underlying noise signal recorded from the microphone with (top-to-bottom) 0, 4, 16, 64 and 256 averages, respectively. The noise level for each of these traces is indicated in Table 5.7, with a calculation of the reduction in noise with each level of averaging, expressed as both a ratio and in dB. Noise level is defined as the root-mean-square (RMS) of the measured signal and so was calculated as the standard deviation of each trace, since these are numerically identical. As such, the noise SPL quoted in this table is the RMS value whereas all other values quoted in this Chapter are peak values. Hence, when signal-to-noise ratio (SNR) is investigated in the following section, the ratio is provided in terms of *peak* SNR.

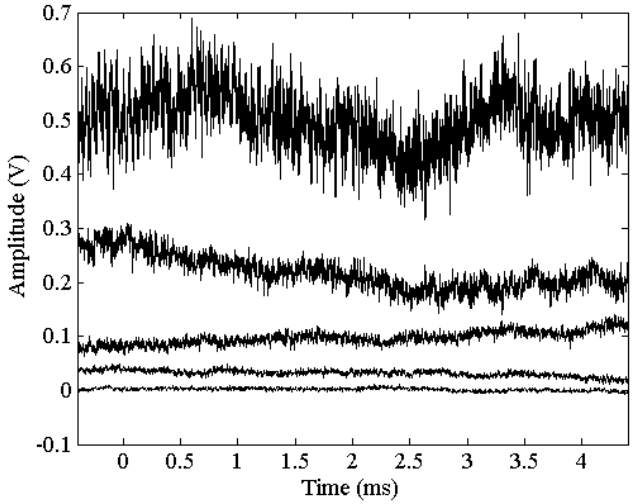

Figure 5.20. The effect of averaging on the noise level measured from the B&K microphone system, using the Agilent Infiniium digital oscilloscope. The traces in this figure were recorded with (top-to-bottom) 0, 4, 16, 64 and 256 averages, respectively.

Number of Averages	0	4	16	64	256
Noise level (mV)	53.9	32.6	13.3	6.2	2.8
Noise reduction (ratio)	n/a	1.7	4.1	8.7	19.3
Theoretical noise reduction	n/a	2	4	8	16
Noise level (dB SPL)	58.6	54.3	46.5	39.8	32.9
Noise reduction (dB)	n/a	4.3	12.1	18.8	25.7
Theoretical noise reduction	n/a	6.0	12.0	18.1	24.1

Table 5.7. Predicted return echo SPL from a 65μm cross-section wire at each range using either the CF-FM call of *A. tridens* or a CF 83kHz call.

It can be seen from these figures that the theoretical and measured reduction in noise levels correlate well, with the 256 averages used as standard throughout the previous section providing approximately 25dB of noise reduction.

5.7.2 The Effect of Averaging on Target Detection

Each of the experimental echolocation traces illustrated thus far have been captured from the oscilloscope using 256 averages. However, a series of tests were also carried out, varying the number of averages employed, to investigate the effect that had on the effectiveness of detecting the wire targets. These results are evaluated in this section. The tests were performed in the same fashion as those presented in section 5.5, but at a single target range of 300mm with the signals captured using

256, 64, 16, 4 and 0 averages. Cross correlation was then used to ascertain at what levels of SNR this process is effective for extracting the return echo from noise, and also to see which echolocation signals are most suited to this process. To prevent repetition, results are presented for target diameters that are at the detection limit for each echolocation signal at the range of 300mm.

Figure 5.21 illustrates the traces recorded using the reproduced call of *R. aegyptiacus* with varying averaging for the 1mm diameter wire target. It can be seen in both the (subtracted) time domain trace, and in the cross correlation, that the echo can be detected in all cases except that using no averaging. By examining the trace recorded with 256 averages, the peak echo amplitude can be measured to be 45.1mV for the 3mm target, whilst for the 1mm target an echo of 9.2mV can just be discerned. The noise level in each trace (RMS) and the resulting peak SNR for each of these targets with varying averages is shown in Table 5.8.

	Number of Averages	0	4	16	64	256
3mm target	Noise level (mV)	60.7	21.1	12.6	7.3	5.2
	Peak SNR (dB)	-2.6	6.5	11.1	15.7	18.6
1mm target	Noise level (mV)	44.7	21.4	9.3	8.9	5.7
	Peak SNR (dB)	-13.7	-7.3	-0.1	0.3	4.2

Table 5.8. Measured noise level and peak SNR for return echoes from the 3mm and 1mm wire targets, with varying levels of averaging using a reproduced *R. aegyptiacus* signal.

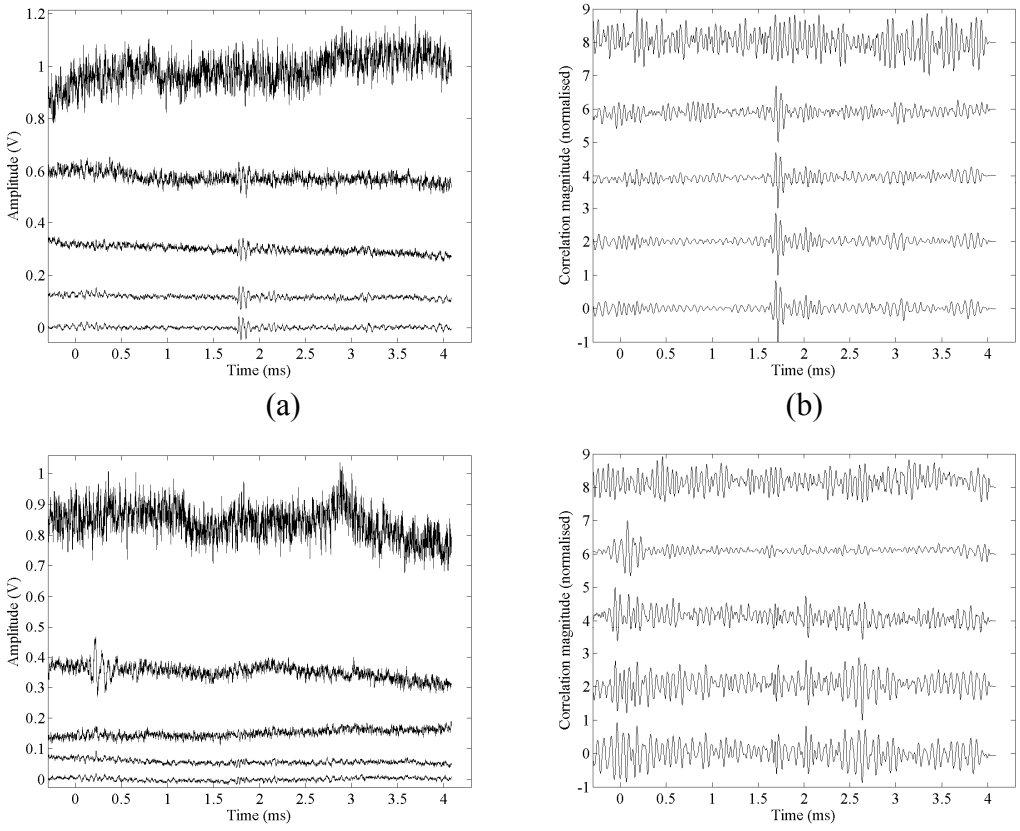

Figure 5.21. Images depicting signals from wire-target echolocation tests using a reproduced call from *R. aegyptiacus*: (a) subtracted and (b) normalised cross-correlation trace for 3mm cross-section target at 300mm; (c) subtracted and (d) normalised cross-correlation trace for 1mm cross-section target at 300mm. The traces in each image were recorded with (top-to-bottom) 0, 4, 16, 64 and 256 averages, respectively.

It can be seen from comparing the results illustrated in Figure 5.21 with the values in Table 5.8, that with these levels of SNR and this particular echolocation signal, there is very little appreciable advantage in using cross correlation; it does not extract the echo from noise in any traces where the echo cannot already be detected in the raw (subtracted) data. It will be illustrated during the rest of this section that this is not the case for the other echolocation signals used.

The results obtained using the 83kHz CF signal are illustrated in Figure 5.22, with parts (a) and (b) relating to the 600µm target, and (c) and (d), 340µm. Immediately, the usefulness of cross correlation becomes apparent as it is capable of extracting the reflected signal from the noise for the 600µm target with zero averages, and the 340µm target with 4 or more averages. With the 600µm target, its peak return

amplitude is 52.0mV, while it is 17.2mV for the 340µm target. The noise level and estimated peak SNR are shown in Table 5.9.

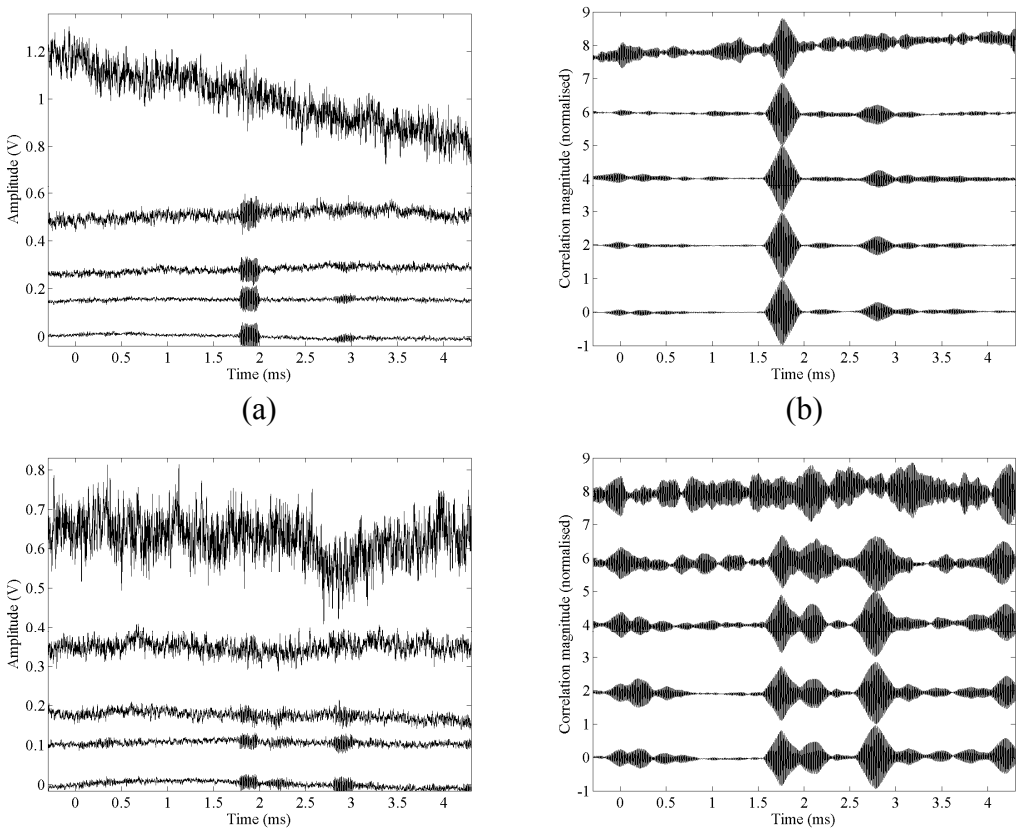

Figure 5.22. Series of figures depicting signals from wire-target echolocation tests using a CF 83kHz signal: (a) subtracted and (b) normalised cross-correlation trace for 600µm cross-section target at 300mm; (c) subtracted and (d) normalised cross-correlation trace for 340µm cross-section target at 300mm. The traces in each image were recorded with (top-to-bottom) 0, 4, 16, 64 and 256 averages, respectively.

	Number of Averages	0	4	16	64	256
600µm target	Noise level (mV)	64.8	18.1	10.1	5.7	4.5
	Peak SNR (dB)	0.8	2.9	5.2	9.1	11.5
340µm target	Noise level (mV)	45.4	15.4	8.8	7.1	6.2
	Peak SNR (dB)	0.4	1.1	1.9	2.4	2.8

Table 5.9. Measured noise level and peak SNR for return echoes from the 600µm and 340µm wire targets, with varying levels of averaging using the CF 83kHz signal.

It can be seen by cross-referencing Table 5.8 with Figure 5.22, that cross correlation in this case is capable of extracting the echo from the noise for peak SNR levels of less than 1dB, which is approaching a SNR ratio of unity.

The results obtained using the reproduced echolocation call of *A.* tridens are illustrated in Figure 5.23, with parts (a) and (b) relating to the 340µm target, and (c) and (d), 250µm. With the 340µm target, its peak return amplitude is 41.1mV, while it is 24.1mV for the 250µm target. The noise level and estimated peak SNR are shown in Table 5.10.

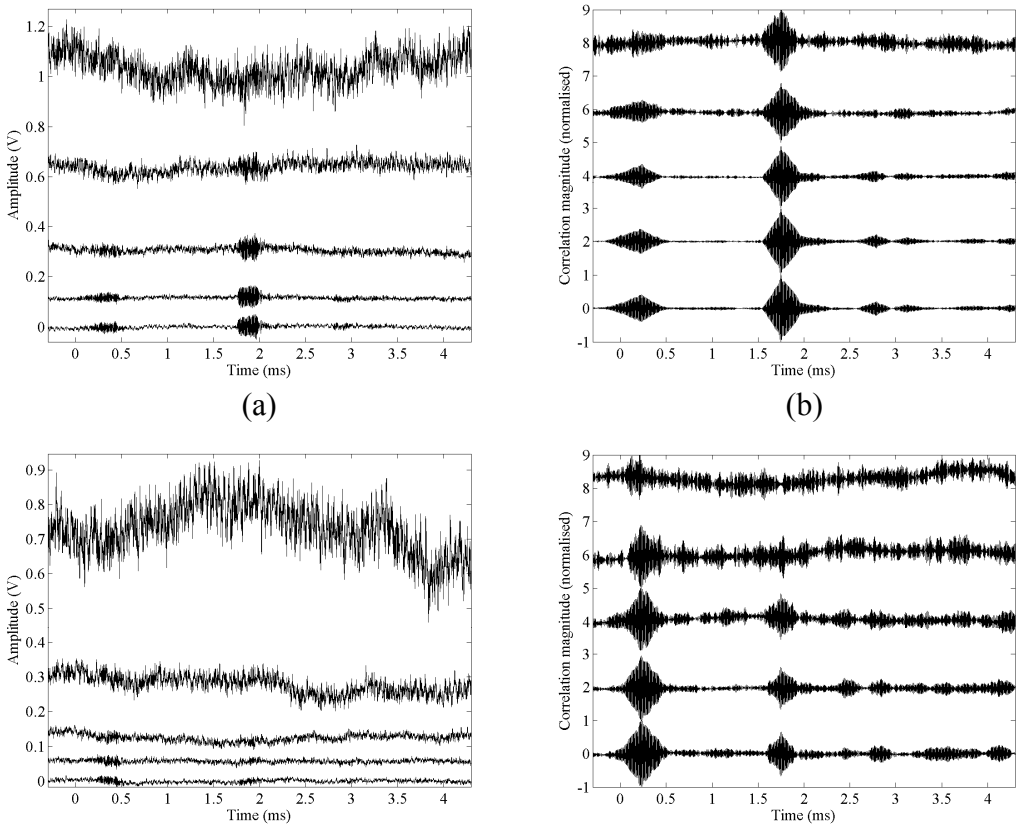

Figure 5.23. Series of figures depicting signals from wire-target echolocation tests using a reproduced call from *A. tridens*: (a) subtracted and (b) normalised cross-correlation trace for 340µm cross-section target at 300mm; (c) subtracted and (d) normalised cross-correlation trace for 250µm cross-section target at 300mm. The traces in each image were recorded with (top-to-bottom) 0, 4, 16, 64 and 256 averages, respectively.

	Number of Averages	0	4	16	64	256
340µm target	Noise level (mV)	57.0	19.8	10.5	5.4	5.9
	Peak SNR (dB)	-2.8	6.3	11.9	17.7	16.8
250µm target	Noise level (mV)	57.7	21.4	10.0	5.8	5.3
	Peak SNR (dB)	-7.6	1.0	7.6	12.4	13.1

Table 5.10. Measured noise level and peak SNR for return echoes from the 600µm and 340µm wire targets, with varying levels of averaging using the CF 83kHz signal.

As with the 83kHz CF signal, cross correlation of the *A. tridens* echolocation call with the recorded echoes plus noise allows signals buried in noise to be extracted, in this case even extracting one signal with a peak amplitude smaller than the RMS noise value (340µm target with 0 averages).

The results obtained using the quadratic FM 180kHz-30kHz chirp are illustrated in Figure 5.24, with parts (a) and (b) relating to the 1mm target, and (c) and (d), 600µm. With the 1mm target, its peak return amplitude is 68.2mV, while it is 43.1mV for the 600µm target. The noise level and estimated peak SNR are shown in Table 5.11.

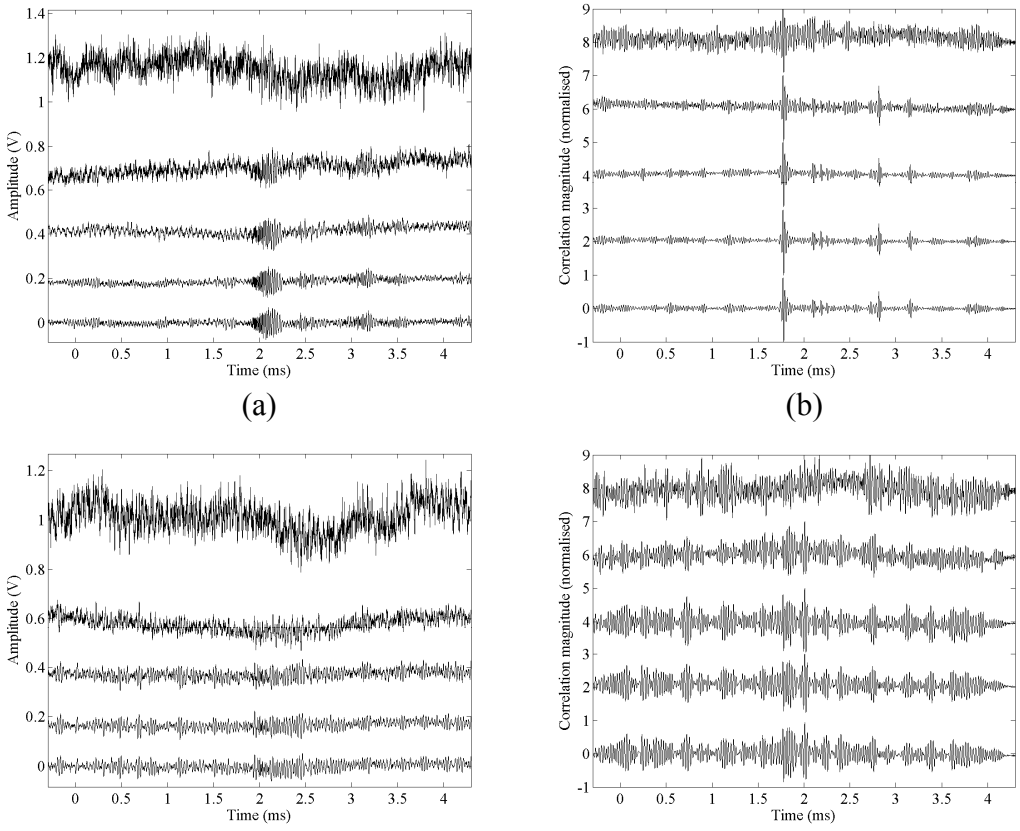

Figure 5.24. Series of figures depicting signals from wire-target echolocation tests using a quadratic FM chirp with initial and terminal frequencies of 180kHz and 30kHz, respectively: (a) subtracted and (b) normalised cross-correlation trace for 1mm cross-section target at 300mm; (c) subtracted and (d) normalised cross-correlation trace for 600µm cross-section target at 300mm. The traces in each image were recorded with (top-to-bottom) 0, 4, 16, 64 and 256 averages, respectively.

	Number of Averages	0	4	16	64	256
1mm target	Noise level (mV)	58.0	34.6	15.7	9.6	9.6
	Peak SNR (dB)	1.4	5.9	12.8	17.0	17.0
600µm target	Noise level (mV)	62.7	33.3	18.0	16.3	16.1
	Peak SNR (dB)	-3.2	2.2	7.5	8.5	8.5

Table 5.11. Measured noise level and peak SNR for return echoes from the 1mm and 600µm wire targets, with varying levels of averaging using the quadratic 180kHz-30kHz FM chirp.

Figure 5.25 displays the results from the multi-harmonic chirp, with (a) and (b) relating to the 1mm target, and (c) and (d), 600µm. With the 1mm target, its peak return amplitude is 91.4mV, and 42.0mV for the 600µm target. The noise level and estimated peak SNR are in Table 5.12.

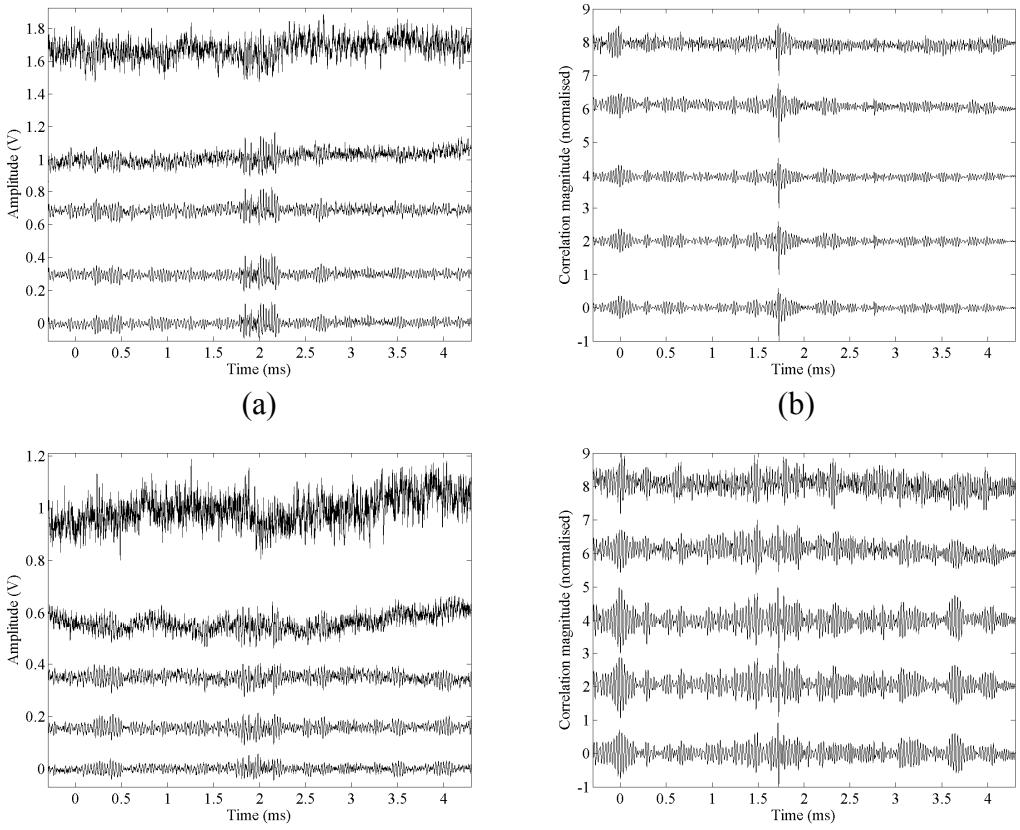

Figure 5.25. Series of figures depicting signals from wire-target echolocation tests using a multiharmonic FM chirp: (a) subtracted and (b) normalised cross-correlation trace for 1mm cross-section target at 300mm; (c) subtracted and (d) normalised cross-correlation trace for 600µm cross-section target at 300mm. The traces in each image were recorded with (top-to-bottom) 0, 4, 16, 64 and 256 averages, respectively.

	Number of Averages	0	4	16	64	256
1mm target	Noise level (mV)	60.1	38.8	25.5	18.2	17.5
	Peak SNR (dB)	3.6	7.4	11.1	14.0	14.3
600µm target	Noise level (mV)	58.6	36.1	17.2	14.3	11.2
	Peak SNR (dB)	-2.9	1.3	7.7	9.3	11.5

Table 5.12. Measured noise level and peak SNR for return echoes from the 1mm and 600µm wire targets, with varying levels of averaging using the multi-harmonic quadratic FM chirp.

It is interesting to note that the cross correlation technique appears to be somewhat less effective at extracting the signal from noise with the wideband chirp signals, than it is with either the 83kHz CF signal or the *A. tridens* call. For example, even with a measured SNR of 7dB-9dB, the cross correlation function struggles to

distinctly extract the echo of either the single-harmonic or multi-harmonic chirp from the 600μm target with 16 or 64 averages. Even examining the time traces by eye, it would seem that these echoes are reasonably easy to locate. Certainly in comparison with the corresponding echoes in the 83kHz CF signal or the *A. tridens* call, the echoes from the FM chirps are more easily discerned visually; however, echoes from either the CF or *A.* tridens call were extracted that had a SNR of less than 1dB.

The reason for this apparent reduction in target detection capability using the cross-correlation function only becomes evident when the structure and frequency content of the signals themselves are examined. As an example, Figure 5.26 illustrates a close-up image of the echoes detected from the 1mm and 600μm targets, and their corresponding frequency spectra, calculated via a FFT. Figures 5.26(a) and (b) correspond to the signals obtained from the 1mm target, whilst (c) and (d) were captured from the 600μm target. It is apparent that, although the amplitude is reduced significantly between the two targets, the form of the echo also undergoes significant variation. In (a) the return echo can be seen to sweep downwards in frequency over the 300μs duration of the call, with the FFT magnitude illustrating the presence of a continuous set of frequency components between approximately 30kHz and 140kHz. In comparison, the echo returning from the 600μm target is far more distorted, as seen in (c) and (d). In the time domain (c) it is difficult to discern the frequency modulation so evident in (a), whilst the echo also seems to be elongated in duration. Furthermore, the FFT plot (d) illustrates significant missing / reduced components, especially amongst the higher frequencies. This indicates that it is the altered nature of the return echo that leads to the reduced capability of the correlation process to extract it from noise, rather than simply being a straight function of the measurable SNR itself. Examination of the results for the triple-harmonic signal demonstrated similar effects with decrease of target diameter, whereas the less wideband CF and *A. tridens* signals demonstrate no such effects, meaning that with these signals the capability to extract the return echo from noise using correlation is related directly to the measurable SNR as illustrated earlier in this section.

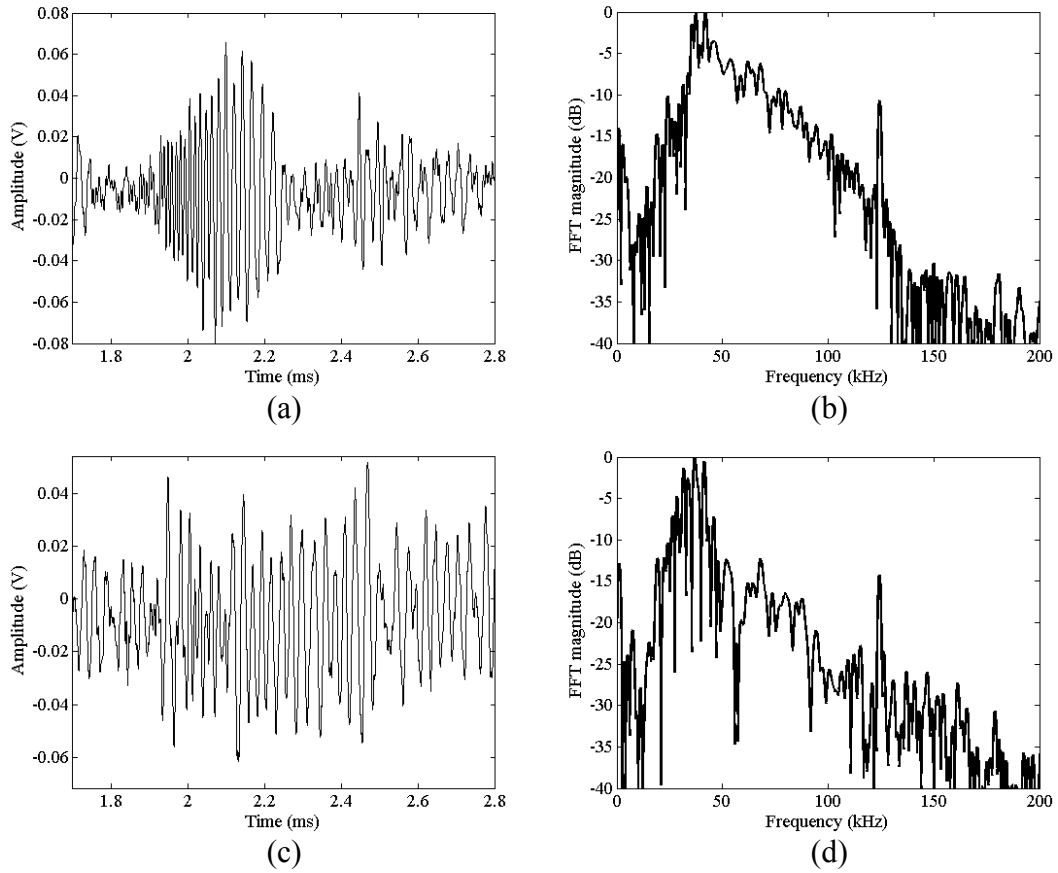

Figure 5.26. Time and frequency domain representations of the detected echo at 300mm target range using the 180kHz-30kHz FM chirp from: a 1mm target (a) and (b); and a 600µm target (c) and (d).

5.8 Conclusions

In this Chapter, the electrostatic transducers described in Chapter 4 have been demonstrated for accurate reproduction of wideband bioacoustic signals and biologically-inspired FM chirps. This capability can enable a variety of applications such as investigation of the echolocation process using accurate bat sonar signals as demonstrated in detail in this Chapter, or ranging with the advantages that can be gleaned from wideband signals. Indeed, these electrostatic transducers have already been demonstrated in a ranging application by a colleague, where the availability of a wideband FM chirp allows both an accurate and precise measurement of time delay to be made (Jackson *et al.,* in review). The wideband nature of the signal allows an extension of the multi-frequency (e.g. Tsai *et al*., 2006; Huang and Huang, 2009) method for ranging to be extended to allow a phase measurement at each frequency component across a wide bandwidth. This allowed an average time delay to be

calculated over a large number of spectral components to generate an accurate (sub-mm) and more repeatable (sub-30μm) result. Furthermore, since the accuracy does not rely on time-domain measurement, it is less reliant on high sampling frequency, allowing improved computation speed and application in lower-specification or mobile platforms.

It has been demonstrated that, despite the non-uniform nature of the frequency response of the transducers (or, indeed, the combined system of the transducer, air channel and microphone) the use of pre-equalisation based on the impulse response of the system was very effective for replicating a variety of signals occupying the frequency spectrum that bats use. These signals ranged from the impulse-like calls of *R. aegyptiacus* occupying the 10kHz – 40kHz region, through the CF-FM calls of *A. tridens* in the 100kHz region, to wideband FM chirps extending over a decade of frequency, from 30kHz – 300kHz. This demonstrated both the effectiveness of the technique as well as the linearity of the transducers themselves. Further proof of the technique's usefulness was illustrated through calculation of the cross-correlation function of the original signal, with the one transmitted using an electrostatic transducer and recorded from the microphone. Without use of the inversion process, the correlation function contained sidelobes of substantial magnitude that could cause confusion in a time-delay or ranging algorithm, especially in the presence of noise. With the inversion process, the cross-correlation function was almost identical to the auto-correlation function of the original signal itself. Coupled with their piston-like behaviour, these characteristics provide a powerful tool for investigating wideband ultrasonic signals in air.

One particular aim of this Chapter was to investigate the effectiveness of a variety of echolocation signals, especially the so-called "rudimentary" (Koay *et al.,* 1998) clicks of *R. aegyptiacus* in comparison with the CF or CF/FM calls of microchiropterans, or bio-inspired FM chirps. This was done by using these signals in a replication of the wire-avoidance tasks detailed in the literature. The results presented here demonstrate that the echolocation performance of the calls of *R. aegyptiacus* is poorer for the detection of small cross-section targets. Although, these calls generated the highest amplitude echo of across all the experiments (from the

largest 5mm diameter wire) this signal was subjected to by far the greatest reduction in echo amplitude for increasing range or decreasing target diameter.

Amongst the other echolocation signals used, the performance of the CF/FM *A. tridens*, and CF-approximated call of *R. ferrumequinum* were the most effective for detecting echoes from the smaller target diameters. This result, in comparison with that from the *R. aegyptiacus* call agreed with results documented in the literature for the wire avoidance capabilities of these species (Gustafson and Schnitzler, 1979; Mogdans *et al*., 1988; Waters and Vollrath, 2003). However, the results for *A. tridens* and *R. ferrumequinum* in these wire-avoidance tasks indicated the capability to detect and avoid targets with a cross section as low as λ/70, or 60μm. This seems to be a quite astonishing feat, and warranted further investigation with respect to the measured return echoes from the wire detection experiments. Further analysis of the echo amplitude returning from these smaller-diameter wires was performed using curve-fitting techniques. This indicated a return echo from the smallest wires detectable by these species in the literature of approximately 30dB pe SPL. Unfortunately, detection thresholds for bats only exist from static laboratory tests, and indicate a passive detection threshold (i.e. the sound is played to the bat via a loudspeaker, rather than the bat echolocating and detecting an echo) of approximately 0dB. However, further publications (e.g. Kick and Simmons, 1984) regarding actively echolocating bats, indicate a reduction in sensitivity of over 25dB at and immediately after call emission, due to the contraction of middle-ear muscles in the bat. This sensitivity is gradually restored over the ensuing few milliseconds as the muscles are relaxed, producing the bats' active gain control that provides both a protection mechanism for the sensitive hearing system, as well as range-compensated hearing sensitivity. Such data is not available for bats echolocating whilst in flight, but environmental noise will undoubtedly add to this figure. As such, the SPL of 27dB – 35dB estimated for the echo from a 65μm diameter wire, with a 100dB SPL incident signal seems to be an entirely reasonable estimation of the detection threshold for an echolocating bat in flight. As such, these bats capability to detect such small targets can be explained in terms of their hearing sensitivity and expected echo amplitude, in conjunction with the dynamic range of the signals bats work with.

It was particularly interesting to observe the performance of the wideband FM chirps, in comparison with the lower bandwidth *A. tridens* call and the constant frequency 83kHz signal. It was assumed that these signals would provide both improvement in timing accuracy through the pulse compression attributes of cross-correlation, as well as a capability for detecting smaller targets courtesy of their higher-frequency components. However, this was not demonstrated by the experimental results. There are a number of possible reasons for this, related to the mechanics of wave scattering from a cylindrical target. When the transmitted wave is incident on the target, there is a scattered wave reflected back towards the source, but in addition to this there may be travelling waves that circumnavigate the cylinder and travel back towards the source (Neubauer, 1968) and also radial (resonant) modes excited in the cylinder (Faran, 1951) that may affect the total energy returned towards the source. It is not expected that any radial modes will be excited, since the lowest frequency at which these are reported for a cylinder correspond to ka = 1.18, whereas the maximum value of ka for the cylindrical targets used here was approximately 0.7 (ka is the dimensionless multiplication of wavenumber, $k=2\pi/\lambda$, with target radius, a, often used for describing the properties of insonified cylinders or spheres; for this calculation λ is calculated within the cylinder material itself). Similarly, travelling waves could cause interference that would distort the signal returning to the microphone, as illustrated by Dardy *et al.* (1977). The values of ka at which such effects would occur is again generally beyond the region of investigation, with $ka>5$ (so at higher frequencies of incident sound). However, it does appear that there is significant distortion of the returned FM chirps, as discussed previously. Another possible explanation is that the large range of ka covered by a chirp, courtesy of its varying frequency, produces a distorted echo. For example, with a copper wire (longitudinal velocity of approximately 4000ms^{-1}) and an FM chirp with initial and terminal frequencies of 180kHz and 30kHz, then ka ranges from 0.14 to 0.02, respectively for a 1mm diameter wire. This will cause the returned signal to be distorted from the original due to varying target strength as discussed in Chapter 2. It could be this effect that means as SNR reduces, the distorted returning echo cannot be detected using cross-correlation techniques. In contrast, the CF and CF / FM calls

have significant portions of constant frequency within the signals, and as such a constant reflection coefficient. The reason the expected detection and resolution improvement did not occur with the wideband chirps appears to be due to the fact that the sub-mm targets did not produce a reflection that was an accurate reproduction of the incident signal. As such, the correlation function itself is less effective for extracting these signals, and performed more poorly in the presence of noise. Such effects were not observed with either of the lower bandwidth signals; the calls were either reflected with little change in their structure, or they were not (detectably) reflected at all.

One further series of experiments was performed. It was interesting to observe the reduction in echolocation performance of the *R. aegyptiacus* call with increasing range and decreasing target diameter, in comparison with the other signals used. While this was not unexpected, due to the low-frequency composition of the call, it is also the case that the call itself is a completely different form to the others consisting of an impulse-like click. As such, the performance of a frequency-doubled *R. aegyptiacus* call was investigated. The call was produced by halving the time-interval between each successive sample in the original call, with this signal then processed using the spectral inversion technique and transmitted via the electrostatic transducer as previously. Again, the peak SPL was set to 100dB at 100mm for comparison purposes, and the traces obtained from the wire detection experiments are displayed in Figure 5.27.

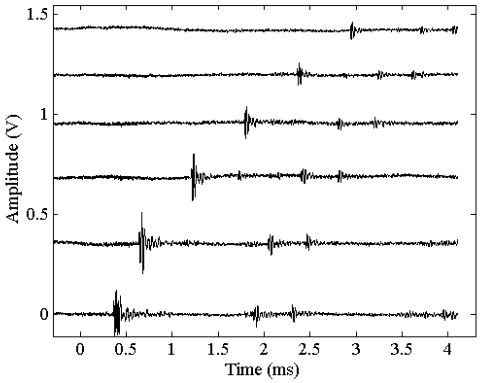
Amplitude (V)
Time (ms)

(a)

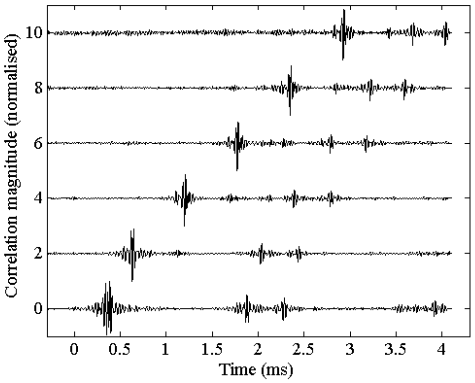
Correlation magnitude (normalised)
Time (ms)

(b)

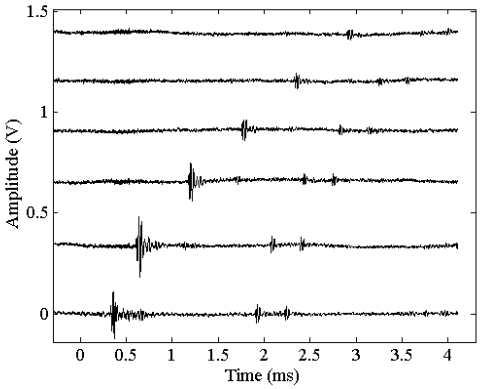
Amplitude (V)
Time (ms)

(c)

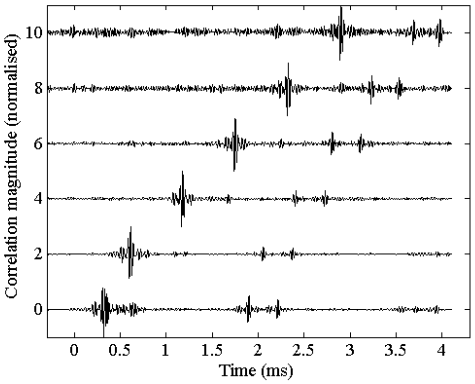
Correlation magnitude (normalised)
Time (ms)

(d)

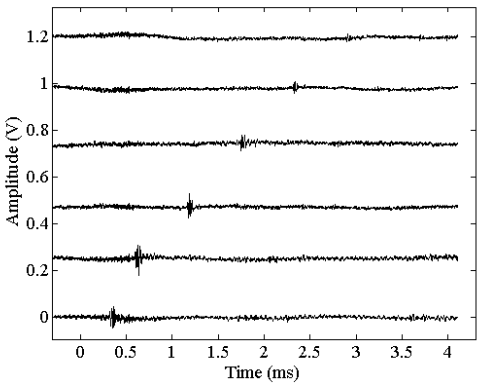
Amplitude (V)
Time (ms)

(e)

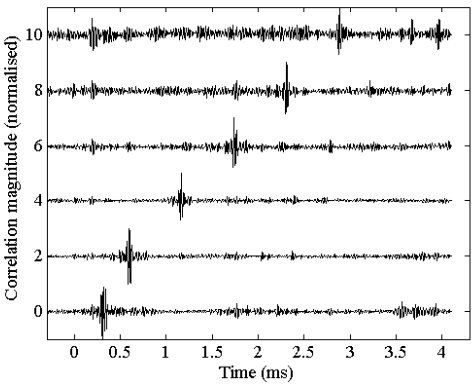
Correlation magnitude (normalised)
Time (ms)

(f)

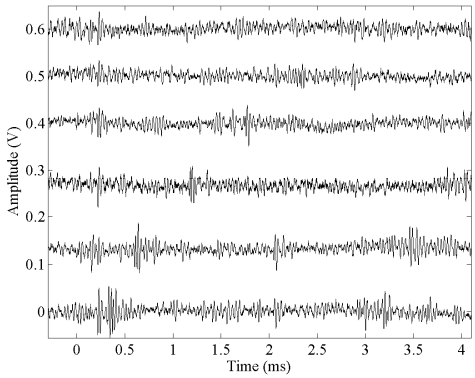
Amplitude (V)
Time (ms)

(g)

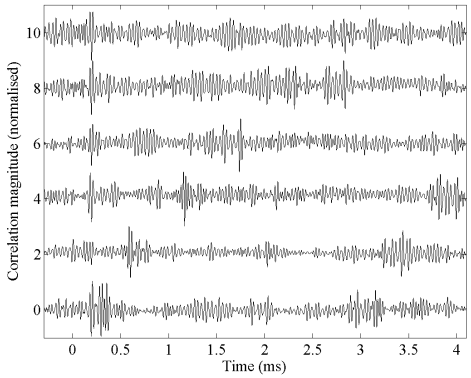
Correlation magnitude (normalised)
Time (ms)

(h)

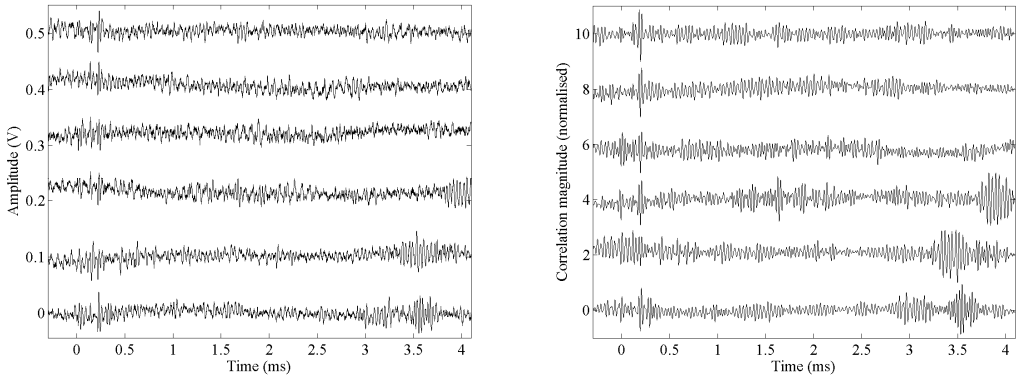

(i) (j)

Figure 5.27. Series of figures depicting signals from wire-target echolocation tests using a frequency-doubled call from *R. aegyptiacus*: (a) subtracted and (b) normalised cross-correlation trace for 5mm cross-section target (with location of target echoes circled); (c) subtracted and (d) normalised cross-correlation trace for 3mm cross-section target; (e) subtracted and (f) normalised cross-correlation trace for 1mm cross-section target; (g) subtracted and (h) normalised cross-correlation trace for 600µm cross-section target; (i) subtracted and (j) normalised cross-correlation trace for 340µm cross-section target.

In comparison with Figure 5.11, the call frequency makes a significant difference to the amplitude of return echoes and the ability to detect the smaller diameter targets at a larger range; in fact it can be seen that the 1mm target is now discernible at double the range that it was with the original call, and furthermore that the 600µm target can now be detected at up to 300mm distance. This in itself may not be surprising, but what is interesting is what this indicates about the way in which *R. aegyptiacus* uses its echolocation. Over millennia, the pressure for evolution would tend to increase the frequency components in the call of *R. aegyptiacus* if that would serve to benefit the species. However, there are obvious trade-offs in increasing the frequency content of the emitted call. Firstly, increased frequency signals are subject to greater attenuation and as such this may be one motivation for *Rousettus* to have a lower frequency call, by enabling the bat to detect objects at a greater distance. However, in this case, the doubling of frequency components and the advantages that brings in terms of detecting smaller targets, occurs by altering the lowest frequency component from approximately 14kHz to approximately 28kHz. The attenuation at these frequencies is $0.27dBm^{-1}$ and $0.81dBm^{-1}$, respectively. Given the maximum unambiguous range of the echolocation calls of *R. aegyptiacus* in the laboratory (see section 3.4.1.1 of this thesis) was measured to be approximately 16m, then the total

round-trip attenuation due to propagation in air is 8.7dB and 26dB respectively, a difference of approximately 18dB. This level of attenuation could indeed be an inhibitor for increasing the call frequency. However, the first echolocation call of any pair has a maximum unambiguous range of only 4m, giving a total round-trip attenuation of 2.2dB and 6.5dB. It would not seem that this level of increase would give the bat any cause to use the lower frequency call. Furthermore, should it to be deemed to provide an evolutionary advantage, there should be no reason why the call could not evolve to contain additional high-frequency components without losing the low-frequency ones, thereby providing the advantage of smaller-target detection, without losing the advantage of the long-range detection capability. As such, it would appear that *R. aegyptiacus* does not require its echolocation system to be capable of detecting small targets; it simply would not convey an ecological advantage to the species. This is further evidence that the bat may use its echolocation system as a form of collision avoidance in navigating through the caves in which it roosts, only requiring a method by which to navigate safely to its roost. This is rather different to the requirements of the sonar system of the microchiropteran species, which must have the capability to detect and locate small prey. Furthermore, given the limited use of correlation in pinpointing the exact time of arrival of a signal such as that used by *R. aegyptiacus* (as opposed to the pulse compression that occurs in the correlation of a FM chirp, or even a CF toneburst) then the requirement for fruitbats to evolve such specialised signals and systems is further negated.

CHAPTER 6

FINITE ELEMENT ANALYSIS OF THE RESPONSE OF A Rousettus leschenaultii BAT EAR

6.1 Introduction

In previous Chapters, various aspects of the bat echolocation system have been investigated. Firstly the calls emitted by, and returned to, the fruitbat *R. aegyptiacus* were recorded using a wireless sensor system to give an insight into the signals actually used by the bat whilst echolocating in flight. Through the design of bespoke electrostatic transducers, these calls, as well as coded FM calls, have been reproduced and used to replicate the wire detection tasks some bats have undertaken. These experiments have allowed the use of echolocation signals to be investigated, shedding light on the echolocation process and the dynamic range over which bats must be capable of operating. However, there is a further aspect of the echolocation process that such techniques cannot explore, and that is the signal that the bat actually hears. This Chapter investigates the response of the external ear, or pinna, of a fruitbat, using PZFlex Finite Element Analysis (FEA) code (Weidlinger Associates, CA, USA) to simulate the signals actually directed into the ear canal and onwards towards the eardrum. It is these signals that are transformed, via the eardrum, middle ear and cochlea, into the sounds actually heard by the bat. This technique is experimentally validated, with these results also reported in this Chapter.

As discussed in Chapter 2, there are a number of studies that demonstrate how the external ear structure alters bats' perception of reflected echolocation calls. For example Mogdans *et al*. (1988) demonstrated how "deflecting" the tragus of a greater horseshoe bat reduced its capability to detect and avoid wires in a wire-avoidance task, especially those which were horizontally oriented. This is interesting because binaural information such as interaural intensity difference (IID) or interaural time difference (ITD), is ineffective in locating horizontally oriented targets (since there is are no horizontal differences to generate these). As such, *monaural* cues, generated by each ear individually become important for such a task. This is also true of targets located on the median sagittal plane (the horizontal plane bisecting the body into right and left halves). The lack of either IID or ITD implies horizontal location on this plane, but its elevation can only be inferred through interpretation of monaural information generated by the interaction between the returning echoes and the external ear. Indeed, it seems logical that the generation of such information is the

very reason for the complex design of the pinna in mammals, including humans. All animals require to be able to locate either predators or prey through the sounds they generate; bats have taken this a further step by actively generating the sounds by which they can navigate and find their prey.

Previous studies, such as those conducted by Fuzessery (1996), Müller (2004), Müller *et al*. (2006) and Wang and Müller (2009) have investigated the response of bat ears using a variety of methods. Furthermore, some work has been done (e.g. Wotton *et al.*, 1995; Fuzessery, 1996; Aytekin *et al.*, 2004) investigating the head-related transfer function (HRTF) to demonstrate the effect the entire head of the bat (including the pinnae) has on the signal heard by the bat. However, it is hoped the technique used here will provide a more powerful and flexible means by which this aspect of the echolocation process can be investigated. Indeed, future work might involve modelling of the entire bat head, should this technique prove successful.

6.2 Methodology

The basis for this work was an X-Ray Computed Tomography (CT) scan of the ear of a *Rousettus leschenaultii* individual, obtained by Dr. Rolf Müller at the University of Shandong, Jinan City, China. At this point, the author would like to note his extreme gratitude to Dr. Muller for the provision of the scan data that made this work possible.

It was considered that these species were similar enough for the ear of the second species to give an accurate representation of the response of the original. Indeed, *R. leschenaultii* is the closest relative of *R. aegyptiacus* as indicated by the phylogram (a branching diagram that biologists use to indicate evolutionary relationships between species) presented by Goodman *et al.* (2010). Furthermore, their calls are similar both in terms of time and frequency content, as indicated by the signals recorded by Zhang *et al.* (2010).

The scan of the bat ear was provided as a series of 2-D image files, each of which represented the structure of a slice through the cross-section of the ear. Each slice was separated by 30μm, and contained pixels of 30μm square. Furthermore, the

slices were parallel and roughly perpendicular to the long axis of the ear. In order to render this ear in 3D, each 2-D slice was stacked using Analyze (AnalyzeDirect Inc., KS, USA), producing a 3D model with voxels of 30μm per side; this was performed by Mr. Martin Connell at the University of Edinburgh, to whom the author would like to express his gratitude. There are a number of image processing packages, such as Avizo (Visualization Sciences Group, MA, USA) or VG Studio (Volume Graphics GmbH, Heidelberg, Germany) suitable for this task. Due to the cost of such packages however, and their limited application to current research activity, no such package was purchased for this work. The 3D image was exported as a stereo-lithography file (.stl; hereafter referred to as an STL file), this having the advantage of being compatible with both PZFlex via a SolidWorks (Dassault Systèmes SolidWorks Corp., MA, USA) import tool and also the micro stereo-lithography (μSL) equipment available within the Department of Design, Manufacturing and Engineering Management (DMEM) at the University of Strathclyde. Through use of these tools, a physical model of the ear was constructed, with a virtual copy being used for simulation.

6.2.1 Manufacturing Using Micro Stereo-lithography

Residing within the Faculty of Engineering at the University of Strathclyde, DMEM provides the capability for manufacture and reverse engineering using a range of scanners, probes and rapid prototyping technology. Among the latter is the Objet Eden 350 (Objet Geometries Inc., MA, USA) 3D printer, which allows a 3D model to be manufactured in a variety of polymer materials though a layered printing process. This machine accepts STL files and, assuming contiguous connection of the solid elements, a 3D representation of the file can be produced. The Objet Eden 350 is capable of 42μm resolution in each of the horizontal axes (x and y) and 16μm in the vertical (z) axis. As such, the original 30μm voxels were resampled by the machine for manufacturing. Given the resolution, the result was a smooth finished object, with no “blocky” rendering detectable. The process itself can be described in the following steps, and is illustrated graphically in Figure 6.1:

1. 3D CAD data imported from STL file
2. CAD data is deconstructed into 2-D slices for printing process
3. Resin layer added for each slice of data
4. Ultraviolet laser scanned to cure the polymer relating to the CAD data
5. Steps 3 and 4 are repeated for each layer of data
6. Excess polymer is removed via immersion in solvent
7. Remaining solid part further cured in UV oven.

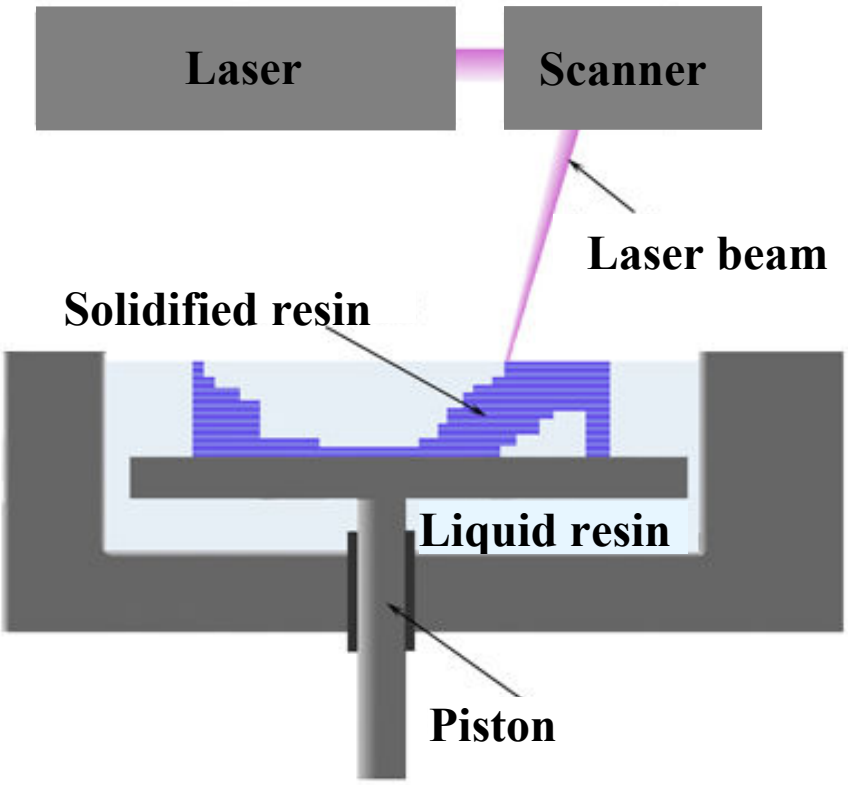

Figure 6.1. Diagrammatic illustration of μSL technique, using a scanned laser to cure each layer of resin thereby producing a solid form using 3-D printing.

This process was used to produce bat ears with a range of scales from 1:1 to 2:1, the larger of which were useful for illustration purposes. Images of the bat ear, in STL format from SolidWorks are depicted in Figure 6.2, with the manufactured μSL ear shown in Figure 6.3. The ear itself is approximately 21mm tall and 11mm at its widest point, with an opening into the ear canal approximately 3mm×2mm. The tragus (bottom centre of the leftmost image in Figure 6.2) is evident, but not particularly prominent, and there are some obvious ridges on the inside of the pinna itself. These ridges, seen on many bat ears, may be for structural rather than acoustic

purposes, given their spacing (~1mm) with respect to the wavelength (~17mm) of the peak frequency of the echolocation calls this bat emits.

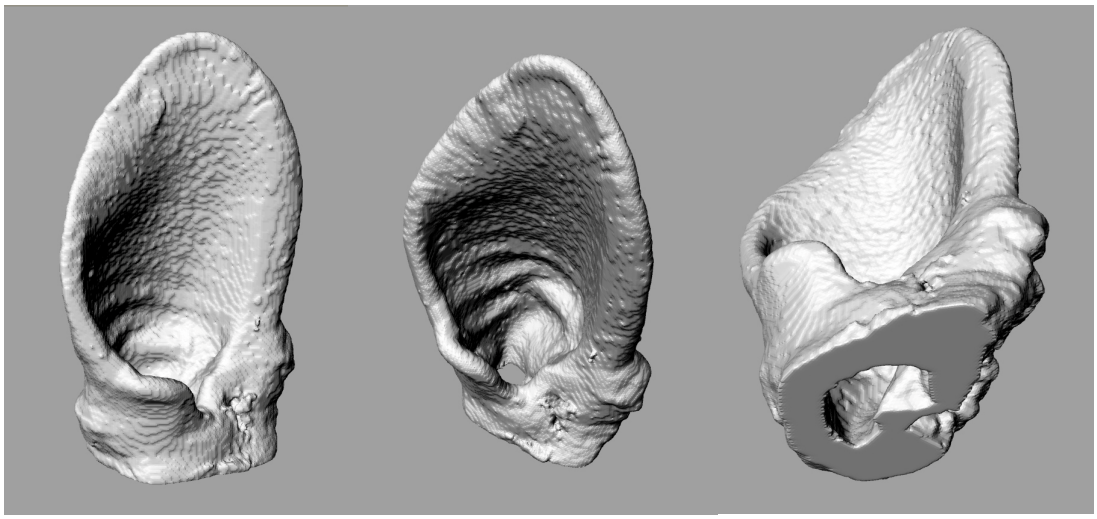

Figure 6.2. Solidworks representation of the *R. leschenaultii* ear.

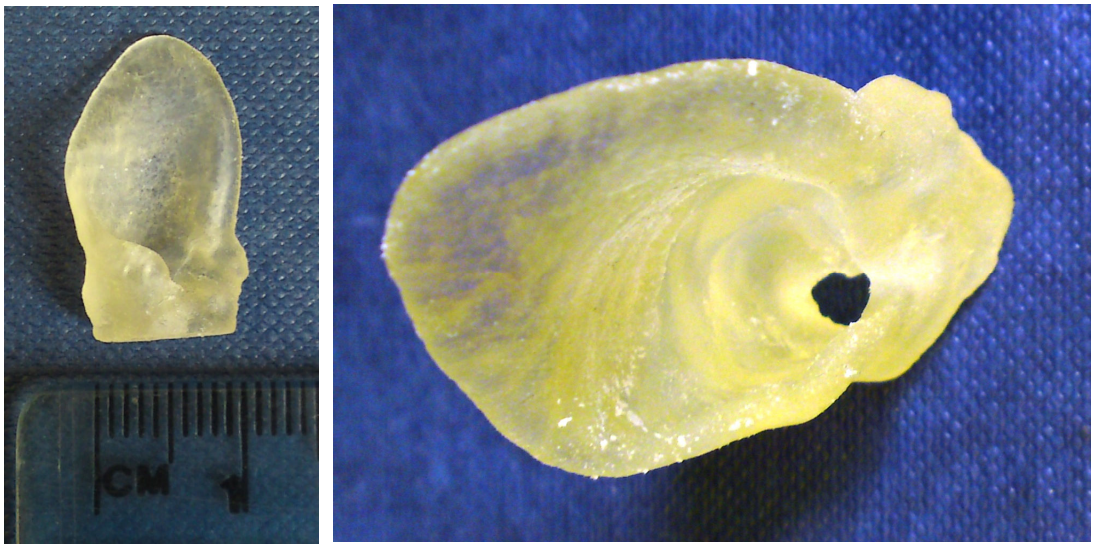

Figure 6.3. Manufactured µSL *R. leschenaultii* ear, in soft polymer.

The physical ear, pictured in Figure 6.3, was constructed of Objet Fullcure 930 TangoPlus (Objet Geometries Inc., MA, USA), a flexible polymer material produced by the µSL machine. In order to accurately simulate its behaviour in PZFlex, its material properties were characterised in the laboratory. The procedures used to generate the measured property values (longitudinal and shear velocities, density, and longitudinal and shear attenuations) are detailed by O'Leary (2003) and Trogé *et al.* (2009), but summarised here. The velocities were calculated in through-transmission configuration by measuring the time-of-flight of a 500kHz toneburst

travelling through a disc of known thickness. This was performed with the disc at normal incidence (for longitudinal velocity, c_l) and at the oblique angle that generated the peak shear wave transmission (for shear velocity, c_s). By accounting for the geometry of the test configuration, and measuring a reference time-of-flight without the disc in place, c_l and c_s can be calculated. A similar measurement relating the amplitude of the received signal in the reference, normal incidence, and oblique incidence configurations was used to calculate the longitudinal and shear attenuation coefficients. This was achieved by fitting to theoretical values over the appropriate range of angles for each property: from 0° to the critical angle for longitudinal attenuation; and a range of angles centred on the angle of peak shear wave transmission for shear attenuation. Given the isotropic nature of the material, the elastic moduli were then calculated from the measured velocities and density. The calculated and derived material properties are listed in Table 6.1.

Longitudinal velocity, c_l (ms^{-1})	1986.8
Shear velocity, c_s (ms^{-1})	626.4
Density, ρ (kgm^{-3})	1197.58
Poisson Ratio, ν	0.445
Young's Modulus, E ($ms^{-2}Kg$)	1.35e09
Impedance, Z ($kgm^{2}s^{-1}$)	2.38e06
Bulk Modulus, B ($ms^{-2k}g$)	4.10e09
Shear Modulus, G ($ms^{-2}kg$)	4.70e08
Longitudinal Attenuation (dBm^{-1})	382
Shear Attenuation (dBm^{-1})	5837

Table 6.1. Material properties of Objet Fullcure 930 TangoPlus from μSL machine.

6.2.2 Experimental Measurement of the Bat Ear Response

Although it was the receive response of the ear that was of interest, the response of the bat ear was actually measured in transmission as illustrated in Figure 6.4. This was done due to the inherent problems of measuring the receive response in an enclosed space; the principle of reciprocity ensured that these measurements were valid. The ear was mounted on a cone that was itself mounted on an Ultra Sound Advice Loudspeaker (Ultra Sound Advice, London, UK), attached to a rotational stage. The cone was used to direct the output from the transducer into the ear. It was machined from PVC with an internal diameter that tapered evenly from 60mm to

5mm over the cone height of 100mm. The ear was bonded to the cone using a quick-setting epoxy. This assembly was mounted on the x-y stage of the scanner detailed in Chapter 4 for ease of location. The B&K4138 microphone was mounted 60mm radially distant from the centre of the ear-canal, attached to the z-stage of the scanner. Given the dimensions of the ear, 60mm was selected to be in the far-field at all relevant frequencies (the largest dimension of the ear is approximately 20mm; using Equation 4.4, this equates to a far-field boundary at approximately 29mm for 100kHz, or 58mm for 200kHz), but close enough to achieve good quality recordings from the microphone. This configuration allowed the ear to be rotated about its axis, as well as being moved vertically via the y-stage of the scanner. This facilitated two types of measurement used to define the response of the ear: firstly, a series of polar directional plots obtained across a range of frequencies and at various heights with respect to the ear; and secondly a series of time domain waveforms recorded at a sub-set of these positions. Both of these measurements were used to validate the PZFlex simulation, as well as provide data on the directionality of the ear itself.

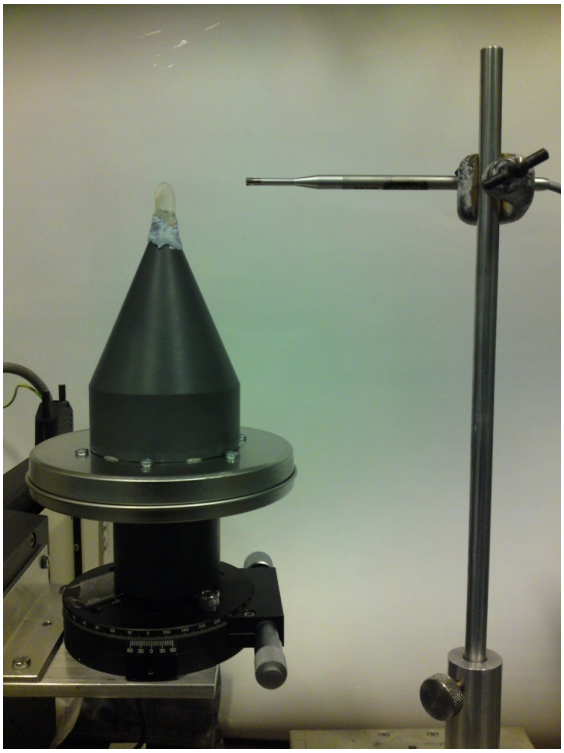

Figure 6.4. Experimental setup for measuring response of μSL ear.

6.2.3 Finite Element Analysis of the Bat Ear Response

FEA using PZFlex has been widely used for pressure wave propagation simulation, and it is for this purpose that it is used here. Although experimental measurements were obtained as indicated in the previous section, the main purpose of these was to validate results obtained from PZFlex simulation. The reason for this is that by producing an accurate simulation of the bat ear, it can be used to obtain a far greater variety of results than could be achieved experimentally. For example, given limited space, it is difficult to configure an accurate experimental system to test the receive response of the bat ear, which would allow its response to a range of signals originating from various origins to be measured. With an accurate FEA representation, this is relatively simple to achieve and, ultimately, this method can generate results more quickly.

PZFlex was specifically designed for piezoelectric, ultrasonic and thermal simulation and is particularly applicable to wave propagation modelling, which is the aspect of particular interest in this problem. PZFlex can be used to simulate the behaviour of the entire system of wave propagation, including the piezoelectric transduction mechanisms. Given this, the transducer structure can be created in the virtual environment (often termed as virtual prototyping) and an arbitrary drive signal, either electrical or mechanical, can be applied to transducer. In the case of an electrical signal applied to the transducer, for example, PZFlex will simulate the mechanical deformation caused in the piezoelectric material, and the ultrasonic pressure wave generated. This wave can then be propagated through a given medium in order to obtain overall system behaviour. In the case investigated here, this is not required, with the pressure wave introduced directly into the model, reducing the simulation to one of fundamental wave propagation.

6.2.3.1 Building the PZFlex Model

Any FEA begins with constructing a virtual representation, or model, of the physical space to be simulated. The model is constructed of individual elements, each of which is given a selection of properties representative of its constituent material, most commonly density, longitudinal and shear velocity, and a measure of damping.

These elements lend an inherent discretisation to the model space, the level of which must be carefully controlled. In PZFlex, it is recommended to have at least 15 elements per wavelength discretisation. This means that the element size must be small enough that there are 15 elements in the wavelength of the highest frequency of interest in the material with the lowest wave velocity (and hence shortest wavelength), thus defining the acceptable limit of discretisation, and hence the maximum element size. Once the model is built and boundary conditions established, then any driving functions are defined and applied. When simulating the bat ear response, a pressure load was applied to user-specified elements to generate suitable wave propagation within the model. PZFlex is capable of modelling in 2D, 2D axisymmetric or 3D. In 2D, any axes of symmetry may be exploited to reduce the computation time of any given model, and often a 2D model (built in the x-y plane, and which assumes an infinite model in the z-direction) can be used to obtain quick and accurate results. However, with the complex geometry of the bat ear, only a 3D model can be constructed in this case. In PZFlex, materials can be isotropic or anisotropic, with the physical properties providing all the information required to simulate how they will react to physical stresses and how waves will propagate through them. In this model, only isotropic materials are required.

Generally, the physical model is constructed using PZFlex code commands to define the geometry of each individual section. However, the only way to accurately represent the structure of the bat ear was to import the STL file directly into the PZFlex environment. As already mentioned, the source for the FEA representation of the bat ear was the original STL file that was used to produce the μSL ear. This file was imported into PZFlex via the SolidWorks importer, which converted the STL file to a PZFlex table file which maps each individual element within a cuboid volume to a specific material. The author would like to express his gratitude to Dr. Gerry Harvey of Weidlinger Associates for his expertise in this matter and in the original PZFlex code. The maximum frequency of interest was defined to be 100kHz (to adequately cover the frequency range of *R. aegyptiacus* as well as provide the capability to simulate some wideband coded FM sequences) and the slowest material in the model was air, with a longitudinal velocity of approximately $345ms^{-1}$. The requirement for at least 15 elements-per-wavelength was doubled to 30, giving an

element size of 115μm. The model was constructed by placing the imported ear structure within a larger cuboid volume of air. This larger cuboid extended outward from the region defined by the table file by approximately 5mm in all directions. This distance was defined to allow the propagation of energy away from the ear. The entire model was constructed of the 115μm-cubed elements. This element size was also applied to the ear, resampled from the original 30μm resolution. This was performed to reduce the number of elements, and so computation time, in the final model; even so, the model still contained some 8 million elements.

As mentioned previously, each element within the model was assigned a material, with associated material properties. The ear structure itself was defined as the Objet Fullcure 930 TangoPlus soft-setting polymer material produced by the μSL machine. Within the model at this point only air and polymer elements existed, defining the ear structure in polymer within a volume of air. In order to correctly excite the model, additional elemental structures were defined. Firstly, two additional regions of air were defined. This can be useful for defining the elements upon which to apply a load, especially if the excitation region is non-planar or difficult to specify otherwise. As an example, two further materials *air2* and *air3* were defined – the original air elements having been defined as *air1*. These have the same material properties as air (and as such, there is no material boundary within the model between an *air1* and *air2* or *air3* element) but a pressure load or indeed an output measurement can be defined as being applied only to the boundaries between *air2* and *air3* for example. In this case a cuboid of *air2* was defined extending beyond the ear structure in the x-y plane, and from the base of the ear to the bottom face of the model in the z-direction. Within this, a further smaller cuboid of *air3* was defined, this time having its x-y extent limited to fit within the base of the ear, and again extending from the base of the ear to the bottom face of the model in the z-direction. As such, the only boundary between *air3* and *air1* elements is within the ear canal itself; it is this boundary that the input pressure load was defined to act upon. Finally, a hollow cylinder of polymer was defined extending from the base of the ear to the base of the model volume. This was put in place to remove any direct air path between the applied load and the rest of the model, preventing wave propagation outwards from underneath the ear. This was necessary since PZFlex induces an equal and opposite

pressure load radiating in the negative direction from the surface to which the pressure load is applied. This ensured that pressure waves radiating into the surroundings of the ear were caused entirely by waves travelling up through the ear canal and radiating out from and around the pinna. The model as viewed in PZFlex is illustrated in several images in Figure 6.5, showing the ear itself, the two additional types of air element and the polymer cylinder extending from the base of the ear, all contained within the larger cuboid of air.

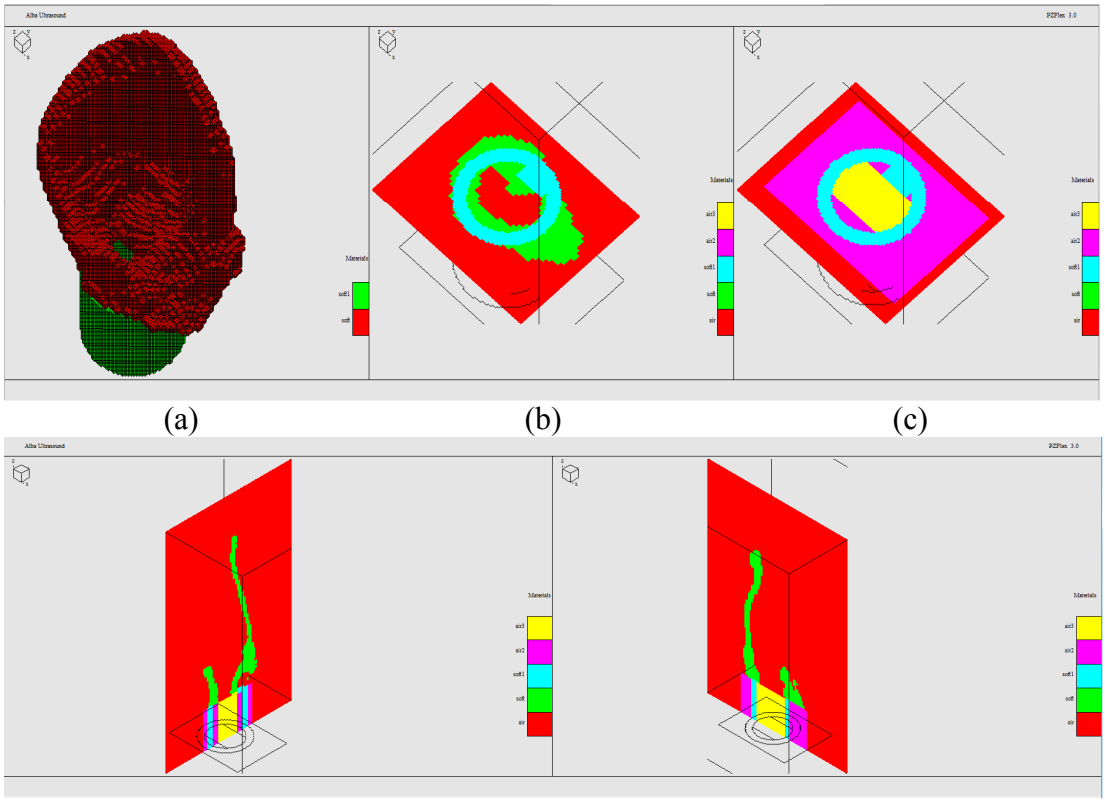

(a) (b) (c)

(d) (e)

Figure 6.5. A series of images depicting various aspects of the model in Flex: (a) the ear (red) and additional cylinder of polymer (green) that was required to prevent energy radiating from under the ear – the inside of the cylinder can be seen through the base of the ear canal; (b) a planar illustration of how the additional cylinder and box of polymer (cyan) connect to the base of the ear (green); (c) an illustration of how the various air materials - air1 (red), air2 (magenta), air3 (yellow) - are used to allow the pressure load to be applied to the ear canal. Part (c) is a slice taken through at a level one box below the slice of part (b). The pressure load is applied to the boundary between air3 (yellow in (c)) and air 1 (red in (b)). The only points at which these materials have a boundary is at the bottom of the ear, fully enclosed within the canal; (d) and (e) show orthogonal cross sections of the ear depicting all materials and clearly showing the spatial relationship between the three types of air element, for pressure loading purposes as described previously.

6.2.3.2 Field Calculation Through Extrapolation in PZFlex

The model volume was approximately 21.3mm×18.6mm×30.9mm, constructed from the 115μm-a-side elements. It can be seen from the dimensions of the model that it did not extend out to the 60mm radial distance at which the microphone was placed to measure the response of the μSL ear. This is because a model of that size would simply take too long to process. In order to compare the response of the PZFlex and experimental results, the extrapolation function of PZFlex was used. Extrapolation techniques allow the field produced by waves propagating in homogeneous media to be predicted without having to construct an explicit model large enough to encompass the area across which results are required. To use the extrapolation function, one or more extrapolation boundaries are defined within the model structure, through which the pressure waves will propagate. The time history of the pressure wave passing through each elemental area of each extrapolation boundary (plane) is then stored as the model progresses, with these time histories used later to extrapolate the pressure wave at any given point beyond the extrapolation boundary.

It is useful at this point to define the notation by which sides of the model are referred to in PZFlex. Any 3D model has 6 sides, being those of the cuboid volume within which the model is defined. There is a convention for naming these sides, providing a basis by which to apply boundary conditions to them. The sides are simply numbered 1 through 6, with 1 and 2 defining the negative and positive boundaries, respectively, of the model in the x-direction. Similarly, sides 3 and 4 define the negative and positive boundaries, in the y-direction, whilst sides 5 and 6 define the negative and positive boundaries, in the z-direction. As such, sides 1 through 4 define the vertical boundaries of the model, whilst sides 5 and 6 define the bottom and top of the model space, respectively. In this case, five individual extrapolation boundaries were defined, parallel to sides 1, 2, 3, 4 and 6, forming a box with the bottom face removed. The bottom (parallel to side 5) was not included for two reasons: firstly, it was not necessary since this is facing below the ear (or into the head of the bat) which is of no interest for investigating the response of the ear; and secondly, extrapolation boundaries must be declared within a uniform material – with the cylindrical extension of polymer extending from below the ear canal all the

way to side 5 of the model, there is no available plane of uniform material. To ensure accurate extrapolation, the vertical extrapolation boundaries were extended by 40 elements (~4.5mm) below the base of the ear to ensure that all energy travelling towards the vertical faces of the model was included. These boundaries were placed approximately 4 elements distant from the ear material, as defined by the PZFlex manual to ensure accurate calculation of extrapolated data. As the energy was simulated to propagate through the model, the time domain trace (known as a time history in PZFlex) was stored for each node on the extrapolation boundaries. With access to this information, the waveform at any point in space beyond the boundaries can be calculated, in a similar fashion to the application of the Rayleigh integral detailed in Chapter 4. The model was completed by attaching boundary conditions to each of the six external sides or faces of the model. Each of these was defined as an absorbing boundary, allowing any energy incident on the edge of the model space to effectively propagate out of the model, with no reflections. As such, the ear was simulated in an infinite volume.

6.2.4 Experimental and Simulation Procedures

Experimental measurements were split into two categories, although they are inherently linked and were performed at the same time, with the same experimental configuration. Firstly, the directional characteristics of the field radiating from the ear were measured at 5° intervals, with this measurement being performed at 10mm height intervals extending from level with the base of ear (defined as 0mm) to 100mm above this (approximately 80mm above the ear tip). As such, the peak output voltage from the B&K microphone system was measured at each point, before the ear was moved rotationally or vertically and a new measurement made. Although this task was relatively time-consuming it did not have to be repeated often and so the rotational movement and measurement was carried out manually, since the time taken to produce an automated solution would have proven to be an inefficient use of time. These measurements were repeated at 10kHz intervals from 10kHz to 100kHz, with the driving function being a 10-cycle toneburst, apodised by a Hanning window. This allowed the directional characteristics of the ear to be measured at each of these frequencies. The second measurement made was the recording of the time domain

traces received by the microphone. These signals were captured at a subset of the points measured for the directional response; at 30° intervals at 0mm, 20mm and 50mm elevation. This was performed as it was felt that validating the directional characteristics of the PZFlex simulation was not in itself sufficient to validate the model. This was especially true since it was the aim of this work to use PZFlex as a tool to simulate the response of the ear to varying incident waves originating from a range of points in space. As such, it would be the time domain signal present in the ear canal at the base of the ear that would be of interest and so the time domain correlation between experimental and simulated results was considered to be at least as important as the directional characteristics, in terms of model validation.

To compare with these experimental measurements, PZFlex was used in a number of different ways. Firstly, it was run with a single-cycle 100kHz sine wave as the pressure load applied to the air elements at the base of the ear canal. By propagating this through the model, and running a series of frequency domain extrapolations, then the directional characteristics of the ear at any frequency can be calculated, on the condition there is a spectral component within the single-cycle signal at the frequency of interest, and furthermore that the frequency of interest is not so high that it flouts the 15-elements-per-wavelength rule in PZFlex. Since the driving function in the experimental results was a windowed tone-burst, the extrapolation was performed at a series of 1kHz-spaced frequencies, with these results then weighted to provide the spectral content of the driving function when added together. For example, a 50kHz 10-cycle, Hanning-apodised toneburst has rather more bandwidth than might be expected, certainly in comparison to the single spectral line of a constant 50kHz sine wave. This is illustrated in Figure 6.6(a), where it can be seen that the -3dB bandwidth is approximately 10kHz, or 20%. Also displayed are the 13 discrete spectral components calculated and added together in PZFlex to approximate the response of the toneburst. Figure 6.6(b) depicts the original analogue windowed toneburst, and the result of the complex inverse FFT of the discrete components. This demonstrates the validity of using these components to generate the response of the toneburst itself.

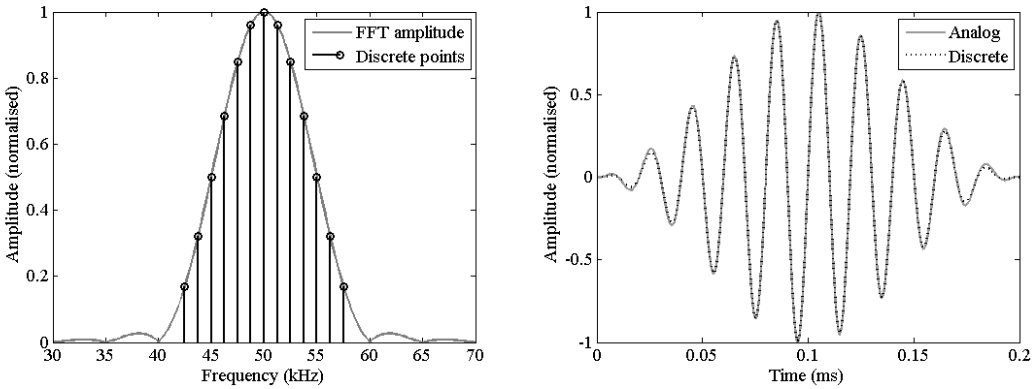

(a) (b)

Figure 6.6. Spectral composition of 10-cycle 50kHz Hanning-windowed toneburst (a) with discrete points used to simulate directionality in frequency domain extrapolation in Flex. (b) Time domain image of the original analog toneburst, and its discretely-formed alternative, constructed using the complex inverse FFT of the 13 discrete points shown in (a).

This method was used to calculate the peak amplitude of the extrapolated signal at 1˚ intervals on a 60mm radius circle, centred on the ear, at heights of 0mm – 100mm above the base of the ear to correspond with the experimental measurements made. In order to validate this methodology, and also to obtain the required waveforms for time domain comparison with experimental results, a time domain extrapolation was also performed in PZFlex. This is a more lengthy process than the frequency domain extrapolation, even accounting for the requirement to calculate several spectral components for each frequency domain result. As such, this process was only run fully at selected frequencies, and the peak amplitude of the resultant signals extracted to validate the frequency domain extrapolation. After this, it was only performed at the reduced number of points at which experimental time domain results were stored.

6.3 Simulation Validation

In this section the results obtained in transmission, both experimentally and virtually will be compared. This comparison is presented as validation of the PZFlex model, demonstrating its accuracy in simulating the response of the ear to an applied pressure load.

6.3.1 Simulation Validation - Directional Response

As indicated previously, the directional response of the ear was measured experimentally at intervals of 10kHz, between 10kHz and 100kHz, using a 10-cycle apodised toneburst. This procedure was then repeated using frequency domain extrapolation to calculate the directional characteristics of the ear in PZFlex. The results presented here compare these results for validation purposes. The data is presented as a series of plots, normalised over the results for the entire ear to illustrate the variation in magnitude response with frequency. The experimental plots were also normalised with respect to the acoustic input to the ear, as the amplitude of the applied signal varied with frequency. To achieve this, the input signal was measured using the B&K microphone placed at the entrance to the ear canal, with the cone and ear in place on the Ultra Sound Advice loudspeaker, with the experimental results referenced to this level. Furthermore, the directional characteristics of the microphone were accounted for as detailed in Appendix A. Alignment of the two plots was carried out by initially finding the position of the maximum output across all frequencies in the experimental system, and designating its horizontal angular direction (θ) as 0˚; this direction with respect to the ear was then defined as 0˚ in the simulation results with the horizontal angle referenced to it. Height was measured relative to the base of the ear, which was defined as the zero point. Finally, to aid comparison, the experimental measurements were interpolated to produce results at 1˚ resolution.

The comparison of PZFlex and experimental directional data is displayed in Figures 6.7 through 6.16. For brevity, the comparisons are displayed every 20mm of elevation, rather than the 10mm measurement resolution. In general terms, the correlation between the simulated and experimental traces is very good. However, looking at the results in more detail reveals interesting features and trends. In terms of comparison between the experimental and simulated results, across all frequencies the correlation tends to be poorer at lower elevation. There are two reasons for this. Firstly, the SNR at lower levels is poorer leading to less accurate experimental measurements of the variation with angular rotation. All experimental measurements were made using the measuring function of the oscilloscope, using 256 averages and

the peak value noted to the nearest 5mV since the result rarely settled to a greater resolution than this, even with averaging. As such, relative amplitude variations were not as accurately represented for low signal amplitudes as for larger signals, as a function of the available signal to noise ratio. Secondly, at low elevations, reflections from the external surface of the feed-cone undoubtedly had a greater influence on the signal transmitted from the ear structure towards the microphone, and this was not included in the PZFlex simulation as it would have significantly increased the size of the model; by approximately 50 times to include the entire cone. In terms of the accuracy of the model, it is most important that the higher amplitude results correlate well with experimental data. This is because when the model is used for its intended purpose of demonstrating the ear response to incoming echolocation signals, it is those directional components with greater amplitude that will contribute more significantly to the signal directed into the ear canal. As such, it can be seen that across all the results, the correlation between simulated and experimental results at the heights with peak amplitude response (generally 40mm – 60mm) is good.

Most results demonstrate that simulated results correlate exceptionally well for the main lobe of the response, with varying degrees of success in reproducing the response at greater angular displacement. It should also be noted that the data indicates that the simulation and experimental data correlates more closely for lower frequencies - up to approximately 60kHz. At frequencies of 70kHz and above, there are more noticeable discrepancies between the two. As an example of this, it is instructive to compare the results at 30kHz, with those at 80kHz. It can be seen across the height-range at 30kHz (Figure 6.9) that the main lobe correlation is extremely good, both in terms of amplitude and beamwidth, with probably the most significant departure between simulated and experimental data being evident at 20mm and 40mm in the form of the secondary lobe in the simulated data at approximately -130˚. In comparison, any secondary lobe in the experimental data is shifted to approximately -170˚ and is less pronounced. It is interesting that all the results up to 50kHz demonstrate similar patterns, with accurate reproduction of the amplitude and form of the main lobe, but simulated data overstating the amplitude of any secondary lobe and also misplacing it by 30˚ to 40˚. Notwithstanding these features however, the correlation is good. At 80kHz (Figure 6.14) however, there are

a number of features that vary between the experimental and simulated data. At lower elevations, the general form of the directional traces is broadly similar. However, at higher elevations, with more intricate field patterns, there are interesting variations to note. It can be seen in the experimental results that as the elevation increases, there is a shift in angular direction of the main lobe from approximately -30˚ to 20˚, with a broadening of the peak, or separation into two distinct peaks, in between. A similar shift can be seen in the simulated data, but the separation into two peaks is more pronounced and the shift in the main lobe occurs at a lower elevation. Even with these variations, however, it is reassuring to note that the trends of both sets of results tie in well. Obviously the ear has a complex geometry, and so generates a more complex field to determine than for that of the flat-faced electrostatic transducers in Chapter 4, but some of the intricacies of the field generated by such a source have been indicated in the simulated results. This is particularly evident in the way in which the main lobe is seen to split and relocate.

In comparing these two sets of results, the reasons for any differences should be considered. As such, the increased variation as the frequency increases is perhaps instructive. Given the three-dimensional nature of the work, it is inconceivable that there was not some spatial variation between the experimental and virtual configuration; this was another reason for keeping the microphone as close to the ear as possible, whilst still working in the far-field. The ear itself has a small (6mm×4mm) planar base, situated on top of the feed-cone. Given this, it is probable that it was not oriented exactly vertically, even though it was ensured that the transducer and rotational stage were horizontal with a spirit level. Any variation in this would obviously give an offset in the field, essentially skewing the horizontal planes on which simulated results were calculated. This effect, when combined with the more detailed and intricate field structures generated at higher frequencies, would cause any physical offset to produce more noticeable variations between the experimental and simulated results, as has been documented. However, over the full range of frequencies and elevation, there is sufficient correlation to suggest that the simulated directional results are accurate.

This is further supported by examining the results from a different perspective, viewed as a whole in 3D space. These results are illustrated in Figure 6.17 where a variety of trends are reinforced or seen fully in a way not possible in the 2D comparisons (although objective comparison of the correlation of the two sets of results is more readily perceived in 2D). In the 3D plots, the colours are simply used to easily distinguish between the results at each elevation, rather than coding the magnitude in some way. This was the least confusing manner in which to present the data and provides an easy way by which to compare each set of results. For example, it can be seen that the elevation at which the maximum amplitude response occurs varies, starting at approximately 20mm at 10kHz and gradually rising with frequency up to 60mm at 40kHz, before falling at 50kHz – 60kHz and rising again at 70kHz at which point it remains relatively static up to 100kHz. Also evident at 100kHz is a splitting of the peak, with two peaks appearing at 20mm-30mm and at 70mm. This is evident in both simulated and experimental data. Also apparent, is the rotation in the angular position of the peak amplitude as the frequency changes. The trends of this variation are depicted in both sets of results except for a discernible offset at 80kHz. Another trend in the results that is more discernible in the 3D plots is that the beamwidth in the vertical direction is rather larger in the simulated results, with PZFlex predicting a broader vertical beam at practically all frequencies, with a rather narrower appearance to the top of the directionality profile of the experimental results. However, over the entire frequency and elevation range, the simulated directional characteristics of this complex structure show consistent correlation with the experimental results. It is also interesting to note that the peak response of the ear was measured and simulated at 50kHz – 60kHz, significantly above the frequency content of the *R. aegyptiacus* call.

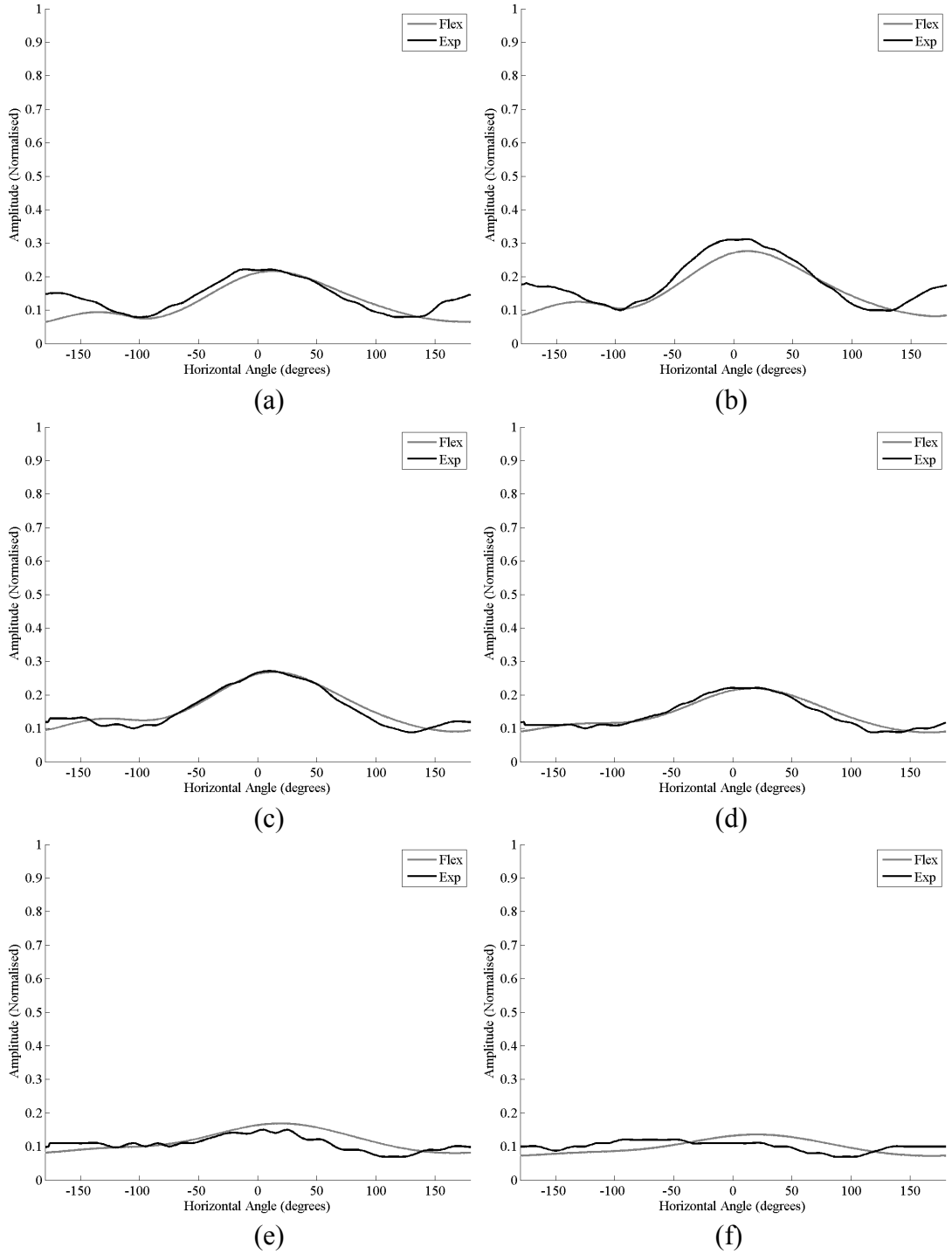

Figure 6.7. Comparison of Flex and experimental directionality from 10kHz windowed toneburst: (a) 0mm; (b) 20mm; (c) 40mm; (d) 60mm; (e) 80mm; and (f) 100mm.

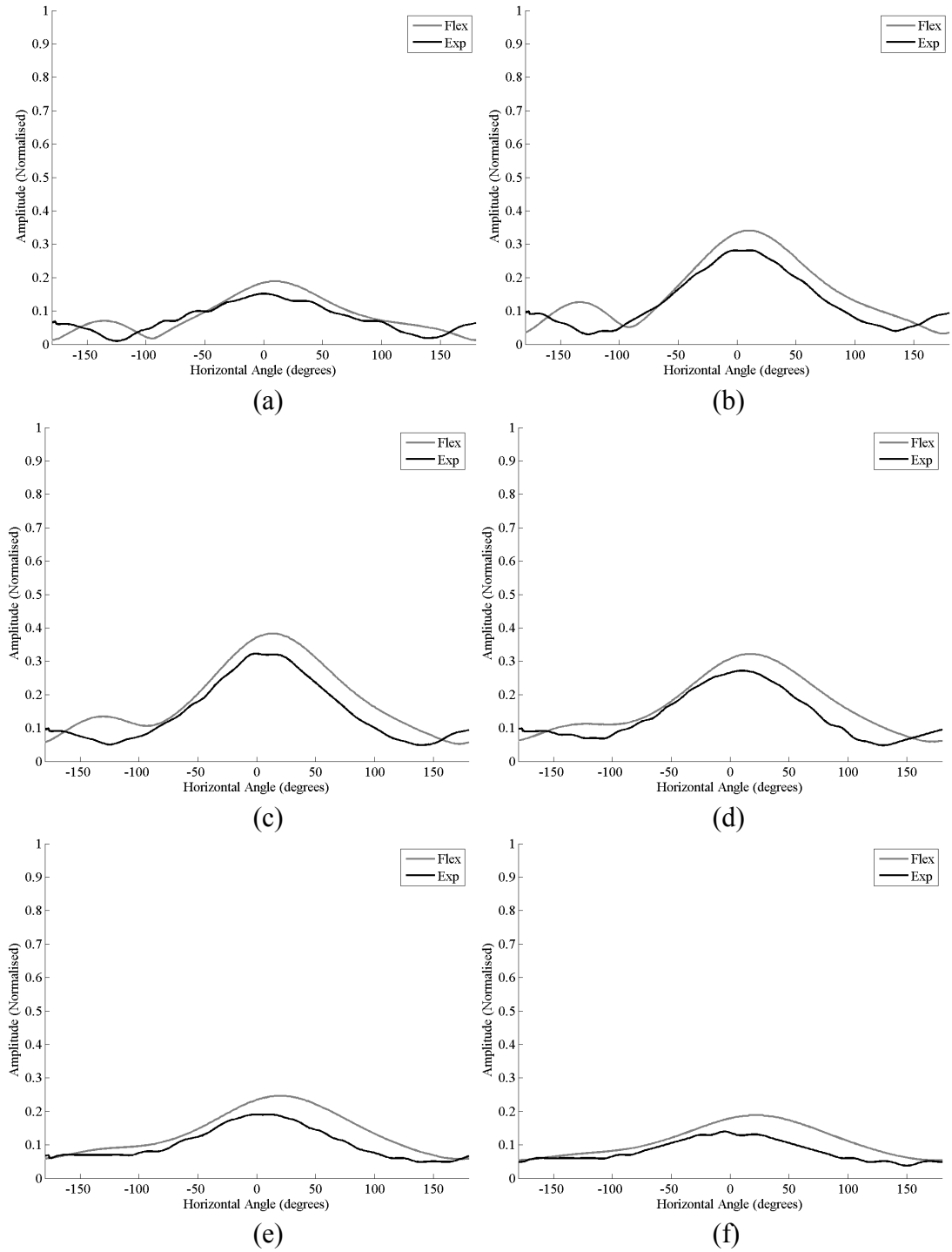

Figure 6.8. Comparison of Flex and experimental directionality from 20kHz windowed toneburst: (a) 0mm; (b) 20mm; (c) 40mm; (d) 60mm; (e) 80mm; and (f) 100mm.

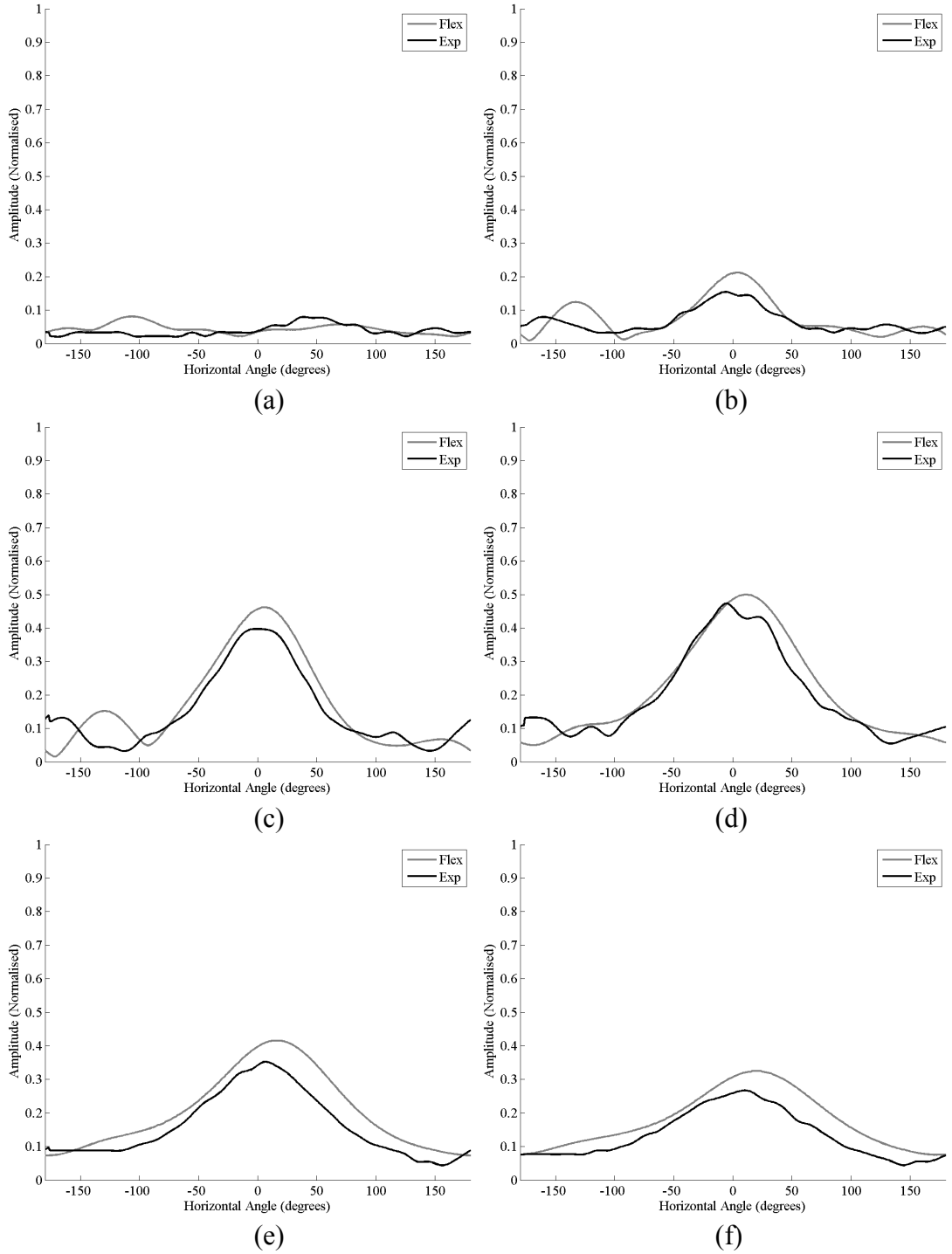

Figure 6.9. Comparison of Flex and experimental directionality from 30kHz windowed toneburst: (a) 0mm; (b) 20mm; (c) 40mm; (d) 60mm; (e) 80mm; and (f) 100mm.

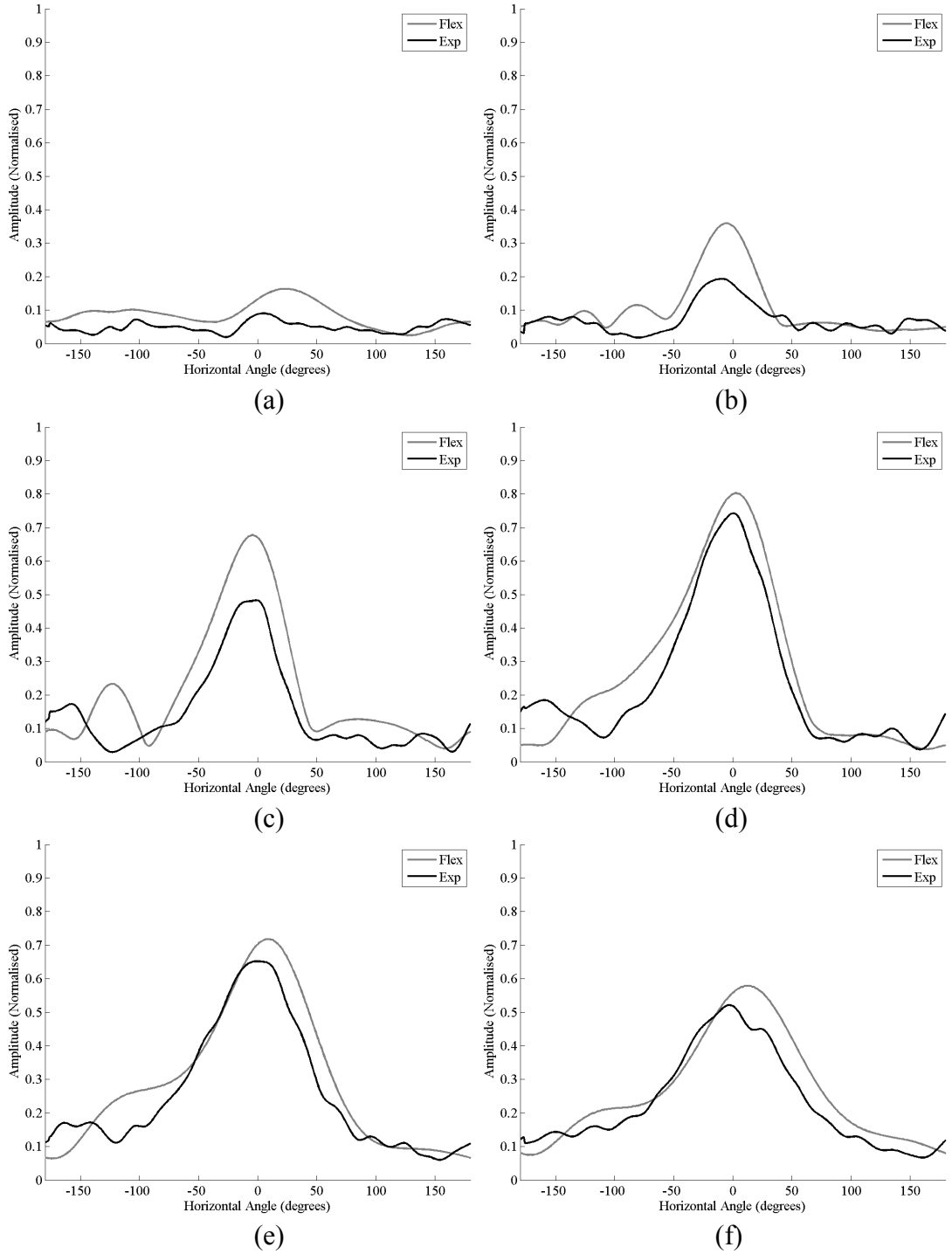

Figure 6.10. Comparison of Flex and experimental directionality from 40kHz windowed toneburst: (a) 0mm; (b) 20mm; (c) 40mm; (d) 60mm; (e) 80mm; and (f) 100mm.

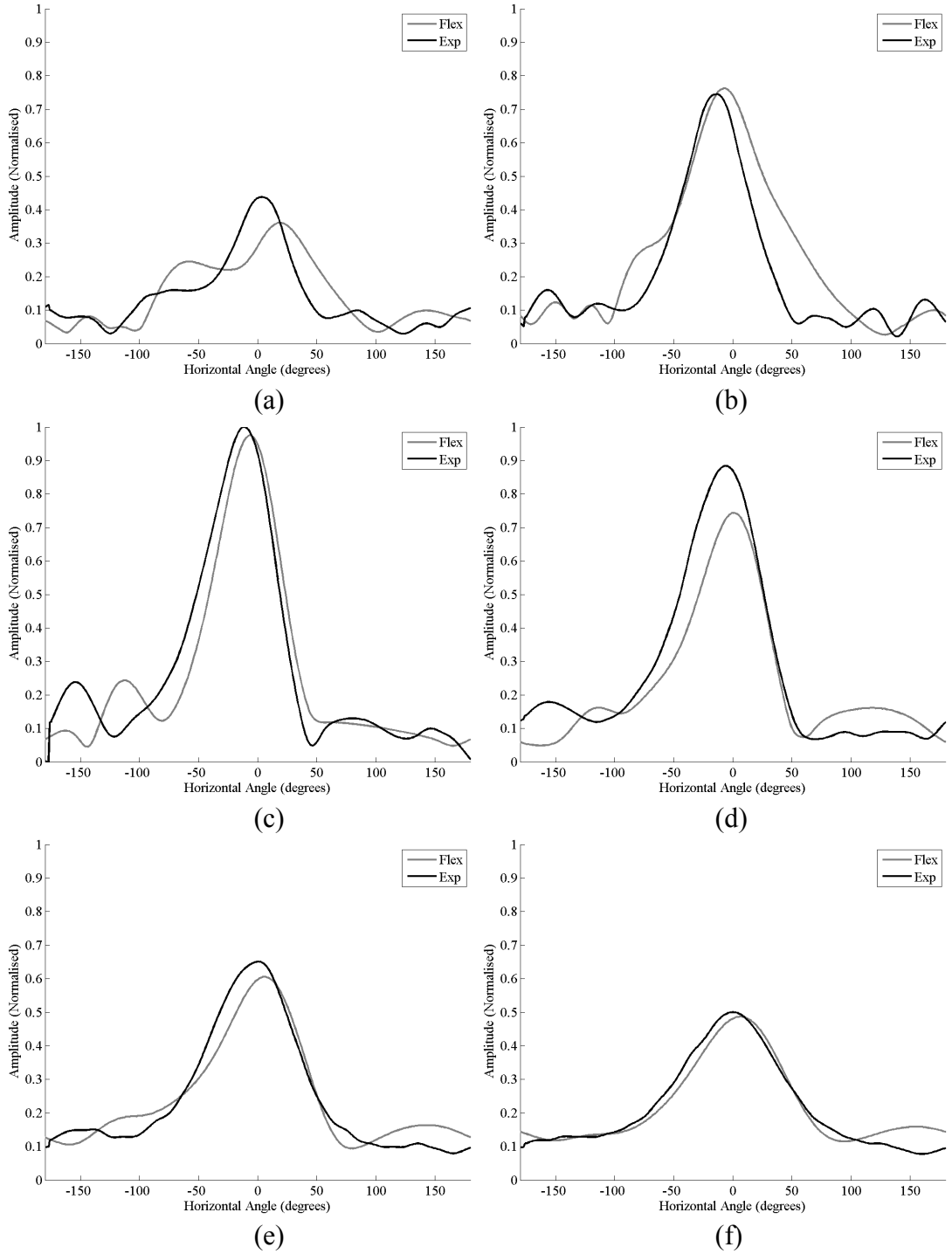

Figure 6.11. Comparison of Flex and experimental directionality from 50kHz windowed toneburst: (a) 0mm; (b) 20mm; (c) 40mm; (d) 60mm; (e) 80mm; and (f) 100mm.

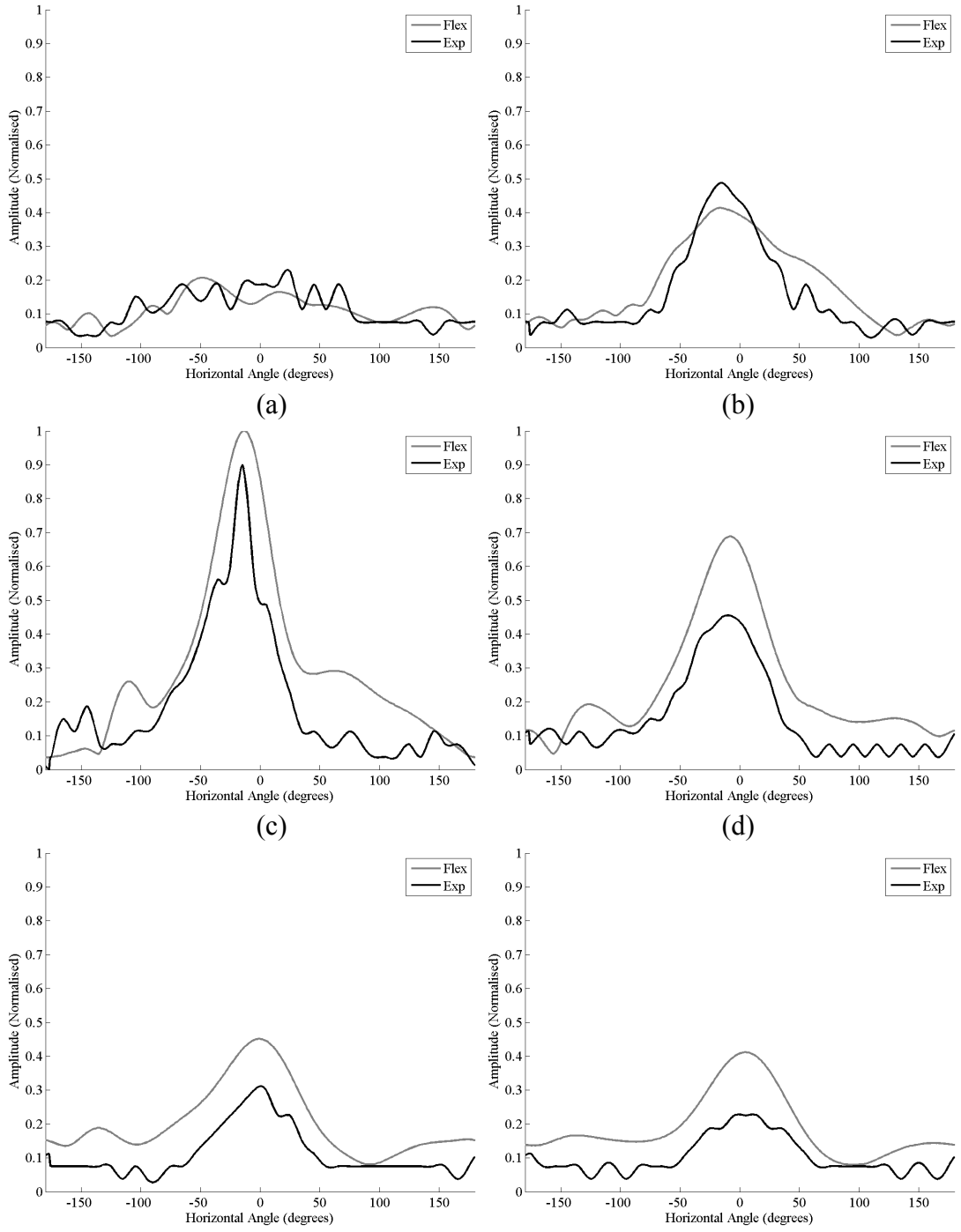

Figure 6.12. Comparison of Flex and experimental directionality from 60kHz windowed toneburst: (a) 0mm; (b) 20mm; (c) 40mm; (d) 60mm; (e) 80mm; and (f) 100mm.

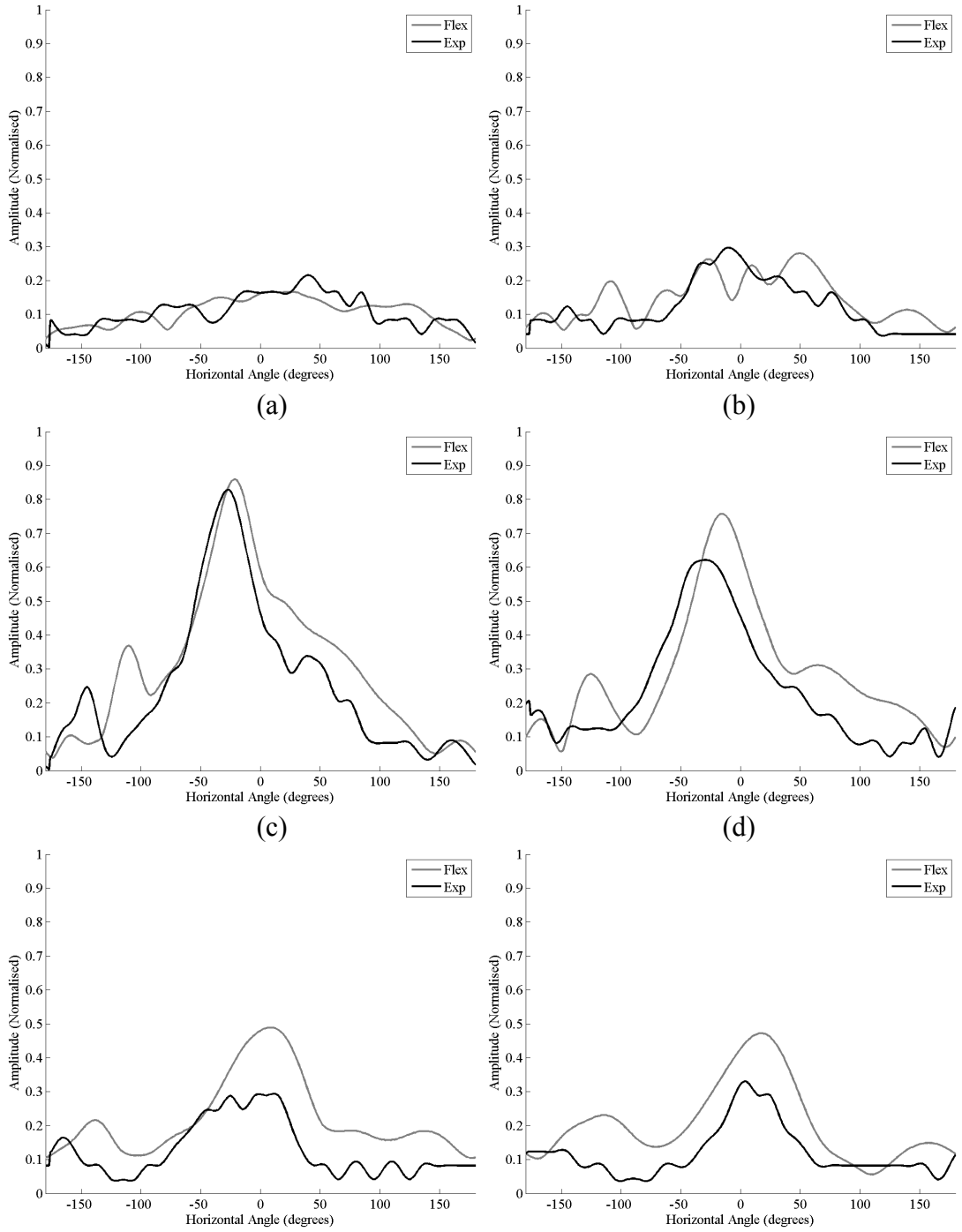

Figure 6.13. Comparison of Flex and experimental directionality from 70kHz windowed toneburst: (a) 0mm; (b) 20mm; (c) 40mm; (d) 60mm; (e) 80mm; and (f) 100mm.

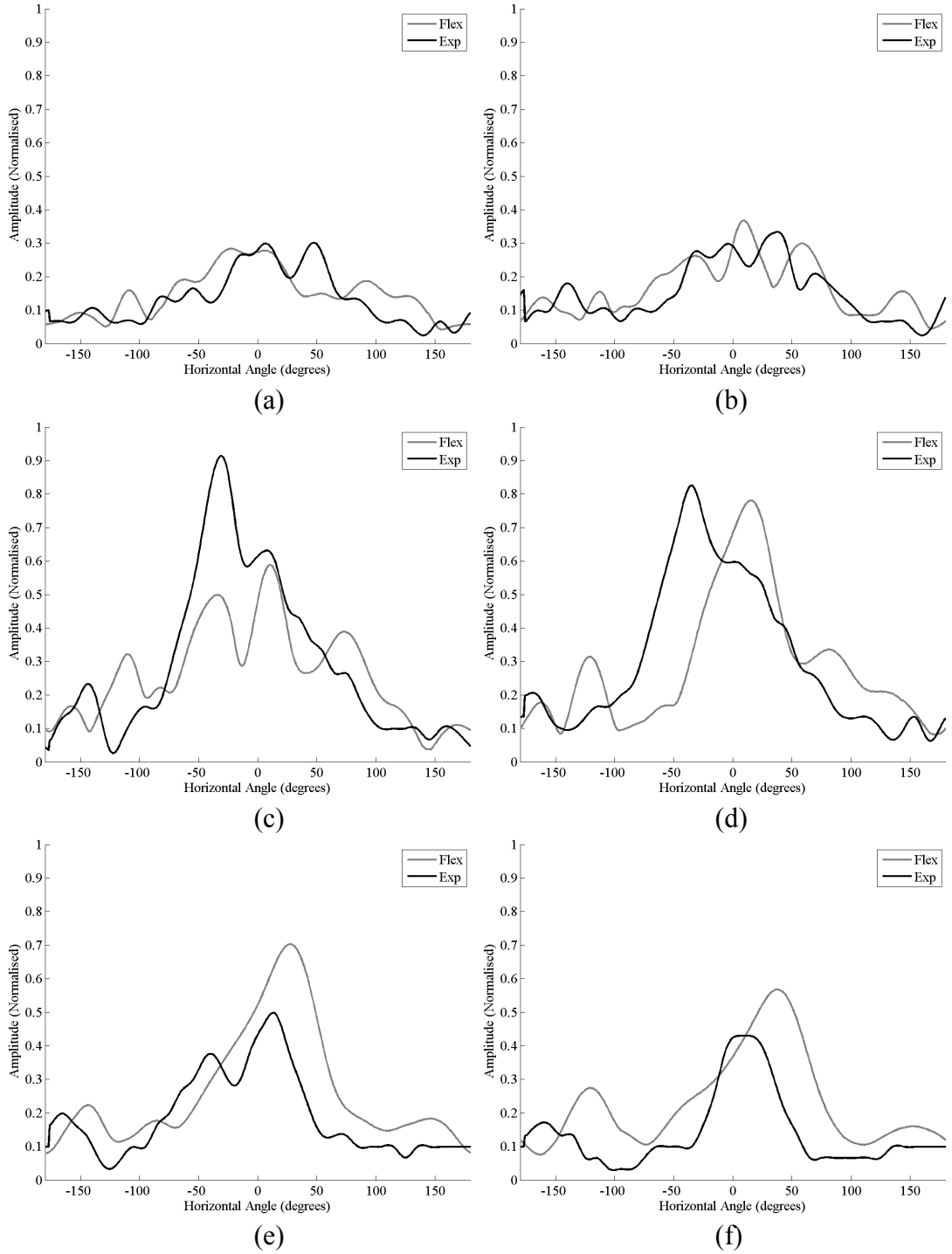

Figure 6.14. Comparison of Flex and experimental directionality from 80kHz windowed toneburst: (a) 0mm; (b) 20mm; (c) 40mm; (d) 60mm; (e) 80mm; and (f) 100mm.

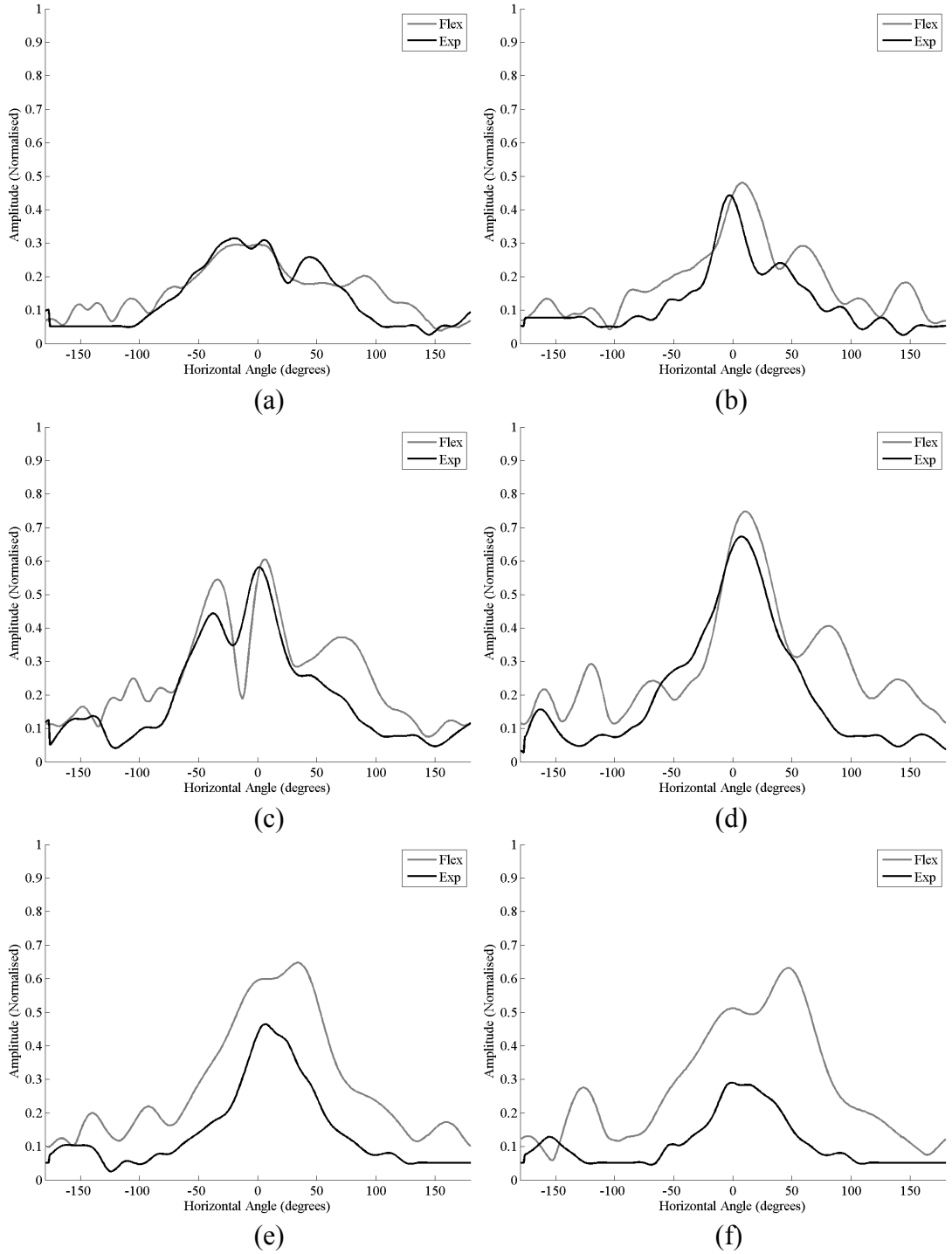

Figure 6.15. Comparison of Flex and experimental directionality from 90kHz windowed toneburst: (a) 0mm; (b) 20mm; (c) 40mm; (d) 60mm; (e) 80mm; and (f) 100mm.

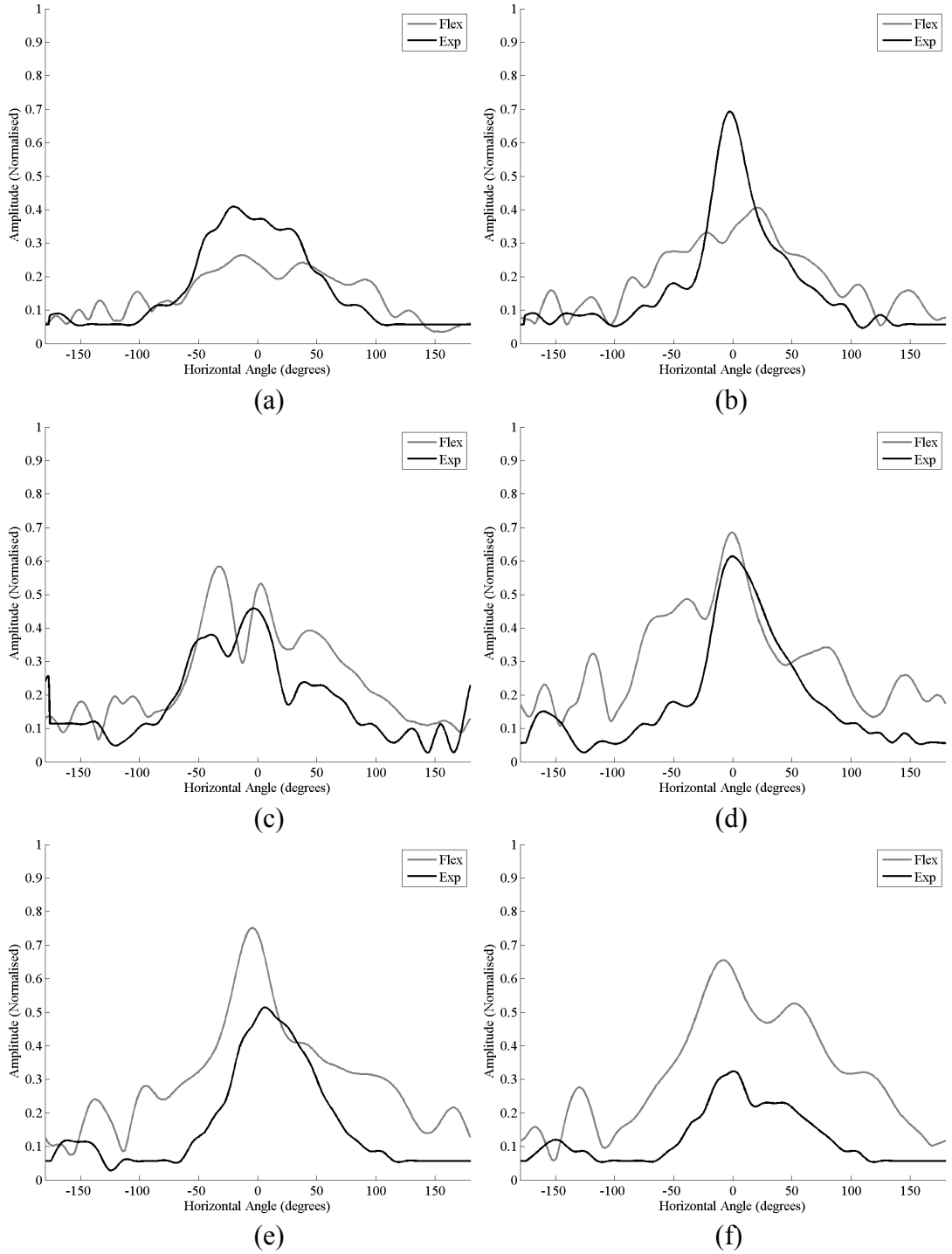

Figure 6.16. Comparison of Flex and experimental directionality from 100kHz windowed toneburst: (a) 0mm; (b) 20mm; (c) 40mm; (d) 60mm; (e) 80mm; and (f) 100mm.

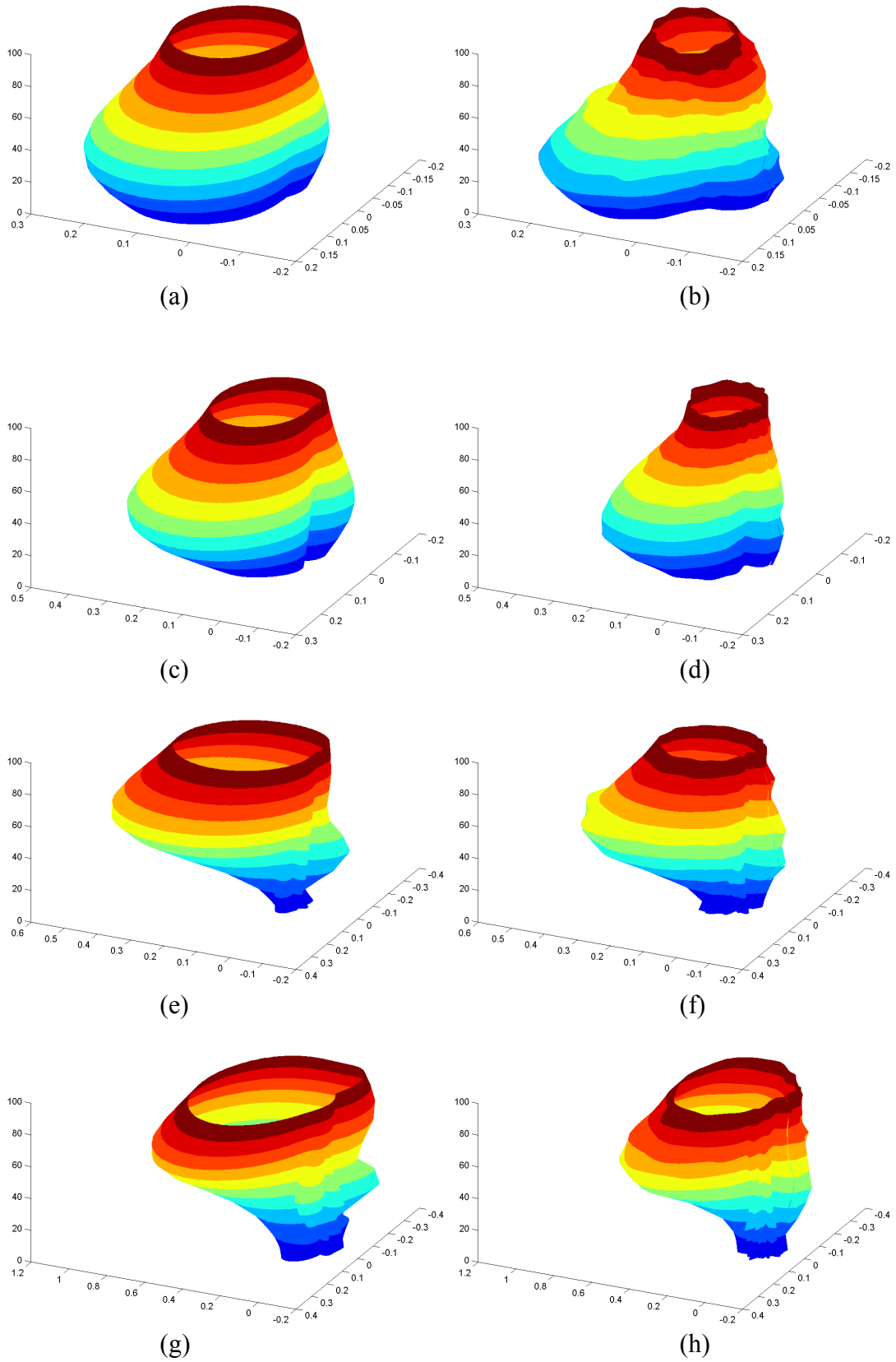
(a)
(b)
(c)
(d)
(e)
(f)
(g)
(h)

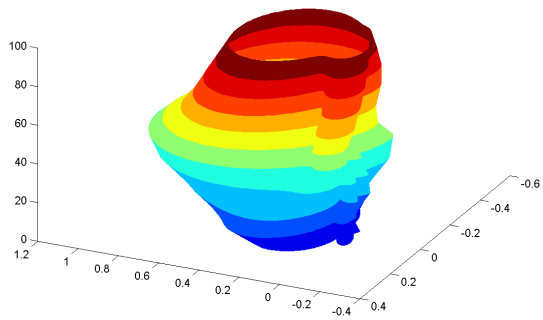

(i)

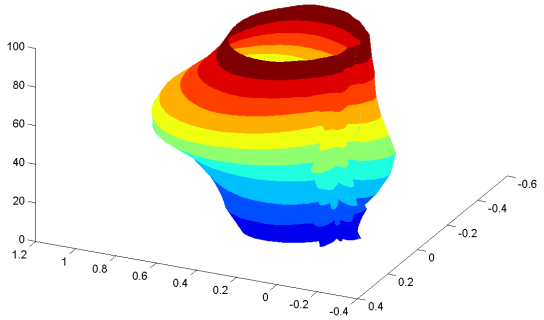

(j)

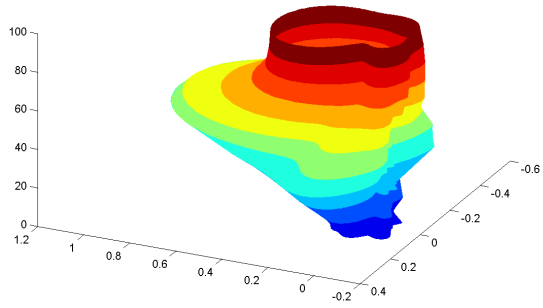

(k)

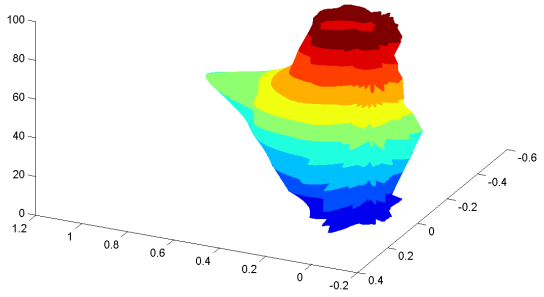

(l)

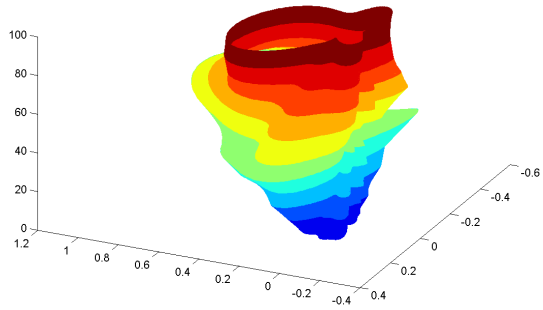

(m)

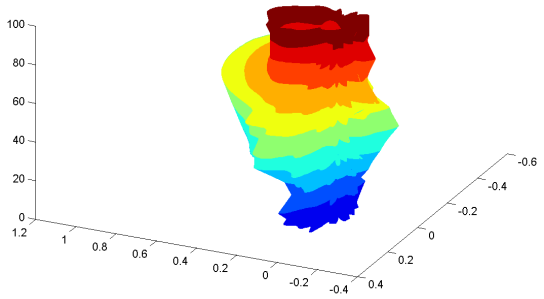

(n)

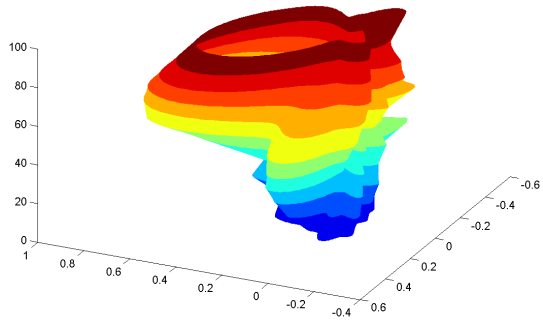

(o)

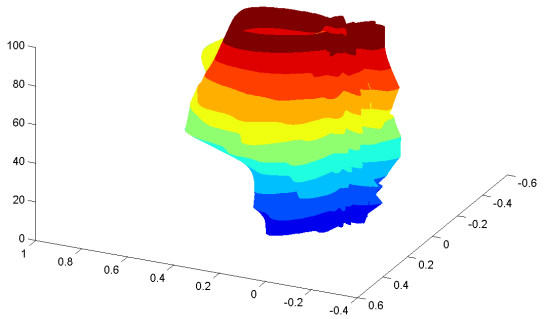

(p)

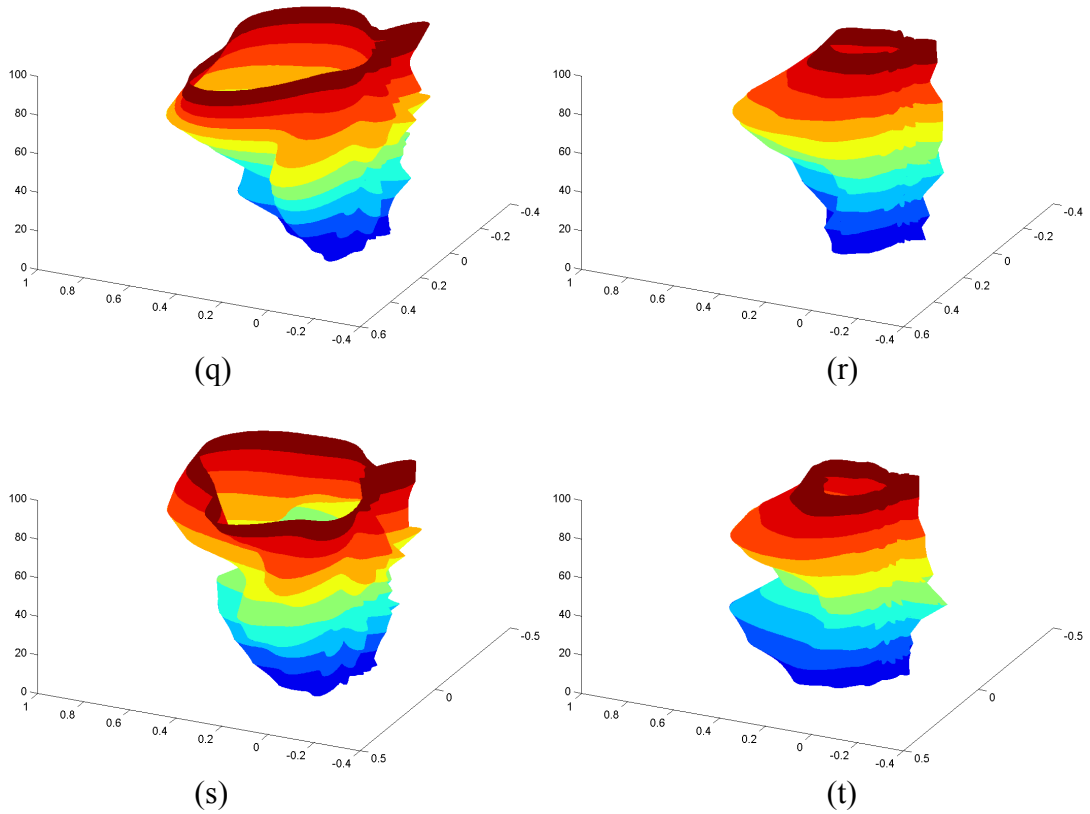

Figure 6.17. Comparison of Flex and experimental directionality from 10 - 100kHz windowed toneburst in 3D. The colours are used simply to delineate between results taken at different heights, and do not relate to any signal characteristic. (a) Flex 10kHz; (b) Experimental 10kHz; (c) Flex 20kHz; (d) Experimental 20kHz; (e) Flex 30kHz; (f) Experimental 30kHz; (g) Flex 40kHz; (h) Experimental 40kHz; (i) Flex 50kHz; (j) Experimental 50kHz; (k) Flex 60kHz; (l) Experimental 60kHz; (m) Flex 70kHz; (n) Experimental 70kHz; (o) Flex 80kHz; (p) Experimental 80kHz; (q) Flex 90kHz; (r) Experimental 90kHz; and (s) Flex 100kHz; (t) Experimental 100kHz.

6.3.2 Simulation Validation – Time Domain Results

It has previously been indicated that, although frequency domain extrapolation was performed to produce the directional plots, time domain extrapolation could equally have been used, with directional response acquired simply by extracting peak amplitude data from the time domain trace at each elevation and angular position. As such, it is to be expected (and indeed is the case) that amplitude comparisons in the time domain provide no further useful information on the correlation between each set of results. Rather, time domain comparisons are made as a means of validating the use of PZFlex for time domain simulation of the signals transferred to the inner ear of the bat as a result of returning echolocation signals.

Time domain comparisons are displayed in Appendix B at 0mm, 20mm and 50mm elevations at an angular resolution of 30˚ for frequencies of 10kHz, 30kHz, 50kHz, 70kHz and 90kHz. In addition to results obtained using the windowed toneburst, a further comparison was made using a recorded *R. aegyptiacus* call as the driving function. To keep this Chapter to a reasonable length, only a limited number of Figures are duplicated here where a specific point or comparison is to be made.

The simulations for these results were run using a different pressure load applied to the base of the ear canal, than was used for the directional comparisons. The input to the ear canal in the experimental configuration was measured using the B&K microphone inserted into the top of the ear; this signal was then applied as the driving function in PZFlex, such that the simulation input waveform was as accurate as possible. This had minimal effect on the simulated amplitude response, but took into account the effect of the feed-cone on the time domain signal propagated via the ear structure.

As with the directional comparison, it can be seen that generally good correlation is seen between experimental and simulated time domain results. The effect of simulating the propagation of the actual signal measured at the input to the ear canal is only really noticeable at 10kHz, where the wavelength of the signal (and hence time duration of the toneburst) allows reverberating echoes from within the feed-cone to overlap. The duration of a 10-cycle 10kHz toneburst is 1ms; the transit time through the cone of 100mm height is approximately 0.3ms, and so reflections occurring within the cone approximately 0.6ms later overlap with the original toneburst. (At higher frequencies, this is no longer the case. For example at 20kHz, the duration of the toneburst is just 0.5ms and so reflections do not quite overlap with the original signal. At 30kHz, the next frequency displayed in the results, the toneburst duration of 0.33ms ensures a significant gap between the original toneburst and subsequent echoes within the cone; the resulting waveforms are very similar to those obtained with a single toneburst input.) At 10kHz, this effect results in the multiple peaks of the signal envelope, with adjacent peaks separated by approximately 0.6ms. This can be seen in Figure 6.18.

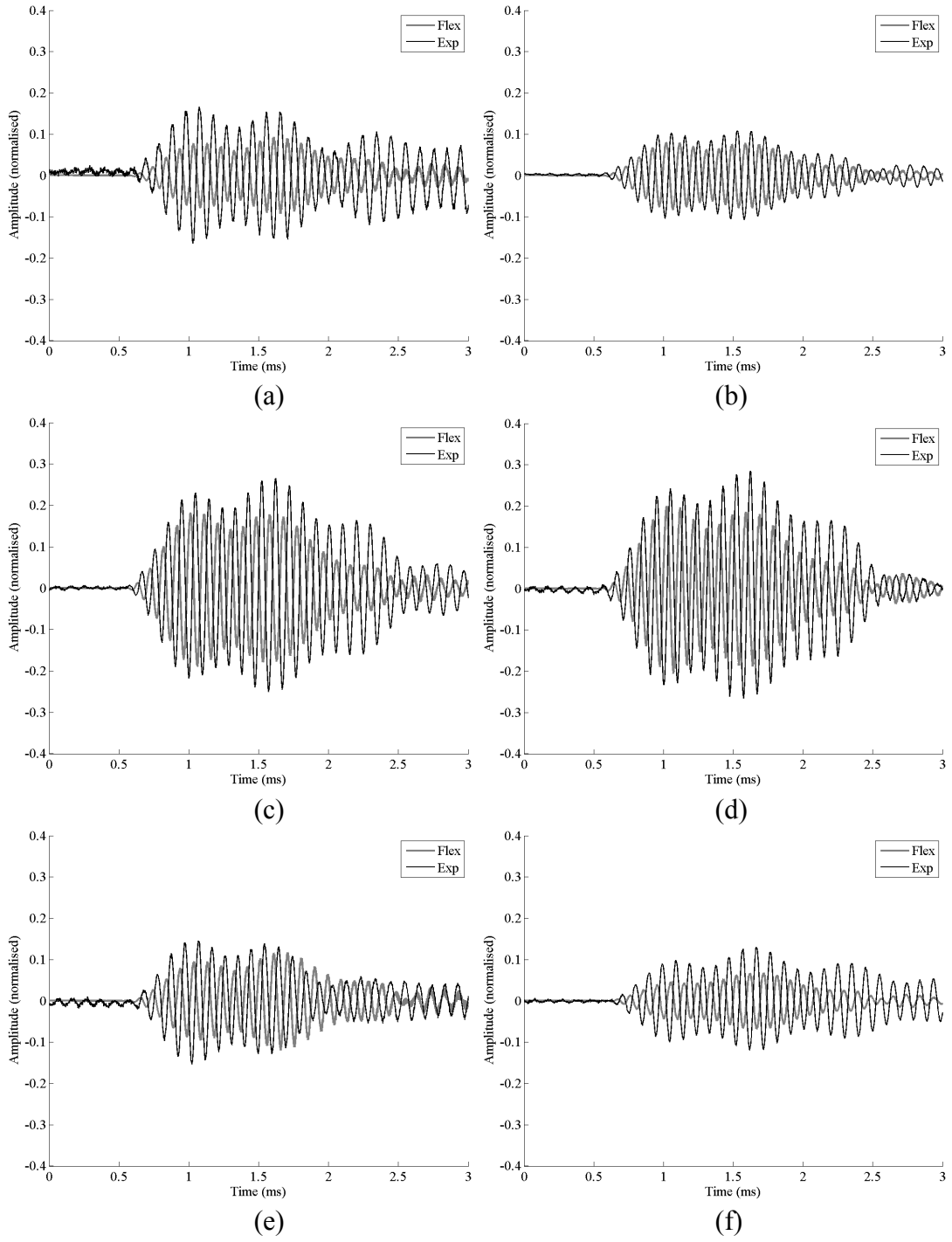

Figure 6.18. Comparison of simulated and experimental waveforms from a 10kHz toneburst at a height of 0mm with respect to the base of the ear at: (a) -120˚; (b) -60˚; (c) 0˚; (d) 60˚; (e) 120˚; (f) 180˚

Given the potential misalignment of the experimental apparatus, with respect to the simulated environment discussed in the previous section, some time domain offset between the two sets of results is inevitable. However, it can be seen that the initial

arrival time of the propagated energy is well matched (within approximately half a wavelength at 10kHz, or 50μs), although the waveforms themselves do not tie up exactly. At 10kHz, the envelope of the experimental signals is well simulated by PZFlex indicating the validity of these results. As the frequency is increased, in general the envelope of the signals is simpler since it is due to only a single toneburst. Examining the results obtained at 30kHz excitation, the comparison between the two sets of results is easier to make since the signal is shorter with less cycles and so easier to judge. It can be seen that at certain points, the simulated and experimental results match almost perfectly in the time domain, as demonstrated in Figure 6.19, although the respective amplitudes vary, as discussed previously.

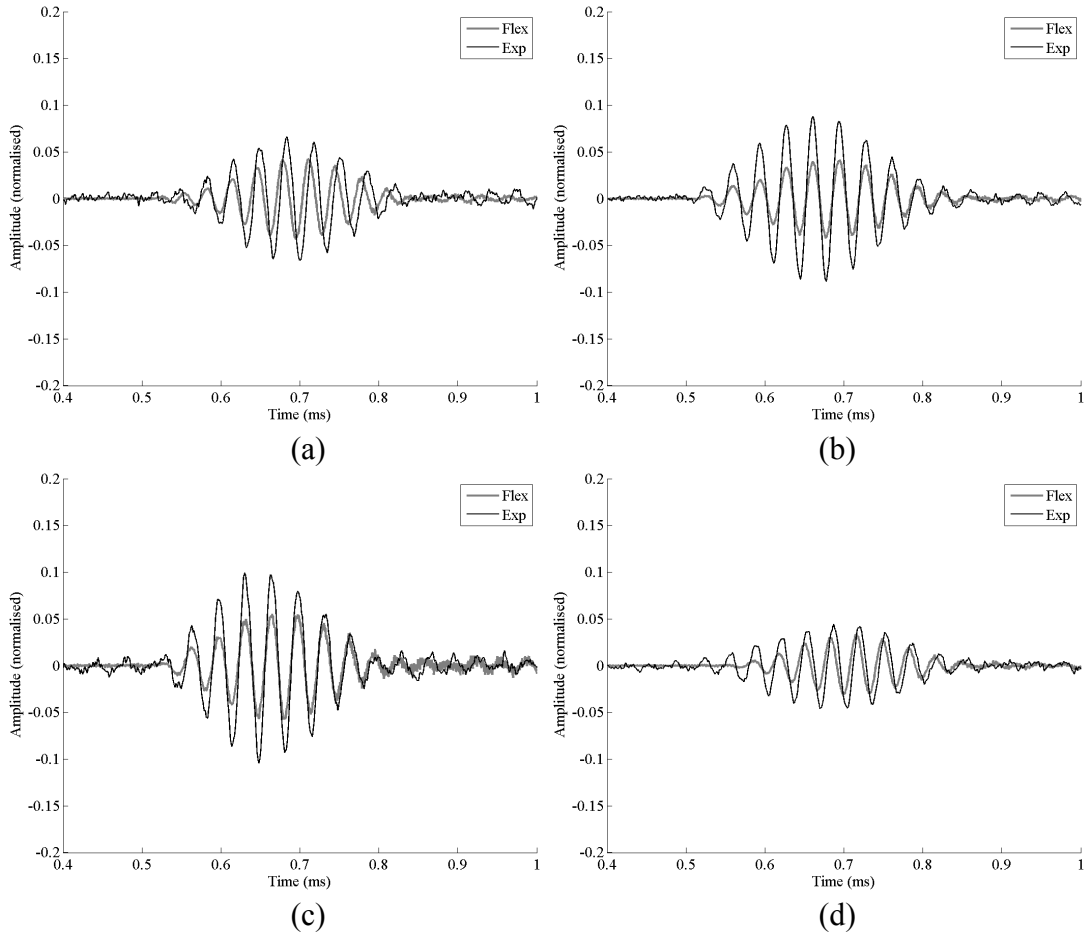

Figure 6.19. Comparison of simulated and experimental waveforms from a 30kHz toneburst at a height of 0mm with respect to the base of the ear at: (a) -120˚; (b) 60˚; (c) 90˚; (d) 150˚.

At most points for these higher frequencies, the envelope of the signal is a simple toneburst. However, there are points at which the response of the ear causes the original toneburst to split, recombining at the microphone to generate interference between two separate tonebursts. At 30kHz this can be seen at 0mm elevation / -60˚ rotation, and at 20mm elevation / 60˚ rotation, as shown in Figure 6.20. Examination of these plots illustrates how accurately the simulated results predict these more complex waveforms with the double-peak of the envelope well defined. It is no coincidence that these interfering waveforms are generated at these lower elevations, as they are the product of the toneburst emanating from the ear canal refracting around the ear in different directions, to recombine in the direction of the microphone. At higher elevations, this will have less effect as the energy travels a more direct route from ear canal to measuring point via the pinna or refraction around the top of the ear, rather than refraction around either side.

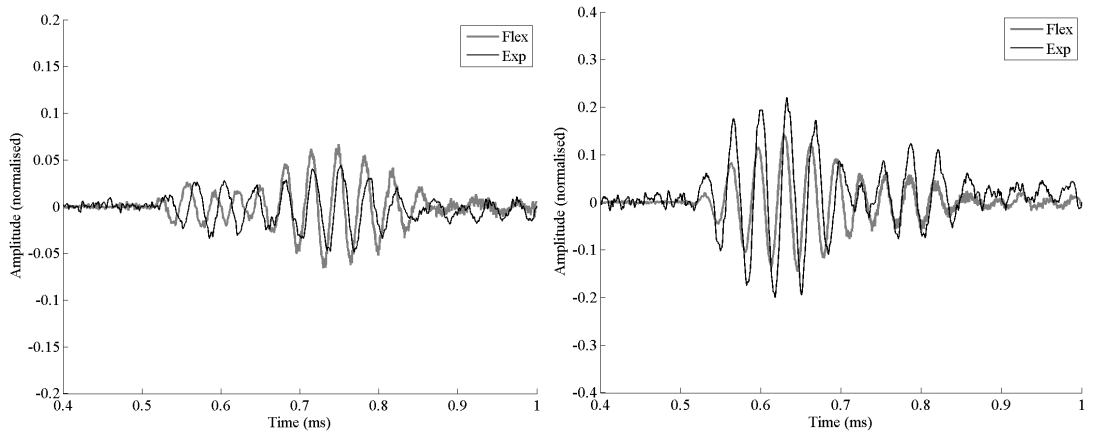

Figure 6.20. Comparison of simulated and experimental waveforms from a 30kHz toneburst at: (a) 0mm elevation / -60˚ rotation; (b) 20mm elevation / 60˚ rotation. This demonstrates how FEA can accurately predict the recombination of two different reflection generated within the ear.

At 50kHz, the correlation across both elevation and rotation is again good, with some exceptions. For example at 0mm / 60˚, the experimental interference envelope is not matched by PZFlex, whilst at 0mm / 150˚ these comparisons are reversed as indicated in Figure 6.21. However, these are the exception rather than the rule. This is true even where some distortion of the original Hanning-window is evident, such as in the elongated envelope of the signals at 0mm / -60˚ and 0mm / 30˚ (Figures 6.22(a) and (b)), the small second peak at 0mm / 180˚ (Figure 6.22(c)), the time-delayed peak at 20mm/150˚ (Figure 6.22(d)) or the asymmetric peak at 50mm / 30˚ (Figure 6.22(e)). These results generate confidence that the simulated results are well matched to the experimental ones, even in areas where the complex geometry of the ear leads to interesting combinations of multiple tonebursts due to refraction and recombination along separate signal paths.

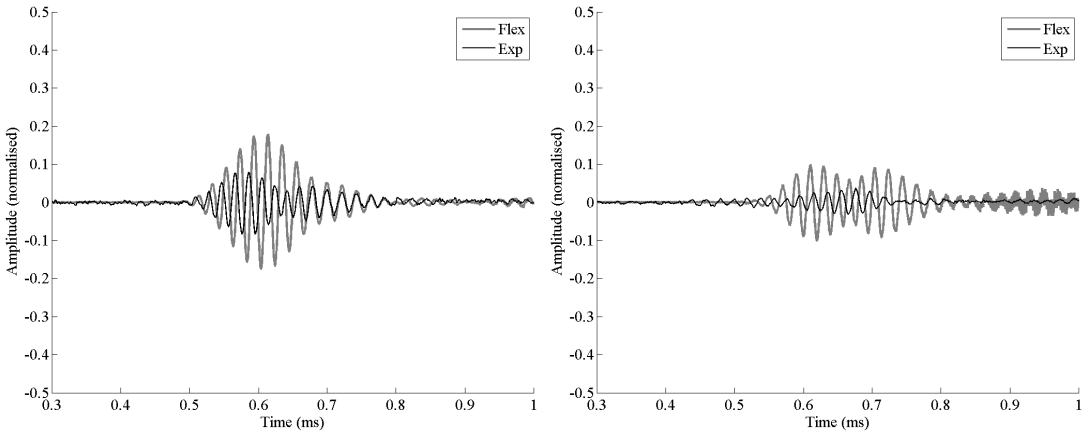

(a) (b)

Figure 6.21. Comparison of simulated and experimental waveforms from a 50kHz toneburst at: (a) 0mm elevation / 60˚ rotation; (b) 0mm elevation / 150˚ rotation. This demonstrates two points at which the envelope of the experimental result is not matched by FEA simulation.

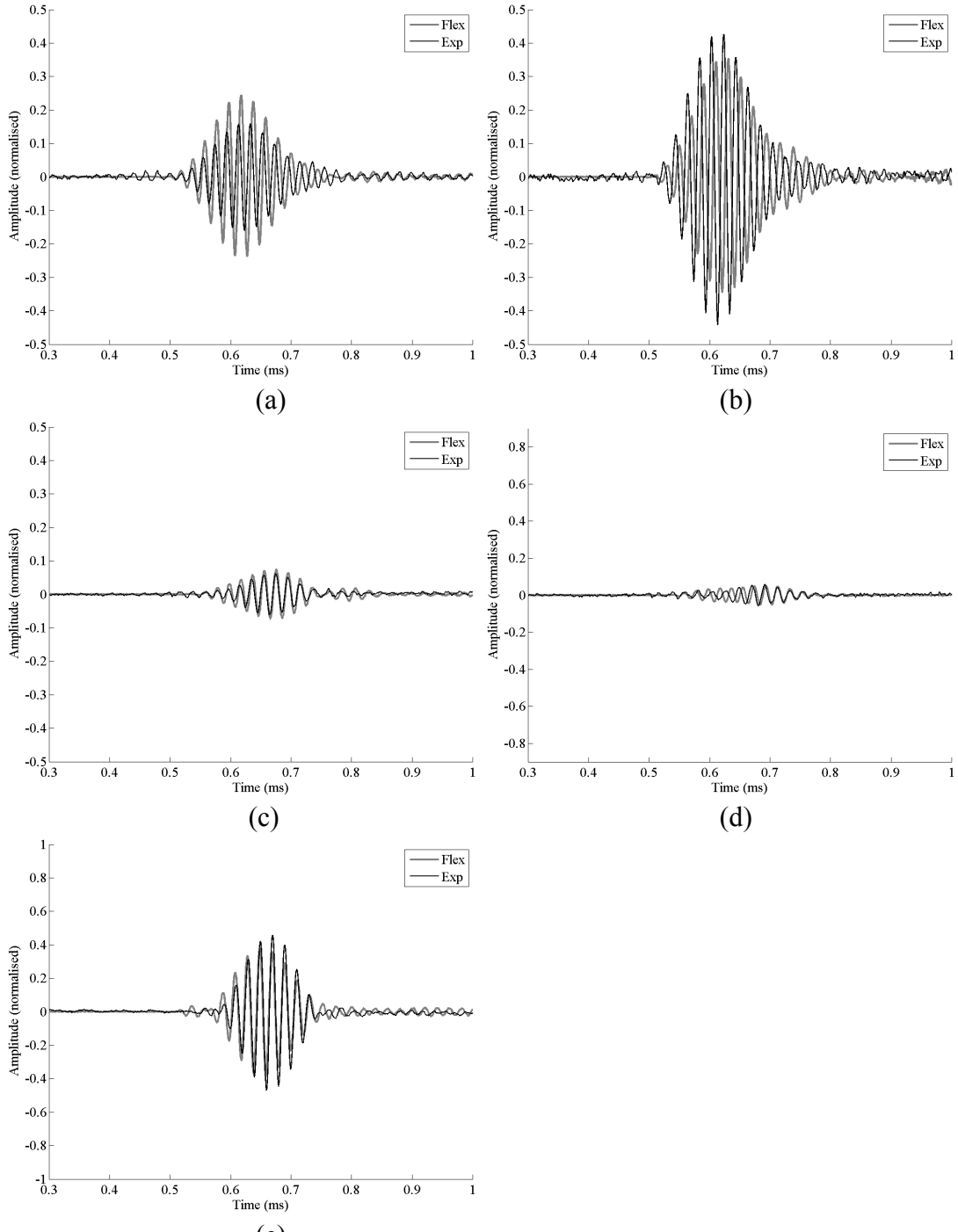

Figure 6.22. Comparison of simulated and experimental waveforms from a 50kHz toneburst at: (a) 0mm elevation / -60˚ rotation; (b) 0mm elevation / 30˚ rotation; (c) 0mm elevation / 180˚ rotation; (d) 20mm elevation / 150˚ rotation; (e) 50mm elevation / 30˚ rotation.

At the higher frequencies, above 50kHz, as with the directional results there is a more noticeable departure between the sets of results, and this is especially true for

the data taken at 0mm elevation. Examples of this can be seen at 70kHz in Figure 6.23. However, even in these figures it can be seen that some form of envelope-splitting is evident in the simulated results, although these tend to be to a greater or lesser extent than indicated by the experimental results. As with the directional results, these discrepancies become less marked at greater elevation; this can be seen in Figure 6.24 at 50mm elevation, with envelope splitting and toneburst distortion well correlated between both results. Even where this correlation is less exact, signal distortion is present, an indication that the experimental misalignment noted previously may again be having an effect. Furthermore, as with the directional comparison, it can be seen that increasing frequency and lower elevation add to any divergence between the two sets of results, due to the increasing complexity these factors bring to the emitted acoustic field, meaning that any positional inaccuracy will have a greater effect. A similar trend of results can be seen in time domain traces obtained at 90kHz.

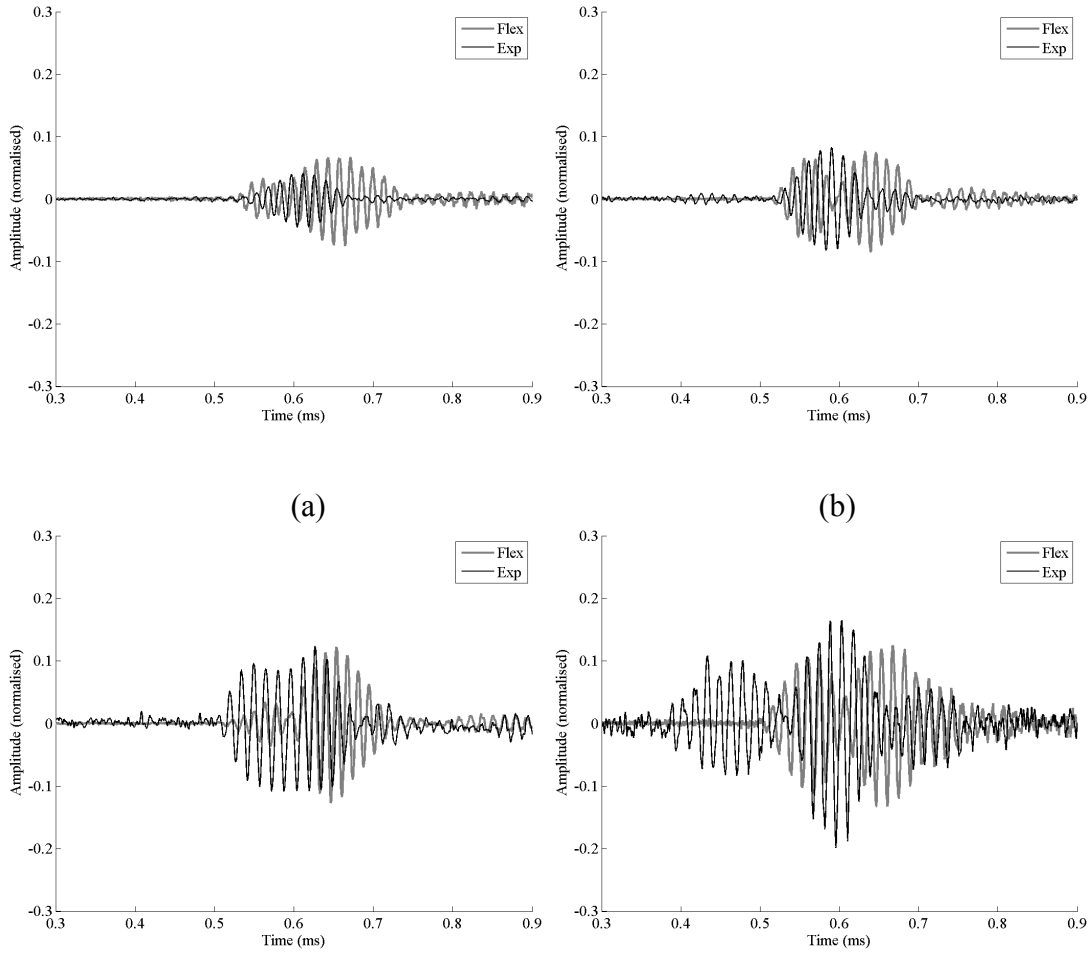

Figure 6.23. Comparison of simulated and experimental waveforms from a 70kHz toneburst at a height of 0mm with respect to the base of the ear at: (a) -120˚; (b) -90˚; (c) -30˚; (d) 120˚.

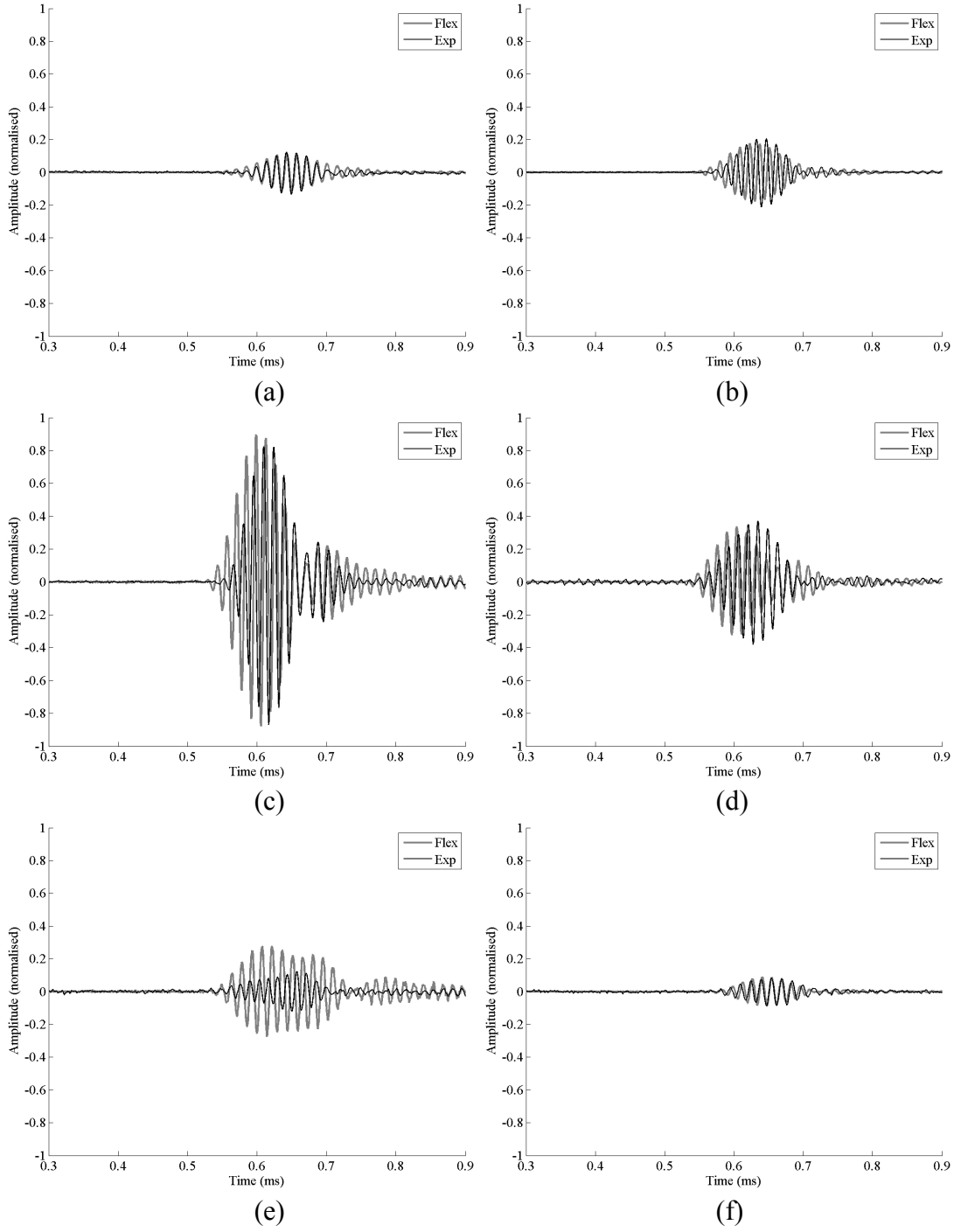

Figure 6.24. Comparison of simulated and experimental waveforms from a 70kHz toneburst at a height of 50mm with respect to the base of the ear at: (a) -120˚; (b) -60˚; (c) 0˚; (d) 60˚; (e) 120˚; (f) 180˚

Final validation of PZFlex simulation was performed using a call recorded from the bat *R. aegyptiacus* itself using the wireless sensor detailed in Chapter 3. This call was transmitted in the same way as the tonebursts used earlier, with the input to the simulation measured in the same way with the B&K microphone inserted into the μSL ear canal. Previous results demonstrate the accuracy of the simulation to tonebursts across a wide frequency range from 10kHz to 100kHz, whereas this simulation was performed to show its validity with a wider-band echolocation signal. As with the 10kHz toneburst, the length of the *R. aegyptiacus* echolocation call generated multiple overlapping echoes within the cone and so propagating into the surrounding air via the ear canal and pinna. Full results are again provided in Appendix B, but results obtained at 0mm are depicted in Figure 6.25. The correlation at all elevations and angular displacements is very good, as would be expected to be the case given the previous results at 10kHz and 30kHz; the spectral composition of the *R. aegyptiacus* echolocation call falls generally within this frequency range (see section 3.4.1.2). It is interesting to note that the temporal alignment of the two sets of results appears to get progressively worse as elevation increases, indicating that the experimental alignment was somewhat inaccurate, as previously noted, in such a way as to cause this effect.

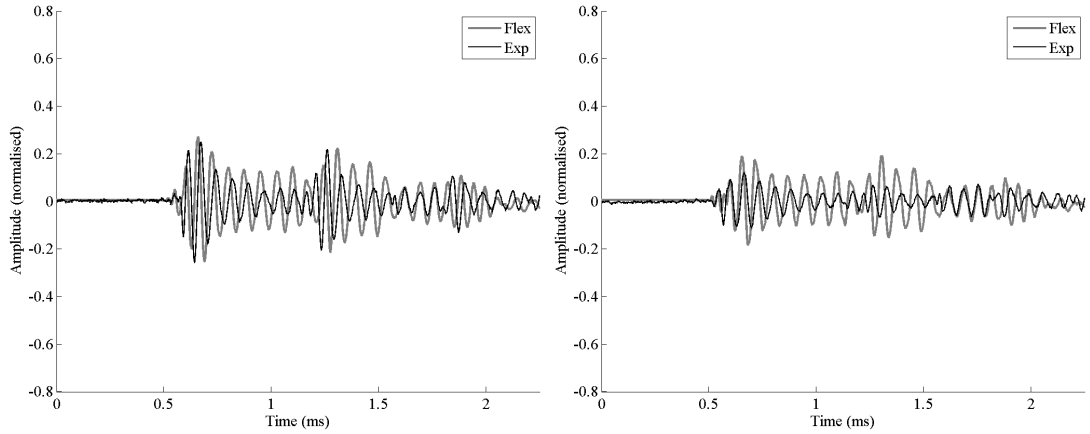
Flex
Exp
Amplitude (normalised)
Time (ms)

(a)

Flex
Exp
Amplitude (normalised)
Time (ms)

(b)

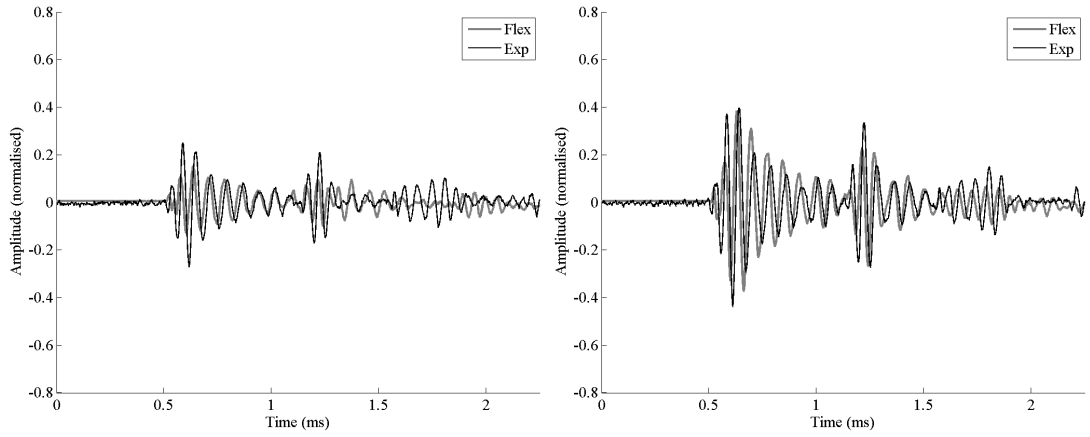
Flex
Exp
Amplitude (normalised)
Time (ms)

(c)

Flex
Exp
Amplitude (normalised)
Time (ms)

(d)

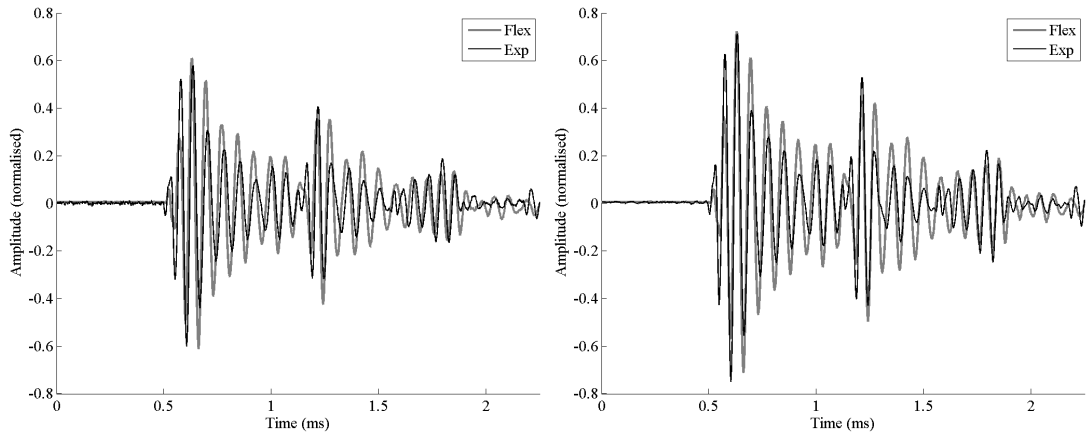
Flex
Exp
Amplitude (normalised)
Time (ms)

(e)

Flex
Exp
Amplitude (normalised)
Time (ms)

(f)

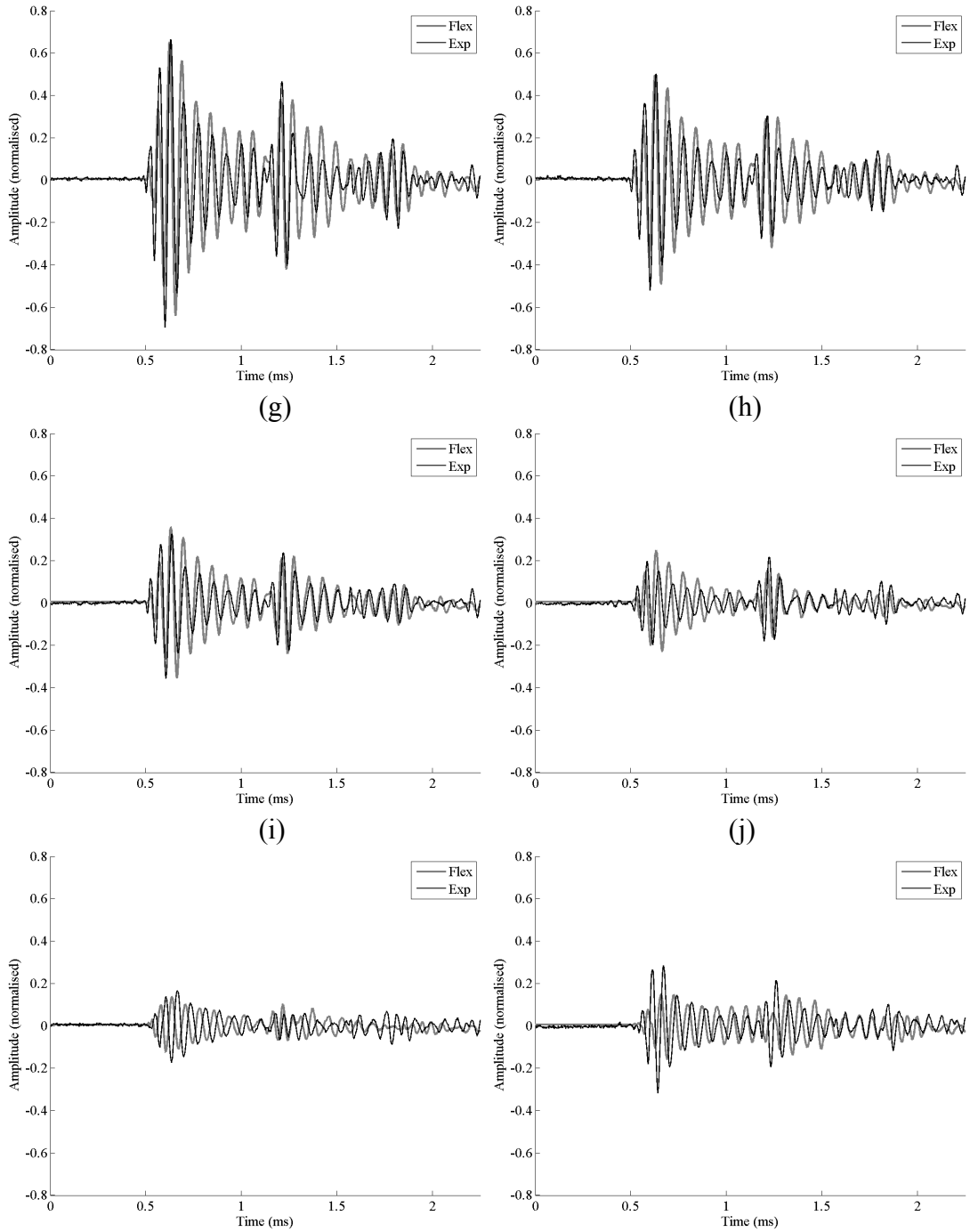

Figure 6.25. Comparison of simulated and experimental waveforms from a *R. aegyptiacus* call at a height of 0mm with respect to the base of the ear at: (a) -150˚; (b) -120˚; (c) -90˚; (d) -60˚; (e) -30˚; (f) 0˚; (g) 30˚; (h) 60˚; (i) 90˚; (j) 120˚; (k) 150˚; (l) 180˚

6.4 Simulation of *Rousettus* Ear Response

The results detailed and discussed in the previous sections validate the use of PZFlex simulation of the *R. leschenaulti* ear. As such, the model was then used to investigate the response of the ear to the call of *R. aegyptiacus* as it impacts on the pinna from a variety of origins in the environment around the ear. This was done to investigate any monaural cues that could be provided to the bat as to the origin of the reflected signal returning to the bat. It is well known that bats use both binaural ITD or IID to determine the origin of an echo, but it has also been demonstrated that transformation of sound by the outer ear structure can provide monaural cues regarding the location of the origin of the echo. Simulation can allow these cues to be investigated by generating a sound field in the model, which propagates as if its origin was at a given location external to the model space itself. The response of the ear to this stimulus is demonstrated by extracting the time-history of the wave as it passes through the same surface of air elements at the base of the ear, inside the ear canal, as was used to apply the pressure load in the validation model. Pressure was extracted as an average across these elements.

6.4.1 Generation of an Origin-Specific Sound Field in the PZFlex Model

As the location of a sound source changes in relation to the ear, then the sound field that impacts on the ear changes correspondingly. The specific pressure field generated by any signal from any given origin can be simulated in PZFlex, providing that the pressure waves incident on the boundaries of the model are accurately applied to the elemental spaces on those boundaries. In the previous validation model, the input pressure load was applied to the boundary between the *air3* and *air1* elements; the plane of air across base of the ear canal. For the purposes of model validation, the input pressure wave was assumed to be planar, and perpendicular to this plane, and so the same input signal was applied to each element. However, when the origin is located at some point external to the ear, then the radiating pressure wave crosses each point (or in the case of PZFlex, each element) on the boundaries of the model with varying phase, related to the varying distance travelled from the sound origin. It is also the case that the amplitude of the signal, and its frequency

content will vary marginally between these points, but given the dimensions of the model these minor variations were considered to be negligible. Similarly, as the wave propagates through air externally to the model, its frequency characteristics will alter according to the frequency-dependent attenuation coefficient of air; again, this has been neglected as the distance considered (1m) is sufficiently short to make little difference across the frequency range considered (approximately 3dB over 10kHz-100kHz) and the only difference this would make would be to affect the relative amplitudes of the spectral components within the signal. In terms of the response of the ear, these external effects are of less interest than the response of the ear to the full-bandwidth signal.

Pressure loads in PZFlex are applied via the PLOD command, which allows an arbitrary signal to be applied to any of a variety of elemental configurations (e.g. single element, rectangular array of elements, boundary between two materials or objects) and further provides the option to apply a defined delay to that signal. As such, by applying the input signal with the appropriate delay to the elements on the boundaries of the model, the wave will propagate through the model space as it would by radiating from a given external point. The appropriate delays were calculated using Matlab. The position of each boundary of the model was defined in Cartesian coordinates, along with the location of the signal source. The source location was initially defined in polar coordinates - (theta, phi, r) or (θ, φ, r) - to easily define both horizontal (θ) and vertical (φ) angular variation, but was converted to Cartesian to simplify the calculation of distance between the source and each element of the boundary. In all results, the source location will be referred to in polar coordinates.

Depending on the location of the sound source, up to three sides of the model could be insonified by the wave on its way *into* the model. The transit time between the source and each element on each of the appropriate sides was calculated – this is particularly efficient when done in Matlab as it can be calculated in matrix form. The *minimum* transit time was then subtracted from each value to produce an array of delays relative the first arrival time of the pressure wave at the external boundaries of the model. Each of these delays was then read into Flex as an individual variable, to

be applied to the appropriate element on the insonified boundaries of the model. In fact, PZFlex limits the number of variables (or *symbols*) that can be declared in a file to 50000. Since the model is made up of 185×162×268 elements, then approximately 123000 symbols would be required to store the delays if three sides on the model were insonified; even two sides would require some 93000. As such, delays were calculated and loaded onto the boundaries in groups of 2×2 elements, with a maximum number of symbols required limited to 31000. Since pressure in Flex is an *elemental* quantity, dividing the boundaries into 2×2 element sources is akin to having a 2D array with an element pitch of 230μm, or λ/15 at 100kHz – more than sufficient to accurately direct the propagating wave.

6.4.2 The Effect of Source Location on the Sound a Bat Hears – *R. aegyptiacus* Call

Using the methodology detailed in the previous section, the call of *R. aegyptiacus* was applied to the model as if generated from a point 1m distant, at an elevation angle of 0˚ (φ = 0˚) and a horizontal angle (θ) varying from -90˚ to +90˚ in steps of 10˚. Effectively this investigated the echo returning to the bat from the hemisphere in front of the bat, disregarding the hemisphere behind the bat from which echoes obviously cannot originate. Whilst in flight and echolocating, *R. aegyptiacus* moves its ears backwards as it emits an echolocation call, and forwards to face the direction of flight (and call emission) in the time interval up to the next call emission (Holland and Waters, 2005). This appears to be used as a gain control mechanism, reducing the level of the emitted call heard by the bat, but increasing the gain produced by the pinna for sounds returning from in front of the bat. This being the case, the reference 0˚ angle was taken to be that which provided the most gain, and generated the largest signal in the ear canal.

The literature indicates that both time and frequency domain information is used by the bat, and so Figure 6.26 depicts the time domain traces generated across the ear canal, whilst the spectral composition of these traces is illustrated in Figure 6.27. The data presented in Figure 6.26 has been normalised across the entire set of results, with the y-axis used to label the traces according to the horizontal angle (θ) of the

sound source. In Figure 6.27, each trace is normalised and displayed over the amplitude range -40dB to 0dB, to demonstrate spectral differences between the traces without any influence from amplitude variation. Probably the most interesting aspect of these results is that there are few differences between the traces, in either the time or frequency domain. In the time domain, the amplitude of the signal can be seen to vary significantly with θ; its time of arrival also varies, but only by approximately 20μs. However, neither of these effects in themselves can provide significant monaural information since there is no "benchmark" signal against which to compare the detected signal in active echolocation. As such, variation in amplitude could be due to angular effects, or target size. Similarly, arrival time could be interpreted in terms of angular or distance variation. In the frequency domain, it can be seen that, with relative amplitude variations removed through normalisation, the traces are very similar. The location and depth of the only significant spectral notch (at approximately 12kHz) is almost constant across the entire set of results. There is some variation in the amplitude of higher frequency components, but it is arguable whether these minor variations would be sufficient for the bat to determine angle. In general, however, angular variation in the horizontal plane can be decoded from binaural information. If variation in the elevation angle (φ) is considered however, especially on the median sagittal plane, then neither IID nor ITD can be used to determine φ, since none will exist. In this case, monaural cues may be important for determining target location. Figures 6.28 and 6.29 depict the time and frequency domain traces resulting from varying φ from 0˚ to 90˚ in 10˚ steps, whilst keeping θ constant at 0˚. Again the time domain traces are normalised across all traces, whilst the frequency domain traces are individually normalised and displayed over a range of -40dB to 0dB. Again, there is a small difference in the arrival time (approximately 15μs) across the set of results and very little to distinguish the frequency domain traces from each other, excepting similar variations in the relative amplitude of the higher frequency energy, from 25kHz to 40kHz. As with the horizontal angle variation, there seem to be few evident cues the bat could take from monaural information to decode angular information. These results take on further significance when considered with those presented in the following section, where a coded FM signal is examined in a similar manner.

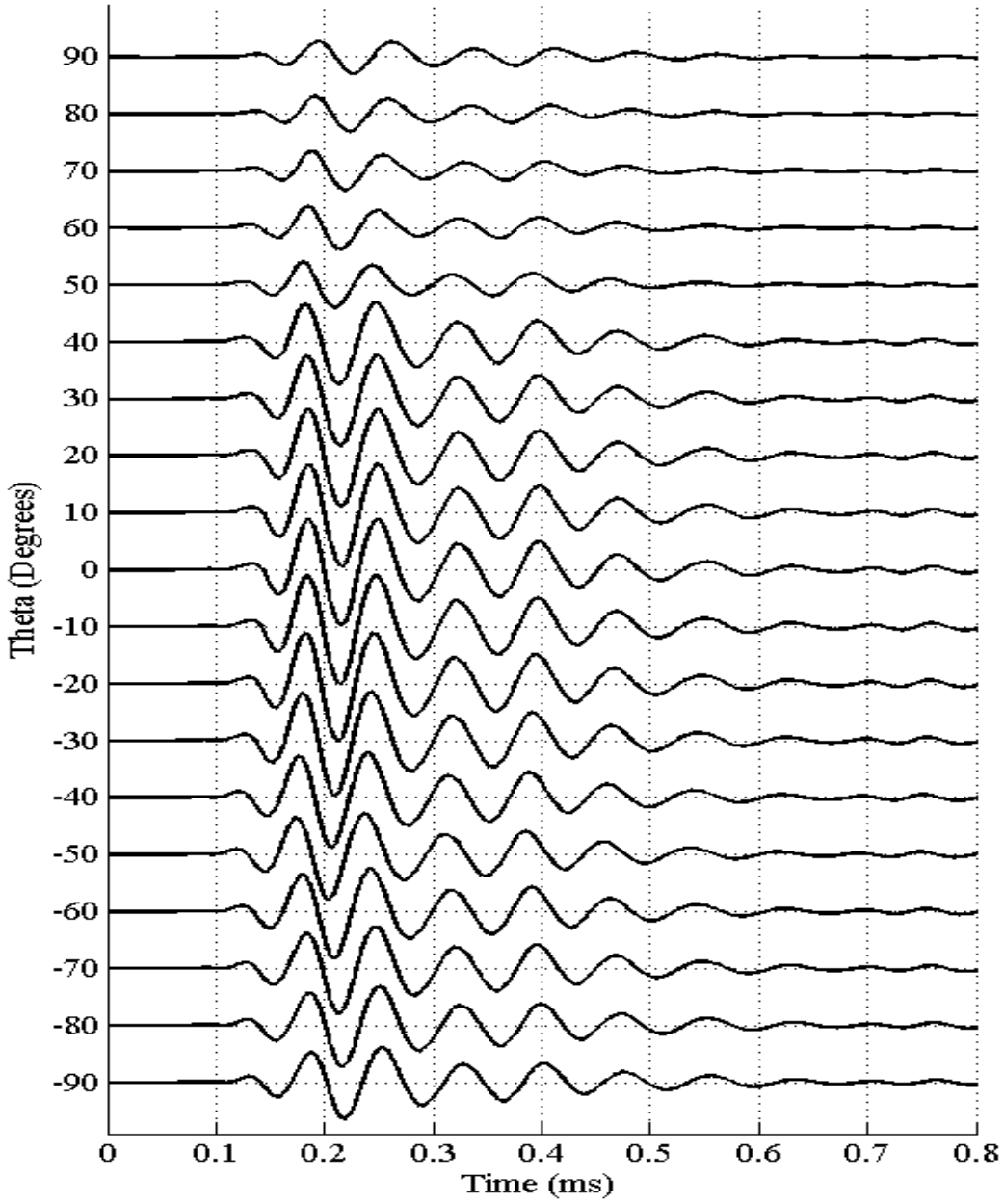

Figure 6.26. Time domain traces for the call of *R. aegyptiacus* as detected at the entrance to the ear canal for varying horizontal angle (θ) of sound source. Vertical angle (φ = 0˚) and distance (r = 1m) are kept constant.

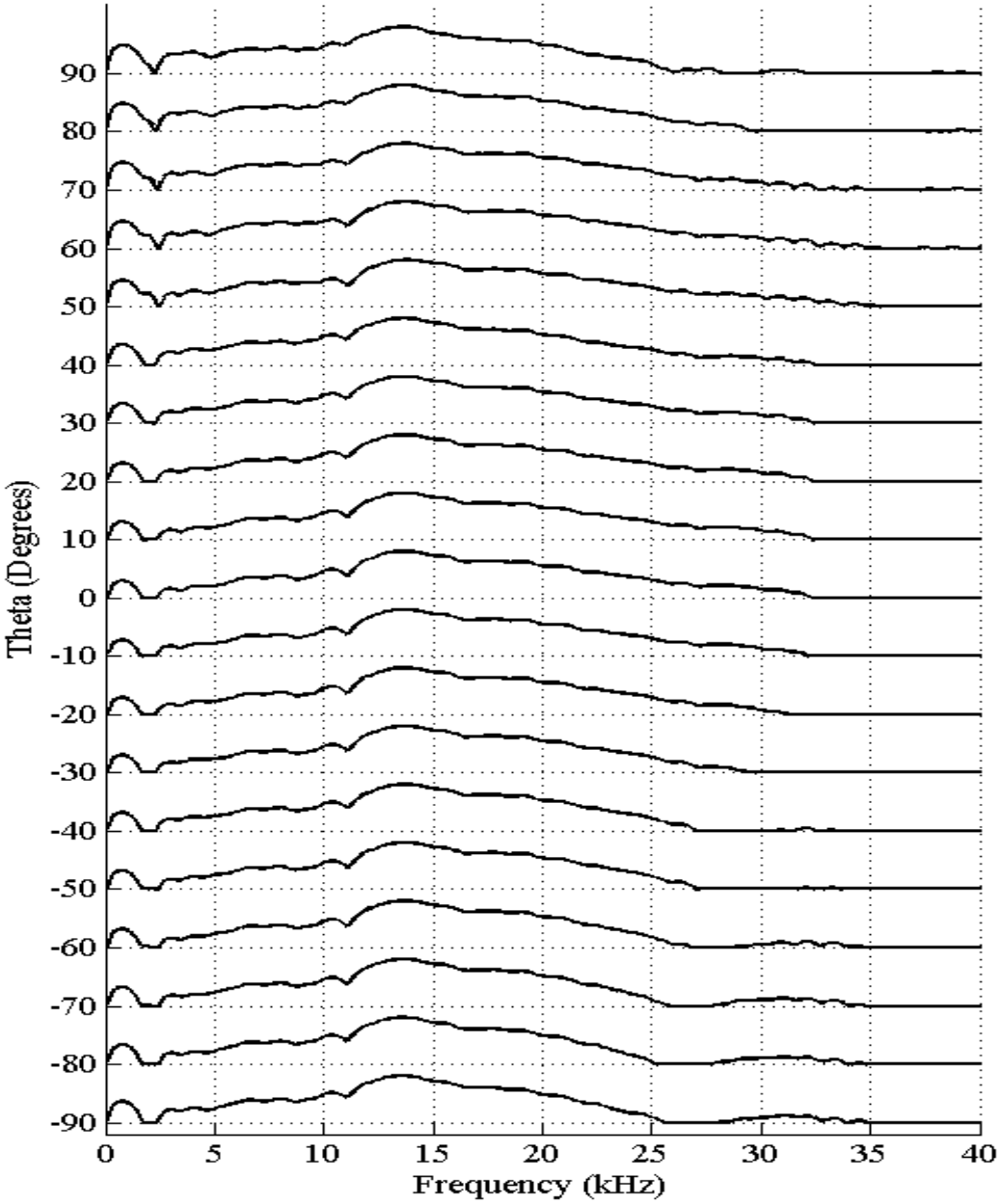

Figure 6.27. Frequency domain traces for the call of *R. aegyptiacus* as detected at the entrance to the ear canal for varying horizontal angle (θ) of sound source. Vertical angle (φ = 0˚) and distance (r = 1m) are kept constant. Each trace is displayed over the amplitude range -40dB to 0dB.

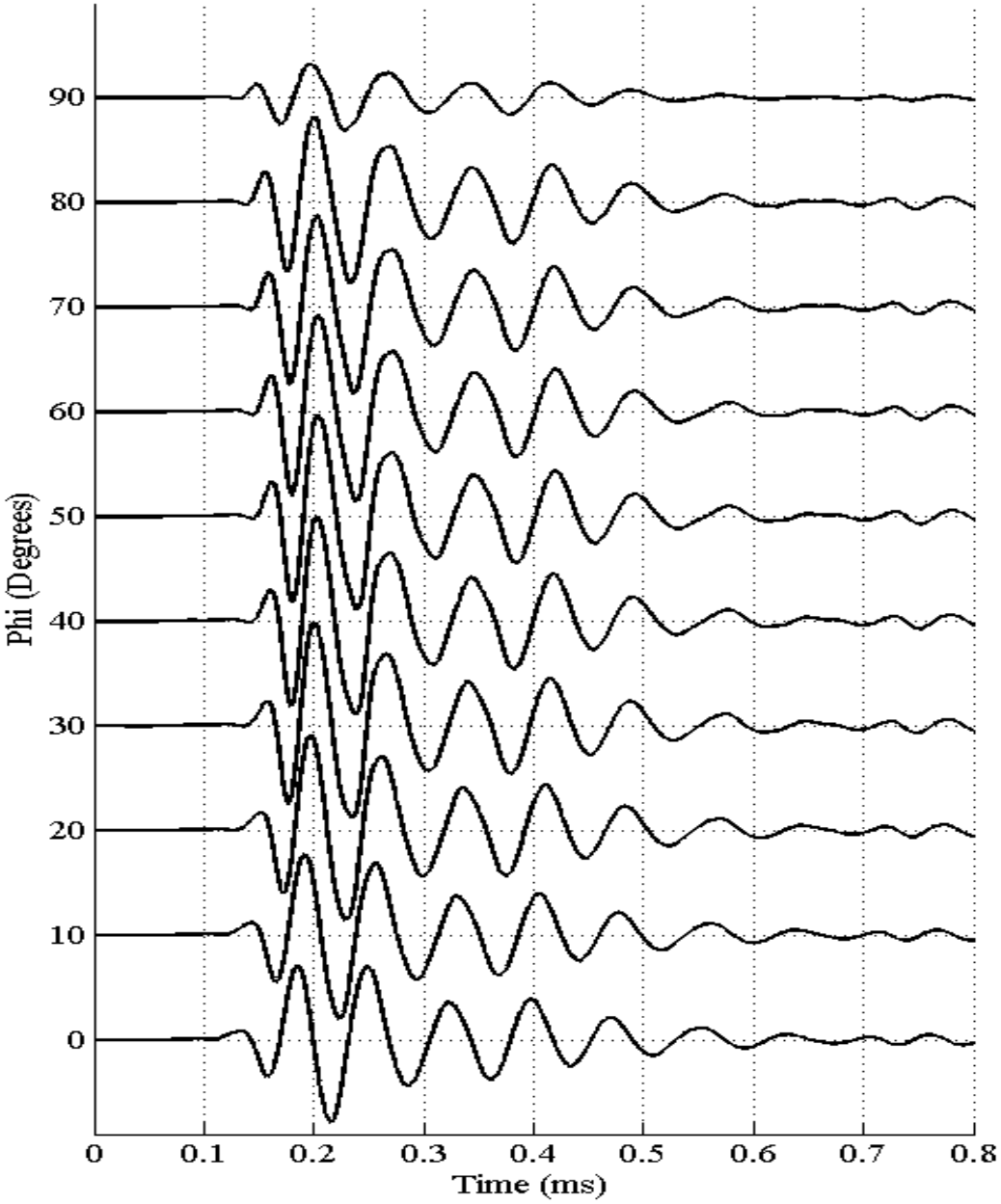

Figure 6.28. Time domain traces for the call of *R. aegyptiacus* as detected at the entrance to the ear canal for varying vertical angle (φ) of sound source. Horizontal angle (θ = 0˚) and distance (r = 1m) are kept constant.

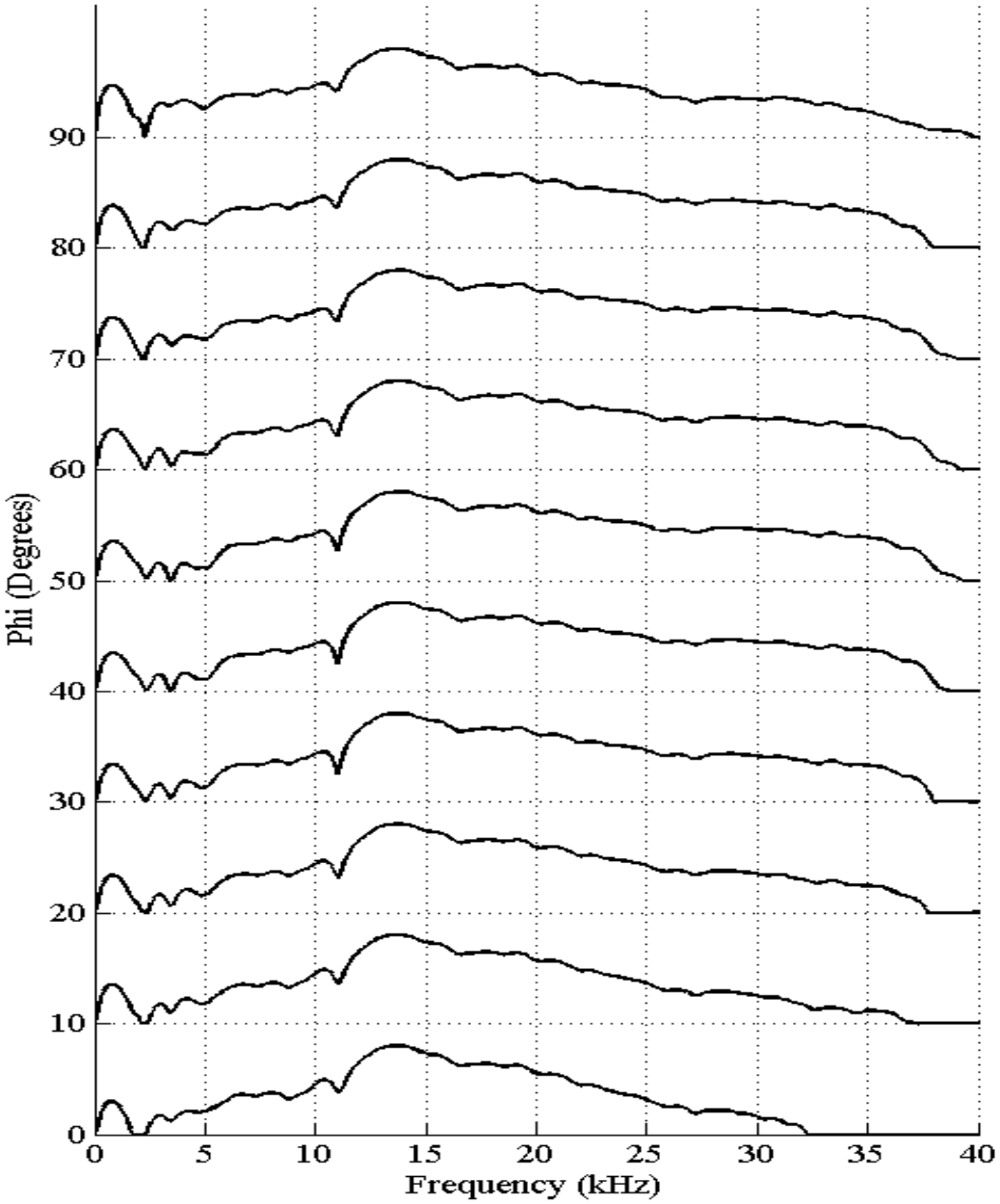

Figure 6.29. Frequency domain traces for the call of *R. aegyptiacus* as detected at the entrance to the ear canal for varying vertical angle (φ) of sound source. Horizontal angle (θ = 0˚) and distance (r = 1m) are kept constant.

6.4.3 The Effect of Source Location on the Sound a Bat Hears – FM Call

The simulations reported in the previous section were repeated, but using a 500μs quadratic FM chirp as the input. It was generated with initial and terminal frequencies of 120kHz and 40kHz respectively, and apodised with a 25% Tukey

window. Figure 6.30 illustrates this signal in the time and frequency domain as a comparison with the results of the simulations. It can be seen that the upper limit of its frequency content extends beyond 120kHz, due to the spectral content of the window function although the spectrogram (limited to -20dB, normalised) indicates limited energy above the 100kHz defined limit of the PZFlex model.

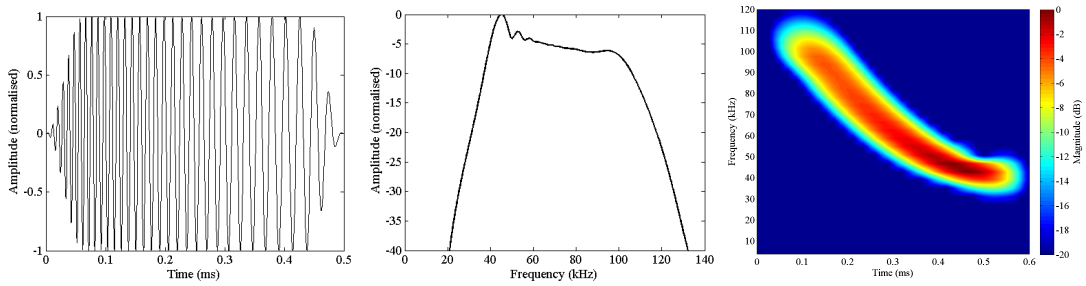

(a) (b) (c)

Figure 6.30. Time (a); frequency (b); and spectrogram (c) representations of the 500μs, 120kHz-40kHz quadratic FM signal.

Although this signal is artificially generated, it covers a very similar frequency range to that used by many FM bats (such as *Pipistrellus pipistrellus* or *Eptesicus fuscus*). As with the previous section, θ is initially varied between ±90˚ in 10˚ increments, with the time and frequency domain traces presented in Figures 6.31 and 6.32. In comparison with the previous results, there is significant variation apparent between each trace. The variation in the time domain is not so much in the time of arrival, but rather it can be seen that there are pronounced dips in the windowed signal. These then correspond with the spectral notches present in Figure 6.32, which vary in frequency and depth, whilst the general form of the FFT trace shows varying undulations. With the operation of the cochlea being time- and frequency dependent (higher frequencies activate cells further into the structure of the cochlea, and hence later in the time domain) it can be seen that this time / frequency information could provide the bat with cues as to the directional origin of each echo. Further evidence of this is provided by the spectrograms of these signals, displayed in Figure 6.33. Simulations were again repeated for varying φ between 0˚ and 90˚ in 10˚ increments to investigate the monaural cues that may be available to decode the vertical angular direction of the sound source. The results from these simulations are displayed in the time domain in Figure 6.34 and frequency domain in Figure 6.35, with the

corresponding spectrograms in Figure 6.36. This provides further evidence of the monaural cues available from a coded FM chirp.

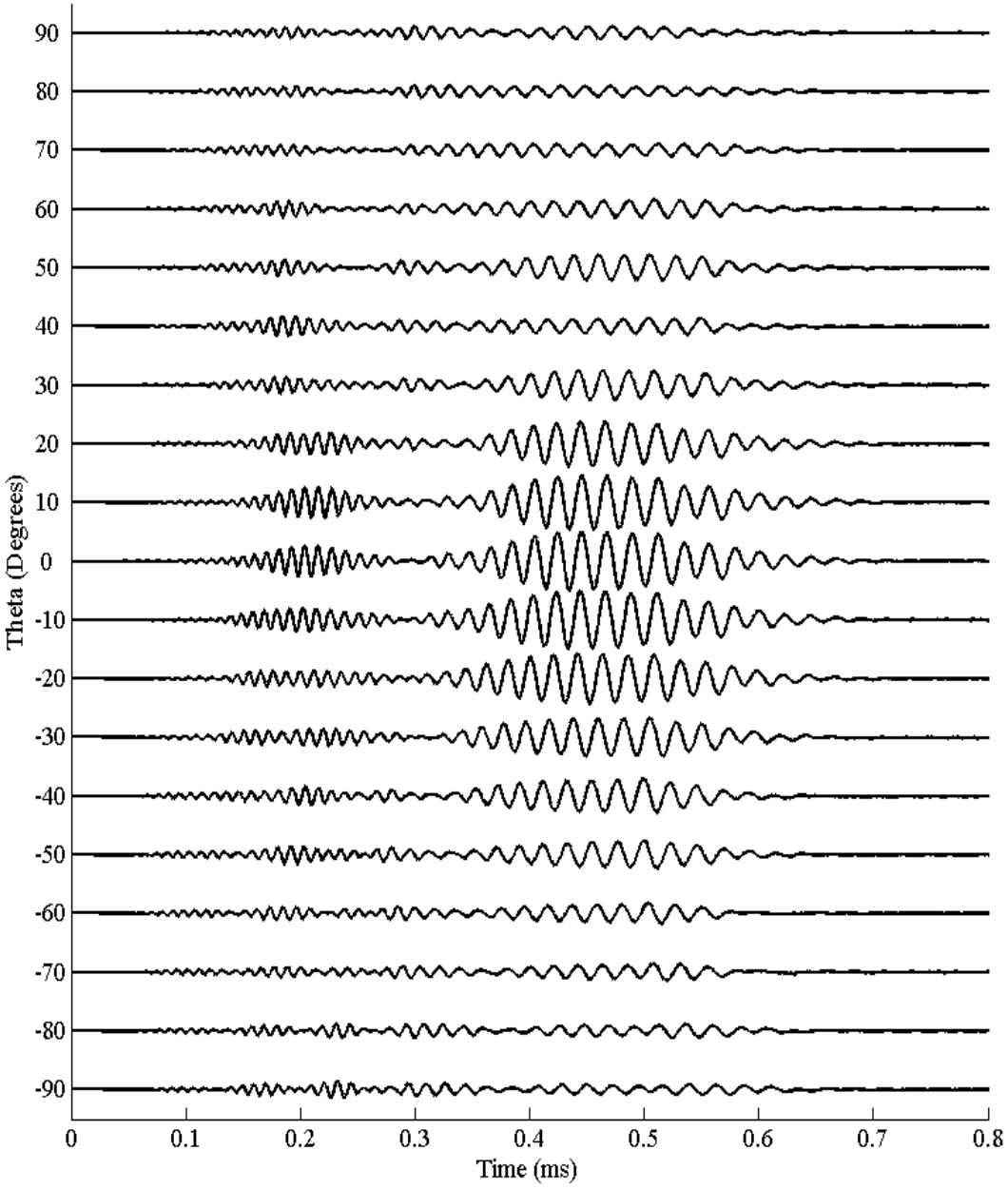

Figure 6.31. Time domain traces for a 500μs quadratic FM call (120kHz – 40kHz) as detected at the entrance to the ear canal for varying horizontal angle (θ) of sound source. Vertical angle (φ = 0˚) and distance (r = 1m) are kept constant.

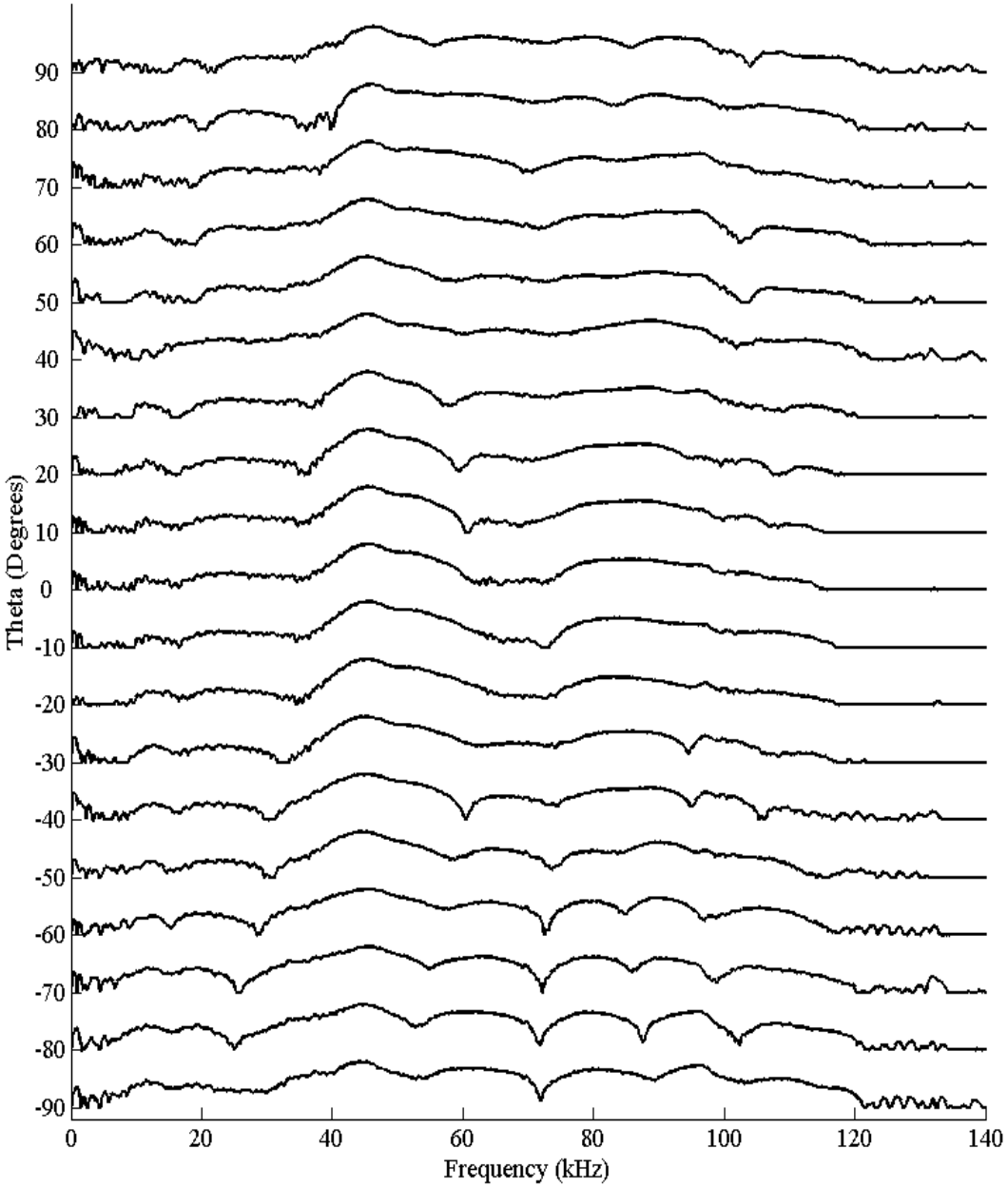

Figure 6.32. Frequency domain traces for a 500μs quadratic FM call (120kHz – 40kHz) as detected at the entrance to the ear canal for varying horizontal angle (θ) of sound source. Vertical angle (φ = 0˚) and distance (r = 1m) are kept constant.

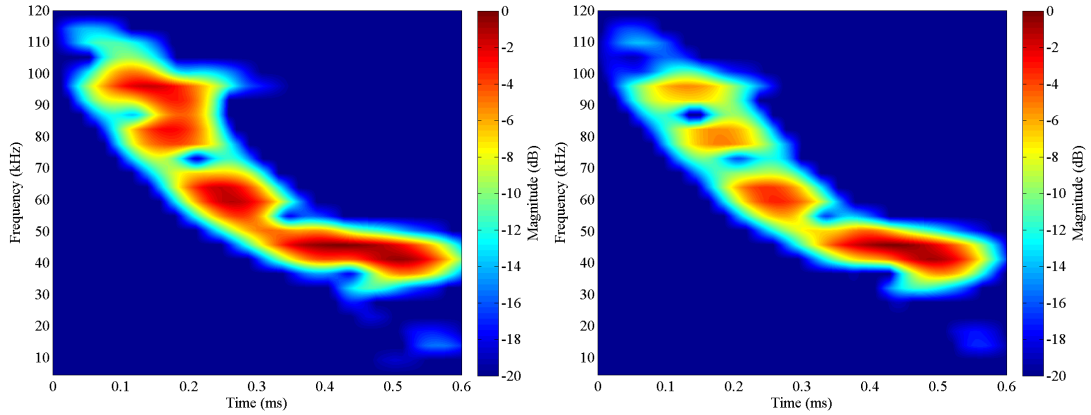
Frequency (kHz)
Time (ms)
Magnitude (dB)

(a) (b)

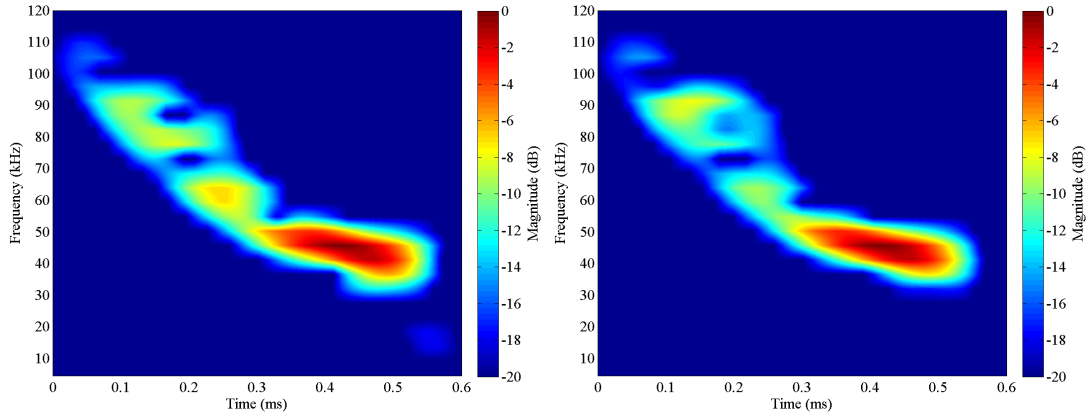
Frequency (kHz)
Time (ms)
Magnitude (dB)

(c) (d)

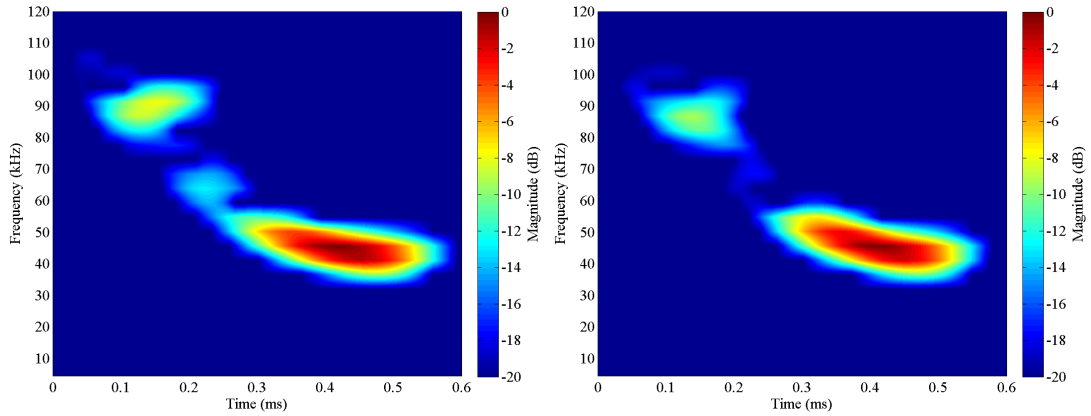
Frequency (kHz)
Time (ms)
Magnitude (dB)

(e) (f)

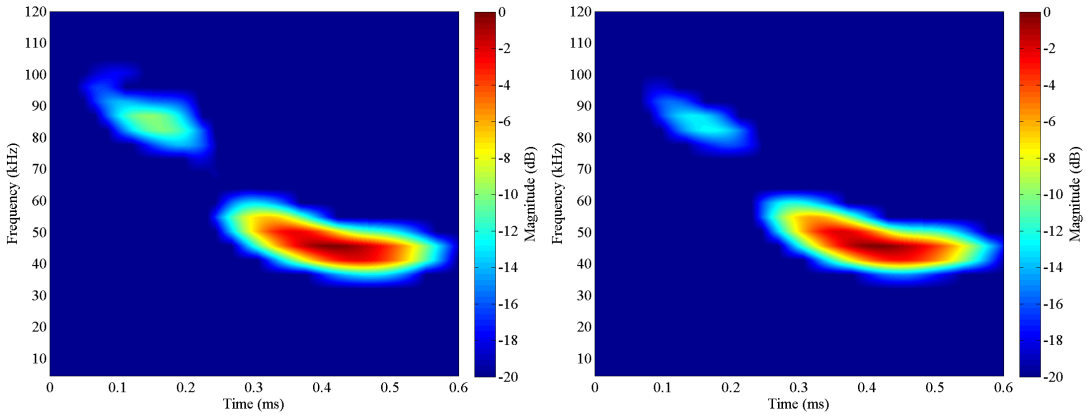
Frequency (kHz)
Time (ms)
Magnitude (dB)

(g) (h)

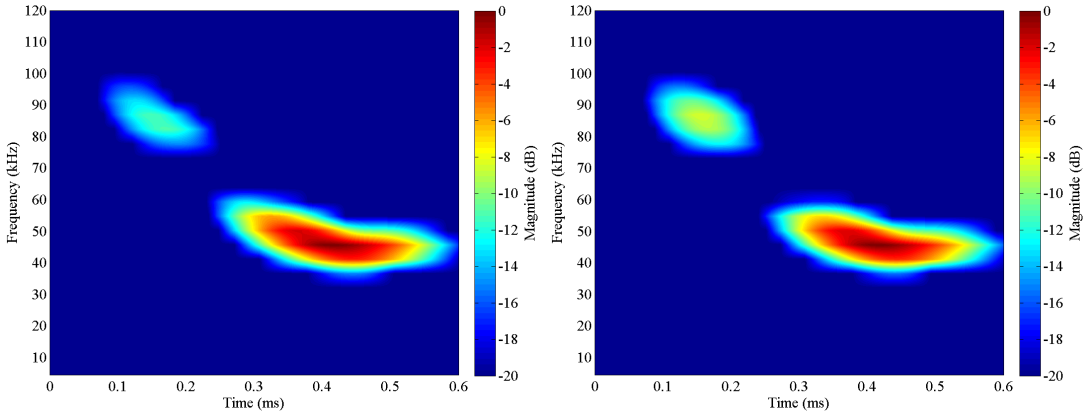
Frequency (kHz)
Time (ms)
Magnitude (dB)

(i) (j)

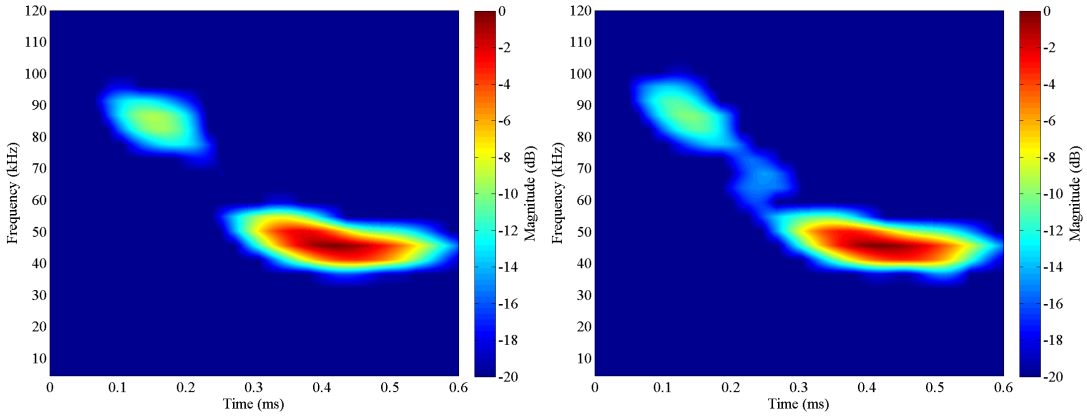
Frequency (kHz)
Time (ms)
Magnitude (dB)

(k) (l)

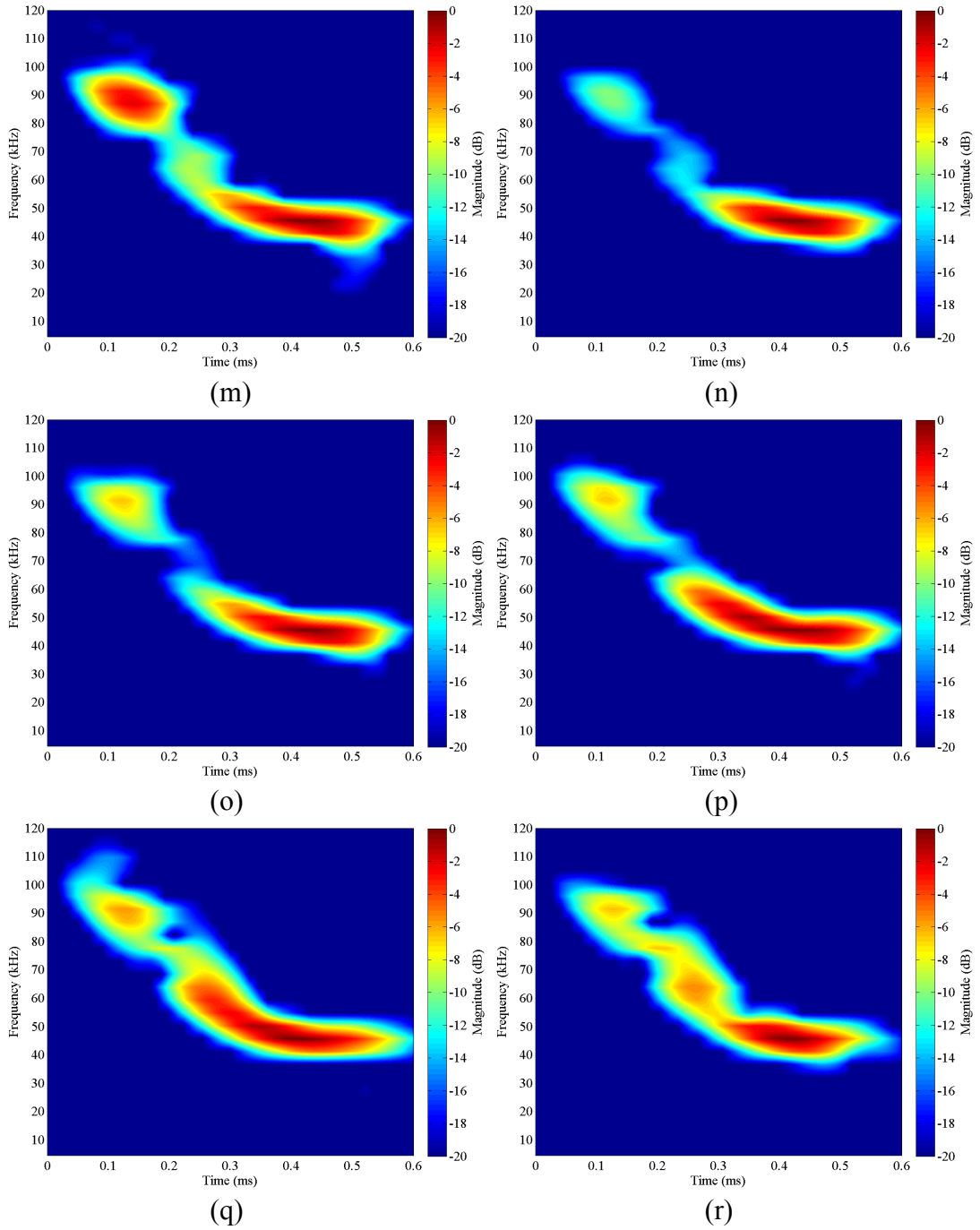

Figure 6.33. Spectrogram representations of the signal received at the ear canal from a 500μs 120kHz-40kHz quadratic FM signal originating from positions with varying θ: (a) -90˚; (b) -80˚; (c) -70˚; (d) -60˚; (e) -50˚; (f) -40˚; (g) -30˚; (h) -20˚; (i) -10˚; (j) 10˚; (k) 20˚; (l) 30˚; (m) 40˚; (n) 50˚; (o) 60˚; (p) 70˚; (q) 80˚; (r) 90˚. Φ = 0˚ and r = 1m are kept constant.

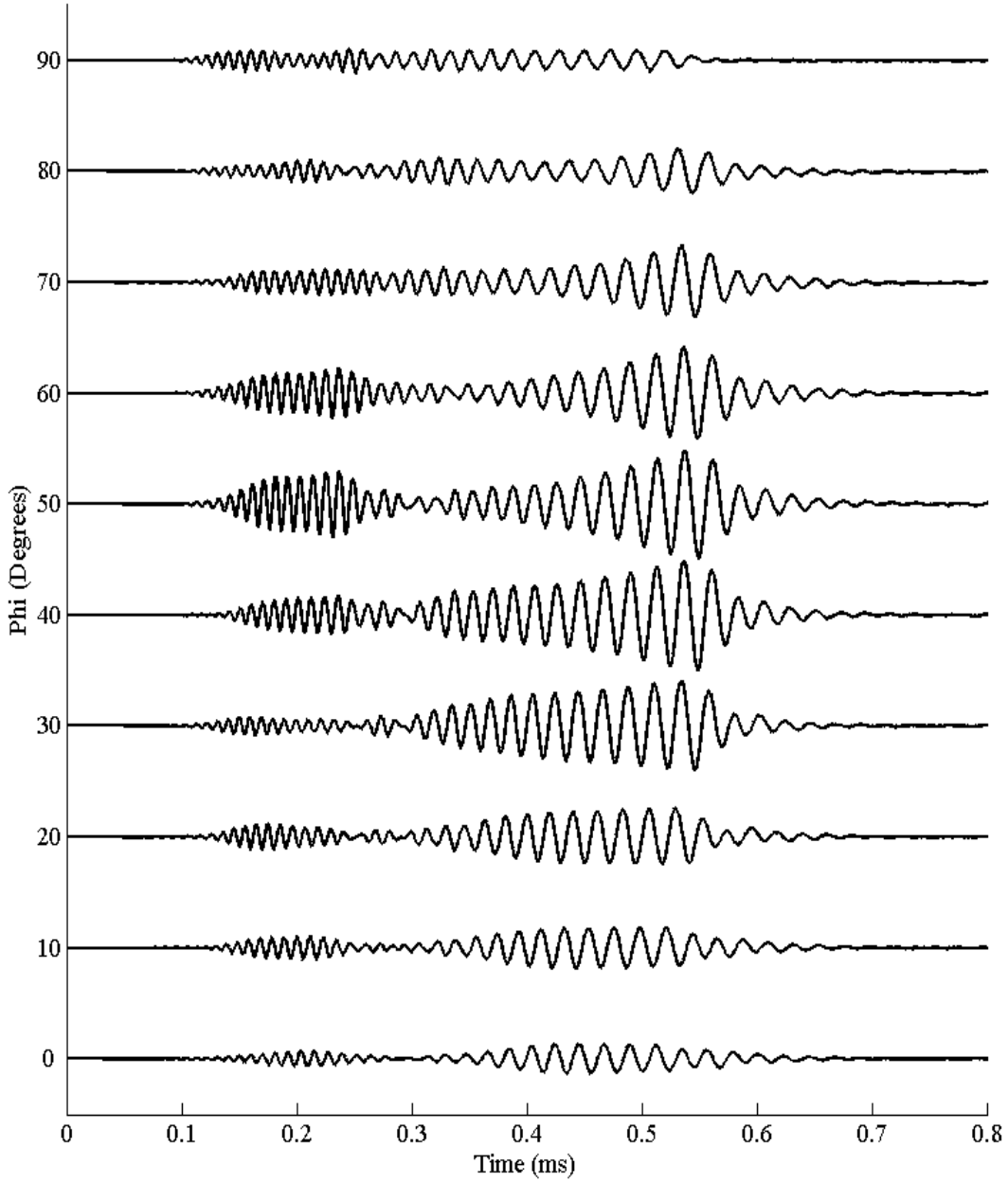

Figure 6.34. Time domain traces for a 500μs quadratic FM call (120kHz – 40kHz) as detected at the entrance to the ear canal for varying vertical angle (φ) of sound source. Horizontal angle (θ = 0˚) and distance (r = 1m) are kept constant.

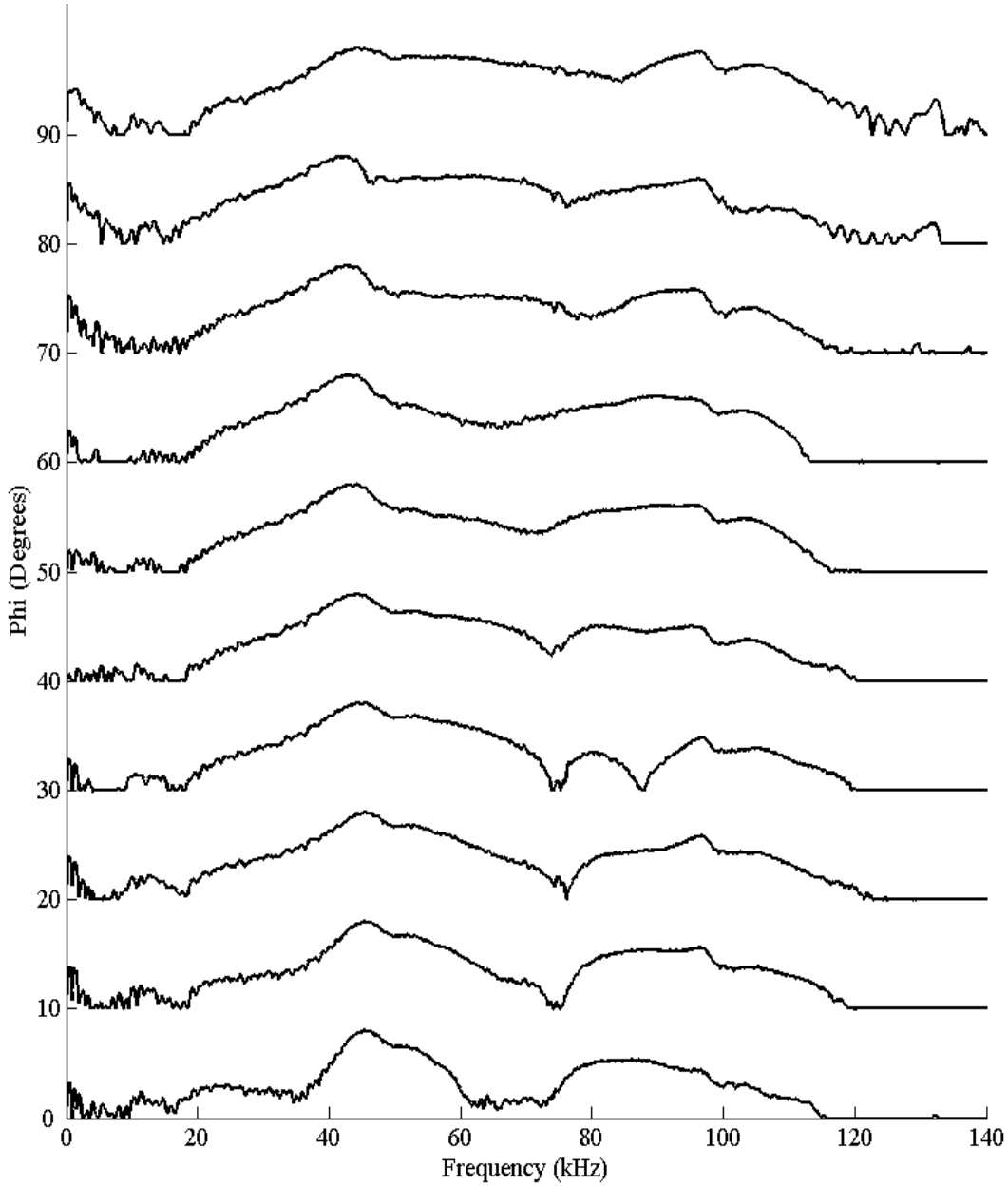

Figure 6.35. Frequency domain traces for a 500μs quadratic FM call (120kHz – 40kHz) as detected at the entrance to the ear canal for varying vertical angle (φ) of sound source. Horizontal angle (θ = 0˚) and distance (r = 1m) are kept constant.

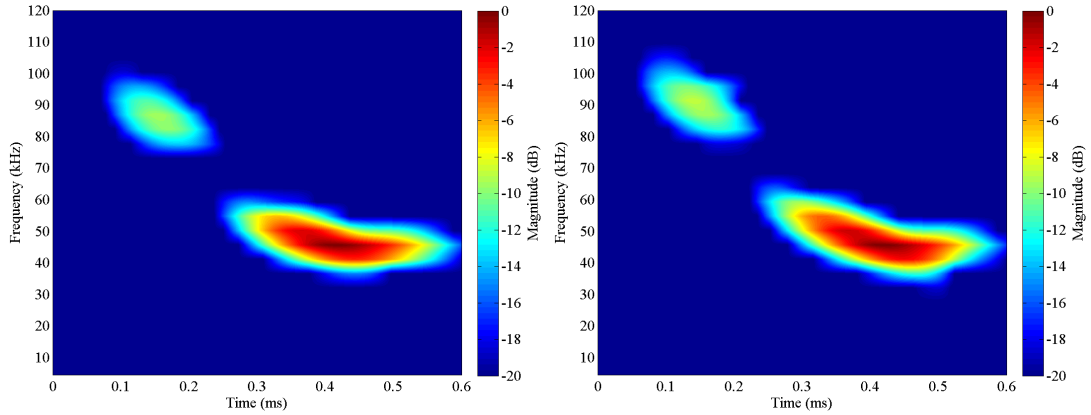
Frequency (kHz)
Time (ms)
Magnitude (dB)

(a)

Frequency (kHz)
Time (ms)
Magnitude (dB)

(b)

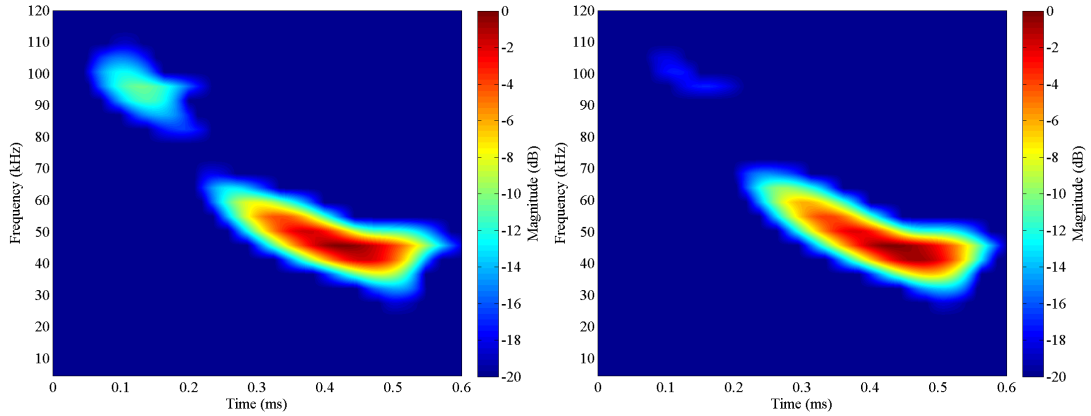
Frequency (kHz)
Time (ms)
Magnitude (dB)

(c)

Frequency (kHz)
Time (ms)
Magnitude (dB)

(d)

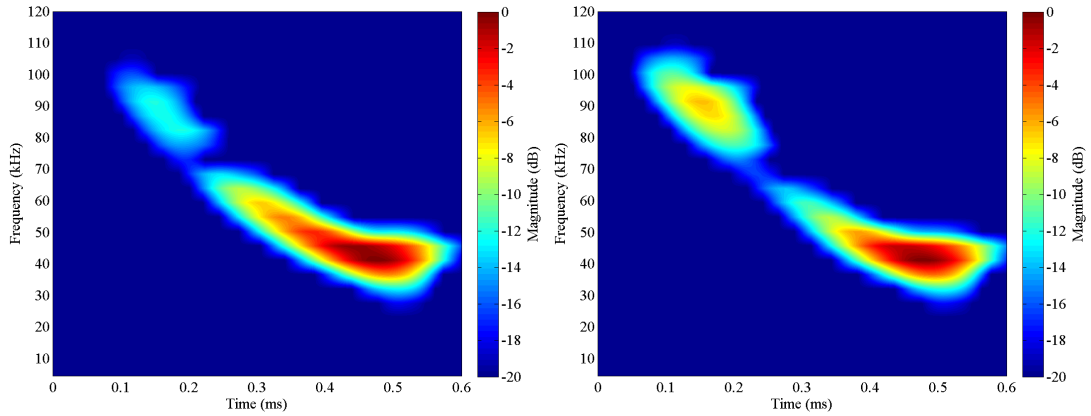
Frequency (kHz)
Time (ms)
Magnitude (dB)

(e)

Frequency (kHz)
Time (ms)
Magnitude (dB)

(f)

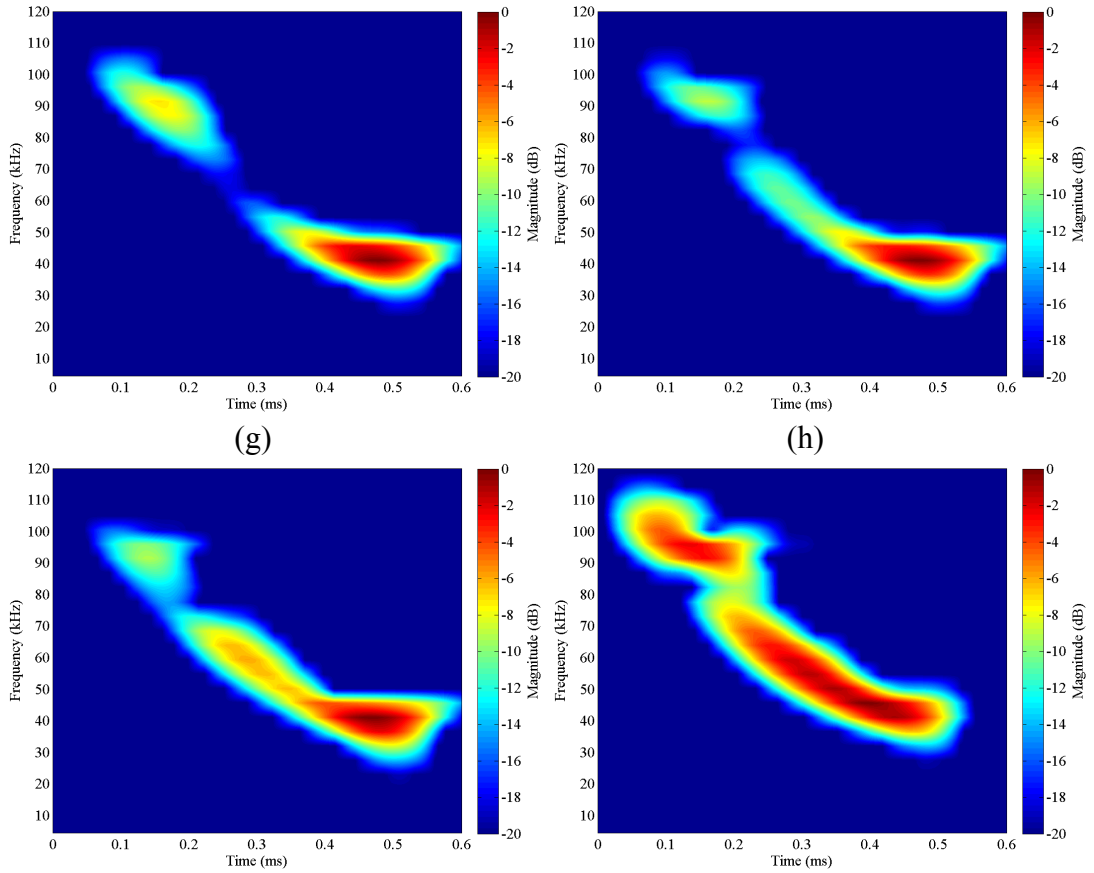

Figure 6.36. Spectrogram representations of the signal received at the ear canal from a 500μs 120kHz-40kHz quadratic FM signal originating from positions with varying φ: (a) 0˚; (b) 10˚; (c) 20˚; (d) 30˚; (e) 40˚; (f) 50˚; (g) 60˚; (h) 70˚; (i) 80˚; (j) 90˚. Φ = 0˚ and r = 1m are kept constant.

6.4.4 Effect of Call Duration and Frequency Content on Monaural Cues

The results presented in the previous section indicate how a bat may obtain information about the angular direction from which an echo is returning via monaural cues. This is in addition to binaural cues, such as IID or ITD, that may also be available. However, the previous results do not indicate whether the observed variation with angular direction are time- or frequency-dependent. For example, if the call has the same frequency content but is of longer duration, do the dips in amplitude occur at the same time relative to the start of the call, or do they produce the same spectral notches regardless of duration. Similarly, if the frequency content of the call changes such that the bandwidth is increased, what effect does this have on the location of the spectral notches? Any effect such changes produce is interesting since bats naturally vary both the duration and frequency content of their

calls, especially during the phases of predation. As such, any variation in the response due to duration or frequency content would imply that the bat must have *a priori* knowledge of the angular effect on *any* of the calls it is likely to use during this process.

To investigate these issues, two further FM signals were created. Firstly, the same initial and terminal frequencies were used, but the duration of the call was doubled to 1ms. Secondly, the duration of the call was held at 500μs, but the initial frequency increased to 220kHz. Since the original frequency limit was specified to be 100kHz in PZFlex, this upper frequency will test the limitations of the model, although the number of elements per wavelength at 100kHz was set to 30, double the recommended figure of 15 and so operation of the model at frequencies up approximately 200kHz should be possible. However, it is actually of most importance that this model is still valid for the frequencies contained in the original chirp, up to 120kHz. This is because this simulation is run to ensure that the features present in the spectrum of that signal still exist with a change in the echolocation call. This would indicate that no *a priori* knowledge the emitted signal would be required for the bat to be able to use spectral cues for sound localisation.

The time domain traces obtained from the 1ms 120kHz-40kHz chirp for variation of θ (with φ = 0°) are depicted in Figure 6.37, where it can be seen that similar envelopes to those of the 500μs chirp (Figure 6.31), albeit lengthened in the time domain, are evident. The similarity of these signals is illustrated effectively in Figure 6.38, which shows a comparison of the frequency domain traces for both the 500μs and 1ms version of the chirp. This demonstrates that the signal propagating into the ear canal of the bat has the same frequency spectrum, dependent on incident angle, irrespective of the duration of the signal. As such, the spectral notches and variations give an *independent* indication of the direction from which the incoming sound has arrived. These results are repeated for variation in φ (with θ = 0°), illustrated in the time and frequency domain in Figures 6.39 and 6.40, respectively. Again it can be seen that the frequency domain traces have almost identical features to those produced from the shorter duration chirp signal, allowing monaural information to be used to indicate the direction from which a signal has arrived.

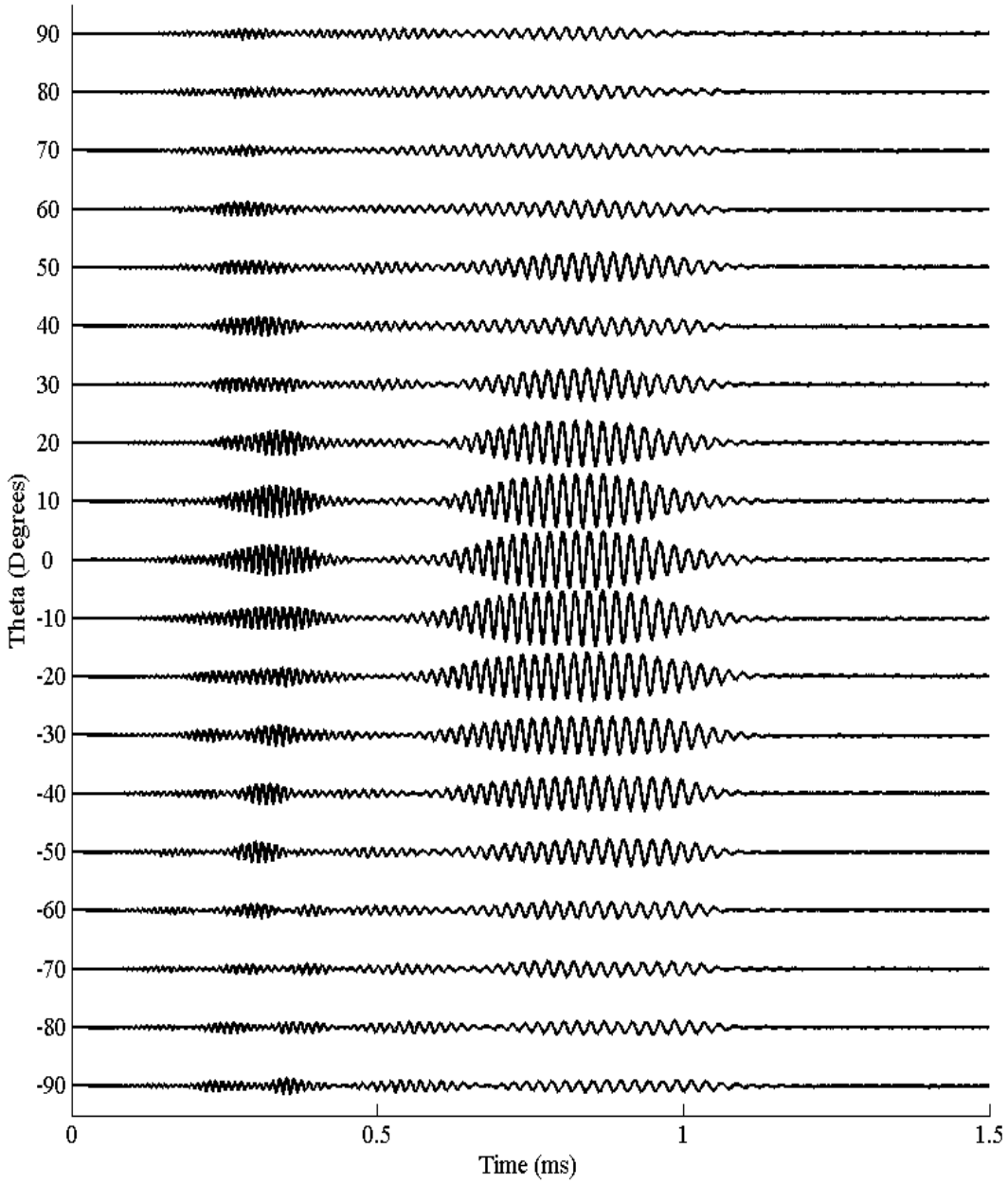

Figure 6.37. Time domain traces for a 1ms quadratic FM call (120kHz – 40kHz) as detected at the entrance to the ear canal for varying horizontal angle (θ) of sound source. Vertical angle (φ = 0˚) and distance (r = 1m) are kept constant.

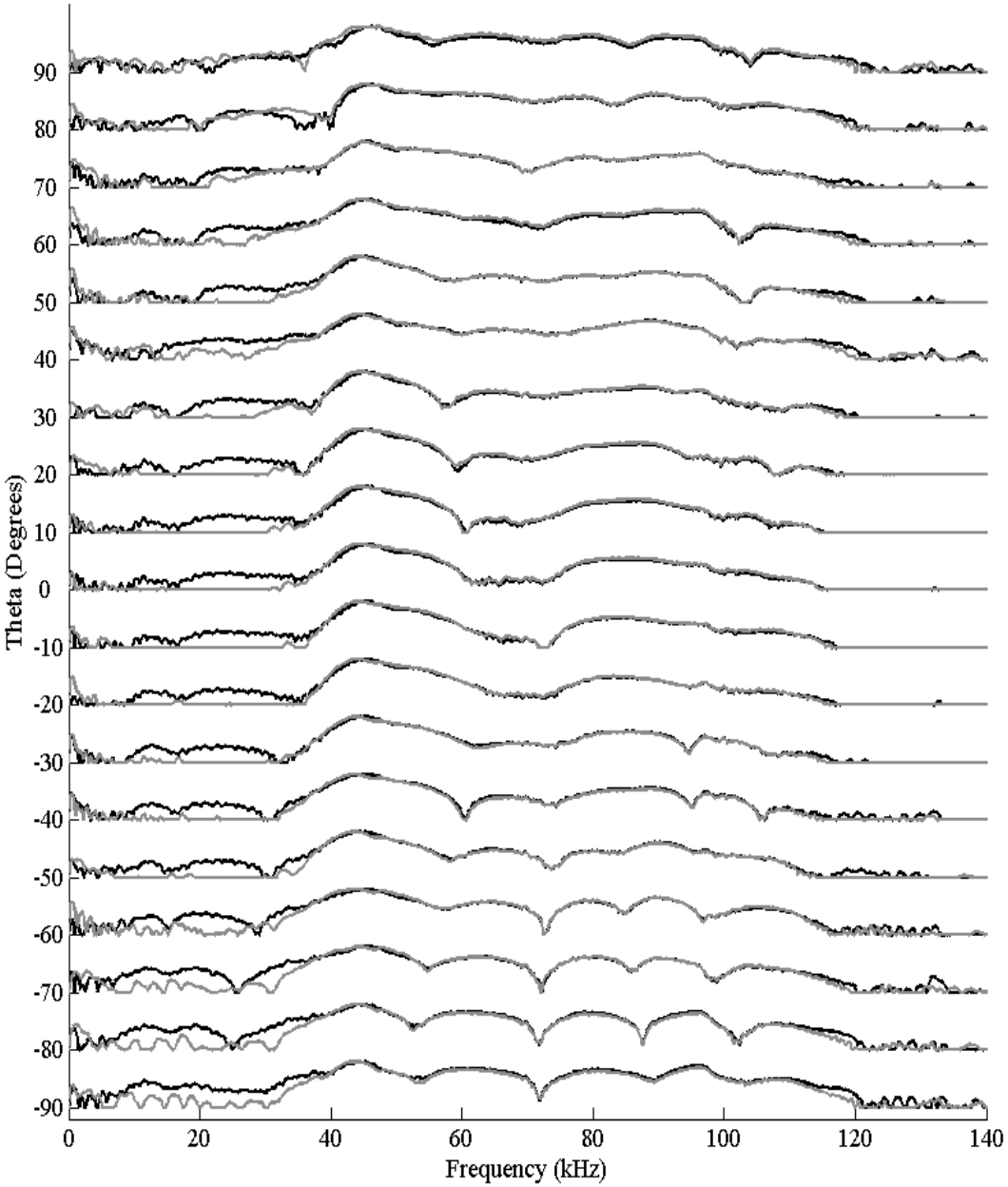

Figure 6.38. Frequency domain traces for a 500μs 120kHz-40kHz quadratic FM call (black), in comparison with those for a 1ms 120kHz-40kHz quadratic FM call (grey), as detected at the entrance to the ear canal for varying horizontal angle (θ) of sound source. Vertical angle (φ = 0˚) and distance (r = 1m) are kept constant.

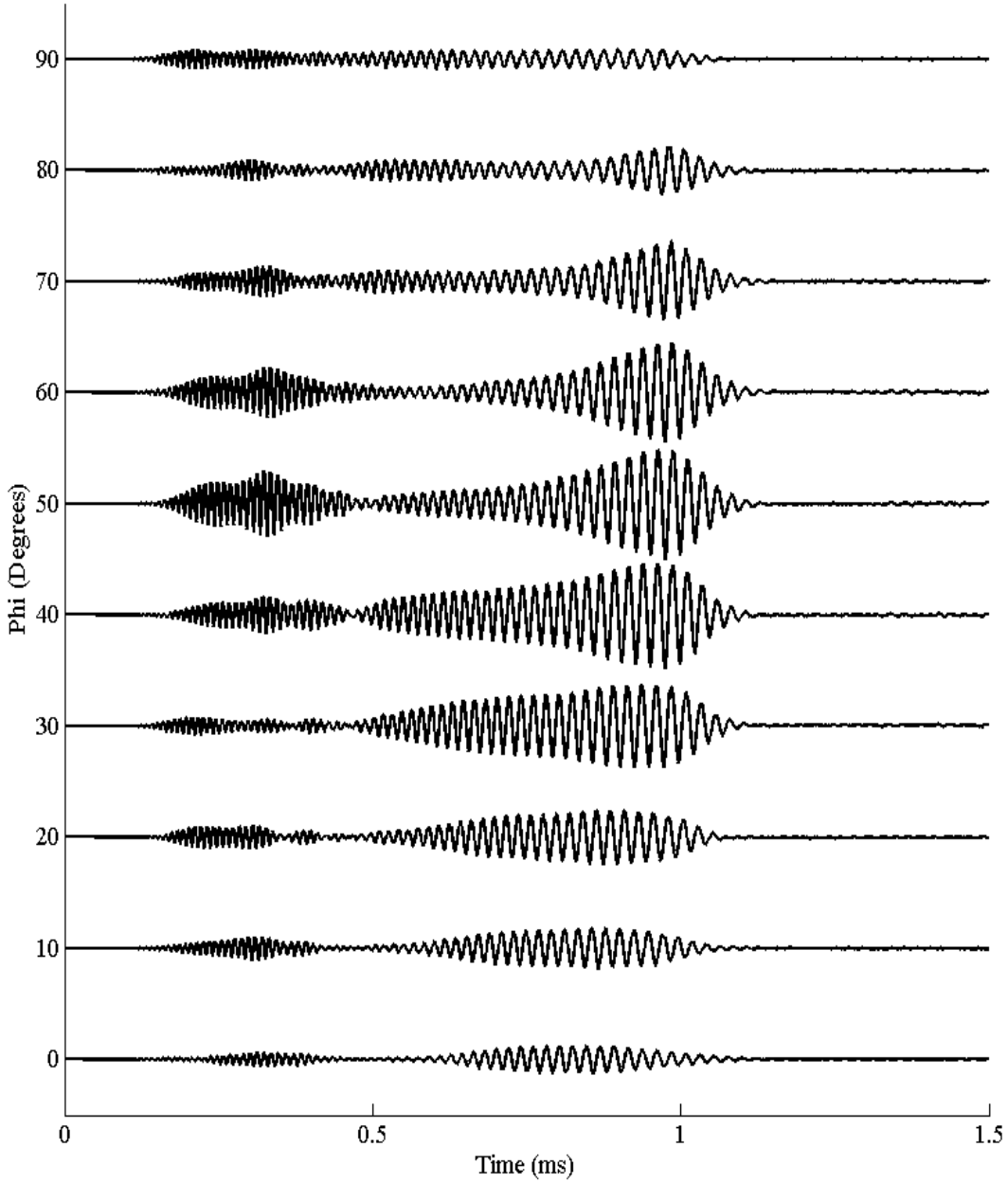

Figure 6.39. Time domain traces for a 1ms quadratic FM call (120kHz – 40kHz) as detected at the entrance to the ear canal for varying vertical angle (φ) of sound source. Horizontal angle (θ = 0˚) and distance (r = 1m) are kept constant.

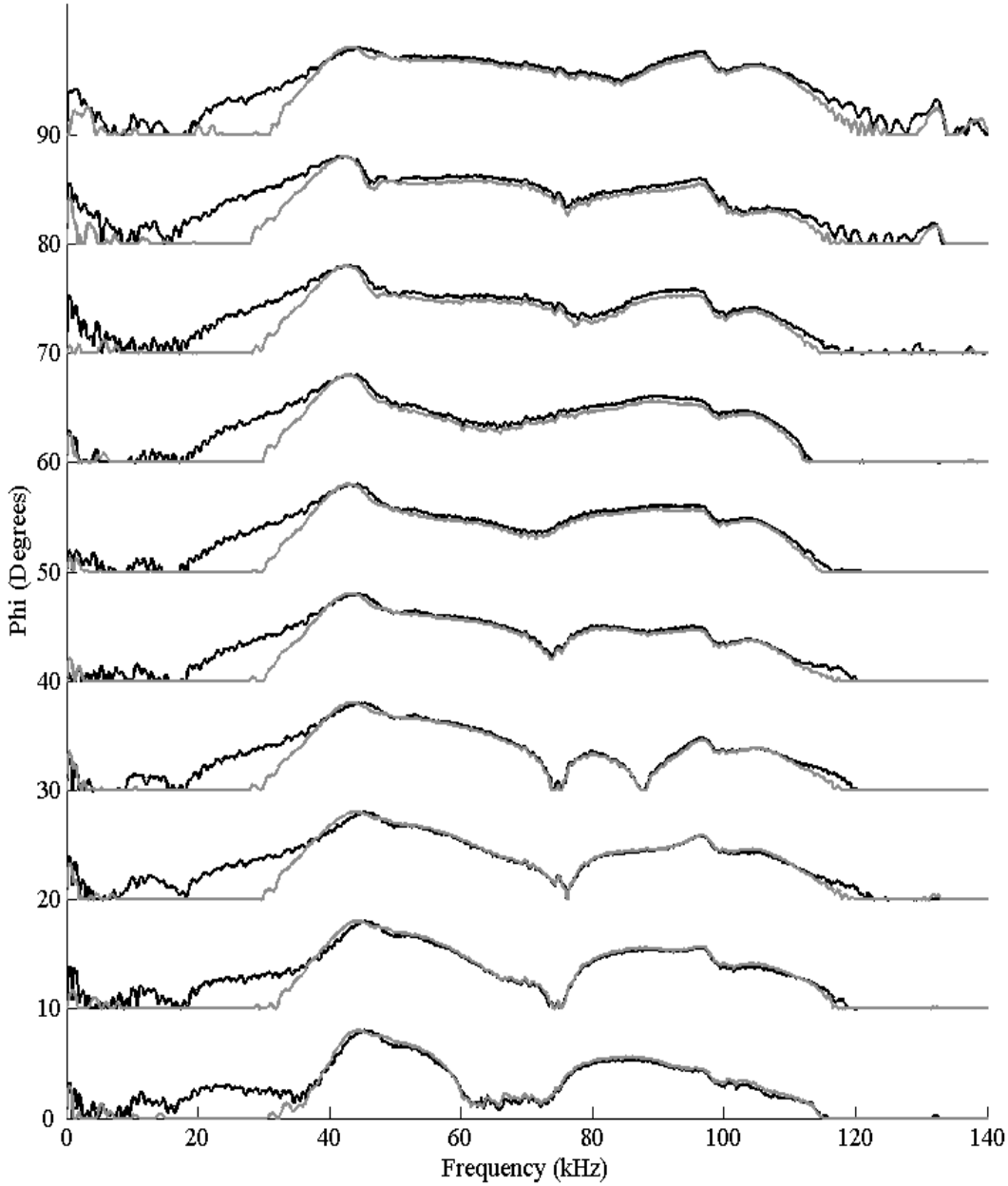

Figure 6.40. Frequency domain traces for a 500μs 120kHz-40kHz quadratic FM call (black), in comparison with those for a 1ms 120kHz-40kHz quadratic FM call (grey), as detected at the entrance to the ear canal for varying vertical angle (φ) of sound source. Horizontal angle (θ = 0˚) and distance (r = 1m) are kept constant.

Further evidence of this is provided by examining the results from the chirp with the additional high frequency content. As for previous signals, Figures 6.41 through 6.44 show time and frequency traces for θ and φ variation. It can once again be seen that the frequency content of the original 120kHz-40kHz chirp is almost identical to that of the 220kHz-40kHz version, at least below approximately 100kHz where the spectral content of the initial signals is comparable. These results are consistent for any angular variation in either the horizontal or vertical plane. As such, they provide information about the direction from which an echo has arrived, independently of the chirp duration or frequency content - assuming there is sufficient bandwidth to cover the frequency range of interest. It should be pointed out that the validity of higher-frequency simulations has not been demonstrated. However, in these results, the important feature is that the spectral content of the 220kHz-40kHz chirp is the same as that for the 120kHz-40kHz chirp, across the extent of the lower bandwidth signal. This illustrates that the ear generates the same spectral profile regardless of the temporal structure of the incoming signal, but reliant only on the spectral content adequately covering this bandwidth. At these frequencies, the simulation has been demonstrated to be valid, and so these comparisons and results are also valid.

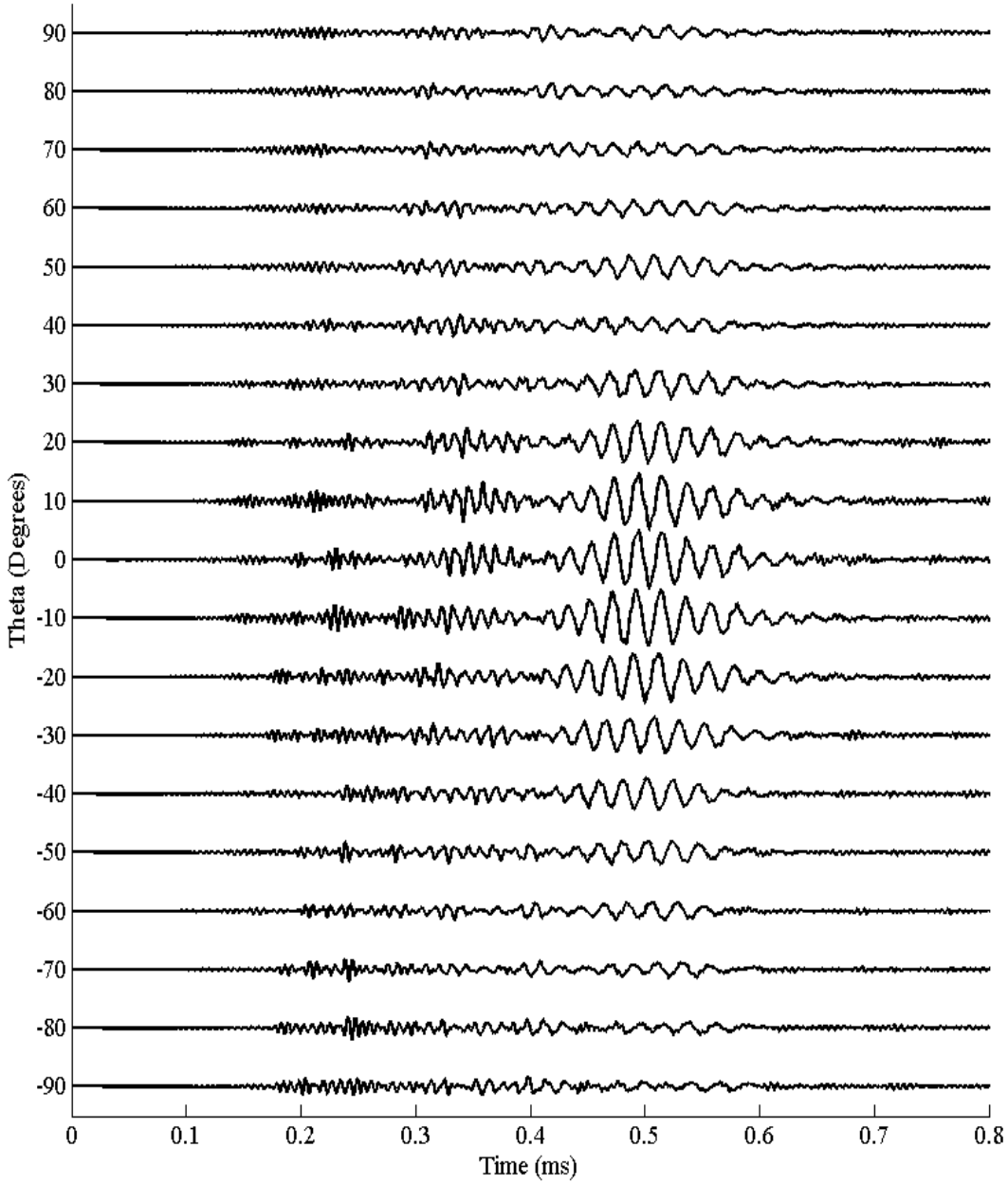

Figure 6.41. Time domain traces for a 500μs quadratic FM call (220kHz – 40kHz) as detected at the entrance to the ear canal for varying horizontal angle (θ) of sound source. Vertical angle (φ = 0˚) and distance (r = 1m) are kept constant.

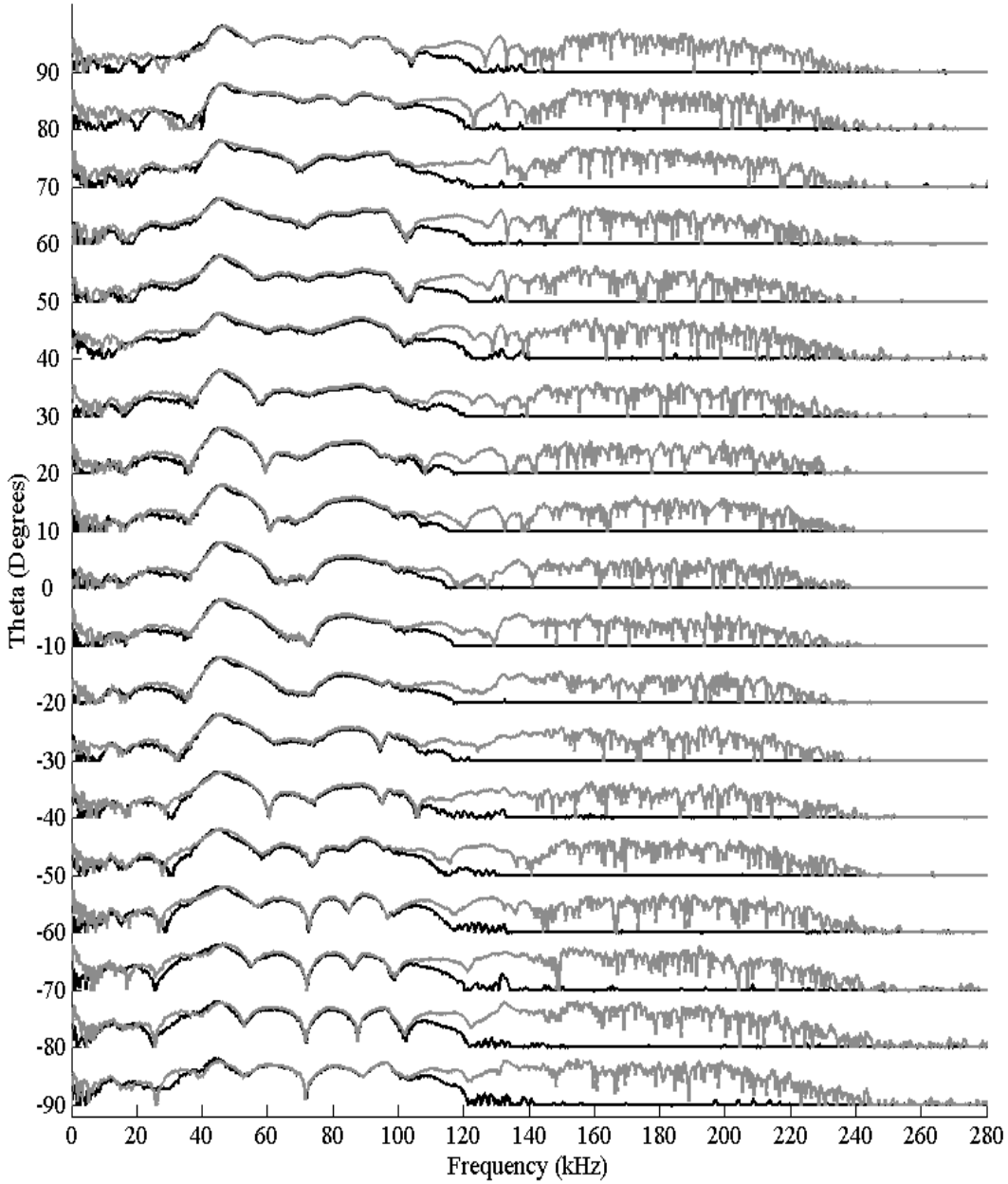

Figure 6.42. Frequency domain traces for a 500μs 120kHz-40kHz quadratic FM call (black), in comparison with those for a 500μs 220kHz-40kHz quadratic FM call (grey), as detected at the entrance to the ear canal for varying horizontal angle (θ) of sound source. Vertical angle (φ = 0˚) and distance (r = 1m) are kept constant.

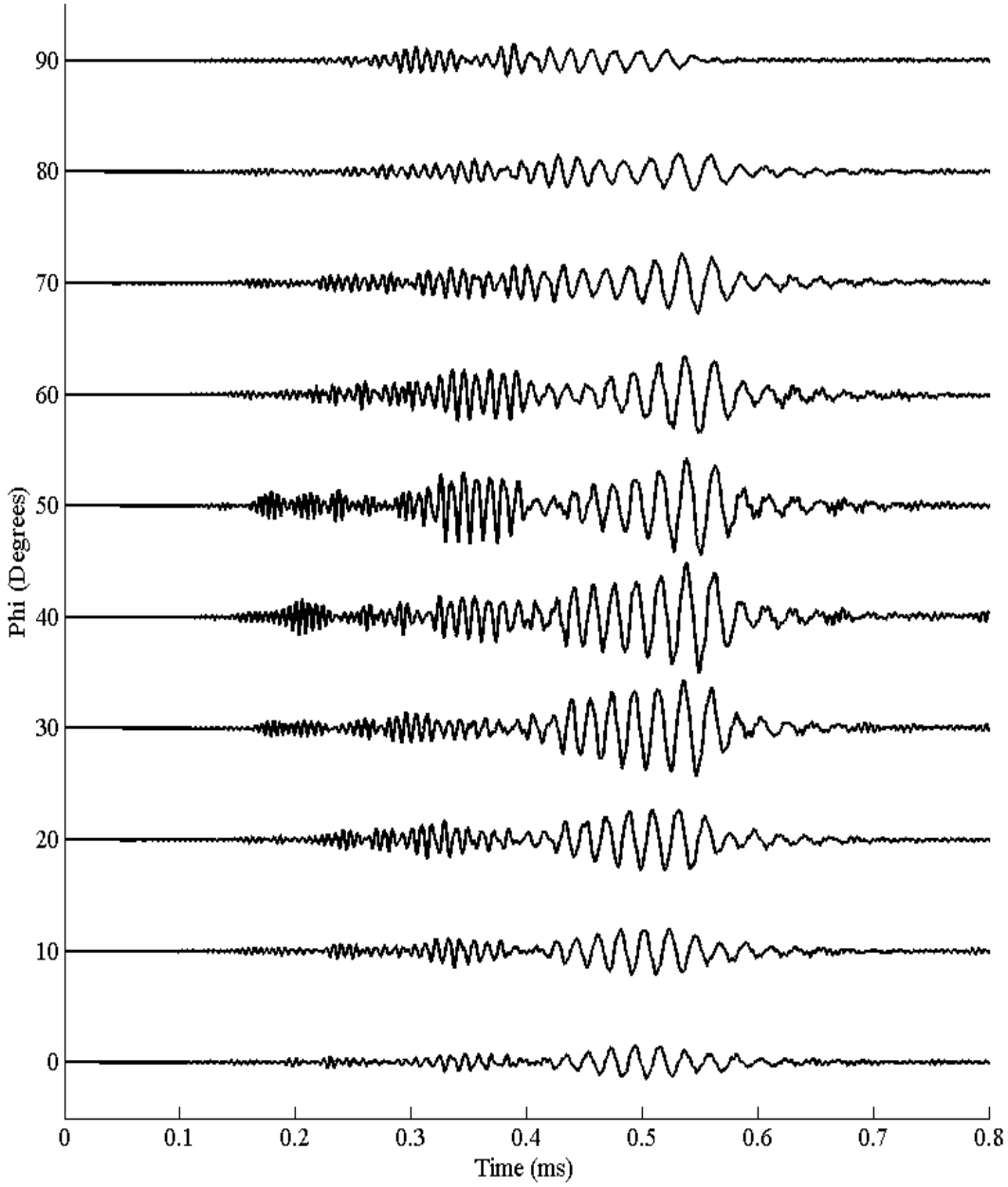

Figure 6.43. Time domain traces for a 500μs quadratic FM call (220kHz – 40kHz) as detected at the entrance to the ear canal for varying horizontal angle (φ) of sound source. Vertical angle (θ = 0˚) and distance (r = 1m) are kept constant.

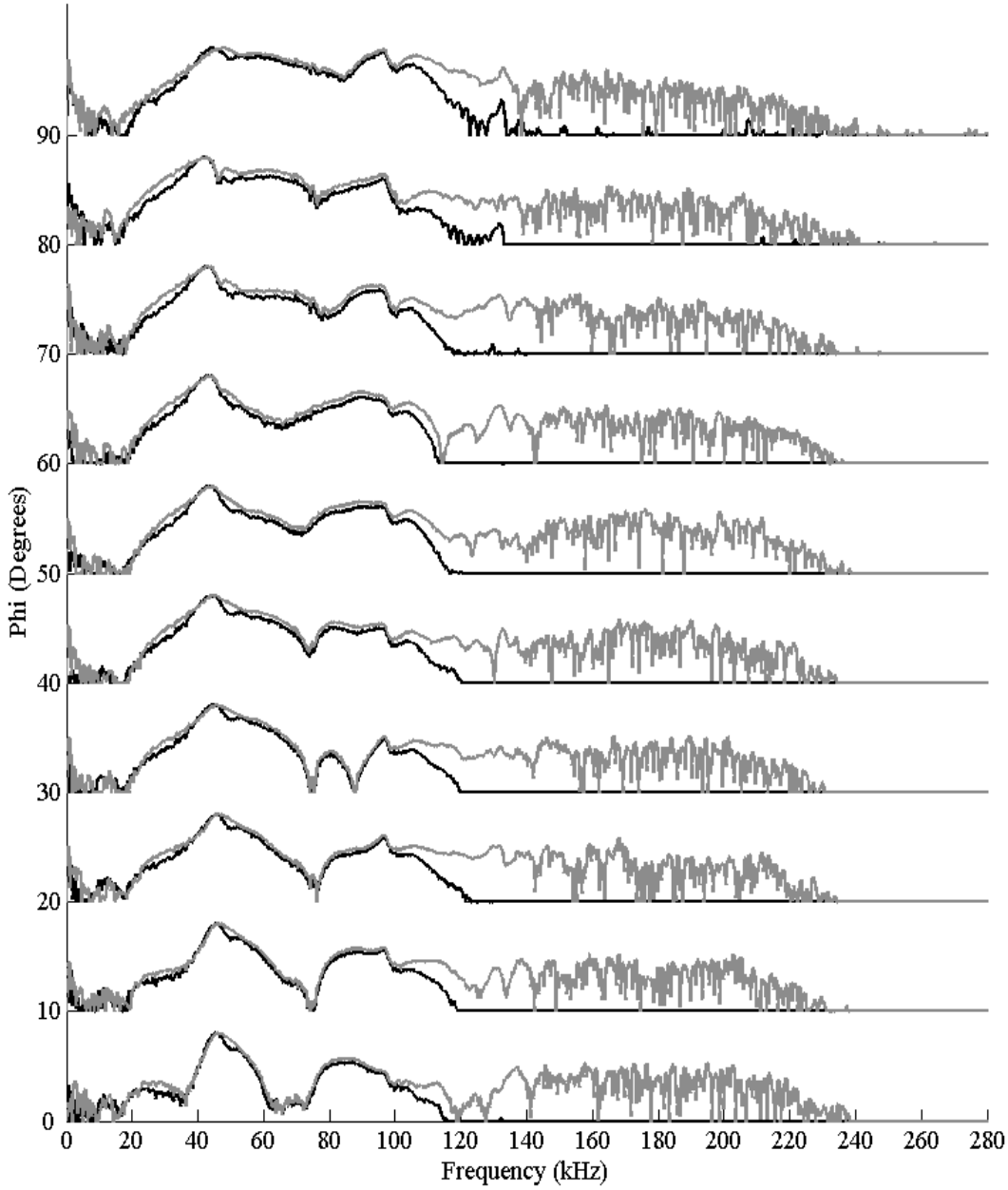

Figure 6.44. Frequency domain traces for a 500μs 120kHz-40kHz quadratic FM call (black), in comparison with those for a 500μs 220kHz-40kHz quadratic FM call (grey), as detected at the entrance to the ear canal for varying horizontal angle (φ) of sound source. Vertical angle (θ = 0˚) and distance (r = 1m) are kept constant.

6.4.5 The Effect of Source Location Within a 30˚ Cone in front of the Bat

As reviewed in Chapter 2, the range of elevation and azimuth angles over which spectral cues are available to bats, as indicated from measured HRTFs, appears to be finite. Indeed, Wotton *et al.* (1997) documented that the region of space within which spectral cues were useful was "restricted to a cone of space of approximately ±30°" from a combination of the HRTF documented in an earlier study (Wotton *et al.*, 1995) and emitted sonar directionality measured by Hartley and Suthers (1989). The earlier study by Wotton *et al.* (1995) had also demonstrated that the HRTF on its own generated a notch frequency that decreased systematically with decreasing elevation, although the "elevation dependence of the most prominent notch…is largely restricted to elevations below the horizontal". With these results in mind, the response of the bat ear to a series of sounds originating from within ±30˚ of the $(\theta,\varphi) = (0^{\circ},0^{\circ})$ direction was investigated in more detail.

It has already been demonstrated that the response of the ear to the call of *R. aegyptiacus* does not vary significantly with source location. As such, the original FM signal (500μs quadratic FM chirp, with initial and terminal frequencies of 120kHz and 40kHz, respectively) was used to investigate the response of the ear within this reduced angular space to demonstrate whether the same trends were observed.

Simulations were performed for a sound source location varying between ±30˚ in elevation and at -30˚, 0˚ and +30˚ in azimuth. In this case, only the frequency domain results are displayed, in Figures 6.45 – 6.47, since these contain the useful information. Comparison of these results does indicate significant differences in the spectral content of the signal reaching the ear, varying with both azimuth and elevation. It is interesting that there is some evidence of a variation of notch frequency with elevation observed by Wotton *et al.* (1995), most notably in the results for an azimuth angle of +30˚, with the elevation decreasing from 30˚ to approximately 10˚. However, the "systematic" nature of this relationship is certainly not observed over the full angular space of these simulations. Interestingly, the similar FEA techniques used by Müller (2004) and Müller *et al*. (2006) indicated that

notches and sidelobes in the *directivity* of the ears of *E. fuscus* and *Nyctalus plancyi* were generated by interaction between a direct signal and one generated by diffraction around the prominent tragus. This may well be the same mechanism that generates the deep notches at a frequency that varies with the elevation angle as reported by Wotton *et al.* (1995) in *E. fuscus*. As such, a tragus that protrudes very little from the pinna structure (as is the case with *R. leschenaultii*) generates no diffraction-based secondary signal that can produce a spectral notch. The notches generated in this case originate from the multiple reflections within the pinna, and this mechanism does not appear to produce the same relationship between notch frequency and source angle.

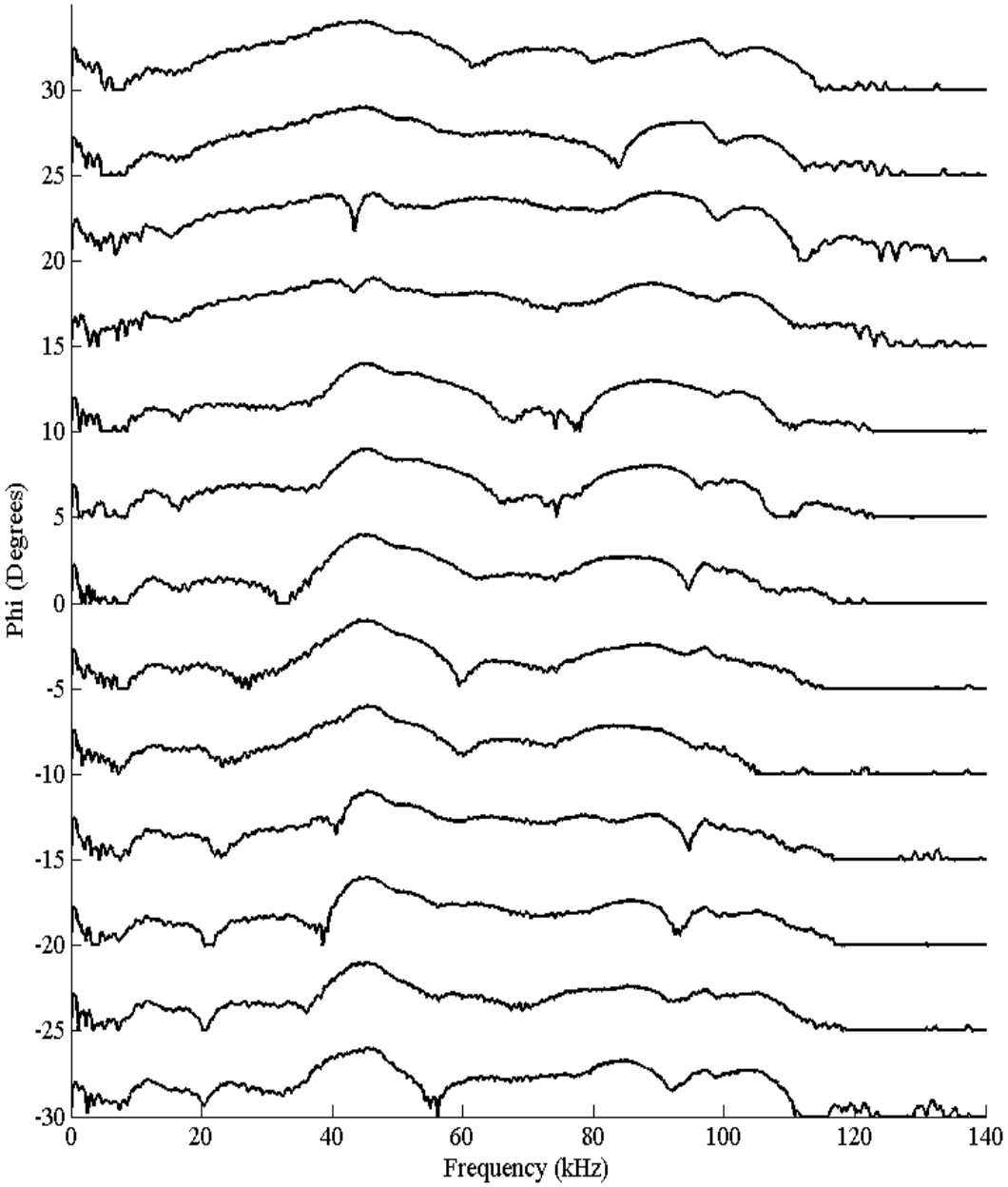

Figure 6.45. Frequency domain traces for a 500μs quadratic FM call (120kHz – 40kHz) as detected at the entrance to the ear canal for varying vertical angle (φ) of sound source. Horizontal angle (θ = -30˚) and distance (r = 1m) are kept constant.

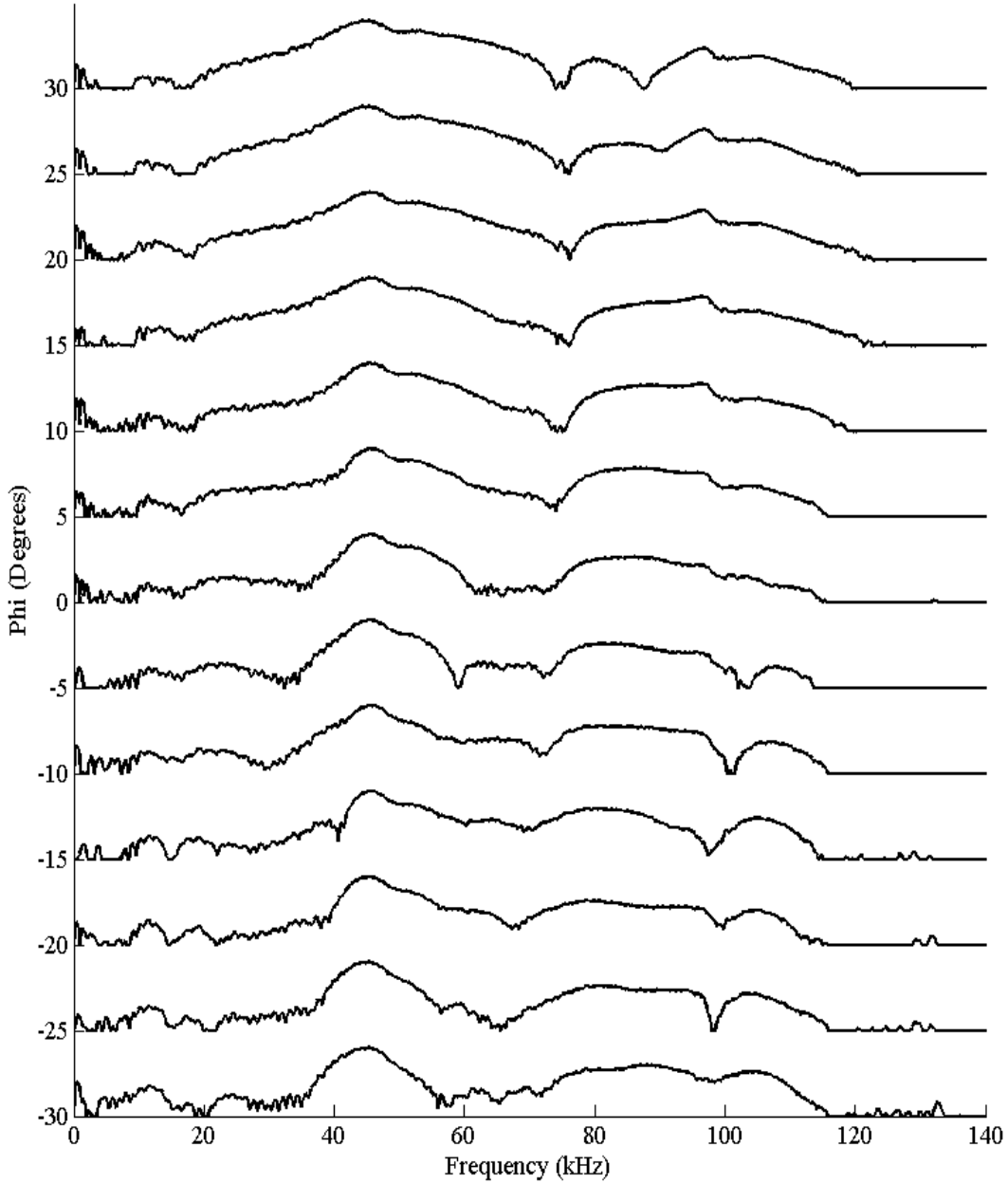

Figure 6.46. Frequency domain traces for a 500μs quadratic FM call (120kHz – 40kHz) as detected at the entrance to the ear canal for varying vertical angle (φ) of sound source. Horizontal angle (θ = 0˚) and distance (r = 1m) are kept constant.

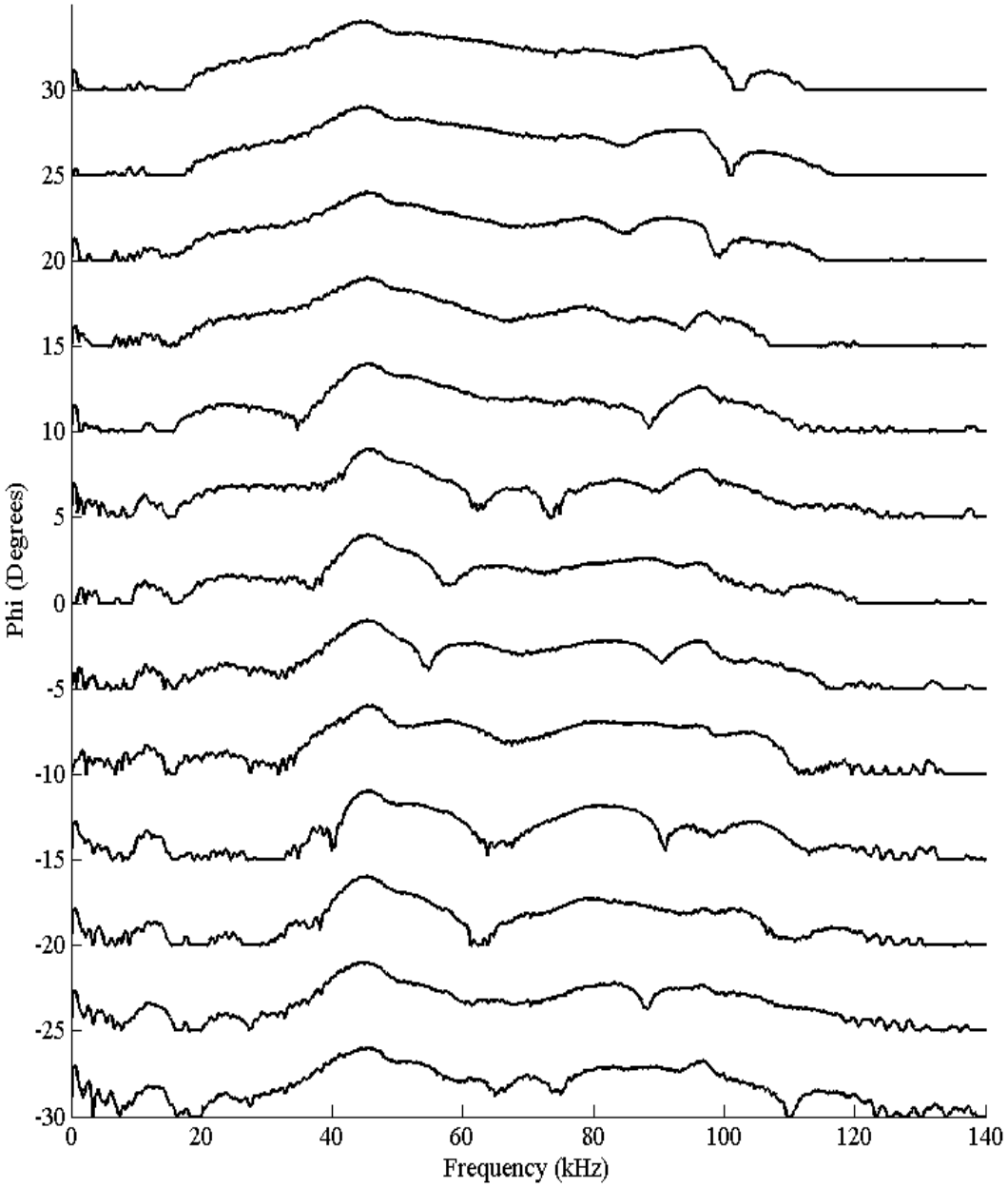

Figure 6.47. Frequency domain traces for a 500μs quadratic FM call (120kHz – 40kHz) as detected at the entrance to the ear canal for varying vertical angle (φ) of sound source. Horizontal angle (θ = +30˚) and distance (r = 1m) are kept constant.

6.5 Discussion and Conclusions

This Chapter set out to validate a new methodology by which the response of a bat ear could be investigated, through FEA using PZFlex. To that end, a copy of the left ear of a *R. leschenaulti* individual was rendered in 3D in the virtual environment, with a physical specimen produced in a soft-setting flexible polymer material using μSL. With these versions of the ear available, experimental measurements were made (in transmission) to validate results generated (also in transmission) using the PZFlex simulation. Assuming validation of the PZFlex method, the model could be used to investigate the response of the ear to a range of echolocation calls, originating from varying locations in space. This would then be used to provide information on the monaural cues available to the bat about the location of the source of echoes returning to it.

The experiments and simulations detailed in the first part of this Chapter demonstrate the validity of the PZFlex method. Although the directional and time domain results are not a perfect match for each other, the trends demonstrated by the two sets of results correlate well. Furthermore, there are many examples of how the interference patterns present in the experimentally received signal, generated by the complex geometry of the bat ear, are predicted accurately by PZFlex. As such, the discrepancies between the two sets of results have been explained by considering that the geometry of the experimental and simulated experiments cannot be entirely consistent with each other, given the complex configuration and many degrees of freedom in the experimental system. As such, the results of these experiments, have been justifiably accepted as validation of the PZFlex model.

With this endorsement, the PZFlex model was used for its intended purpose – to simulate the response of the ear to echolocation calls arriving at the ear as if originating from a range of source locations, varying in horizontal and vertical angular location. The results of these simulations were successful, both in terms of demonstrating a new and powerful technique for simulating the mechanics of echolocation, as well as interesting in what they revealed about the response of the bat ear to different echolocation calls. *R. leschenaulti* is closely related, and similar

physically, to *R. aegyptiacus* – the species that had its echolocation call accurately recorded using the wireless sensor reported in Chapter 3. As such, the response of the ear to its own echolocation call could be investigated. The results of this were very interesting, in that there appeared to be very little difference in the time or spectral content of the calls as transformed into the ear canal with varying angular position. This suggests one of two things: either that *R. leschenaultii* is incapable of using monaural cues to locate a sound source; or that it uses some other mechanism not demonstrated through the simulations performed here. This is not to say that the bat is incapable of locating a sound source in azimuth and elevation, simply that it may use techniques other than the monaural spectral characteristics investigated here. It is interesting to consider the reasons for this, and possibly to revisit the concept of the echolocation system of *Rousettus* as "rudimentary" (Koay *et al.,* 1998). As discussed at the end of Chapter 3, it may be that the requirement for *Rousettus* to use echolocation is in its habit of roosting in the darkness of caves, necessitating a collision avoidance system, but not requiring the type of complex scene analysis microchiropterans are capable of. The results obtained using PZFlex simulation may enhance this belief; certainly the signals used by the genus do not provide the capability for the external ear to generate obvious spectral cues as to the location of the echo source, beyond the binaural ITD and IID.

A further aspect of the ear response was investigated through simulation. By varying the time and frequency characteristics of the FM chirp, it was demonstrated that the spectral content of the signal detected by the bat was dependent only on the angular direction from which the sound originated. This was demonstrated by simulating the response of the ear to three different chirp signals, each windowed with a 25% Tukey window:

1. 500µs quadratic FM chirp, with initial and terminal frequencies of 120kHz and 40kHz
2. 1ms quadratic chirp, with initial and terminal frequencies of 120kHz and 40kHz
3. 500µs quadratic FM chirp, with initial and terminal frequencies of 220kHz and 40kHz

The spectral content of the signals transmitted into the canal of the *R. leschenaulti* ear, below approximately 100kHz where all signals had similar spectral content, was dependent solely on the angular direction, both horizontal (θ) and vertical (φ), of the sound source. Since it is thought that bats are capable of analysing the spectral content of the sounds they hear, then these results are certainly significant in quantifying a monaural method by which echo directionality could be determined. In conjunction with accurate timing information available from cross-correlation type processing, then this information can give a bat a precise indication of the location of the source of a returning echo. It has been shown (Mogdans *et al*., 1988) that the capability of certain bats to locate horizontally-oriented wires (i.e. variation in vertical angle, φ) decreases when the pinna of the bat was deformed in some way. This indicates that monaural information is important to the bat for this skill; indeed it can be appreciated that for an object located on the median sagittal plane, or for a long thin horizontal target such as a wire, with no variation in the horizontal plane, then monaural cues may be the only method by which (vertical) location can be determined. As such, the results indicated here, with vertical angular location encoded into the spectral content of the sound the bat hears, are important in demonstrating how a bat may achieve this. Furthermore, the methodology applied in this Chapter is exceptionally flexible, allowing the response of the ear to any arbitrary sound originating from any given location to be simulated.

CHAPTER 7

CONCLUSIONS AND SUGGESTIONS FOR FURTHER WORK

7.1 Conclusions

7.1.1 General Overview

The biosonar systems that have evolved over millennia in certain mammals have enabled these creatures to take advantage of specific ecological niche environments. This has allowed toothed whales in the order Odontoceti to find prey over great distances in the world's oceans, and bats – in conjunction with their unique mammalian capacity for powered flight – to navigate and hunt in the night sky. It is the biosonar systems of bats with which this Thesis has been concerned, and what can be learned from these systems that can be used in human ultrasonic systems. As such, many of the facets of a biosonar system have been investigated or replicated in this work. Indeed, one method of leveraging any advantageous methods and characteristics from biosonar systems is through a biomimetic or biologically-inspired approach, thereby applying useful biological techniques in an engineered ultrasonic system.

This work investigated biosonar systems using techniques borrowed from a range of scientific and engineering disciplines. Advances in microelectronics enabled the design of the wireless ultrasonic sensor described in Chapter 3. A rigorous application of acoustics techniques, in conjunction with laser doppler vibrometry, allowed the electrostatic transducers detailed in Chapter 4 to be fully characterised. Finite element modelling was used to simulate the response of a bat ear to an incoming acoustic signal. Underpinning all this was the background gained through an in-depth review of the literature, covering the subject area from a biological and engineering viewpoint. Each Chapter has presented the results of investigations into a different aspect of biological or engineered airborne sonar systems, as summarised in the following paragraphs.

Chapter 2 presented an in-depth review of the mechanics and capabilities of bat sonar systems, along with a history of human study of what became known as Spallanzani's Bat Problem, after the Italian monk who first described a study into bats' ability to fly and hunt unhindered in the dark, in the late 18th century. Several characteristics of bats' biosonar systems documented in the literature are

fundamentally important to Chiropterans' success. Firstly, bats use signals that cover a considerable dynamic range, which is required for them to detect and locate the small prey insects on which the microchiroptera feed; there can be in excess of 100dB difference between the intense emitted signal and faint reflected echo from a prey target. Secondly, bats are capable of using these echoes to accurately image objects and their environment, decoding range to fractions of a millimetre, and angular location to approximately 1˚ to 3˚. Thirdly, microchiropteran bats use a variety of signals, with a relatively larger or smaller proportion of constant frequency and frequency modulated content dependent on task, environment and species. These characteristics can certainly be employed in engineering systems. Chapter 2 also investigated various mechanisms for recording bat echolocation calls, and the findings these recordings have generated. Another aspect of the literature that is reviewed are techniques that have been used to investigate the sounds actually heard by bats, through measurement and modelling of the effect the bat's head and ears have on returning echoes. Finally, techniques for the generation of echolocation calls (or wideband signals in general) in air were reviewed. These subject areas cover the various aspects of biosonar and biologically-inspired sonar systems investigated in the rest of the Thesis.

Chapter 3 presented the design of a wireless microphone sensor that was built to be mounted on the back of the fruitbat *Rousettus aegyptiacus*, to record its echolocation calls whilst in flight. Firstly the sensor was accurately calibrated in the laboratory, before being used to record the emitted echolocation call. Furthermore, through use of a variable-gain stage, it was capable of detecting the echoes returning to the bat from the surrounding environment. This demonstrated the complexity of the signals returning to the bat. Chapter 4 covered a range of topics linked to the generation of ultrasonic signals in air, from theoretical field calculation to the design and test of wideband electrostatic transducers. The characterisation of these transducers is described in detail, with their operation across the frequency range of bat echolocation (approximately 20kHz-200kHz) demonstrated. Characterisation was performed using both field measurement techniques as well as measuring the motion of the transmitting membrane using laser vibrometry techniques. This combined approach is one rarely documented in the literature, but is essential to obtain a

complete understanding of the operation of the transducer. Chapter 5 demonstrated the use of these transducers for generating biological and biologically-inspired wideband signals in air. These signals were then used to investigate bats' documented ability to detect and avoid wires with a cross-section fractions of a wavelength in diameter. The findings from this work indicated that it is bats' ability to work over a very large (>100dB) dynamic range that is key to their detection of small targets. Finally, Chapter 6 investigated the response of the external ear of the fruitbat *R. leschenaultii*, a close relation of the bat studied in Chapter 3, *R. aegyptiacus*. This work demonstrated the use of PZFlex, a finite element analysis package, in simulating the response of the ear to incoming sounds, thereby predicting the signals transferred to the middle ear and actually heard by the bat. This indicated that the combined response of the calls and ears of the *Rousettus* family, do not generate significant monaural spectral cues for sound localisation, in contrast to microchiropteran species in the literature (Wotton *et al.*, 1997).

7.2 Review of Achievements

This work investigated biosonar systems and techniques, and demonstrated similar methods applied to engineered air-coupled ultrasonic systems. This work has made some significant advances:

- Design and manufacture of a wireless ultrasonic sensor allowing the calls of fruitbats to be recorded as they echolocated whilst in free flight. Through novel use of variable gain, mimicking techniques used by bats, the attenuated return echoes were also well represented in the recordings.
- An inexpensive electrostatic transducer was designed and tested that operates in piston-mode fashion over a wide frequency range, including the range used by echolocating bats. These transducers are also capable of generating acoustic signals in air in excess of 100dB SPL with a 20Vp-p excitation signal, comparable to the signal levels used by bats.
- The link between the surface profile of the backplate of electrostatic transducers, and their magnitude and phase operation was demonstrated

through precise mapping of the backplate surface, in conjunction with laser vibrometry and field measurement techniques.

- Reproduction of echolocation calls and biologically inspired signals allowed bats' capability of detecting wires of small cross-section to be investigated in the laboratory. Using a calibrated microphone to quantify the process, it was demonstrated that bats achieve this via the considerable (>100dB) dynamic range between the calls they emit, and the return echoes they are capable of detecting.
- The response of the external ear of *R. leschenaultii* was predicted via a combined measurement and FEA approach. Using finite element code (PZFlex) the response of a bat ear to arbitrary signals, originating from a user-specified location, was simulated. This approach was verified by measuring the response of an ear reproduced using rapid prototyping techniques, thereby verifying the FEA technique. This simulation approach was then used to demonstrate the response of a fruitbat ear and also to investigate the advantage of using a wideband FM chirp, favoured by many microchiropteran species, over the impulsive click used by *Rousettus* in terms of the potential for gathering monaural cues regarding the origin of an echo.

The work presented in this Thesis has been successful in investigating biological and physical aspects of biosonar systems, and applying some of these techniques in engineering applications. The multi-disciplinary approach meant that many aspects of biosonar were investigated, with the result being a more complete view of the echolocation system than might be appreciated otherwise.

7.3 Suggestions for Further Work

There are several areas within the scope of this Thesis that warrant additional investigation, which would further the application of useful biosonar techniques in engineered ultrasonic and sonar systems.

7.3.1 Wireless Microphone Sensor Development

The aim of designing the miniature bat-mounted wireless sensor was two-fold. Firstly, it was desired to obtain accurate recordings of the calls emitted by a flying bat, without the issues related to changing distance and orientation between the bat and a static microphone. Secondly, using variable gain, the echoes returning to the bat were to be recorded. Both of these aims were achieved, although the extent to which the emitted call can be *accurately* recorded without having the microphone positioned in front of the bat's mouth (and therefore forming an acoustic obstruction) is questionable given the directivity of echolocation calls, especially the higher-frequency components. However, what cannot be disputed is that the microphone mounted between the ears of the bat is an *ideal* position for the recording of returning echoes. There were two specific aspects of the echolocation recordings that were not ideal. Firstly, the environment was artificial, and secondly, the calls of the bat used were not as interesting from an engineering viewpoint as the wideband FM chirps used by many microchiropteran bats. At one stage it was planned that the sensor would be further miniaturised, to enable it to be used with smaller species of bat resident in the British Isles. It was envisaged that this smaller sensor could be used on bats flying in a more natural environment by capturing foraging bats, mounting the sensor, and allowing them to fly in a outdoor cage constructed of a frame and netting. In this way, the bats would behave in a more natural way, and presumably allow the calls used during the phases of predation to be recorded. The use of variable gain to record emitted and returning calls would undoubtedly add more detail to our understanding of the signals employed. As such, this work could still be undertaken, although there are significant obstacles. Miniaturisation of the sensor is possible, though brings certain compromises. Firstly, the mass of the sensor is made up almost entirely of the large battery. This was required mainly for two components – the VGA and VCO. Both of these components could be replaced by a discrete design using surface mount transistors, thereby reducing the power requirements of the sensor. Whilst this may be possible for the amplifier, without too many compromises (although the same level of gain variation would be difficult to achieve), the same cannot be said of the VCO. Although the VCO is relatively power-hungry, it is also capable of generating a significant level of RF transmitted

signal, making it possible to use the sensor outwith a screened environment. The only other wireless bat-mounted microphone the author is currently aware of is the *Telemike* system designed at the University of Doshisha in Japan (e.g. Hiryu *et al.*, 2008). Telemike uses an oscillator based on discrete transistors, thereby allowing it to be miniaturised and run from a low-power and lightweight zinc-air battery. However, the low-power nature of the design means that the sensor must be used within a Faraday cage environment to screen out external sources of RF interference. As such, miniaturisation of the sensor for use with microchiropteran species would undoubtedly produce useful and interesting results. However, it is far from straightforward, especially if the variable-gain functionality was to be maintained, and an outdoor environment, with inevitable RF interference, was desired. Within the scope of this work, the design of a wideband microphone to cover the entire frequency range of interest, would also be beneficial given the null that exists in the electret microphone used on the current sensor design. This may be possible through use of a piezoelectric polymer such as PVDF, though this would certainly necessitate the use of a high-impedance FET-input amplifier, placing further restrictions on the electronic design.

7.3.2 Electrostatic Transducer Development

As noted during Chapter 4, the design of an air-coupled transducer capable of reproducing the wideband calls of bats was achieved with an electrostatic design. Furthermore, this design was demonstrated to operate in a piston-mode fashion over an extended frequency range, producing an efficient wideband source. However, one improvement that would bring many benefits, especially within the field of NDE, would be if the piston-mode characteristic could be maintained but the transducer made more sensitive through increased membrane motion. This would enable wideband signals, and the many benefits they could bring in terms of resolution, to be used in air-coupled NDE. It would also enable Lamb waves to be launched into test plates of varying thickness without altering the angle of incidence, by changing the frequency of operation; this would allow a device to be designed with a static transducer, courtesy of the frequency agility of the system.

It was demonstrated that the transducers with a PCB backplate showed improved sensitivity over those built with vitreous carbon (VC). It was hypothesised that this was due to increased membrane motion promoted by the additional air trapped between the membrane and backplate courtesy of the increased surface roughness. Indeed, vibrometry measurements appeared to back this up, indicating areas of increased membrane motion that corresponded with the weave structure of the PCB material itself. The average velocity of the transmitting membrane was also significantly higher for the PCB devices than the VC ones. One method of improving sensitivity was thus trialled, through micromachining a series of pits, of approximately 20μm diameter, in a VC backplate using a laser micromachining system. The objective of this was to trap additional air under the membrane over which it could vibrate, thereby increasing its range of motion. The results from the micromachined backplates proved to be disappointing, however. No increase in membrane motion or, correspondingly, device sensitivity was observed.

As such, the way forward in this regard is not clear. There *are* examples of micromachined electrostatic transducers (as opposed to cMUTs) in the literature (e.g. Schindel *et al.*, 1995). However, the effect of micromachining on device operation was not investigated through comparison with a non-micromachined version. It is interesting to note that the extremely smooth surface of the VC backplate promoted tight phase correlation across the membrane; according to Schindel *et al.* this is one of the advantages of the micromachining approach. Given that those backplates were manufactured from a silicon wafer type structure, itself very smooth, it would be surprising, given the response of the VC transducer, if the results from a non-micromachined device indicated poor phase correlation. As such, the function of the micromachining is not clearly demonstrated. Furthermore, no sensitivity data was presented on any of these devices meaning that a full comparison with the devices produced during the work presented here could not be made. Interestingly, very little consideration is given to the sensitivity of electrostatic devices in the literature, or how this might be improved.

One possible reason for the lack of improved sensitivity with the laser micromachining approach adopted here may be the large spacing between

micromachined pits (375μm) with respect to their diameter (approximately 20μm); the aggregate area of the pits accounted for just 1% of the surface of the backplate. In the case of the devices built by Schindel *et al*., the pits accounted for some 20% of the backplate area. As such, a series of backplates should be micromachined with a greater density of small pits. Assuming circular pits with a diameter of 20μm, then the theoretical limit on the spacing (assuming adjacent pits do not impinge on each other) would itself be 20μm. This imposes a limit that would mean the total pit area would account for almost 80% of the surface of the backplate, comprised of some 2.25 million pits. This certainly leaves sufficient margin to investigate, starting from the 1% of the surface area occupied by the pits in the backplate machined in Chapter 4. It is difficult to believe that the operation of the device would not be altered, either for better or worse, as the density of the pits was increased towards this limiting point. It would be interesting to observe at what point the excellent phase correlation reported for the VC backplates was disrupted as the surface was more drastically altered through more densely-packed pits. Or, indeed, at what point the expected improvement in sensitivity was obtained. It may be that the motion of the membrane can indeed be increased using this method, but that any increase in sensitivity is compromised due a decrease in phase correlation. This relationship requires investigation.

It should be highlighted at this point that the intention of micromachining the backplate was *not* to create pits over which the membrane would *resonate* – by definition a relatively narrowband phenomenon. The intention instead was that there would be additional air between the membrane and backplate over which the membrane could *vibrate*, without setting up resonant behaviour. However, resonant structures are the second method by which improved sensitivity may be promoted. Indeed, the means by which the sensitivity of a transducer may be increased in a narrowband fashion has already been documented by Campbell *et al.* (2006) on transducers with resonant pipes and cavities machined in the backplate. These structures were designed to have a narrowband response, and a device manufactured with a cavity matched to a resonant (open-ended) pipe was demonstrated to generate a 16-fold (24dB) improvement over a cavity alone.

Although this operation was demonstrated at a low frequency (approximately 8kHz) and generated devices with a limited bandwidth (<15% fractional bandwidth), the methodology may have some merit in application to wideband transducers, operating at a higher centre frequency. Given the potential for very finely spaced cavities, a range of cavities or pipes relating to a range of resonant frequencies could be created in a backplate. Assuming an upper frequency limit of 500kHz for use in NDE, then a cavity spacing of double the 20μm diameter would mean approximately 17 cavities per wavelength, or nearly 300 in a square of a wavelength per side. This would allow enough cavities at each frequency to generate a piston-mode acoustic field. The manufacture of such a device would be problematic however, in terms of controlling the dimensions of each size of cavity or pipe. Theoretically, it could generate a wideband transducer with significantly improved sensitivity however.

7.3.3 Simulation of Echolocation Systems

One area that has significant opportunities for further research is that of Finite Element Analysis (FEA) and simulation of the biological structures involved in echolocation. The simulation of the response of the *R. leschenaultii* ear described in the previous Chapter demonstrates a new and flexible method by which the response of these structures can be simulated, and their role in the echolocation process can be investigated. By obtaining an accurate 3D scan of the structure of interest, modelling accuracy can also be assured – although it should be noted that the nature of bat echolocation is certainly dynamic, with many species moving the ears, mouth and entire head during this process. This is not a factor that can be easily accounted for. However, the process demonstrated here could certainly be extended. Initially, it would be of great interest to investigate the response of more complex bat ears. The simulated response of *R. leschenaultii* ears reported in Chapter 6 demonstrated that the calls of *R. aegyptiacus* do not generate spectral cues that are strongly correlated with angular position of a sound source. However, such cues were more visible when FM chirps were used. The ears of the genus *Rousettus* have not evolved to make use of these complex chirps; it would be more interesting to investigate the response of an FM bat's ear to its own calls. In general these ears are more complex, with a prominent tragus that both simulation (Müller, 2004; Müller *et al*., 2008) and

measurement using dead bats (Wotton *et al.*, 1995; Aytekin, 2004) suggests plays a prominent role in generating correlated spectral cues regarding the angular location of a sound source. This could be investigated using the same method as used in this Thesis. In addition to simulating the response of bat ears, this method could also be used to investigate the response of the whole head of a bat by simulating the HRTF. This would be somewhat more challenging, given the sheer size of the model required to accurately represent the whole head in 3D. However, given modern distributed computing hardware, such as the High Performance Computer at the University of Strathclyde, such complex simulations are certainly possible. Further opportunities would be presented if the full 3D representation of a bat head was available.

Crucially, the x-ray techniques used to generate such models allow both the external and *internal* structures to be imaged. This could allow the *generation* of echolocation calls to be investigated using similar techniques. As demonstrated in Chapter 6 when the technique was being verified, a sound source can be applied within a structure and the sound propagated through the structure using FEA, and then beyond the model boundaries using extrapolation tools. If the internal airways of a bat could be imaged in sufficient detail, then this technique could be used to investigate how these structures and the oral cavity and mouth affect the sound emitted by the bat. These techniques would provide a flexible method by which the emission and detection of ultrasound by bats could be investigated. Furthermore, in comparison to the laborious and time-consuming alternative methods, such as mounting microphones within the ear cavities of dead bats (e.g. Fuzessery, 1996) or holding a bat stationary and stimulating its brain to force emissions that can be measured using a microphone or microphone array (e.g. Hartley and Suthers, 1989) these methods are relatively simple. Furthermore, it has the potential for generating a far greater range of accurate data than any method demonstrated to date in the literature.

7.3.4 Biomimetic Ultrasonic Sensors

There is one final area for research that warrants a brief mention. It has been amply demonstrated in the literature (as reviewed in detail in Section 2.4) that the external

ears of bats can encode the angular location of an echo source into the spectral content of the sound transferred to the inner ear. This process occurs as a result of the interaction between the incoming echo and the shape of the external ear. As such, there is a mechanism to determine the direction from which a sound has originated, without recourse to using an array and array signal processing algorithms. It would be interesting to apply these techniques to electrostatic transducers, by manufacturing ear-like structures that could be mounted on the front of the transducers to similarly encode sound directionality into the signal that impacts on the membrane. Such structures could be built relatively easily using the MSL equipment described in Chapter 6, allowing structures to be designed using CAD and even simulated in PZFlex to allow the most effective designs to be modelled beforehand. In conjunction with wideband time-of-flight measurement techniques, an echo source could potentially be accurately located in 3D space using a single transducer.

REFERENCES

Aldridge, H.D.J.N. and Brigham, R.M. 1988 Load carrying and maneuverability in an insectivorous bat: a test of the 5% rule of radio-telemetry. *J. Mammal.*, **69**(2), 379-82

Aytekin, M., Grassi, E., Sahota, M., and Moss, C. 2004 The bat head-related transfer function reveals binaural clues for sound localization in azimuth and elevation, *J. Acoust. Soc. Am.* **116**(6), 3594-605

Bashford, A.G., Hutchins, D.A. and Schindel, D.W. 1996 Radiated fields of an air-coupled ultrasonic capacitance transducer. *Ultrasonics*, **34**, 169-172

Bashford, A.G., Schindel, D.W., Hutchins, D.A. and Wright, W.M.D. 1997 Field characterisation of an air-coupled micromachined ultrasonic capacitance transducer, *Journal of the Acoustical Society of America*, **101**(1), 315-322

Bass, H.E., Sutherland, L.C., Zuckerwar, A.J., Blackstock, D.T. and Hester, D.M. 1995 Atmospheric absorption of sound: further developments, *Journal of the Acoustical Society of America*, **62** (6), 1373-1376 **97** (1), 680-3

Benny, G., Hayward, G. and Chapman, R. 2000 Beam profile measurements and simulations for ultrasonic transducers operating in air, *Journal of the Acoustical Society of America*, **107** (4), 2089-2100

Bernard, E and Fenton, M.B. 2003 Bat mobility and roosts in a fragmented landscape in Central Amazonia, Brazil, *Biotropica*, **35** (2), 262-277

Blum, F., Jarzynski, J. and Jacobs, L.J. 2005 A focused two-dimensional air-coupled ultrasonic array for non-contact generation, *NDT&E International* **38** 634-642

Bobber, R.J. 1988 Underwater Electroacoustic Measurements. ISBN 0-932146-19-8

Bontadina, F., Schofield, H. and Naef-Daenzer, B. 2002 Radio-tracking reveals that lesser horseshoe bats (Rhinolophus hipposideros) forage in woodland. *Journal of Zoology (London)*, **258**, 281-290

Boonman, A. and Jones, G. 2002 Intensity control during target approach in echolocating bats; stereotypical sensori-motor behaviour in Daubenton's bats, Myotis daubentonii. *Journal of Experimental Biology*, **205**, 2865-2874

Britton, A. R. C., Jones, G. and Rayner, J. M. V. 1997 Flight performance, echolocation and foraging behaviour in pond bats, *Myotis dasycneme* (Chiroptera: Vespertilionidae). *Journal of Zoology (London)*, **241**, 503–522.

Campbell, E., Galbraith, W. and Hayward, G. 2006 A new electrostatic transducer incorporating fluidic amplification, *IEEE Ultrasonics Symposium*, 1445-1448

Dardy, H.D., Bucaro, J.A., Schuetz, L.S. and Dragonette, L.R. 1977 Dynamic wide-bandwidth acoustic form-function determination, *Journal of the Acoustical Society of America*, **62** (6), 1373-1376

Faran, J.J. 1951 Sound scattering by solid cylinders and spheres, *Journal of the Acoustical Society of America*, **23** (4), 405-418

Faure P.A., Barclay R.M.R. 1994 Substrate gleaning versus aerial-hawking: plasticity in the foraging and echolocation behaviour of the long-eared bat, *Myotis evotis*. *Journal of Comparative Physiology A* , **174,** 651-660

Fenton, M.B. and Bell, G.P. 1981. Recognition of species of insectivorous bats by their echolocation calls. *J. Mammal*. 62, 233-43

Fuzessery, Z.M. 1996 Monaural and binaural spectral cues created by the external ears of the pallid bat. *Hearing Research*, **95**, 1-17

Gachagan, A., Hayward, G., Kelly, S.P., Galbraith, W. 1996 Characterization of air-coupled transducers. *IEEE Transactions on Ultrasonics, Ferroelectrics and Frequency Control*, **43** (4), 678-689

Galambos, R. 1942 Cochlear potentials elicited from bats by supersonic sounds. *Journal of the Acoustical Society of America*, **13**, 41-49

Ge, L.-F. 1999 Electrostatic airborne ultrasonic transducers: modelling and characterisation. *IEEE Transactions on Ultrasonics, Ferroelectrics and Frequency Control*, **46** (5), 1120-1127

Goodman, S.M., Chan, L.M., Nowak, M.D. and Yoder, A.D. 2010 Phylogeny and biogeography of western Indian Ocean *Rousettus* (Chiroptera: Pteropodidae). *Journal of Mammalogy*, **91** (3), 593-606

Griffin, D.R. 1944 How bats guide their flight by supersonic echoes. *American Journal of Physics* **12**, 342-5

Griffin DR. *Listening in the Dark*. Yale University Press, 1958. ISBN 0486217140

Griffin, D.R., Novick, A. and Kornfield, M. 1958 The sensitivity of echolocation in the fruit bat rousettus. *Biological Bulletin* **115** (1) 107-113

Grinnell, A.D. 1995 in Hearing by bats, p.4 Popper A.N. and Fay R.R. (Eds.) Springer-Verlag. ISBN 0387978445

Gustafson, Y. and Schnitzler, H.-U. 1979 Echolocation and obstacle avoidance in the Hipposiderid bat *Asellia tridens*, Journal of Comparative Physiology A, **131**, 161-167

Habersetzer J. and Vogler B. 1983 Discrimination of surface-structured targets by the echolocating bat, *Myotis myotis*, during flight. Journal of Comparative Physiology A, **152**, 275-282

Hamilton I.M. and Barclay R.M.R. 1998 Ontogenetic influences on foraging and mass accumulation by big brown bats (*Eptisicus fuscus*). Journal of Animal Ecology, **67**, 930-940

Haller, M.I. and Khuri-Yakub, B.T. 1996 A surface micromachined electrostatic ultrasonic air transducer. *IEEE Transactions on Ultrasonics, Ferroelectrics and Frequency Control*, **43** (1), 1-6

Hansen, S.T., Ergun, A.S., Liou, W., Auld, B.A. and Khuri-Yakub, B.T. 2004 Wideband micromachined capacitive microphones with radio frequency detection. *Journal of the Acoustical Society of America*, **116** (2), 828-842

Hartley, D.J. 1992 Stabilization of perceived echo amplitudes in echolocating bats. II. The acoustic behaviour of the big brown bat, *Eptesicus fuscus*, when tracking moving prey. *Journal of the Acoustical Society of America*, **91** (2), 1133-1149

Hartley, D.J., Campbell, K.A. and Suthers, R.A. 1989 The acoustic behaviour of the fish-catching bat, *Noctilio leporinus*, during prey capture. *Journal of the Acoustical Society of America*, **86** (1), 8-27

Hartley, D.J. and Suthers, R.A. 1989 The sound emission pattern of the echolocating bat, *Eptesicus fuscus*. *Journal of the Acoustical Society of America*, **85** (3), 1348-1351

Hartridge, H. 1920 The avoidance of objects by bats in their flight. *Journal of Physiology*, **54** (1-2), 54-57

Hayward, G., Benny, G., Banks, R. and Galbraith, W. 2000 The radiation field characteristics of piezoelectric polymer membrane transducers when operating in air. *IEEE Transactions on Ultrasonics, Ferroelectrics and Frequency Control*. **47** (6), 1438-1447

Henson Jr., O.W. 1965. The activity and function of the middle ear muscles in echolocating bats. *Journal of Physiology* (London) **180**, 871-87

Henson Jr., O.W., Bishop, A., Keating, A., Kobler, J., Henson, M., Wilson, B. and Hansen, R. 1987 Biosonar imaging of insects by *Pteronotus p. parnellii*, the mustached bat. *National Geographic Research*, **3** (1), 82-101

Hietanen, J., Matilla, P., Stor-Pellinen, J., Tsukuki, F., Vaataja, H., Sasaki, K. and Luukala, M. 1993 Factors affecting the sensitivity of electrostatic ultrasonic transducers. *Measurement Science and Technology*, **4**, 1138-1142

Hietanen, J. 1998 Closed-form formulation for sensitivity of capacitive ultrasonic transducers using V-grooved backplates. *Sensors and Actuators A*, **69**, 138-142

Hill JE, Smith JD (1984) Bats: A Natural History. Rigby Publishers. ISBN 072702003X

Hiryu, S., Katsura, K., Lin, L.-K., Riquimaroux, H. and Watanabe, Y. 2005 Doppler-shift compensation in the Taiwanese leaf-nosed bat (*Hipposideros terasensis)* recorded with a telemetry microphone system during flight. *Journal of the Acoustical Society of America* **118** (6), 3927-3933

Hiryu, S., Hagino, T., Riquimaroux, H. and Watanabe, Y. 2007 Echo-intensity compensation in echolocating bats (Pipistrellus abramus) during flight measured by a telemetry microphone. *Journal Of The Acoustical Society Of America* **121**, 1749-1757.

Hiryu, S., Shiori, Y., Hosokawa, T., Riquimaroux, H. and Watanabe, Y. 2008 On-board telemetry of emitted sounds from free-flying bats: compensation for velocity and distance stabilises echo frequency and amplitude. *Journal of Comparative Physiology A*, **194**, 841-851

Holderied, M.W., Korine, C., Fenton, M., Parsons, S., Robson, S. and Jones, G. 2005 Echolocation call intensity in the aerial hawking bat *Eptesicus bottae* (Vespertilionidae) studied using stereo videogrammetry. *Journal of Experimental Biology*, **208**, 1321-1327

Holland, R. A., Waters, D. A. and Rayner, J. M. V. 2004. Echolocation signal structure in the Megachiropteran bat Rousettus aegyptiacus Geoffroy 1810. *Journal Of Experimental Biology*, **207**, 4361-4369

Holland, R.A. and Waters, D.A. 2005 Echolocation signals and pinnae movement in the fruitbat *Rousettus aegyptiacus*. *Acta Chiropterologica*, **7** (1), 83-90

Huang, A.Y. and May, B.J. 1996 Sound orientation behavior in cats. II. Mid-frequency spectral cues for sound localization. *Journal of the Acoustical Society of America*, **100** (2), 1070-1080

Huang, K.-N. and Huang, Y.-P. 2009 Multiple-frequency ultrasonic distance measurement using direct digital frequency synthesizers. *Sensors and Actuators A: Physical*, **149** (1), 42-50

Jackson, J.C., Summan, R., Dobie, G., Whiteley, S., Pierce, G. and Hayward, G. Time-of-flight measurement techniques for airborne ultrasonic ranging. *IEEE Transactions of Ultrasonics, Ferroelectrics and Frequency Control* (in press)

Jen, P. H.-S. and Chen, D. 1988 Directionality of sound pressure transformation at the pinna of echolocating bats. *Hearing Research*, **34** (2), 101-117

Jen, P.H.-S. and Suga, N. 1975 Coordinated activities of the middle-ear and laryngeal muscles in echolocating bats. *Science* **191**, 950-2

Jimenez, A., Hernandez, A., Urena, J., Perez, M.C., Alvarez, F.J., De Marziani, C., Garcia, J.J. and Villadangos, J.M. 2008 EMFi-based ultrasonic transducer for robotics applications. *Sensors and Actuators A*, **148**, 342-349

Jones, G. (1999) Scaling of echolocation call parameters in bats. *The Journal of Experimental Biology* **202**, 3359-3367

Jones, G. and Teeling, E.C. 2006 The evolution of echolocation in bats. *Trends in Ecology and Evolution* **21** (3), 149-156

Kalko, E.K.V. 1994 Coupling of sound emission and wingbeat in naturally foraging European pipistrelle bats (Microchiroptera: Vespertillionidae). *Folia Zoologica*, **43**, 363-376

Kelly, S.P., Farlow, R. and Hayward, G. 1996 Applications of through-air ultrasound for rapid NDE scanning in the aerospace industry. *IEEE Transactions of Ultrasonics, Ferroelectrics and Frequency Control*, **43** (4), 581-591

Kelly, S.P., Hayward, G. and Alvarez-Arenas, T.E.G. 2004 Characterization and assessment of an integrated matching layer for air-coupled ultrasonic applications. *IEEE Transactions of Ultrasonics, Ferroelectrics and Frequency Control*, **51** (10), 1314-23

Kick, S.A. and Simmons, J.A. 1984 Automatic gain control in the bat's sonar receiver and the neuroethology of echolocation. *Journal of Neuroscience*, **11** (4), 2725-37

Koay, G., Heffner, R.S., Bitter, K.S. and Heffner, H.E. 2003 Hearing in leaf-nosed bats II: *Carollia perspicillata. Hearing Research*, **178**, 27-34

Koay, G., Heffner, R.S. and Heffner, H.E. 1998 Hearing in a megachiropteran fruit bat (*Rousettus aegyptiacus*). *Journal of Comparative Psychology*, **112** (4), 371-82

Kober, R. and Schnitzler, H.-U. 1990 Information in sonar echoes of fluttering insects available for echolocating bats. *Journal of the Acoustical Society of America*, **87** (2), 882-896

Korine, C., Speakman, J. and Arad, Z. 2004 Reproductive energetics of captive and free-ranging Egyptian Fruit Bats (*Rousettus aegyptiacus*). *Ecology*, **85** (1), 220-30

Kuhl, W., Schodder, G.R. and Schroder, F.-K. 1954 Condenser transmitters and microphones with solid dielectric for airborne ultrasonics. *Acustica*, **4**, 519-532

Lancaster, W.C., Keating, A.W. and Henson, O.W. 1992 Ultrasonic vocalizations of flying bats monitored by radiotelemetry. *Journal of Experimental Biology*, **173**, 43-58

Lancaster, W.C., Henson, O.W. and Keating, A.W. 1995 Respiratory muscle activity in relation to vocalization in flying bats. *J. Exp. Biol.* **198**, 175-91

Lawrence B.D. and Simmons, J.A. 1982 Echolocation in bats: The external ear and perception of vertical targets. *Science* **218**, 481-3

Lerch, R. and Friedrich, W. 1986 Ultrasound fields in attenuating media. *Journal of the Acoustical Society of America*, **80** (4), 1140-1147

Lockley RM (1979) Whales, Dolphins and Porpoises. David & Charles. ISBN 0715377310

Manthey, W., Kroemer, N. and Magori, V. 1992 Ultrasonic transducers and transducer arrays for applications in air. *Measurement Science and Technology*, **3**, 249-61

Menne, D., Kaipf, I., Wagner, I., Ostwald, J. and Schnitzler, H.-U. 1989 Range estimation by echolocation in the bat *Eptesicus fuscus*: Trading of phase versus time cues. *Journal of the Acoustical Society of America*, **85** (6), 2642-2650

Mergell, P., Fitch, W.T. and Herzel, H. 1999 Modeling the role of non-human vocal membranes in phonation. *Journal of the Acoustical Society of America*, **105** (3), 2020-2028

Mogdans, J., Ostwald, J. and Schnitzler, H.-U. 1988 The role of pinna movement for the localization of vertical and horizontal wire obstacles in the greater horseshoe bat, *Rhinolophus ferrumequinum*, *Journal of the Acoustical Society of America*, **84** (5), 1676-1679

Moss, C.F. and Schnitzler, H.-U. 1989 Accuracy of target ranging in echolocating bats: acoustic information processing. *Journal of Comparative Physiology A*, **165**, 383-93

Moss, C.F. and Schnitzler, H.-U. 1995 in Popper A.N., Fay R.R. (Eds.) Hearing by Bats. Springer Verlag. ISBN 0387978445 (p.134)

Moss, C.F. and Surlykke, A. 2001 Auditory scene analysis by echolocation in bats. *Journal of the Acoustical Society of America*,. **110** (4), 2207-2226

Müller, R. 2004 A numberical study of the role of the tragus in the big brown bat. *Journal of the Acoustical Society of America*, **116** (6), 3701-3712

Müller, R., Lu, H., Zhang, S. And Peremans, H. 2006 A helical biosonar scanning pattern in the Chinese Notule, *Nyctalus plancyi*. *Journal of the Acoustical Society of America*, **119** (6), 4083-4092

Müller, R., Lu, H. and Buck, J.R. 2008 Sound diffracting flap in the ear of a bat generates spatial information. *Physical Review Letters*, **100**, 108701, 1-4

Neubauer, W.G. 1968 Experimental measurement of creeping waves on solid aluminium cylinders in water using pulses. *Journal of the Acoustical Society of America*, **44** (1), 298-299

Neuweiler, G., Singh, S. and Sripathi, K. 1984 Audiograms of a South Indian bat community. *J. Comp. Physiol. A* **154**, 133-42

Noyes, A. and Pierce, G.W. 1938 Apparatus for acoustic research in the supersonic frequency range. *Journal of the Acoustical Society of America* **9** (3)**,** 205-211

Obrist, M.K., Fenton, M.B., Eger, J.L. and Schlegel, P.A. 1993 What ears do for bats: a comparative study of pinna sound pressure transformation in chiroptera. *Journal of Experimental Biology*, **180**, 119-152

Oksanaen, M., Varis, J., Hietanen, J. and Wu, J. 1997 Quantitative theory for v-groove capacitive transmitting transducers. *Ultrasonics*, **35**, 205-211

Paajanen, M., Lekkala, J. and Kirjavainen, K. 2000 Electromechanical film (EMFi) – a new multipurpose electret material. *Sensors and Actuators A*, **84**, 95-102

Pallav, P., Hutchins, D.A. and Gan, T.H. 2009 Air-coupled ultrasonic evaluation of food materials. *Ultrasonics*, **49**, 244-253

Pollack, G.D. 1993 Some comments on the proposed perception of phase and nanosecond time disparities by echolocating bats. *Journal of Caomparative Physiology A*, **172**, 523-531

Rafiq, M. and Wykes, C. 1991 The performance of capacitive ultrasonic transducers using v-grooved backplates. *Measurement Science and Technology*, **2**, 168-74

Riquimaroux, H., and Watanabe, Y. 2000 Characteristics of bat sonar sounds recorded by a telemetry system and a fixed ground microphone. *Proceedings WESTPRAC VII*, 233-238

Riquimaroux, H., Watanabe, Y. and Lin, L.-K. 2002 Ultrasonic echolocation behavior of a flying bat measured by a telemetry system and a high-speed video system. *Proceedings Forum Acoustica Sevilla*

Roberts, L.H. 1975 Confirmation of the echolocation pulse production mechanism of Rousettus. *Journal of Mammalogy*, **56** (1), 218-220

Robertson, T.J., Hutchins, D.A. and Billson, D.R. 2002 Capacitive air-coupled cylindrical transducers for ultrasonic imaging applications. *Measurement Science and Technology*, **13**, 758-769

Roverud, R.C., Volker, N., Neuweiler, G. 1991 Discrimination of wingbeat motion by bats, correlated with echolocation sound pattern. *Journal of Comparative Physiology A*, **168,** 259-263

Sales, G. and Pye, D. 1974 Ultrasonic Communication by Animals. Chapman and Hall. ISBN 0470749857

Schindel, D.W. and Hutchins, D.A. 1995 Applications of micromachined capacitance transducers in air-coupled ultrasonics and nondestrcutive evaluation. *IEEE Transactions on Ultrasonics Ferroelectrics and Frequency Control*, **42** (1), 51-58

Schindel, D.W., Hutchins, D.A., Zou, L. and Sayer, M. 1995 The design and characterization of micromachined air-coupled capacitive transducers. *IEEE Transactions on Ultrasonics Ferroelectrics and Frequency Control*, **42**(1), 42-50

Schnitzler, H.-U. and Kalko, E.K.V. 2001 Echolocation by insect-eating bats, *Bioscience*, **51** (7), 557-569

Schnitzler, H.-U., Moss, C.F. and Denzinger, A. 2003 From spatial orientation to food acquisition in echolocating bats. *Trends in Ecology and Evolution*, **18** (8), 386-394

Schumm, A., Krull, D. and Neuweiler, G. 1991 Echolocation in the notch-eared bat, *Myotis emarginatus*. *Behavioral Ecology and Sociobiology*, **28**, 255-261

Shiori, Y., Hiryu, S., Watanabe, Y., Riquimaroux, H. and Watanabe, Y. 2009 Pulse-echo interaction in free-flying horseshoe bats, *Rhinolophus ferrumequinum Nippon*. *Journal of the Acoustical Society of America Express Letters*, **126** (3), EL80-EL85

Simmons, J.A. 1973 The resolution of target range by echolocating bats. *Journal of the Acoustical Society of America*, **54** (1), 157-173

Simmons, J.A. 1979 Perception of echo phase information in bat sonar. *Science*, **204**, 1336-1338

Simmons, J.A. 1989 A view of the world through the bat's ear: the formation of acoustic images in echolocation. *Cognition*, **33**, 155-199

Simmons, J.A., Fenton, M.B. and O'Farrell, M.J.O. 1978 Echolocation and pursuit of prey by bats. *Science* **203**, 16-21

Simmons, J.A., Lavender, W.A., Lavender, B.A., Childs, J.E., Hulebak, K., Ridgen, M.R., Sherman, J. and Woolman, B. 1978 Echolocation by free-tailed bats (*Tadarida*). *Journal of Comparative Physiology A*, **125**, 291-299

Simmons, J.A. and Stein, R.A. 1980 Acoustic imaging in bat sonar: echolocation signals and the evolution of echolocation. *Journal of Comparative Physiology A*, **135**, 61-84

Simmons, J.A. and Vernon, J.A. 1971 Echolocation: Discrimination of targets by the bat *Eptesicus fuscus*, *Journal of Experimental Zoology*, **176**, 315-328

Simmons, J.A., Lavender, W.A., Lavender, B.A., Doroshow, C.A., Kiefer, S.W., Livingston, R., Scallet, A.C. and Crowley, D.E. 1974 Target structure and echo spectral discrimination by echolocating bats. *Science*, **186,** 1130-1132

Simmons, J.A., Kick, S.A., Lawrence, B.D., Hale, C., Bard, C. and Escudie, B. 1983 Acuity of horizontal angle discrimination by the echolocating bat, *Eptisicus fuscus*. *Journal of Comparative Physiology A.* **153**, 321-30

Simmons, J.A., Ferragamo, M., Moss, C.F., Stevenson, S.B. and Altes, A. 1990 Discrimination of jittered sonar echoes by the echolocating bat, *Eptesicus fuscus*: The shape of target images in echolocation. *Journal of Comparative Physiology A*. **167**, 589–616

Simmons, J.A., Moffat, A.J., and Masters, W.M. 1992 Sonar gain control and echo detection thresholds in the echolocating bat, *Eptesicus fuscus*. *J. Acoust. Soc. Am.* **91**, 1150–63.

Song, J. and Chimenti, D.E. 2006 Design, fabrication and characterization of a spherically focused capacitive air-coupled ultrasonic transducer. *International Journal of Applied Science and Engineering*, **4** (1), 1-19

Speakman, J.R., Anderson, M.E. and Racey, P.A. 1989 The energy cost of echolocation in pipistrelle bats (*Pipistrellus pipistrellus*). *Journal of Comparative Physiology A*. **165**, 679-685

Speakman, J.R. and Racey, P.A. 1991 No cost of echolocation for bats in flight. *Nature* **350**, 421-3

Streicher, A., Kaltenbacher, M., Lerch, R. and Peremans, H. 2005 Broadband EMFi ultrasonic transducer for bat research, *Proceedings IEEE Ultrasonics Symposium 2005*, 1629-1632

Surlykke, A. and Kalko, E.K.V. 2008 Echolocating bats cry out loud to detect their prey. *PLoS ONE*, **3** (4), e2036

Suthers, R.A. and Fattu, J.M. 1973 Mechanisms of sound production by echolocating bats. *American Zoology*, **13**, 1215-1226

Suthers, R.A. 2004 Vocal mechanisms in birds and bats: a comparative view. *Anais da Academia Brasileira de Ciências*, **76** (2), 247-252

Suzuki, K., Higuchi, K. And Tanigawa, H. 1989 A silicon electrostatic ultrasonic transducer. *IEEE Transactions on Ultrasonics Ferroelectrics and Frequency Control*, **36** (6), 620-627

Takahashi, S. and Ohigashi, H. 2009 Ultrasonic imaging using air-coupled P(VDF/TrFE) transducers at 2MHz. *Ultrasonics*, **49**, 495-498

Thomas, S.P. 1981 Ventilation and oxygen extraction in the bat *Pteropus gouldii* during rest and steady flight. *Journal of Experimental Biology*, **94**, 231-250

Trogé, A., O'Leary, R.L., Hayward, G., Pethrick, R.A. and Mullholland, A.J. 2009 Properties of photocured epoxy resin materials for application in piezoelectric ultrasonic transducer matching layers. *Journal of the Acoustical Society of America*, **128** (5), 2704-2714

Tsai, W.-Y., Chen, H.-C. and Liao, T.-L. 2006 High accuracy ultrasonic air temperature measurement using multi-frequency continuous wave. *Sensors and Actuators A: Physical*, **132** (2), 526-532

Ulanovsky, N. and Moss, C.F. 2008 What the bat's voice tells the bat's brain. *Proceedings of the National Academy of Sciences of the USA*, **105** (25), 8491-8498

Urban, H.G., 2002 Handbook of Underwater Acoustic Engineering STN ATLAS Elektronik GmbH, Breman

Van Wanrooij, M.M. and Van Opstal, A.J. 2004 Contribution of head shadow and pinna cues to chronic monaural sound localization. *Journal of Neuroscience*, **24** (17), 4163-4171

Van Wanrooij, M.M. and Van Opstal, A.J. 2006 Sound localization under perturbed binaural hearing. *Journal of Neurophysiology*, **97**, 715-726

Von der Emde, G. and Menne, D. 1989 Discrimination of wingbeat frequencies by the bat *Rhinolophus ferrumequinum*. *Journal of Comparative Physiology A*, **164** 663-671

Wang, X. and Müller, R. 2009 Pinna-rim skin folds narrow the sonar beam in the lesser false vampire bat (*Megaderma spasma*). *Journal of the Acoustical Society of America*, **126** (6), 3311-3318

Waters, D.A. and Jones, G. 1995 Echolocation call structure and intensity in five species of insectivorous bats. *Journal of Experimental Biology*, **198**, 475-489

Waters, D.A. and Vollrath, C. 2003 Echolocation performance and call structure in the megachiropteran fruit-bat *Rousettus aegyptiacus*. *Acta Chiropterologica*, **5** (2), 209-219

Waters, D.A., Rydell, J. and Jones, G. 1995 Echolocating call design and limits on prey size: a case study using the aerial hawking bat *Nyctalus leisleri*. *Behavioral and Ecological Sociobiology* **37**, 321-328

Wightman, F.L. and Kistler, D.J. 1989 Monaural sound localisation revisited. *Journal of the Acoustical Society of America*, **101** (2), 1050-1063

Wong, J. G. and Waters, D. A. 2001 The synchronisation of signal emission with wingbeat during the approach phase in soprano pipistrelles (*Pipistrellus pygmaeus*). *Journal Of Experimental Biology*, **204**, 575-583.

Wotton, J.M., Haresign, T and Simmons, J.A. 1995 Spatially dependent acoustic cues generated by the external ear of the big brown bat, *Eptesicus fuscus*. *Journal of the Acoustical Society of America*, **98** (3), 1423-1445

Wotton, J.M., Haresign, T., Ferragamo, M.J. and Simmons, J.A. 1996 Sound source elevation and external ear cues influence the discrimination of spectral notches by

the big brown bat, *Eptesicus fuscus*. *Journal of the Acoustical Society of America*, **100** (3), 1764-1776

Wotton, J.M., Jenison, R.L. and Hartley, D.J. 1997 The combination of echolocation emission and ear reception enhances directional spectral cue of the big brown bat, *Eptesicus fuscus*. *Journal of the Acoustical Society of America*, **101** (3), 1723-1733

Wotton, J.M. and Simmons, J.A. 2000 Spectral cues perception of the vertical position of targets by the big brown bat, *Eptesicus fuscus*. *Journal of the Acoustical Society of America*, **107** (2), 1034-1041

Zhang, J.-S, Jones, G., Zhang, G.-J. and Zhang, S.-Y. 2010 Recent surveys of bats (Mammalia: Chiroptera) from China II. Pteropodidae. *Acta Chiropterologica*, **12** (1), 103-116

Appendix A - Calibration of Sound Pressure Level as measured using B&K Type 4138 Microphone Coupled to Nexus 2670 Pre-amp.

All calibrated sound pressure level (SPL) measurements and field measurements presented in the course of this Thesis were produced using a Brüel & Kjær (B&K, Nærum, Denmark) Type 4138 1/8" microphone, in conjunction with a Nexus 2670 preamplifier (also supplied by B&K). There were two specific issues that needed to be addressed in correcting for the response of the microphone: frequency response such that the absolute pressure level generated by the transducers was accurately measured across a range of frequencies; and directional response to enable the effect of the microphone on the measured field structure to be ascertained. The purpose of this Appendix is to describe how correction data for each of these effects was calculated, and then how these data were applied.

A1.1 Microphone Frequency Response Data Provided by the Manufacturer

In correcting for the frequency response of the B&K system, two factors were taken into account: its pressure field response, measured using the electrostatic actuator method; and a correction for measurements in a free-field. An electrostatic actuator is a stiff metal plate that is brought into close proximity of the microphone membrane (~0.5mm). An AC signal (tens of volts) at the frequency of interest is then applied in addition to a DC signal (hundreds of volts), which will generate a periodic deflection of the microphone membrane, in the same way as an incident pressure wave would. This can then be measured and the frequency response of the microphone cartridge calculated. This is use in conjunction with a measurement of absolute sensitivity carried out using a calibrated sound source at a reference frequency to produce a calibration curve referenced to an absolute sensitivity. This response refers to the cartridge response in a pressure field, which is characterised by a sound pressure with the same magnitude and phase anywhere in the field (as occurs in enclosures that are small with respect to the sound wavelength). To convert this calibration curve for use in a free field (i.e. where sound waves are free to propagate) requires the addition of the free field correction. Each B&K microphone is provided with an individual calibration chart of its electrostatic actuator / pressure field response,

whilst a general free field correction curve is provided in the product data sheet (available at http://www.bksv.co.uk/doc/bp2030.pdf), whilst the Microphone Handbook (available at http://www.bksv.co.uk/doc/ba5105.pdf) contains a full description of microphone design, calibration and operation.

The pressure field response for the microphone used in this study is pictured in Figure A1.

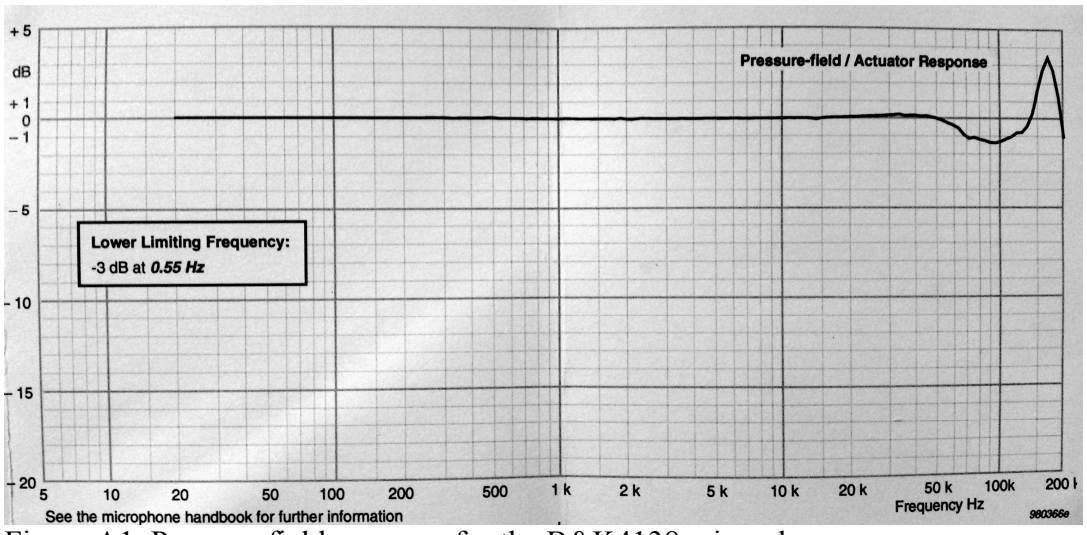

Figure A1. Pressure field response for the B&K4138 microphone.

This calibration curve was referenced to a sensitivity of -60.5dB re. 1V/Pa, which is equivalent to 0.941mV/Pa. The associated free-field correction curves are illustrated in Figure A2 with (a) and without (b) the protection grid attached to the microphone.

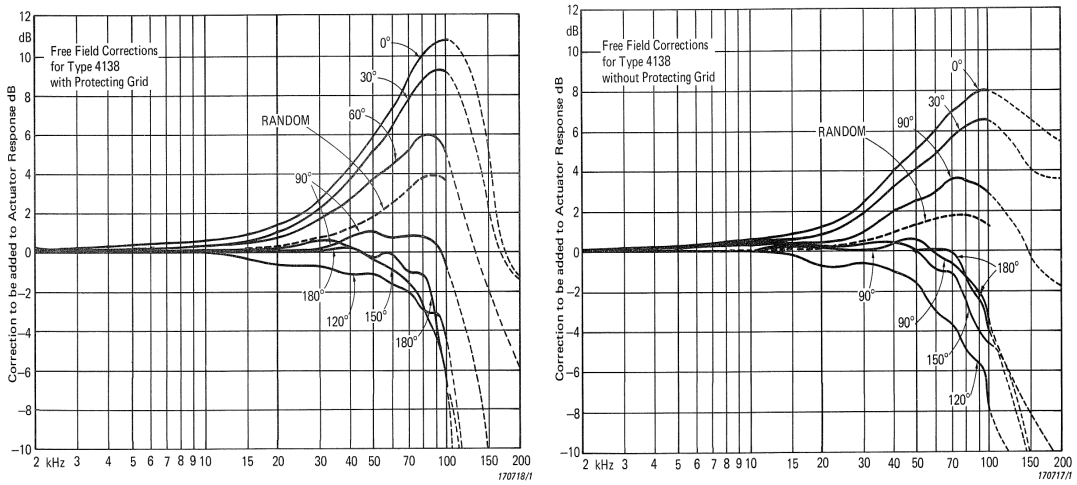

(a) (b)

Figure A2. Free-field correction curves for the B&K 4138 microphone with (a) and without (b) the protection grid.

Unfortunately these graphs were not available in tabulated format and so these correction curves had to be converted through measurement of the graphs into a suitable format for application to the measurements made during the course of this Thesis. This required these curves to be interpreted in two ways in order to calibrate for the absolute received sound pressure level (SPL) at normal incidence, and secondly to account for the angular sensitivity change in field measurements.

A1.2 Sound Pressure Level Calibration – Normal Incidence

For SPL calibration, an estimate was made from the 0° incidence curve on the graph at 10kHz intervals from 10kHz to 200kHz. All measurements were made with the protection grid removed, and so it is these data points that were used, which were then interpolated using Matlab to obtain correction factors at 1kHz intervals, to apply directly to the measured values. The values measured from each graph are indicated in Table A1.

Frequency (kHz)	Actuator Response (dB)	Free Field Correction (no grid, dB)
10	0.0	0.5
20	0.1	1.35
30	0.2	2.7
40	0.1	4.1
50	0.0	5.0
60	-0.4	5.6
70	-1.0	6.0
80	-1.2	6.2
90	-1.4	6.55
100	-1.3	6.7
110	-1.1	6.7
120	-0.8	6.7
130	-0.45	6.75
140	0.0	6.9
150	1.5	8.0
160	2.5	8.8
170	3.5	9.5
180	2.5	8.3
190	1.0	6.7
200	-1	4.5

Table A1. Calibration estimates for B&K 4138 microphone taken at 10kHz intervals from graphical data.

After interpolation of these data points to provide 1kHz intervals, the curves used in SPL measurement calibration are displayed in Figure A3.

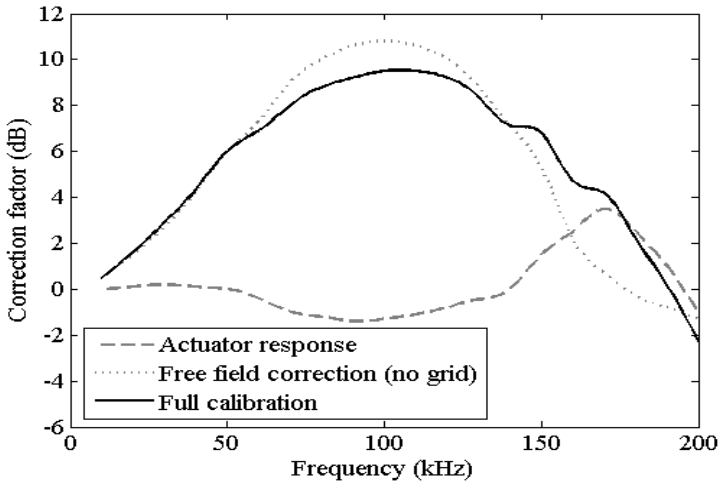

Figure A3. Actuator response, free field correction and full calibration curves for the B&K 4138 microphone without the protection grid in place.

The data points on these curves were then used to properly compensate for the response of the microphone when used to make single-frequency toneburst calibration measurements. As such, the measurement of SPL at each frequency was performed using equation A1.1:

$$SPL = 20\log_{10}\left(\frac{V_p}{20e-6}\frac{1}{\gamma}\right) - \zeta \qquad \text{(A1.1)}$$

Where v_p is peak voltage from the microphone amplifier, 20e-6 is the reference pressure in Pascals (Pa), γ is microphone system sensitivity (V/Pa), and ζ is the full calibration factor, in dB, at the correct frequency.

A1.3 Angular Sensitivity – Relative Calibration

The response of the microphone to varying angles of sound incidence was important since, during field measurement, the angle of incidence of sound on the microphone varies for each point in the field. Furthermore, at small axial distances from the transducer, the sound angle of incidence actually varied significantly depending on where on the transducer surface it originated. As such, to accurately simulate the field as received by the microphone, this effect needs to be incorporated into the field prediction algorithm. To enable this, the free-field correction values at 20kHz, 50kHz, 100kHz, 150kHz, 200kHz and 250kHz were estimated for 0° to 90° at 10° increments from the graphs in Figure A2. These estimates are detailed in Table A2 below.

Frequency	Correction Factor at Given Angle (dB)									
	0°	±10°	±20°	±30°	±40°	±50°	±60°	±70°	±80°	±90°
20kHz	1.2	1.05	0.9	0.8	0.65	0.5	0.4	0.35	0.25	0.2
50kHz	5.0	4.85	4.6	4.2	3.8	3.2	2.5	2.0	1.3	0.5
100kHz	8.0	7.7	7.3	6.5	5.5	4.4	3.0	1.2	-1.0	-3.0
150kHz	6.5	5.9	5.1	4.0	2.8	1.5	-0.2	-2.2	-4.7	-8.0
200kHz	5.5	5.0	4.4	3.6	2.1	0.3	-1.7	-4.2	-7.2	-11.0
250kHz	6.0	5.4	4.8	3.4	2.0	0.0	-2.2	-4.5	-8.0	-12.5

Table A2. Correction factor estimates over frequency range of interest at 10° increments taken from graphical data.

These data were then interpolated using Matlab to produce data at 1° increments, as displayed in Figure A4. This data was then used in field predictions by calculating the angle of incidence, to the nearest degree, from each point on the transducer surface to the each field point as the Rayleigh integral was calculated (see section 4.2), and applying the appropriate correction factor. This allowed accurate field structures, including the reduction in on-axis amplitude variation caused by microphone directionality, to be calculated.

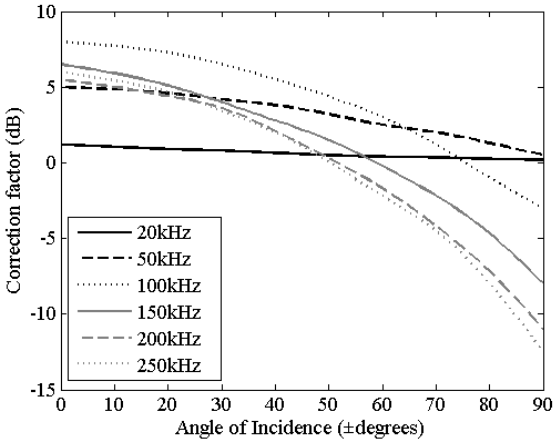

Figure A4. Free field correction factor for angle of incidence across frequency range of interest.

It can be seen that, through use of the data provided by the microphone manufacturer, that its response was properly compensated for in each measurement made.

Appendix B – Graphical Comparison of Time-Domain Results for Experimental and FEA Measurement of Ear Respsonse

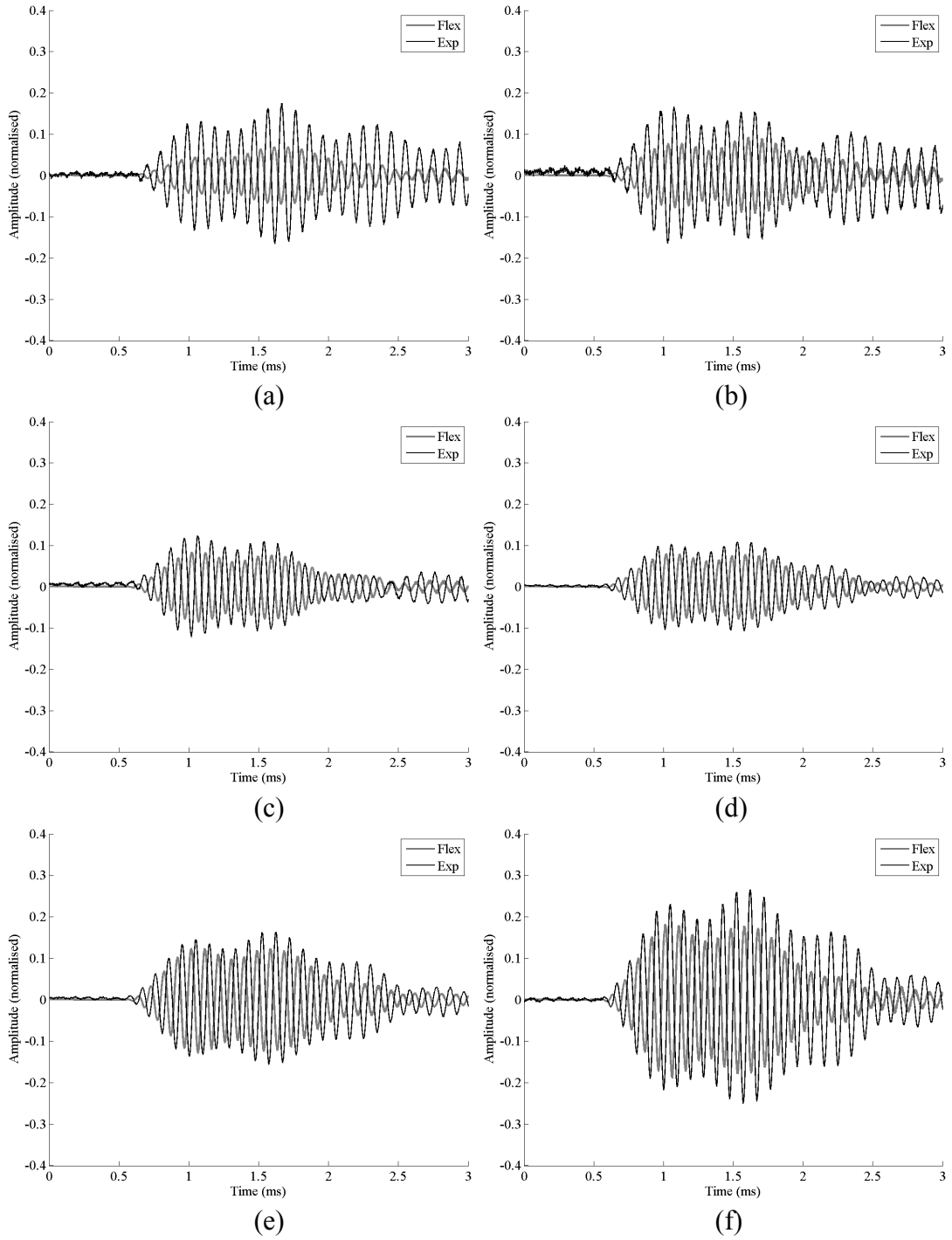

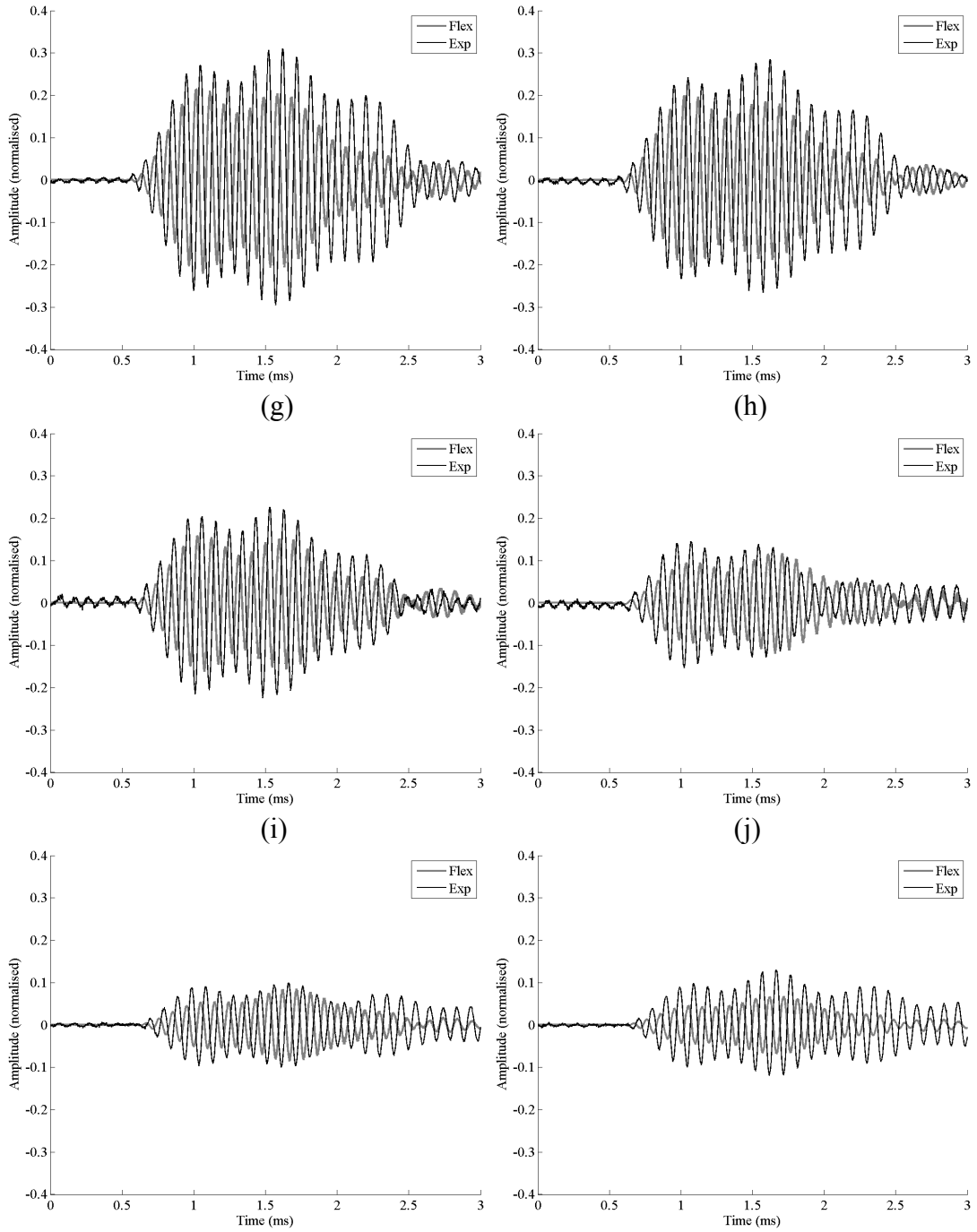

Figure B1. Comparison of simulated and experimental waveforms from a 10kHz toneburst at a height of 0mm with respect to the base of the ear at: (a) -150˚; (b) -120˚; (c) -90˚; (d) -60˚; (e) -30˚; (f) 0˚; (g) 30˚; (h) 60˚; (i) 90˚; (j) 120˚; (k) 150˚; (l) 180˚

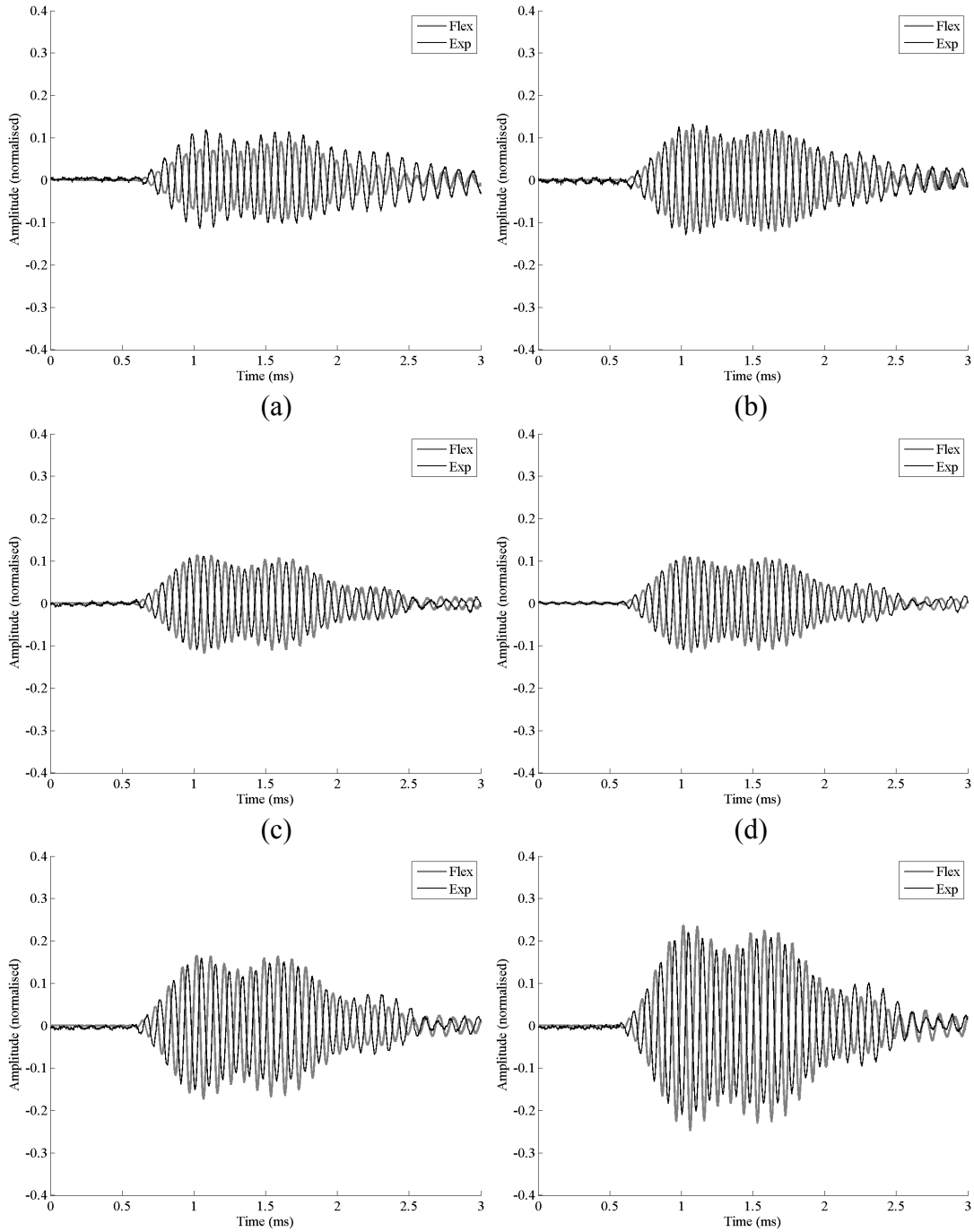
Flex
Exp
Amplitude (normalised)
Time (ms)
(a)
(b)
(c)
(d)
(e)
(f)

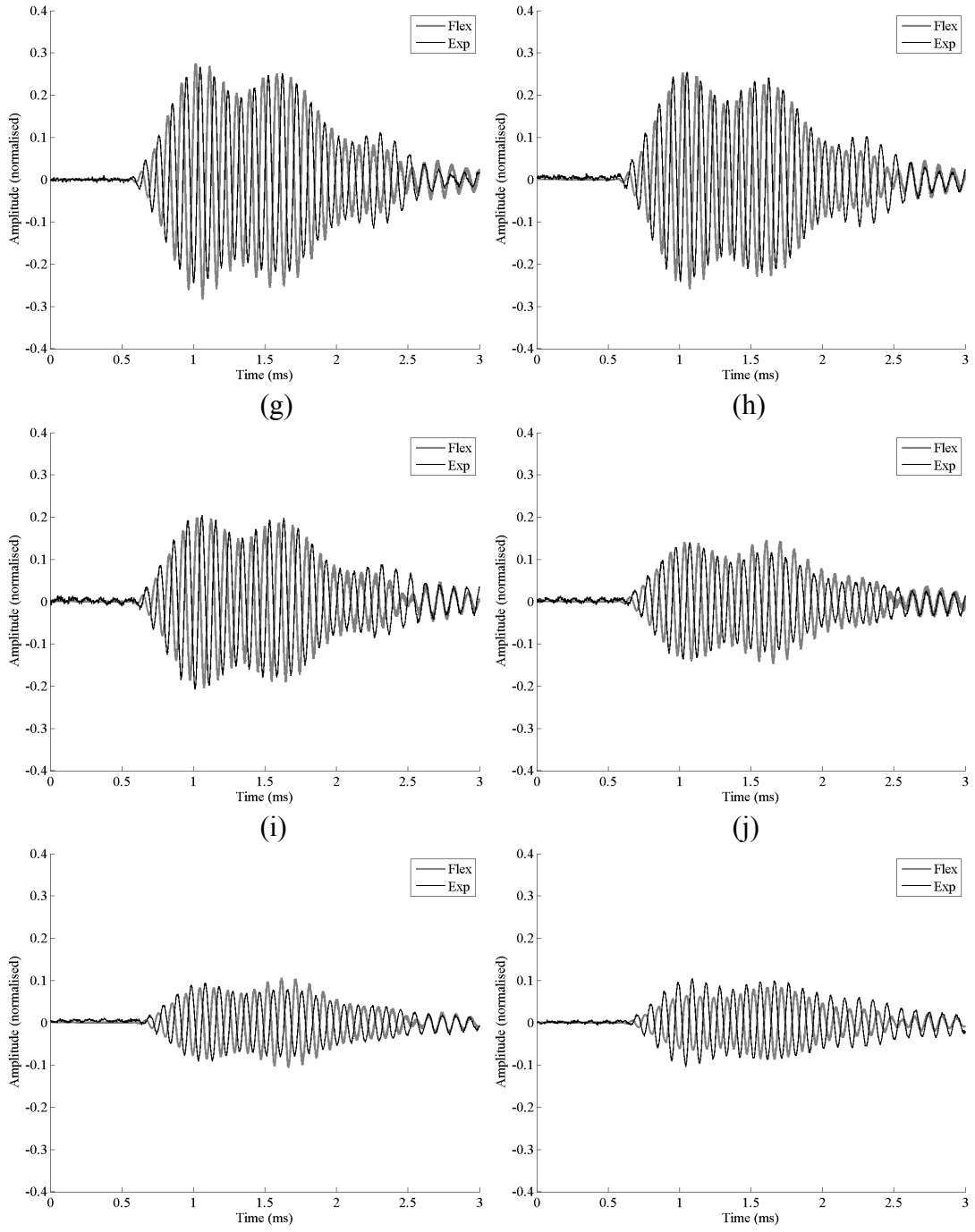

Figure B2. Comparison of simulated and experimental waveforms from a 10kHz toneburst at a height of 20mm with respect to the base of the ear at: (a) -150˚; (b) -120˚; (c) -90˚; (d) -60˚; (e) -30˚; (f) 0˚; (g) 30˚; (h) 60˚; (i) 90˚; (j) 120˚; (k) 150˚; (l) 180˚

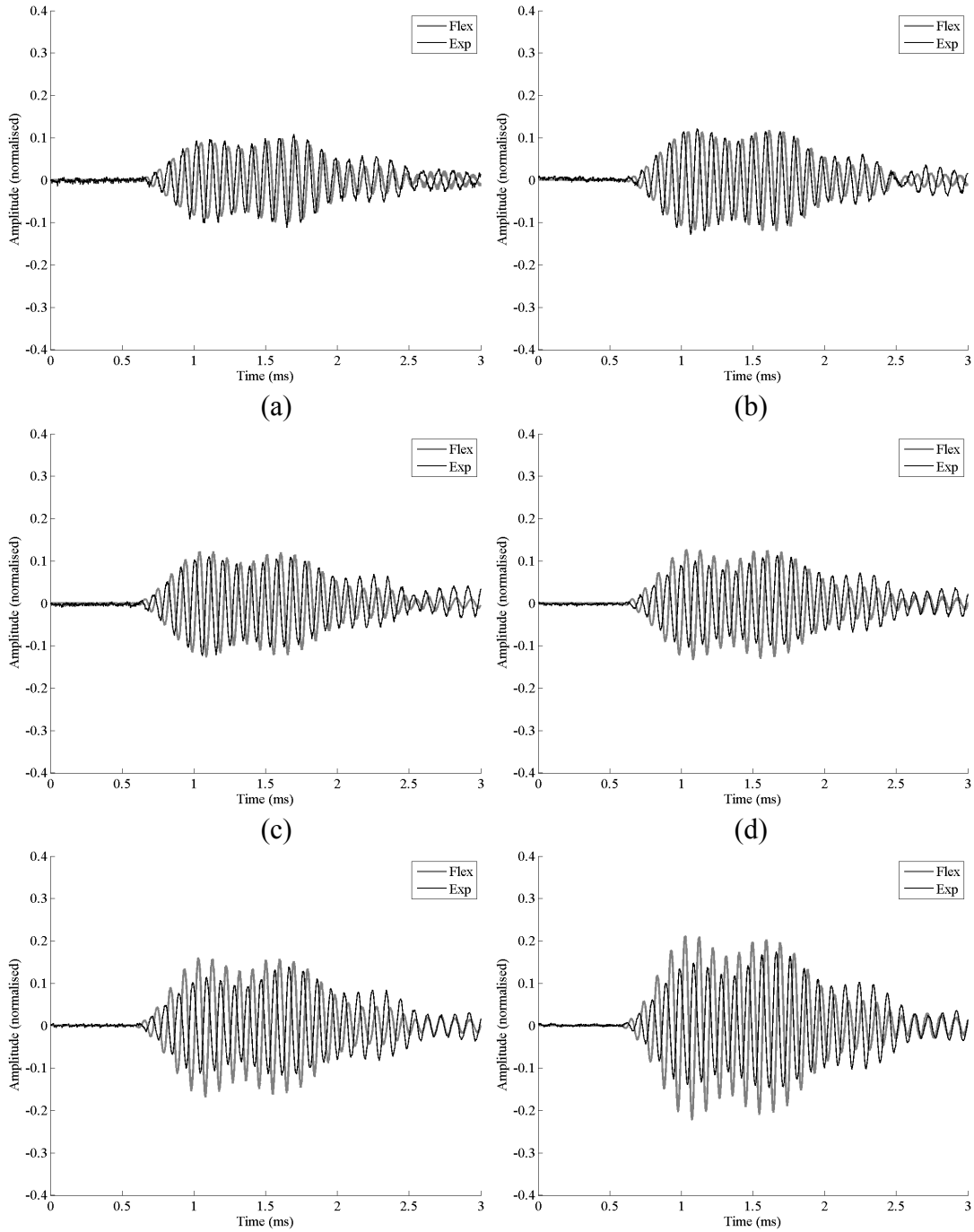
Flex
Exp
Amplitude (normalised)
Time (ms)
(a)
(b)
(c)
(d)
(e)
(f)

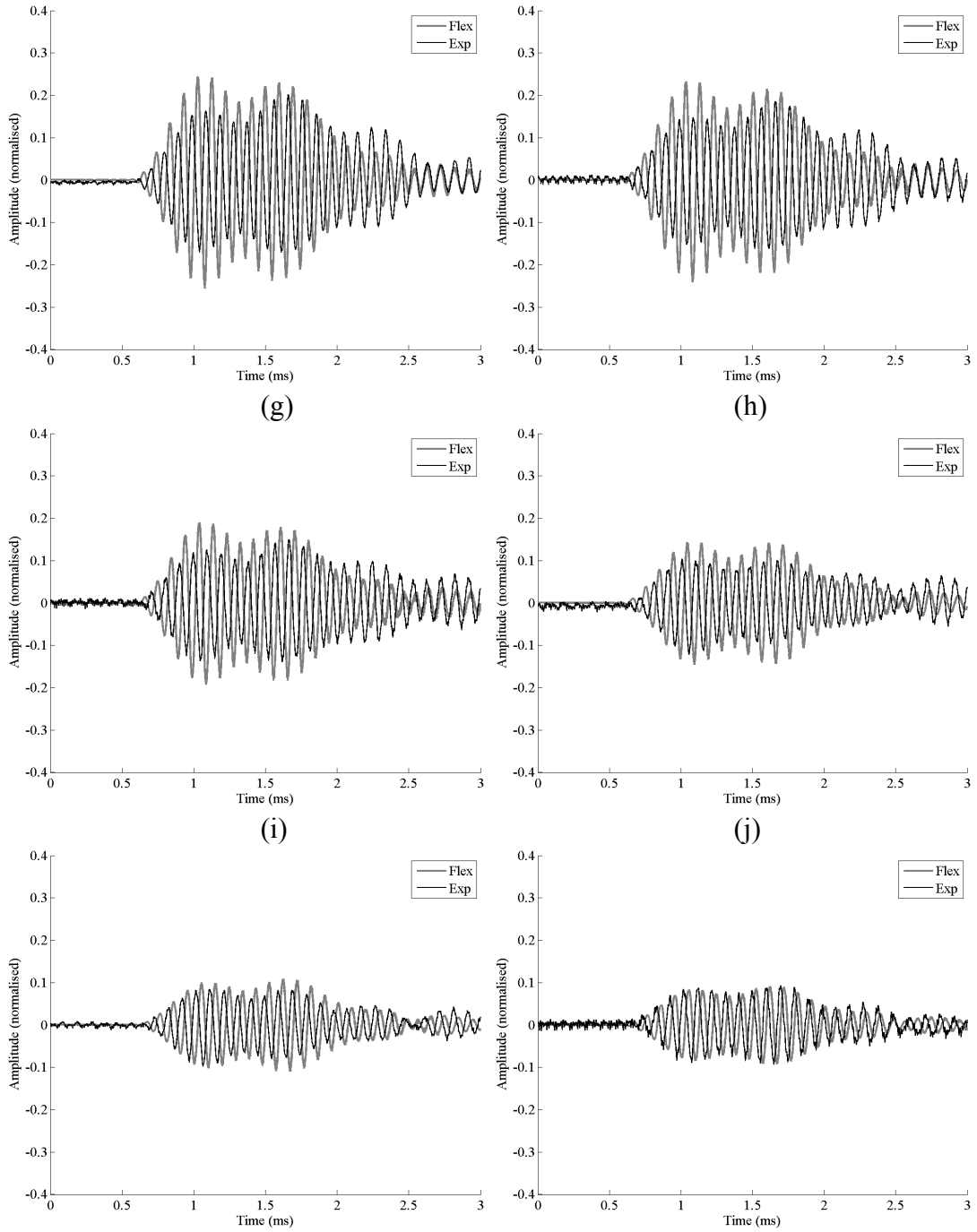

Figure B3. Comparison of simulated and experimental waveforms from a 10kHz toneburst at a height of 50mm with respect to the base of the ear at: (a) -150˚; (b) -120˚; (c) -90˚; (d) -60˚; (e) -30˚; (f) 0˚; (g) 30˚; (h) 60˚; (i) 90˚; (j) 120˚; (k) 150˚; (l) 180˚

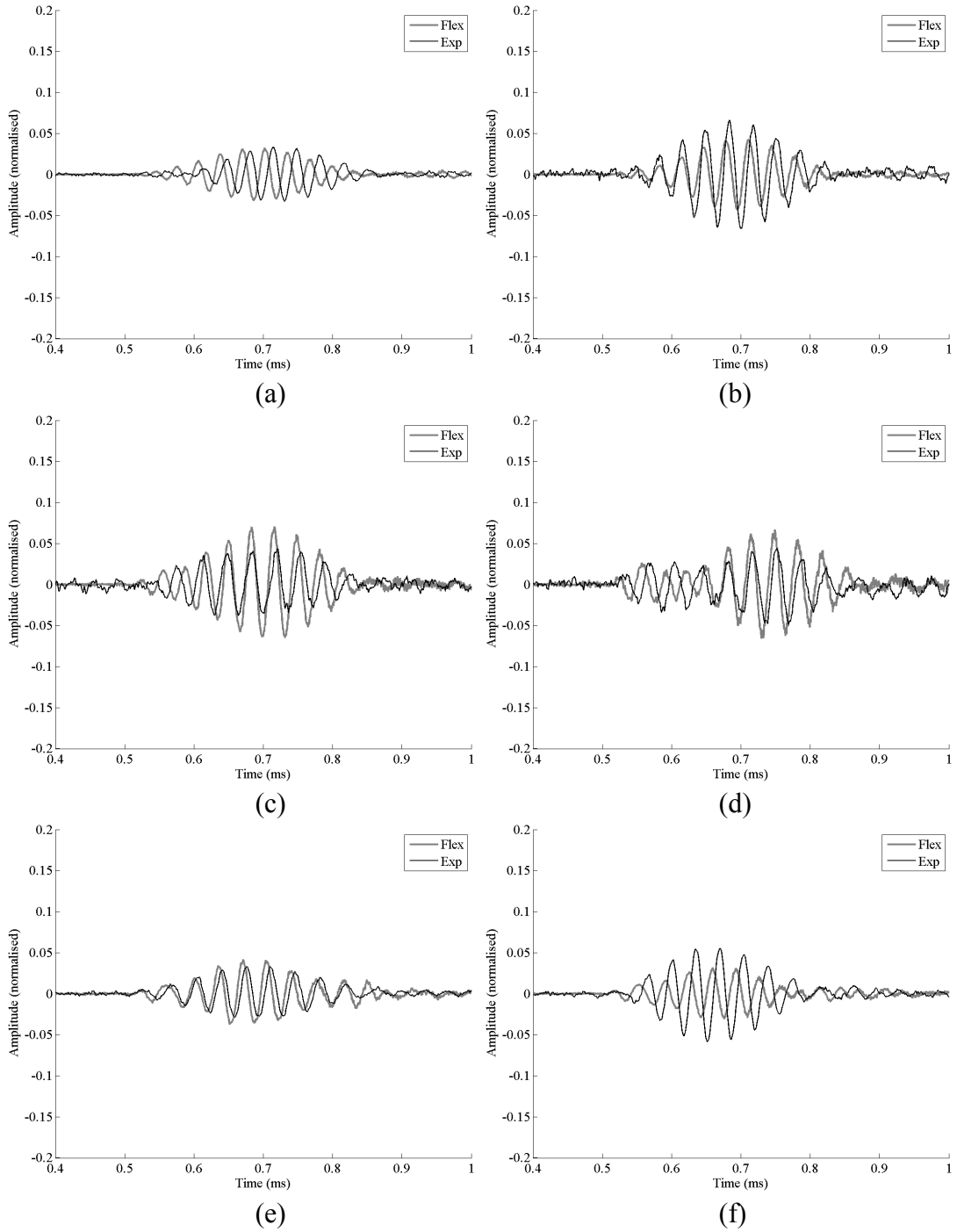
Flex
Exp
Amplitude (normalised)
Time (ms)
(a)
(b)
(c)
(d)
(e)
(f)

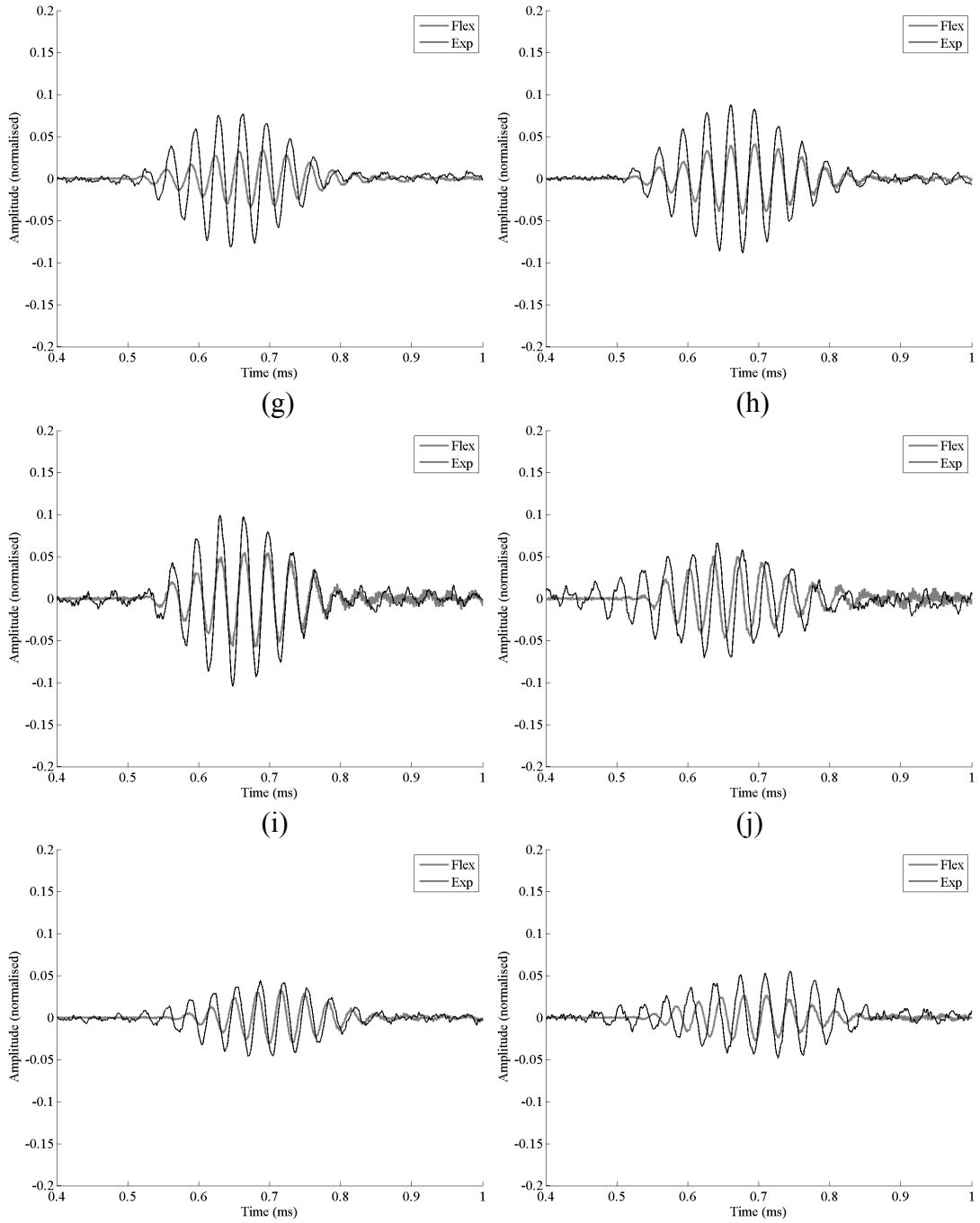

Figure B4. Comparison of simulated and experimental waveforms from a 30kHz toneburst at a height of 0mm with respect to the base of the ear at: (a) -150˚; (b) -120˚; (c) -90˚; (d) -60˚; (e) -30˚; (f) 0˚; (g) 30˚; (h) 60˚; (i) 90˚; (j) 120˚; (k) 150˚; (l) 180˚

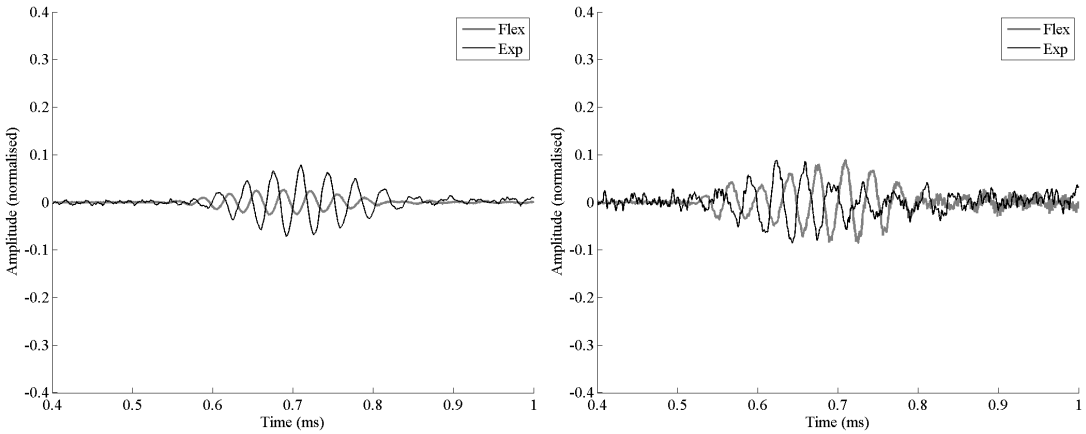
Flex
Exp
Amplitude (normalised)
Time (ms)

(a)

Flex
Exp
Amplitude (normalised)
Time (ms)

(b)

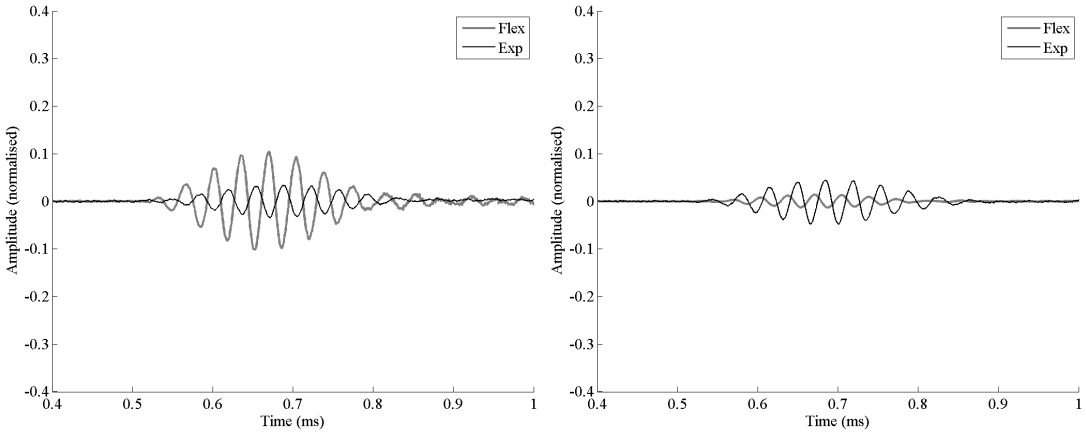
Flex
Exp
Amplitude (normalised)
Time (ms)

(c)

Flex
Exp
Amplitude (normalised)
Time (ms)

(d)

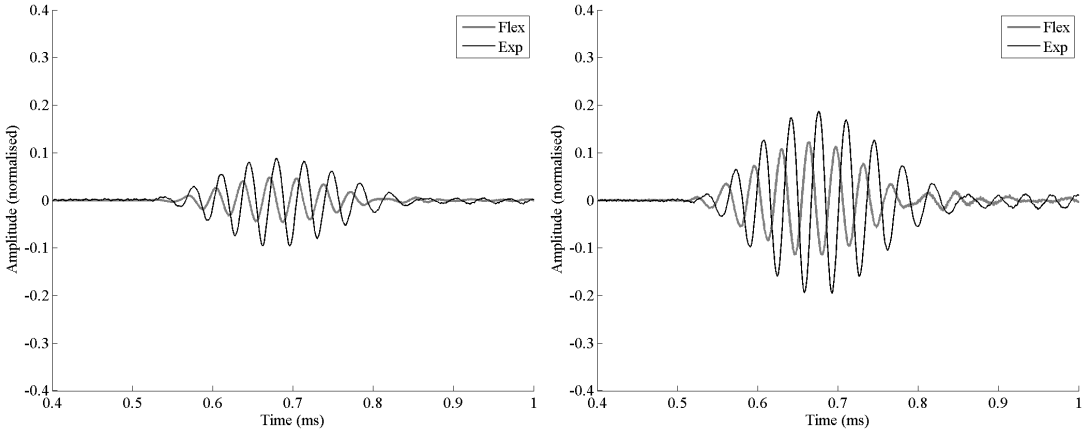
Flex
Exp
Amplitude (normalised)
Time (ms)

(e)

Flex
Exp
Amplitude (normalised)
Time (ms)

(f)

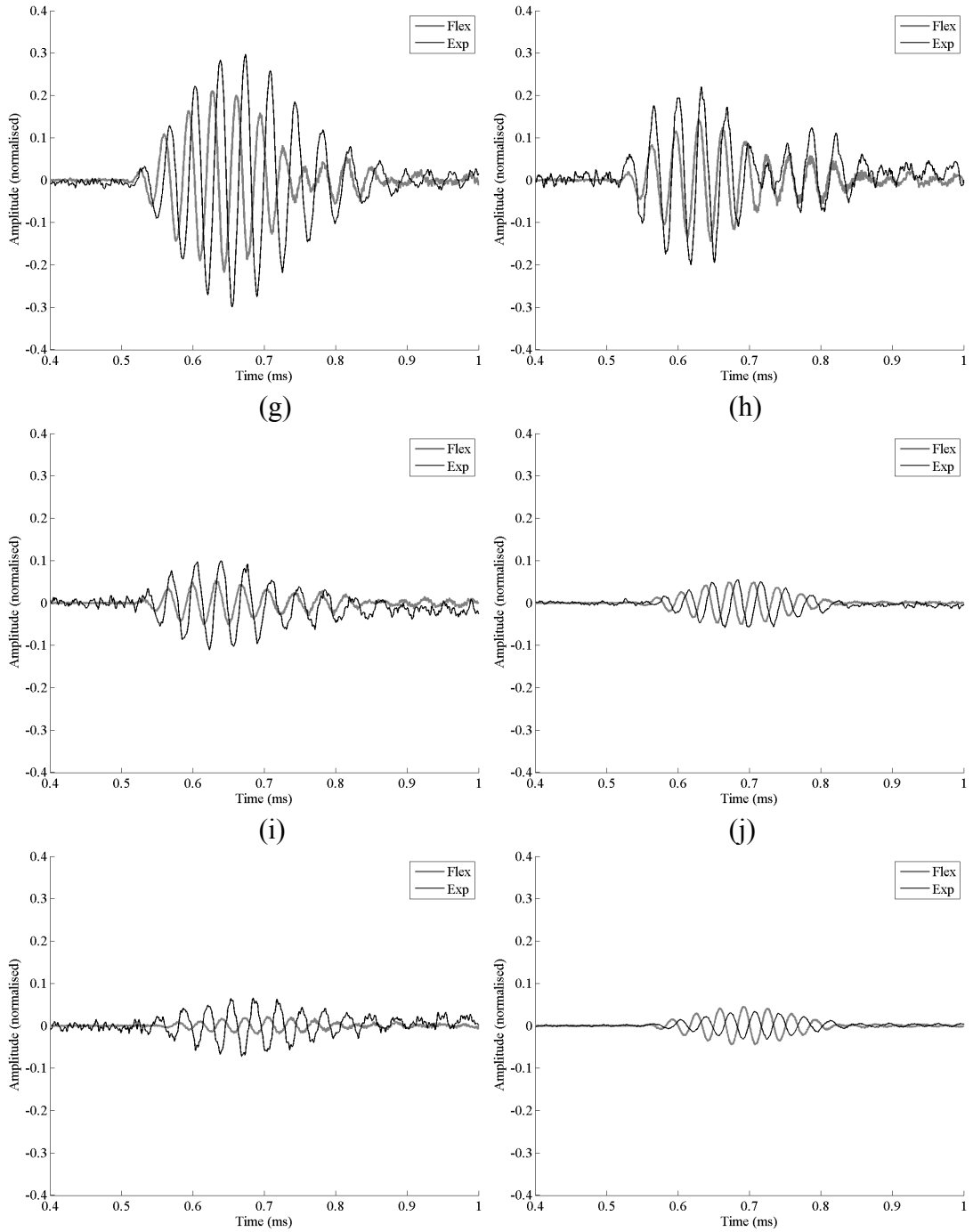

Figure B5. Comparison of simulated and experimental waveforms from a 30kHz toneburst at a height of 20mm with respect to the base of the ear at: (a) -150˚; (b) -120˚; (c) -90˚; (d) -60˚; (e) -30˚; (f) 0˚; (g) 30˚; (h) 60˚; (i) 90˚; (j) 120˚; (k) 150˚; (l) 180˚

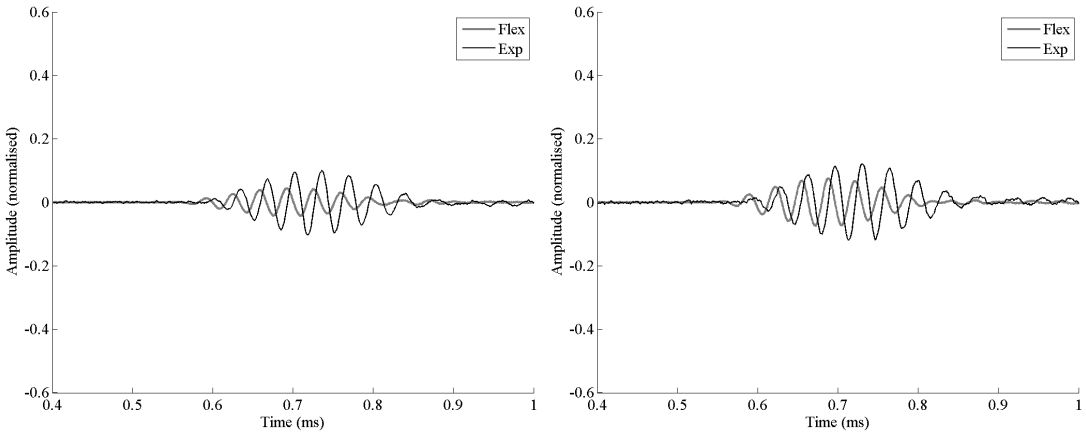
Flex
Exp
Amplitude (normalised)
Time (ms)

(a)

Flex
Exp
Amplitude (normalised)
Time (ms)

(b)

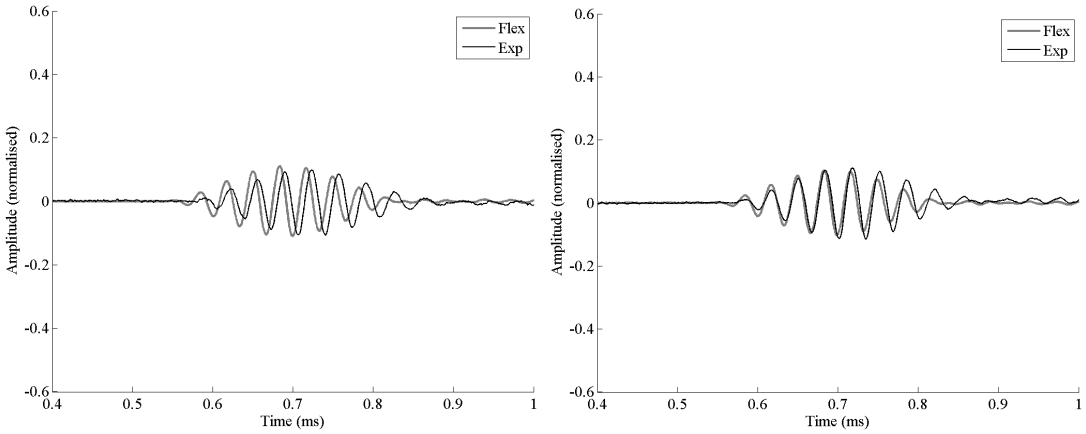
Flex
Exp
Amplitude (normalised)
Time (ms)

(c)

Flex
Exp
Amplitude (normalised)
Time (ms)

(d)

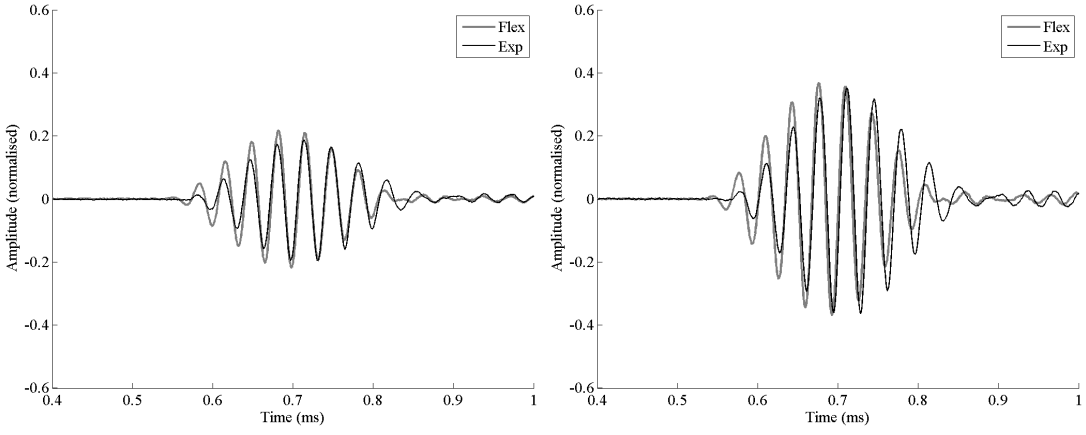
Flex
Exp
Amplitude (normalised)
Time (ms)

(e)

Flex
Exp
Amplitude (normalised)
Time (ms)

(f)

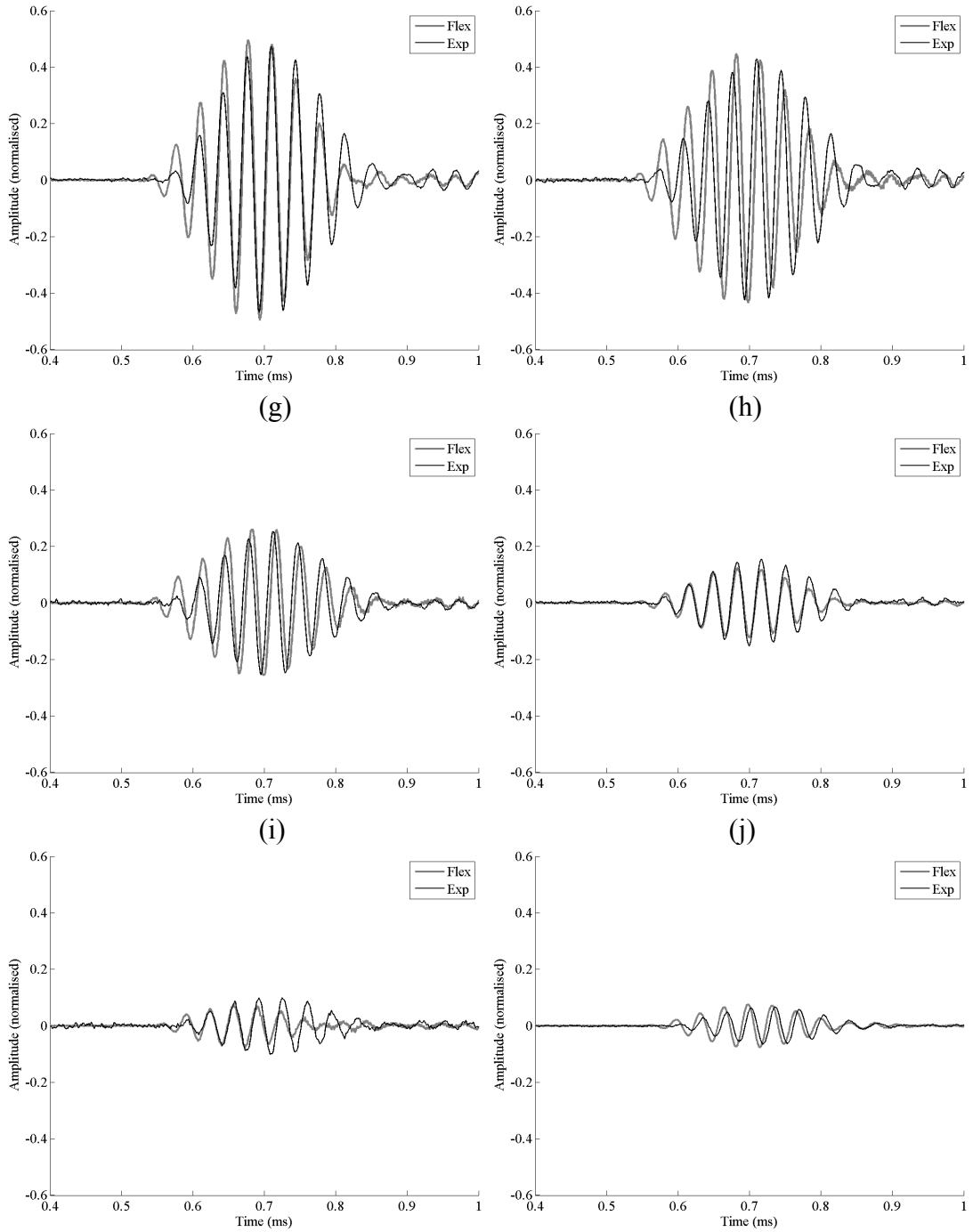

Figure B6. Comparison of simulated and experimental waveforms from a 30kHz toneburst at a height of 50mm with respect to the base of the ear at: (a) -150˚; (b) -120˚; (c) -90˚; (d) -60˚; (e) -30˚; (f) 0˚; (g) 30˚; (h) 60˚; (i) 90˚; (j) 120˚; (k) 150˚; (l) 180˚

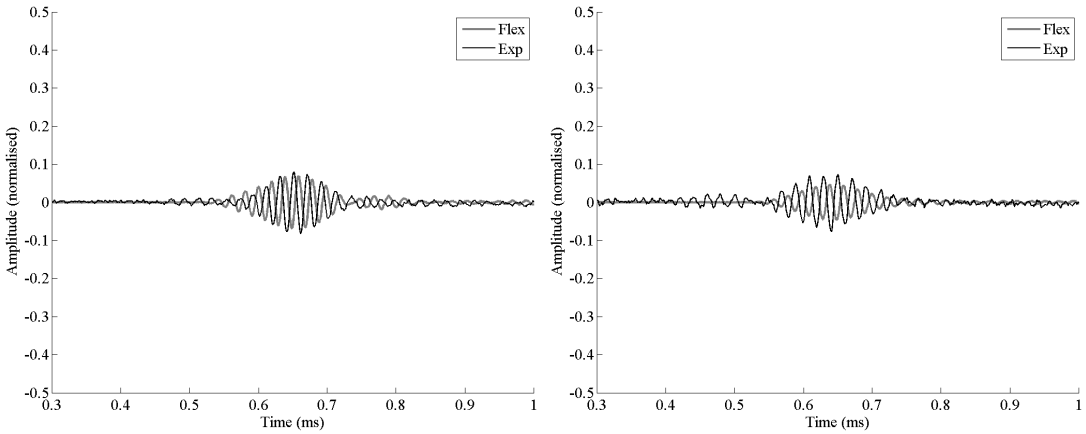
Flex
Exp
Amplitude (normalised)
Time (ms)

(a)

Flex
Exp
Amplitude (normalised)
Time (ms)

(b)

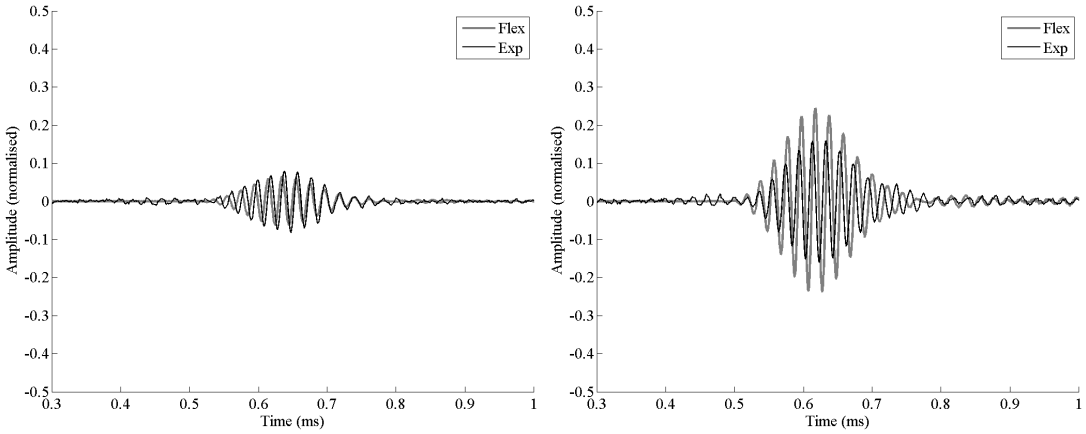
Flex
Exp
Amplitude (normalised)
Time (ms)

(c)

Flex
Exp
Amplitude (normalised)
Time (ms)

(d)

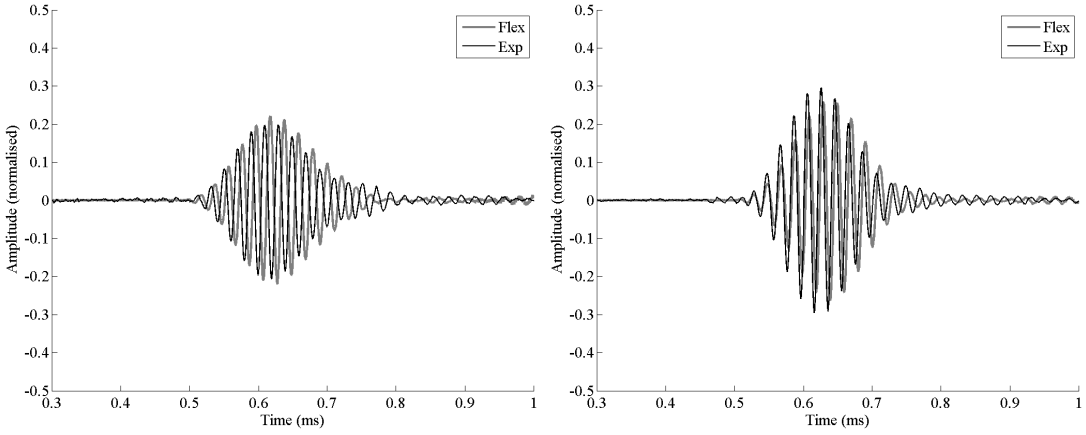
Flex
Exp
Amplitude (normalised)
Time (ms)

(e)

Flex
Exp
Amplitude (normalised)
Time (ms)

(f)

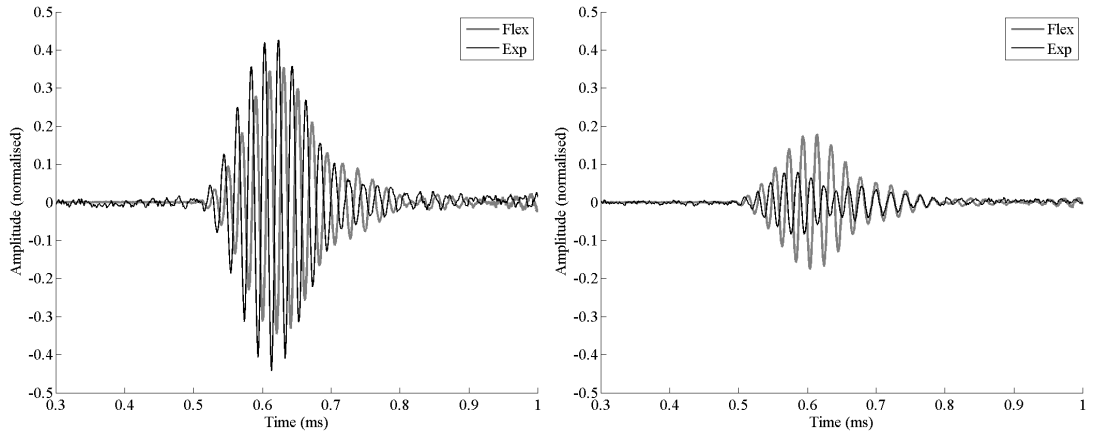

(g)

(h)

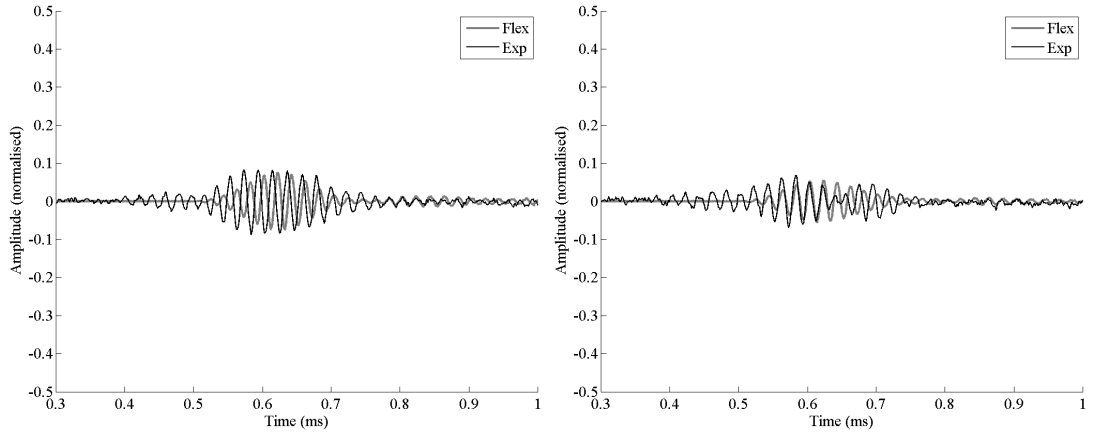

(i)

(j)

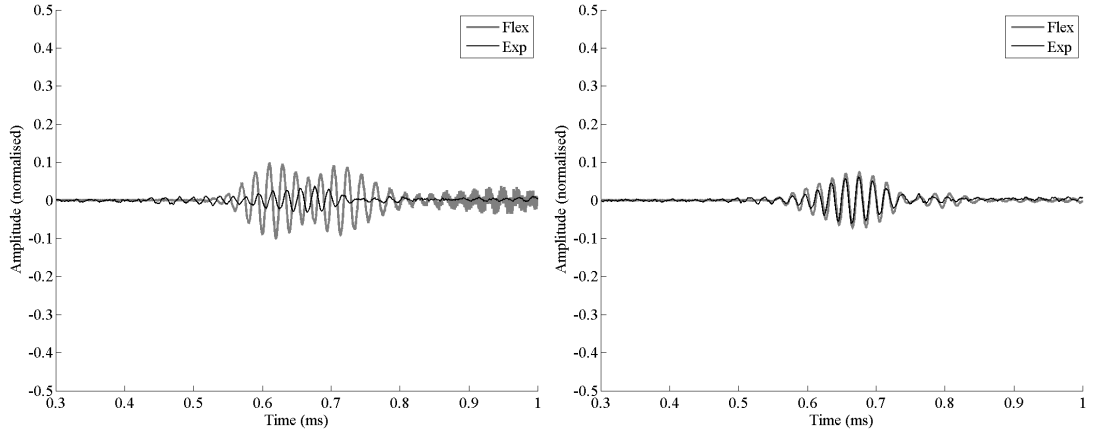

(k)

(l)

Figure B7. Comparison of simulated and experimental waveforms from a 50kHz toneburst at a height of 0mm with respect to the base of the ear at: (a) -150˚; (b) -120˚; (c) -90˚; (d) -60˚; (e) -30˚; (f) 0˚; (g) 30˚; (h) 60˚; (i) 90˚; (j) 120˚; (k) 150˚; (l) 180˚

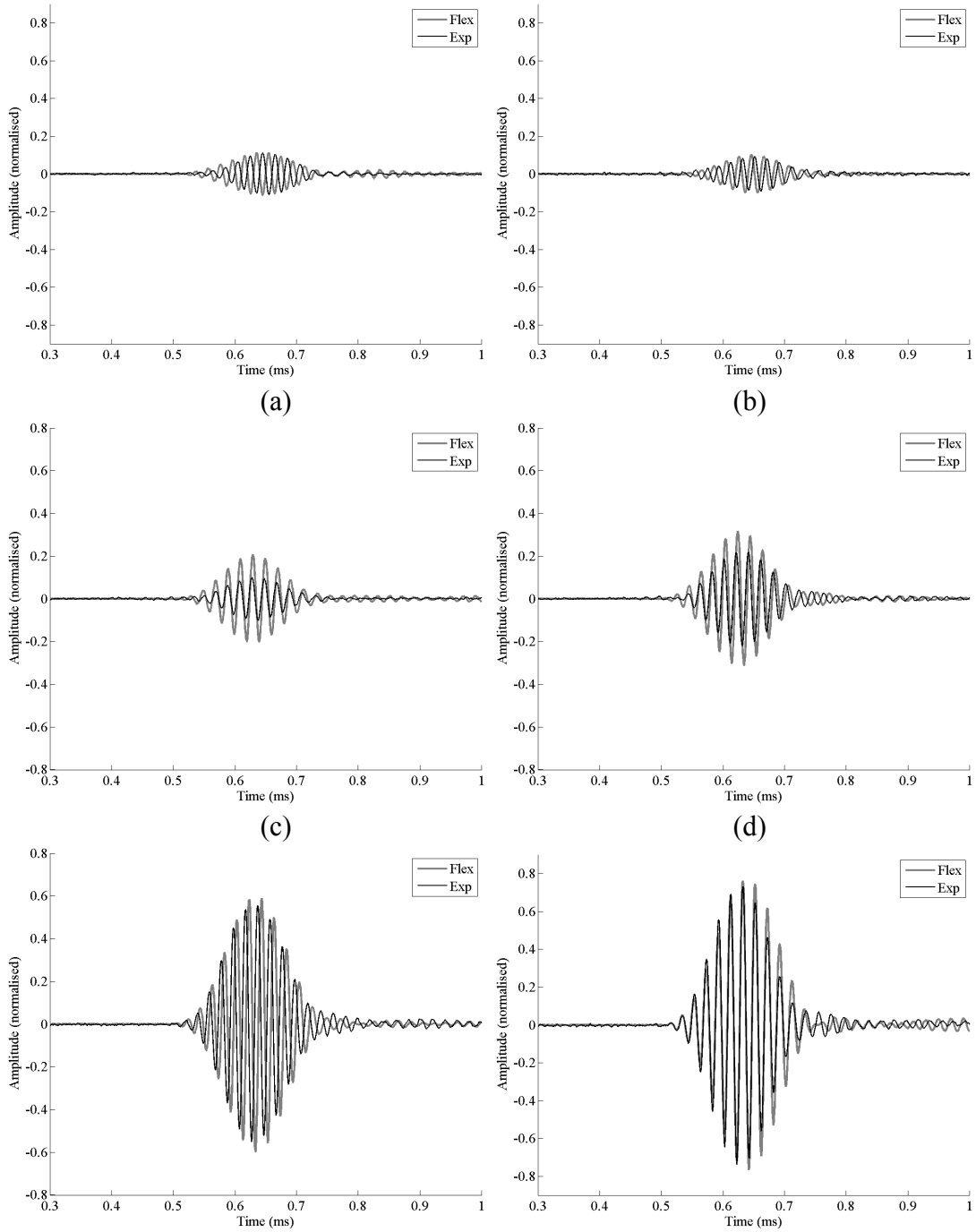
Flex
Exp
Amplitude (normalised)
Time (ms)
(a)
(b)
(c)
(d)
(e)
(f)

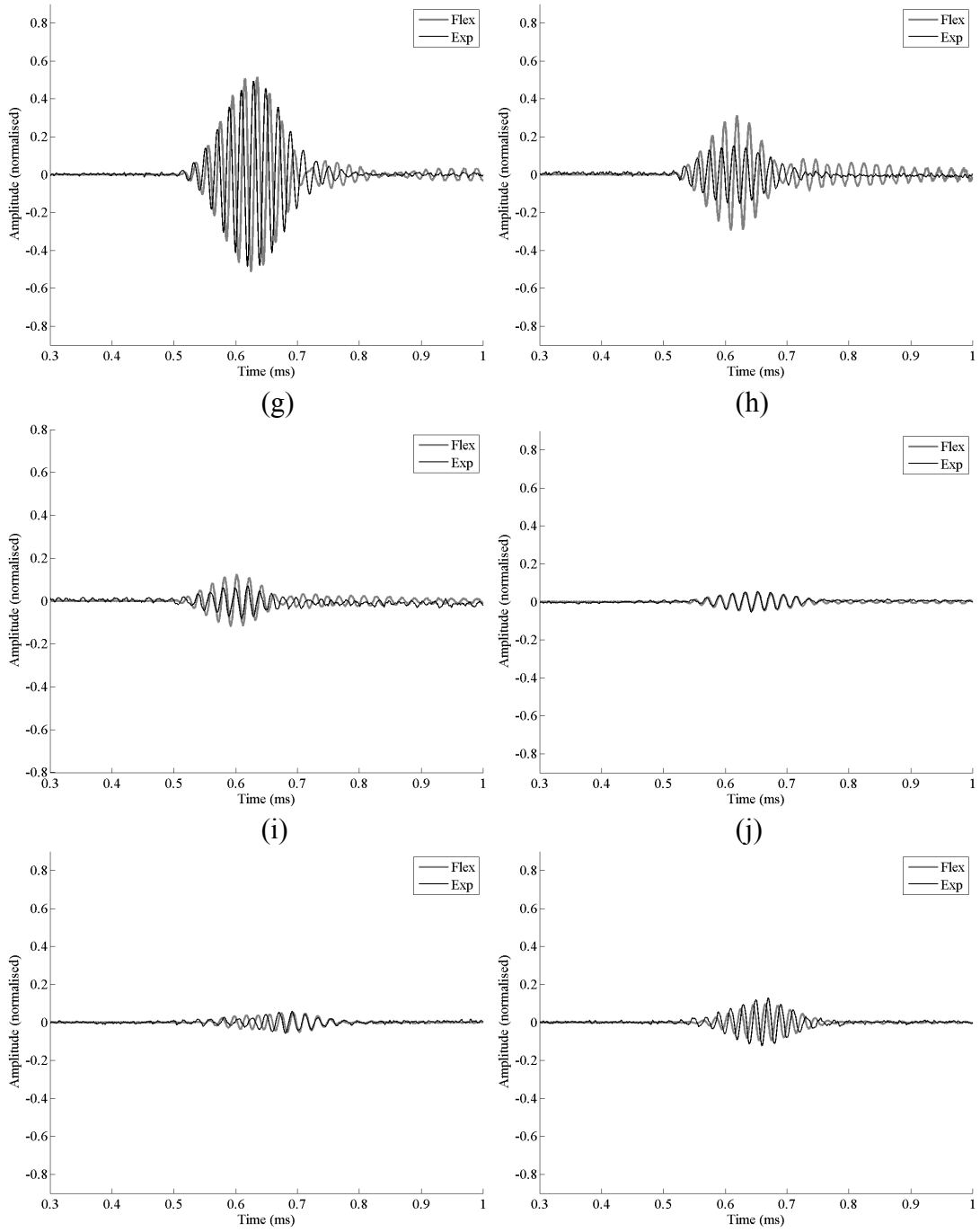

Figure B8. Comparison of simulated and experimental waveforms from a 50kHz toneburst at a height of 20mm with respect to the base of the ear at: (a) -150˚; (b) -120˚; (c) -90˚; (d) -60˚; (e) -30˚; (f) 0˚; (g) 30˚; (h) 60˚; (i) 90˚; (j) 120˚; (k) 150˚; (l) 180˚

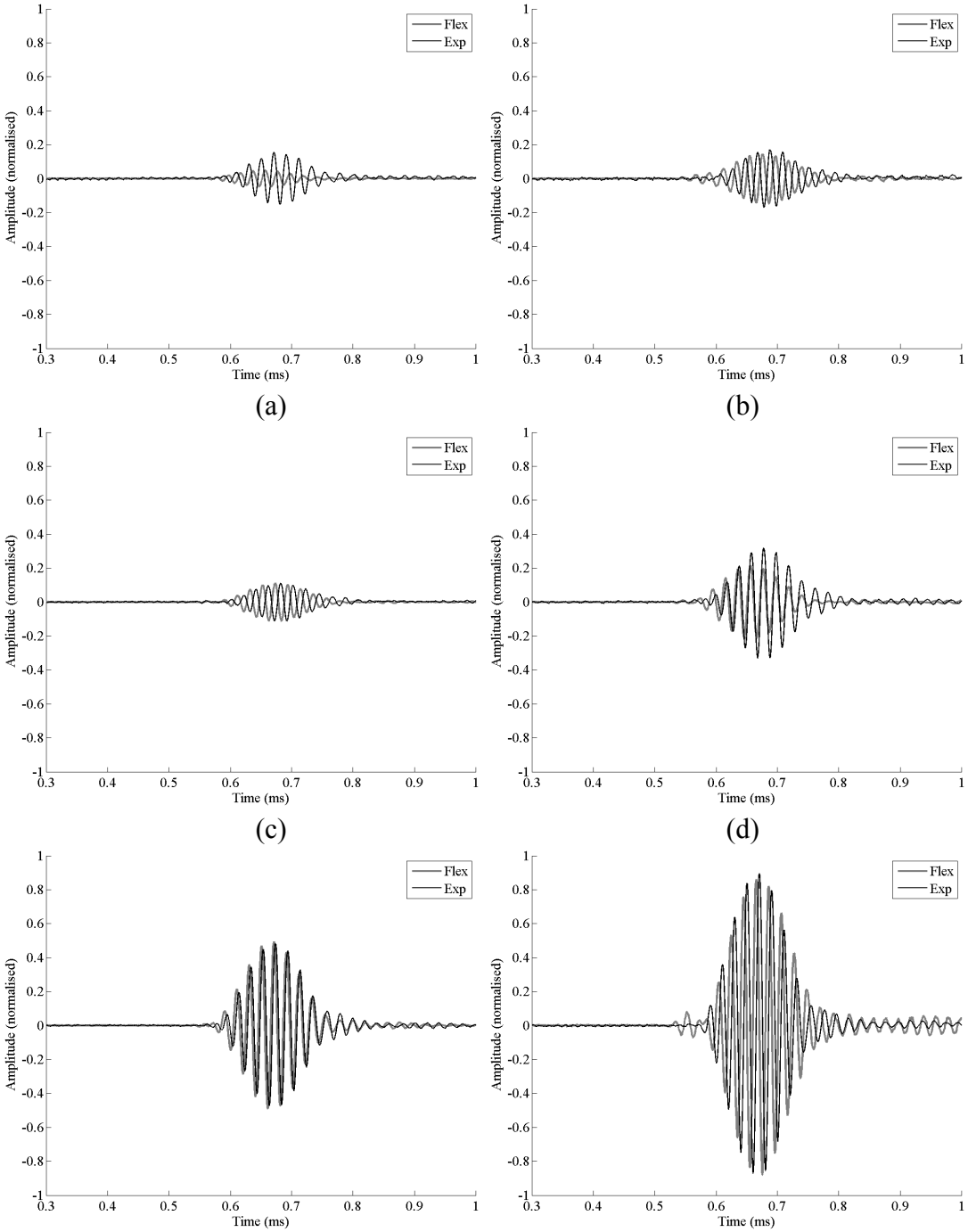
Flex
Exp
Amplitude (normalised)
Time (ms)
(a)
(b)
(c)
(d)
(e)
(f)

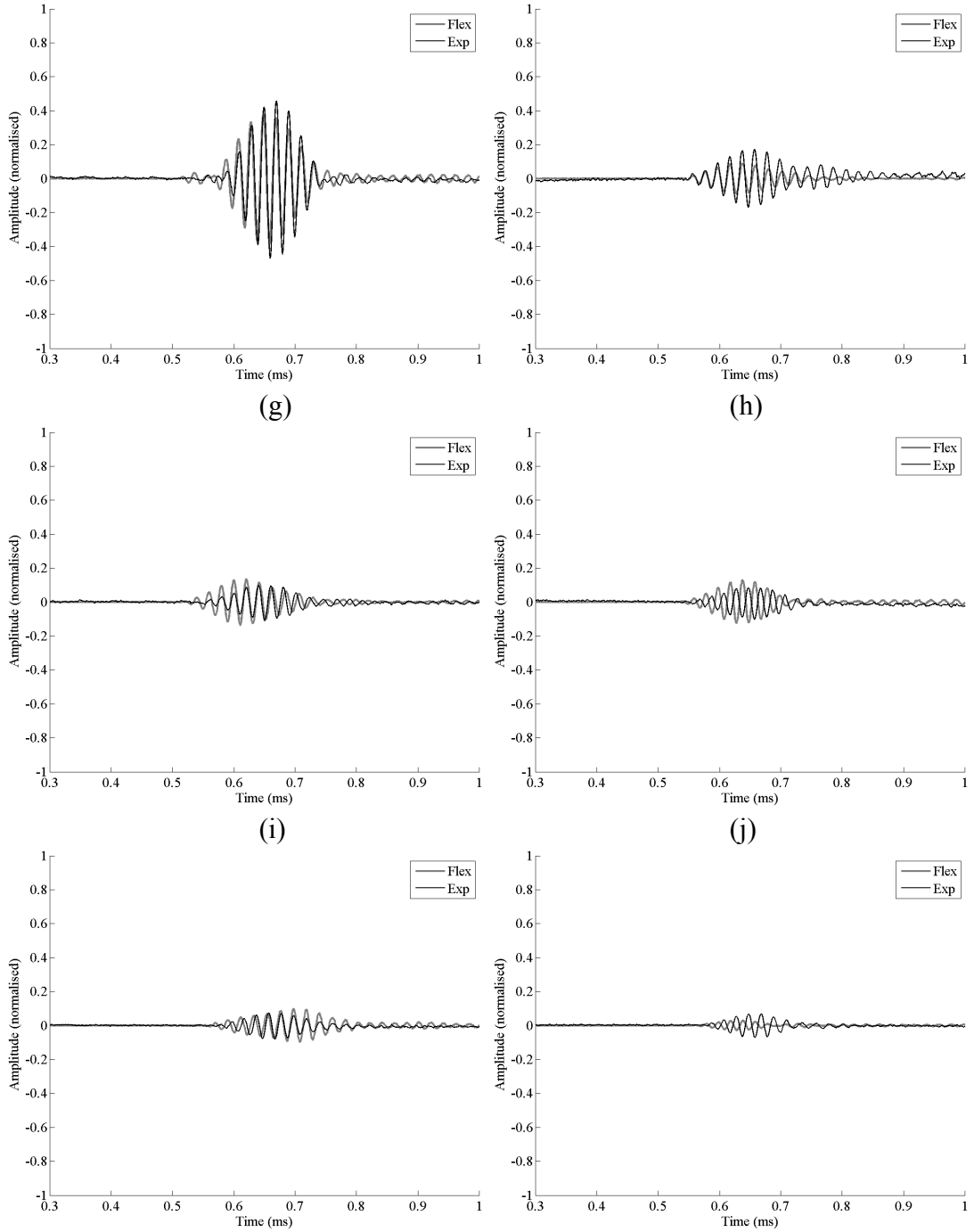

Figure B9. Comparison of simulated and experimental waveforms from a 50kHz toneburst at a height of 50mm with respect to the base of the ear at: (a) -150˚; (b) -120˚; (c) -90˚; (d) -60˚; (e) -30˚; (f) 0˚; (g) 30˚; (h) 60˚; (i) 90˚; (j) 120˚; (k) 150˚; (l) 180˚

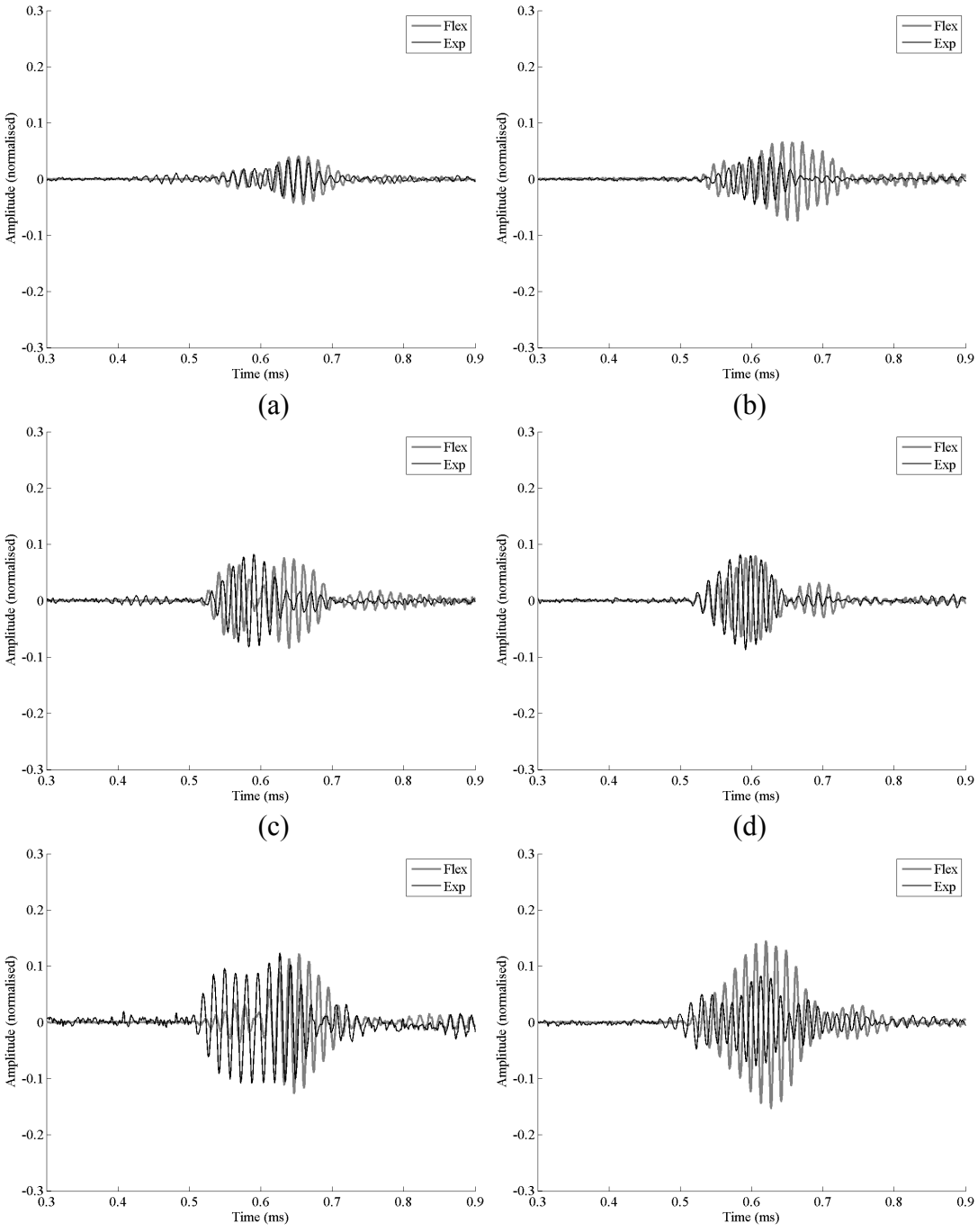
Flex
Exp
Amplitude (normalised)
Time (ms)
(a)
(b)
(c)
(d)
(e)
(f)

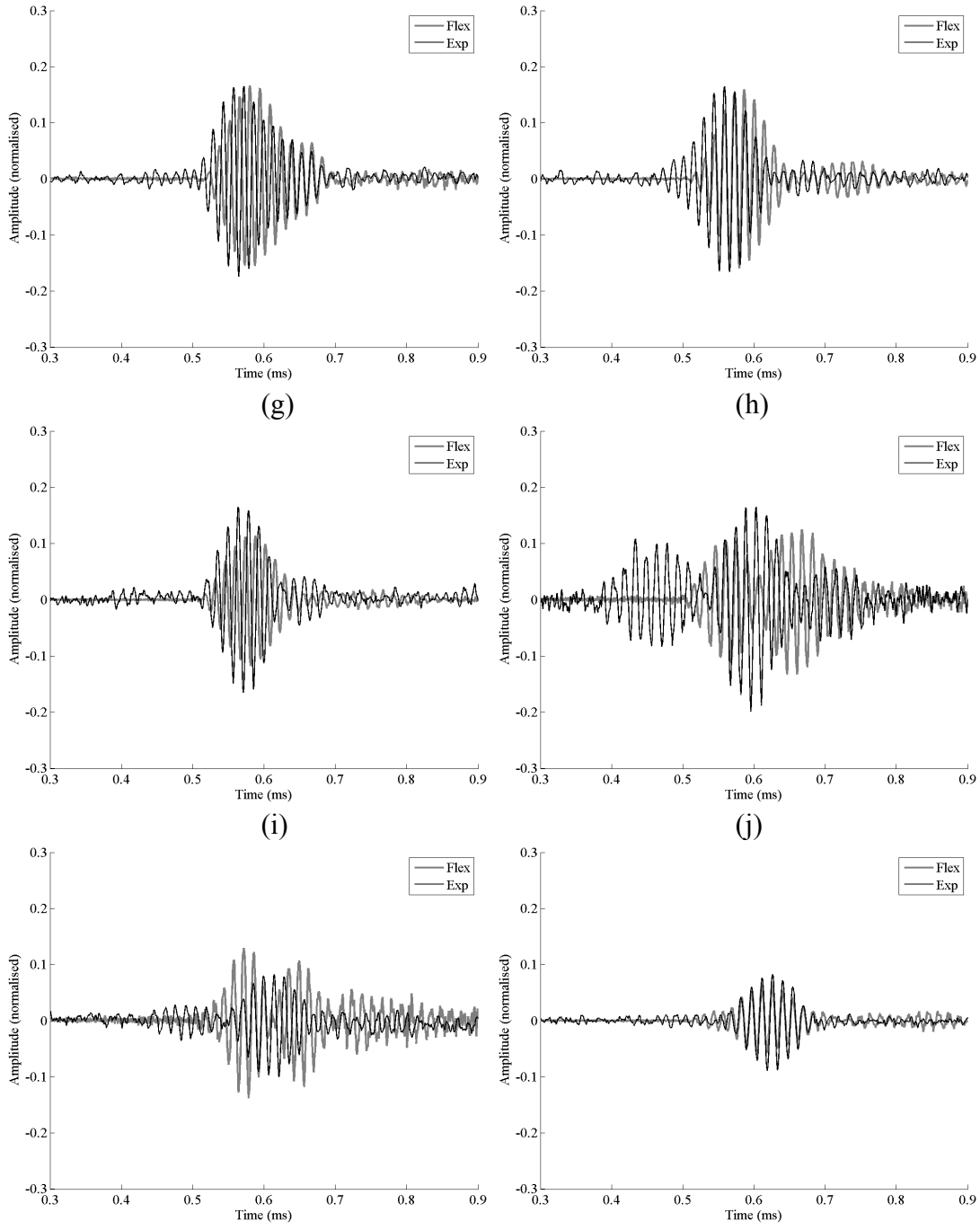

Figure B10. Comparison of simulated and experimental waveforms from a 70kHz toneburst at a height of 0mm with respect to the base of the ear at: (a) -150˚; (b) -120˚; (c) -90˚; (d) -60˚; (e) -30˚; (f) 0˚; (g) 30˚; (h) 60˚; (i) 90˚; (j) 120˚; (k) 150˚; (l) 180˚

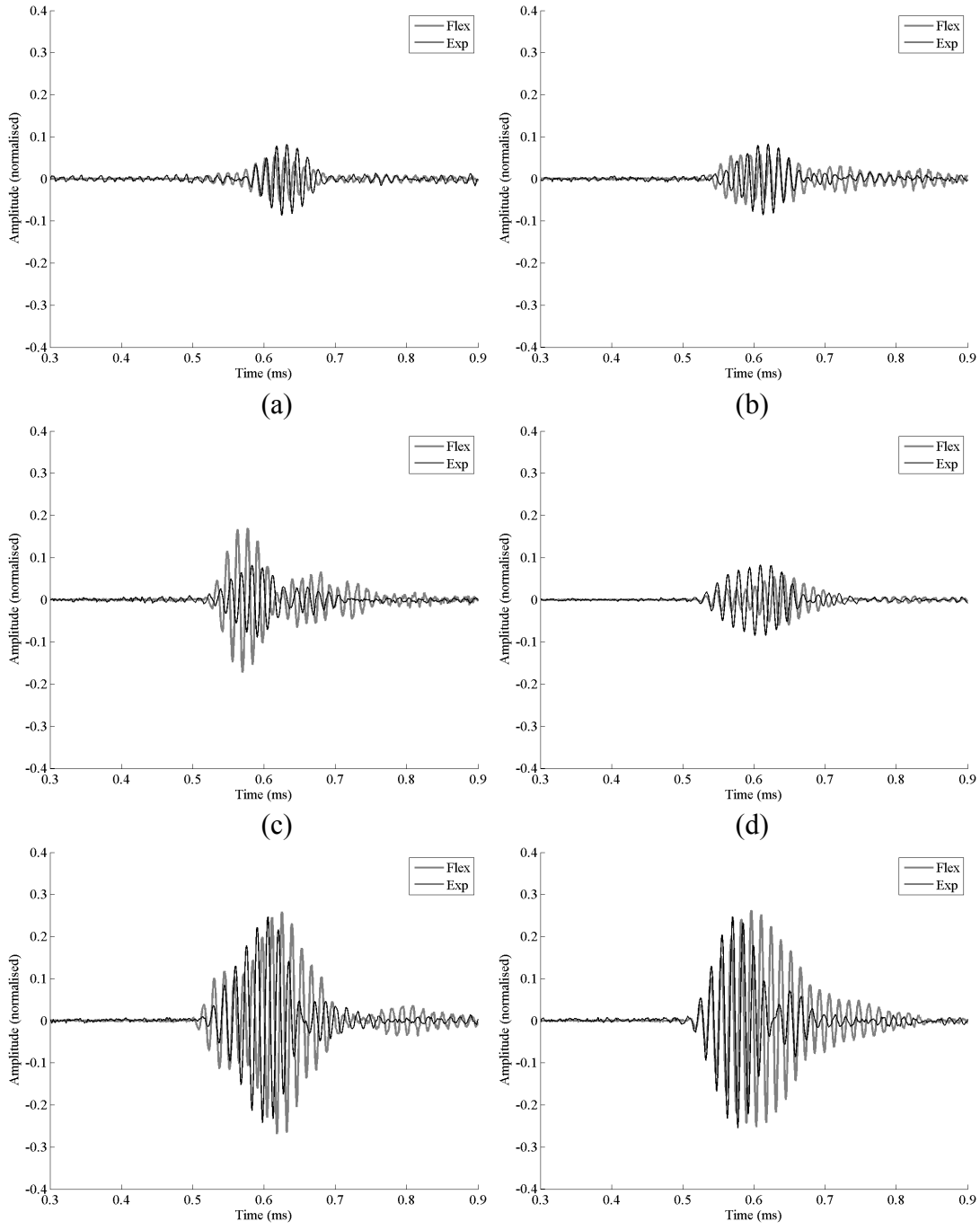
Flex
Exp
Amplitude (normalised)
Time (ms)
(a)
(b)
(c)
(d)
(e)
(f)

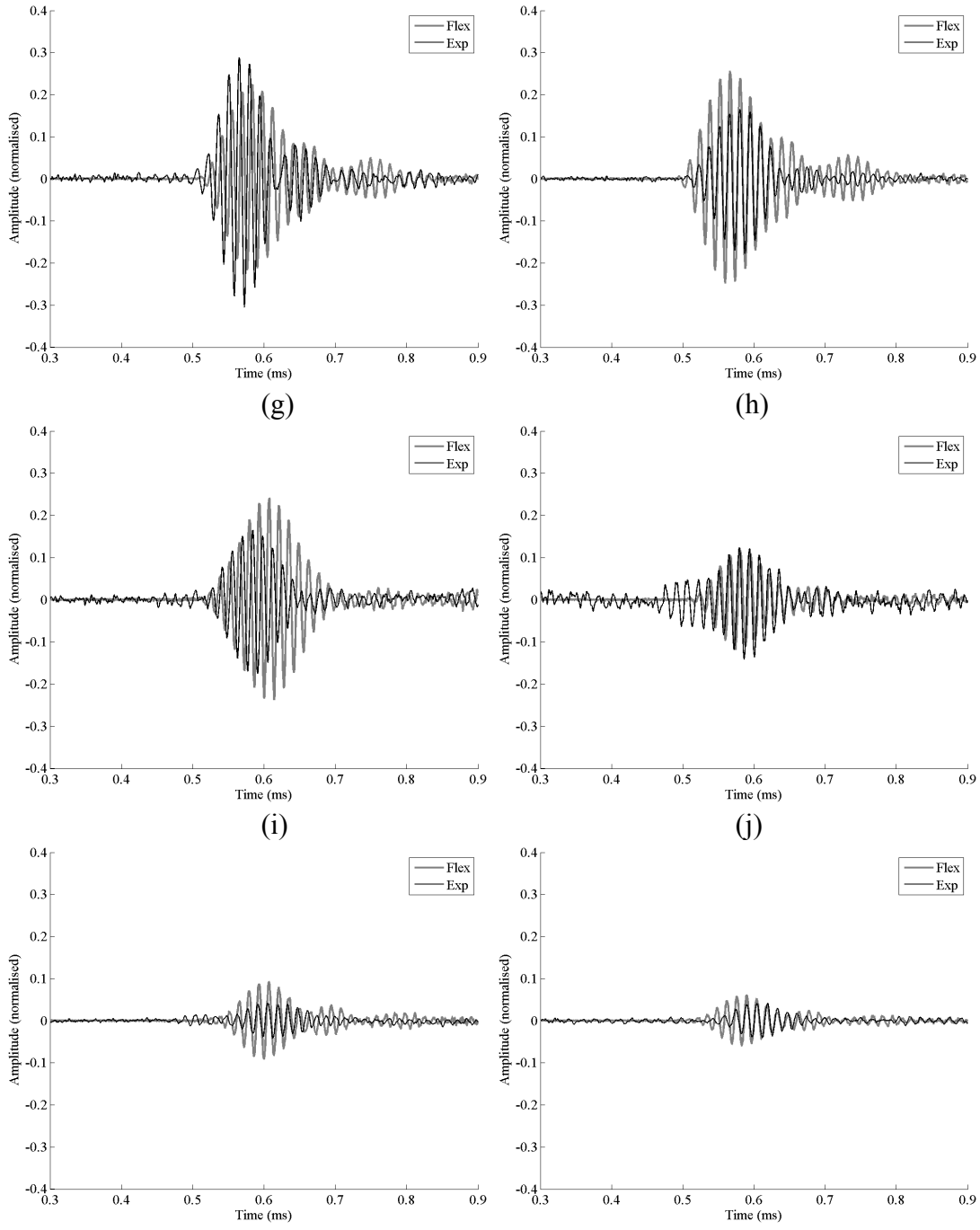

Figure B11. Comparison of simulated and experimental waveforms from a 70kHz toneburst at a height of 20mm with respect to the base of the ear at: (a) -150˚; (b) -120˚; (c) -90˚; (d) -60˚; (e) -30˚; (f) 0˚; (g) 30˚; (h) 60˚; (i) 90˚; (j) 120˚; (k) 150˚; (l) 180˚

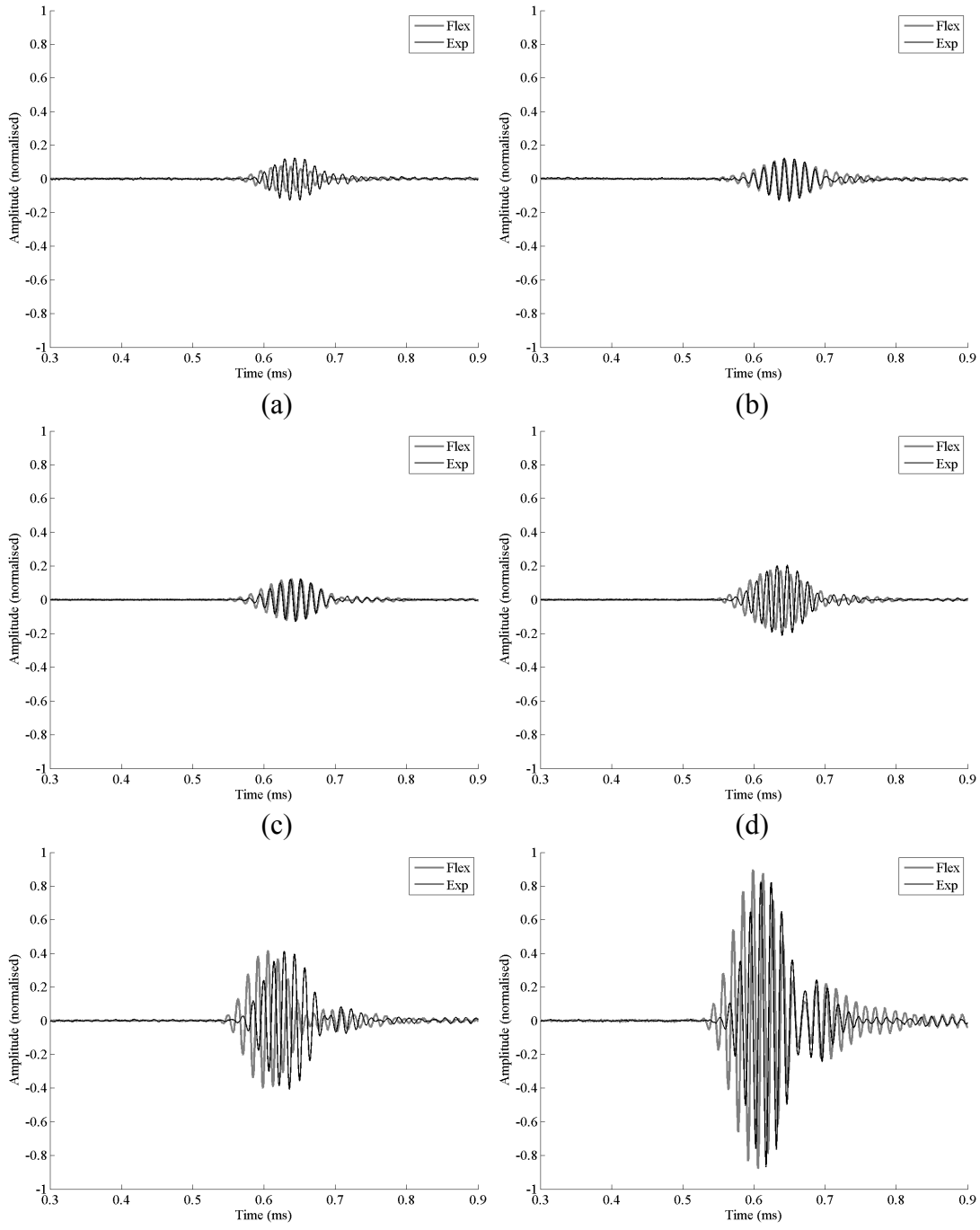
Flex
Exp
Amplitude (normalised)
Time (ms)
(a)
(b)
(c)
(d)
(e)
(f)

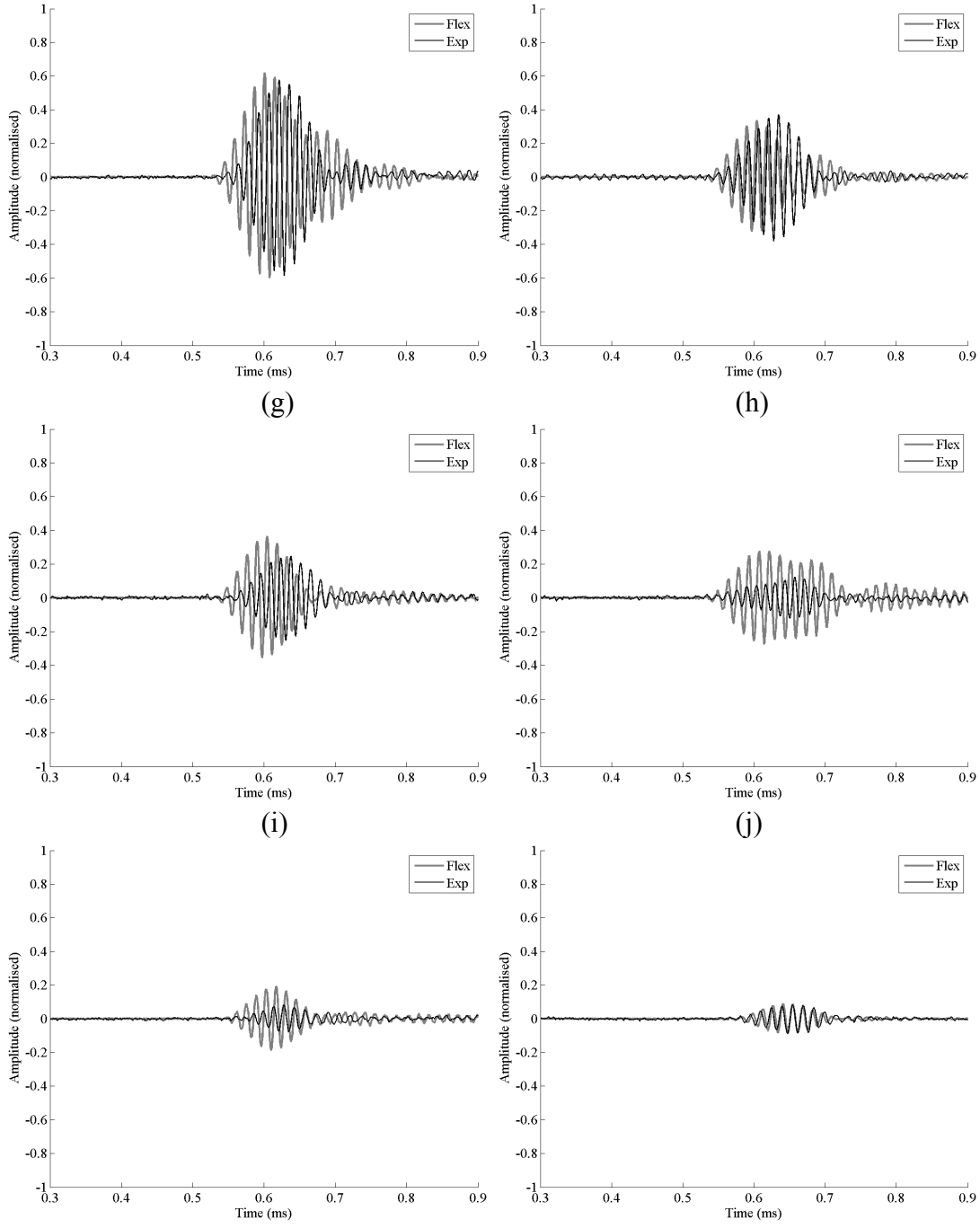

Figure B12. Comparison of simulated and experimental waveforms from a 70kHz toneburst at a height of 50mm with respect to the base of the ear at: (a) -150˚; (b) -120˚; (c) -90˚; (d) -60˚; (e) -30˚; (f) 0˚; (g) 30˚; (h) 60˚; (i) 90˚; (j) 120˚; (k) 150˚; (l) 180˚

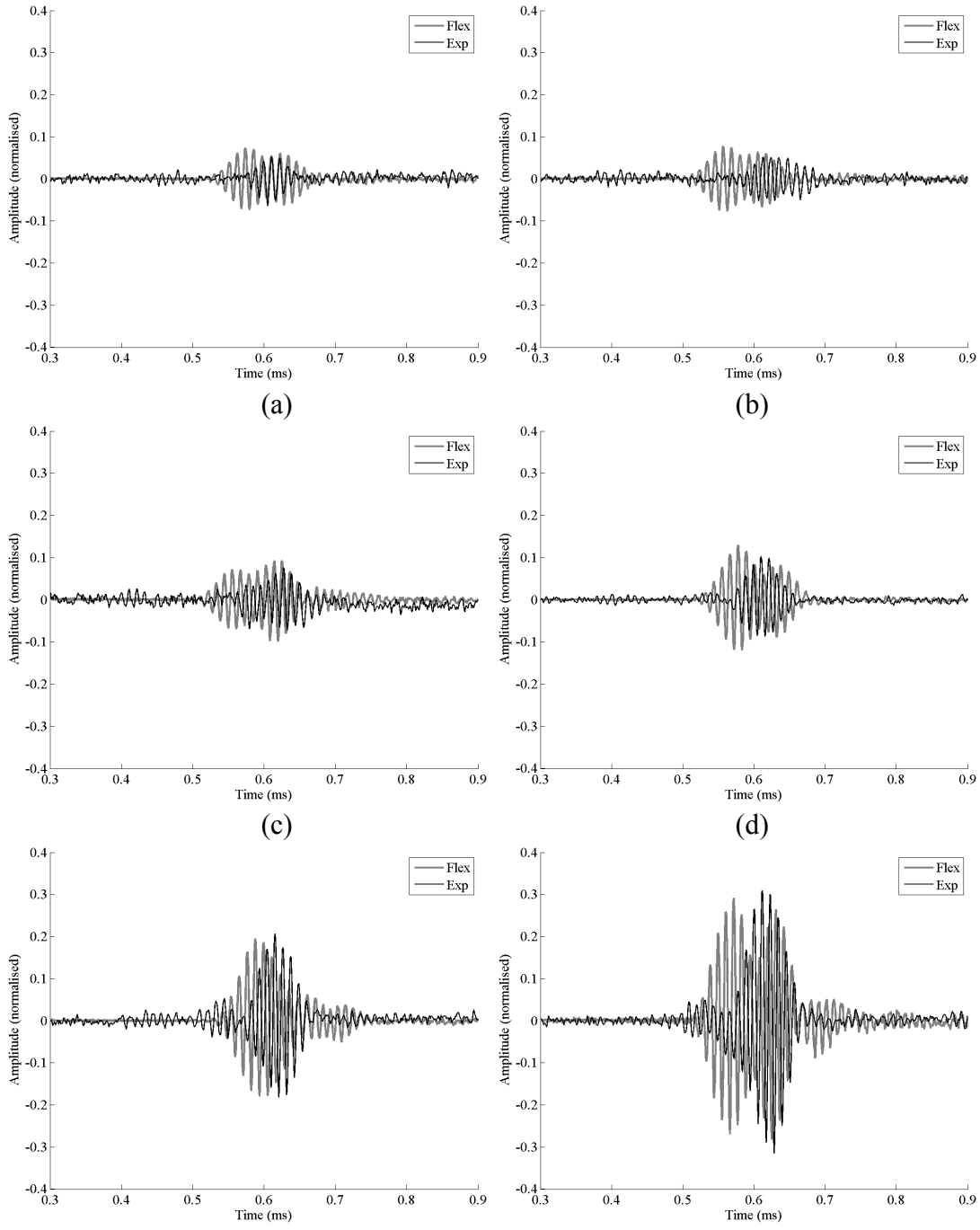
Flex
Exp
Amplitude (normalised)
Time (ms)
(a)
(b)
(c)
(d)
(e)
(f)

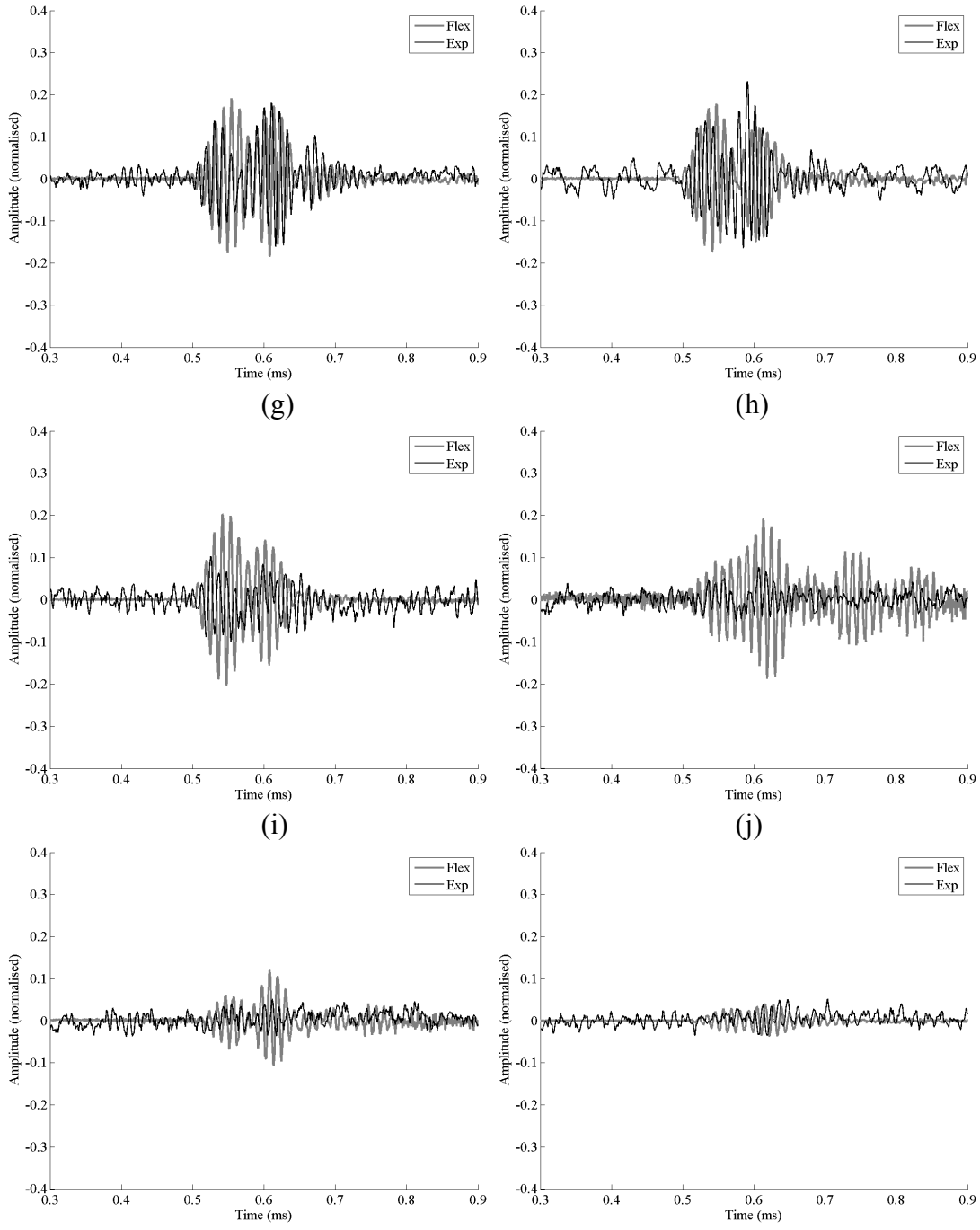

Figure B13. Comparison of simulated and experimental waveforms from a 90kHz toneburst at a height of 0mm with respect to the base of the ear at: (a) -150˚; (b) -120˚; (c) -90˚; (d) -60˚; (e) -30˚; (f) 0˚; (g) 30˚; (h) 60˚; (i) 90˚; (j) 120˚; (k) 150˚; (l) 180˚

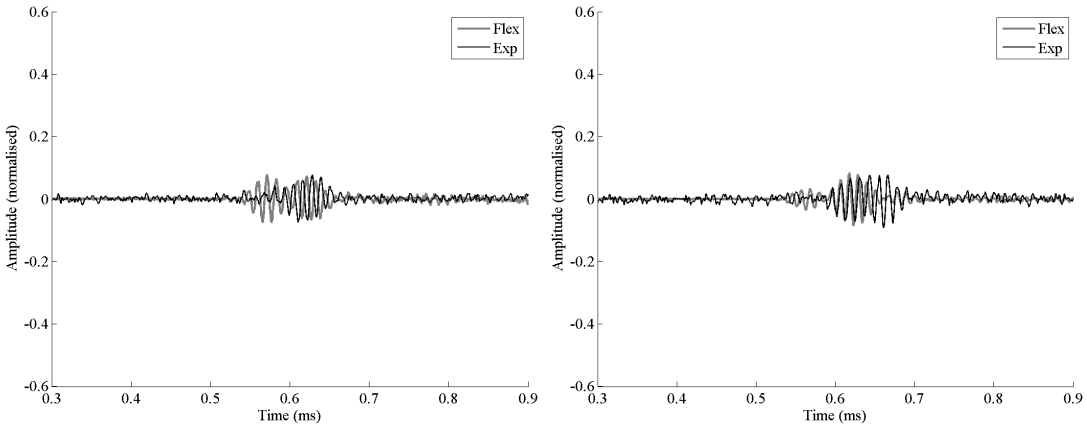
Flex
Exp
Amplitude (normalised)
Time (ms)

(a)

Flex
Exp
Amplitude (normalised)
Time (ms)

(b)

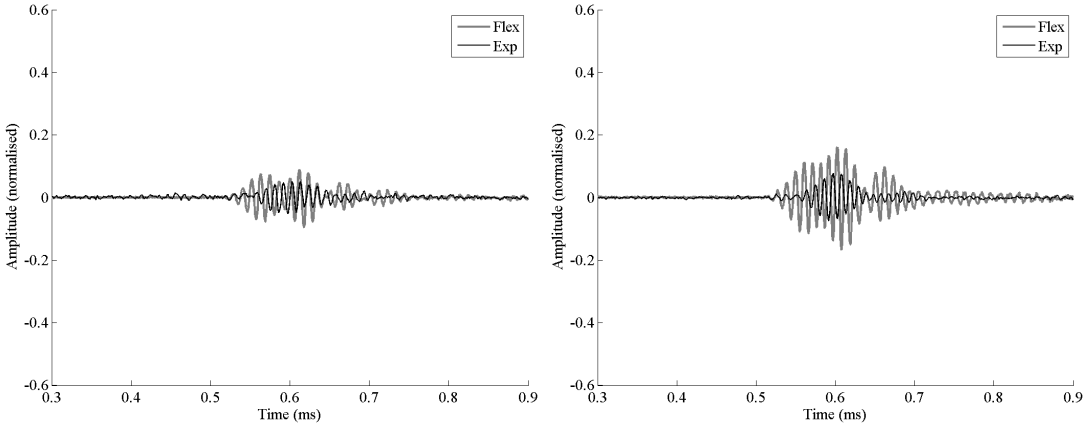
Flex
Exp
Amplitude (normalised)
Time (ms)

(c)

Flex
Exp
Amplitude (normalised)
Time (ms)

(d)

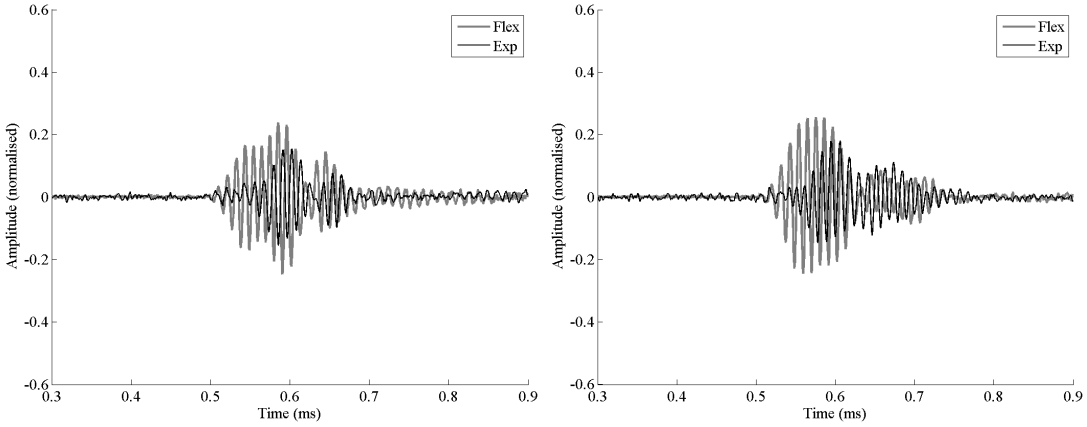
Flex
Exp
Amplitude (normalised)
Time (ms)

(e)

Flex
Exp
Amplitude (normalised)
Time (ms)

(f)

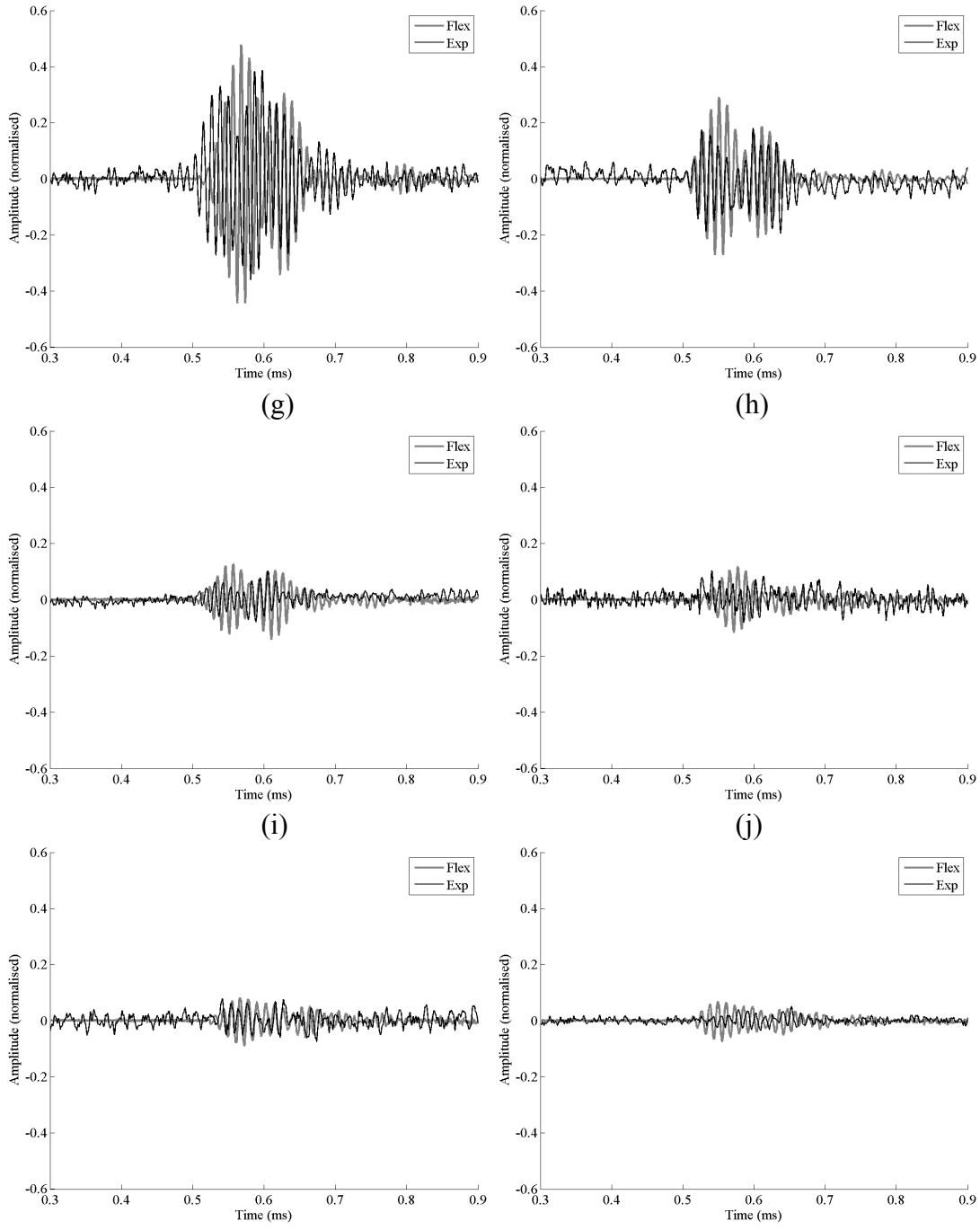

Figure B14. Comparison of simulated and experimental waveforms from a 90kHz toneburst at a height of 20mm with respect to the base of the ear at: (a) -150˚; (b) -120˚; (c) -90˚; (d) -60˚; (e) -30˚; (f) 0˚; (g) 30˚; (h) 60˚; (i) 90˚; (j) 120˚; (k) 150˚; (l) 180˚

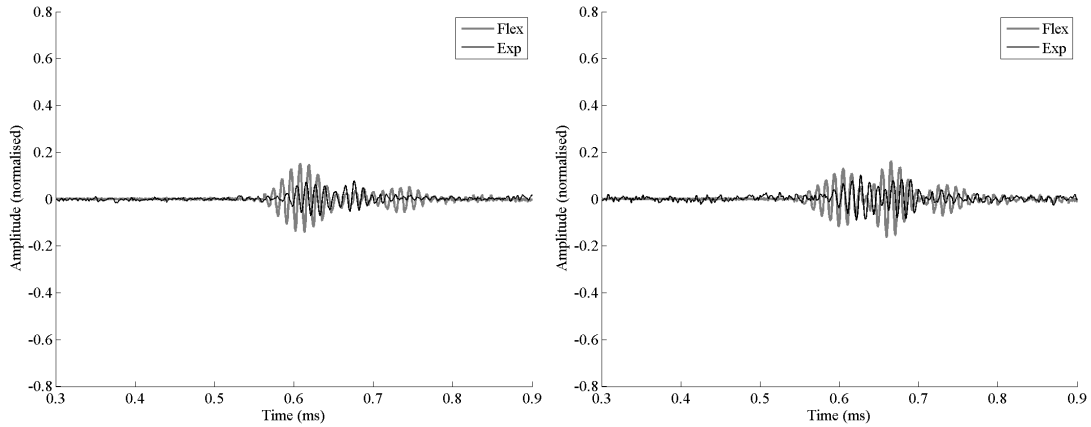
Flex
Exp
Amplitude (normalised)
Time (ms)

(a)

Flex
Exp
Amplitude (normalised)
Time (ms)

(b)

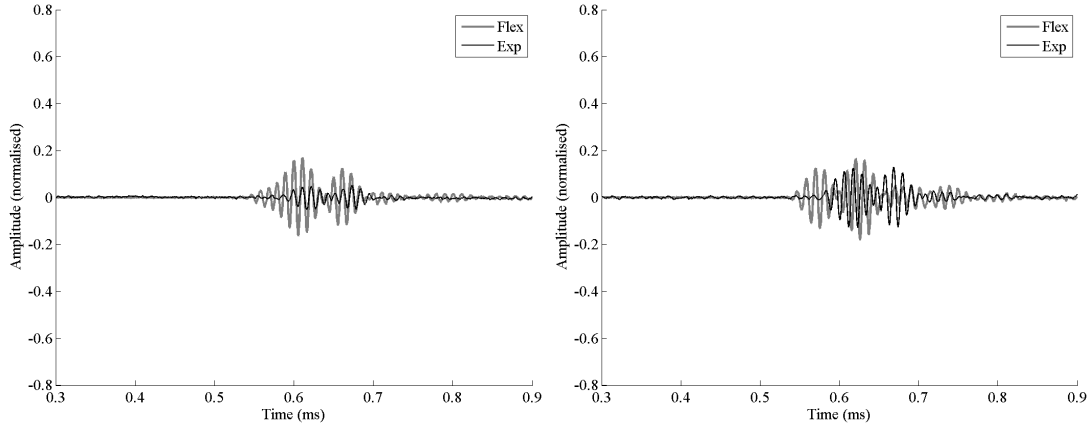
Flex
Exp
Amplitude (normalised)
Time (ms)

(c)

Flex
Exp
Amplitude (normalised)
Time (ms)

(d)

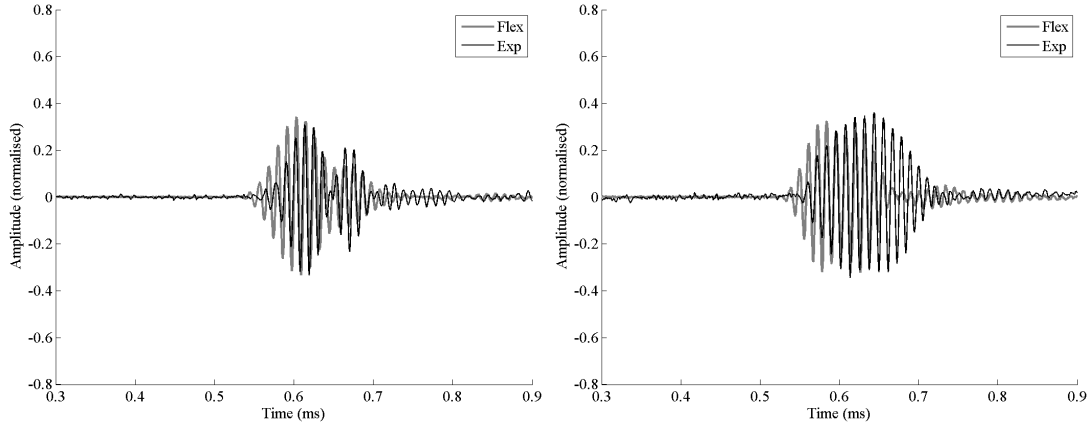
Flex
Exp
Amplitude (normalised)
Time (ms)

(e)

Flex
Exp
Amplitude (normalised)
Time (ms)

(f)

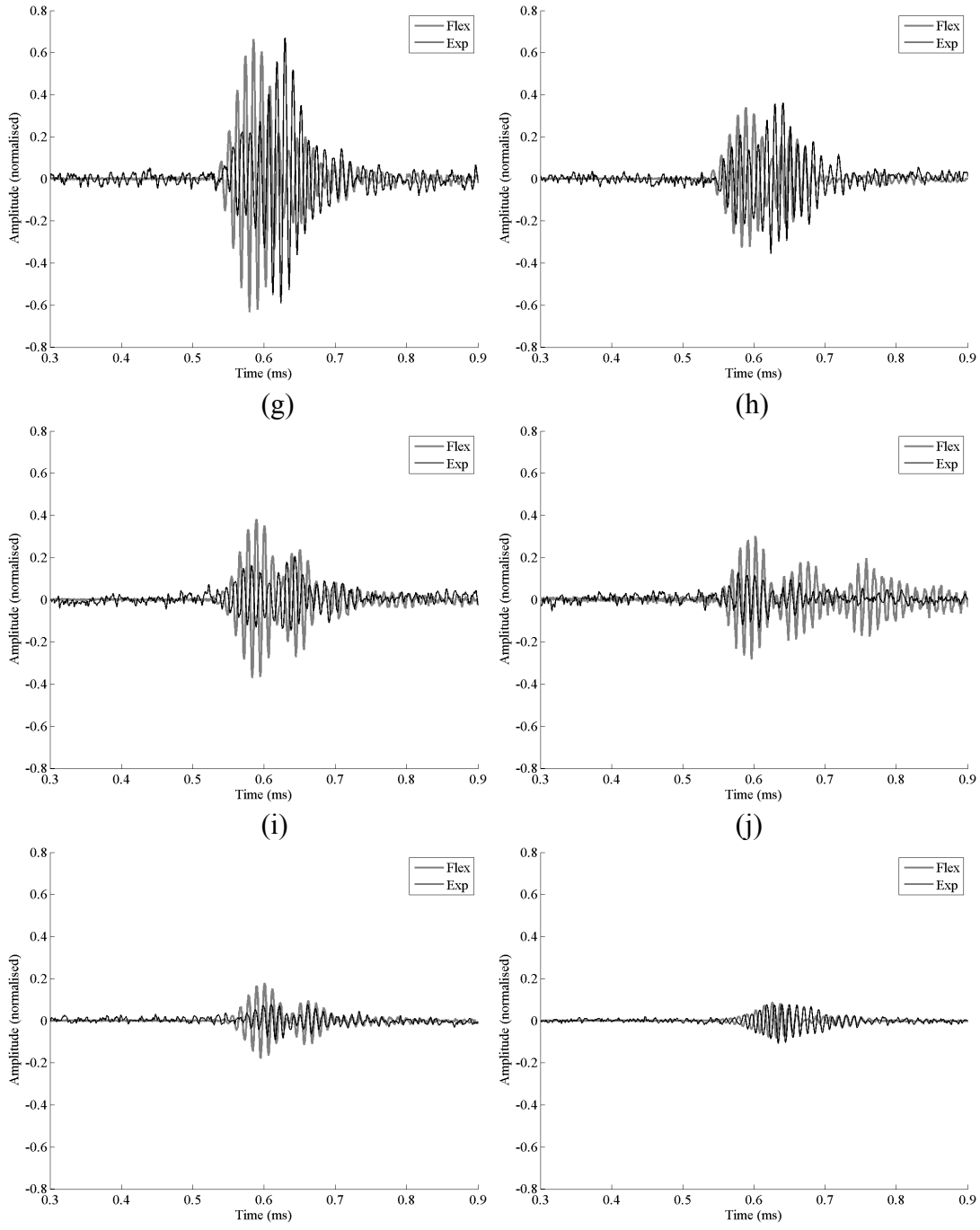

Figure B15. Comparison of simulated and experimental waveforms from a 90kHz toneburst at a height of 50mm with respect to the base of the ear at: (a) -150˚; (b) -120˚; (c) -90˚; (d) -60˚; (e) -30˚; (f) 0˚; (g) 30˚; (h) 60˚; (i) 90˚; (j) 120˚; (k) 150˚; (l) 180˚

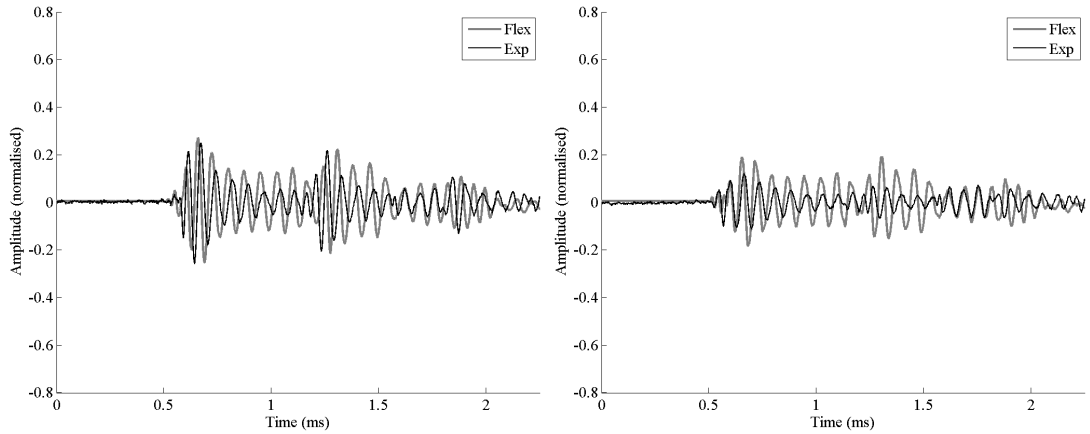
Flex
Exp
Amplitude (normalised)
Time (ms)

(a)

Flex
Exp
Amplitude (normalised)
Time (ms)

(b)

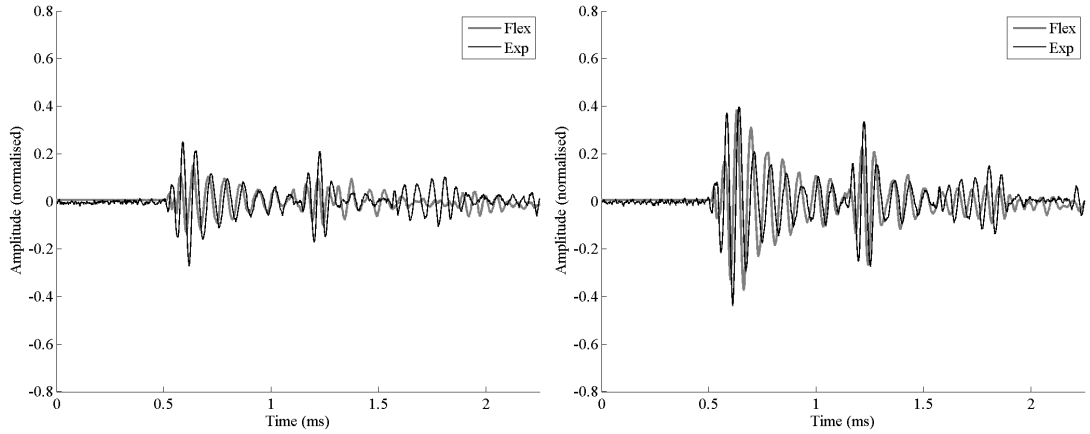
Flex
Exp
Amplitude (normalised)
Time (ms)

(c)

Flex
Exp
Amplitude (normalised)
Time (ms)

(d)

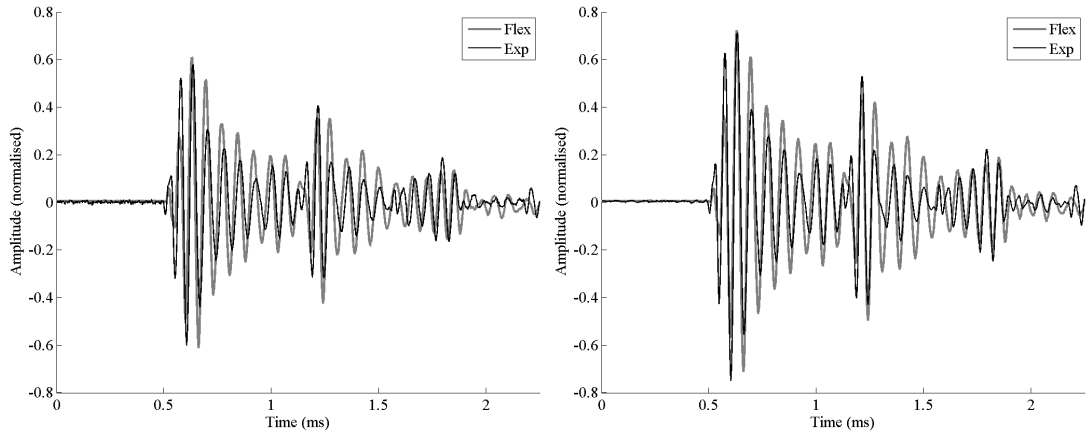
Flex
Exp
Amplitude (normalised)
Time (ms)

(e)

Flex
Exp
Amplitude (normalised)
Time (ms)

(f)

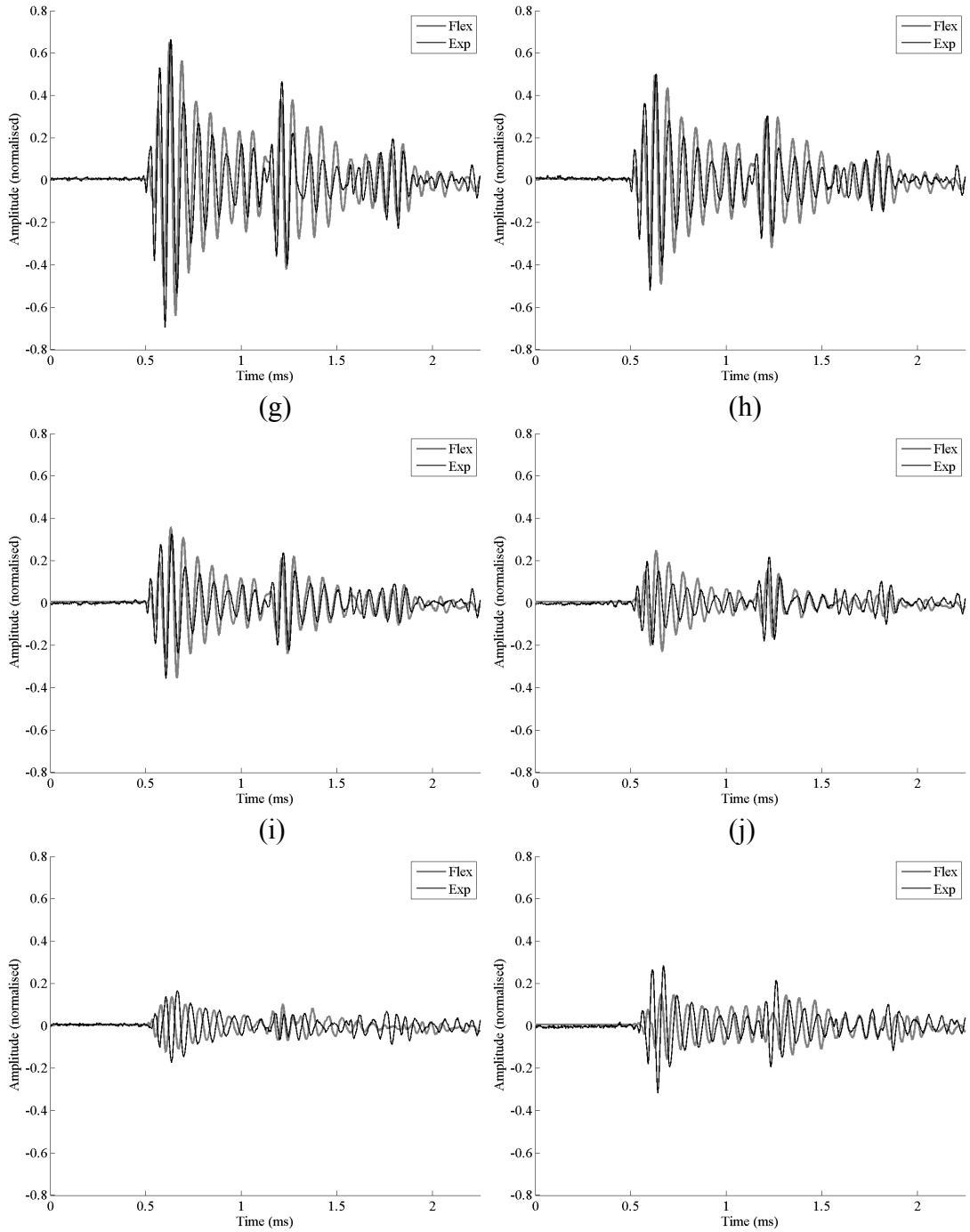

Figure B16. Comparison of simulated and experimental waveforms from a *R. aegyptiacus* call at a height of 0mm with respect to the base of the ear at: (a) -150˚; (b) -120˚; (c) -90˚; (d) -60˚; (e) -30˚; (f) 0˚; (g) 30˚; (h) 60˚; (i) 90˚; (j) 120˚; (k) 150˚; (l) 180˚

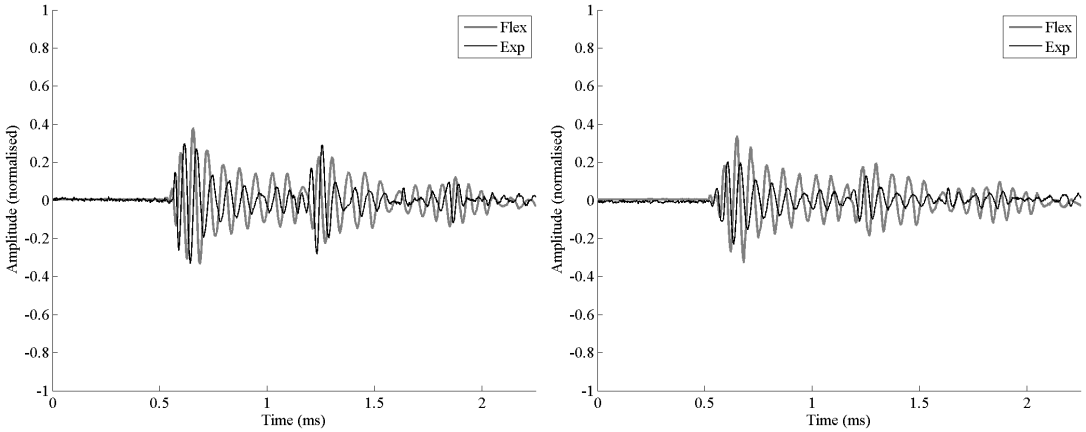
Flex
Exp
Amplitude (normalised)
Time (ms)

(a)

Flex
Exp
Amplitude (normalised)
Time (ms)

(b)

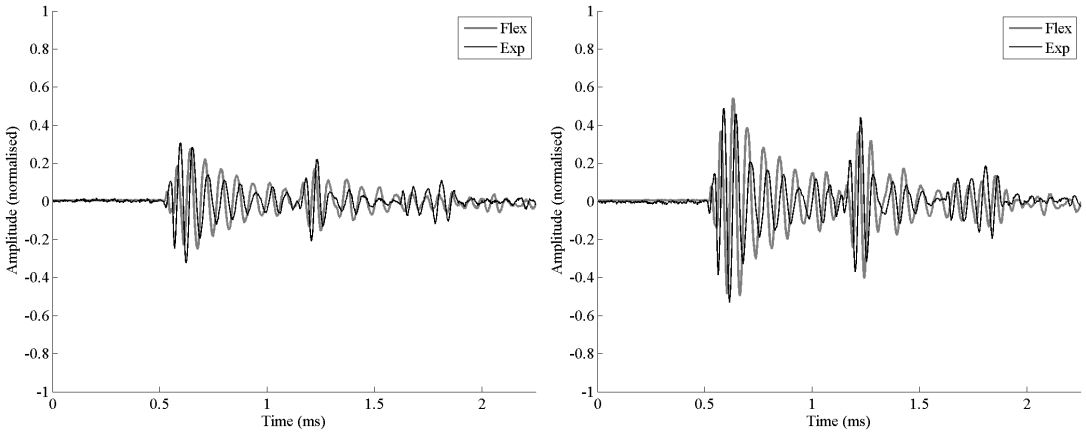
Flex
Exp
Amplitude (normalised)
Time (ms)

(c)

Flex
Exp
Amplitude (normalised)
Time (ms)

(d)

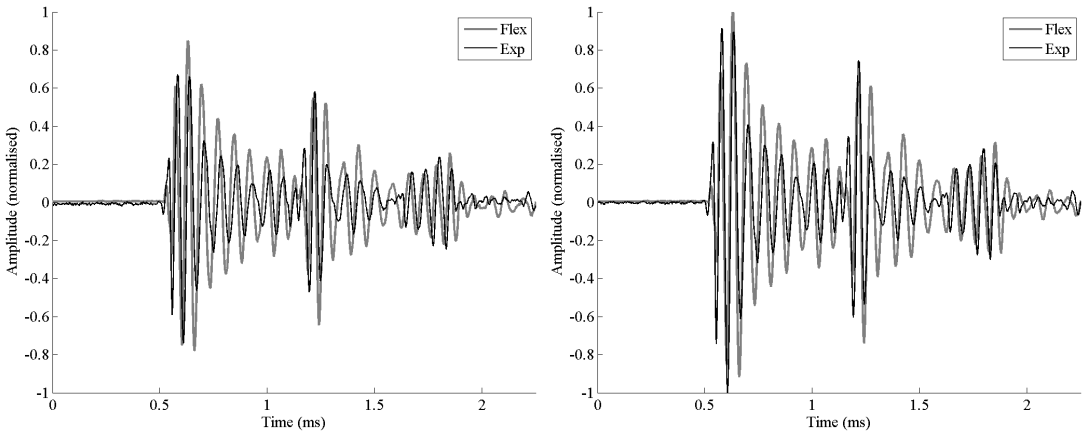
Flex
Exp
Amplitude (normalised)
Time (ms)

(e)

Flex
Exp
Amplitude (normalised)
Time (ms)

(f)

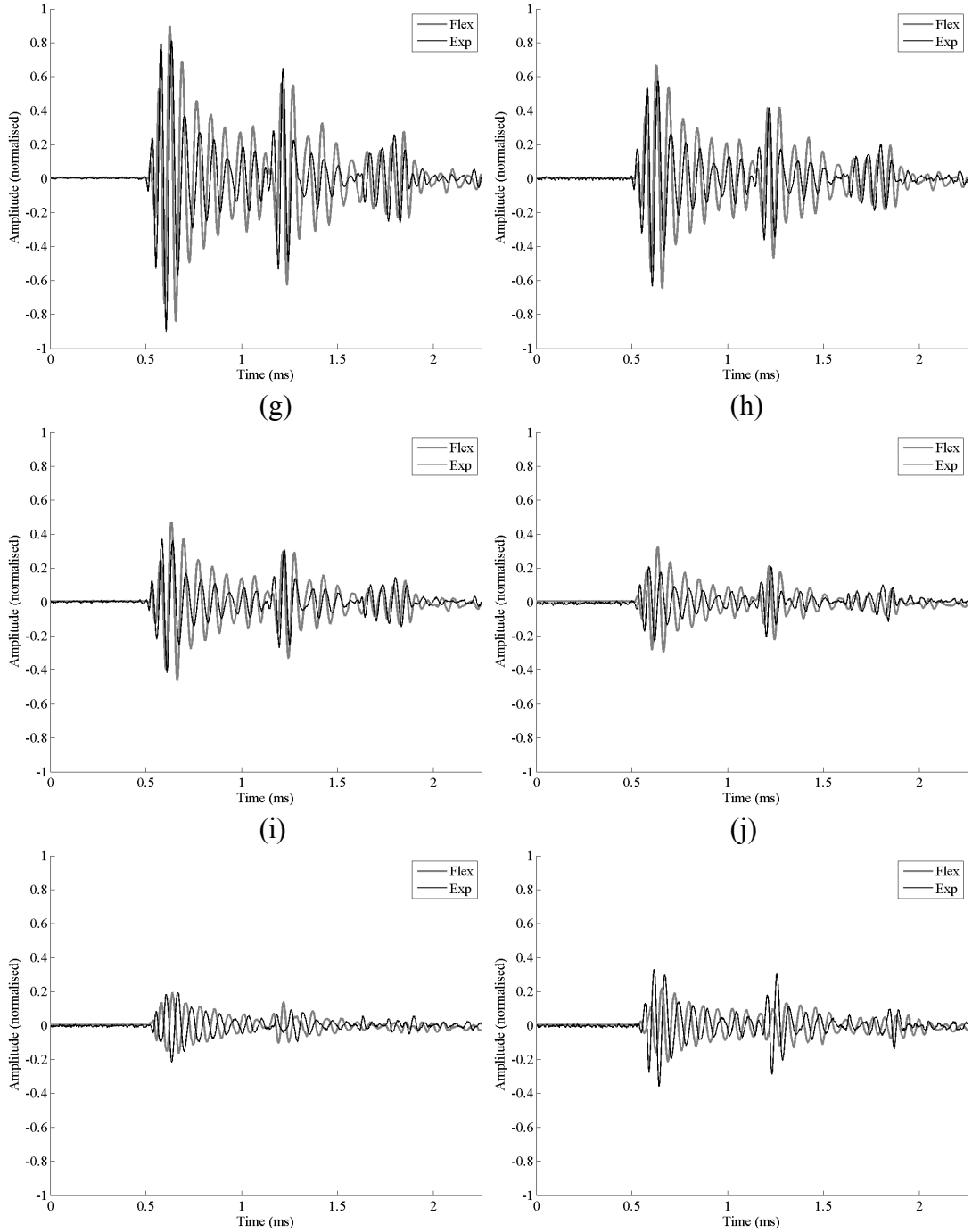

Figure B17. Comparison of simulated and experimental waveforms from a *R. aegyptiacus* call at a height of 20mm with respect to the base of the ear at: (a) -150˚; (b) -120˚; (c) -90˚; (d) -60˚; (e) -30˚; (f) 0˚; (g) 30˚; (h) 60˚; (i) 90˚; (j) 120˚; (k) 150˚; (l) 180˚

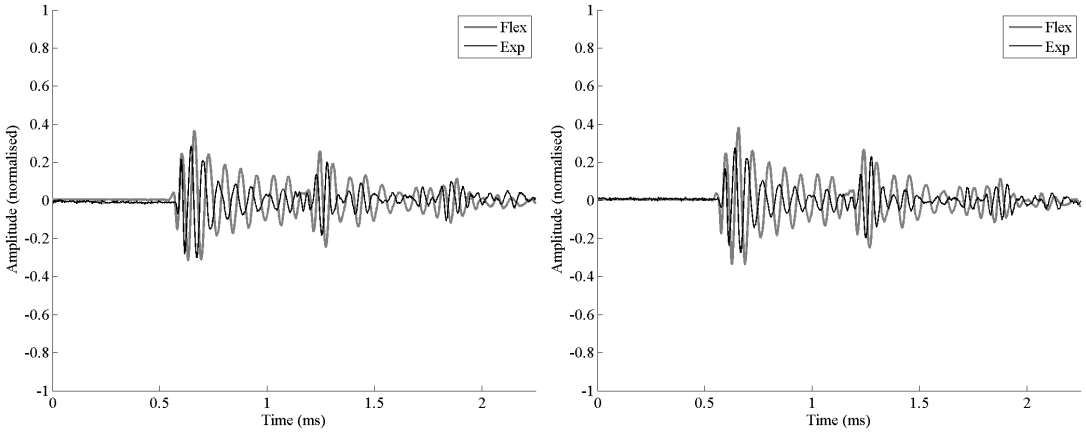
Flex
Exp
Amplitude (normalised)
Time (ms)

(a)

Flex
Exp
Amplitude (normalised)
Time (ms)

(b)

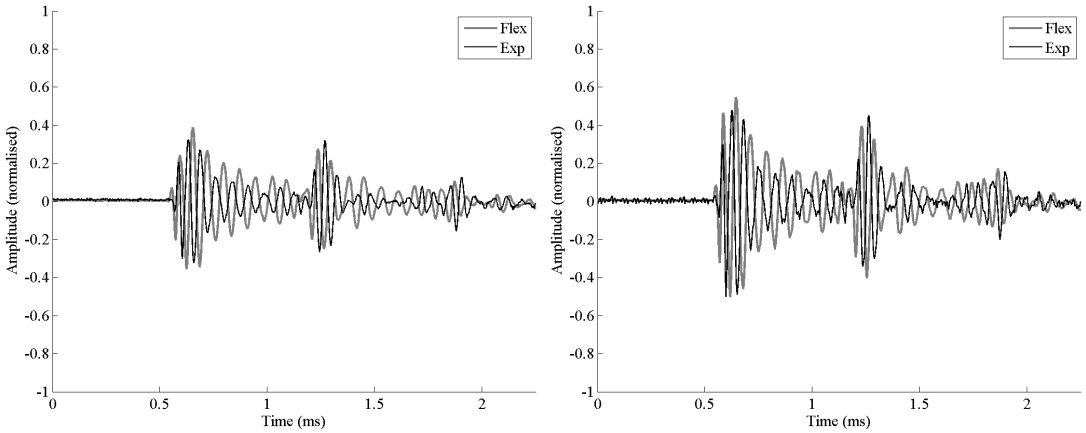
Flex
Exp
Amplitude (normalised)
Time (ms)

(c)

Flex
Exp
Amplitude (normalised)
Time (ms)

(d)

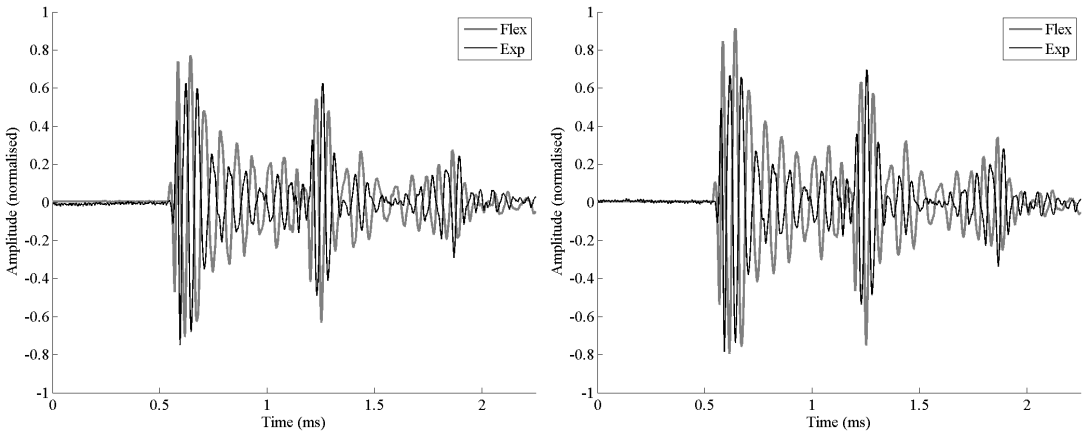
Flex
Exp
Amplitude (normalised)
Time (ms)

(e)

Flex
Exp
Amplitude (normalised)
Time (ms)

(f)

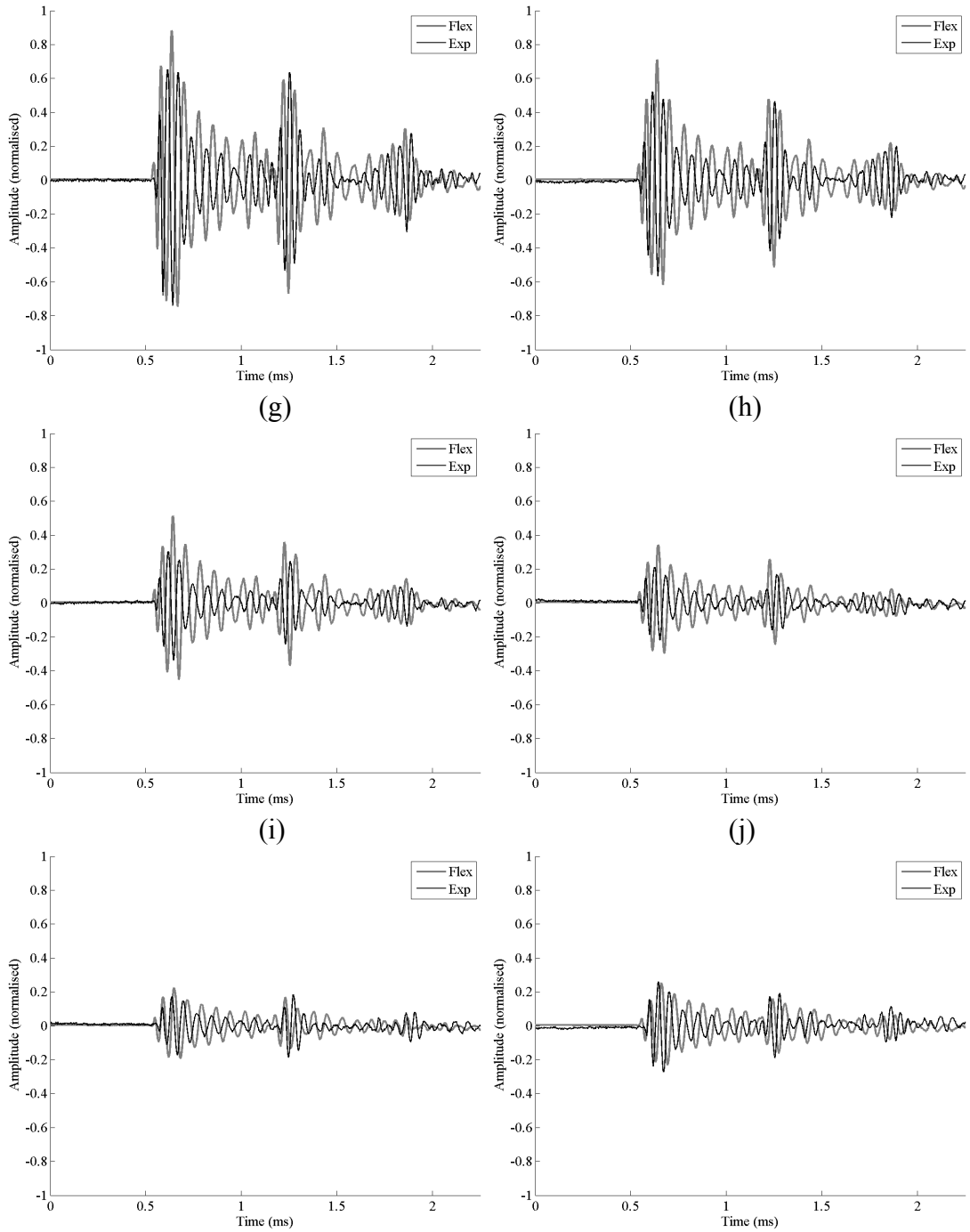

Figure B18. Comparison of simulated and experimental waveforms from a *R. aegyptiacus* call at a height of 50mm with respect to the base of the ear at: (a) -150˚; (b) -120˚; (c) -90˚; (d) -60˚; (e) -30˚; (f) 0˚; (g) 30˚; (h) 60˚; (i) 90˚; (j) 120˚; (k) 150˚; (l) 180˚